

Finite Element Modelling of Anchorage to Concrete
Systems at Different Strain Rates

by

Lenda T. Ahmed Al Saeab

A thesis submitted to the Faculty of Graduate and Postdoctoral
Affairs in partial fulfillment of the requirements for the degree of

Doctor of Philosophy

in

Civil Engineering

Carleton University
Ottawa, Ontario

© 2019

Lenda T. Ahmed Al Saeab

Abstract

Demand for flexibility in design and faster construction times has resulted in the increasing use of fasteners in a variety of concrete structures. These structures are exposed to static and dynamic loading conditions. Furthermore, these structures can be exposed to high strain rate loading such as encountered in impact and blast loads. Thus, anchorage systems used to fasten elements to concrete structures are also exposed to the high strain rates of loading which can be tensile and shear loads. If not adequately designed and constructed, anchorages can fail in a catastrophic manner and pose significant threat to building safety and the life of building occupants.

Behaviour of anchors embedded into concrete and subjected to static load has been widely investigated experimentally. However, despite the fact that many structures that contain anchorage systems are exposed to dynamic loads, the research in this vital area is limited. Currently, no guidance is available in design codes for the anchorage response under high strain rate loading. The American Concrete Institute and Concrete Capacity Design methods are recommended for anchorage system subjected to static and low cycle dynamic loading only. Hence, there is a need to develop a design method to predict the anchorage response and capacity under impact and blast loading.

The project presented in this thesis aims to investigate the tensile and shear behaviour of cast-in-place, adhesive and undercut anchors subjected to different strain rates using LS-DYNA software. Numerical models of the anchorage systems with different design parameters were developed and mesh sensitivity analyses were carried out to determine mesh sizes that best simulated the experimental results obtained from the literature. The

ultimate static capacity results were verified with the design methods. Effect of strain rate, embedment depth, and anchor diameter on the tensile and shear failure loads was investigated. Failure modes for the anchorage systems were also examined at different strain rates. Concrete cone breakout diameter and failure cone angles were investigated. A relation between the ultimate loads and the strain rates was investigated and dynamic increase factors (DIF) for design were determined. Regression analysis was performed to predict a relation that accurately represents the finite element results. Results of the tensile and shear loading of the anchorage to concrete systems show that anchorage to concrete system capacity increases with an increase in the strain rates. The failure mode of the anchorage systems is influenced by the strain rate. Maximum DIFs of 1.74, 1.13 and 1.58 were obtained for the cast-in-place, adhesive and undercut anchors under tensile load respectively where concrete cone breakout failure mode was observed. Maximum DIFs of 1.17, 1.13 and 1.44 respectively were obtained for the cast-in-place, adhesive and undercut anchors exhibited steel failure mode. The maximum DIFs were 1.15, 1.18 and 1.45 respectively for the anchors subjected to shear load where steel failure was observed.

Acknowledgements

I would like to express my sincere thanks and gratitude to my supervisor Professor Braimah for his continuous support, suggestions and valid advice throughout this research and during the preparation of this thesis. I greatly thank Prof. Braimah for his constructive and invaluable recommendations in all phases of the research.

I would like to thank Carleton University, Department of Civil and Environmental Engineering for giving me the support during my study to accomplish my research. Also, I would like to thank Mr. Kenneth Akhiwu for his kind assistance.

Finally, I would like to extend my sincere thanks to my parents, my husband, my brothers and sisters for their continuous encouragement and support.

Dedication

To my father and mother,

To my husband,

To the memory of my brother.

Table of contents

Abstract	ii
Acknowledgements	iv
Dedication	v
Table of contents	vi
List of Figures	xv
List of Tables.....	xxxix
Notations	xliv
Chapter 1 : Introduction	1
1.1 Background	1
1.2 Objectives and significance of research program	4
1.3 Methodology	6
1.4 Scope of the research.....	11
1.5 Structure of the thesis.....	12
Chapter 2 : Literature review	15
2.1 Introduction	15
2.2 Classification of anchors	18
2.3 Classification of adhesive materials	22
2.4 Bond strength	23
2.5 Cast-in-place anchors	29
2.5.1 Cast-in-place anchors under tensile load	29
2.5.2 Cast-in-place anchors under shear load	34

2.6 Adhesive anchors	39
2.6.1 Adhesive anchors under tensile load	39
2.6.2 Adhesive anchors under shear load	47
2.7 Undercut anchors.....	49
2.7.1 Undercut anchors under tensile load	49
2.7.2 Undercut anchors under shear load	51
2.8 Strain rate effect on material properties	52
2.8.1 Effect of strain rate on concrete.....	52
2.8.2 Effect of strain rate on steel.....	57
2.9 Design methods for anchorage system.....	60
2.9.1 American Concrete Institute (ACI)	60
2.9.2 Concrete Capacity Design (CCD)	61
2.10 Anchorage failure modes	62
2.10.1 Failure modes of cast-in-place anchors under tensile load.....	62
2.10.2 Failure modes of cast-in-place anchors under shear load.....	63
2.10.3 Failure modes of adhesive anchors under tensile load	64
2.10.3.1 Concrete cone breakout failure.....	65
2.10.3.2 Bond failure	65
2.10.3.3 Combined cone-bond failure	65
2.10.3.4 Steel anchor failure	66
2.10.4 Failure modes of adhesive anchors under shear load	66
2.10.5 Adhesive bond failure.....	66
2.10.6 Failure modes of undercut anchors under tensile load	67

2.10.7 Failure modes of undercut anchors under shear load	67
2.11 Summary	67
Chapter 3 : Finite element modelling of anchorage systems.....	70
3.1 Introduction	70
3.2 Implicit and explicit analysis.....	71
3.3 Theoretical aspects (hydrocode)	75
3.4 Finite element type	76
3.4.1 Solid element	77
3.5 Meshing technique	78
3.6 Material constitutive models	79
3.6.1 Concrete models	79
3.6.1.1 Concrete Model (MAT_CSCM_CONCRETE).....	81
3.6.2 Steel anchor models.....	86
3.6.3 Adhesive modelling.....	89
3.6.3.1 Adhesive model (MAT_ARUP_ADHESIVE).....	90
3.7 Design parameters	92
3.8 Materials properties.....	93
3.9 Contact modelling	94
3.10 Boundary conditions	96
3.10.1 Load conditions	97
3.11 Quasi-static simulation using LS-DYNA.....	99
3.12 Summary	100

Chapter 4 : Strain rate effect on cast-in-place anchors.....	101
4.1 Cast-in-place anchors under tensile load.....	101
4.1.1 Finite element modelling of cast-in-place anchors under tensile load	101
4.1.2 Validation of cast-in-place anchor model under tensile load	102
4.1.3 Comparison of finite element results with the ACI and CCD design methods	105
4.1.4 Effect of strain rate on the level of damage and failure mode of cast-in-place anchors.....	108
4.1.5 Effect of design parameters on failure mode and ultimate tensile load.....	118
4.1.6 Effect of anchor embedment depth on the concrete cone depth.....	121
4.1.7 Effect of strain rate on concrete cone breakout diameter	124
4.1.8 Effect of strain rate on the tensile behaviour of cast-in-place anchors.....	125
4.1.9 Effect of strain rate on the ultimate tensile load and dynamic increase factor of cast-in-place anchors	133
4.1.10 Regression Analysis for cast-in-place anchors under tensile load	141
4.2 Cast-in-place anchors under shear load.....	151
4.2.1 Finite element modelling for cast-in-place anchors under shear load	151
4.2.2 Validation of cast-in-place anchor model under shear load	151
4.2.3 Comparison of finite element results with design method	153
4.2.4 Crack pattern for cast-in-place anchors under shear load.....	156
4.2.5 Effect of strain rate on the level of damage and failure mode.....	158
4.2.6 Effect of design parameters on failure mode and ultimate shear load.....	164
4.2.7 Effect of strain rate on the shear behaviour of cast-in-place anchors.....	166

4.2.8 Effect of strain rate on the ultimate shear load and DIF of cast-in-place anchors	172
4.2.9 Regression analysis for cast-in-place anchors under shear load.....	177
4.2.10 Case study: effect of concrete compressive strength on the shear behaviour of cast-in-place anchors	182
4.2.10.1 Level of damage and failure mode	182
4.2.10.2 Effect of strain rate and concrete compressive strength on shear behaviour	185
4.3 Summary	191
Chapter 5 : Strain rate effect on adhesive anchors.....	193
5.1 Finite element modelling for adhesive anchors under tensile load	193
5.1.1 Validation of adhesive anchor model under tensile load.....	194
5.1.2 Comparison of finite element results with ACI and CCD design methods....	199
5.1.3 Effect of strain rate on the level of damage and failure mode of adhesive anchors	200
5.1.4 Effect of design parameters on failure mode and ultimate tensile load.....	209
5.1.5 Effect of anchor embedment depth on concrete cone depth.....	212
5.1.6 Concrete cone breakout diameter for adhesive anchors	215
5.1.7 Effect of strain rate on the tensile behaviour of adhesive anchors	216
5.1.8 Effect of strain rate on the ultimate tensile load and DIF of adhesive anchors	225
5.1.9 Regression Analysis for adhesive anchors under tensile load	232
5.2 Adhesive anchors under shear load.....	242

5.2.1 Finite element modelling for adhesive anchors under shear load	242
5.2.2 Validation of adhesive anchor model under shear load.....	242
5.2.3 Comparison of finite element results with design methods.....	245
5.2.4 Crack pattern for adhesive anchors under shear load	246
5.2.5 Effect of strain rate on the level of damage and failure mode.....	248
5.2.6 Effect of design parameters on failure mode and ultimate shear load.....	252
5.2.7 Effect of strain rate on the shear behaviour of adhesive anchors	256
5.2.8 Effect of strain rate on the ultimate shear load and DIF of adhesive anchors	262
5.2.9 Regression analysis for adhesive anchor under shear load.....	268
5.3 Summary	272
Chapter 6 : Strain rate effect on the undercut anchors	274
6.1 Finite element modelling for undercut anchors under tensile load	274
6.1.1 Validation of undercut anchor model under tensile load.....	275
6.1.2 Comparison of FEA results with the ACI and CCD design methods	278
6.1.3 Effect of strain rate on the level of damage and failure mode.....	279
6.1.4 Effect of design parameters on failure mode and ultimate tensile load.....	283
6.1.5 Effect of anchor embedment depth on the ultimate tensile load	286
6.1.6 Effect of strain rate on concrete cone breakout diameter and cone propagation angle.....	288
6.1.7 Effect of strain rate on the tensile behaviour of the undercut anchors	290
6.1.8 Effect of strain rate on the ultimate tensile load and DIF of undercut anchors	298
6.1.9 Regression analysis for the undercut anchors under tensile load	303

6.2 Finite element modeling for undercut anchors under shear load	309
6.2.1 Validation of undercut anchor model under shear load.....	309
6.2.2 Comparison of finite element results with design methods.....	311
6.2.3 Crack pattern for the undercut anchors under shear load	313
6.2.4 Effect of strain rate on the level of damage and failure mode.....	314
6.2.5 Effect of design parameters on failure mode and ultimate shear load.....	321
6.2.6 Effect of strain rate on the shear behaviour of undercut anchors	323
6.2.7 Effect of strain rate on the ultimate shear load and DIF of undercut anchors	329
6.2.8 Regression analysis for undercut anchors under shear load	334
6.3 Summary	338
Chapter 7 :Conclusions and recommendations for future research	340
7.1 Introduction	340
7.2 General conclusions	341
7.3 Behaviour of cast-in-place anchorage system under different strain rates.....	342
7.4 Behaviour of adhesive anchorage system under different strain rates	344
7.5 Behaviour of undercut anchorage system under different strain rates	345
7.6 Research limitations	346
7.7 Future resreach	347
7.8 Contributions.....	348
7.8.1 Journal papers	348
7.8.2 Conference papers	348
References	349

Appendix A: Design methods for cast-in-place anchors	370
A.1 Design methods for cast-in-place anchors under tensile load	370
A.1.1 American Concrete Institute (ACI)	370
A.1.2 Concrete Capacity Design (CCD)	375
A.2 Design methods for cast-in-place anchors under shear load	378
A.2.1 American concrete institute (ACI).....	378
A.2.2 Concrete Capacity Design (CCD)	383
Appendix B: Design methods for adhesive anchors	385
B.1 Design methods for adhesive anchors under tensile load.....	385
B.1.1 Concrete cone breakout failure	385
B.1.2 Anchor steel failure.....	386
B.1.3 Bond failure	386
B.1.4 Combined cone-bond failure.....	388
B.2 Design methods for adhesive anchors under shear load.....	390
Appendix C: Tensile load-displacement relation for cast-in place anchors	393
Appendix D: Shear load-displacement relation for cast-in-place anchors	399
Appendix E: Tensile load-displacement relation for adhesive anchors.....	405
Appendix F: Shear load-displacement relation for adhesive anchors	411
Appendix G: Tensile load-displacement relation for undercut anchors.....	417
Appendix H: Shear load-displacement relation for undercut anchors.....	423
Appendix I: LS-DYNA keyword files for anchorage to concrete systems.....	429

Cast-in-place anchor under tensile load	429
Cast-in-place anchor under shear load	432
Adhesive anchor under tensile load	440
Adhesive anchor under shear load	445
Undercut anchor under tensile load.....	453
Undercut anchor under shear load.....	457

List of Figures

Figure 1-1: Anchorage systems	9
Figure 1-2: Flow chart for the methodology of the project	10
Figure 2-1: Applications of anchorage system in rock burst (Cai et al., 2010)	16
Figure 2-2: Applications of anchorage system in window; (a) glass window under blast load (Madico Safety Shield Premier Partener, 2012), (b) anchorage to base-plate (Johnson window films, 2018)	17
Figure 2-3: Types of anchors: (a) cast-in-place anchors, (b) post installed anchors (ACI Committee 318, 2011)	19
Figure 2-4: Undercut anchor types	21
Figure 2-5: Failure modes under tensile loading: (a) steel anchor failure, (b) concrete cone breakout, (c) side face blowout, (d) concrete splitting (Cement Association of Canada 2010; ACI Committee 318, 2011)	63
Figure 2-6: Failure modes for anchors under shear load (a) steel anchor failure preceded by concrete spall; (b) concrete pryout failure; (c) concrete breakout failure; (d) thin concrete breakout; (e) edge breakout, corner breakout (f) narrow concrete edge breakout (Cement Association of Canada 2010; ACI Committee 318, 2011)	64
Figure 2-7: Failure modes for adhesive anchors, (a) concrete cone breakout failure; (b) combined cone-bond failure (bond failure at adhesive/concrete interface; (c) combined cone-bond failure (bond failure at steel/adhesive interface); (d) combined cone-bond failure (bond failure at combination of adhesive/concrete and steel/adhesive interface); (e) steel anchor failure (Cook et al., 1998).....	64

Figure 3-1: Eight node hexahedron solid element (Livermore Software Technology Corporation, 2015).....	77
Figure 3-2: Four node tetrahedron solid element (Livermore Software Technology Corporation, 2015).....	78
Figure 3-3: General shape of the concrete model yield surface (Murray, 2007).....	82
Figure 3-4: Yield surface (LSTC, 2014).....	91
Figure 3-5: Stress-displacement relation of MAT_169 for (a) tension and (b) shear (LSTC, 2014).....	91
Figure 3-6: Boundary conditions for the anchorage models under (a) tensile load and (b) shear load	97
Figure 4-1: Schematic view of the cast-in-place anchor.....	101
Figure 4-2: Geometric configuration with boundary condition of cast-in-place anchor model.....	102
Figure 4-3: Comparison of experimental and numerical tensile load-displacement behaviour of 8-mm diameter cast-in-place anchor with 50 mm embedment depth	104
Figure 4-4: Comparison of experimental and numerical tensile load-displacement behaviour of 24-mm diameter cast-in-place anchor with 150 mm embedment depth ...	104
Figure 4-5: Plastic strain contours for cast-in-place anchor at strain rate of 10^{-5} s^{-1}	110
Figure 4-6: Effect of anchor embedment depth on the concrete cone diameter	111
Figure 4-7: Cone breakout and crack propagation angles on the cast-in-place anchorage to concrete system.....	112
Figure 4-8: Failure mode of 12.7 mm diameter cast-in-place anchor at different strain rates	114

Figure 4-9: Failure mode of 15.9 mm diameter cast-in-place anchor at different strain rates	115
Figure 4-10: Failure mode of 19.1 mm diameter cast-in-place anchor at different strain rates	116
Figure 4-11: Strain rate effect on the failure mode and ultimate tensile load for cast-in-place anchor diameter of 12.7 mm.....	119
Figure 4-12: Strain rate effect on the failure mode and ultimate tensile load for cast-in-place anchor diameter of 15.9 mm.....	120
Figure 4-13: Strain rate effect on the failure mode and ultimate tensile load for cast-in-place anchor diameter of 19.1 mm.....	121
Figure 4-14: Effect of anchor embedment depth on the concrete cone depth and ultimate tensile load for 12.7 mm diameter cast-in-place anchor	122
Figure 4-15: Effect of anchor embedment depth on the concrete cone depth and ultimate tensile load for 15.9 mm diameter cast-in-place anchor	123
Figure 4-16: Effect of anchor embedment depth on the concrete cone depth and ultimate tensile load for 19.1 mm diameter cast-in-place anchor	123
Figure 4-17: Displacement contours of 15.9 mm diameter cast-in-place anchor at strain rates ranging from 10^{-5} s^{-1} to 10^3 s^{-1}	124
Figure 4-18: Tensile load-displacement graph for 12.7 mm diameter cast-in-place anchor at strain rate of 10^{-5} s^{-1}	125
Figure 4-19: Tensile load-displacement graph for 12.7 mm diameter cast-in-place anchor at strain rate of 10^{-3} s^{-1}	126

Figure 4-20: Tensile load-displacement graph for 12.7 mm diameter cast-in-place anchor at strain rate of 10^{-1} s^{-1}	126
Figure 4-21: Tensile load-displacement graph for 12.7 mm diameter cast-in-place anchor at strain rate of 10 s^{-1}	127
Figure 4-22: Tensile load-displacement graph for 12.7 mm diameter cast-in-place anchor at strain rate of 10^2 s^{-1}	127
Figure 4-23: Tensile load-displacement graph for 12.7 mm diameter cast-in-place anchor at strain rate of 10^3 s^{-1}	128
Figure 4-24: Ultimate tensile load and DIF versus strain rate for the cast-in-place anchor of 76.2 mm embedment depth	136
Figure 4-25: Ultimate tensile load and DIF versus strain rate for the cast-in-place anchor of 101.6 mm embedment depth	136
Figure 4-26: Ultimate tensile load and DIF versus strain rate for the cast-in-place anchor of 127 mm embedment depth	137
Figure 4-27: Ultimate tensile load and DIF versus strain rate for the cast-in-place anchor of 152.4 mm embedment depth	138
Figure 4-28: Effect of strain rate ratio on the DIF for cast-in-place anchor exhibiting concrete cone breakout failure	142
Figure 4-29: Effect of strain rate ratio on the DIF for cast-in-place anchor exhibiting steel failure	142
Figure 4-30: Residual versus strain rate ratio for the cast-in-place anchors exhibited concrete cone breakout failure	145

Figure 4-31: Residual versus strain rate ratio for the cast-in-place anchors exhibited steel failure	146
Figure 4-32: DIF obtained from the finite element analysis versus the predicted DIF for the cast-in-place anchor exhibited concrete cone breakout failure.....	147
Figure 4-33: DIF obtained from the finite element analysis versus the predicted DIF for the cast-in-place anchor exhibited steel failure.....	148
Figure 4-34: Geometric configuration of cast-in-place anchor model under shear load	151
Figure 4-35: Applied shear load in the direction parallel to the edge distance c_1 and perpendicular to the edge distance c_2	152
Figure 4-36: Plastic strain contours for cast-in-place anchor under shear load at strain rate of 10^{-5} s^{-1}	157
Figure 4-37: Pryout failure mechanism of the cast-in-place anchor.....	158
Figure 4-38: Failure mode for 12.7 mm diameter cast-in-place anchor at different strain rates.....	160
Figure 4-39: Failure mode for 15.9 mm diameter cast-in-place anchor at different strain rates.....	160
Figure 4-40: Failure mode for 19.1 mm diameter cast-in-place anchor at different strain rates.....	161
Figure 4-41: Steel failure process of 19.1 mm diameter cast-in-place anchor with 101.6 mm embedment depth; (a) stress concentration around the anchor, (b) anchor bending, (c) initiation of anchor fracture and (d) complete anchor fracture	163
Figure 4-42: Effect of strain rate on the failure mode and ultimate shear load for the cast-in-place anchor diameter of 12.7 mm	165

Figure 4-43: Effect of strain rate on the failure mode and ultimate shear load for the cast-in-place anchor diameter of 15.9 mm	165
Figure 4-44: Effect of strain rate on the failure mode and ultimate shear load for the cast-in-place anchor diameter of 19.1 mm	166
Figure 4-45: Shear load-displacement graph for 12.7 mm diameter cast-in-place anchor at strain rate of 10^{-5} s^{-1}	167
Figure 4-46: Shear load-displacement graph for 12.7 mm diameter cast-in-place anchor at strain rate of 10^{-3} s^{-1}	167
Figure 4-47: Shear load-displacement graph for 12.7 mm diameter cast-in-place anchor at strain rate of 10^{-1} s^{-1}	168
Figure 4-48: Shear load-displacement graph for 12.7 mm diameter cast-in-place anchor at strain rate of 10 s^{-1}	168
Figure 4-49: Shear load-displacement graph for 12.7 mm diameter cast-in-place anchor at strain rate of 10^2 s^{-1}	169
Figure 4-50: Shear load-displacement graph for 12.7 mm diameter cast-in-place anchor at strain rate of 10^3 s^{-1}	169
Figure 4-51: Ultimate shear load and DIF versus strain rate for cast-in-place anchor with 76.2 mm embedment depth.....	174
Figure 4-52: Ultimate shear load and DIF versus strain rate for cast-in-place anchor with 101.6 mm embedment depth.....	174
Figure 4-53: Ultimate shear load and DIF versus strain rate for cast-in-place anchor with 152.4 mm embedment depth.....	175

Figure 4-54: Effect of strain rate ratio on the DIF for cast-in-place anchors exhibit steel failure under shear load.....	178
Figure 4-55: Residual versus strain rate ratio for the cast-in-place anchor subjected to shear load and exhibited steel failure	180
Figure 4-56: DIF obtained from the finite element analysis versus the predicted DIF for the cast-in-place anchor exhibited steel failure under shear load	181
Figure 4-57: Effect of strain rate and concrete compressive strength on the failure mode for the 12.7 mm diameter cast-in-place anchors.....	183
Figure 4-58: Effect of strain rate and concrete compressive strength on the failure mode for the 19.1 mm diameter cast-in-place anchors.....	184
Figure 4-59: Shear load-displacement response of 12.7 mm cast-in-place anchor diameter with 76.2 mm embedment depth at strain rate of 10^{-5} s^{-1}	186
Figure 4-60: Shear load-displacement response of 12.7 mm cast-in-place anchor diameter with 152.4 mm embedment depth at strain rate of 10^{-5} s^{-1}	187
Figure 4-61: Shear load-displacement response of 19.1 mm cast-in-place anchor diameter with 76.2 mm embedment depth at strain rate of 10^{-5} s^{-1}	187
Figure 4-62: Shear load-displacement response of 19.1 mm cast-in-place anchor diameter with 152.4 mm embedment depth at strain rate of 10^{-5} s^{-1}	188
Figure 4-63: Shear load-displacement response of 12.7 mm cast-in-place anchor diameter with 76.2 mm embedment depth at strain rate of 10^3 s^{-1}	189
Figure 4-64: Shear load-displacement response of 12.7 mm cast-in-place anchor diameter with 152.4 mm embedment depth at strain rate of 10^3 s^{-1}	189

Figure 4-65: Shear load-displacement response of 19.1 mm diameter cast-in-place anchor with 76.2 mm embedment depth at strain rate of 10^3 s^{-1}	190
Figure 4-66: Shear load-displacement response of 19.1 mm cast-in-place anchor diameter with 152.4 mm embedment depth at strain rate of 10^3 s^{-1}	190
Figure 5-1: A schematic view of the adhesive anchorage to concrete system.....	193
Figure 5-2: Geometric configuration with boundary condition for the adhesive anchor model.....	194
Figure 5-3: Comparison of tensile load-displacement response between FEA and experimental results obtained by Braimah et al. (Braimah et al., 2004) for anchor diameter of 6.4 mm.....	197
Figure 5-4: Failure mode obtained from the finite element analysis and the experimental results obtained by Braimah et al. (Braimah et al., 2004).....	197
Figure 5-5: Comparison of tensile load-displacement response between FEA and experimental results obtained by Braimah et al. (Braimah et al., 2004) for anchor diameter of 9.5 mm.....	198
Figure 5-6: Plastic strain contours for adhesive anchor with different anchor diameters and embedment depths at strain rate of 10^{-5} s^{-1}	202
Figure 5-7: Cone breakout angle on the adhesive anchorage to concrete system.	203
Figure 5-8: Failure mode of 12.7-mm diameter adhesive anchor at different strain rates	206
Figure 5-9: Failure mode of 15.9-mm diameter adhesive anchor at different strain rates	207

Figure 5-10: Failure mode of 19.1-mm diameter adhesive anchor at different strain rates	208
Figure 5-11: Strain rate effect on the failure mode and ultimate tensile load for adhesive anchor diameter of 12.7 mm	209
Figure 5-12: Strain rate effect on the failure mode and ultimate tensile load for adhesive anchor diameter of 15.9 mm	210
Figure 5-13: Strain rate effect on the failure mode and ultimate tensile load for adhesive anchor diameter of 19.1 mm	211
Figure 5-14: Effect of anchor embedment depth on the concrete cone depth and ultimate tensile load for 12.7 mm diameter adhesive anchor	214
Figure 5-15: Effect of anchor embedment depth on the concrete cone depth and ultimate tensile load for 15.9 mm diameter adhesive anchor	214
Figure 5-16: Effect of anchor embedment depth on the concrete cone depth and ultimate tensile load for 19.1 mm diameter adhesive anchor	215
Figure 5-17: Displacement contours for adhesive anchors at strain rate of 10^{-5} with diameters of: (a) 12.7 mm, (b) 15.9 mm and (c) 19.1 mm.....	216
Figure 5-18: Tensile load-displacement graph for 12.7 mm diameter adhesive anchor at strain rate of 10^{-5} s^{-1}	217
Figure 5-19: Tensile load-displacement graph for 12.7 mm diameter adhesive anchor at strain rate of 10^{-3} s^{-1}	217
Figure 5-20: Tensile load-displacement graph for 12.7 mm diameter adhesive anchor at strain rate of 10^{-1} s^{-1}	218

Figure 5-21: Tensile load-displacement graph for 12.7 mm diameter adhesive anchor at strain rate of 10 s^{-1}	218
Figure 5-22: Tensile load-displacement graph for 12.7 mm diameter adhesive anchor at strain rate of 10^2 s^{-1}	219
Figure 5-23: Tensile load-displacement graph for 12.7 mm diameter adhesive anchor at strain rate of 10^3 s^{-1}	219
Figure 5-24: Ultimate tensile load and DIF versus strain rate for the adhesive anchor at 76.2 mm embedment depth.....	228
Figure 5-25: Ultimate tensile load and DIF versus strain rate for the adhesive anchor at 101.6 mm embedment depth.....	229
Figure 5-26: Ultimate tensile load and DIF versus strain rate for the adhesive anchor at 127 mm embedment depth.....	229
Figure 5-27: Ultimate tensile load and DIF versus strain rate for the adhesive anchor at 152.4 mm embedment depth.....	230
Figure 5-28: Effect of strain rate ratio on DIF for adhesive anchor exhibited combined cone bond failure under tensile load.....	232
Figure 5-29: Effect of strain rate ratio on DIF for adhesive anchor exhibited steel failure under tensile load	233
Figure 5-30: Residual versus strain rate ratio for the adhesive anchor exhibited combined cone bond failure.....	235
Figure 5-31: Residual versus strain rate ratio for the adhesive anchor exhibited steel failure	236

Figure 5-32: DIF obtained from the finite element analysis versus the predicted DIF for the adhesive anchors exhibited combined cone bond failure	237
Figure 5-33: DIF obtained from the finite element analysis versus the predicted DIF for the adhesive anchors exhibited steel failure	237
Figure 5-34: Geometric configuration and boundary conditions of adhesive anchor model	242
Figure 5-35: Comparison of shear load-displacement relation between FEA and experimental results obtained by Cattaneo et al. (Cattaneo & Muciaccia, 2015).....	244
Figure 5-36: Failure mode obtained from:(a) finite element analysis and (b) experimental results obtained by Cattaneo et al. (Cattaneo & Muciaccia, 2015).....	244
Figure 5-37: Plastic strain contours for adhesive anchor under shear load at strain rate of 10^{-5} s^{-1}	247
Figure 5-38: Failure mode for 12.7 mm diameter adhesive anchor at different strain rates	249
Figure 5-39: Failure mode for 15.9 mm diameter adhesive anchor at different strain rates	249
Figure 5-40: Failure mode for 19.1 mm diameter adhesive anchor at different strain rates	250
Figure 5-41: Failure mechanism of 19.1 mm diameter adhesive anchor with 152.4 mm embedment depth; (a) stress concentration around the anchor, (b) anchor bending with bond failure, (c) initiation of anchor fracture, (d) complete anchor failure	251
Figure 5-42: Effect of strain rate on the failure mode and ultimate shear load for the adhesive anchor diameter of 12.7 mm	254

Figure 5-43: Effect of strain rate on the failure mode and ultimate shear load for the adhesive anchor diameter of 15.9 mm	255
Figure 5-44: Effect of strain rate on the failure mode and ultimate shear load for the adhesive anchor diameter of 19.1 mm	255
Figure 5-45: Shear load-displacement graph for 12.7-mm diameter adhesive anchor at strain rate of 10^{-5} s^{-1}	256
Figure 5-46: Shear load-displacement graph for 12.7-mm diameter adhesive anchor at strain rate of 10^{-3} s^{-1}	257
Figure 5-47: Shear load-displacement graph for 12.7-mm diameter adhesive anchor at strain rate of 10^{-1} s^{-1}	257
Figure 5-48: Shear load-displacement graph for 12.7-mm diameter adhesive anchor at strain rate of 10 s^{-1}	258
Figure 5-49: Shear load-displacement graph for 12.7-mm diameter adhesive anchor at strain rate of 10^2 s^{-1}	258
Figure 5-50: Shear load-displacement graph for 12.7-mm diameter adhesive anchor at strain rate of 10^3 s^{-1}	259
Figure 5-51: Ultimate shear load and DIF versus strain rate for adhesive anchors at 76.2 mm embedment depth.....	265
Figure 5-52: Ultimate shear load and DIF versus strain rate for adhesive anchors at 101.6 mm embedment depth.....	266
Figure 5-53: Ultimate shear load and DIF versus strain rate for adhesive anchors at 152.4 mm embedment depth.....	266

Figure 5-54: Effect of strain rate ratio on the DIF for adhesive anchor exhibiting steel failure under shear load.....	269
Figure 5-55: Residual versus strain rate ratio for the adhesive anchor subjected to shear load and exhibited steel failure	271
Figure 5-56: DIF obtained from the finite element analysis versus the predicted DIF for the adhesive anchor exhibited steel failure under shear load.....	272
Figure 6-1: A schematic view for the undercut anchor model.....	274
Figure 6-2: Geometric configuration and boundary conditions for the undercut anchor model.....	275
Figure 6-3: Tensile load-displacement response of the FEA and experimental results obtained by Mahadik et al. (Mahadik et al., 2016)	277
Figure 6-4: Failure mode of the undercut anchors under tensile load observed from the finite element analysis and the experimental results by (Mahadik et al., 2016).....	277
Figure 6-5: Plastic strain contours for the undercut anchors at strain rate of 10^{-5} s^{-1}	280
Figure 6-6: Failure mode of 12 mm diameter undercut anchor at different strain rates. .	281
Figure 6-7: Failure mode of 16 mm diameter undercut anchor at different strain rates. .	281
Figure 6-8: Failure mode of 20 mm diameter undercut anchor at different strain rates. .	282
Figure 6-9: Strain rate effect on the failure mode and ultimate tensile load for undercut anchor diameter of 12 mm	283
Figure 6-10: Strain rate effect on the failure mode and ultimate tensile load for undercut anchor diameter of 16 mm	284
Figure 6-11: Strain rate effect on the failure mode and ultimate tensile load for undercut anchor diameter of 20 mm	284

Figure 6-12: Effect of anchor embedment depth on the concrete cone depth and ultimate tensile load for 12 mm diameter undercut anchor	287
Figure 6-13: Effect of anchor embedment depth on the concrete cone depth and ultimate tensile load for 16 mm diameter undercut anchor	287
Figure 6-14: Effect of anchor embedment depth on the concrete cone depth and ultimate tensile load for 20 mm diameter undercut anchor	288
Figure 6-15: Displacement contours for 20 mm undercut anchor diameter at strain rates ranging from 10^{-5} s^{-1} to 10^3 s^{-1}	289
Figure 6-16: Tensile load-displacement graph for the 12-mm diameter undercut anchor at strain rate of 10^{-5} s^{-1}	291
Figure 6-17: Tensile load-displacement graph for the 12-mm diameter undercut anchor at strain rate of 10^{-3} s^{-1}	291
Figure 6-18: Tensile load-displacement graph for the 12-mm diameter undercut anchor at strain rate of 10^{-1} s^{-1}	292
Figure 6-19: Tensile load-displacement graph for the 12-mm diameter undercut anchor at strain rate of 10 s^{-1}	292
Figure 6-20: Tensile load-displacement graph for the 12-mm diameter undercut anchor at strain rate of 10^2 s^{-1}	293
Figure 6-21: Tensile load-displacement graph for the 12-mm diameter undercut anchor at strain rate of 10^3 s^{-1}	293
Figure 6-22: Tensile load-displacement response of 100 mm embedment depth undercut anchors at strain rate of 10^{-5} s^{-1}	295

Figure 6-23: Tensile load-displacement response of 190 mm embedment depth undercut anchors at strain rate of 10^{-5} s^{-1}	295
Figure 6-24: Ultimate tensile load and DIF versus strain rate for the undercut anchor at 100 mm embedment depth.....	300
Figure 6-25: Ultimate tensile load and DIF versus strain rate for the undercut anchor at 125 mm embedment depth.....	301
Figure 6-26: Ultimate tensile load and DIF versus strain rate for the undercut anchor at 190 mm embedment depth.....	301
Figure 6-27: Ultimate tensile load and DIF versus strain rate for the undercut anchor at 250 mm embedment depth.....	302
Figure 6-28: Effect of strain rate ratio on the DIF for the undercut anchors exhibited steel failure under tensile load.....	304
Figure 6-29: Residual versus strain rate ratio for the undercut anchors exhibited steel failure	306
Figure 6-30: DIF obtained from the finite element analysis versus the predicted DIF for the undercut anchors exhibited steel failure	307
Figure 6-31: Geometric configuration and boundary conditions for the undercut anchor model.....	309
Figure 6-32: Comparison of shear load-displacement relation between FEA and experimental results obtained by Mahadik et al. (Mahadik et al., 2016).....	311
Figure 6-33: Failure mode obtained from:(a) finite element analysis and (b) experimental results obtained by Mahadik et al. (Mahadik et al., 2016).....	311

Figure 6-34: Plastic strain contours for undercut anchors under shear load at strain rate of 10^{-5} s^{-1}	314
Figure 6-35: Failure mode of 12-mm diameter undercut anchor at different strain rates	316
Figure 6-36: Failure mode of 16-mm diameter undercut anchor at different strain rates	317
Figure 6-37: Failure mode of 20-mm diameter undercut anchor at different strain rates	318
Figure 6-38: Failure process of 12-mm diameter undercut anchor with 190 mm embedment depth; (a) stress concentration around the undercut anchor, (b) anchor bending, (c) crack initiation and (d) anchor fracture	320
Figure 6-39: Effect of strain rate on the failure mode and ultimate shear load for the undercut anchor diameter of 12 mm	321
Figure 6-40: Effect of strain rate on the failure mode and ultimate shear load for the undercut anchor diameter of 16 mm	322
Figure 6-41: Effect of strain rate on the failure mode and ultimate shear load for the undercut anchor diameter of 20 mm	322
Figure 6-42: Shear load-displacement graph for 12-mm diameter undercut anchor at strain rate of 10^{-5} s^{-1}	324
Figure 6-43: Shear load-displacement graph for 12-mm diameter undercut anchor at strain rate of 10^{-3} s^{-1}	324
Figure 6-44: Shear load-displacement graph for 12-mm diameter undercut anchor at strain rate of 10^{-1} s^{-1}	325
Figure 6-45: Shear load-displacement graph for 12-mm diameter undercut anchor at strain rate of 10 s^{-1}	325

Figure 6-46: Shear load-displacement graph for 12-mm diameter undercut anchor at strain rate of 10^2 s^{-1}	326
Figure 6-47: Shear load-displacement graph for 12-mm diameter undercut anchor at strain rate of 10^3 s^{-1}	326
Figure 6-48: Ultimate shear load and DIF versus strain rate for undercut anchors at 100 mm embedment depth.....	331
Figure 6-49: Ultimate shear load and DIF versus strain rate for undercut anchors at 125 mm embedment depth.....	331
Figure 6-50: Ultimate shear load and DIF versus strain rate for undercut anchors at 190 mm embedment depth.....	332
Figure 6-51: Ultimate shear load and DIF versus strain rate for undercut anchors at 250 mm embedment depth.....	332
Figure 6-52: Effect of strain rate ratio on the DIF for undercut anchors exhibited steel failure under shear load.....	335
Figure 6-53: Residual versus strain rate ratio for the undercut anchors under shear load exhibited steel failure	337
Figure 6-54: DIF obtained from the finite element analysis versus the predicted DIF for the undercut anchors exhibited steel failure under shear load	338
Figure A-1: Calculation of Projected area A_{No} and actual area A_N for single anchor and double anchors (Cement Association of Canada 2010; ACI Committee 318 2011)	374
Figure A-2: Calculation of projected area A_{vco} for single anchor (Cement Association of Canada, 2010; ACI Committee 318, 2011)	381

Figure C-1: Tensile load-displacement graph for 15.9 mm diameter cast-in-place anchor at strain rate of 10^{-5} s^{-1}	393
Figure C-2: Tensile load-displacement graph for 15.9 mm diameter cast-in-place anchor at strain rate of 10^{-3} s^{-1}	393
Figure C-3: Tensile load-displacement graph for 15.9 mm diameter cast-in-place anchor at strain rate of 10^{-1} s^{-1}	394
Figure C-4: Tensile load-displacement graph for 15.9 mm diameter cast-in-place anchor at strain rate of 10 s^{-1}	394
Figure C-5: Tensile load-displacement graph for 15.9 mm diameter cast-in-place anchor at strain rate of 10^2 s^{-1}	395
Figure C-6: Tensile load-displacement graph for 15.9 mm diameter cast-in-place anchor at strain rate of 10^3 s^{-1}	395
Figure C-7: Tensile load-displacement graph for 19.1 mm diameter cast-in-place anchor at strain rate of 10^{-5} s^{-1}	396
Figure C-8: Tensile load-displacement graph for 19.1 mm diameter cast-in-place anchor at strain rate of 10^{-3} s^{-1}	396
Figure C-9: Tensile load-displacement graph for 19.1 mm diameter cast-in-place anchor at strain rate of 10^{-1} s^{-1}	397
Figure C-10: Tensile load-displacement graph for 19.1 mm diameter cast-in-place anchor at strain rate of 10 s^{-1}	397
Figure C-11: Tensile load-displacement graph for 19.1 mm diameter cast-in-place anchor at strain rate of 10^2 s^{-1}	398

Figure C-12: Tensile load-displacement graph for 19.1 mm diameter cast-in-place anchor at strain rate of 10^3 s^{-1}	398
Figure D-1: Shear load-displacement graph for 15.9 mm diameter cast-in-place anchor at strain rate of 10^{-5} s^{-1}	399
Figure D-2: Shear load-displacement graph for 15.9 mm diameter cast-in-place anchor at strain rate of 10^{-3} s^{-1}	399
Figure D-3: Shear load-displacement graph for 15.9 mm diameter cast-in-place anchor at strain rate of 10^{-1} s^{-1}	400
Figure D-4: Shear load-displacement graph for 15.9 mm diameter cast-in-place anchor at strain rate of 10 s^{-1}	400
Figure D-5: Shear load-displacement graph for 15.9 mm diameter cast-in-place anchor at strain rate of 10^2 s^{-1}	401
Figure D-6: Shear load-displacement graph for 15.9 mm diameter cast-in-place anchor at strain rate of 10^3 s^{-1}	401
Figure D-7: Shear load-displacement graph for 19.1 mm diameter cast-in-place anchor at strain rate of 10^{-5} s^{-1}	402
Figure D-8: Shear load-displacement graph for 19.1 mm diameter cast-in-place anchor at strain rate of 10^{-3} s^{-1}	402
Figure D-9: Shear load-displacement graph for 19.1 mm diameter cast-in-place anchor mm at strain rate of 10^{-1} s^{-1}	403
Figure D-10: Shear load-displacement graph for 19.1 mm diameter cast-in-place anchor at strain rate of 10 s^{-1}	403

Figure D-11: Shear load-displacement graph for 19.1 mm diameter cast-in-place anchor at strain rate of 10^2 s^{-1}	404
Figure D-12: Shear load-displacement graph for 19.1 mm diameter cast-in-place anchor at strain rate of 10^3 s^{-1}	404
Figure E-1: Tensile load-displacement graph for 15.9 mm diameter adhesive anchor at strain rate of 10^{-5} s^{-1}	405
Figure E-2: Tensile load-displacement graph for 15.9 mm diameter adhesive anchor at strain rate of 10^{-3} s^{-1}	405
Figure E-3: Tensile load-displacement graph for 15.9 mm diameter adhesive anchor at strain rate of 10^{-1} s^{-1}	406
Figure E-4: Tensile load-displacement graph for 15.9 mm diameter adhesive anchor at strain rate of 10 s^{-1}	406
Figure E-5: Tensile load-displacement graph for 15.9 mm diameter adhesive anchor at strain rate of 10^2 s^{-1}	407
Figure E-6: Tensile load-displacement graph for 15.9 mm diameter adhesive anchor at strain rate of 10^3 s^{-1}	407
Figure E-7: Tensile load-displacement graph for 19.1 mm diameter adhesive anchor at strain rate of 10^{-5} s^{-1}	408
Figure E-8: Tensile load-displacement graph for 19.1 mm diameter adhesive anchor at strain rate of 10^{-3} s^{-1}	408
Figure E-9: Tensile load-displacement graph for 19.1 mm diameter adhesive anchor at strain rate of 10^{-1} s^{-1}	409

Figure E-10: Tensile load-displacement graph for 19.1 mm diameter adhesive anchor at strain rate of 10 s^{-1}	409
Figure E-11: Tensile load-displacement graph for 19.1 mm diameter adhesive anchor at strain rate of 10^2 s^{-1}	410
Figure E-12: Tensile load-displacement graph for 19.1 mm diameter adhesive anchor at strain rate of 10^3 s^{-1}	410
Figure F-1: Shear load-displacement graph for 15.9 mm diameter adhesive anchor at strain rate of 10^{-5} s^{-1}	411
Figure F-2: Shear load-displacement graph for 15.9 mm diameter adhesive anchor at strain rate of 10^{-3} s^{-1}	411
Figure F-3: Shear load-displacement graph for 15.9 mm diameter adhesive anchor at strain rate of 10^{-1} s^{-1}	412
Figure F-4: Shear load-displacement graph for 15.9 mm diameter adhesive anchor at strain rate of 10 s^{-1}	412
Figure F-5: Shear load-displacement graph for 15.9 mm diameter adhesive anchor at strain rate of 10^2 s^{-1}	413
Figure F-6: Shear load-displacement graph for 15.9 mm diameter adhesive anchor at strain rate of 10^3 s^{-1}	413
Figure F-7: Shear load-displacement graph for 19.1 mm diameter adhesive anchor at strain rate of 10^{-5} s^{-1}	414
Figure F-8: Shear load-displacement graph for 19.1 mm diameter adhesive anchor at strain rate of 10^{-3} s^{-1}	414

Figure F-9: Shear load-displacement graph for 19.1 mm diameter adhesive anchor at strain rate of 10^{-1} s^{-1}	415
Figure F-10: Shear load-displacement graph for 19.1 mm diameter adhesive anchor at strain rate of 10 s^{-1}	415
Figure F-11: Shear load-displacement graph for 19.1 mm diameter adhesive anchor at strain rate of 10^2 s^{-1}	416
Figure F-12: Shear load-displacement graph for 19.1 mm diameter adhesive anchor at strain rate of 10^3 s^{-1}	416
Figure G-1: Tensile load-displacement graph for the 16 mm diameter undercut anchor at strain rate of 10^{-5} s^{-1}	417
Figure G-2: Tensile load-displacement graph for the 16 mm diameter undercut anchor at strain rate of 10^{-3} s^{-1}	417
Figure G-3: Tensile load-displacement graph for the 16 mm diameter undercut anchor at strain rate of 10^{-1} s^{-1}	418
Figure G-4: Tensile load-displacement graph for the 16 mm diameter undercut anchor at strain rate of 10 s^{-1}	418
Figure G-5: Tensile load-displacement graph for the 16 mm diameter undercut anchor at strain rate of 10^2 s^{-1}	419
Figure G-6: Tensile load-displacement graph for the 16 mm diameter undercut anchor at strain rate of 10^3 s^{-1}	419
Figure G-7: Tensile load-displacement graph for the 20 mm diameter undercut anchor at strain rate of 10^{-5} s^{-1}	420

Figure G-8: Tensile load-displacement graph for the 20 mm diameter undercut anchor at strain rate of 10^{-3} s^{-1}	420
Figure G-9: Tensile load-displacement graph for the 20 mm diameter undercut anchor at strain rate of 10^{-1} s^{-1}	421
Figure G-10: Tensile load-displacement graph for the 20 mm diameter undercut anchor at strain rate of 10 s^{-1}	421
Figure G-11: Tensile load-displacement graph for the 20 mm diameter undercut anchor at strain rate of 10^2 s^{-1}	422
Figure G-12: Tensile load-displacement graph for the 20 mm diameter undercut anchor at strain rate of 10^3 s^{-1}	422
Figure H-1: Shear load-displacement graph for 16 mm diameter undercut anchor at strain rate of 10^{-5} s^{-1}	423
Figure H-2: Shear load-displacement graph for 16 mm diameter undercut anchor at strain rate of 10^{-3} s^{-1}	423
Figure H-3: Shear load-displacement graph for 16 mm diameter undercut anchor at strain rate of 10^{-1} s^{-1}	424
Figure H-4: Shear load-displacement graph for 16 mm diameter undercut anchor at strain rate of 10 s^{-1}	424
Figure H-5: Shear load-displacement graph for 16 mm diameter undercut anchor at strain rate of 10^2 s^{-1}	425
Figure H-6: Shear load-displacement graph for 16 mm diameter undercut anchor at strain rate of 10^3 s^{-1}	425

Figure H-7: Shear load-displacement graph for 20 mm diameter undercut anchor at strain rate of 10^{-5} s^{-1}	426
Figure H-8: Shear load-displacement graph for 20 mm diameter undercut anchor at strain rate of 10^{-3} s^{-1}	426
Figure H-9: Shear load-displacement graph for 20 mm diameter undercut anchor at strain rate of 10^{-1} s^{-1}	427
Figure H-10: Shear load-displacement graph for 20 mm diameter undercut anchor at strain rate of 10 s^{-1}	427
Figure H-11: Shear load-displacement graph for 20 mm diameter undercut anchor at strain rate of 10^2 s^{-1}	428
Figure H-12: Shear load-displacement graph for 20 mm diameter undercut anchor at strain rate of 10^3	428

List of Tables

Table 3-1: Material specifications for concrete models (LSTC, 2014)	80
Table 3-2: Boundary conditions of the anchorage to concrete systems.....	97
Table 3-3: Material models specifications (LSTC, 2014)	99
Table 4-1: Effect of mesh size refinement on the convergence of ultimate tensile load for cast-in-place anchors.....	103
Table 4-2: Comparison of ultimate tensile loads obtained from FEA with ACI and CCD design methods.....	107
Table 4-3: Concrete cone diameter and cone breakout angle for the cast-in-place anchor at the static strain rate	112
Table 4-4: Failure mode for cast-in-place anchors under tensile load at different strain rates	117
Table 4-5: Crack propagation angle for the cast-in-place anchors at different strain rates	118
Table 4-6: Ultimate tensile load and displacement results for the 12.7 mm diameter cast-in-place anchor	130
Table 4-7: Ultimate tensile load and displacement results for the 15.9 mm diameter cast-in-place anchor.....	130
Table 4-8: Ultimate tensile load and displacement results for the 19.1 mm diameter cast-in-place anchor.....	131
Table 4-9: Maximum dynamic increase factor for the cast-in-place anchors under tensile load.....	140

Table 4-10: Statistical models and coefficient of determination to predict the DIF for cast-in-place anchors exhibited concrete cone breakout failure under tensile load	143
Table 4-11: Statistical models and coefficient of determination to predict the DIF for cast-in-place anchors exhibited steel failure under tensile load	143
Table 4-12: Comparison between ultimate dynamic load obtained from the FEA and proposed equations by Fujikake et al. (2003) for the cast-in-place anchor exhibited concrete cone breakout failure.....	150
Table 4-13: Effect of mesh size refinement on the convergence of ultimate shear load for cast-in-place anchor	153
Table 4-14: Comparison between FEA and ACI 318 method.....	155
Table 4-15: Failure mode for cast-in-place anchors under shear load at different strain rates	164
Table 4-16: Ultimate shear load and displacement results for the 12.7 mm diameter cast-in-place anchor.....	170
Table 4-17: Ultimate shear load and displacement results for the 15.9 mm diameter cast-in-place anchor.....	171
Table 4-18: Ultimate shear load and displacement results for the 19.1 mm diameter cast-in-place anchor.....	172
Table 4-19: Maximum DIF for the cast-in-place anchors under shear load.....	176
Table 4-20: Statistical models and coefficient of determination to predict the DIF for cast-in-place anchor exhibited steel failure under shear load.....	178
Table 5-1: Effect of mesh size refinement on the convergence of ultimate tensile load for adhesive anchor.....	195

Table 5-2: Comparison of ultimate tensile loads obtained from FEA with ACI and CCD methods.....	199
Table 5-3: Concrete cone diameter and cone breakout angle for the adhesive anchor...	204
Table 5-4: Failure mode for adhesive anchors under tensile load at different strain rates	212
Table 5-5: Ultimate tensile load and displacement results for the 12.7 mm diameter adhesive anchor.....	221
Table 5-6: Ultimate tensile load and displacement results for the 15.9 mm diameter adhesive anchor.....	222
Table 5-7: Ultimate tensile load and displacement results for the 19.1 mm diameter adhesive anchor.....	223
Table 5-8: Maximum dynamic increase factor for the adhesive anchors under tensile load	231
Table 5-9: Statistical models and coefficient of determination to predict the DIF for adhesive anchors exhibited combined cone bond failure under tensile load.....	233
Table 5-10: Statistical models and coefficient of determination to predict the DIF for adhesive anchors exhibited steel failure under tensile load.....	234
Table 5-11: Comparison between ultimate load obtained from the FEA and the proposed equations by Fujikake et al. (2003) for concrete cone breakout failure mode.....	239
Table 5-12: Comparison between ultimate dynamic load obtained from the FEA and the proposed equations by Fujikake et al. (2003) for combined cone bond failure mode....	240
Table 5-13: Effect of mesh size refinement on the convergence of ultimate shear load for adhesive anchor.....	243

Table 5-14: Comparison between FEA and ACI 318 method.....	245
Table 5-15: Failure mode for adhesive anchors under shear load at different strain rates	251
Table 5-16: Ultimate shear load and displacement results for the 12.7-mm diameter adhesive anchor.....	261
Table 5-17: Ultimate shear load and displacement results for the 15.9-mm diameter adhesive anchor.....	261
Table 5-18: Ultimate shear load and displacement results for the 19.1-mm diameter adhesive anchor.....	262
Table 5-19: Maximum dynamic increase factor for the adhesive anchors under shear load	268
Table 5-20: Statistical models and coefficient of determination to predict the DIF for adhesive anchor exhibited steel failure under shear load.....	270
Table 6-1: Effect of mesh size refinement on the convergence of ultimate tensile load for undercut anchor.....	276
Table 6-2: Comparison of ultimate tensile loads obtained from FEA with ACI and CCD methods.....	279
Table 6-3: Failure mode for undercut anchors under tensile load at different strain rates	285
Table 6-4: Crack propagation angle for the undercut anchors at different strain rates...	290
Table 6-5: Ultimate tensile load and displacement for the 12 mm diameter undercut anchor	296

Table 6-6: Ultimate tensile load and displacement for the 16 mm diameter undercut anchor	297
Table 6-7: Ultimate tensile load and displacement for the 20 mm diameter undercut anchor	298
Table 6-8: Maximum Dynamic increase factor for the undercut anchors under tensile load	303
Table 6-9: Statistical models and coefficient of determination to predict the DIF for the undercut anchors exhibited steel failure under tensile load	304
Table 6-10: Comparison between ultimate dynamic load for the undercut anchor obtained from the FEA and proposed equation by Fujikake et al. (2003)	308
Table 6-11: Effect of mesh size refinement on the convergence of ultimate shear load for undercut anchor	310
Table 6-12: Comparison of ultimate shear load obtained from FEA and ACI 318 method	312
Table 6-13: Failure mode for the undercut anchors under shear load at different strain rates	323
Table 6-14: Ultimate shear load and displacement results for the 12-mm diameter undercut anchor	328
Table 6-15: Ultimate shear load and displacement results for the 16-mm diameter undercut anchor	328
Table 6-16: Ultimate shear load and displacement results for the 20-mm diameter undercut anchor	329
Table 6-17: Maximum dynamic increase factor for the undercut anchors under shear load	334
Table 6-18: Statistical models and coefficient of determination to predict the DIF for the undercut anchors exhibited steel failure under shear load	335

Notations

a	Acceleration
A_{brg}	Bearing area
A_e	Projected area of concrete cone failure
A_N	Actual projected area of stress cone of a single anchor in tension
A_{No}	Projected area of stress cone of a single anchor unlimited by edge effect or spacing between anchors in tension
A_s	Effective cross-sectional area of the anchor
A_v	Actual projected area considering edge effects and overlap with adjacent anchors in shear
A_{vo}	Projected area for one anchor unlimited by edge effects, concrete depth or cone overlapping in shear
a^n	Nodal acceleration at time step (n)
a^{n+1}	Nodal acceleration at time step (n+1)
c	Distance from center of anchor to edge of concrete
c_1	Edge distance parallel to the direction of the applied load
c_2	Edge distance perpendicular to the direction of the applied load
c_c	Critical distance
C, p	Cowper-Symonds constants
d	Diameter of the anchor
d_{cone}	Cone diameter
d_h	Anchor head diameter
d_o	Diameter of the hole

d^n	Nodal displacement at time step (n)
e'_N	Distance between the resultant tensile force of the group anchors and the centroid of the group anchors
e'_v	Distance between resultant shear force of the anchor group and the centroid of the anchors
E_p	Plastic hardening modulus
E_t	Tangent modulus
f'_c	Compressive strength of concrete measured on cylinder
f'_{cc}	Compressive strength of concrete measured on cube
F_{cd}	Ultimate dynamic concrete cone breakout
f_{ct}	Concrete capacity
$f'_{c,low}$	Low strength concrete
F_s	Tensile static load
F_{td}	Tensile dynamic load
F_u	Ultimate tensile load for anchors with eccentricity effect and/or edge effect
F_{uo}	Ultimate tensile load without eccentricity effect and/or edge effect
f_{ut}	Ultimate tensile strength of the steel
f_{in}	Internal force
$F(t)$	External force
F_f	Shear (failure) surface
F_c	Hardening cap surface
G	Shear modulus
h	Concrete depth

h_{cone}	Concrete cone depth
h_{ef}	Effective embedment depth
J_1	First invariant of the stress tensor
J'_2	Second invariant of the deviatoric stress tensor
J'_3	Third invariant of the deviatoric stress tensor
k, k_1, k_2, k_3	Calibrated factors
k_{cp}	Calibrated factor
m	Mass
n	Number of anchors
N_a	Nominal bond strength for single adhesive anchor
N_b	Basic concrete breakout strength in tension of a single anchor
N_{cb}	Nominal concrete breakout strength in tension for a single anchor
N_{cbg}	Concrete breakout strength in tension for a group of anchors
N_u	Ultimate tensile load with edge effect and spacing
N_{uo}	Ultimate tensile load
N_{sb}	Side face blowout strength for single anchor
N_{sbg}	Side face blowout strength for a group of anchors
N_{pn}	Pullout load of single anchor
N_p	Nominal pullout stress
N_{cone}	Concrete cone failure load
N_{bond}	Bond failure load
P	Pressure
$PWRT$	Power law term for tension

$PWRS$	Power law term for shear
s	Distance between anchors (spacing)
S_{ij}^*	Trial deviatoric stress
S_{ij}, S_{jk}, S_{ki}	Deviatoric stress tensors
SHT_SL	Slope of the yield surface at zero tension
v	Velocity
V_{cb}	Nominal concrete breakout strength for a single anchor in shear
V_b	Basic concrete breakout strength of a single anchor in shear in cracked concrete
V_{cbg}	Concrete breakout capacity for a group of anchors in shear
V_{cp}	Pryout capacity of single cast-in anchor
V_{cpg}	Pryout capacity of a group of cast-in anchors
V_n	Ultimate shear load for anchors considering the effect of edge distance, concrete depth, and spacing
V_{no}	Ultimate shear load
v^n	Nodal velocity at time step (n)
v^{n+1}	Nodal velocity at time step (n+1)
Y	Yield function of the concrete material
ρ	Density
p	Hydrostatic pressure
ψ_1	Factor taking into account the eccentricity of the resultant tensile force on the anchors
ψ_2	Modification factor considers disorder of the radial symmetric stress

	distribution due to the edge effect for the anchors far from the edge
ψ_4	Eccentricity effect of shear load on anchor groups
ψ_5	Modification factor considers disorder of symmetric stress distribution in shear
$\psi_{ec,N}$	Modification factor account for eccentricity effect for group anchors in tension
$\psi_{ed,N}$	Modification factor account for edge effect in tension
$\psi_{c,N}$	Modification factor account for cracking under tensile load
$\psi_{ec,v}$	Modification factor accounts for eccentricity effect for group anchors subjected to eccentric shear load
$\psi_{ed,v}$	Modification factor accounts for edge effect in shear
$\psi_{c,v}$	Modification factor accounts for cracking under shear load
$\psi_{cp,N}$	Modification factor account for post installed anchors embedded in uncracked concrete
$\psi_{h,v}$	Modification factor account of the thickness of concrete
Σ_0	Nominal perimeter of the reinforcing
σ_u	Ultimate strength of the anchor
σ_0	Initial yield stress
σ_y	Yield stress
σ_s	Tensile stress of the steel bar
τ	Shear stress
τ_o	Uniform bond stress in the adhesive layer
τ_{max}	Maximum bond stress in the adhesive layer

λ'	Elastic constant
\mathfrak{R}	Rubin three invariant reduction factor
$\alpha, \lambda, \beta, \theta$	Constants
θ_a	Cone breakout angle
θ_b	Crack propagation angle
Δt	Time step
$\dot{\epsilon}$	Effective strain rate
ϵ_{eff}^p	Effective plastic strain
$\dot{\epsilon}_{ij}^e$	Elastic strain rate
$\dot{\epsilon}_{ij}^p$	Plastic strain rate
$\dot{\epsilon}_{ij}$	Total strain rate
ϵ_{ij}	Strain
$\Delta\epsilon_{eff}^p$	Effective plastic strain increment
$f_h(\epsilon_{eff}^p)$	Hardening function

Chapter 1 : Introduction

1.1 Background

Modern construction techniques depend on the ability to connect or join building components. There are different joining techniques depending on the construction materials, structural system, and building design requirements (Eligehausen et al., 2006). Steel anchorage techniques are widely used for joining steel structural components to concrete structures (Eligehausen et al., 2006; Fuchs, 2001; Zamora et al., 2003; Eligehausen et al., 2001; Çalışkan et al., 2013).

There are two broad anchorage techniques for fastening structural components to concrete structure: cast-in-place and post-installed anchorage systems. Cast-in-place anchors are installed before casting the concrete, while post-installed anchors are installed in hardened concrete by drilling holes and inserting the steel anchors. The connections between parts in a structure are important to transfer the load between these parts (Primavera et al., 1997). Load transfer mechanism for cast-in-place anchors is mainly by mechanical interlocking between anchor and the concrete. The load transfer mechanism in post-installed anchorage systems is by mechanical interlocking, friction and bonding (adhesion) (Çalışkan et al., 2013; Eligehausen et al., 2001; Eligehausen et al., 2006; Fuchs, 2001; Zamora et al., 2003).

Many factors influence the strength of the anchorage system to concrete. These are:

- a) factors related to the anchor such as anchor type (cast-in-place or post installed), anchor strength, embedment depth, edge distance and spacing (in multi-anchor applications);
- b) factors related to the base material such as type of the base material (concrete or masonry), strength and condition of the base material (cracked or uncracked), and reinforcement detailing of the base material;
- c) factors related to the applied load such as direction of the applied load (shear, tension, combined shear-tension load), and type of load (static or dynamic); and
- d) factors related to the environmental conditions such as corrosion and temperature (Committee Euro-International du Beton (CEB), 1994).

Failure load of the anchorage system can be determined either by experimental testing, numerical modelling or by predictive methods. The predictive methods are such as American Concrete Institute (ACI) (ACI Committee (349), 1990; Fuchs, 2001; Zamora et al., 2003) and Concrete Capacity Design (CCD) (Committee Euro-International du Beton (CEB) 1994; Fuchs et al., 1995; Subramanian, 2000; Fuchs, 2001; Ashour and Alqedra, 2005). Behaviour of anchors embedded into concrete and subjected to static load has been widely investigated experimentally (Cook et al., 1992; Fuchs, 2001; Hashimoto and Takiguchi, 2004; Yilmaz et al., 2013; Zamora et al., 2003; Çalışkan et al., 2013; Eligehausen et al., 2001; Eligehausen et al., 2006). Although many structures that contain anchorage systems are exposed to dynamic loads, most of the research is under static loading conditions. Research focusing on the effects of dynamic loads from structural

vibration, earthquakes, impacts and blasts is limited. Investigating the dynamic response of the anchorage systems at high strain rates is crucial for the following reasons:

- Complex concrete response at high dynamic loading (Tu and Lu, 2009).
- Significant increase in the strength of concrete and steel due to high strain rate (Malvar & Crawford, 1998; Shkolnik, 2008; Min et al., 2014).
- The high strain rate has an influence on the properties and deformation of concrete (Park et al., 2001) and steel (Lee et al., 2007) materials.
- Exposure to high strain rate can result in a catastrophic anchorage failure such as in the structures under the earthquake, impact or blast events.
- Lack of a comprehensive and validated database on the behaviour of anchorage to concrete systems in structures subjected to different strain rates is considered a critical barrier to the designers to estimate the performance of these systems under different strain rate loading conditions.
- Current codes and guidelines for the design of anchorage systems such as ACI and CCD methods address anchorage designs under static and low cycle dynamic loading. Hence, there is a need to develop a design method to predict the anchorage response under high dynamic loading to ensure structural safety and to minimize or prevent anchorage failure.

1.2 Objectives and significance of research program

A review of the literature shows little information on the response of anchorage systems under high strain rates arising from blast and impact loading. Moreover, there is no accepted method for the design of anchorages subjected to high strain rates. Experimental research involving high strain rate loading can be complex, time consuming and expensive. Consequently, numerical analysis using a commercially available finite element package, LS-DYNA, was used to investigate the response of steel anchorage systems under high strain rates. The results of the numerical analyses will enable the prediction of the structural response of the anchorage systems under different strain rates.

The main objective of this research project is to investigate the effect of strain rate on the tensile and shear behaviour of cast-in-place, adhesive and undercut anchors. The main objectives of the research were achieved through the following research tasks:

- Development of finite element models for the cast-in-place, adhesive and undercut anchors to investigate the effect of strain rate on the tensile and shear behaviour of the anchorage to concrete systems.
- Investigation of the effect of strain rate on the load-displacement relation for the anchorage system.
- Examination of the effect of anchor diameter and embedment depth on the capacity of anchorage to concrete systems at different strain rates.
- Determination of the concrete cone breakout angle and cone breakout diameter for the anchorage systems.

- Establishment of dynamic increase factors (DIF) to relate the static and dynamic capacity of anchorage systems at high strain rates.
- Prediction and discussion of the failure mode of the cast-in-place, adhesive and undercut anchorage to concrete at different strain rates.
- Examination of the level of damage of the anchorage to concrete under different design parameters and strain rates.
- Development of analytical equations to relate DIF and strain rate for the anchorage to concrete systems.

It has been experimentally established that both concrete and steel experience an increase in strength under high strain rate loading. The combined effect of strength increase of concrete and steel has not been adequately investigated under strain rates experienced under blast and impact. This research presents a numerical investigation carried out to study the tensile and shear behaviour of cast-in-place, adhesive and undercut anchorage to concrete systems under strain rates ranging from 10^{-5} s^{-1} to 10^3 s^{-1} . Predicting the failure mode of anchorage to concrete system and the relationship between the anchorage system strength increase and strain rate will provide designers with the requisite information to design safe and cost-effective anchorage systems. Also, the effect of anchor diameter and embedment depth on the anchorage system capacity at different strain rates will be invaluable to designers. In addition, the research aims to provide a proven design methodology for the cast-in-place, adhesive and undercut anchorage to concrete systems under different strain rates. The findings of this research will contribute to the design of

anchorage systems capable of resisting high strain rate loading and predicting the failure load and failure mode of the anchorage systems under these loading conditions.

1.3 Methodology

In this project, behaviour of anchorage to plain concrete at strain rates in the range of 10^{-5} s⁻¹ to 10^3 s⁻¹ was investigated using finite element analysis package - LS-DYNA software. Single cast-in-place, adhesive and undercut anchors were selected for the analysis. Effect of group anchors on the tensile and shear behaviour of anchorage to concrete system was not considered for the analysis in this thesis. Standard anchor diameters of 12.7-mm, 15.9 mm and 19.1-mm with embedment depths (h_{ef}) of 76.2 mm, 101.6 mm, 127 mm and 152.4 mm for the cast-in-place and adhesive anchors were selected for the analysis. Three undercut anchors with nominal diameters of 12-mm, 16-mm and 20-mm and recommended embedment depths of 125 mm, 190 mm and 250 mm were considered for this investigation according to Hilti Inc. (Hilti, 2011). In addition, embedment depth of 100 mm was investigated. Effect of edge distance was not considered in the analyses. To preclude edge effects on the behaviour of the anchors, concrete block size of $(4h_{ef} + 125)$ mm \times $(4h_{ef} + 125)$ mm \times $(2h_{ef})$ mm was selected to model the tensile behaviour of the steel anchorage systems. For modelling the shear behaviour of the steel anchorage system, concrete block size of $(2h_{ef} + 150)$ mm \times $(2h_{ef} + 150)$ mm \times $(1.5h_{ef} + 50)$ mm was selected to minimize the effect of edge distance on the behaviour of the anchors.

Solid elements were used to model the steel anchor, sleeve, adhesive, plate, nut, washer and the concrete. The solid elements for the anchor, sleeve, plate, nut and washer were

formulated using constant stress while the solid elements for the concrete were formulated using one point integrated tetrahedron. Details of the solid element types used for the analyses are presented in Chapter 3. Several material constitutive models are available in LS-DYNA to model concrete, steel and adhesive materials. Some of the commonly used material constitutive models were evaluated to select the most suitable material models that can best represent the behaviour of concrete, steel and adhesive under the strain rates investigated. Continuous Surface Cap Model (MAT_CSCM_CONCRETE) was selected to model the concrete, Piecewise Linear Plasticity Model (MAT_024) was used to model the steel anchor, and Arup Adhesive Model (MAT_169) was used to model the adhesive material.

Three contact definitions were used to model the interaction between the components of the anchorage system: CONTACT_AUTOMATIC_SURFACE_TO_SURFACE, CONTACT_TIED_SURFACE_TO_SURFACE and CONTACT_AUTOMATIC_ONE_WAY_SURFACE_TO_SURFACE_TIEBREAK. Bonding between the concrete and the anchor for the cast-in-place and undercut anchors was performed using CONTACT_AUTOMATIC_SURFACE_TO_SURFACE. This contact keyword simulates a two-way contact where the penetration of the slave nodes (the anchor) are checked against master segment (the concrete) and master nodes are checked against slave segment. For the adhesive anchor, CONTACT_AUTOMATIC_ONE_WAY_SURFACE_TO_SURFACE_TIEBREAK was used to model the steel to adhesive bond, CONTACT_TIED_SURFACE_TO_SURFACE was used for bonding between the adhesive and the concrete. CONTACT_ERODING_SINGLE_SURFACE was implemented to remove any distorted elements of the adhesive material. All the nodes at

the bottom surface of the concrete block were fixed to prevent displacement and rotation during the loading regime. Using symmetry, a quarter of the anchorage system with two symmetry planes boundary condition was used to model the tensile behaviour. Half of the anchorage system with one symmetry plane boundary condition was used to model the shear behaviour.

The strain rate was imposed on the steel anchor by imposing BOUNDARY_PRESCRIBED_MOTION_SET keycard, in z-direction and y-direction, to model the tensile and shear loads respectively. After completing the finite element models, finite element analysis was carried out using explicit solver of LS-DYNA.

The cast-in-place, adhesive and undercut anchor models were validated with experimental test data and compared with results from the analytical prediction methods (ACI and CCD). Effect of strain rate on the tensile and shear capacity of the cast-in-place, adhesive and undercut anchors was investigated for the different anchor diameters and embedment depths. Ultimate load values for the anchors were determined for the investigated strain rates. The DIF, defined as the ratio of dynamic to static capacity was determined at each strain rate. The relation between the DIF and strain rate was established and an equation relating the DIF and strain rate was proposed. The adequacy of the proposed equation was verified by comparing the DIF obtained from the predicted equation with the DIF obtained from new developed numerical models of the anchorage systems with different design parameters. Figure 1-1 shows the anchorage to concrete systems used in this research. The methodology of the project can be summarized as in the flow chart shown in Figure 1-2.

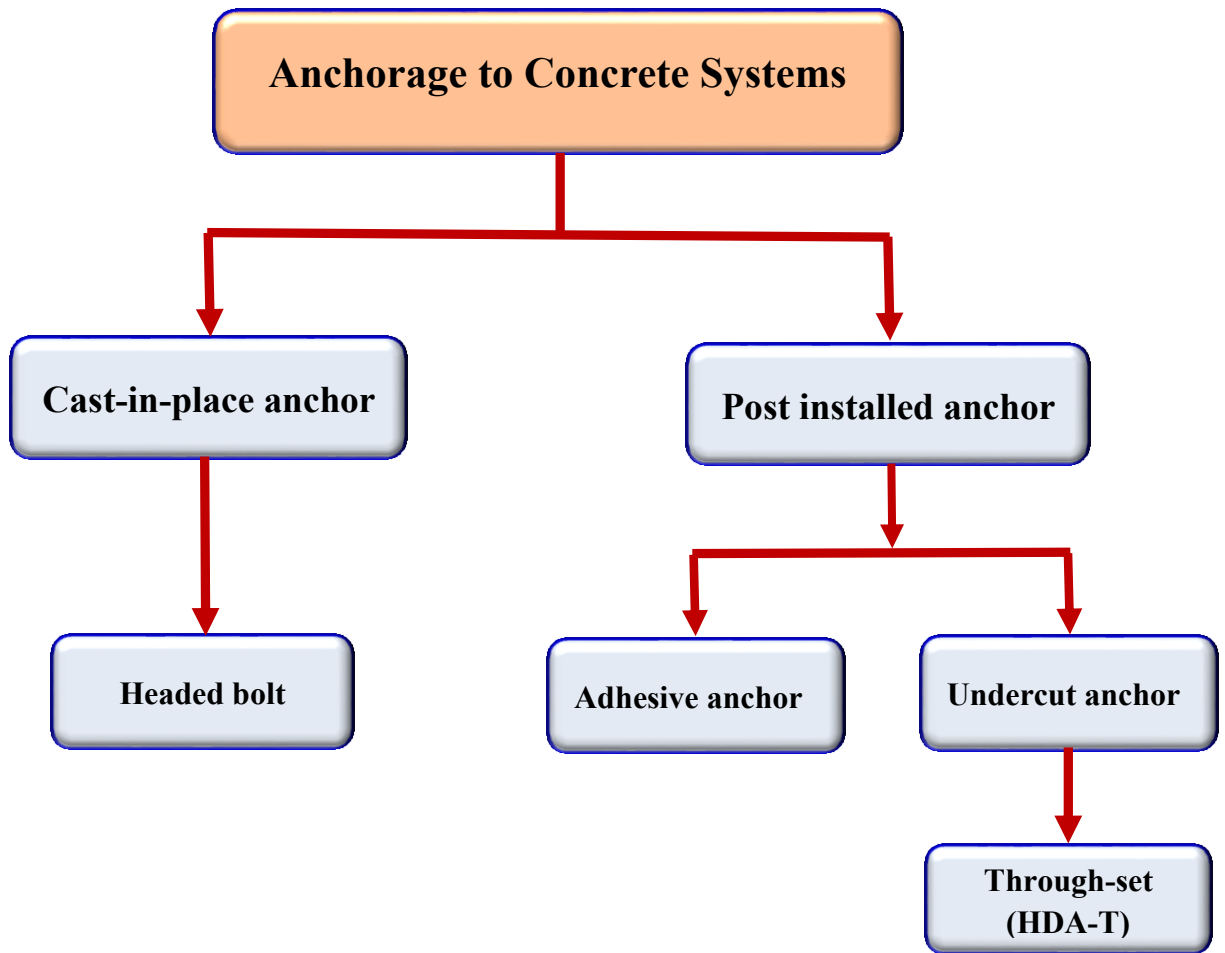


Figure 1-1: Anchorage systems

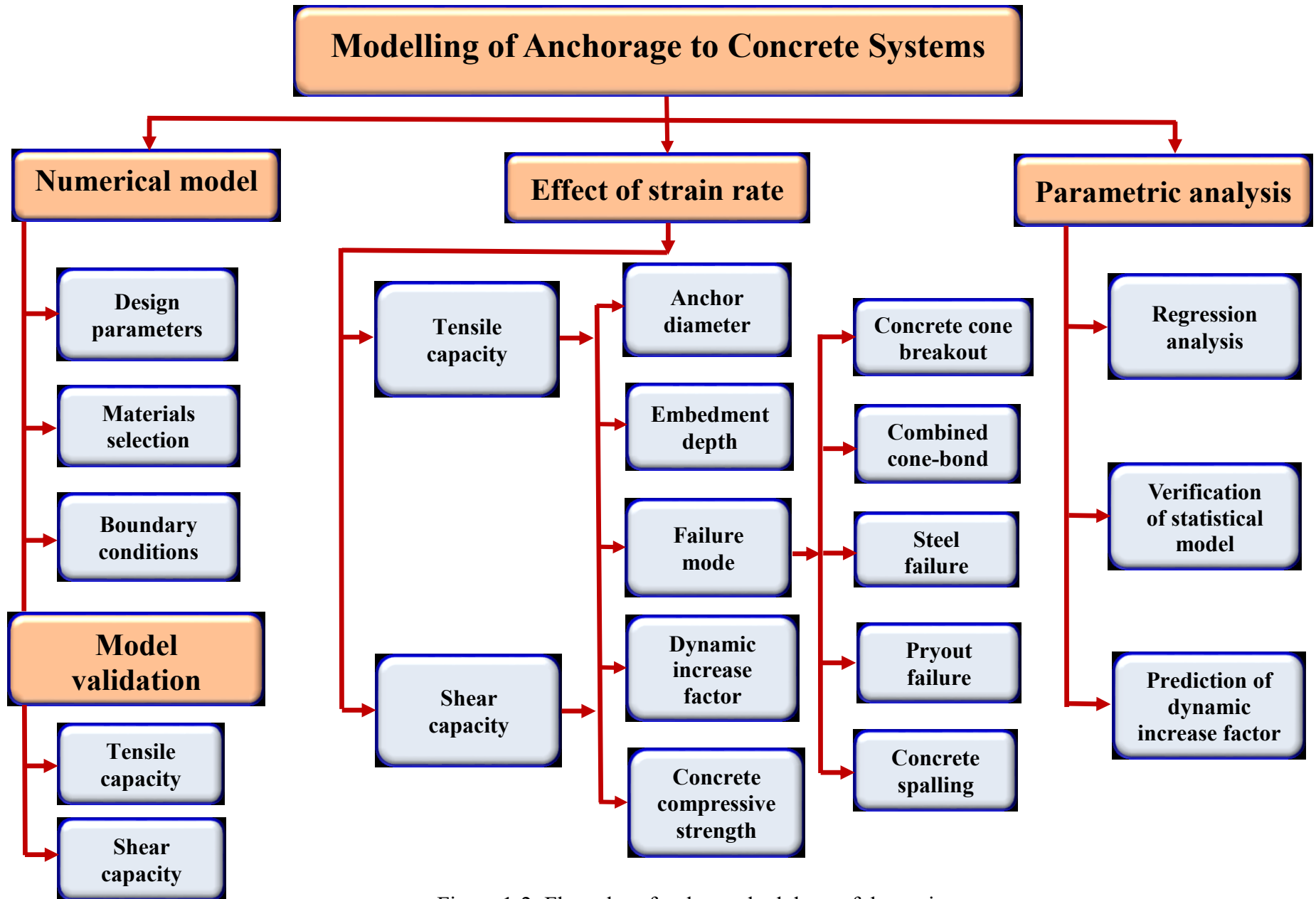


Figure 1-2: Flow chart for the methodology of the project

1.4 Scope of the research

In this research, anchorage to concrete system models of different design parameters were developed using LS-DYNA software to investigate the tensile and shear behaviour of the anchorage systems embedded in plain concrete. Six strain rates of 10^{-5} s^{-1} , 10^{-3} s^{-1} , 10^{-1} s^{-1} , 10 s^{-1} , 10^2 s^{-1} and 10^3 s^{-1} that represent various loading conditions were considered in the analysis. Low strain rate of 10^{-5} s^{-1} is considered to represent the static loading, moderate strain rates of 10^{-3} s^{-1} and 10^{-1} s^{-1} are considered to represent the earthquake, strain rate of 10 s^{-1} is considered for impact and high strain rates of 10^2 s^{-1} and 10^3 s^{-1} are associated with blast loading. The scope of this research can be summarized as follows:

1. Analyses on the behaviour of cast-in-place anchorage to concrete systems subjected to tensile and shear loads at strain rates ranging from 10^{-5} s^{-1} to 10^3 s^{-1} .
2. Analyses on the behaviour of post-installed adhesive anchorage to concrete systems subjected to tensile and shear loads at strain rates ranging from 10^{-5} s^{-1} to 10^3 s^{-1} .
3. Analyses on the behaviour of post-installed undercut anchorage to concrete systems subjected to tensile and shear loads at strain rates ranging from 10^{-5} s^{-1} to 10^3 s^{-1} .

1.5 Structure of the thesis

This thesis has been organized into seven chapters. The contents in each chapter are summarized as follows:

Chapter one outlines the background of anchorage to concrete systems, followed by the objectives of the research. The methodology of the research is also presented in this chapter with a flow chart that shows the process of developing the anchorage to concrete models and the factors that are investigated. Chapter one ends with the structure of the thesis that outlines all the chapters of the thesis.

Chapter two presents a comprehensive literature review on steel to concrete anchorage systems. Chapter two addresses the classifications of anchors and adhesive materials. The chapter includes a literature review on the behaviour of cast-in-place and post-installed anchors under static and dynamic tensile and shear loading. A literature survey on the effect of bond strength, embedment depth, anchor diameter, edge distance, anchor spacing, and failure mode is presented. Effect of strain rate on the concrete and steel materials is also presented. This is followed by introduction of the design methods for cast-in-place and post-installed anchors under tensile and shear loads. Failure modes of the cast-in-place and post-installed anchors and summary of the literature review are presented at the end of the chapter.

Chapter three presents the modelling and finite element analyses of the cast-in-place, adhesive and undercut anchors using LS-DYNA software. The chapter begins with introduction and presentation of the most commonly used finite element software packages in engineering applications and the main features of LS-DYNA. Implicit and explicit

analyses methods implemented in LS-DYNA are introduced, followed by the theoretical aspects of LS-DYNA. The considerations used to select constitutive materials models, element type, and bonding type for the concrete, steel and adhesive are presented. Meshing technique, boundary conditions, contact modelling and loading conditions that accurately represents the behaviour of anchorage to concrete system are introduced. Procedure to perform quasi static analysis using LS-DYNA software is presented. Finally, a summary of chapter three is presented.

Chapter four begins with modelling the cast-in-place anchorage system using LS-DYNA software. Results and discussion of the effect of strain rate on the behaviour of cast-in-place anchors subjected to tensile and shear loads are presented. Static and dynamic loading conditions using LS-DYNA software are carried out in this chapter. Mesh sensitivity analysis is carried out to improve the accuracy of the analysis. Model validation with experimental test data in the literature as well as comparison with analytical prediction methods (ACI and CCD methods) is presented. The effect of strain rate on the ultimate tensile and shear loads, the effect of strain rate on the level of damage and failure mode as well as the DIF, the effect of anchor embedment depth on concrete cone depth, the effect of strain rate on concrete breakout diameter and crack propagation angle, and effect of concrete compressive strength on the level of damage and failure mode are presented in Chapter four. Regression analysis is performed for the cast-in-place anchors under tensile and shear loads to develop a relationship between DIF and strain rate.

Chapter five begins with modelling the adhesive anchorage to concrete system using LS-DYNA software. Mesh sensitivity analysis is carried out to establish the element size and

mesh density to maximize accuracy at least resource cost. Results and discussion of the effect of strain rate on the behaviour of adhesive anchors subjected to tensile and shear loads are presented. The adhesive anchor model is validated with experimental test data in the literature and presented in this chapter. Comparison with the ACI and CCD analytical prediction methods is presented. Level of damage and failure mode at different strain rates, the effect of strain rate on the ultimate loads and DIF, the effect of anchor embedment depth on concrete cone depth, the effect of strain rate on concrete cone breakout diameter are presented in chapter 5. Regression analysis is performed to develop a relationship between DIF and strain rate for the adhesive anchors under tensile and shear loads.

Chapter six presents modelling of the undercut anchorage to concrete system under tensile and shear loads using LS-DYNA software. Model validation with the experimental data is performed. Comparison of the finite element results with the ACI and CCD design methods is presented. Results and discussion of the effect of strain rate on the tensile and shear behaviour of undercut anchors are presented. Effect of strain rate on the ultimate loads and DIF, failure mode and crack propagation angle at different strain rates, the effect of anchor embedment depth on concrete cone depth and cone diameter are presented. Regression analysis is performed for the undercut anchors under tensile and shear loads to develop relationship between DIF and strain rate.

Chapter seven presents the main conclusions of the analyses and introduces recommendations for future work.

Chapter 2 : Literature review

2.1 Introduction

Construction of buildings and building components requires joining or connecting parts together. Different anchorage techniques are widely used for joining concrete and steel structures and components. Anchorage to concrete systems can be exposed to static or dynamic loading conditions resulting from use and occupancy or from the environment or climate. Static load results from self-weight of the structure and when the live load is applied slowly. Dynamic loads result from structural vibration, earthquake, impact and blast events.

Structures can be exposed to low and high strain rate loading conditions such as encountered with creep, quasi-static, earthquake, impact and blast loads. It is essential for the structures to retain suitable structural safety with durable anchorage system. The damage that occurs due to high loading rate such as under earthquake loading, motivate researchers to study the behaviour of anchor connections at these rates. In the 1994 Northridge earthquake in the USA, anchor failures caused damage of transformers and resulted in electrical power outage to the Veteran's hospital (Zhao, 2014). In 1995 an earthquake in Osaka, Japan resulted in anchorage failure and caused transformers to slip off their foundations, resulting in power outage and severe damage to power transmission lines (Zhao, 2014). Low loading rates such as creep, on the other hand, may result in degradation of the adhesive materials and lead to failure of anchorage systems. An example of adhesive anchor failure is the collapse of part of concrete ceiling in Boston tunnel where

adhesive anchors were used to secure the ceiling to the tunnel walls. The National Transportation Safety Board found that the collapse resulted from creep of the adhesive due to long term loading (Vuletic and Pearson, 2008).

Investigating the behaviour of anchors under high loading rates is important in roadway support and design. Anchors can be used in applications that require high loading rates such as rock burst where the anchors can be used to reduce the damage induced by rock burst (Zhao et al., 2015). For example, in mining, anchors used to secure steel mesh against rock bursts are subjected to very high impact loading (Ansell, 2006). Figure 2-1 shows applications of anchorage system in rock burst.



Figure 2-1: Applications of anchorage system in rock burst (Cai et al., 2010)

In addition, bolts can be used to attach blast protection appliques (such as armor) to combat vehicles, where the appliques are used to mitigate the effect of explosions. However, these

bolts shear off under blast loads resulting in secondary fragments that may damage the vehicle and/or cause injury to people (Lou and Perciballi, 2008).

When a structure subjected to blast loading, the fractured glass windows can cause injury and fatality to the occupants of the building and the people around it. According to the Oklahoma State Department of Health, most of the injuries in the Oklahoma City bombing were caused by window glass shards (Mallonee et al., 1996; Norville & Conrath, 2001, 2006; Shariat et al., 1998). People within a distance of 3 m from the windows reporting injuries due to the window glass shards represented over 40% of the total injured (Norville et al., 1999). Upgrading window glazing and using laminated glass can mitigate the injuries and fatalities. However, the load are transferred from the window glazing to the window frame and then from the window frame to the structure through the bolts (Braumah et al., 2014). Figure 2-2 shows the applications of anchors in the window to resist blast load.

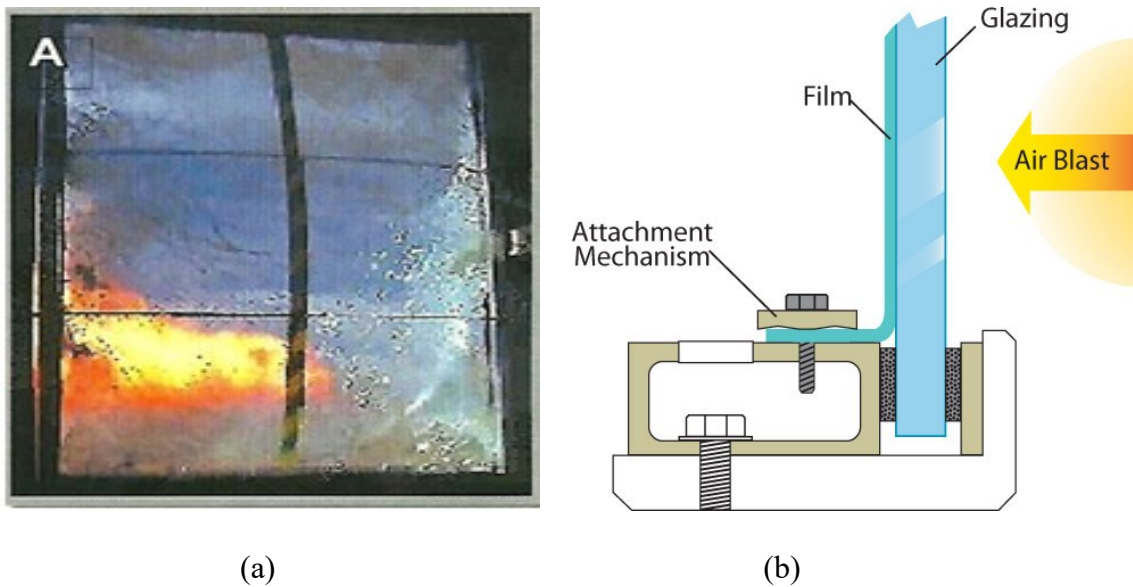
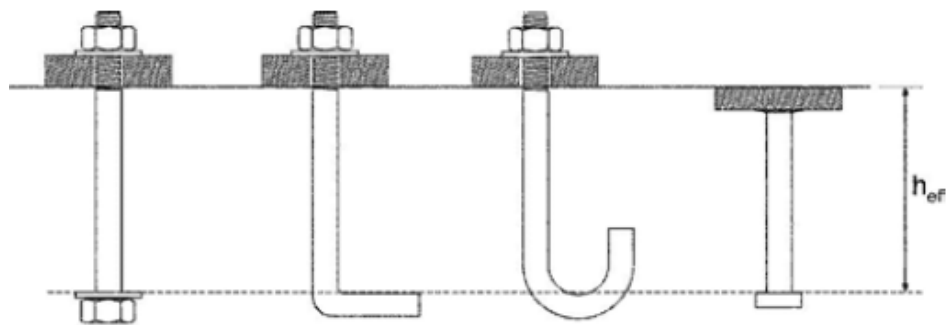


Figure 2-2: Applications of anchorage system in window; (a) glass window under blast load (Madico Safety Shield Premier Partener, 2012), (b) anchorage to base-plate (Johnson window films, 2018)

2.2 Classification of anchors

The main function of the anchors is to connect structural components. As mentioned in chapter one, there are two categories of anchors commonly used for joining concrete to steel structures: cast-in-place and post-installed anchors. Cast-in-place anchors are cast into fresh concrete during forming and have been used in a wide range of structural applications for decades (Hawkins, 1987). Cast-in-place anchors are used to fasten equipment to concrete in construction in order to avoid drilling in hardened concrete, a process that creates microcracking in the concrete member as well as requiring additional finishing work (Delhomme et al., 2015a). The cast-in-place anchors can be classified according to their shape as hexagonal headed bolt, hooked L-bolt, hooked J-bolt and welded headed stud (Figure 2-3 a). Some errors may occur due to improper installation of the cast-in-place anchor and affect its performance. These errors include: inappropriate location of the anchor installation, incorrect implementation of the detailing drawing, neglect of changes that may occur in the concrete geometry during the casting, curing and under sustained loading; e.g. creep and shrinkage (Spyridis and Bergmeister, 2014).



(i) hexagonal headed bolt (ii) hooked L-bolt (iii) hooked J-bolt (iv) welded headed stud
(a)

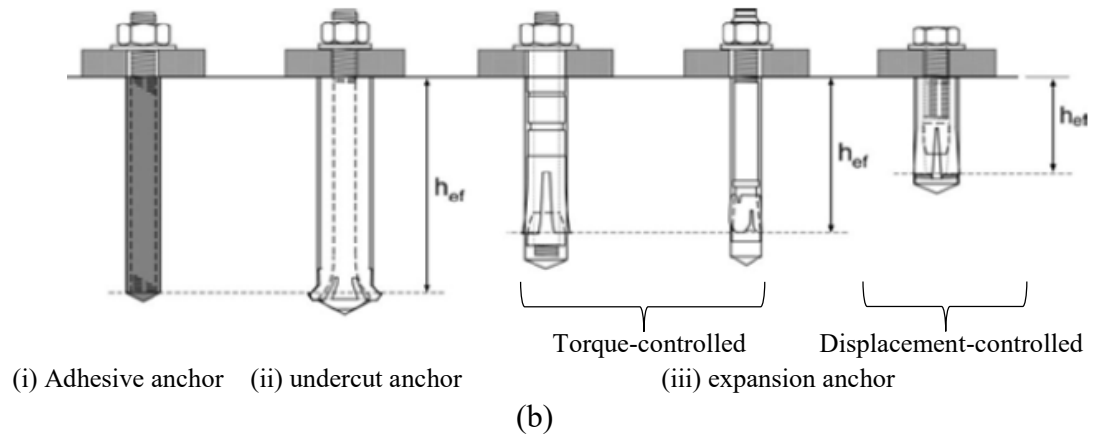


Figure 2-3: Types of anchors: (a) cast-in-place anchors, (b) post installed anchors (ACI Committee 318, 2011)

Post-installed anchors are increasingly used in construction due to their flexibility of installation in any position in a substrate material and the increasing demand for shorter construction times. Post-installed anchors have found use in a variety of applications including: new construction, retrofit and rehabilitation, and repair of concrete and masonry structures (Cook, 1993). Post-installed anchors have also found use in blast retrofit applications to resist, minimize or mitigate the influence of blast load where they are subjected to high strain rate loading. Post-installed anchors are classified according to the load transfer mechanism into mechanical and bonded anchors (McMullin et al., 2016). Mechanical anchors are further classified as undercut and expansion anchors, while bonded anchors can be either adhesive anchors or grouted anchors (Figure 2-3 b). The load transfer mechanism for the undercut anchors to the substrate material is by mechanical interlocking which is similar to the cast-in-place anchors. The applied tensile load is transferred from the anchor stud to the sleeve by bearing which in turns bears on the concrete (A Mitek' Company, 1997). For expansion anchors the load transfer mechanism is by friction. On the

other hand, the load transfer mechanism for the bonded anchors to the substrate material is by chemical bonding (Fuchs et al., 1995).

Undercut anchors are mechanical anchors. The undercutting is made either by a special drill bit or self-drilling anchor with carbide tipped segments used to undercut concrete during the installation process (ACI Committee 318, 2011). The undercut anchor is characterized by its performance that is comparable to the cast-in-place anchor with more flexibility of installation (Mackay-Sim, 1990; Hilti, 2011). In addition, undercut anchors are shown to safely and reliably resist dynamic loads and are thus suitable for applications that require high level of safety such as in nuclear power plants (Trautwein, 2017). The anchor installation can be accomplished in one of three techniques: load-controlled, displacement-controlled or torque-controlled (ACI Committee 355, 2000; Eligehausen et al., 1998). The installation by load controlled is performed by applying tensile load on the undercut anchor that expands the sleeve into a drilled hole. The displacement-controlled installation method can be performed either by applying compression force on the sleeve of the undercut anchor or by pulling out the cone and expanding the sleeve. The installation by the torque-controlled method is performed by applying a torque and resulting in expansion of the sleeve. The displacement-controlled undercut anchor is used for low strength concrete while the load-controlled and torque-controlled undercut anchors are used for low and high strength concrete.

Hilti Inc. produces two types of undercut anchors: Hilti design anchor pre-set (HDA-P) and Hilti design anchor through-set (HDA-T). In the through-set anchor type the sleeve continues through the base plate while the sleeve ends before the base plate for the pre-set

anchor type. Through-set undercut anchor is capable of withstanding higher shear strength than the pre-set undercut anchor. This is attributed to the contribution of the sleeve to the anchor shear resistance. For the pre-set anchor type on the other hand, the shear force is transmitted from the anchor to the sleeve and then to the concrete by bearing (Hilti, 2011). Hence, the through-set undercut anchors are selected for the analysis presented in this thesis. Figure 2-4 presents the pre-set and through-set types undercut anchors.

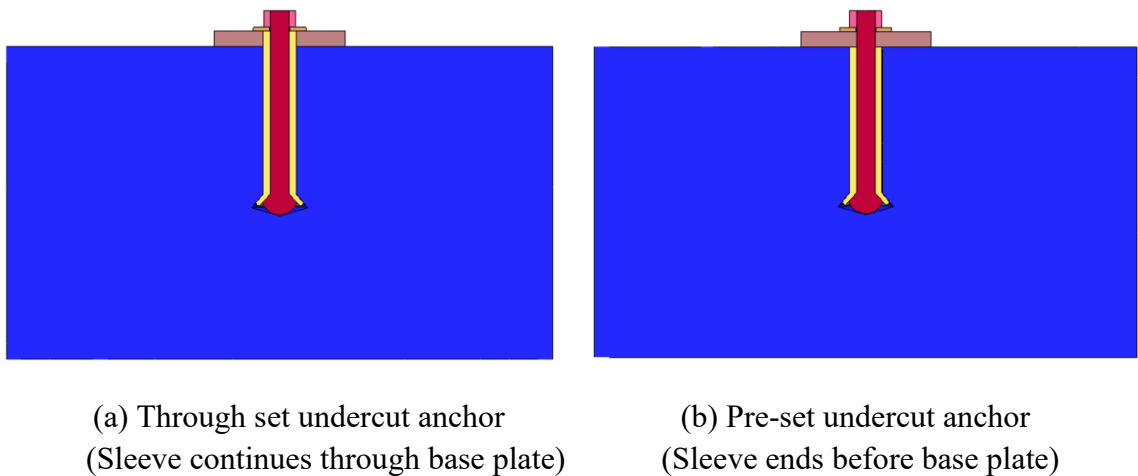


Figure 2-4: Undercut anchor types

The expansion anchors are post-installed mechanical anchors inserted in a drilled hole in hardened concrete. When torque is applied on the expansion anchor, the lower part of the expansion anchor expands resulting in increased friction and bearing against the sides of the hole. Two techniques are used to achieve the expansion of the anchor; torque-controlled and displacement-controlled techniques. Torque-controlled technique is achieved by applying a torque on the anchor, while the displacement controlled technique is achieved by applying impact force on the sleeve of anchor, the expansion is controlled by distance that the sleeve travels (ACI Committee 318, 2011).

Adhesive anchor systems involve drilling a hole in hardened concrete and then filling the hole with an adhesive material. The anchor is then inserted in the hole, where the adhesive material serves as a bonding agent between the anchor and the concrete (Cook et al., 2007). In grouted anchors, the drilled hole in hardened concrete is grouted after placement of the steel anchor. Different types of bonding agents can be used for bonded anchors. Epoxies, polyesters and vinylesters are used as bonding agents for the adhesive anchors, while cementitious bonding agents are used for the grouted anchors.

Selection of a suitable type of anchor in construction, whether cast-in-place or post installed, can be decided based on the application, cost, and performance of the anchor.

2.3 Classification of adhesive materials

Adhesive materials are used to bond two or more materials together. Adhesive materials can be classified into six categories based on:

- origin e.g. natural and synthetic;
- functionality e.g. thermosetting and thermoplastic;
- chemical composition e.g. epoxy, silicon and polyurethane;
- physical form e.g. paste and liquid;
- type e.g. hot melt; and
- load carrying capacity e.g. structural, semi structural and non-structural (da Silva et al. 2011).

Structural adhesive is used in the structural applications to sustain a long term applied load on a structure. There are several types of structural adhesives such as: epoxy and polyurethane (Goncalves and Margarido, 2015). Epoxy can be formed as two components or one component cartridges. The two component epoxies consists of resin and hardener which can be mixed together and cured at room temperature (Kinsho et al., 2000). One component epoxy can be found in liquid or paste form. Heat is required for curing the one component epoxy (Kinsho et al., 2000; da Silva et al., 2011).

2.4 Bond strength

The strength of anchorage system whether cast-in-place or post installed is influenced by the bond strength. In steel reinforced concrete, force is transmitted from steel to concrete through interface bond (Nammur and Naaman, 1989). The concrete composition and the surface condition of the steel influence the interface bond between concrete and steel, which in turns influences the load resistance of the reinforced concrete element (Fu and Chung, 1999). There are two types of bond models used in analysis and design: elastic and inelastic. Elastic bond is exhibited when the bond at the interface is less than the bond strength and the shear stresses depend on the relative displacement between the steel and the concrete (Nammur and Naaman, 1989).

For the adhesive anchors, the force from the anchor is transmitted to the concrete through the adhesive material. The bond strength of adhesive anchorage system is affected by two main factors: internal and external. Internal factors such as adhesive formulations, processing and packaging are under the control of the manufacturer, while external factors

such as installation and in-service factors are under the control of the designer and installer. The installation factors include the hole condition and the strength of the substrate material while in-service factors include curing time of adhesive, thickness of adhesive layer, type of loading and environmental conditions such as temperature (high and low), moisture, and freeze-thaw cycles (Cook and Konz, 2001; Cook et al., 2007).

There are two models available to predict the bond strength of the adhesive anchors: uniform bond stress and elastic bond stress models (Cook, 1993). Bond failure occurs at the steel-adhesive interface or at the adhesive-concrete interface. The pullout force for the steel-adhesive and concrete-adhesive interfaces can be predicted from the uniform bond stress model and the elastic bond stress model. For the uniform bond stress model the pull out force can be predicted according to (Equations B.7 and B.8 in Appendix B) (McVay et al., 1996; Cook et al., 1998; Cook, 1993; Eligehausen et al., 2007). The elastic bond stress model considers the compatibility between the concrete, bonding agent and the steel anchor, while the uniform bond stress model does not (Cook et al., 1993). For the elastic bond stress model, the pullout force can be predicted according to Equation (B.9 in Appendix B) (McVay et al., 1996; Cook et al., 1998; Cook et al., 1993; Cook, 1993).

Chapman and Shah (1987) conducted pullout test to investigate bond strength between concrete and reinforcing bars at different curing ages from 1 to 28 days. They tested both smooth bars and deformed bars for different embedment lengths. They stated that bond strength of smooth bar is not affected by curing age while, bond strength of deformed bar is significantly affected by curing age. The researchers observed three types of failure: steel

yield and fracture failure, anchor pullout (or bond) failure, and concrete splitting failure. Pullout failure was observed at early concrete ages, while yield failure was observed at later concrete ages. Splitting failure was observed at early age for embedment depth of 175 mm and at later ages for embedment depth of 76.2 mm. The authors concluded that as the embedment depth increases the pullout load increases while the average bond strength decreases. The increase in the pullout load is not proportional to that of the embedment depth. The failure mode of the bond for deformed bars is influenced by the embedment depth and compressive strength. Pullout failure occurs for shallow embedment depths and low concrete compressive strengths. Splitting failure is observed for short embedment depth with high concrete compressive strength and for deep embedment depth with low concrete compressive strength. Yield failure occurs for deep embedment depths with high concrete compressive strength (Chapman and Shah, 1987). By assuming a uniform stress distribution in the pullout test, the bond stress (u) is determined from Equation (2.1) (Chapman and Shah, 1987; Chan et al., 2003; Xing et al., 2015; Benmokrane et al., 1996; Larrard et al., 1993; Fabbrocino et al., 2005):

$$u = \frac{A_s \sigma_s}{\Sigma_0 \cdot l_d} = \frac{F}{\pi d_b l_d} \quad (2.1)$$

Where A_s is the cross-sectional area of the bar, σ_s is the tensile stress of the steel bar, F is the applied tensile load, $\Sigma_0 = \pi d_b$ is the nominal perimeter of the reinforcing bar, d_b is the bar diameter, l_d is the embedment length of the bar.

Chan et al. (2003) conducted pullout tests to investigate the bond strength of steel reinforcement in self-consolidating concrete (SCC). The authors used ordinary Portland cement concrete (OPC) for comparison purpose. Effect of age, level of reinforcing bars, and concrete type on bond strength were investigated. The authors concluded that the bond strength of reinforcement in SCC is higher than that for the OPC. Maximum bond strength of 9.51 MPa and 6.31 MPa were obtained for the SCC and OPC respectively. The decrease in the bond strength of the OPC is attributed to the bleeding and inhomogeneity of the concrete. The bond strength is very low at the early age; up to three days. The bond strength is fully developed after seven days for the OPC and after 15 days for SCC. Chan et al. (2003) stated that the bond strength varies linearly with the square root of the compressive strength. The bond strength of top reinforcement is lower than that of bottom reinforcement in an OPC and SCC member. However, the difference in bond strength for the top and bottom reinforcements in SCC members was observed to be less than that in OPC members (Chan et al., 2003).

Fu and Chung (1999) conducted electromechanical pullout tests to investigate the effect of steel rebar surface treatment and concrete composition on the bond strength. The electromechanical pullout is conducted by measuring the contact electrical resistivity and bond strength of the specimen. They concluded that the rebar surface treatment such as adding polymer (latex and Methelcellose) to the concrete and increased water-cement ratio increases the bond strength. Surface treatment involving use of ozone is more effective than use of sand blasting and acetone. The authors stated that the effectiveness of

adding latex to the concrete is the same as using ozone surface treatment to the rebar (Fu and Chung, 1999).

Toikka et al. (2015) conducted experimental work to investigate the effect of strain rate on the bond strength and development length of steel reinforcement in concrete beams under blast loading. The authors found that the bond strength increased while the required development length decreased at high strain rate associated with blast loading. The authors concluded that dynamic increase factor for bond stress increased with the increase in the reinforcement bar diameter (Toikka et al., 2015).

Xing et al. (2015) investigated the bond strength between the reinforcing bar and concrete. They studied the effect of bar surface type, embedment length, bar type and diameter. The authors concluded that the bond strength of plain bar is less than that of the deformed bar. The bond strength of plain bars increases significantly as the embedment depth increases from 80 mm to 120 mm. As the embedment depth increases, the bond stress distribution becomes uniform. The bond strength of deformed bars is composed of mechanical interlock, friction and adhesion. It is mainly governed by the mechanical interlock. Hence, the bond strength of the deformed bars is influenced by the concrete strength. The bond strength of plain bars is composed of friction and adhesion. It mainly depends on the friction. Thus, its bond strength is not influenced by the concrete strength (Xing et al., 2015). Increasing the bar diameter decreases the bond strength (Xing et al., 2015; Larrard et al., 1993).

Shima et al. (1987) investigated the bond mechanism in reinforced concrete using microscopic and macroscopic models. In the microscopic model, they represented the relationship between the local bond stress and local slip. In the macroscopic model, they represented the relationship between the pullout load and the displacement. Shima et al. (1987) determined the tensile stiffness in reinforced concrete. The pullout of the anchored bars resulted in large cracks at the connection area. The authors represent two types of the deformational behaviour of bond: relative displacement of anchored bars in concrete, and tension stiffness of cracked concrete (Shima et al., 1987).

Larrard et al. (1993) studied the bond strength of reinforcing bars embedded in high performance concrete (HPC) of 95 MPa compressive strength, and ordinary concrete of 42 MPa compressive strength. They used smooth and deformed bars with different diameters. They stated that the increase in the tensile strength of the concrete increases the bond strength. The increase in the bond strength of HPC was of 80% and 30% for bar diameters of 10 mm and 25 mm respectively. They observed that, slip of the reinforcement starts at the beginning of the loading for ordinary concrete, while the slip didn't start at the beginning of the loading due to the high rigidity of the bond in the high performance concrete (Larrard et al., 1993).

Barnat et al. (2012) studied the bond strength of chemical anchors embedded in high strength concrete in the range between 71.8 MPa to 80.7 MPa under pullout load. The authors concluded that the performance of chemical anchorage in high strength concrete depends on the properties of the adhesive material (Barnat et al., 2012). Also, the authors

concluded that the bond strength of the adhesive is not influenced by the concrete strength (Barnat et al., 2012). However, Cook and Konz (2001) stated that bond strength increased slightly with the increase in the concrete strength (Cook and Konz, 2001). Cook and Konz (2001) conducted tensile tests to investigate factors affecting the bond strength of adhesive anchors. The authors investigated the effect of installation condition, concrete strength, concrete aggregate types, adhesive curing time and effect of loading at high temperature. The authors found that the hole condition can have a detrimental effect on bond strength, where the bond strength decrease for anchors embedded into wet, damp and uncleaned holes. Unsuitable curing and hole preparation lead to bond failure where bond strength is insufficient. The authors used two types of aggregates: river gravel and limestone. The authors stated that the effect of using river gravel aggregates on increasing the bond strength is more than the effect of using limestone. The authors concluded that the increase in the porosity of the aggregates decrease the bond strength. Also, they concluded that the increase in the temperature to 43°C affects the bond strength (Cook and Konz, 2001).

2.5 Cast-in-place anchors

2.5.1 Cast-in-place anchors under tensile load

Hawkins (1987) and Delhomme et al. (2015) investigated the strength of cast-in-place headed anchors embedded in reinforced concrete and subjected to static tensile loading. Hawkins (1987) observed two types of concrete failure modes: concrete cone breakout and concrete splitting failure. Concrete cone breakout failure occurred for shallow embedment depth of 76 mm, while concrete splitting occurred for deeper embedment depths of 127 mm and 187 mm (Hawkins, 1987). Similar observation was reported by Delhomme et al.

(2015) where concrete cone breakout failure is observed at embedment depth of 80 mm. In addition, Delhomme et al. (2015) observed steel failure at embedment depths of 100 mm, 120 mm and 130 mm. Furthermore, Delhomme et al. (2015) studied effect of embedment depth for quadruple anchors. The authors observed concrete cone breakout failure at embedment depths of 80 mm, 100 mm, 120 mm, and 130 mm and steel failure at embedment depth of 310 mm. The authors concluded that the failure mode changed from concrete cone breakout to steel failure at embedment depth of 130 mm for the quadruple anchors (Delhomme et al., 2015b).

Solomos and Berra (2006) performed experimental test on the pullout strength of anchors under static and dynamic loads. The authors used Hopkinson bar technique to apply dynamic pullout loads on post-installed and cast-in-place anchors. The authors stated that the stresses and damage generated in the concrete due to the applied load and method of installation, whether cast-in-place or post-installed, affected the failure load of anchors. Moreover, same strength for post-installed and cast-in-place anchors can be obtained when adequate installation for post-installed anchors is achieved. The authors concluded that the failure load in the dynamic test is higher than that in the static test (Solomos and Berra, 2006).

Fujikake et al. (2003), Sato et al. (2004) and Ozbolt et al. (2006) investigated the effect of loading rate on the cone resistance for cast-in-place headed anchors. Fujikake et al. (2003) and Sato et al. (2004) studied loading rates of 1×10^{-1} kN/s, 4×10^2 kN/s, 4×10^3 kN/s, and 4×10^4 kN/s and found that the increase in the loading rate from 1×10^{-1} kN/s to 4×10^4 kN/s

resulted in increase in the ultimate cone resistance (Fujikake et al., 2003; Sato et al., 2004). Ozbolt et al. (2006) studied loading rates ranging from 5 mm/s to 2×10^4 mm/s and found similar results for the static and dynamic analysis for intermediate loading rate where the microcracks are dominant. For very high loading rates, the structural behaviour is controlled by the structural inertia. The authors concluded that when the loading rate increases, the size effect on the nominal pullout strength increases significantly for the moderate high loading rates. Size effect is neglected for very high loading rates and as the embedment depth increases the nominal strength increases (Ožbolt et al., 2006).

Choi et al. (2015) studied the behaviour of cast-in-place anchors in ultra-high performance fibre-reinforced concrete (UHPFRC) under monotonic shear and tensile loads. The authors observed that the tensile and shear load capacities for cast-in-place anchors in UHPFRC are higher than that for anchors in normal concrete. The authors related this increase in the capacities to the increase in the tensile and strain capacity in UHPFRC. The authors studied the effect of embedment depth and edge distance in UHPFRC. They observed that the concrete breakout capacity increased as the embedment depth increased. They also stated that the increase in the edge distance resulted in increase in the concrete breakout capacity. The authors observed shallower angle of the failure cone for the anchors embedded in UHPFRC compared to the 35° proposed in the CCD method. The authors proposed three equations to determine the tensile and shear concrete breakout capacity and anchor pryout capacity in UHPFRC (Choi et al., 2015).

Ozbolt and Eligehausen (1990) conducted numerical analysis to investigate the behaviour of headed studs embedded in large plain concrete and subjected to tensile load. They studied the effect of concrete properties and head size on the anchor behaviour. They stated that the failure of the headed stud is induced by circumferential concrete cracking, while the displacement at failure load is induced by the concrete compression behaviour under the head. As the anchor head increased from 35 mm to 52 mm, the average compression stress under the anchor head decreased and this resulted in small displacement under the anchor head. Hence, the smaller the head diameter the larger displacement at failure (Ozbolt and Eligehausen, 1990).

Jang and Suh (2006) investigated the effect of cracks on the anchorage capacity for cast-in-place anchors subjected to tensile load. Influence of crack depth, crack width, and distance between the cracks and the anchor was studied. The authors found that brittle failure of cracked concrete propagated the cracks faster than for anchors in uncracked concrete. The authors concluded that anchorage in uncracked concrete has higher capacity than that obtained from anchorage in cracked concrete. The authors found that, a side crack (far from the anchor) has more effect on anchorage capacity than central cracks (passing through the anchor). They stated that the crack depth and the distance between the anchor and the cracks has more influence on the anchorage capacity compared to the crack width (Jang and Suh, 2006).

Hashimoto and Takiguchi (2004) investigated the strength of cast-in-place anchor embedded 30 mm in concrete and subjected to tensile load under high temperature. Results

of their study show that, the increase in the temperature decreases tensile strength (Hashimoto and Takiguchi, 2004).

Fuchs et al. (1995) proposed Concrete Capacity Design (CCD) Method to predict failure loads of cast-in-place and post-installed anchors subjected to static tensile and shear loads. Fuchs et al. compared the results of the proposed CCD method with ACI 349-85. The authors investigated the effect of edge distance, anchor spacing under tensile and shear loads. They concluded that the CCD method gives accurate results of the failure load, while the ACI method can give conservative results for the failure load when the anchors are embedded into concrete with small edge distance or unconservative results for the failure load when the edge distance is large and for deep embedment depth anchors. The size of the concrete cone breakout for the shear loading is calculated based on the edge distance, while for the tensile loading it is calculated based on the anchor depth. The anchor diameter and stiffness were found to have an effect on the failure load of the anchors (Fuchs et al., 1995).

Nilforoush et al. (2017 and 2018) investigated the tensile behaviour of cast-in-place anchors embedded into plain and fibre reinforced concrete. The authors investigated the effect of concrete thickness and adding steel fibres on the anchor capacity and failure mode. They found that the increase in the concrete thickness exhibited a slight increase in the anchor capacity. Also, the authors observed that adding steel fibres to the concrete increased the tensile capacity (Nilforoush et al., 2017; Nilforoush et al., 2018). Nilforoush et al. (2017) found that the anchorage tensile capacity and stiffness increased with the

increase in the concrete compressive strength. Concrete cone breakout failure was observed for the anchors embedded in plain concrete while concrete splitting was observed for the anchors embedded in thin plain concrete members (Nilforoush et al., 2017). In addition, Nilforoush et al. (2018) investigated the effect of anchor head size on the tensile capacity of the cast-in-place anchors. The authors found that the increase in anchor head size resulted in a significant increase in the tensile capacity and anchor stiffness (Nilforoush et al., 2018).

Hariyadi et al. (2017) investigated the pullout capacity of anchors embedded in concrete and subjected to static pullout loads. The authors conducted experimental work on anchors with shallow embedment depth (embedment depth-to-diameter ratio is equal to 3.5) and observed combination of cone breakout and bond failure mode. The authors obtained lower tensile capacity from the experimental results in comparison with the concrete cone method (CCM) and concrete capacity design method (CCD). The authors obtained cone breakout angle in the range of 15° to 23° (Hariyadi et al., 2017).

2.5.2 Cast-in-place anchors under shear load

Shear strength of anchors embedded in concrete has been investigated experimentally by Ueda et al. (1990). The authors observed concrete failure with wedge cone for most of the tested specimens. The authors concluded that an increase in edge distance increases the shear strength of single and double anchors embedded in concrete. They also found that the shear strength for double anchors increased with the increase in anchor spacing (Ueda et al., 1990).

In another study, Ueda et al. (1991) investigated the shear strength of steel anchor groups. The authors applied shear loads parallel and perpendicular to the edge and observed that the increase in the spacing for double anchors increased the shear capacity in the parallel and perpendicular directions to the edge. Similar observation was obtained for the adhesive anchors by Eligehausen et al. (2006) when the load was applied perpendicular to the edge (Eligehausen et al., 2006). Ueda et al. (1991) and Eligehausen et al. (2006) stated that there is a critical edge distance when the load is applied perpendicular to the edge after which the value of failure load remain constant (Eligehausen et al., 2006, Ueda et al., 1991). Ueda et al. suggested empirical equations to determine the ultimate shear strength for single and grouped anchors involving two or four anchors (Ueda et al., 1991).

Performance of cast-in-place anchors with large diameters (more than 50 mm), large edge distances and deep embedment depths (more than 635 mm) subjected to shear load was investigated by Lee et al. (2011). The authors made an assessment of the methods available for predicting the capacity of anchorage systems and applied them to large anchor diameters and deep embedment depths. Based on the results, the authors concluded that current prediction methods are unsuitable for large anchors with large edge distance and deep embedment depths. The authors reported that the capacity of large anchor diameters and deep embedment depths, was overestimated by the CCD method (Lee et al., 2011).

Hawkins (1987) investigated the strength of cast-in-place headed anchors embedded in reinforced concrete and subjected to static shear loading. The author stated that the increase

in concrete compressive strength increased the ultimate shear capacity significantly (Hawkins, 1987).

Gross et al. (2001) investigated the behaviour of single and double cast-in-place, undercut and expansion anchors under static and dynamic shear loading. The anchors were installed with limited edge distance. The authors reported that the shear capacity under dynamic loading is higher than that under static loading for the anchors they tested. They also observed that the shear capacity in cracked concrete increased under dynamic loading and decreased under static loading. The authors concluded that when anchor spacing for double anchors is equal to or more than two times the embedment depth, the shear capacity of the two-anchor group is equal to the sum of the individual anchor capacities (Gross et al., 2001).

Statistical analysis on concrete breakout capacity for anchors subjected to static and dynamic shear loading has been conducted by Muratli et al. (2001). The authors compared the results of the ACI method, CCD method, and a regression analysis on the variation of CCD method. The authors used Monte Carlo analysis to predict the probability of failure of steel anchor systems including cast-in-place, undercut, expansion, and sleeve anchors. An increase of 20% in anchor capacity under dynamic loading in comparison with static capacity was reported by the authors. The shear breakout capacity of cast-in-place anchors was observed to be 10% higher than that for the post-installed anchors. The authors assessed the accuracy of ACI and CCD method using probability of failure and found that steel anchorage systems designed in accordance with CCD method has lower probability

of failure than that designed in accordance with ACI method (Muratli et al., 2001). The authors also concluded that the CCD method is more accurate and thus more suitable for predicting the shear breakout capacity than the ACI method (Muratli et al., 2001; Muratli et al., 2004).

Petersen et al. (2013) investigated the shear behaviour of cast-in-place anchors subjected to seismic loading experimentally and numerically using ABAQUS finite element software. The authors investigated the exposed anchor length for the anchors of fixed ends and for the anchors of limited end rotations of 7° and 14° . Where the exposed length is the distance between the surface of the concrete and bottom edge of loading plate. The anchors were placed in oversized hole of 3 mm larger than the anchor diameter in a thick load plate and fixed plate. The thick load plate is the plate where the load is applied, while the fixed plate is the plate where the anchor is fixed. The oversized holes of the thick fixed plate and load plate allow 7° and 14° anchor end rotations respectively. The authors stated that the exposed length has an influence on the failure mode. Shear failure mode was observed for the specimens with exposed length of $0.2d$, while flexural dominant deformations were observed for the exposed length of $2d$, where d is the anchor diameter. Strain hardening was observed for the exposed length of $4d$, where the stiffness was increased at larger displacement. Also, the authors reported that the limited end rotation increases the ultimate shear strength and stiffness of the specimens and that the increase in the exposed length up to $4d$ resulted in decrease of the ultimate shear load. No further decrease in the shear load was observed for anchors with larger exposed lengths than $4d$ (Petersen et al., 2013).

Zhao (2014) studied the behaviour of single cast-in place anchors in tension and shear installed in plastic hinge zone of concrete column. The author proposed anchor reinforcement in seismic zone to enhance the behaviour of anchors by providing protection to the concrete around the anchors. The author observed concrete spalling and cracking in the seismic zone, however, the anchor failure was due to ductile steel failure. The author concluded that the confined concrete in the plastic hinge zones can improve the performance of the anchorage system. The author stated that the anchor reinforcement play a role in carrying the load from the anchor and protecting the core concrete around the anchor from crushing and spalling (Zhao, 2014).

Jebara et al. (2016) conducted experimental work to investigate the pryout mechanism for cast-in-place welded stud subjected to shear load. They assumed pryout mechanism for cast-in-place welded studs as a pseudo-tension breakout induced by two forces: the tensile force in the stud and compression force in the plate. The authors assumed triangular compression stress distribution along the embedment depth in front of the stud. They found that the ultimate shear load increases with the increase in the anchor diameter. The increase in the anchor diameter increases the stiffness and resistance. Furthermore, the authors found that the increase in the concrete pryout capacity is proportional to the square root of the stud diameter. The authors proposed equations to calculate the pryout capacity for welded stud embedded in normal concrete and subjected to shear load (Jebara et al., 2016).

2.6 Adhesive anchors

The use of adhesive anchors has gained popularity in the past decades due to the fast curing time in comparison with grouted anchors and their associated superior cost-effectiveness (Upadhyaya & Kumar, 2015). Furthermore, the use of adhesive anchors is very common compared to other types of post installed anchors due to the flexibility of adhesive anchors in installation (Cattaneo and Muciaccia, 2015; Cook, 1993). Experimental and numerical work has been conducted by several researchers to investigate the behaviour of adhesive anchors under different loading conditions and the results of these tests are summarized in the following sections.

2.6.1 Adhesive anchors under tensile load

Epacakchi et al. (2015) and Eligehausen et al. (2006) investigated the pullout behaviour of single and group adhesive anchors. The authors studied the influence of anchor spacing on the failure mode of adhesive anchors. Epacakchi et al. (2015) used single anchors and groups of 4, 6, and 9 anchors. Anchor diameter of 20 mm with embedment depth of 200 mm and anchor spacing of 150 mm and 200 mm were investigated. Epacakchi et al. (2015) observed combined cone-bond failure and steel fracture for the single anchor and concrete cone breakout failure for the groups of 4 anchors while combined cone-splitting failure was observed for the groups of 6 and 9 anchors. In the combined cone-splitting failure, splitting cracks formed in the concrete after formation of the concrete cone breakout. The authors found that the decrease in anchor spacing decreased the tensile strength of group anchors (Epacakchi et al., 2015). Similar observation was reported by Li et al. (2002) for the quadruple anchor fastening. Eligehausen et al. (2006) observed that concrete breakout cone

is initiated at the base of the anchor and propagated along the embedment depth for the anchor spacing $s = 4d$, while concrete breakout cone is initiated near the surface of the concrete for the anchor spacing $s = 8d$, and that the failure of anchor groups is similar to that of single anchor for the large spacing distance of $s = 16d$ where combined cone bond failure is observed for the deep embedment depths. Eligehausen et al. (2006) obtained concrete cone breakout failure for the high bond strength, when the mean bond strength (τ) was equal to maximum mean bond strength (τ_{max}), while pullout failure is obtained for the very low bond strength ($\tau \leq 0.3 \tau_{max}$). The authors reported that the critical spacing and critical edge distance were influenced by the bond strength and anchor diameter (Eligehausen et al., 2006).

Cook et al. (1998) and McVay et al. (1996) studied the behaviour of single adhesive anchor embedded in uncracked concrete subjected to tensile load. The authors designed models for single adhesive anchor and compared it with the worldwide database of anchor test results (Cook et al., 1998; McVay et al., 1996). Cook et al. (1998) stated that the design model based on a uniform bond stress showed good agreement with the non-linear analytical studies and the results from the worldwide database with an error of about 3% (Cook et al., 1998). McVay et al. (1996) stated that the use of the uniform bond stress model will reduce the error to less than 4% (McVay et al., 1996).

Cook et al. (1998), McVay et al. (1996) and Cattaneo and Muciaccia (2015) observed three types of failure for the adhesive anchors: concrete cone breakout failure, steel failure and combined cone-bond failure (Cook et al., 1998; McVay et al., 1996; Cattaneo and

Muciaccia, 2015). Concrete cone breakout failure occurred for shallow embedment depth anchors (Cook et al., 1998). Steel failure induced by yielding and fracture of the steel anchor occurred for deep embedment depths where the tensile strength of the steel anchor is less than the strength of the embedded part of the anchor in the substrate (Cook et al., 1998; Cook, 1993). Combined cone-bond failure characterized by shallow concrete cone breakout at the upper embedded part of the anchor with bond failure at the lower embedded part of the anchor. In addition, Cook et al. (1998) and McVay et al. (1996) observed bond failure when the strength of the bond surface was small, as in the case of inadequate curing or improper hole preparation. The bond failure may occur either at steel-adhesive interface or at concrete-adhesive interface or at both interfaces (Cook et al., 1998).

Li et al. (2002) studied the failure mode for the adhesive anchors subjected to tensile loading. The authors observed concrete cone breakout failure for quadruple adhesive anchors with embedment depth less than or equal to 96 mm and small spacing, while combined cone-bond failure was observed for the large embedment depth. Pullout failure was observed for the quadruple adhesive anchors with large spacing (Li et al., 2002).

Cattaneo and Muciaccia (2015) investigated the behaviour of adhesive anchors in normal and two high performance concretes (concrete compressive strength of 75 MPa and 90 MPa) under tensile load. The authors studied the effect of embedment depth and steel fibres on the behaviour of adhesive anchors. Anchor diameter of 12 mm with embedment depths of 50 mm, 75 mm and 110 mm were investigated. The authors found that the ultimate tensile load was increased by adding steel fibres to the concrete. Adding steel fibre to the

concrete resulted in combined concrete cone-bond failure mode for the embedment depth of 50 mm. They obtained brittle/ductile failure mode for the adhesive anchors in high performance concrete and brittle failure mode for the adhesive anchors in normal concrete. They concluded that the fibre reinforced concrete is a viable alternative when there is a need to use short anchor spacing, edge distance and thinner member (Cattaneo and Muciaccia, 2015).

Yilmaz et al. (2012) investigated the behaviour of post-installed anchors embedded in low strength concrete under tensile load. The authors compared the results of the failure loads with the ACI 318 code and reported that the ACI 318 code overestimates the anchor strength in comparison with experimental data for low strength concrete. They observed that the failure mechanism depends on the concrete strength and edge distance for the anchors having an edge distance ≥ 15 times the anchor diameter (Yilmaz et al., 2013).

Upadhyaya and Kumar (2015) introduced analytical model to predict the pullout capacity of adhesive anchors. The authors investigated the effect of material properties and design parameters (embedment depth, adhesive thickness and the relative stiffness between the steel anchor and the adhesive) on the pullout capacity of adhesive anchors. The authors stated that, using stiff anchor, the anchor can sustain higher loads before bond failure, where the adhesive layer is subjected to lower stresses. The authors investigated embedment depths in the range from 40 mm to 1000 mm and adhesive thickness in the range from 0.25 mm to 1.25 mm. The authors concluded that the adhesive anchor load capacity increased with the increase in the embedment depth until a critical embedment

depth was reached where no further increase in the anchor capacity was observed as the failure was governed by steel fracture. Also, they concluded that increase of the thickness of the adhesive layer from 0.25 mm to 1.25 mm decreases the peak stresses in the adhesive layer. The authors compared the analytical results with finite element analyses results using ABAQUS finite element analysis (FEA) package and reported good agreement (Upadhyaya and Kumar, 2015).

Cook et al. (1993) investigated the behaviour of adhesive anchors with embedment depths of 100 mm, 150 mm and 200 mm under tensile loading. The authors used fully bonded and partially bonded adhesive anchors. A debonding agent was placed at the top 50 mm of the embedment depth for the partially bonded adhesive anchors. The authors found that the fully bonded anchors fail either by steel anchor failure or by concrete cone breakout with the adhesive pullout, while partially bonded anchors failed by steel anchor failure or adhesive bond failure. They obtained similar failure behaviour for the fully bonded double anchors as single anchors. They found that the strength of fully bonded anchors and partially bonded anchors is nearly equal at the same embedment depth (Cook et al., 1993).

Sato et al. (2004) and Fujikake et al. (2003) investigated the pullout behaviour of adhesive anchors subjected to loading rates ranging from 1×10^{-1} kN/s to 4×10^4 kN/s. The authors found that the increase in the loading rate increases the failure load for bond failure of the adhesive anchors (Sato et al., 2004; Fujikake et al., 2003). Sato et al. concluded that the embedment depth has no influence on the average dynamic bond strength for the same loading rate. The authors observed bond failure at the concrete/adhesive interface at all

loading rates tested (Sato et al., 2004). Fujikake et al. (2003) reported that bonding agent has significant effect on the performance of adhesive anchors subjected to static loading. This effect of bonding agent is probably applicable for dynamic loading condition (Fujikake et al., 2003).

Zamora et al. (2003) investigated the behaviour of single, headed and unheaded, grouted anchors subjected to static tensile load. Results of their study show identical behaviour for the adhesive and grouted unheaded anchors. Also, identical tensile behaviour was found for the headed grouted and cast-in-place anchors. The authors concluded that bond failure at the steel-grout interface is the predominant failure for the unheaded grouted anchors. However, bond failure may also occur at the grout-concrete interface. Concrete breakout cone failure or bond failure at the grout/concrete interface was observed for the headed grouted anchors. They found that the nominal bond stress at the steel-grout and concrete-grout interfaces are important to identify the interface at which the bond failure occurred. The embedment strength is thus controlled by the lowest bond strength of the two interfaces (Zamora et al., 2003).

Braimah et al. (2009) investigated the behaviour of adhesive steel anchors embedded into concrete and limestone substrates and subjected to impulsive loading. The authors found that the substrate material has an influence on the failure mode. Steel failure was observed for the concrete substrate, while steel failure and limestone failure were observed for the anchors embedded into limestone substrate at similar embedment depths. The authors investigated the effect of penetration angle on the dynamic increase factor (DIF). The

authors found that the DIF for the substrate penetration angle of 45° is higher than that of 90° penetration angle. The authors recommended DIF of 1.2 for the adhesive anchor of 90° penetration angle for both concrete and limestone substrates, while they recommended DIF of 2.5 and 3.2 for the adhesive anchor of 45° penetration angle for the limestone and concrete substrates, respectively (Brimah et al., 2009). In another study, Brimah et al. (2014) carried out impact test on the adhesive anchors embedded into concrete masonry and clay brick substrate. The authors recommended DIF of less than one for the adhesive anchor subjected to high strain rate and embedded into clay brick, and DIF greater than one for the adhesive anchor embedded into concrete masonry (Brimah et al., 2014).

Zhao et al. (2015) investigated the pullout behaviour of anchorage body under different loading rates using practical flow code (PFC) numerical software, where the anchorage body consists of the anchor, bonding materials and the concrete matrix. Loading rates in the range between 0.5 mm/s to 1000 mm/s corresponding to strain rates in the range from 10^{-5} s^{-1} to 10 s^{-1} were investigated. The authors studied the interfacial shear stress distribution along the anchorage embedment depth and the failure mode of the anchors. They observed irregular distribution of the axial force and interfacial shear stress. As the loading rate increases, the axial force and interfacial shear stress increase in the upper anchorage section. No clear increase of the axial force and interfacial shear stresses in the lower anchorage section was observed. The authors proposed a linear relationship between the pullout failure load and the loading rate. The authors obtained three failure modes for the anchorage substrate matrix: matrix cracking in addition to a main crack along the bottom matrix at loading rates less than 10 mm/s, crack propagation in the upper portion

of the matrix with the main crack along the bottom matrix for the loading rates greater than 10 mm/s, pullout failure accompanied by large fracture area at loading rates greater than 100 mm/s where the cracks propagated in the middle and top part of the bolt resulted in large fracture area. The authors attributed this failure mode at high strain rates to the breakage of the bond between the matrix and the anchors resulting from high stress concentration along the top part of the anchorage section (Zhao et al., 2015).

Kim et al. (2013) performed experimental tests and finite element analysis on the tensile behaviour of post-installed anchors. They studied the effect of torque ratio, embedment depth and anchor diameter on the tensile strength. The authors applied torque ratios of 30%, 50% and 70% of the total torque to tighten the nut during anchor installation. Where, the torque ratio is the ratio between the applied torque to the total torque that can be applied on the anchor. The authors used anchor diameters of 10 mm and 12 mm with embedment depths of 50 mm and 100 mm. They concluded that the tensile strength is dependent on the torque ratio, embedment depth and anchor diameter. The authors stated that, the maximum load capacity for tensile tests increase with the increase in the embedment depths. The authors stated that the finite element model using ABAQUS is suitable to predicting the failure load (Kim et al., 2013).

Mahrenholtz and Eligehausen (2015) investigated the behaviour of post-installed anchors under tensile and shear loads for safety relevant applications such as nuclear power plant. The authors observed concrete breakout failure and steel anchor failure for the tensile and shear tests, respectively for the tested post-installed anchors. They also observed that the

ultimate tensile load decreased slightly in cracked concrete. They obtained linear relationship between the displacement and cyclic loading. They found that increasing the number of load cycles increases the displacement. At the beginning of cyclic loading, large initial displacement is observed followed by a slight increase in displacement. They related the increase in the displacement to hole clearance, therefore, they suggested that a proper filler has to be used to fill the gap (Mahrenholtz and Eligehausen, 2015).

González et al. (2018) studied the tensile behaviour of post-installed (adhesive and grouted) anchors at different construction conditions. The authors used conventional (vibrated concrete) and self-compacting concrete. The authors investigated several factors such as type of hole drilling machine, type of filling material, hole condition (moisture and cleanliness) and condition of installation. The authors found that the capacity of the anchor is influenced significantly by the installation condition and the drilling machine. Also, the authors found that the hole condition has an influence on the anchor capacity (González et al., 2018).

2.6.2 Adhesive anchors under shear load

Caliskan et al. (2013) performed cyclic shear test on adhesive anchors embedded in low strength concrete of 5.9 MPa and 10.9 MPa. The authors used three anchor diameters of 12 mm, 16 mm and 20 mm and three embedment depths for each anchor diameter (d). Embedment depths of $10d$, $15d$ and $20d$ were investigated. The authors found that the shear strength decreased significantly for anchor diameter more than 16 mm embedded into low strength concrete. Also, the authors concluded that there is no influence on the shear

capacity of the anchors when the embedment depth was larger than 10 times the anchor diameter (Çalışkan et al., 2013).

Shear behaviour of adhesive anchors in normal and high performance concretes was investigated by Cattaneo and Muciaccia (2015). The authors studied the effect of edge distance and the effect of using steel fibre reinforced concrete on the behaviour of adhesive anchor concrete system. The authors reported increase in failure load with increase in the edge distance of adhesive anchors subjected to shear loading. Adding steel fibres to the concrete increased the ultimate shear load. The addition of steel fibres to the concrete affect the failure mode when the edge distance increased from 40 mm to 55 mm, where the failure mode changed from concrete breakout to steel failure at the edge distance of 55 mm (Cattaneo & Muciaccia, 2015).

Kim et al. (2013) performed experimental tests and finite element analysis on the shear behaviour of post-installed anchors. They studied the effect of torque ratio, embedment depth and anchor diameter on the shear strength. They concluded that the shear strength is dependent on the embedment depth and anchor diameter and not on the torque ratio. The authors stated that, the maximum load capacity for shear tests increase with the increase in the embedment depth (Kim et al., 2013).

Lou and Perciballi (2008) performed three point bending test on beam with bolts at the end supports. Static loads were applied on bolts with and without preloading using LS-DYNA and NEi Nastran software. The authors used preloaded bolts to ensure that the anchor will

not fail and prevent connection separation. The authors stated that the bolts can be under tensile, shear or combined tensile and shear loads in service. The shear load on the bolts generated from joint slip or friction. Failure was analyzed using the two software programs. They observed less deformation in the beam when using preloaded anchors subjected to static loads. Higher failure loads were obtained for the preloaded bolts compared to that without preload. Quite similar results were obtained from the two software programs (Lou and Perciballi, 2008).

Epackachi et al. (2015) investigated the shear behaviour of single and group of adhesive anchors. Embedment depth of 200 mm, anchor spacing of 150 mm and 200 mm were investigated. The authors stated that the shear strength of the adhesive anchors is not affected by the anchor spacing. The results show that, the shear strength of group of anchors can be determined by multiplying the shear strength of one anchor by the number of anchors for the spacing ranging from 150 mm to 200 mm. Steel failure and concrete bearing failure were observed for the tested adhesive anchors (Epackachi et al., 2015).

2.7 Undercut anchors

2.7.1 Undercut anchors under tensile load

Primavera et al. (1997) investigated the tensile behaviour of undercut anchors in high strength concrete. Anchor embedment depth of 203 mm was investigated. The authors obtained shallow concrete cone breakout for the tested anchor. The authors found that the increase in the concrete compressive strength increased the pullout capacity. The authors compared the pullout capacity with the ACI and CCD methods and reported that the CCD

method underpredicted while the ACI method overpredicted the pullout capacity of the undercut anchor (Primavera et al. 1997).

Ashour and Alqedra (2005) investigated the pullout capacity of post installed (expansion and undercut) anchors using neural network modelling under static tensile load. The authors compared the neural network results with previous experimental results and they found it to be in good agreement. The authors found that the pullout capacity for the post-installed anchors is influenced by the anchor embedment depth (Ashour & Alqedra, 2005).

Marcon et al. (2018) investigated the influence of the aggregate on the tensile capacity of the undercut anchors subjected to static load. The authors used three mixes of the concrete depending on the type, size and mechanical properties of the aggregate. Undercut anchors embedded in concrete at age of 28 days and 70 days were investigated. The authors stated that the size of coarse aggregate has an effect on the concrete properties and tensile capacity of the undercut anchors. However, the influence of the aggregate is within the range of the predictive equations results. Also, the authors concluded that the tensile capacity of the anchors embedded in concrete at age of 70 days is higher than that for the anchors embedded in concrete at age of 28 days (Marcon et al., 2018).

Rodriguez et al. (1997) investigated the behaviour of the post-installed (expansion and undercut) anchors in concrete subjected to static and dynamic tensile load. The authors calculated the normalized tensile capacity of the undercut and grouted anchors considering the failure mode is concrete cone breakout. They concluded that the normalized tensile

capacity under dynamic load increased 30% compared to the normalized capacity under static load (Rodriguez et al., 1997).

2.7.2 Undercut anchors under shear load

Mahrenholtz and Eligehausen (2013) investigated the qualifications of the undercut anchors in nuclear power plants subjected to seismic dynamic tensile and shear loads. Two conditions, service condition and extreme cracked condition, were investigated. The authors found that the seismic dynamic load increased the cumulative displacement of the anchor causing steel failure (Mahrenholtz & Eligehausen, 2013). In another research, Mahrenholtz and Eligehausen (2015) applied cyclic tension and shear loads on the undercut anchors used for nuclear power plants and reported that crack widths affected the strength of the anchors when subjected to tensile loading and no significant influence on the anchor strength under shear loading. The authors observed concrete failure mode under cyclic tensile loading and steel fracture failure mode under cyclic shear loading (Mahrenholtz & Eligehausen, 2015).

Eligehausen et al. (1998) investigated the behaviour of post-installed anchors in cracked and uncracked concrete. The post installed anchors investigated were torque controlled expansion, displacement-controlled expansion (drop-in), undercut and adhesive anchors. The authors found that the capacity of the anchors decreased in the cracked concrete. The reduction in the capacity for the displacement-controlled expansion (drop-in) anchors is higher than the undercut anchors and torque controlled expansion anchors. Undercut anchors, adhesive anchors and properly designed torque controlled expansion anchors are

suitable to install in cracked concrete where the tensile load can be transferred to the concrete (Eligehausen et al., 1998).

2.8 Strain rate effect on material properties

2.8.1 Effect of strain rate on concrete

The level of the strain rate applied on concrete structures has an effect on its capacity. Static loading is obtained at a strain rate ranging from 10^{-6} s^{-1} to 10^{-5} s^{-1} . Low dynamic loading and earthquake results in strain rates ranging from 10^{-4} s^{-1} to 10^{-1} s^{-1} . Impact loading results in strain rate in the range between 10^0 s^{-1} to 10 s^{-1} , while very high strain rate ranging from 10^2 s^{-1} to 10^3 s^{-1} can be achieved with blast loading (Bischoff and Perry, 1991).

Different testing machines can be used to apply various loading conditions on concrete structures at different levels of strain rates. Hydraulic testing machine can be used to apply static load at strain rate of 10^{-5} s^{-1} to 10^{-1} s^{-1} . Charpy impact testing machine can be used to apply dynamic load at strain rate up to 10^0 s^{-1} , while strain rate up to 10^1 s^{-1} can be achieved by using drop weight impact. Higher strain rates up to 10^2 s^{-1} can be reached by using Split Hopkinson Pressure Bar. Strain rates equal or higher than 10^3 s^{-1} can be obtained using explosive charges (Bischoff and Perry, 1991; Hentz et al., 2004).

Effect of strain rate on the strength of concrete has been investigated by several researchers (Malvar and Crawford, 1998; Malvar and Ross, 1998; Bischoff and Perry, 1991; Georgin and Reynouard, 2003; Hentz et al., 2004; Ross et al., 1995; Fu et al., 1991; Shkolnik, 2008; Min et al., 2014; Park et al., 2001; Cadoni et al. 2001; Tedesco et al. 1994; Ross et al. 1996;

Rossi et al. 1994). The authors found that the increase in the strain rate increases the tensile and compressive strength of concrete.

Ross et al. (1989) investigated the behaviour of concrete and mortar subjected to quasi-static and dynamic loads at strain rate in the range between 10 s^{-1} to 10^2 s^{-1} . The authors observed similar failure for the quasi static and dynamic tensile test. They concluded that both tensile and compressive strengths increase at high strain rate. However, the increase in the tensile strength at high strain rate is larger than that for the compressive strength. They found that the tensile strength of the mortar at high strain rate of 10^2 s^{-1} is equal to three times that obtained from quasi-static load while it is equal to six times that obtained from quasi-static load when using concrete substrate (Ross et al. 1989).

Ross et al. (1995), Georgin and Reynouard (2003) and Min et al. (2014) conducted numerical analysis on the effect of strain rate on the strength of the concrete. The authors observed that the increase in the strain rate increases the concrete compressive strength. Georgin and Reynouard (2003) attributed the increase in the compression strength of concrete at high strain rates to the inertial force, the inertial confinement, structural effect and rate effect (Georgin and Reynouard, 2003). Ross et al. (1995) found that the increase in the strain rate from 10^{-7} s^{-1} to 300 s^{-1} increases the tensile and compressive strength of the concrete. However, there is a critical value of strain rate of 5 s^{-1} for the tensile strength and 60 s^{-1} for the compressive strength at which the percentage increase in the tensile strength of the concrete becomes higher than the percentage increase in the compressive strength. When the strain rate exceed the critical value, the strength of the concrete is

significantly increased. Ross et al. (1995) also investigated the effect of strain rate on wet, partially wet and dry concrete. The authors found that the wet and partially wet concretes are more sensitive to high strain rate than the dry concrete (Ross et al., 1995). Similar observation was obtained by Ross et al. (1996), Reinhardt et al. (1990) and Rossi et al. (1994). The increase in the sensitivity in wet concrete is due to the existence of water in the wet concrete (Ross et al., 1996; Reinhardt et al., 1990; Rossi et al., 1994).

Min et al. (2014), Malvar and Crawford (1998), Hentz et al. (2004) and Shkolnik (2008) found that the strain rate sensitivity on the tensile strength of the concrete is higher than that on the compressive strength. A relationship between DIF and strain rate was introduced by Min et al. (Min et al., 2014). Malvar and Crawford (1998) stated that the DIF is very important in the design of structures subjected to high strain rates and can be expressed as a bilinear function of the strain rate. The authors obtained DIF greater than 2 and 6 for the concrete subjected to compression and tension loads, respectively (Malvar and Crawford, 1998). Moreover, Rossi et al. (1994) found that the DIF for wet concrete is higher than that obtained for the dry concrete (Rossi et al., 1994).

Hentz et al. (2004) and Shkolnik (2008) investigated the effect of strain rate on the modulus of elasticity of concrete under tensile and compressive loading. The authors found that the modulus of elasticity increased with the increase in the strain rate (Hentz et al., 2004; Shkolnik, 2008). Similar observation was obtained by Rossi et al. (1994) for the effect of strain rate on the modulus of elasticity of the wet concrete under tensile loading (Rossi et al., 1994). Shkolnik (2008) obtained linear relationship between the stress and the strain of

concrete at high strain rate of 150 s^{-1} (Shkolnik, 2008). Hentz et al. (2004) observed that the strain rate has less effect on the Poisson's ratio, energy absorption and strain at ultimate strength of the concrete compared to the tensile and compressive strengths (Hentz et al., 2004).

Park et al. (2001) conducted finite element analysis on the behaviour of concrete and mortar under high strain rate of 10^4 s^{-1} . The authors observed inelastic deformation in the mortar with less inelastic strains in the aggregates under impact loading. They stated that the increase in the aggregate volume fraction to 42% increases the strength of the concrete by 30% and increases the energy absorption 15% (Park et al., 2001). The finite element modelling can predict the material response and provide an assessment to the strain rate effect (Ross et al., 1995; Georgin and Reynouard, 2003).

Tedesco et al. (1994) performed finite element analysis on the concrete subjected to compression load. The authors stated that the type of failure depends on the strain rate. At strain rate of 17 s^{-1} no cracking was observed. At strain rate of 25 s^{-1} cracking initiated which led to compression failure of about 35% of the concrete specimen. Strain rate of 200 s^{-1} resulted in about 85% concrete compression failure (Tedesco et al., 1994).

Bischoff and Perry (1991) investigated effect of concrete quality, water cement ratio, aggregate type, aging and curing time on concrete compressive strength at low and high strain rates. The authors observed that the increase in compressive strength of lower compressive strength concrete is greater than that for higher compressive strength concrete

at high strain rate. The effect of the strain rate on the compressive strength is influenced by type of aggregate; stiffer aggregate is less sensitive to strain rate. Aggregates of good bond and smaller maximum size enhanced the concrete compressive strength at high strain rate. Also, the authors found that the compressive strength of concrete is affected by the method of curing and moisture content. Cured wet specimen exhibits higher compressive strength than the wet specimen. The increase in the age of the concrete shows less sensitivity to the increase in the strain rate (Bischoff and Perry, 1991).

Fu et al. (1991) investigated the effect of loading rate on reinforced concrete. They observed 30% increase in the strength of the reinforced concrete at high loading rate; the yield strength of the steel is also increased. The failure mode is affected by the loading rate. At high loading rate the tensile and bond strength of concrete increase resulted in few cracks and sharp strain gradient. The increase in the bond strength at high loading rate decreased the ductility at failure (Fu et al., 1991).

Cadoni et al. (2001) investigated effect of strain rate on the tensile behaviour of concrete. They applied quasi static tensile loading at strain rate of 10^{-6} s^{-1} and impact loads at strain rates of 10^0 s^{-1} and 10^1 s^{-1} on the concrete at different humidity levels. The increase in the relative humidity of the concrete increases the tensile strength for the impact loading. The tensile strength decreases slightly for the saturated concrete subjected to quasi static load (Cadoni et al., 2001).

Kulkarni and Shah (1998) investigated the effect of high loading rate on concrete beams. They applied static and high loading rates (piston velocity) of 0.00071 cm/s and 38 cm/s respectively. They found that the increase in the strain rate increases the ultimate load and the energy absorption capacity and that the failure mode is influenced by the strain rate. Shear failure mode was obtained for the concrete beam at the static test while flexural failure mode was obtained when similar beams were tested at high strain rate. The difference in the failure mode was attributed to the inertia forces. Flexural failure mode is attributed to yielding of reinforcement, beam rotation, opening up of cracks and reducing compression zone lead to concrete crushing in compression. The post peak behaviour of the load-deflection curve shows a gradual decrease in the load with increase in the deflection. Shear failure mode is attributed to the shear cracks. The post peak behaviour of the load-deflection curve shows a sharp decrease in the load (Kulkarni and Shah, 1998).

2.8.2 Effect of strain rate on steel

The strain rate has an effect on the mechanical properties of the steel material. The yield and tensile strength of the steel increases with the increase in the strain rate (Fu et al., 1991; Yu et al., 2009; Hopperstad et al., 2003), while the Young's modulus remain constant (Fu et al., 1991). This is due to the increase in the deformations and dislocations in the steel structure at high strain rate (Lee et al., 2007). The deformation of the steel material at low strain rate or quasi-static loading is nearly homogeneous and controlled by slip and twin plastic deformation mechanisms. However, the deformation of the steel material at high strain rate is more complicated where the strains extremely concentrated along narrow area called adiabatic shear band. The cracks are initiated and propagated from these shear bands

leading to fracture. At high strain rate the formation of the shear band in steel is affected by several factors such as chemical composition of the steel components, strain rate and heat treatment (Odeshi et al., 2005).

Lee et al. (2007) investigated the fracture response of stainless steel under high strain rate loading. They found that strain rate has an influence on the flow stress-strain behaviour and the microstructure of the specimen. The increase in the strain rate increased the level of deformation of the grain. The authors stated that the adiabatic shear band created plastic instability that leads to fracture (Lee et al., 2007).

Xiong et al. (2009) conducted tensile test of twin induced plasticity (TWIP) steel at strain rate ranging from 10^{-5} s^{-1} to 10^3 s^{-1} . The authors investigated two types of TWIP steel. Each steel type has different chemical composition according to the manganese (Mn) percent in the composition; steel 1[#] (14.3% Mn) and steel 3[#] (25.41% Mn). The authors stated that the tensile properties of steel exhibit strain rate sensitivity. Similar observation was obtained by Xu et al. (2013). In addition, Xiong et al. (2009) found that the yield strength and ultimate tensile strength of the steel 3[#] increased with the increase in the strain rate. The increase in ultimate tensile strength of steel 1[#] was higher than that reported for steel 3[#] (Xiong et al., 2009). On the other hand, Xu et al. (2013) observed no change in the yield strength at strain rate in the range from 10^{-3} s^{-1} to 10^{-2} s^{-1} while a significant increase in the yield strength was observed at high strain rate of 400 s^{-1} (Xu et al., 2013).

Børvik et al. (2003) conducted non-linear finite element analysis using LS-DYNA on smooth and notched axisymmetric specimens of steel to investigate the tensile behaviour under quasi static and high strain rate loading. They concluded that the finite element models have the capability to represent the quasi static and dynamic behaviour of the material and give accurate results (Børvik et al., 2003).

Lee and Lam (1996) investigated the deformation behaviour of AISI 4340 alloy steel at low and high strain rates using Hopkinson pressure bar. They concluded that AISI 4340 alloy steel is sensitive to strain rate. They proposed an equation to predict the relation between the work hardening and strain rate sensitivity (Lee and Lam, 1996).

Yu et al. (2009) studied the effect of strain rate in the range from 10^{-4} s^{-1} to 10^3 s^{-1} on dual phase steel (DP600 steel). The DP600 steel has tensile strength higher than 600 MPa and composed of ferrite and martensite. They found that the mechanical behaviour of the steel is influenced by the strain rate. The authors proposed a new constitutive model to predict the mechanical behaviour of the steel (Yu et al., 2009).

Das et al. (2017) investigated the deformation of micro-mechanisms in dual phase steel at strain rates ranging from 10^{-3} s^{-1} to 800 s^{-1} . The authors used two types of dual phase steel (DP600 and DP800) with different martensite percent. The authors found that the strain rate affects the steel deformation through formation of dislocation cells. The authors stated that the size and the extent of these cells depend on the strain rate and the fraction of

martensite. The size of the dislocation cells become finer as the strain rate increase (Das et al., 2017).

Lu et al. (2013) investigated the effect of strain rate on the fracture surface and tensile behaviour of AISI304 stainless steel in the range from 10^{-4} s^{-1} to 10^{-1} s^{-1} . The authors concluded that the ultimate tensile strength is affected significantly by the strain rate. The increase in the strain rate increased the tensile strength and flow stress. Also, the authors stated that the strain rate has an influence on the fracture surface. Microvoid coalescence is observed at low strain rate, while equiaxed dimple (having equal dimensions in all directions) with narrow diameter is observed at high strain rates (Lu et al., 2013).

2.9 Design methods for anchorage system

There are two common design methods proposed in building codes to predict the tensile and shear capacities of anchorage to concrete system. These methods are: American Concrete Institution (ACI) method (ACI Committee 349, 1990; ACI Committee 318, 2005; ACI Committee 318, 2011), and Concrete Capacity Design (CCD) method (Fuchs et al., 1995).

2.9.1 American Concrete Institute (ACI)

Several versions of ACI code include provision to predict the tensile and shear capacities of anchors. ACI method 349-85 was developed in 1975 (Fuchs et al., 1995) and proposed for the design of nuclear power structures or nuclear safety related concrete structures (Fuchs et al., 1995; Subramanian, 2000). The method assumes that anchor failure is by

steel fracture to provide a ductile failure mode and to improve the design reliability. Brittle failure is avoided by providing deep embedment (h_{ef}) to prevent concrete failure. The concrete capacity is determined by assuming cone failure where the failure surface forms a 45°-cone. The failure load depends on the concrete tensile capacity and increases as a function of a square of h_{ef} (Subramanian, 2000; Rao and Arora, 2013). The proposed equations to predict the tensile and shear capacity of anchorage system based on the ACI method are included in appendices A and B.

2.9.2 Concrete Capacity Design (CCD)

Concrete Capacity Design (CCD) method, which is equivalent to Kappa method in the Eurocode, was proposed in 1995 based on extensive experimental work conducted by Eligehausen (Fuchs et al, 1995). The CCD method depends on fracture mechanics (size effect) theory in predicting the failure load based on 35° failure angle (or concrete cone breakout). The reliance of the CCD method on the fracture mechanics theory is attributed to existence of the high tensile stresses around the anchor head (Cement Association of Canada 2010).

The failure load according to the CCD method increases as a function of $h_{ef}^{1.5}$ (Yoon et al., 2001; Gesoglu et al., 2005; Cement Association of Canada, 2010). Furthermore, the CCD method can be used for cracked and uncracked concrete and can predict the concrete breakout capacity for different anchor types and design cases (Cement Association of Canada, 2010). The proposed equations to predict the tensile and shear capacity of anchorage system based on the CCD method are included in appendices A and B.

Fuchs (2001) carried out extensive comparison between the ACI and CCD methods to predict the failure load of steel anchorage systems. The author investigated the ultimate tensile capacity and shear capacity of steel anchorage systems. Fuchs confirmed that the CCD method is a more accurate method for predicting failure loads of the anchorage system (Fuchs, 2001).

2.10 Anchorage failure modes

2.10.1 Failure modes of cast-in-place anchors under tensile load

When a steel anchor is subjected to tensile loading, five types of failure mechanisms are commonly observed: anchor bolt failure, concrete cone breakout failure, side face blowout failure, concrete splitting, and anchor pullout (Cement Association of Canada, 2010). Anchor bolt failure occurs when the strength of the anchor is less than the applied tensile stress. Concrete cone breakout failure occurs for shallow embedment depths where the applied tensile stress is greater than the strength of the concrete. Side face blowout failure occurs when there is insufficient edge distance. Concrete splitting occurs when the concrete tensile capacity is less than the bolt capacity with insufficient concrete member depth. Anchor pullout failure occurs when the friction between the anchor and the concrete is less than the applied tensile load for the anchors without head (Fuchs et al., 1995; Cement Association of Canada, 2010). Figure 2-5 shows the failure modes for the cast-in-place anchors under tensile loading.

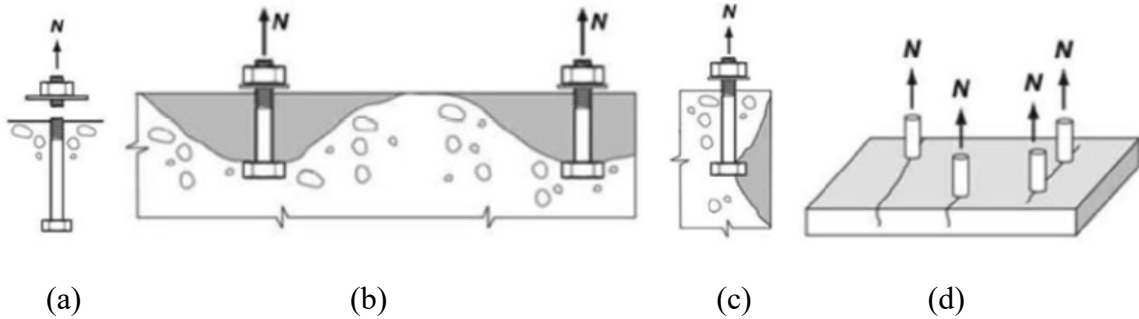
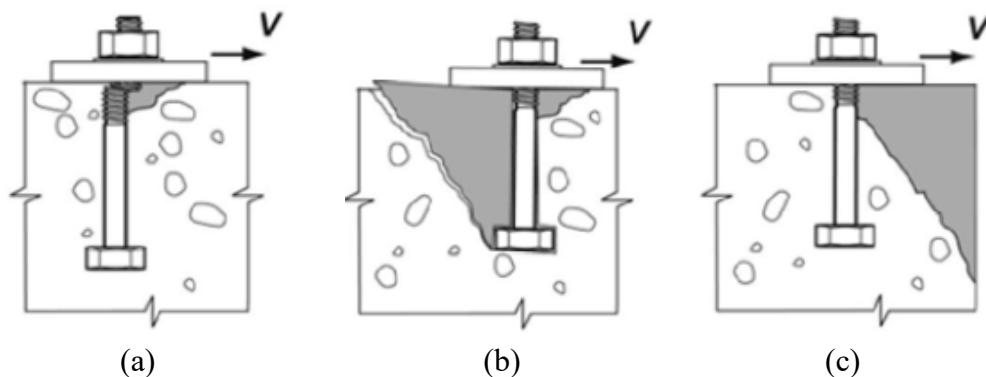


Figure 2-5: Failure modes under tensile loading: (a) steel anchor failure, (b) concrete cone breakout, (c) side face blowout, (d) concrete splitting (Cement Association of Canada 2010; ACI Committee 318, 2011)

2.10.2 Failure modes of cast-in-place anchors under shear load

When a steel anchorage system is subjected to shear loading, three types of failure mechanisms are commonly observed: steel anchor failure, concrete pryout, and concrete breakout (Fuchs et al., 1995; Cement Association of Canada, 2010). Steel anchor failure occurs when adequate embedment is provided without concrete edge effects, while concrete pryout is common in steel anchors without adequate embedment depth and when anchors are placed far away from the concrete free edge (Mahrenholtz & Eligehausen, 2015). Concrete breakout failure (or side blowout) can occur for anchors close to a concrete edge or when insufficient embedment is provided. Figure 2-6 shows the failure modes for cast-in-place anchors under shear load.



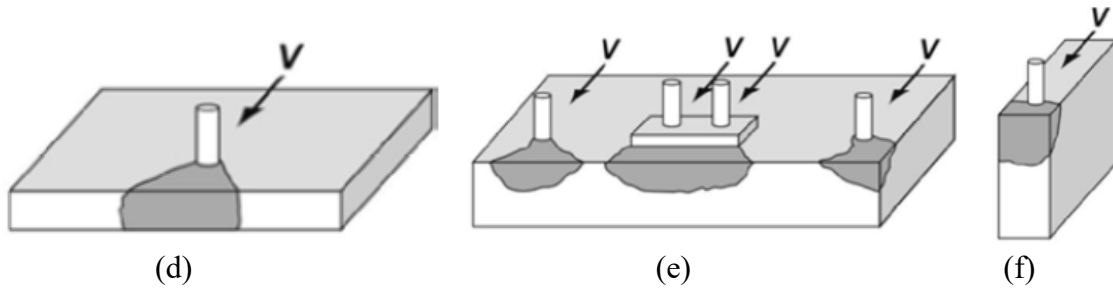


Figure 2-6: Failure modes for anchors under shear load (a) steel anchor failure preceded by concrete spall; (b) concrete pryout failure; (c) concrete breakout failure; (d) thin concrete breakout; (e) edge breakout, corner breakout (f) narrow concrete edge breakout (Cement Association of Canada 2010; ACI Committee 318, 2011)

2.10.3 Failure modes of adhesive anchors under tensile load

There are four types of failure modes that can be seen in adhesive anchorage systems: concrete cone breakout failure, bond failure (including: adhesive-concrete interface, steel-adhesive interface, combined adhesive-concrete and steel-adhesive interface), combined cone-bond failure, and steel anchor failure (Cook, 1993; McVay et al., 1996; Cook et al., 1998). Figure 2-7 shows the failure modes for the adhesive anchors under tensile loading (Cook et al., 1998). Each type of the failure modes is introduced in the following sections.

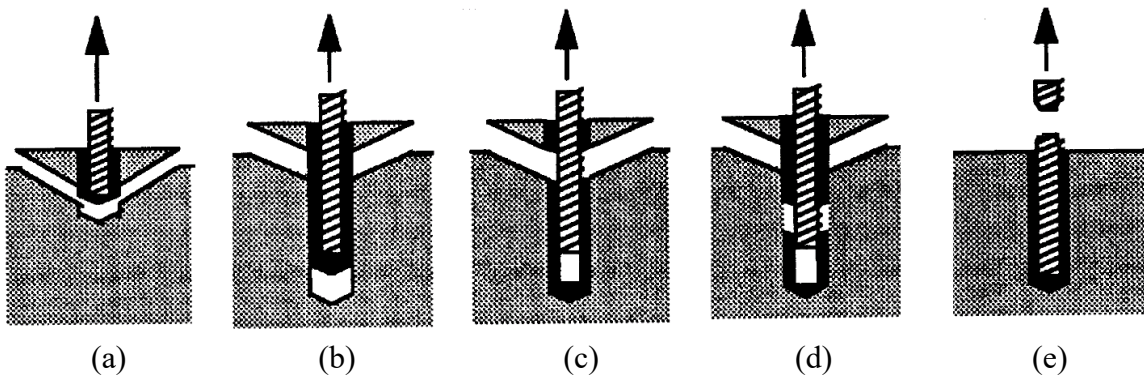


Figure 2-7: Failure modes for adhesive anchors, (a) concrete cone breakout failure; (b) combined cone-bond failure (bond failure at adhesive/concrete interface); (c) combined cone-bond failure (bond failure at steel/adhesive interface); (d) combined cone-bond failure (bond failure at combination of adhesive/concrete and steel/adhesive interface); (e) steel anchor failure (Cook et al., 1998)

2.10.3.1 Concrete cone breakout failure

This type of failure occurs for shallow embedment depths (Cook et al., 1993; Cook, 1993; Gesoglu et al., 2005) (Figure 2-7a). The strength of the concrete and the embedment depth of the steel anchor are the main factors that affect the ultimate failure load (Cook et al., 1998).

2.10.3.2 Bond failure

Bond failure occurs at the interface between the adhesive and the concrete, or at the interface between the steel anchor and the adhesive, or at both of the adhesive-concrete interface and steel-adhesive interface (Figure 2-7). The factors that could cause bond failure are: low bond strength of the adhesive, insufficient curing time, improper hole preparation (Cook et al., 1993).

The ultimate pullout load for bond failure mode at the steel-adhesive interface depends on the bond stress of the adhesive, anchor diameter and embedment depth. There are two models of the bond stresses: uniform bond stress model and elastic bond stress model. The equations to calculate the bond strength according to these two models are presented in Appendix B.

2.10.3.3 Combined cone-bond failure

The combined cone-bond failure is most likely to occur when the embedment depth to the anchor diameter ratio is more than 5 (McVay et al., 1996). The combined cone bond failure is characterized by a shallow cone at the top surface of the concrete accompanied by

adhesive bond failure at the embedded part below the shallow concrete cone breakout (Figure 2-7(b),(c),(d)).

2.10.3.4 Steel anchor failure

This type of the failure is likely to occur for long embedment depth anchors, where the strength of the embedded part of the anchor into concrete is higher than the strength of the steel anchor (McVay et al., 1996; Cook, 1993). The failure occurs by steel yielding and fracture of the steel anchor (Figure 2-7e).

2.10.4 Failure modes of adhesive anchors under shear load

For adhesive anchors subjected to shear loading, three types of failure mechanisms similar to that obtained for the cast-in-place anchors can be observed: steel anchor failure, concrete pryout and concrete breakout (Epackachi et al., 2015). In addition, adhesive bond failure may occur in some areas along the anchor embedment depth associated with the aforementioned failure modes.

2.10.5 Adhesive bond failure

The exposure of adhesive material to temperature, solvents, physical stresses and environment may weaken the adhesive material and cause adhesive failure (da Silva et al., 2011). When cracks occur in the adhesive layer and lead to failure, the failure mode is called cohesive failure. When the cracks appear at the interface between the adhesive material and the adherend, the failure is called adhesive failure (Keller and Vallée, 2005). Mixed mode failure occurs when the cracks are initiated at both of the adhesive layer and the interface.

2.10.6 Failure modes of undercut anchors under tensile load

Three types of failure modes are often observed for the undercut anchor-concrete systems under tensile load similar to that observed for the cast-in-place anchors: concrete cone breakout failure, anchor pullout and steel fracture failure (Cement Association of Canada, 2010; ACI Committee 355, 2000; Eligehausen et al., 1998).

2.10.7 Failure modes of undercut anchors under shear load

Three types of failure modes can be observed for the undercut anchors subjected to shear loads similar to that observed for the cast-in-place and adhesive anchors; pryout failure, concrete breakout and steel anchor failure (Mahrenholtz & Eligehausen, 2015; Epackachi et al., 2015).

2.11 Summary

The literature review presented in this chapter has shown that the behaviour of steel anchorage systems, whether cast-in-place or post-installed, subjected to static and dynamic loads was investigated by several researchers. However, very limited attention has been allocated to these anchors at high strain rates. Hence, for the accurate and economical design of anchorages under impact and blast loading, further investigation of the effects of high strain-rates on anchorage behaviour is required. Based on the literature review presented in this chapter the main gaps in the literature can be summarized as follows:

- Several researchers investigated the tensile behaviour of cast-in-place anchors at different loading rates. Ozbolt et al. (2006) studied the size effect at different loading rate. Fujikake et al. (2003), Sato et al. (2004) and Solomos and Berra (2006)

studied the effect of loading rate for shallow embedment depth anchors. However, effect of strain rate on the tensile behaviour of cast-in-place anchors with different design parameters has not been studied adequately.

- Most of the available studies on the effect of concrete compressive strength on the behaviour of anchorage system are focused on the anchorage behaviour under static loading. Effect of concrete compressive strength on the shear behaviour of cast-in-place anchors at low and high strain rates can help in investigating how the shear capacity and failure mode is influenced by the concrete compressive strength.
- The tensile behaviour of adhesive anchors under static load was investigated by several researches. Although loading rate effect on the tensile behaviour of adhesive anchors has been studied, effect of strain rate on the tensile behaviour of adhesive anchor has not been investigated thoroughly.
- Limited research was found on the shear behaviour of adhesive anchors under static load (Cattaneo and Muciaccia (2015), Epackachi et al. (2015)). Moreover, the shear behaviour of adhesive anchors at different strain rates has not been investigated.
- Tensile and shear behaviour of undercut anchors under static and seismic dynamic load have been studied. However, based on the literature review presented in this chapter, no studies have been found on the strain rate effect on the tensile and shear behaviour of the undercut anchors.
- Failure mode, dynamic increase factor and concrete breakout angle of the anchorage systems subjected to different strain rates have not been investigated thoroughly.

This project aims to investigate the tensile and shear behaviour of cast-in-place, adhesive and undercut anchorage systems subjected to static and dynamic loading using LS-DYNA software. Effect of strain rate on the tensile and shear behaviour of the cast-in-place, adhesive and undercut anchors is investigated. Also, the project aims to investigate the failure mechanism and crack propagation angle of the anchorage systems at different strain rates. Additionally, this research aims to propose an equation to relate the dynamic increase factor with the strain rate for the anchorage systems.

Chapter 3 : Finite element modelling of anchorage systems

3.1 Introduction

The demand to design structures to resist high dynamic loading has been increasing in recent years. When a structure is subjected to high dynamic loading, a large amount of energy is released in a very short time leading to generation of high pressure and high strain rates in the structure. Designing such structures is a challenging task to designers due to the limited information on the response of materials to high dynamic loads (Gebben et al., 2001). Experimental tests are costly and require a long time to complete compared to numerical analysis which can be used to predict the structural response under different loading conditions for a wide range of structures (Davidson et al., 2005; Wu et al., 2012). In addition, numerical analysis has flexibility to change geometry, design parameters, material properties and loading condition of the structural component. Furthermore, the numerical analysis has the ability to investigate the internal damage to the structure that is difficult to be investigated by the experimental tests (Qian and Li, 2011).

LS-DYNA software was selected for the analysis in this research. LS-DYNA is a nonlinear explicit finite element code developed by Livermore Software Technology Corporation (LSTC, 2014). The original version of LS-DYNA, DYNA3D, was designed for stress analysis of structures under impact loading, and then later developed to be used for different applications (Hallquist, 2006). In early 1989 a commercial version of DYNA3D was introduced as LS-DYNA. LS-DYNA is a high fidelity software that can solve non-linear dynamic problems and perform the analysis efficiently with less computation cost

(Liu, 2008). It can analyze the behaviour of structures under static and dynamic loads for a wide range of variables (Hallquist, 2006). The failure mechanism can be illustrated using LS-DYNA software through its capability to calculate the strain distribution in the elements at each time step (Davidson et al., 2005). Finite element analysis using LS-DYNA software can analyze problems that involves high deformation, strain rate, high loading conditions such as impact and blast (Hallquist, 2006; Chen and Hao, 2012). Several researchers have predicted the structural response under high strain rates using LS-DYNA software (Zhao et al., 2012; Bermejo et al., 2011; Kyei and Braimah, 2013; Wu et al. 2012; Chen and Hao, 2012).

In this chapter, finite element modelling for the tensile and shear behaviour of cast-in-place, adhesive and undercut anchors subjected to static and dynamic loading using LS-DYNA software is introduced. Implicit and explicit analyses for structures are presented. Material constitutive models for concrete, steel anchor and adhesive are described. Considerations to select suitable material constitutive models, boundary conditions are also presented. Finite element type, meshing and bonding techniques to model the steel anchor and concrete substrate systems are addressed.

3.2 Implicit and explicit analysis

Material response to applied loading can be linear or non-linear. The linear behaviour is observed in the elastic range, while the nonlinear behaviour can result from geometric effect, inelastic behaviour of materials, and large deformations. The general equations of

motion for linear damped single-degree-of-freedom (SDOF) system can be represented by Equation (3.1) (Hallquist, 2006):

$$ma + cv + kd = F(t) \quad (3.1)$$

and for the nonlinear damped SDOF systems by Equation (3.2):

$$ma + cv + f_{in}(d) = F(t) \quad (3.2)$$

Where m = mass, c = damping coefficient, k = stiffness, a = acceleration, v = velocity, d = displacement, f_{in} = internal force, $F(t)$ = external force.

Linear behaviour problems can be solved by using analytical equations, while nonlinear behaviour problems can be solved by numerical methods such as Newton-Raphson method (with using direct or iterative solvers) (Rust & Schweizerhof, 2003) and finite difference method (Remani, 2013).

Explicit central difference method is used in LS-DYNA to solve the equations of motion and to find the parameters of acceleration, velocity and displacement (Hallquist, 2006).

For time step t^{n+1} the central difference method can be represented by the following equations:

$$V^{n+1/2} = V^{n-1/2} + A^n \Delta t^n \quad (3.3)$$

$$D^{n+1} = D^n + V^{n+1/2} \Delta t^{n+1/2} \quad (3.4)$$

$$\Delta t^{n+1/2} = \frac{\Delta t^n + \Delta t^{n+1}}{2} \quad (3.5)$$

Where D is the global nodal displacement vector, V is the global nodal velocity vector.

LS-DYNA consists of implicit solver with limited capabilities and an explicit solver. For the implicit analysis, the solution is performed by integrating the nodal displacement with large time step size, the nodal displacement is determined by multiplying nodal force by the inverse of the stiffness matrix (k). The user can specify the time step size for the implicit analysis. However, the implicit analysis depends on the iterative method to get the solution and uses a small number of time steps. This requires enormous computational effort and large storage capacity (Jensen et al., 2007). The explicit solver can be used for both quasi-static and dynamic analysis (Hallquist, 2006). The solution for the explicit analysis is performed by integrating the nodal acceleration with a small time step size. Where the nodal acceleration is calculated by dividing the total of internal and external forces to the nodal mass (Jensen et al., 2007). In the explicit analysis, nodal displacement, velocity, and acceleration at time step (n) are known hence direct solution for the nodal displacement at the next time step can be obtained. Equation (3.6) expresses the explicit analysis.

$$d^{n+1} = f(d^n, v^n, a^n, d^{n-1}, \dots) \quad (3.6)$$

On the other hand, implicit analysis requires to identify the nodal velocity and acceleration at time step (n+1) (Jensen et al., 2007).

$$d^{n+1} = f(v^{n+1}, a^{n+1}, d^n, v^n, \dots) \quad (3.7)$$

Where d^n, v^n, a^n are the nodal displacement, velocity and acceleration at time step (n), respectively, v^{n+1}, a^{n+1} are the nodal velocity and acceleration at time step (n+1), respectively.

The nonlinear dynamic analysis can be used to evaluate the structural response and is considered an accurate technique (Kwasniewski, 2010). However, using non-linear analysis requires an understanding of the non-linear problem and its numerical solution. Nonlinear problems can have multiple degrees of freedom and require solution of a number of equations. In the field of structural mechanics, the nonlinear problems can be either path dependent or have multiple solutions. Therefore, it is necessary to select reliable solutions that can represent the nonlinear structural problems (Bergan et al., 1978). Unlike linear problems, in nonlinear problems, it is difficult to develop a method that is valid for all applications. Many of the solutions for nonlinear problems are either for specific types of non-linear problems or need specific requirement to be achieved to get converged solution. Hence, set of alternative algorithms to solve the non-linear problems have been implemented in the computer program. The computer program can control the solution through a number of parameters that are implemented in it. So that, the flexibility, reliability and efficiency to solve a specific problem will increase (Bergan et al., 1978).

3.3 Theoretical aspects (hydrocode)

The dynamic response of a structure to high strain rate loading can be predicted using simplified method such as SDOF method of analysis. The SDOF method is not able to predict localized structural damage (Zhou et al., 2008). The development in the computer programming has produced hydrocodes such as AUTODYN and LS-DYNA to predict the dynamic response of a structure (Tu and Lu, 2009). Hydrocode depends on three fundamentals postulations: conservation of mass, momentum and energy (Gebbeken and Ruppert, 2000). In hydrocodes there are two stress components: volumetric and deviatoric stresses to deal with stresses and strains individually. In the volumetric stress component, the relationship between hydrostatic pressure, local density, and local energy can be identified by the equation of state. The deviatoric stress component is dependent on the strength of the surface which in turns depends on the first stress invariant J_1 , second invariant of deviatoric stress J_2' and third invariant of deviatoric stress J_3' (Zhou et al., 2008). Tensile and compressive strength of concrete is sensitive to strain rate effect. Dynamic increase factor is used to express the effect of strain rate on concrete strength (Zhou et al., 2008). When concrete is subjected to compression load it behaves as a nonlinear material, hence the yielding (decrease in the strength and stiffness) depends on the hydrostatic pressure. Ductile behaviour of concrete is obtained at high hydrostatic pressure, where the strain rate has an effect on the tensile and compressive strength of the concrete. On the other hand, according to plasticity theory, yielding does not rely on the hydrostatic pressure; this gives a possibility of separation of hydrostatic tensor from stress tensor. As a result, deviatoric stress tensor is generated. The deviatoric stresses (s_{ij}) can be expressed as in Equation (3.8) (Gebbeken & Ruppert, 2000; Gebbeken et al., 2001):

$$s_{ij} = f\{\varepsilon_{ij}, \dot{\varepsilon}_{ij}, G[\varepsilon_{ij}, s_{ij}(p)], K(p, \rho)\} \quad (3.8)$$

Where ε_{ij} and $\dot{\varepsilon}_{ij}$ are the strain and strain rate respectively, and G the shear modulus, K the bulk modulus, ρ the density, and p the hydrostatic pressure. However, G and K vary under high loading rates.

Concrete constitutive models can be identified depending on the volumetric and deviatoric response characteristics. The common form of yield function of the concrete material can be represented by Equation (3.9), considering the volumetric response represented by first invariant of the stress tensor J_1 , and the deviatoric response is represented by second and third invariant of the deviatoric stress tensors J'_2 and J'_3 , respectively (Wu et al., 2012).

$$Y(J_1, J'_2, J'_3) = 0 \quad (3.9)$$

3.4 Finite element type

LS-DYNA software provides different types of elements such as solid, beam, spring, cohesive and shell elements. For each element type there is an option for element formulation to best describe the material of the model (Hallquist, 2006). Solid elements are used for modelling the anchorage system and are described in the following subsections.

3.4.1 Solid element

Eight-noded hexahedron solid elements were used to model the anchor, sleeve, steel plate, washer and nut. The solid elements for the anchor, sleeve, steel plate, washer and nut were formulated using constant stress. Four-noded tetrahedron solid elements were used to model the concrete in this research. Tetrahedron element is a fast, stable and simple solid element. The tetrahedron elements permit transition from fine mesh to coarse mesh (Livermore Software Technology Corporation, 2015). Tetrahedron solid elements were used by Fang and Zhang to model the reinforced concrete under dynamic load (Fang & Zhang, 2013). The solid elements for the concrete were formulated using one point integrated solid tetrahedron (Fang & Zhang, 2013). Each node of the solid element has three translational degrees of freedom in (x, y, and z directions). The geometry of the eight-noded hexahedron solid element is shown in Figure 3-1 while the geometry of the tetrahedron solid element is shown in Figure 3-2.

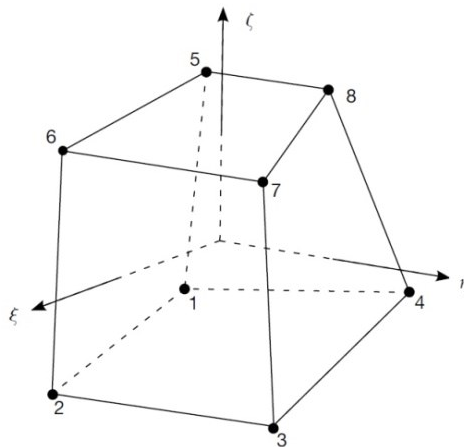


Figure 3-1: Eight node hexahedron solid element (Livermore Software Technology Corporation, 2015)

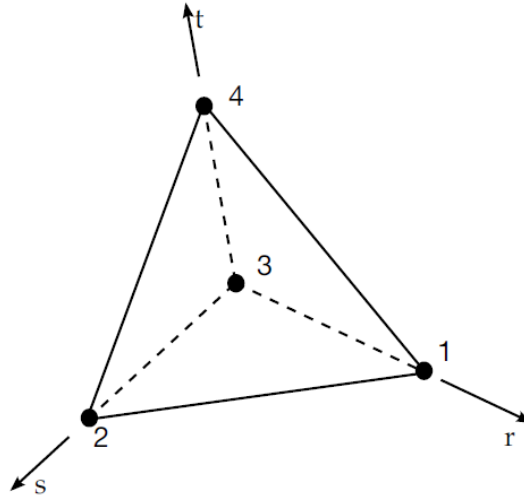


Figure 3-2: Four node tetrahedron solid element (Livermore Software Technology Corporation, 2015)

3.5 Meshing technique

The dynamic analysis of the structures can be performed analytically using mathematical equations or numerically using the finite element method by dividing the volume of the structure into finite elements linked at nodal points and forming a mesh. In the finite element method two types of errors may appear; numerical errors and discretizing errors that can cause the numerical model to give different answers from the analytical model. The discretizing errors can be minimized through mesh refinement (Paultre, 2010). Mesh size has an influence on the accuracy of the results and the time required to perform the analysis. Fine mesh size increases the accuracy and computation time resulting in a high overall computation cost (LSTC, 2014a).

3.6 Material constitutive models

Selecting a suitable material model is important to get a reliable prediction of the structural response to applied load. A wide range of materials constitutive models have been implemented in the LS-DYNA software to represent the behaviour for different materials. In addition, the software gives the user additional options to add new materials to LS-DYNA materials library using the keyword User Defined Material (Hallquist, 2006). Different options can be considered in LS-DYNA to select the appropriate material model for a specific application.

3.6.1 Concrete models

Concrete is a heterogeneous material consisting of aggregate and cement paste. It is ductile in compression and brittle in tension and shear (Gebben and Ruppert, 2000). The heterogeneity and porosity of concrete leads to complex response especially at high dynamic load where the internal energy cannot be neglected (Tu and Lu, 2009). A variety of constitutive models implemented in LS-DYNA library can be used to model the concrete materials. These include:

- Karagozian and Case concrete damage model Release III (MAT_concrete_damage_rel3, MAT_72_R3)
- Winfrith concrete model (MAT_084)
- Johnson Holmquist concrete model (MAT_111)
- Continuous surface cap model for concrete (MAT_CSCM_CONCRETE) (MAT_159)

Table 3-1 shows the material specifications and capabilities of the concrete models presented above.

Table 3-1: Material specifications for concrete models (LSTC, 2014)

Material No. in LS-DYNA	Material model title	Element formulation	Strain rate effects	Failure criteria	Equation of state requirement	Anisotropic	Damage effects	Applications
72	Concrete damage	Solid, thick shell, SPH element	Yes	Yes	Yes	No	Yes	Soil, concrete, rock
84	Winfrith concrete	Solid	Yes	No	No	No	No	Soil, concrete, rock, foam
111	Johnson Holmquist	Solid, thick shell, SPH element	Yes	Yes	No	No	Yes	Soil, concrete, rock
159	CSCM	Solid, thick shell, SPH element	Yes	Yes	No	No	Yes	Soil, concrete, rock

In concrete material models MAT_72_R3, MAT_84 and MAT_111, the erosion criteria for deletion of highly distorted elements are not included implicitly in the formation of these models. Therefore, these material models require an additional element erosion model. This can be done by using MAT_ADD_EROSION. However, the erosion criteria for MAT_ADD_EROSION does not have a direct relation to concrete damage under impact (Sagals et al., 2011). Element erosion is necessary to simulate material damage, failure and prevent non convergence resulting from exaggerated deformation in affected area (Sagals et al., 2011). In addition, the simulation time may be increased due to the distorted elements. Material Erosion card is included in MAT_CSCM_CONCRETE material model to represent element deletion upon failure.

MAT_CSCM_CONCRETE has been used in many applications (Wu et al., 2012) due to its simple input parameters represented by uniaxial compressive strength and maximum aggregate size. Other concrete material models on the other hand require many input parameters (Mousavi et al., 2016). In addition to the simplified input, MAT_CSCM_CONCRETE has key card to include or exclude rate effect. Furthermore, MAT_CSCM_CONCRETE model is able to represent the nonlinear behaviour of concrete material and complex concrete response in tension and compression (damage in tension and softening in compression), strain rate effect, and erosion (Bermejo et al., 2011; Wu et al., 2012). The Continuous Surface Cap Model (MAT_CSCM_CONCRETE) was thus selected to model the concrete in this research.

3.6.1.1 Concrete Model (MAT_CSCM_CONCRETE)

Continuous Surface Cap Model (MAT_CSCM_CONCRETE) (MAT_159) model was originally designed for roadside safety analysis in 1990 and then incorporated in LS-DYNA in 2005 to analyze many different types of applications (Wu et al., 2012). MAT_159 can be used for solid elements to predict the elastic-plastic behaviour of concrete (Wu et al., 2012). Where concrete material is assumed to be an isotropic material and behaves as elastic material obeying Hooke's law before cracking. After cracking and as the stress increases, the concrete material yields and behaves plastically (Murray, 2007).

MAT_159 model is characterized by smooth intersection between two failure surfaces; shear failure surface (F_f) and hardening cap (F_c) surface. Both surfaces: F_f and F_c are combined through multiplication form ($F_f^2 F_c$) into the yield equation. This multiplication form provides the smooth and continuous intersection between the cap (F_c) and shear (F_f)

surfaces. The smooth intersection makes the numerical analysis simple and removes the intricacy induced by the existence of corner region between the failure surface and the hardening cap. Three dimensional yield surface can be used to represent the yield stresses in the concrete model (LSTC, 2014). Figure 3-3 shows the general shape of the concrete model yield surface in two and three dimensions.

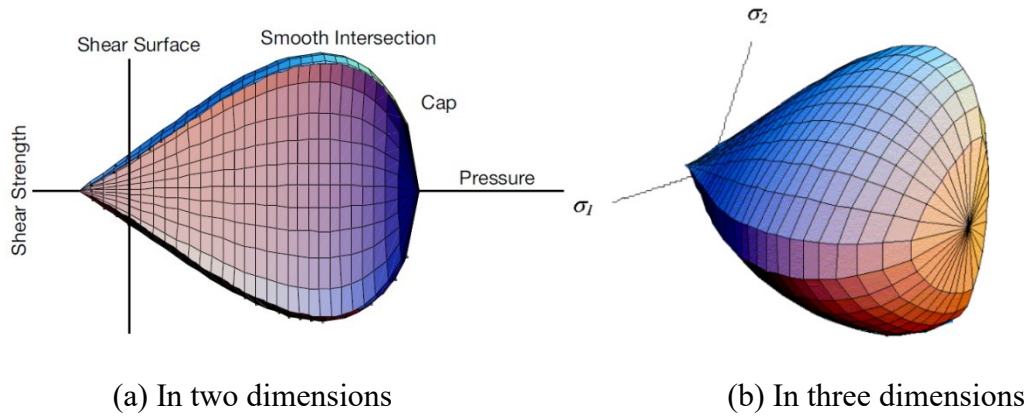


Figure 3-3: General shape of the concrete model yield surface (Murray, 2007)

The yield function for the MAT_159 model is represented by three stress invariants (J_1, J_2', J_3') and cap hardening (k) in Equation (3.10) (LSTC, 2014):

$$f(J_1, J_2', J_3', k) = J_2' - \mathfrak{R}^2 F_f^2 F_c \quad (3.10)$$

$$J_1 = 3P \quad (3.11)$$

$$J_2' = \frac{1}{2} S_{ij} S_{ij} \quad (3.12)$$

$$J'_3 = \frac{1}{3} S_{ij} S_{jk} S_{ki} \quad (3.13)$$

Where J_1 is the first invariant for the stress tensor, J'_2 and J'_3 are the second and third invariant for the deviatoric stress tensor, respectively, k is the cap hardening parameter, \mathfrak{R} is the Rubin three invariant reduction factor. The concrete strength can be calculated by the Rubin scaling factor (\mathfrak{R}) at different stress states relative to concrete strength for triaxial compression (TXC). S_{ij}, S_{jk}, S_{ki} are the deviatoric stress tensor.

LS-DYNA software provides updated values of the stress (J_1^T, J_2^T, J_3^T) at each time step. If the updated stress value is located on or inside the yield surface, $f(J_1^T, J_2^T, J_3^T, k) \leq 0$ the concrete behaves as elastic material. If the updated stress value is located outside the yield surface, $f(J_1^T, J_2^T, J_3^T, k) > 0$, the concrete behaves as elastic-plastic material, where the updated stress is returned to the yield surface, $f(J_1^p, J_2^p, J_3^p, k) = 0$, by a plasticity algorithm (Murray, 2007).

The shear failure surface can be expressed as follows:

$$F_f(J_1) = \alpha - \lambda \exp^{-\beta J_1} + \theta J_1 \quad (3.14)$$

Where α, λ, β and θ are constants measured from a triaxial compression test.

The plastic volume change (expansion and compaction) can be simulated using the cap surface, where the cap movement can represent the expansion or compaction. The hardening cap surface can be represented as follows:

$$F_c(J_1, k) = \begin{cases} 1 - \frac{[J_1 - L(k)] [|J_1 - L(k)| + J_1 - L(k)]}{2[X(k) - L(k)]^2} & \text{if } J_1 > L(k) \\ 1 & \text{if } J_1 \leq L(k) \end{cases} \quad (3.15)$$

Where

$$L(k) = \begin{cases} k & \text{if } k > k_o \\ k_o & \text{if } k \leq k_o \end{cases} \quad (3.16)$$

The hardening cap function (F_c) is either unity or an ellipse depending on the stress state. Unity function ($F_c = 1$) is obtained when ($J_1 \leq L(k)$), where the stress is located in the tensile or low confining pressure zone, consequently, the yield function depends on the shear surface only. Ellipse function is obtained when ($J_1 > L(k)$), where the stress located in low to high confining pressure zone and the yield function is dependent on both the cap surface and the shear surface.

The shear failure surface intersects the cap failure surface when $J_1 = k$. At the initial intersection between shear surface and cap surface $J_1 = k_o$ (Murray, 2007).

MAT_159 has built-in erosion criterion that can represent the concrete failure (Bermejo et al., 2011). When the damage (d) is equal to or greater than 1 and the maximum principal strain is greater than 1-ERODE, the element is eroded. When the damage is less than 1 the

erosion does not occur (Murray, 2007). Furthermore, MAT_159 has built-in damage criterion to represent the damage of the concrete when subjected to compression or tension load. The value of damage parameter (d) is ranging from zero to one and allows for the prediction of crack initiation and propagation in concrete. The MAT_159 material model has been reported to be more suitable for modelling concrete compared to the other material models available in LS-DYNA (Jaime, 2011).

Murray (2004) conducted finite element analysis to investigate the damage on reinforced concrete beam subjected to impact load using MAT_159. Murray's analysis revealed that the damage and displacement were adequately simulated when using MAT_159. Moutossamy et al. (2011) investigated the validation of MAT_159 concrete model using Lagrange in solid to connect the reinforcement with the concrete using analytical and numerical analysis on frame structure. The authors reported that MAT_159 model can represent the real behaviour of the concrete in many conditions. The authors also reported that the cracks in the concrete structure can be modeled properly using plastic strain contours (Moutoussamy et al., 2011).

Rate Effect:

Rate effect is used to model a materials dependence on loading or strain rates. LS-DYNA has a built-in parameter (IRATE) to represent the strain rate effect on the concrete strength. By activating the IRATE formulation, increase in the strain rate increases the strength of the concrete material. The rate effect is applied through using viscoplastic parameters on

the plasticity surface, damage surface and fracture energy. The viscoplastic parameters are used for compatibility of the uniaxial tensile and compressive strength data (Murray, 2007).

3.6.2 Steel anchor models

PIECEWISE_LINEAR_PLASTICITY (MAT_024) and MAT_PLASTIC_KINEMATIC (MAT_003) material models can be used to model the steel material. Rate effect is included in both material models. The two material models are cost effective and commonly used to model steel material and take into account the isotropic and kinematic hardening plasticity of steel (Bi and Hao, 2013; Livermore software technology Corporation, 2012). Analysis has been made on the anchorage to concrete system using MAT_024 and MAT_003. Results show that both material models give same load-displacement response, ultimate load and failure mode. MAT_024 is the most commonly used to model steel and hence MAT_024 is used to model steel material in this research. MAT_024 is an elasto-plastic material model that can represent failure depending on plastic strain or a minimum time step size.

The deviatoric stresses required to attain the yield function for MAT_024 can be expressed by Equation (3.17) (Livermore Software Technology Corporation, 2015):

$$\phi = \frac{1}{2} S_{ij} S_{ij} - \frac{\sigma_y^2}{3} \leq 0 \quad (3.17)$$

$$\sigma_y = \beta [\sigma_0 + f_h(\epsilon_{eff}^p)] \quad (3.18)$$

Where

β is a constant representing strain rate effect, σ_0 is the initial yield stress, and $f_h(\varepsilon_{eff}^p)$ is the hardening function. The hardening function can be represented in linear hardening form expressed in Equation (3.19).

$$f_h(\varepsilon_{eff}^p) = E_p(\varepsilon_{eff}^p) \quad (3.19)$$

$$E_p = \frac{E_t E}{E - E_t} \quad (3.20)$$

$$\varepsilon_{eff}^p = \int_0^t \left(\frac{2}{3} \dot{\varepsilon}_{ij}^p \dot{\varepsilon}_{ij}^p \right)^{1/2} dt \quad (3.21)$$

$$\dot{\varepsilon}_{ij}^p = \dot{\varepsilon}_{ij} - \dot{\varepsilon}_{ij}^e \quad (3.22)$$

Where E_p is the plastic hardening modulus, E_t is the tangent modulus, ε_{eff}^p is the effective plastic strain, $\dot{\varepsilon}_{ij}^p$ is the plastic strain rate, $\dot{\varepsilon}_{ij}^e$ is the elastic strain rate, $\dot{\varepsilon}_{ij}$ is the total strain rate.

The deviatoric stresses are calculated and updated elastically to satisfy the aforementioned yield function. If the yield function is not satisfied, then the increase in the effective plastic strain is calculated according to Equation (3.23).

$$\Delta \varepsilon_{eff}^p = \frac{(\frac{3}{2} S_{ij}^* S_{ij}^*)^{\frac{1}{2}} - \sigma_y}{3G + E_p} \quad (3.23)$$

Where

$\Delta \varepsilon_{eff}^p$ is the effective plastic strain increment, G is the shear modulus, S_{ij}^* is the trial deviatoric stress. If the deviatoric stresses S_{ij}^* is higher than the yield stress σ_y , it is scaled back to the yield surface and the updated deviatoric stress, S_{ij}^{n+1} is given by Equation (3.24).

$$S_{ij}^{n+1} = \frac{\sigma_y}{\left(\frac{3}{2}S_{ij}^*S_{ij}^*\right)^{\frac{1}{2}}} S_{ij}^* \quad (3.24)$$

Rate effect

The strain rate effect is considered for Piecewise Linear Plasticity model (MAT_024) as follows:

- The Cowper-Symonds model which scales the yield stress with a factor as per Equation (3.25) (Livermore Software Technology Corporation, 2015):

$$\beta = 1 + \left(\frac{\dot{\varepsilon}}{C}\right)^{1/p} \quad (3.25)$$

$$\dot{\varepsilon} = \sqrt{\dot{\varepsilon}_{ij}\dot{\varepsilon}_{ij}} \quad (3.26)$$

Where C and P, are Cowper-Symonds constants and $\dot{\varepsilon}$ is the strain rate.

Cowper-Symonds parameters C of 40 s⁻¹ and P of 5 are recommended for steel (Boh et al., 2004) and were used in this research to represent the strain rate effect.

- Using a table if there are different stress-strain curves for different strain rates where a curve ID can be defined for each strain rate. If the strain rate is not in the range included in the table (higher or lower than the strain rate in the table), then effective stress-strain curve for the maximum value of strain rate in the table is used for the strain rates higher than the maximum value. Effective stress-strain curve for the minimum strain rate in the table is used for the strain rates lower than the minimum value (Livermore Software Technology Corporation, 2015).

3.6.3 Adhesive modelling

The adhesive layer in post-installed adhesive anchorage systems can be modeled by using either a mesh dependent or mesh independent method. The mesh dependent method can be implemented by using identical connection between the adhesive and the adherents, while the mesh independent method can be implemented by using CONTACT_TIED_NODES_TO_SURFACE keycard where the connection between the adhesive and the adherents is incompatible (Marzi et al., 2008).

There are two approaches that can be used to describe failure behaviour of the adhesive layer: cohesive zone model (CZM) and continuum damage mechanics (CDM) approach. The CZM describes the damage and failure of adhesive material efficiently by employing simple traction separation law (Marzi et al., 2008; Marzi et al., 2009; May et al., 2014).

The CDM approach on the other hand describes the damage of the adhesive material by employing damage parameter to include the stiffness degradation of the adhesive material (Tserpes & Koumpias, 2012). Both CZM and CDM approaches can represent the damage initiation until complete failure (Sugiman & Ahmad, 2017). However, the CZM approach

is faster and less complicated than the continuum damage mechanics approach (Marzi et al., 2008; Marzi et al., 2009; May et al., 2014). In addition, the continuum damage mechanics approach depends more on mesh size compared to the (CZM) (Tserpes & Koumpias, 2012; Sugiman & Ahmad, 2017).

There are several cohesive zone models that can be used to model the adhesive material implemented in LS-DYNA. These models include ARUP_ADHESIVE (MAT_169), COHESIVE_MIXED_MODE (MAT_138), COHESIVE_ELASTIC (MAT_184), COHESIVE_THERMAL (MAT_185) and COHESIVE_GENERAL (MAT_186) (LSTC, 2014). MAT_138, MAT_184, MAT_185, MAT_186 don't have a keycard to represent the rate effect. However, MAT_169 has rate dependent keycard that can represent the strain rate (LSTC, 2014). Hence, among these models MAT_ARUP_ADHESIVE (MAT_169) was selected to model the adhesive material. MAT_ARUP_ADHESIVE is structural adhesive and can represent the behaviour of the adhesive anchor (Graf et al., 2014).

3.6.3.1 Adhesive model (MAT_ARUP_ADHESIVE)

MAT_ARUP_ADHESIVE (MAT_169) was used to model the adhesive material. Solid element formulations 1, 2 and 15 are suitable to model the adhesive material. The yield function and the failure surfaces for the MAT_169 model is represented by a power-law combination of direct tension and shear as in Equation (3.27) (LSTC, 2014).

$$\left(\frac{\sigma}{\sigma_{max}}\right)^{PWRT} + \left(\frac{\tau}{\tau_{max} - SHT_{SL} \times \sigma}\right)^{PWRS} = 1 \quad (3.27)$$

Where

$PWRT$, $PWRS$ are power law terms for tension and shear respectively. σ is the tensile stress, τ is the shear stress, SHT_SL is the slope of the yield surface at zero tension.

Figure 3-4 shows the yield surface for MAT_169.

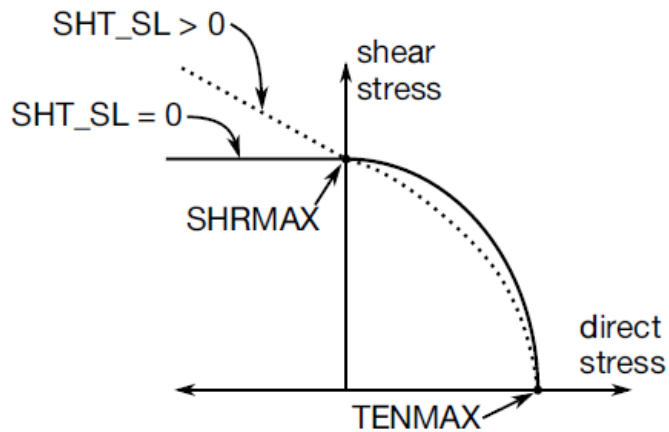


Figure 3-4: Yield surface (LSTC, 2014)

Figure 3-5 shows the stress-displacement relation for MAT_169 in tension and shear.

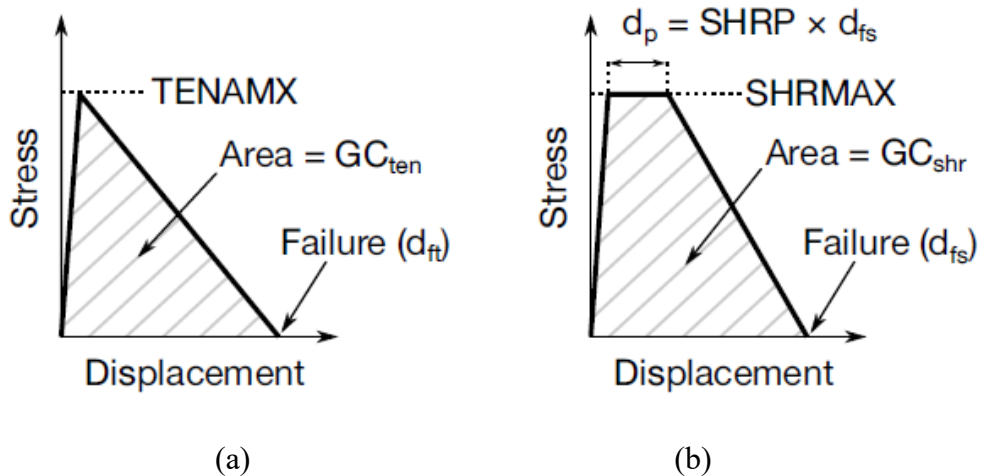


Figure 3-5: Stress-displacement relation of MAT_169 for (a) tension and (b) shear (LSTC, 2014)

Rate effect:

The strain rate effect is considered for MAT_ARUP_ADHESIVE model (MAT_169) through parameters EDOT0 and EDOT2 for the static and dynamic strain rates respectively (LSTC, 2015).

3.7 Design parameters

Concrete block size of $(4h_{ef} + 125)mm \times (4h_{ef} + 125)mm \times (2h_{ef})mm$ was modeled and used for the tensile analysis of anchorage systems. The size of the concrete block for the tensile analyses was selected to preclude edge effect on the failure of concrete cone formation. A concrete block size of $(2h_{ef} + 150)mm \times (2h_{ef} + 150)mm \times (1.5h_{ef} + 50)mm$ was used for the shear analysis to minimize concrete edge effects on the behaviour of the anchors. Single anchor was used for the analysis. The anchor placement in the concrete block was such that the edge distance (c) does not affect the concrete breakout cone formation. Anchorage failure by concrete breakout near the free edge is not considered in this research.

Cast-in-place and adhesive anchor diameters of 12.7 mm, 15.9 mm and 19.1 mm were used. According to the design guidelines of ASTM A 307, the recommended effective embedment depths are 101.6 mm, 127 mm and 152.4 mm for the 12.7-mm 15.9-mm and 19.1-mm diameters anchors, respectively were used for the analysis (Bridge Design Aids, 2012). In this research, anchor embedment depths of 76.2 mm, 101.6 mm, 127 mm and 152.4 mm were investigated for each anchor diameter to investigate the influence of various embedment depths (the recommended, less than the recommended and higher than

the recommended embedment depths) on the behaviour of the anchorage to concrete system, ultimate load, level of damage and the failure mode.

According to Hilti Inc. the minimum embedment depths for adhesive anchor diameters of 12.7 mm, 15.9 mm and 19.1 mm are 70 mm, 79 mm and 89 mm respectively (Hilti, 2014). Cast-in-place anchors with hexagonal head were used for the analysis. The hexagonal head sizes ($D \times H$) of (19×8) mm, (24×10) and (28.5×12) were used for anchor diameters of 12.7 mm, 15.9 mm and 19.1 mm respectively (Cement Association of Canada, 2010). Three nominal undercut anchor diameters of 12 mm, 16 mm and 20 mm with effective embedment depths of 125 mm, 190 mm and 250 mm recommended by Hilti (Hilti, 2011) were investigated. In this research embedment depths of 100 mm, 125 mm, 190 mm and 250 mm were investigated for all the anchor diameters to investigate the behaviour of anchorage system, ultimate load, failure mode and level of damage for various embedment depths (the recommended, less than and higher than the recommended embedment depths). The embedment depth (h_{ef}) of the undercut anchor is measured from the surface of the concrete to the end of the sleeve.

3.8 Materials properties

The cast-in-place, adhesive and undercut anchorage systems consisted of steel anchor, steel plate, washer, nut and concrete block. In addition to the adhesive material for the adhesive anchorage system and sleeve for the undercut anchorage system. The concrete blocks were modeled using continuous surface cap model (MAT_159) while the steel anchor, steel plate, sleeve, washer and nut were modeled using piecewise linear plasticity model (MAT_024). MAT_ARUP_ADHESIVE (MAT_169) was used to model the adhesive

material. The concrete material was modeled with a density of 0.0024 g/mm^3 and compressive strength (f'_c) of 30 MPa. The concrete material is assumed free from cracking or damage, and this is implemented in the concrete material model (MAT_159) through the pre-existing damage parameter PRED equal to zero.

For the cast-in-place and adhesive anchors the properties of the steel anchor, steel plate, washer and nut were in accordance with ASTM A354 specification with yield strength of 896 MPa, ultimate tensile strength of 1034 MPa, density of 0.00785 g/mm^3 , Young's modulus of 200000 MPa, failure strain of 14% and Poisson's ratio of 0.3. The adhesive material was modeled with a density of 0.0012 g/mm^3 , tensile strength of 56 MPa, shear strength of 44 MPa (Dogan et al., 2012), Elastic modulus of 3034 MPa and Poisson's ratio of 0.4.

For the undercut anchors the steel anchor, sleeve, steel plate, washer and nut were modeled in accordance with Hilti Inc. specification with yield strength of 640 MPa and tensile strength of 800 MPa (Hilti, 2011).

3.9 Contact modelling

There are different types of contacts that can be applied using LS-DYNA software. In general, the contact between two surfaces can be automatic or non-automatic. Automatic contact can be used for explicit analysis while, non-automatic contact can be used for implicit analysis (LSTC, 2014).

In the present investigation, CONTACT_AUTOMATIC_SURFACE_TO_SURFACE was used to define the contact interfaces between the concrete, steel anchor, washer, nut and anchor plate for cast-in-place and undercut anchors. This contact bonds the steel anchor and concrete surfaces. The contact algorithm is characterized by its dual treatment, where the slave and master nodes checked against penetration in each other. Hence, the user has flexibility to switch slave part/ master part and obtain identical behaviour. This contact formulation is useful to prevent penetration between contacted surfaces (LSTC, 2014).

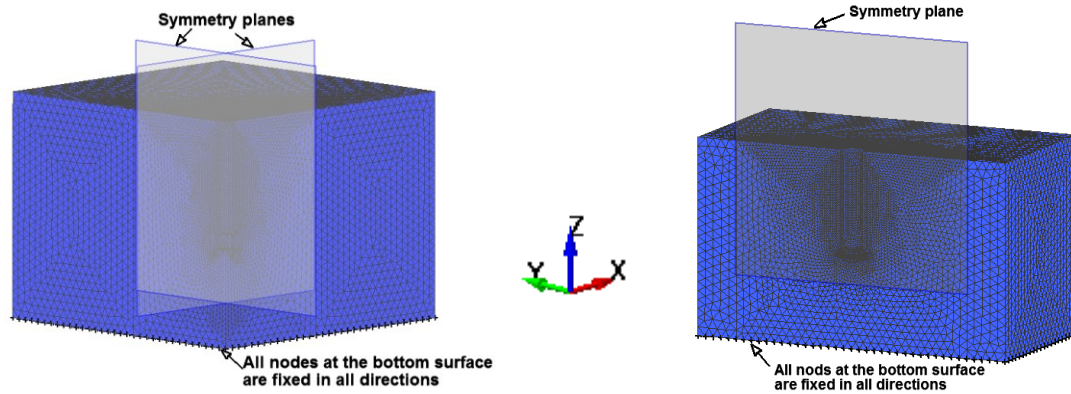
For the adhesive anchor CONTACT_AUTOMATIC_ONE_WAY_SURFACE_TO_SURFACE_TIEBREAK was used to model the interaction between the adhesive and anchor. The tiebreak contact is penalty-based contact which allows transmission of the forces in normal and tangential directions and has the capability to model the failure (LSTC, 2014a). Before failure, the tiebreak contact prevents the separation between slave node (adhesive) and the master segment. After failure, the coupling in normal direction is eliminated and the contact behaves as surface to surface contact with thickness offset (LSTC, 2014). CONTACT_ERODING_SINGLE_SURFACE was used to remove the distorted elements of the adhesive material. ENMASS parameter is set equal to one in the CONTROL_CONTACT key card to retain the mass of these removed distorted elements and they remain active in contact (LSTC, 2014a).

CONTACT_TIED_SURFACE_TO_SURFACE key card was used to model the bond between adhesive and the concrete. The tied contact is a constrained-based contact used to ensure that the adhesive material is tied to the concrete material with no gap (LSTC, 2014).

The tied contact is used when the mesh sizes of two surfaces in contact are different to ensure that the slave nodes (adhesive) located on the master segment (concrete) with no gap (LSTC, 2014; Bala, 2008). LS-DYNA updates the coordinates of the slave nodes to be identical on the master surface and neglect the slave nodes that are located far from the master surface (Bala, 2008). Moreover, the tied contact allows mesh transition (Hallquist, 2006). When the failure of the elements in contact occurs, the elements in the tied contact are automatically deleted (Chen et al., 2017). The interaction between the anchor plate, washer, nut, steel anchor and the concrete was modeled using CONTACT_AUTOMATIC_SURFACE_TO_SURFACE.

3.10 Boundary conditions

Bottom surface of the concrete block (XY plane) was fixed to prevent translational and rotational motion during the application of loading. Due to the symmetry of the geometric configuration of the anchorage system, a quarter of the anchorage to concrete system was modelled to investigate the tensile behaviour while half of the anchorage to concrete system was modelled to investigate the shear behaviour. Using the symmetry increases the efficiency and reduces the computational time. Symmetry planes boundary conditions were applied on the anchorage to concrete models. Two symmetry planes (XZ and YZ) boundary conditions were applied to represent the tensile behaviour. One symmetry plane (YZ) was applied to represent the shear behaviour. Figure 3-6 shows the geometric configuration and boundary conditions for the anchorage system model under tensile and shear loads. Table 3-2 summarizes the boundary conditions used for the anchorage models.



(a) Quarter of the concrete block

(b) Half of the concrete block

Figure 3-6: Boundary conditions for the anchorage models under (a) tensile load and (b) shear load

Table 3-2: Boundary conditions of the anchorage to concrete systems

Boundary conditions	*Degree of freedom					
	Translational			Rotational		
	x	y	z	rx	ry	rz
XZ symmetry plane	0	1	0	1	0	1
YZ symmetry plane	1	0	0	0	1	1
XY plane (at the bottom of the concrete)	1	1	1	1	1	1

*Degree of freedom: 1= fixed, 0= free

3.10.1 Load conditions

The load in LS-DYNA can be applied using five options: BOUNDARY_SPC_SET, INITIAL_VELOCITY, LOAD_SEGMENT_SET, LOAD_NODE_SET, and BOUNDARY_PRESCRIBED_MOTION_SET. The BOUNDARY_SPC_SET (single point constraint) can be applied to determine the reaction force. INITIAL_VELOCITY can be used to apply the velocity to all nodes of the object. LOAD_SEGMENT_SET can be used to apply pressure load (Chou et al, 2004). LOAD_NODE_SET can be used to apply

static load (Abebe & Qiu, 2016). `BOUNDARY_PRESCRIBED_MOTION_SET` is used to apply the quasi static loading (Kashani et al., 2013) and dynamic loading (Abebe & Qiu, 2016) and to maintain uniform rate of velocity. `DATABASE_CROSS_SECTION_PLANE` command is used to specify the location of the applied load, where the load-displacement relation can be drawn. `BOUNDARY_PRESCRIBED_MOTION_SET` is used to apply the tensile and shear loads. In this research, `BOUNDARY_PRESCRIBED_MOTION_SET` was applied in z-direction at the top nodes of the anchor to simulate the tensile load on the anchorage systems. `BOUNDARY_PRESCRIBED_MOTION_SET` was applied in y-direction on the anchor plate to simulate the shear load on the anchorage systems. When using `BOUNDARY_PRESCRIBED_MOTION_SET`, velocity, or displacement can be prescribed. The displacement is used for the implicit analysis (Maker & Zhu, 2000), whereas the velocity is recommended for explicit analysis. The strain rate is applied using the velocity-time curve in the `DEFINE_CURVE` command in LS-DYNA. The applied strain rate can be checked using `SRate` in the fringe component of the LS-DYNA post processor and history-scalar option. Also, the strain rate can be measured using `DATABASE_EXTENT_BINARY`, setting the strain rate flag (`STRFLG`) to one and the energy output (`N3THDT`) to one to minimize the output (LSTC, 2014b). In this research, for the anchors subjected to tensile and shear loads, the strain rate has been measured using `SRate` in the fringe component of the LS-DYNA post processor (`Fcomp`) that presents strain rate plot and then using History-Scalar-option that plots a time history of the strain rate (LSTC, 2014b).

3.11 Quasi-static simulation using LS-DYNA

Explicit LS-DYNA code is designed for dynamic analysis; however quasi-static analysis is performed by decreasing the loading rate and scaling up the mass of the anchor, adhesive and concrete materials by a factor of 1000. This procedure decreases the number of time steps required, reduces the simulation time and improve the computation efficiency. To ensure that the static analysis is achieved, the ratio of the kinetic energy to the internal energy has to be less than 5% during the analysis (Bathe et al., 1999; El-Hage et al., 2005; Han et al., 2007). On the other hand, implicit solver can also be used to perform the static analysis. However, the analysis using the implicit solver generates few number of time steps with large disk storage requirements. This increases the computation time and requires a lot of effort and large computer capacity to complete the run and store the file. As a result, the computational cost will increase (Jensen et al., 2007). Table 3-3 shows the specifications for the material models used in the analysis.

Table 3-3: Material models specifications (LSTC, 2014)

Material No. in LS-DYNA	Material title	Element formulation	Strain rate effects	Failure criteria	Equation of state requirement	Anisotropic	Damage effects	Applications
24	Piecewise Linear Plasticity	Solid, beam, shell, SPH, ALE solid	Yes	Yes	No	No	No	Metal, plastic
159	CSCM	Solid, thick shell, SPH	Yes	Yes	No	No	Yes	Soil, concrete, rock
169	Arup Adhesive	Solid	Yes	Yes	No	Yes	No	Adhesive

3.12 Summary

This chapter presents finite element modelling for cast-in-place, adhesive and undercut anchorage systems. The chapter started with introduction on the development of the LS-DYNA code and its capabilities to predict the structural response under low and high strain rates. The characteristics of the LS-DYNA finite element software package are introduced. Implicit and explicit solvers of LS-DYNA software and their capabilities are presented. Theoretical aspects of LS-DYNA hydrocode used to predict the dynamic response of a structure are presented. Finite element types are introduced and selection criteria for element type are presented. Solid elements that are used to model anchorage to concrete system are described.

Meshing technique to discretize the model in small elements is presented. Material constitutive models for the anchorage to concrete system are presented, followed by selecting the suitable material models to model the concrete, steel anchor and adhesive. Selection criteria are presented for each material model. Materials properties and design parameters for the anchorage systems are presented. Contact keycard to model the interaction between the materials is introduced. Boundary conditions to capture the tensile and shear behaviour of the anchorage to concrete systems are introduced. Application of tensile and shear loads is introduced. Performing quasi static analysis using LS-DYNA software is presented at the end of the chapter.

Chapter 4 : Strain rate effect on cast-in-place anchors

4.1 Cast-in-place anchors under tensile load

4.1.1 Finite element modelling of cast-in-place anchors under tensile load

Analysis of the behaviour of cast-in-place anchors embedded into concrete under tensile loading at different strain rates was performed using the explicit commercial finite element code LS-DYNA (LSTC, 2014). Strain rates ranging from low (static) to high (10^{-5} s^{-1} , 10^{-3} s^{-1} , 10^{-1} s^{-1} , 10 s^{-1} , 10^2 s^{-1} and 10^3 s^{-1}) were investigated. The design parameters, materials properties, boundary conditions and contacts for the anchorage to concrete system were introduced in chapter 3 sections 3.7 to 3.11. The friction between the cast-in-place anchor and the concrete and between the anchor and the anchor plate was neglected. For the cast-in-place anchor, the anchor head has a major role on resisting the applied load on the anchor. A schematic view of the cast-in-place anchor is shown in Figure 4-1. The geometric configuration and boundary condition for the cast-in-place anchor model are shown in Figure 4-2. The mesh of the concrete block was biased (refined) towards the cast-in-place anchor and along the embedment depth to improve the accuracy of the finite element analysis and to minimize discretization errors.

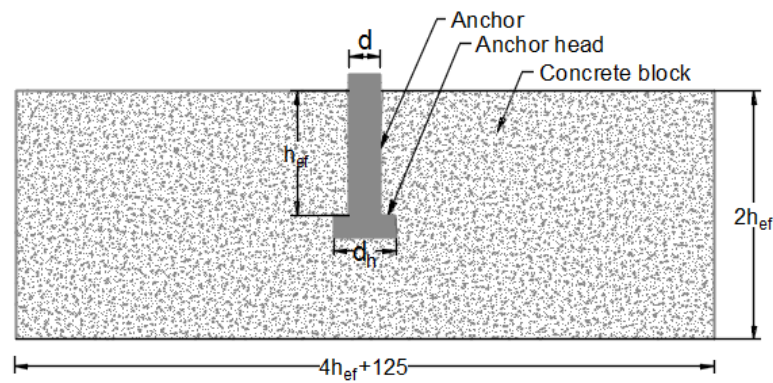
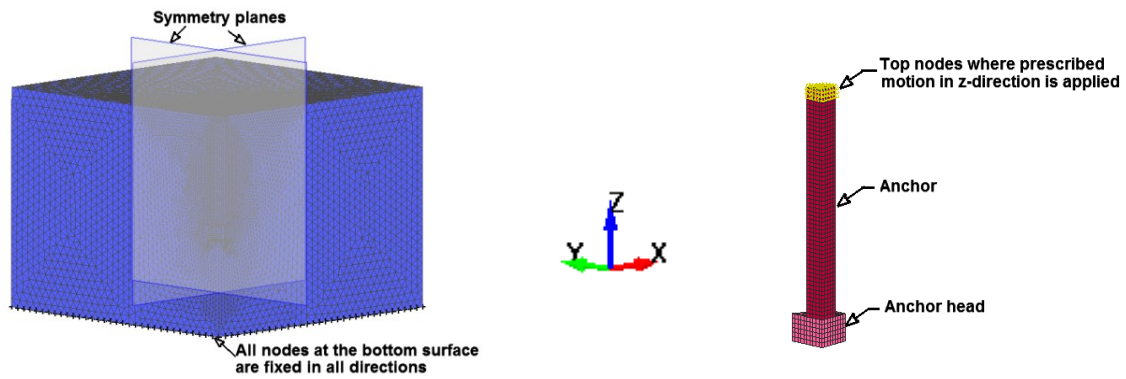


Figure 4-1: Schematic view of the cast-in-place anchor



(a) Concrete mesh

(b) Cast-in-place anchor mesh

Figure 4-2: Geometric configuration with boundary condition of cast-in-place anchor model

4.1.2 Validation of cast-in-place anchor model under tensile load

The finite element model was validated by comparing the ultimate tensile load obtained from the finite element analysis with the experimental test results in the literature. Two finite element models, representing the test specimen used by Eligehausen et al. (Eligehausen et al., 1992) were developed and used to validate the numerical model. The concrete block size was $(4h_{ef} + 200)\text{mm} \times (4h_{ef} + 200)\text{mm} \times (2h_{ef})\text{mm}$ and the steel anchor diameters were 8-mm and 24-mm with embedment depths of 50 mm and 150 mm respectively. The authors used concrete block of 31 MPa cube compressive strength (f'_{cc}) that is approximately equivalent to 25.7 MPa cylinder compressive strength (British Standards Institution Draft for development, 1992; Committee Euro-International du Beton (CEB), 1994). Finite element analysis (FEA) was performed under static loading (strain rate of 10^{-5} s^{-1}).

Mesh sensitivity analysis was carried out to obtain the optimum mesh size that gives converged results with the experimental results. Several models with different mesh sizes

were developed for the cast-in-place anchors. Table 4-1 presents the effect of mesh size refinement on the ultimate tensile load for the cast-in-place anchor.

Table 4-1: Effect of mesh size refinement on the convergence of ultimate tensile load for cast-in-place anchors

Model No.	d (mm)	h_{ef} (mm)	Mesh size (mm)			Ultimate tensile load (kN)		Displacement (mm)		Failure mode
			Anchor	Concrete		FEA	EXP.	FEA	EXP.	
				Min.	Max.					
1	8	50	1	2	8	30.23	31.48	1.92	1.68	Concrete cone breakout
2			1	1	8	30.45		1.87		
3			0.75	1	8	32.15		1.75		
4	24	150	1	2	8	143.98	152.66	4.19	4.43	Concrete cone breakout
5			1	1	8	147.14		4.16		
6			0.75	1	8	156.47		4.41		

Mesh sizes of $1 \times 2 \times 8$ mm, $1 \times 1 \times 8$ mm and $0.75 \times 1 \times 8$ mm were investigated. The mesh sizes of $1 \times 1 \times 8$ mm and $0.75 \times 1 \times 8$ mm give ultimate load and displacement results converged to the experimental results. The ultimate load and displacement at maximum load obtained using mesh size of $0.75 \times 1 \times 8$ mm were found closer 1.3% and 7.1% respectively than that obtained using mesh size of $1 \times 1 \times 8$ mm for the anchor diameter of 8 mm. The ultimate load and displacement were found closer 1.3% and 6.1% respectively for the anchor diameter of 24 mm. Mesh size of ($0.75 \times 1 \times 8$) mm exhibits good agreement with the experimental results obtained by Eligehausen et al. (Eligehausen et al., 1992) and was selected for the analysis.

Figures 4-3 and 4-4 present a comparison of tensile load-displacement results from experimental tests by Eligehausen et al. (Eligehausen et al., 1992) and the finite element analysis for anchor embedment depths of 50 mm and 150 mm respectively. Ultimate tensile load obtained from the FEA (mesh size of $0.75 \times 1 \times 8$ mm) was found to be 2.1% and 2.5%

higher than the experimental results for the 8-mm and 24-mm diameter anchors respectively while the initial stiffness of the concrete anchorage system is almost the same.

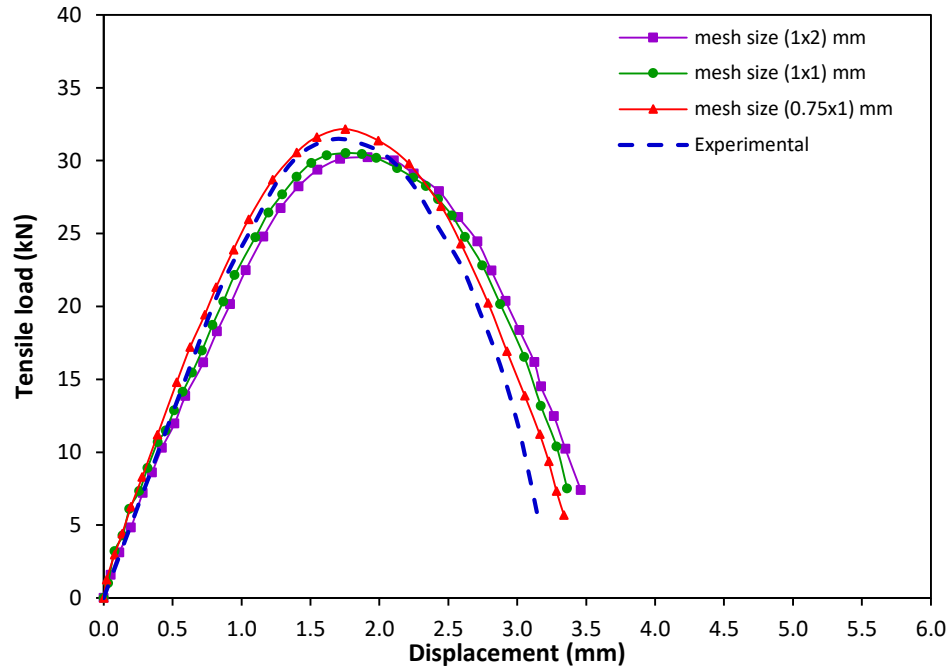


Figure 4-3: Comparison of experimental and numerical tensile load-displacement behaviour of 8-mm diameter cast-in-place anchor with 50 mm embedment depth

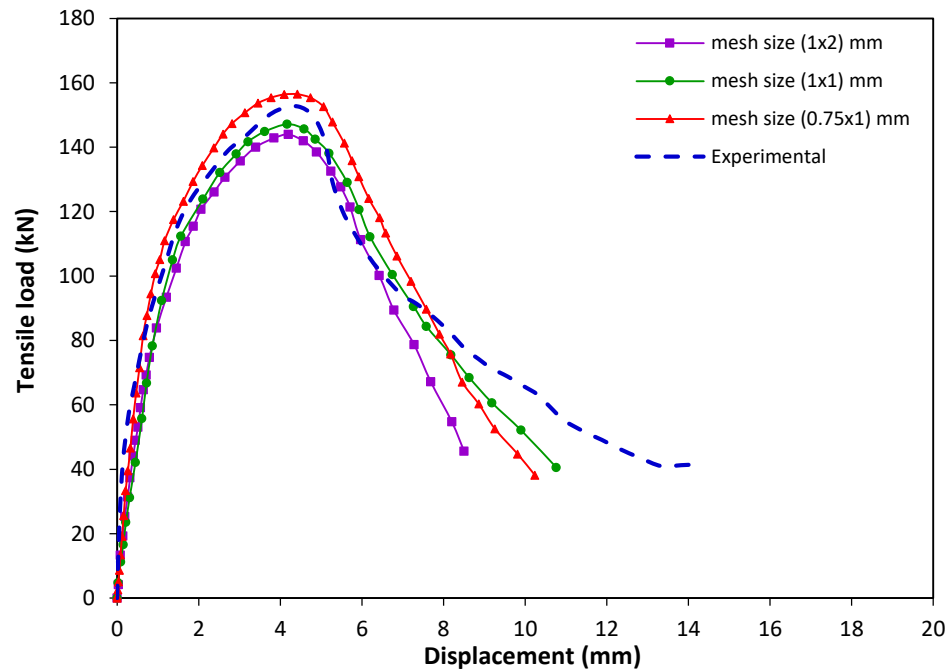


Figure 4-4: Comparison of experimental and numerical tensile load-displacement behaviour of 24-mm diameter cast-in-place anchor with 150 mm embedment depth

Concrete cone breakout failure mode was observed from the finite element analysis similar to that obtained from the experimental tests conducted by Eligehausen et al. (Eligehausen et al., 1992). Concrete breakout cone diameters of 160 mm and 494 mm were obtained from the FEA analyses for 8-mm and 24-mm diameter anchors with 50 mm and 150 mm embedment depths respectively. A good agreement was obtained with the experimental results by Eligehausen et al. (1992) where the concrete cone breakout diameter was reported to be less than $4h_{ef}$ (200 mm and 600 mm for the 8-mm and 24-mm diameter anchors respectively).

After validation of the cast-in-place anchorage to concrete system numerical model, it was used to investigate the effect of strain rate on the capacity of the anchorage system for various design parameters (anchor diameter and embedment depth). The results of the analysis are presented in the following sections.

4.1.3 Comparison of finite element results with the ACI and CCD design methods

Ultimate tensile loads obtained from the finite element analysis at the static strain rate of 10^{-5} s^{-1} were compared with the results obtained from American Concrete Institute (ACI 349-85) (Fuchs, 2001; Fuchs et al., 1995) and Concrete Capacity Design (CCD) methods. According to ACI design method, the ultimate tensile load of the cast-in-place anchors is the minimum of the concrete breakout load and the steel fracture load. The concrete cone breakout failure load (N_{uo}) can be determined from Equation (4.1) (Fuchs et al., 1995).

$$N_{uo} = 0.96 \sqrt{f'_{cc}} h_{ef}^2 \left(1 + \frac{d_h}{h_{ef}} \right) \quad (4.1)$$

Where f'_{cc} is the cube compressive strength of concrete, h_{ef} is the effective embedment depth, d_h is anchor head diameter. Anchor head diameters of 19 mm, 24 mm and 28.5 mm were used for anchor diameters of 12.7-mm, 15.9-mm and 19.1-mm respectively (Cement Association of Canada, 2010).

The tensile load for steel anchor failure mode can be determined by Equation (4.2).

$$N_{uo} = A_s f_{ut} \quad (4.2)$$

Where N_{uo} , is the tensile load, A_s is the effective cross-sectional area of the anchor, f_{ut} is the ultimate tensile strength of the steel. The minimum value of the ultimate tensile load obtained from Equations (4.1) and (4.2) is considered for comparing the design capacity by the ACI method with the finite element results and presented in Table 4-2.

According to CCD Method (Ashour & Alqedra, 2005; Committee Euro-International du Beton (CEB), 1994; Fuchs, 2001; Fuchs et al., 1995; Subramanian, 2000), the ultimate tensile load of the cast-in-place anchors can be determined for the concrete cone breakout from Equation 4.3.

$$N_{uo} = K \sqrt{f'_{cc}} h_{ef}^{1.5} \quad (N) \quad (4.3)$$

Where

$K= 13.5$ for post installed anchors embedded in uncracked concrete

= 15.5 for the cast-in-place anchors embedded in uncracked concrete (Ashour & Alqedra, 2005; Committee Euro-International du Beton (CEB), 1994; Fuchs, 2001; Fuchs et al., 1995; Subramanian, 2000).

Concrete cube compressive strength of 37 MPa, equivalent to a concrete cylinder compressive strengths of 30 MPa, was used in Equation (4.1) and Equation (4.3) (British Standards Institution Draft for development, 1992; British Standards Institution, 2013; Committee Euro-International du Beton (CEB), 1994).

Table 4-2 presents a comparison of ultimate tensile loads obtained from the finite element analysis, ACI and CCD methods for the cast-in-place anchors. As shown in the Table 4-2, the ultimate tensile load increased with increasing anchor embedment depth for the finite element analysis and the design methods. In general the results show that the ACI method underpredicts the capacity of the anchorage system. The CCD method gives a better agreement with the finite element method. Similar observation was reported by Fuchs et al. (1995) where the ACI method was reported to underpredict the failure load for shallow embedment depths and unconservative for the deep embedment depths (Fuchs et al., 1995).

Table 4-2: Comparison of ultimate tensile loads obtained from FEA with ACI and CCD design methods

d (mm)	h _{ef} (mm)	Ultimate tensile load (kN)			FEA/ACI	FEA/CCD	*Failure mode (FEA)
		ACI	CCD	FEA			
12.7	76.2	42.36	62.71	64.48	1.52	1.03	CC
	101.6	71.55	96.55	98.03	1.37	1.02	S
	127	108.28	130.98	98.64	0.91	0.75	S
	152.4	130.98	130.98	99.86	0.76	0.76	S

15.9	76.2	44.59	62.71	68.61	1.54	1.09	CC
	101.6	74.52	96.55	104.17	1.40	1.08	CC
	127	111.98	134.94	163.26	1.46	1.21	S
	152.4	156.98	177.38	166.35	1.06	0.94	S
19.1	76.2	46.59	62.71	72.88	1.56	1.16	CC
	101.6	77.19	96.55	116.65	1.51	1.21	CC
	127	115.32	134.94	181.29	1.57	1.34	CC
	152.4	160.99	177.38	241.37	1.50	1.36	S

*Failure mode: CC=concrete cone breakout, S=steel anchor failure

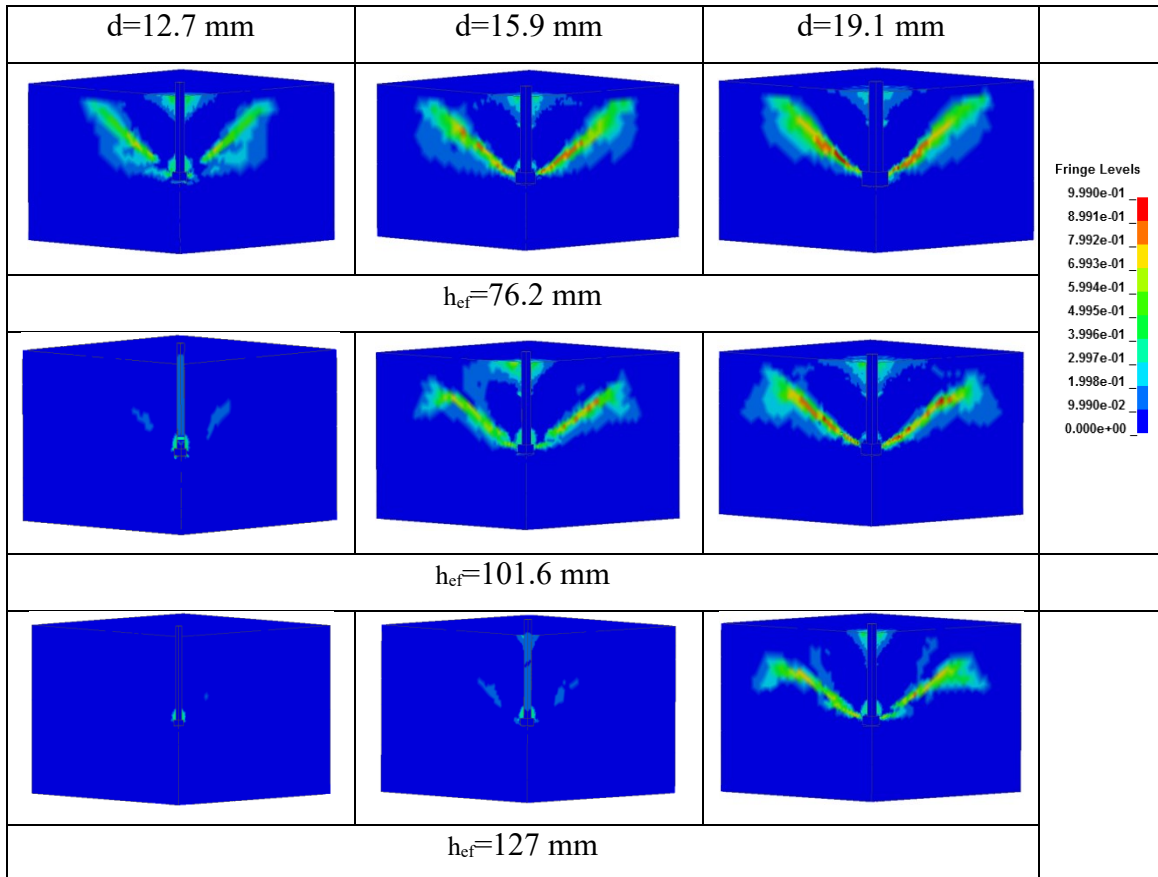
4.1.4 Effect of strain rate on the level of damage and failure mode of cast-in-place anchors

Plastic strain contours can be used to represent level of damage for concrete (Moutoussamy et al., 2011; Wu et al., 2012). The range of the damage in the concrete is expressed by fringe levels associated with crack pattern. The fringe level ranges from no damage at a value of 0 to complete damage at a value of 1.

Contours of effective plastic strain for cast-in-place anchor with diameters of 12.7-mm, 15.9-mm and 19.1-mm and different embedment depths are shown in Figure 4-5 at strain rate of 10^{-5} s^{-1} . As shown in the figure, for all embedment depths investigated, two failure modes were observed: concrete cone breakout failure and steel anchor failure. Concrete cone breakout failure was observed at embedment depth of 76.2 mm for all the anchor diameters investigated. At embedment depth of 101.6 mm, concrete cone breakout failure was observed for 15.9 mm and 19.1-mm diameter anchors while steel anchor failure was observed for the 12.7 mm diameter anchor. With the increase in the anchor embedment

depth, the anchor requires higher loads to break the concrete and form concrete cone failure. When the anchor is not capable to afford the high applied tensile load, anchor fracture will occur.

At embedment depths of 127 mm and 152.4 mm, steel anchor failure was observed for all anchor diameters except for anchor diameter of 19.1-mm with embedment depth of 127 mm where concrete cone breakout failure was observed. As shown in Figure 4-5, the damage increases with the increase in the anchor diameter from 12.7-mm to 19.1-mm. The increase in the anchor diameter increases the anchor head diameter and in turns the amount of cracking in the concrete is increased.



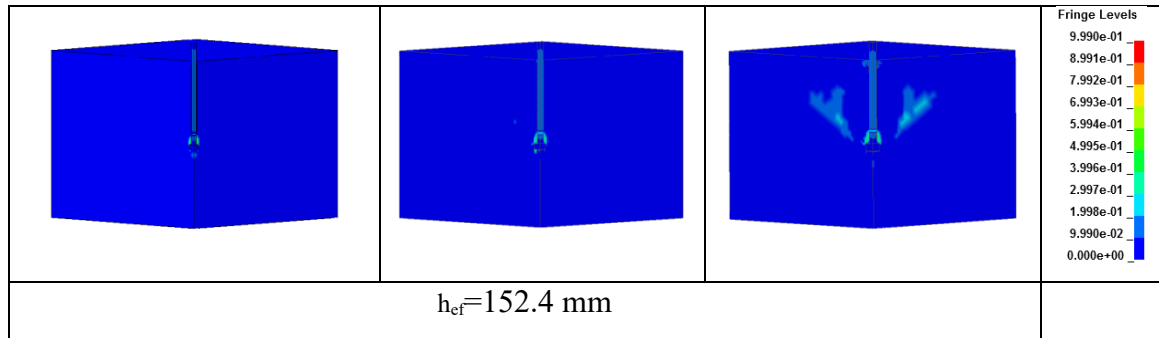


Figure 4-5: Plastic strain contours for cast-in-place anchor at strain rate of 10^{-5} s^{-1}

Concrete cone breakout diameter (d_{cone}) of 230 mm was obtained for the 12.7-mm diameter anchor with embedment depth of 76.2 mm. An increase in the concrete cone breakout diameter from 246 mm to 292 mm was obtained for the increase in the embedment depth from 76.2 mm to 101.6 mm for the 15.9-mm diameter anchor. The increase in the concrete cone breakout diameter was from 255 mm to 390 mm for the increase in the embedment depth from 76.2 mm to 127 mm for the 19.1-mm diameter anchor. The concrete cone breakout diameter increased with increase in the anchor embedment depth. Hence, the load required to cause failure in the concrete increased due to the increase in the size of concrete above the anchor head for the deep embedment depths. Figure 4-6 shows the relation between the concrete cone breakout diameter, embedment depth and anchor diameter.

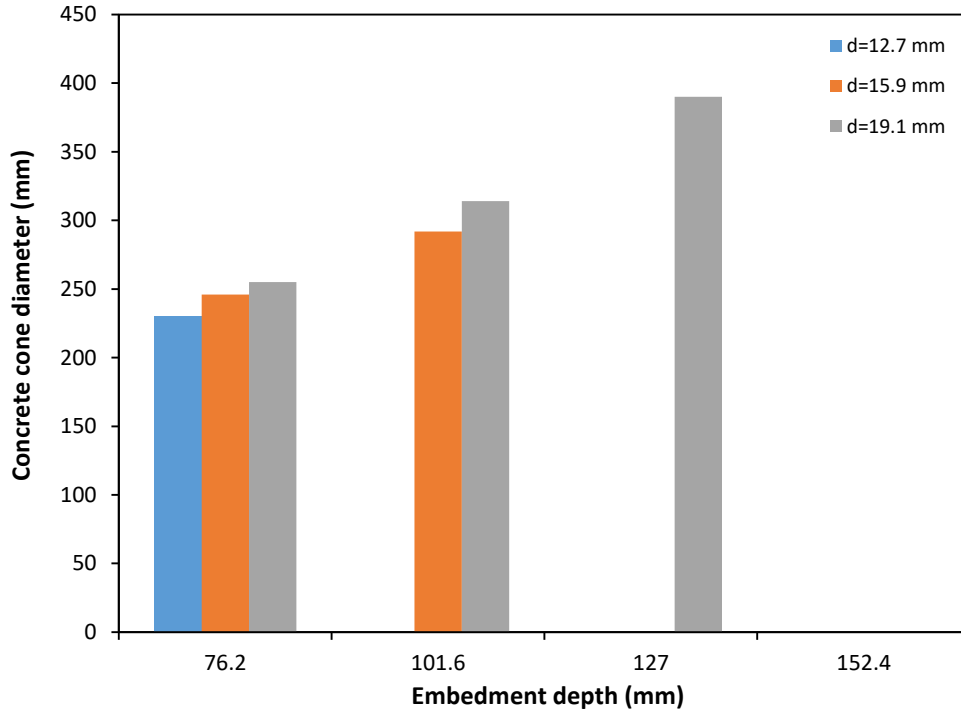


Figure 4-6: Effect of anchor embedment depth on the concrete cone diameter

The concrete cone breakout angle was determined by measuring the angle of inclination of the failure surface. Figure 4-7 shows the concrete cone breakout angle (θ_a) and the crack propagation angle (θ_b). Where, the crack propagation angle is equal to $90-\theta_a$. Table 4-3 shows the concrete cone breakout angle, cone diameter and corresponding failure mode for the embedment depths and diameters of the cast-in-place anchor under tensile load investigated. As shown in Table 4-3, average concrete cone breakout angle was 31.8° .

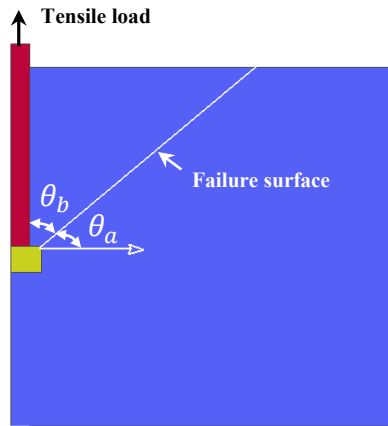


Figure 4-7: Cone breakout and crack propagation angles on the cast-in-place anchorage to concrete system

Table 4-3: Concrete cone diameter and cone breakout angle for the cast-in-place anchor at the static strain rate

h_{ef} (mm)	d (mm)	d_{cone} (mm)	θ_a (deg)	Failure mode
76.2	12.7	230	32	CC
	15.9	246	32	CC
	19.1	255	33	CC
101.6	12.7	-	-	S
	15.9	292	31	CC
	19.1	314	31	CC
127	12.7	-	-	S
	15.9	-	-	S
	19.1	390	32	CC
152.4	12.7	-	-	S
	15.9	-	-	S
	19.1	-	-	S

The failure mode of 12.7-mm, 15.9-mm and 19.1-mm diameter cast-in-place anchors with different embedment depths at strain rates ranging from 10^{-3} s^{-1} to 10^3 s^{-1} is presented in Figures 4-8, 4-9 and 4-10 respectively. At early stage of loading, cracks started to appear above the anchor head, and with further increase in time the cracks appeared on the top

surface of the concrete around the anchor circumference. As shown in Figure 4-8, for the anchor diameter of 12.7-mm with shallow embedment depth of 76.2 mm, cracks grow along the embedment depth and transferred to a wider area on the concrete. These cracks then propagated diagonally forming concrete cone and leads to concrete cone breakout failure at strain rates up to 10 s^{-1} . At high strain rates of 10^2 s^{-1} and 10^3 s^{-1} steel anchor failure was observed. For embedment depths of 101.6 mm, 127 mm and 152.4 mm, steel anchor failure is the dominant failure mode at the strain rates ranging from 10^{-3} s^{-1} to 10^3 s^{-1} .

As shown in Figure 4-9, the failure mode is concrete cone breakout failure for the anchor diameter of 15.9-mm with embedment depths of 76.2 mm and 101.6 mm at strain rates of 10^{-3} s^{-1} to 10 s^{-1} . Concrete cracking was observed at strain rate of 10^2 s^{-1} whereas steel anchor failure was observed at strain rate of 10^3 s^{-1} . For the anchor embedment depths of 127 mm and 152.4 mm steel anchor failure was observed at all the strain rates investigated.

Figure 4-10 shows concrete cone breakout failure mode for the 19.1-mm anchor diameter with embedment depths of 76.2 mm and 101.6 mm at strain rates ranging from 10^{-3} s^{-1} to 10 s^{-1} . Concrete cracking was observed at strain rates of 10^2 s^{-1} while steel anchor failure was observed at strain rate of 10^3 s^{-1} . The increase in the strain rate increased the concrete strength and thus resulting in steel anchor failure. At embedment depth of 127 mm concrete cone breakout failure was observed at strain rates of 10^{-3} s^{-1} to 10 s^{-1} . Steel anchor failure was observed at strain rates of 10^2 s^{-1} and 10^3 s^{-1} . Also, steel anchor failure was observed at embedment depth of 152.4 mm at all the strain rates investigated.

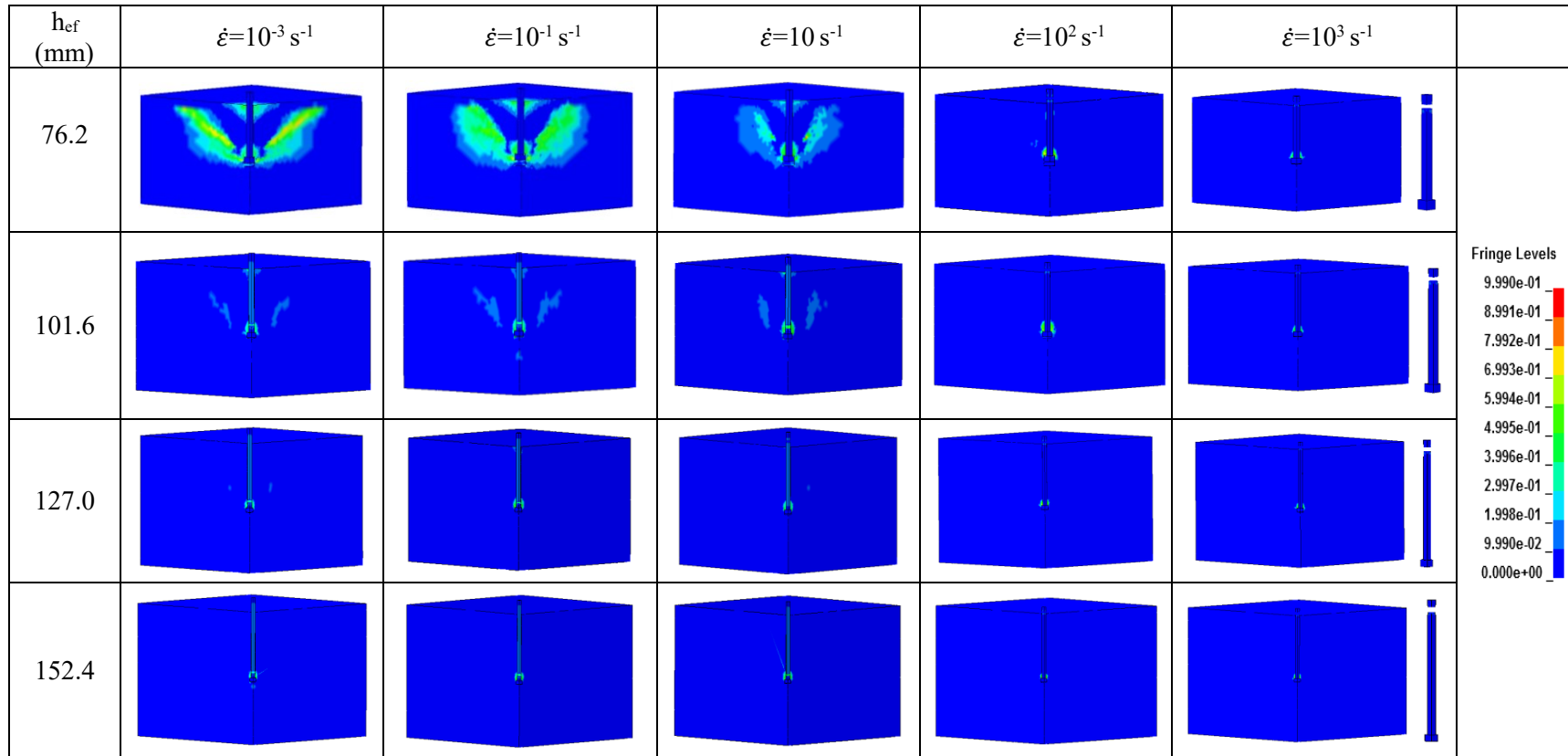


Figure 4-8: Failure mode of 12.7 mm diameter cast-in-place anchor at different strain rates

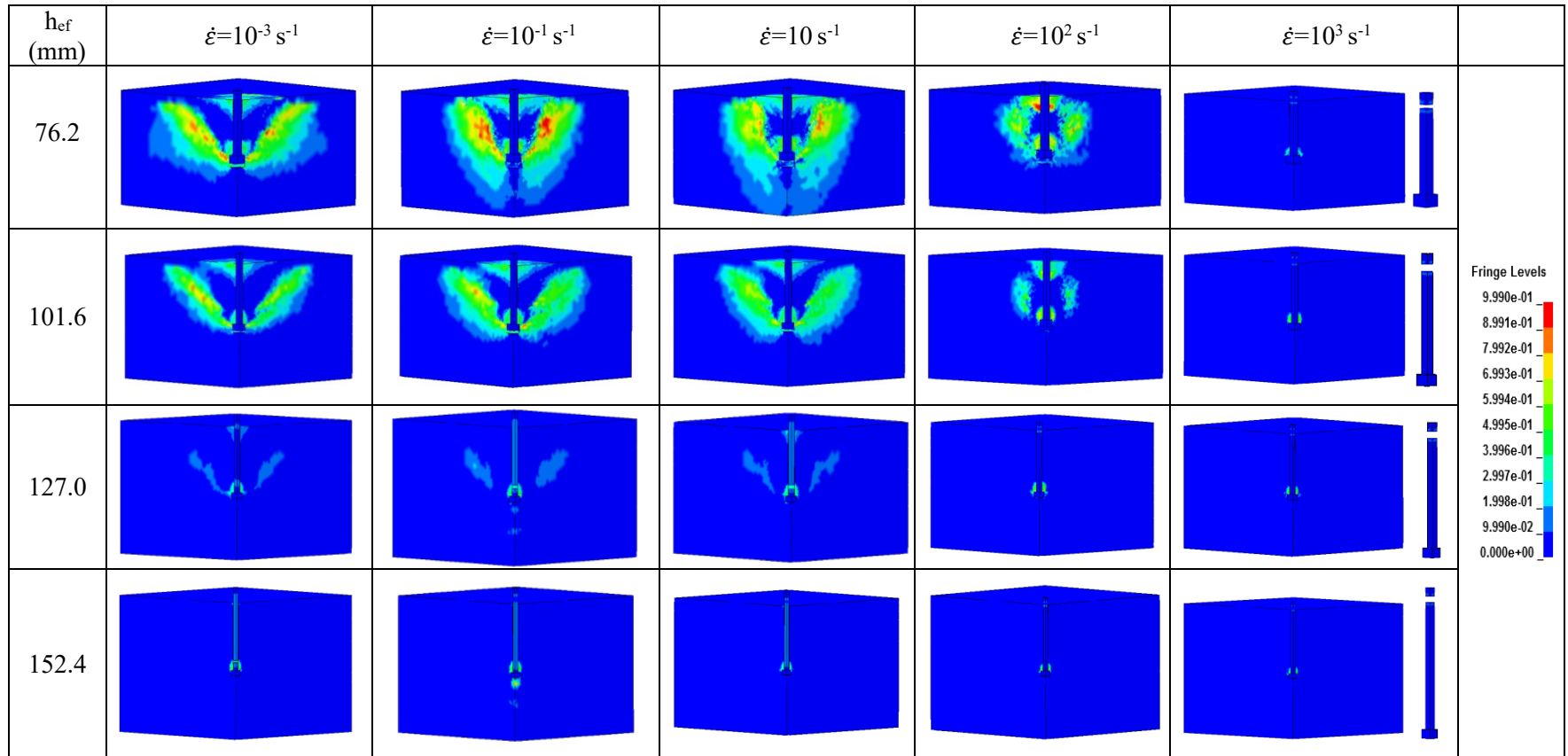


Figure 4-9: Failure mode of 15.9 mm diameter cast-in-place anchor at different strain rates

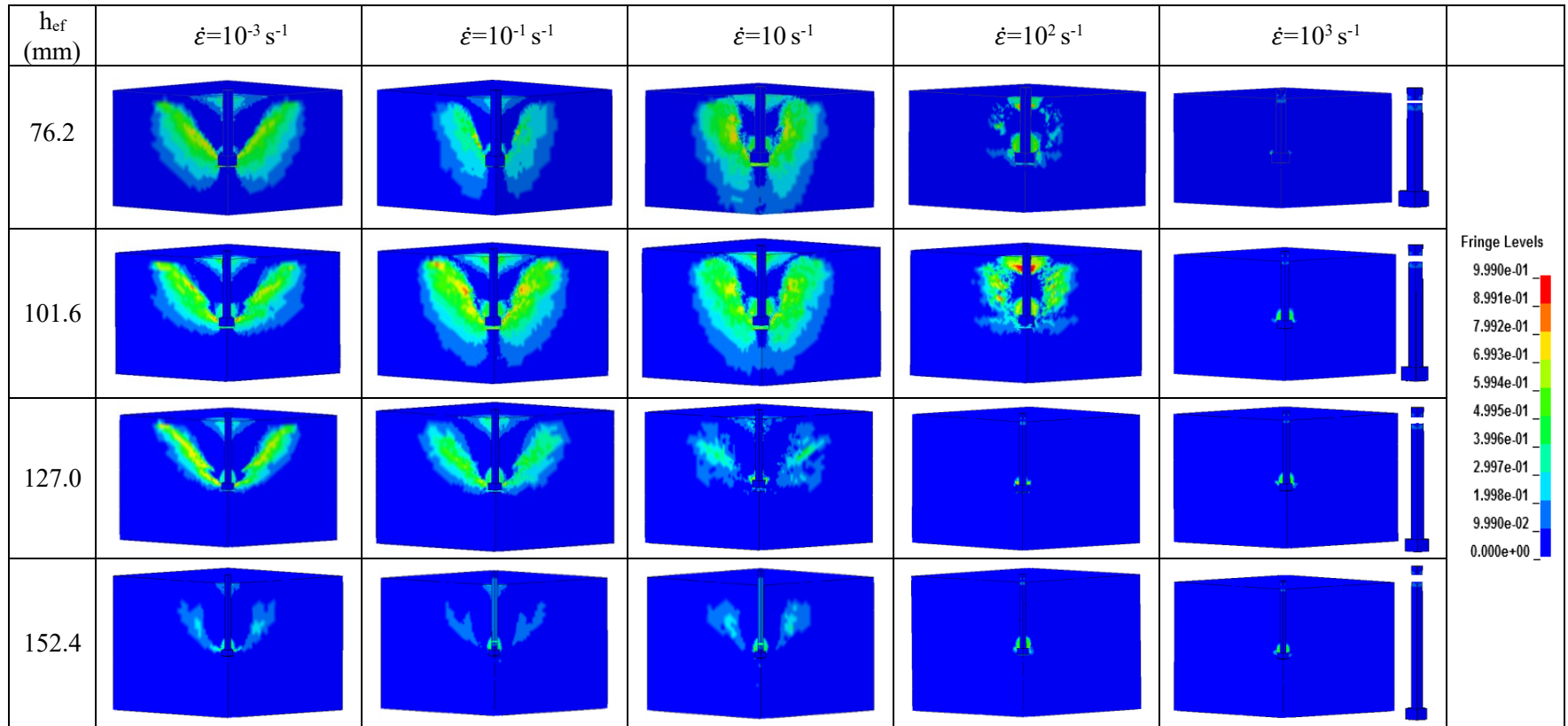


Figure 4-10: Failure mode of 19.1 mm diameter cast-in-place anchor at different strain rates

From Figures 4-8, 4-9 and 4-10, it can be seen that the failure mode is affected by the strain rate. The increase in the strain rate decreased the concrete cone breakout diameter, however the increase in the strain rate increased the strength of the concrete and steel resulted in increasing the failure load. Table 4-4 shows the failure mode for cast-in-place anchors under tensile load at different strain rates.

Table 4-4: Failure mode for cast-in-place anchors under tensile load at different strain rates

Model No.	d (mm)	h _{ef} (mm)	Failure mode*					
			Strain rate (s ⁻¹)					
			$\dot{\epsilon}=10^{-5}$	$\dot{\epsilon}=10^{-3}$	$\dot{\epsilon}=10^{-1}$	$\dot{\epsilon}=10$	$\dot{\epsilon}=10^2$	$\dot{\epsilon}=10^3$
1	12.7	76.2	CC	CC	CC	CC	S	S
2	12.7	101.6	S	S	S	S	S	S
3	12.7	127.0	S	S	S	S	S	S
4	12.7	152.4	S	S	S	S	S	S
5	15.9	76.2	CC	CC	CC	CC	COC	S
6	15.9	101.6	CC	CC	CC	CC	COC	S
7	15.9	127.0	S	S	S	S	S	S
8	15.9	152.4	S	S	S	S	S	S
9	19.1	76.2	CC	CC	CC	CC	COC	S
10	19.1	101.6	CC	CC	CC	CC	COC	S
11	19.1	127.0	CC	CC	CC	CC	S	S
12	19.1	152.4	S	S	S	S	S	S

*Failure mode: CC= concrete cone breakout, COC= concrete cracking, S=steel anchor failure

The crack propagation angle (θ_b) was measured for the cast-in-place anchors at the ultimate tensile load and presented in Table 4-5. As shown in Table 4-5 and Figures 4-8, 4-9 and 4-10, the crack propagation angle decreased with increasing the strain rate for the cast-in-place anchors where concrete cone breakout failure is observed.

Table 4-5: Crack propagation angle for the cast-in-place anchors at different strain rates

Model No.	d (mm)	h _{ef} (mm)	Crack propagation angle (deg)					
			Strain rate (s ⁻¹)					
			$\dot{\epsilon}=10^{-5}$	$\dot{\epsilon}=10^{-3}$	$\dot{\epsilon}=10^{-1}$	$\dot{\epsilon}=10$	$\dot{\epsilon}=10^2$	$\dot{\epsilon}=10^3$
1	12.7	76.2	58	56	53	50	-	-
2	12.7	101.6	-	-	-	-	-	-
3	12.7	127.0	-	-	-	-	-	-
4	12.7	152.4	-	-	-	-	-	-
5	15.9	76.2	58	56	53	48	-	-
6	15.9	101.6	59	57	55	50	-	-
7	15.9	127.0	-	-	-	-	-	-
8	15.9	152.4	-	-	-	-	-	-
9	19.1	76.2	57	55	50	46	-	-
10	19.1	101.6	59	56	50	46	-	-
11	19.1	127.0	58	55	51	48	-	-
12	19.1	152.4	-	-	-	-	-	-

4.1.5 Effect of design parameters on failure mode and ultimate tensile load

Figures 4-11, 4-12 and 4-13 show the effect of strain rate on the failure mode and ultimate tensile load for the 12.7-mm, 15.9-mm and 19.1-mm diameter cast-in-place anchors respectively. As shown in Figure 4-11, the tensile load increased from 64.5 kN to 79.4 kN for the 76.2 mm embedment depth at the strain rates up to 10 s^{-1} where concrete cone breakout failure was observed. At strain rate of 10^2 s^{-1} the ultimate tensile load increased to 105.3 kN where steel anchor failure was observed. At high strain rate of 10^3 s^{-1} insignificant increase in the ultimate tensile load was obtained where steel anchor failure was observed. Steel anchor failure was observed for 101.6 mm, 127 mm and 152.4 mm embedment depths for all the strain rates investigated. The increase in the strain rate from 10^{-5} s^{-1} to 10^3 s^{-1} increased the ultimate tensile load 12.6%, 12% and 10.6% for the anchor embedment depths of 101.6 mm, 127 mm and 152.4 mm respectively.

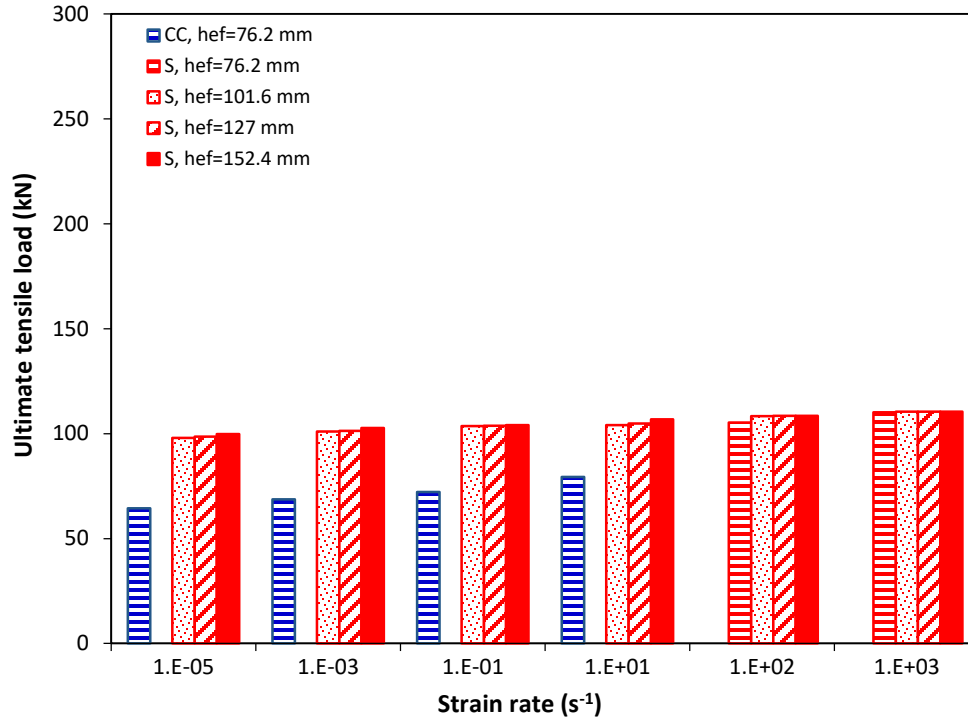


Figure 4-11: Strain rate effect on the failure mode and ultimate tensile load for cast-in-place anchor diameter of 12.7 mm

As shown in Figure 4-12, the tensile load increased from 68.61 kN to 98.14 kN and from 104.17 kN to 128.75 kN for the 76.2 mm and 101.6 mm embedment depths as the strain rate increased from 10^{-5} s^{-1} to 10 s^{-1} where concrete cone breakout failure was observed. Further increase in the strain rate to 10^2 s^{-1} and 10^3 s^{-1} increased the ultimate tensile load, where concrete cracking and steel anchor failure were observed at strain rates of 10^2 s^{-1} and 10^3 s^{-1} respectively. Also, steel anchor failure was observed for 127 mm and 152.4 mm embedment depths for all the strain rates investigated. The increase in the strain rate from 10^{-5} s^{-1} to 10^3 s^{-1} increased the ultimate tensile load 17.4% and 16.5% for the anchor embedment depths of 127 mm and 152.4 mm respectively.

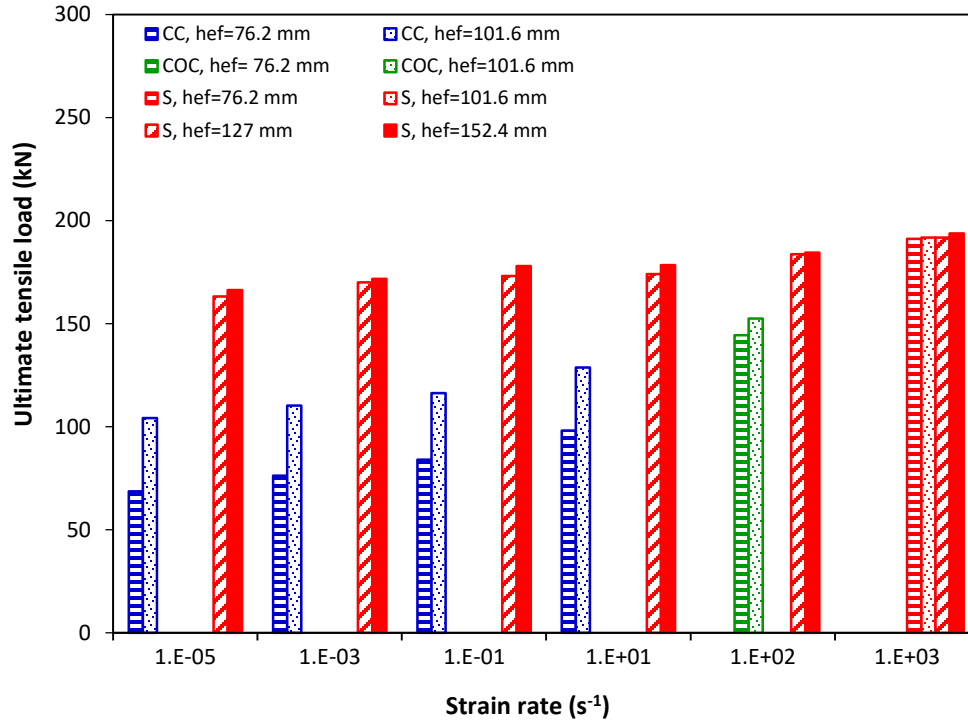


Figure 4-12: Strain rate effect on the failure mode and ultimate tensile load for cast-in-place anchor diameter of 15.9 mm

As shown in Figure 4-13, the tensile load increased with the increase in the strain rates up to 10 s^{-1} for anchor embedment depths of 76.2 mm, 101.6 mm and 127 mm where concrete cone breakout failure was observed. The ultimate tensile load increased with further increase in the strain rate to 10^2 s^{-1} where concrete cracking was observed for embedment depths of 76.2 mm and 101.6 mm while steel anchor failure was observed for embedment depth of 127 mm. At high strain rate of 10^3 s^{-1} , the ultimate tensile load increased where steel anchor failure was observed. Also, steel anchor failure was observed for 152.4 mm embedment depth at all the strain rates investigated with an increase in the ultimate tensile load of 13.4%.

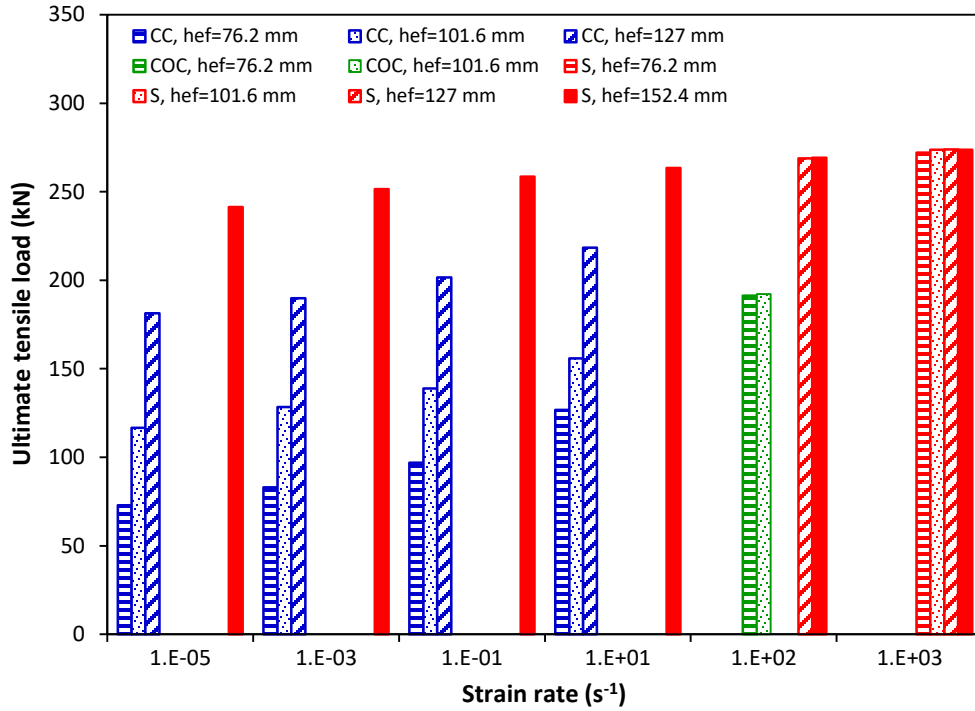


Figure 4-13: Strain rate effect on the failure mode and ultimate tensile load for cast-in-place anchor diameter of 19.1 mm

4.1.6 Effect of anchor embedment depth on the concrete cone depth

Figures 4-14, 4-15 and 4-16 show the effect of anchor embedment depth on concrete cone depth and ultimate tensile load for 12.7-mm, 15.9-mm and 19.1-mm diameter cast-in-place anchors respectively. Different concrete cone depths are obtained from the models for tension response at strain rate of 10^{-5} s^{-1} for the embedment depths of 76.2 mm, 101.6 mm, 127 mm, and 152.4 mm. As shown in Figure 4-14, for the 12.7-mm diameter cast-in-place anchor, concrete cone breakout is obtained at embedment depth of 76.2 mm. For anchor embedment depths of 101.6 mm, 127 mm and 152.4 mm steel anchor failure mode was observed. For the anchor diameter of 15.9-mm (Figure 4-15), concrete cone breakout failure is obtained for the embedment depths of 76.2 mm and 101.6 mm whereas steel

anchor failure is observed for the embedment depths of 127 mm and 152.4 mm. For the 19.1-mm diameter cast-in-place anchor, as shown in Figure 4-16, the concrete cone depth increased with the increase in the embedment depth from 76.2 mm to 127 mm where concrete cone breakout failure was observed. Steel anchor failure was observed at embedment depth of 152.4 mm. From Figures 4-14, 4-15 and 4-16, it can be seen that the ultimate tensile load increases with the increase in the anchor diameter. Also, the ultimate tensile load increased with the increase in the embedment depth when the concrete cone breakout failure or transition from concrete cone breakout failure to steel anchor failure is observed.

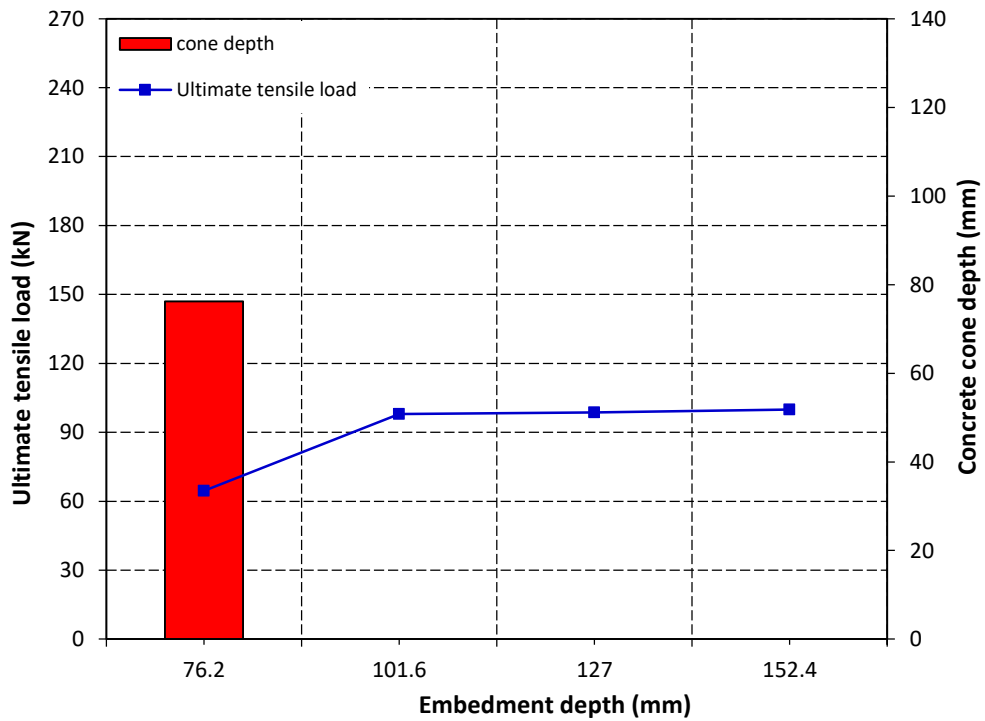


Figure 4-14: Effect of anchor embedment depth on the concrete cone depth and ultimate tensile load for 12.7 mm diameter cast-in-place anchor

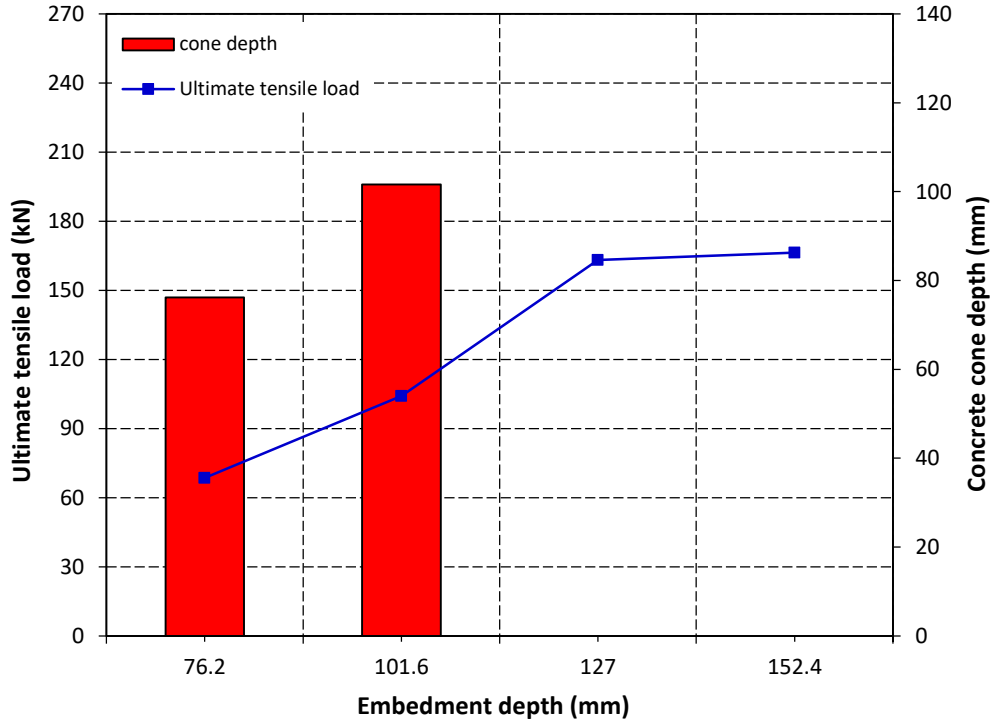


Figure 4-15: Effect of anchor embedment depth on the concrete cone depth and ultimate tensile load for 15.9 mm diameter cast-in-place anchor

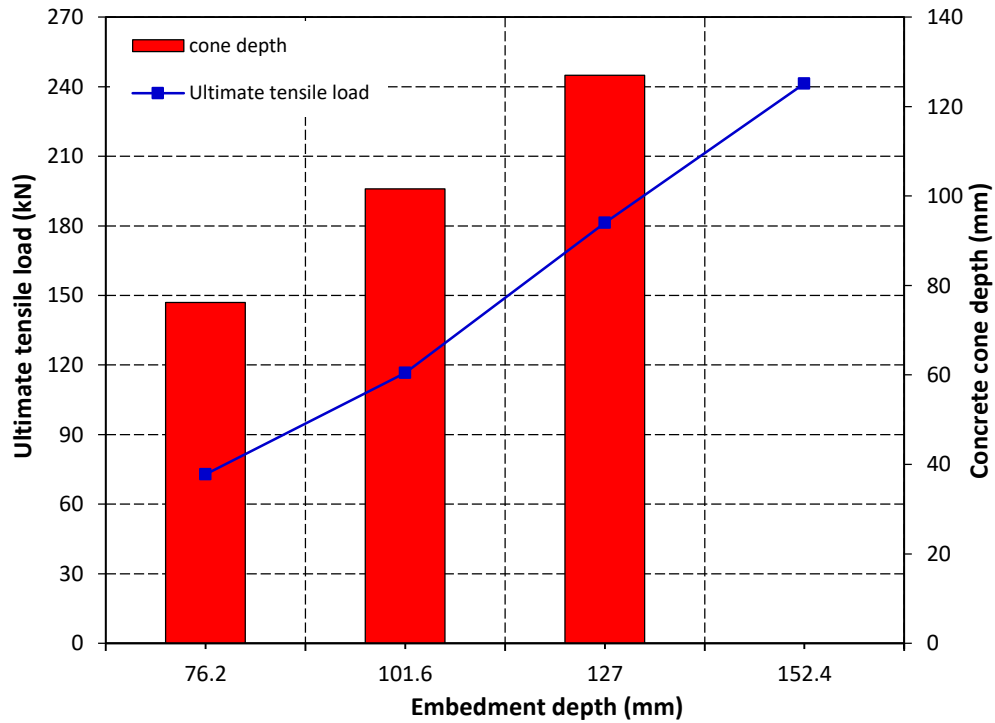


Figure 4-16: Effect of anchor embedment depth on the concrete cone depth and ultimate tensile load for 19.1 mm diameter cast-in-place anchor

4.1.7 Effect of strain rate on concrete cone breakout diameter

Figure 4-17 shows the displacement contours for 15.9-mm diameter cast-in-place anchor with embedment depth of 76.2 mm under tensile load at strain rates of 10^{-5} s^{-1} , 10^{-3} s^{-1} , 10^{-1} s^{-1} , 10 s^{-1} , 10^2 s^{-1} and 10^3 s^{-1} . As shown in the figure, the increase in the strain rate decreased the concrete cone breakout diameter. The decrease in the concrete cone breakout diameter is significant at strain rate of 10^2 s^{-1} while steel anchor failure is observed at highest strain rate of 10^3 s^{-1} .

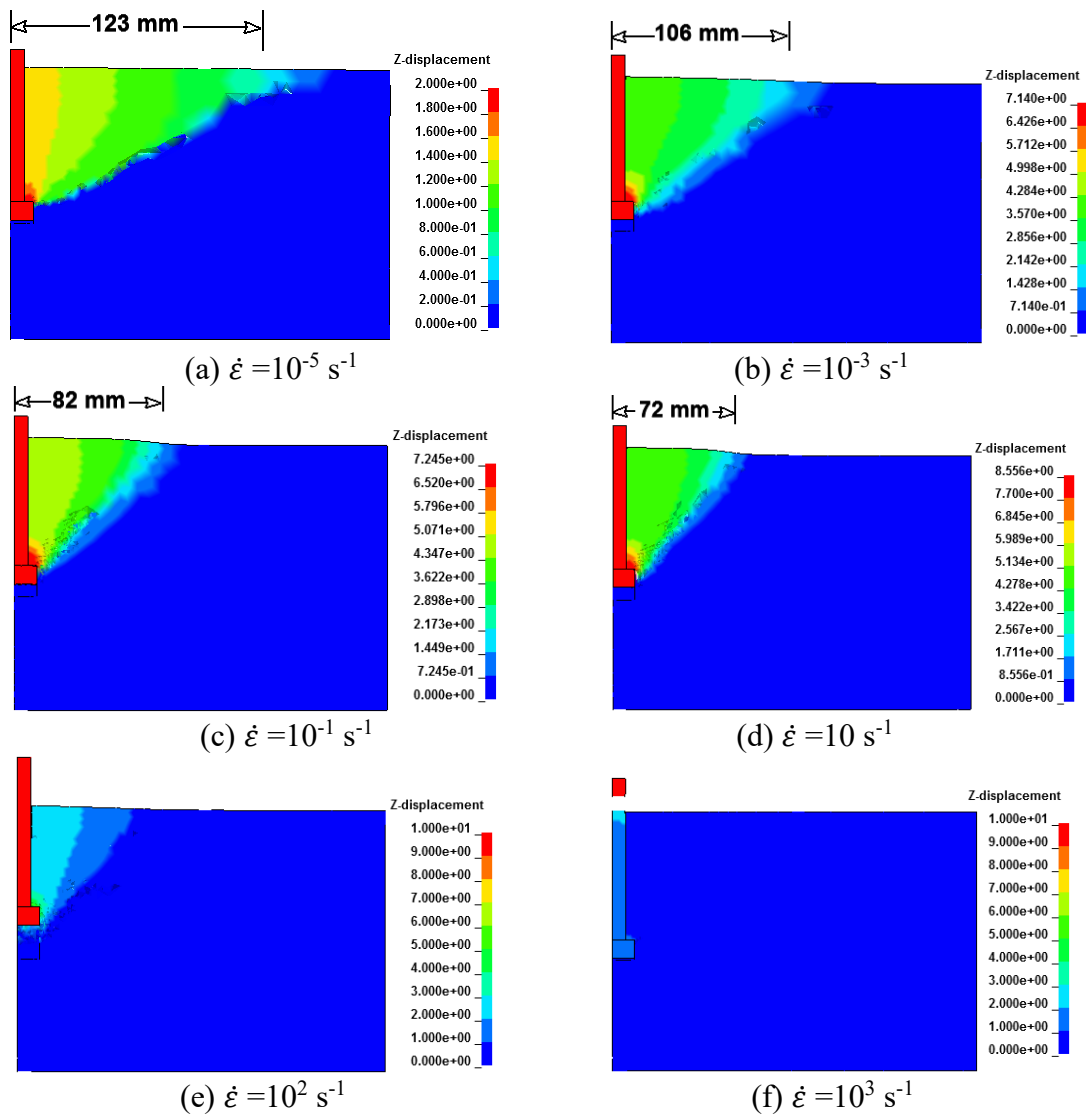


Figure 4-17: Displacement contours of 15.9 mm diameter cast-in-place anchor at strain rates ranging from 10^{-5} s^{-1} to 10^3 s^{-1}

4.1.8 Effect of strain rate on the tensile behaviour of cast-in-place anchors

Tensile behaviour of cast-in-place anchor embedded into concrete was investigated at strain rates ranging from 10^{-5} s^{-1} to 10^3 s^{-1} . Figures 4-18, 4-19, 4-20, 4-21, 4-22 and 4-23 present the load-displacement response for the 12.7-mm diameter cast-in-place anchor at strain rates of 10^{-5} s^{-1} , 10^{-3} s^{-1} , 10^{-1} s^{-1} , 10 s^{-1} , 10^2 s^{-1} and 10^3 s^{-1} respectively. The displacement in the z-direction (shown in Figure 4-2) was measured at the top of the anchor using History-Nodal-z-displacement in LS-DYNA post processor.

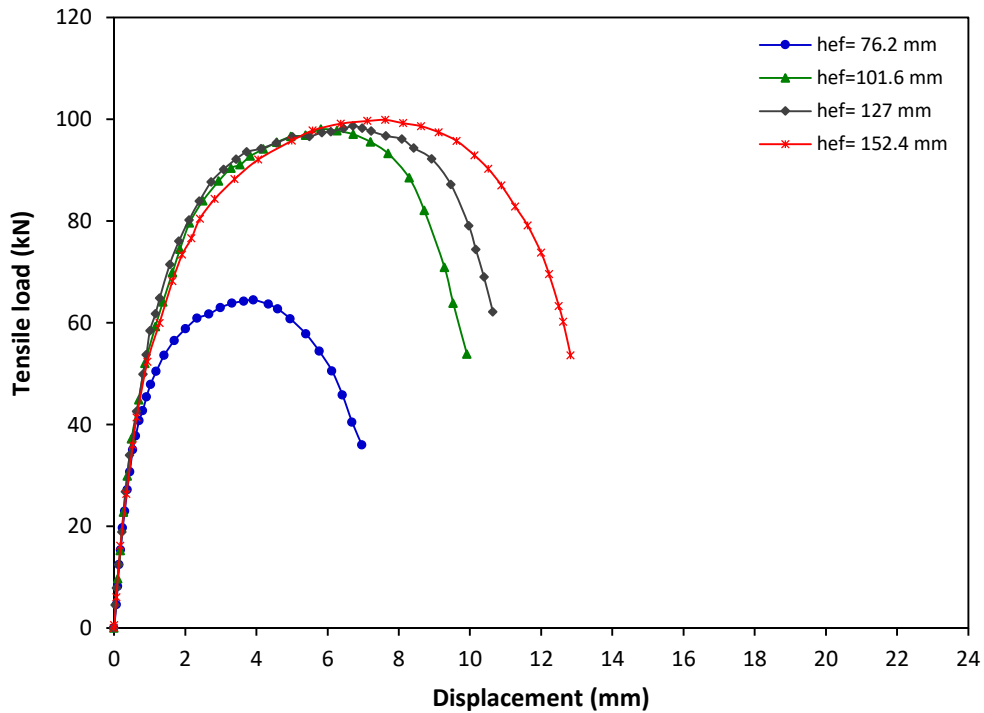


Figure 4-18: Tensile load-displacement graph for 12.7 mm diameter cast-in-place anchor at strain rate of 10^{-5} s^{-1}

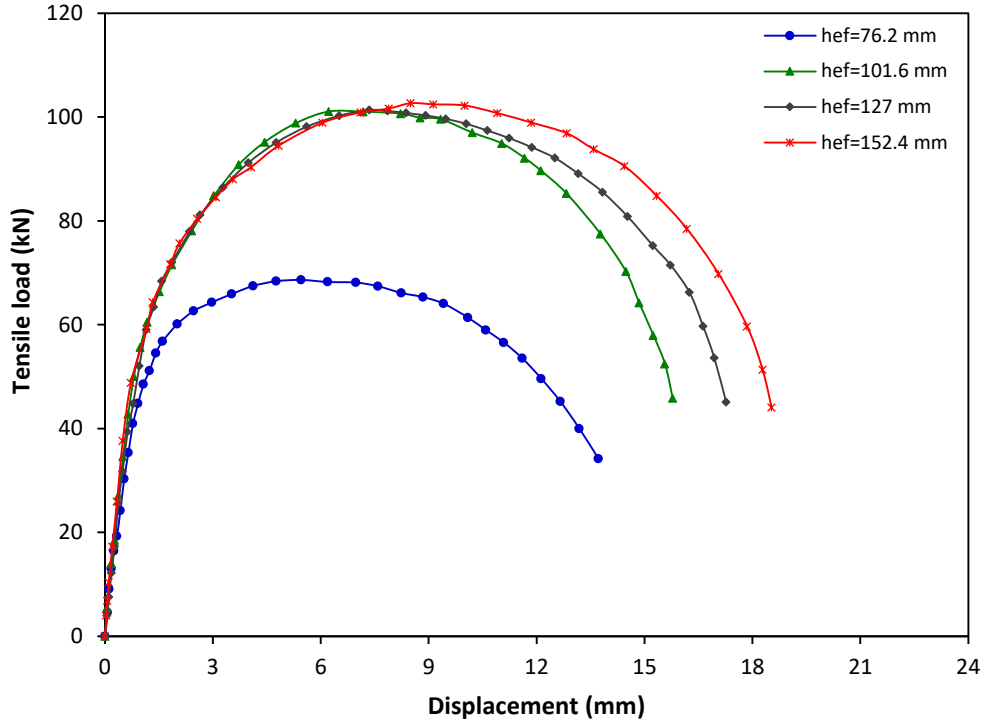


Figure 4-19: Tensile load-displacement graph for 12.7 mm diameter cast-in-place anchor at strain rate of 10^{-3} s^{-1}

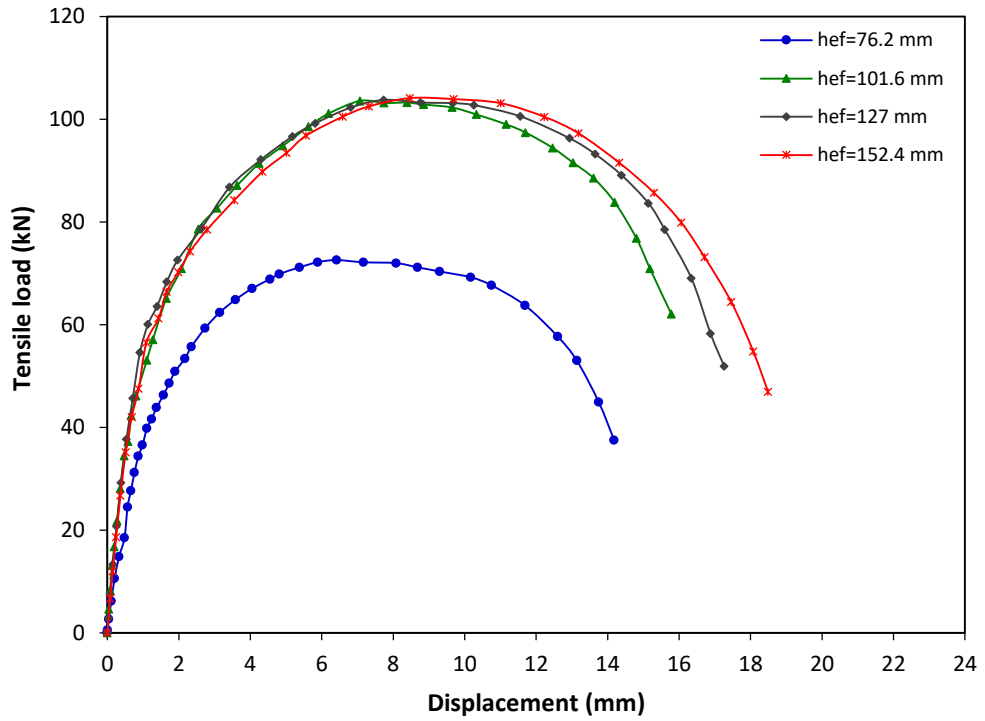


Figure 4-20: Tensile load-displacement graph for 12.7 mm diameter cast-in-place anchor at strain rate of 10^{-1} s^{-1}

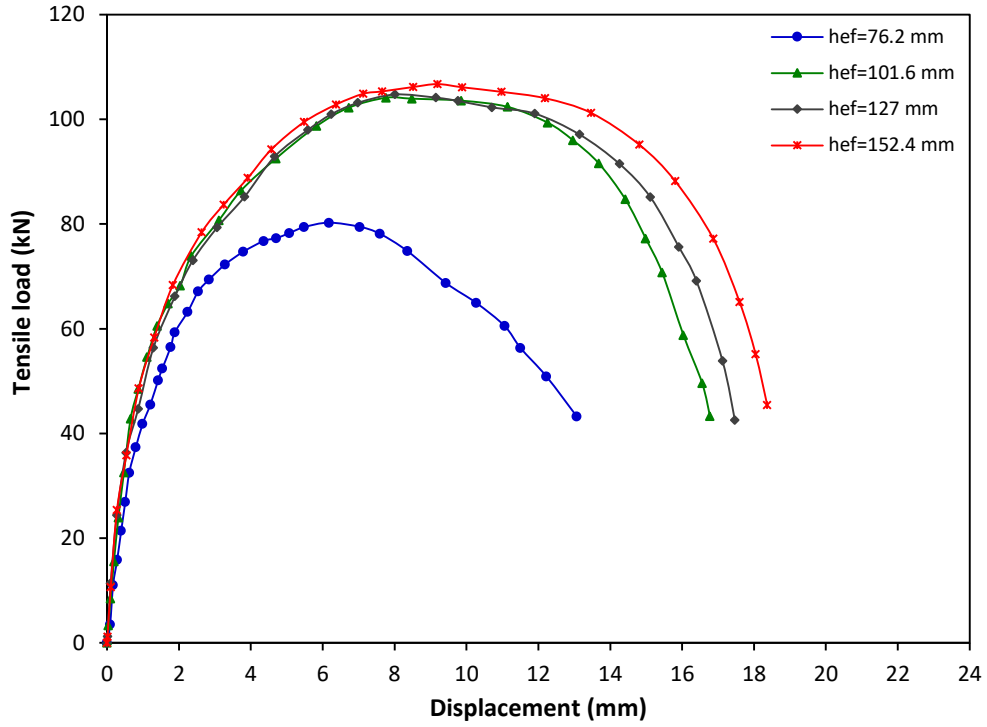


Figure 4-21: Tensile load-displacement graph for 12.7 mm diameter cast-in-place anchor at strain rate of 10^{-1} s^{-1}

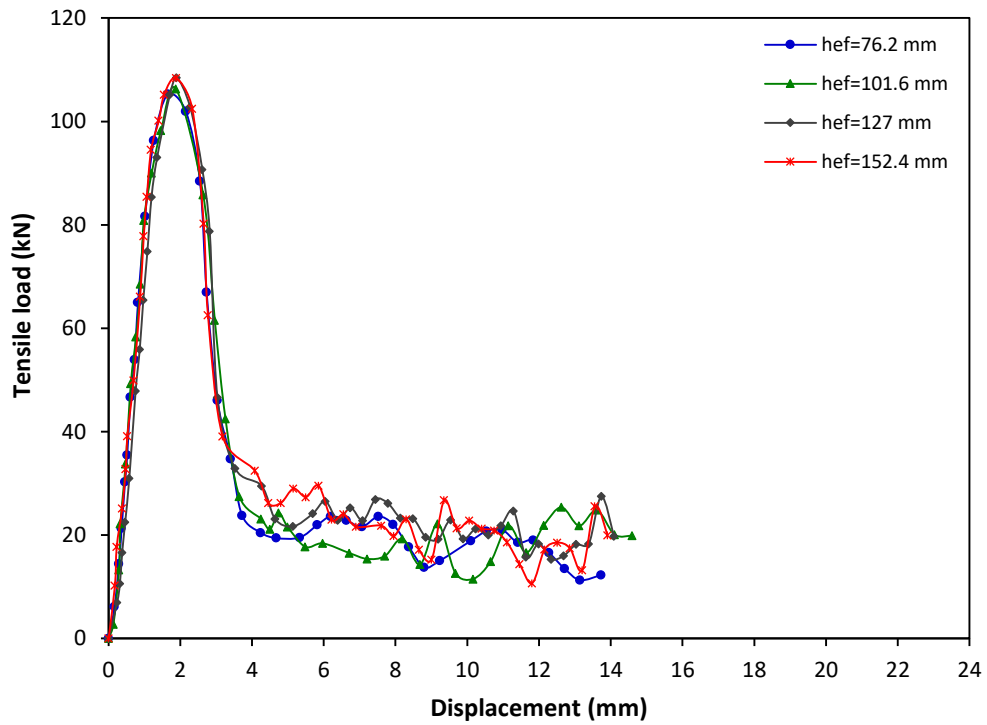


Figure 4-22: Tensile load-displacement graph for 12.7 mm diameter cast-in-place anchor at strain rate of 10^2 s^{-1}

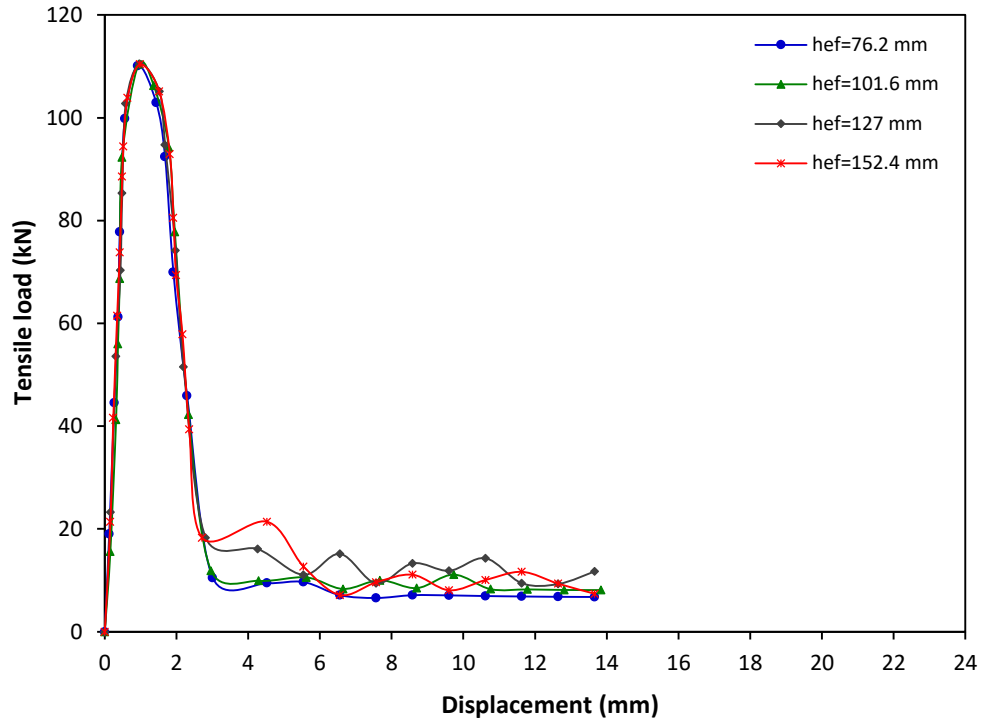


Figure 4-23: Tensile load-displacement graph for 12.7 mm diameter cast-in-place anchor at strain rate of 10^3 s^{-1}

As shown from the figures, the tensile load increased with the displacement until it reaches the ultimate load, then the load decreased with further increase in displacement until failure. The increase in the embedment depth from 76.2 mm to 101.6 mm shows an increase in the ultimate tensile load for the cast in place anchor. This is attributed to the increase in the amount of concrete above the anchor head and increase in the failure area as the embedment depth increased. The increased failure surface area results in increased loads required to breakout the concrete. Same trend for the effect of anchor embedment depth on the tensile load was reported by Eligehausen et al. (Eligehausen et al., 1992). The increase in embedment depth from 101.6 mm to 152.4 mm show very little increase in the ultimate tensile load of the cast-in-place concrete anchorage system as the failure mode was by steel anchor failure. As the strain rate increased the failure mode transitions from concrete cone

breakout failure to steel anchor failure. At this point the ultimate failure load of the anchorage systems is the same irrespective of embedment depth. This trend is observed at strain rate of 10^2 s^{-1} and higher for 12.7-mm diameter anchor.

In general, the increase in the strain rate from 10^{-5} s^{-1} to 10^3 s^{-1} increases the ultimate tensile load. The ultimate tensile load increased from 64.48 kN to 110.13 kN for the anchor embedment depth of 76.2 mm when the strain rate increased from 10^{-5} s^{-1} to 10^3 s^{-1} . The load-displacement response of the cast-in-place anchorage system at increased strain rate of 10^2 s^{-1} and 10^3 s^{-1} is characterized by a linear response to the peak load and then shows a drop in load.

Tensile load-displacement response of the 15.9-mm and 19.1-mm diameter cast-in-place anchors with embedment depths of 76.2 mm, 101.6 mm, 127 mm and 152.4 mm at strain rates of 10^{-5} s^{-1} , 10^{-3} s^{-1} , 10^{-1} s^{-1} , 10 s^{-1} , 10^2 s^{-1} and 10^3 s^{-1} show similar trends to the 12.7-mm diameter anchor and are presented in Appendix C.

Tables 4-6, 4-7 and 4-8 show the ultimate tensile load (F_u) and corresponding displacements (δ) for the 12.7-mm, 15.9-mm and 19.1-mm diameter cast-in-place anchors at strain rates ranging from 10^{-5} s^{-1} to 10^3 s^{-1} . As shown in the tables, the increase in the strain rate from 10^{-5} s^{-1} to 10^3 s^{-1} increases the ultimate tensile load for the cast-in-place anchors.

Table 4-6: Ultimate tensile load and displacement results for the 12.7 mm diameter cast-in-place anchor

Model No.	d (mm)	h_{ef} (mm)	$\dot{\epsilon}$ (s^{-1})	F_u (kN)	δ (mm)	*Failure mode
1	12.7	76.2	10^{-5}	64.48	3.91	CC
2		101.6		98.03	5.82	S
3		127		98.64	6.72	S
4		152.4		99.86	7.62	S
5	12.7	76.2	10^{-3}	68.63	5.46	CC
6		101.6		101.05	6.22	S
7		127		101.37	7.35	S
8		152.4		102.63	8.49	S
9	12.7	76.2	10^{-1}	72.16	5.89	CC
10		101.6		103.55	7.07	S
11		127		103.74	7.74	S
12		152.4		104.10	8.47	S
13	12.7	76.2	10	79.39	5.49	CC
14		101.6		104.13	7.76	S
15		127		104.76	8.01	S
16		152.4		106.75	9.19	S
17	12.7	76.2	10^2	105.30	1.65	S
18		101.6		108.28	1.88	S
19		127		108.48	1.89	S
20		152.4		108.41	1.88	S
21	12.7	76.2	10^3	110.13	0.93	S
22		101.6		110.40	0.94	S
23		127		110.49	0.97	S
24		152.4		110.42	0.98	S

Table 4-7: Ultimate tensile load and displacement results for the 15.9 mm diameter cast-in-place anchor

Model No.	d (mm)	h_{ef} (mm)	$\dot{\epsilon}$ (s^{-1})	F_u (kN)	δ (mm)	*Failure mode
1	15.9	76.2	10^{-5}	68.61	1.34	CC
2		101.6		104.17	3.77	CC
3		127		163.26	6.23	S
4		152.4		166.35	7.14	S
5	15.9	76.2	10^{-3}	76.32	3.20	CC

6		101.6		110.25	3.86	CC
7		127		170.01	7.54	S
8		152.4		171.81	8.17	S
9	15.9	76.2	10^{-1}	83.96	3.08	CC
10		101.6		116.33	6.22	CC
11		127		173.22	7.68	S
12		152.4		177.95	8.58	S
13	15.9	76.2	10	98.14	3.67	CC
14		101.6		128.75	6.91	CC
15		127		174.02	8.06	S
16		152.4		178.35	9.29	S
17	15.9	76.2	10^2	144.46	1.05	COC
18		101.6		152.52	1.32	COC
19		127		183.74	1.54	S
20		152.4		184.52	1.30	S
21	15.9	76.2	10^3	191.15	1.24	S
22		101.6		191.71	1.39	S
23		127		191.73	1.36	S
24		152.4		193.82	1.41	S

Table 4-8: Ultimate tensile load and displacement results for the 19.1 mm diameter cast-in-place anchor

Model No.	d (mm)	h_{ef} (mm)	$\dot{\epsilon}$ (s^{-1})	F_u (kN)	δ (mm)	*Failure mode
1	19.1	76.2	10^{-5}	72.88	0.82	CC
2		101.6		116.65	1.31	CC
3		127		181.29	2.76	CC
4		152.4		241.37	6.91	S
5	19.1	76.2	10^{-3}	83.09	1.76	CC
6		101.6		128.44	3.45	CC
7		127		189.80	4.63	CC
8		152.4		251.55	6.88	S

9	19.1	76.2	10^{-1}	96.94	1.90	CC
10		101.6		138.88	3.98	CC
11		127		201.63	5.59	CC
12		152.4		258.58	7.82	S
13	19.1	76.2	10	126.83	2.14	CC
14		101.6		155.88	3.55	CC
15		127		218.48	4.19	CC
16		152.4		263.37	7.09	S
17	19.1	76.2	10^2	191.30	1.70	COC
18		101.6		192.14	1.98	COC
19		127		268.75	2.19	S
20		152.4		269.15	2.25	S
21	19.1	76.2	10^3	272.09	1.74	S
22		101.6		273.78	2.07	S
23		127		273.95	1.83	S
24		152.4		273.79	1.93	S

Tables 4-6, 4-7 and 4-8 show that the increase in the anchor diameter from 12.7 mm to 19.1 mm increased the ultimate tensile load for all the embedment depths and strain rates investigated. The increase in the anchor diameter requires larger anchor head that increase the bearing area above the anchor head and the failure surface area. Also, it can be seen that the embedment depth has a greater effect on the ultimate tensile load at the same strain rate when concrete cone breakout failure is the dominant failure mode. However, the increase in the embedment depth has no influence on the ultimate tensile load when steel anchor failure is the dominant failure mode. The increase in the ultimate tensile load with the increase in the strain rate is attributed to the increase in concrete resistance under increased strain rate (Ožbolt et al., 2006; Sato et al., 2004; Solomos and Berra, 2006).

4.1.9 Effect of strain rate on the ultimate tensile load and dynamic increase factor of cast-in-place anchors

Investigating the influence of strain rate on the behaviour of anchors is necessary to predict a suitable DIF that can be used for design of anchorage systems subjected to different strain rates. The ratio of the dynamic to static strength of the cast-in-place anchor is defined as the dynamic increase factor (DIF). A safe and economical design of the anchors under dynamic loading can be achieved by applying the DIF to the ultimate load measured under static loading (Brimmah et al., 2009). The DIF can be used to represent the effect of strain rate on concrete strength (compressive and tensile), yield and ultimate strength of steel (Malvar and Crawford, 1998; Murray, 2007; Solomos and Berra, 2006; Zhou et al., 2008). The common approach to model the effect of strain rate on the concrete under tension and compression loading is proposed by Committee Euro International du Beton (CEB) code that introduced equations to predict the DIF of the concrete subjected to different strain rates (Malvar & Ross, 1998). The CEB proposed equations demonstrate that the DIF is a power function of the strain rate ratio (Malvar & Crawford, 1998; Malvar & Ross, 1998; Gebbeken & Ruppert, 2000). In this research, in order to predict the increase in strength of anchorage system due to increase in the steel and concrete strength with the increase in the strain rate, DIF for the anchorage to concrete system was investigated. The lowest strain rate of 10^{-5} s^{-1} is representative of static loading and will be used as the baseline for comparison with cast-in-place anchor capacity at the higher strain rates for the anchors exhibiting concrete cone breakout failure. For the anchors exhibiting steel failure mode at strain rate higher than 10^{-5} s^{-1} , the dynamic increase factor is taken as the ratio of ultimate dynamic load to the ultimate static steel failure load.

Figures 4-24, 4-25, 4-26 and 4-27 present the ultimate tensile load and DIF plotted as a function of the strain rate for the 12.7-mm, 15.9-mm and 19.1-mm diameter cast-in-place anchors with embedment depths of 76.2 mm, 101.6 mm, 127 mm and 152.4 mm respectively. As shown in the figures, the ultimate tensile load increases with increase in the anchor diameter from 12.7-mm to 19.1-mm. It can be seen from Figures 4-24 and 4-25, the ultimate tensile load versus strain rate relationship is bilinear with a change in slope at strain rate of 10 s^{-1} for anchor diameters of 15.9-mm and 19.1-mm. The ultimate tensile load increases with increase in the strain rate from 10^{-5} s^{-1} to 10 s^{-1} . A significant increase in the ultimate tensile load is observed when the strain rate increased from 10 s^{-1} to 10^3 s^{-1} for anchor diameters of 15.9-mm and 19.1-mm. The increase in the strain rate from 10^2 s^{-1} to 10^3 s^{-1} for the anchor diameter of 12.7-mm with embedment depth of 76.2 mm has a slight influence on the ultimate tensile load where steel anchor failure is observed (Figure 4-24). For the anchor diameter of 12.7-mm with embedment depth of 101.6 mm (Figure 4-25), an increase in the ultimate tensile load from 98.03 kN to 110.4 kN (12.6% increase) was obtained where steel anchor failure is observed at all strain rates investigated.

Figure 4-24 is representative of DIF of anchorage systems failing by concrete cone breakout. It can be seen from Figure 4-24 for anchor embedment depth of 76.2 mm the DIF increased with the increase in the strain rate from 10^{-5} s^{-1} to 10^2 s^{-1} for all anchor diameters, except for anchor diameter of 12.7 mm where the dynamic increase factor is measured as the ratio of the dynamic load to the steel failure load. The increase in the strain rate from 10^{-5} s^{-1} to 10^{-1} s^{-1} increased the DIF from 1 to 1.1, 1.2 and 1.3 for the anchor diameters of 12.7-mm, 15.9-mm and 19.1-mm respectively. The increase in the strain rate from 10 s^{-1}

to 10^2 s^{-1} increased the DIF significantly from 1.43 to 2.11 and 1.74 to 2.62 for the anchor diameters of 15.9-mm and 19.1-mm respectively. For the anchor diameter of 12.7 mm, DIF of 1.07 was obtained where steel failure was observed. At high strain rate of 10^3 s^{-1} , DIF of 1.12, 1.17 and 1.13 were obtained for the anchor diameters of 12.7-mm, 15.9-mm and 19.1-mm respectively where steel failure was observed.

Figure 4-25 for anchor embedment depth of 101.6 mm shows that the DIF increased with the increase in the strain rate from 10^{-5} s^{-1} to 10^2 s^{-1} for the 15.9-mm and 19.1-mm diameter cast-in-place anchors where concrete cone failure was observed. At high strain rate of 10^3 s^{-1} , DIF of 1.17 and 1.13 were obtained for the anchor diameters of 15.9 mm and 19.1 mm where steel failure was observed. A slight increase in the DIF to 1.13 was obtained for the anchor diameter of 12.7 mm with the increase in the strain rate from 10^{-5} s^{-1} to 10^3 s^{-1} where steel anchor failure was the dominant failure mode at all the strain rates investigated. This increase is attributed to the increase in the strength of steel with the increase in the strain rate.

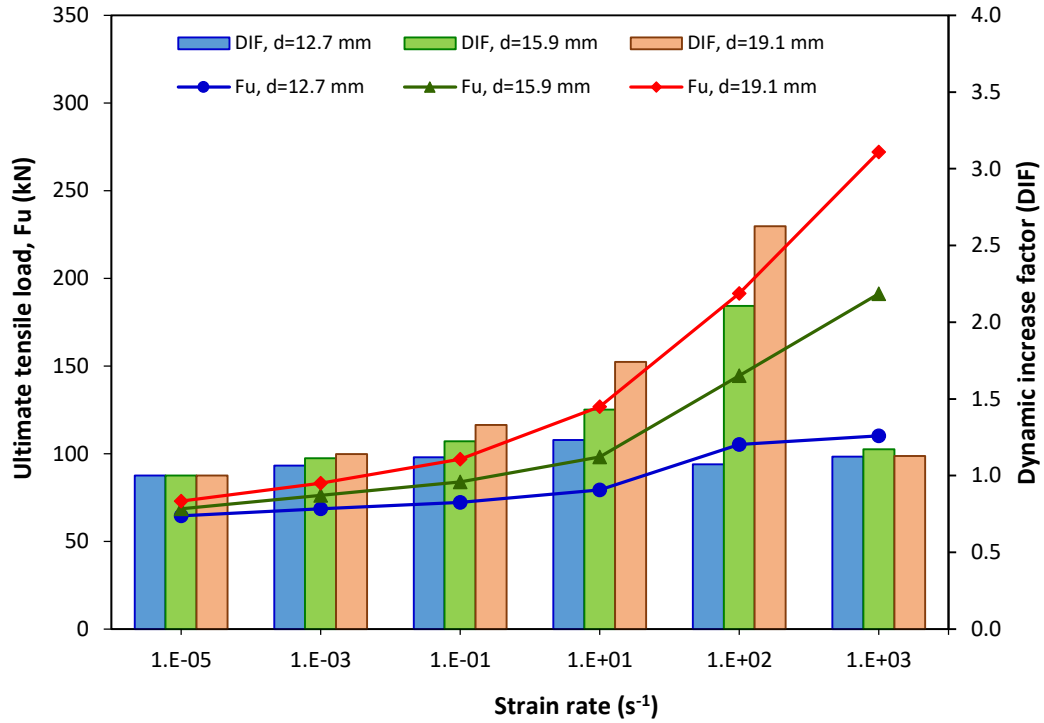


Figure 4-24: Ultimate tensile load and DIF versus strain rate for the cast-in-place anchor of 76.2 mm embedment depth

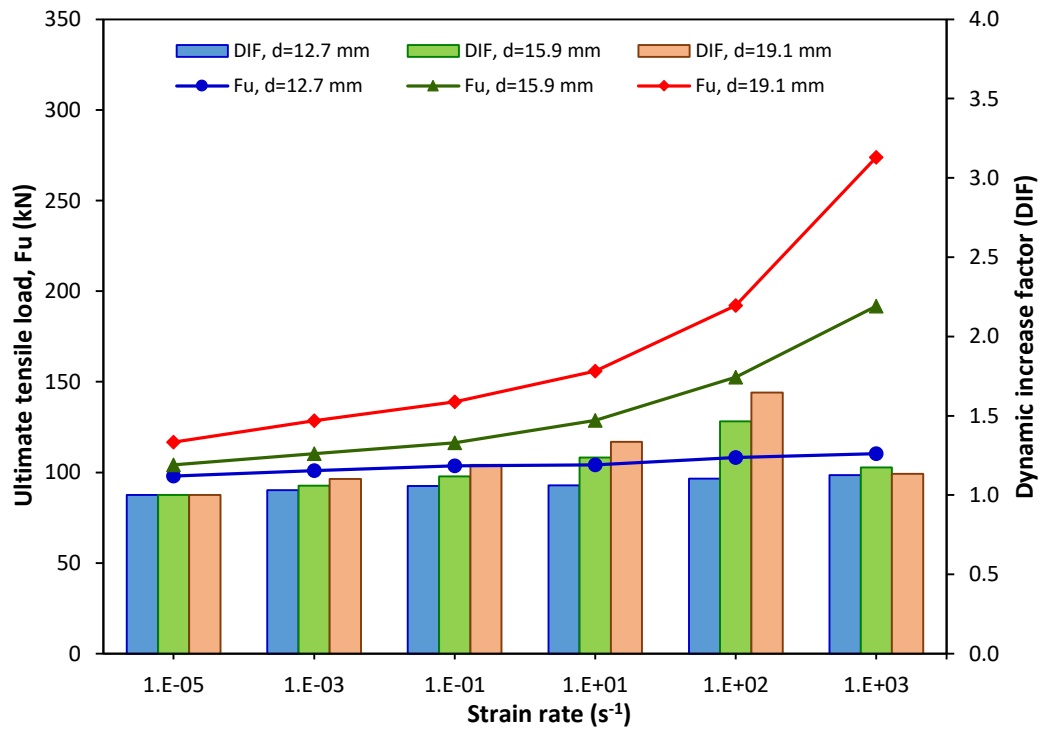


Figure 4-25: Ultimate tensile load and DIF versus strain rate for the cast-in-place anchor of 101.6 mm embedment depth

As shown in Figure 4-26 for the embedment depth of 127 mm, the ultimate tensile load increased 12% and 17.4% as the strain rate increased from 10^{-5} s^{-1} to 10^3 s^{-1} for anchor diameters of 12.7-mm and 15.9-mm respectively. For the cast-in-place anchor diameter of 19.1-mm, the ultimate tensile load increased 20.5% when the strain rate increased from 10^{-5} s^{-1} to 10 s^{-1} where concrete cone breakout failure was observed. The increase in the ultimate load was 25.4% when the strain rate increased from 10 s^{-1} to 10^3 s^{-1} . Transition from concrete cone breakout to steel anchor failure was observed at strain rate of 10^2 s^{-1} . DIF of 1.12 and 1.17 are obtained when the strain rate increased from 10^{-5} s^{-1} to 10^3 s^{-1} for anchor diameters of 12.7-mm and 15.9-mm respectively. For anchor diameter of 19.1 mm the DIF increased to 1.21 at strain rate of 10 s^{-1} where concrete cone breakout failure is observed. The DIF of 1.11 and 1.13 were obtained at strain rates of 10^2 s^{-1} and 10^3 s^{-1} where steel anchor failure is observed.

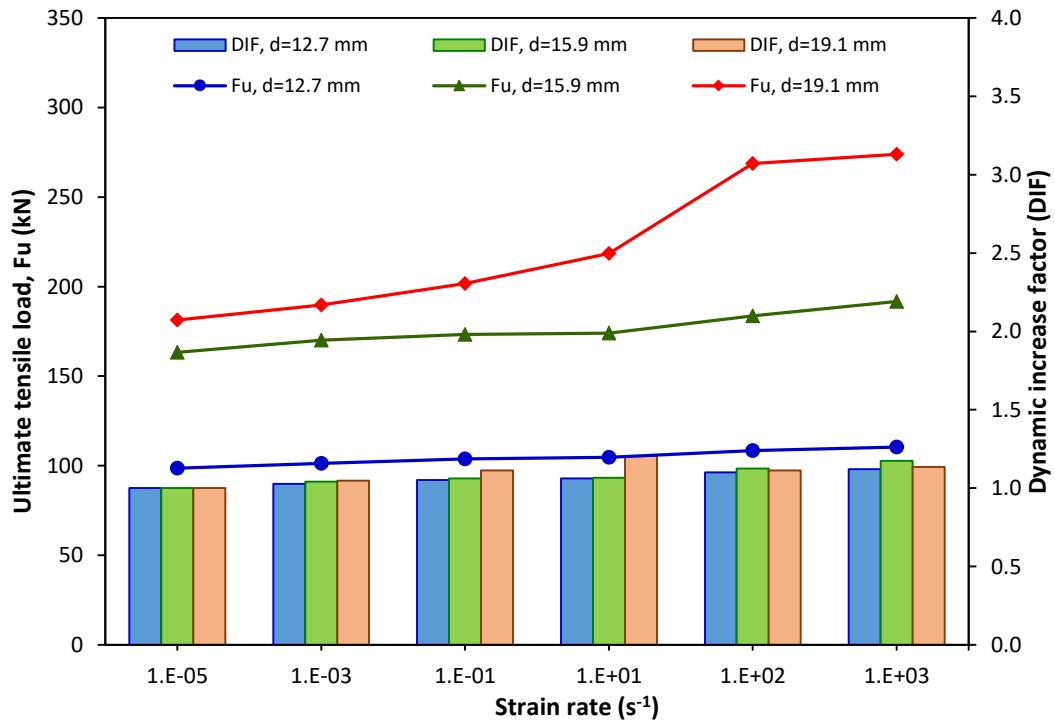


Figure 4-26: Ultimate tensile load and DIF versus strain rate for the cast-in-place anchor of 127 mm embedment depth

As shown in Figure 4-27, at embedment depth of 152.4 mm, the ultimate tensile load increased 10.6%, 16.5% and 13.4% for the 12.7-mm, 15.9-mm and 19.1-mm diameter cast-in-place anchors when the strain rate increased from 10^{-5} s^{-1} to 10^3 s^{-1} where the steel fracture is the dominant failure mode. It can be seen that, approximately linear relation is obtained between the ultimate tensile load and the strain rate. Figure 4-27 is representative of the DIF of cast-in-place anchorage system failing by steel anchor fracture. DIF of 1.11, 1.17 and 1.13 were obtained for anchor diameters of 12.7 mm, 15.9 mm and 19.1 mm with embedment depth of 152.4 mm at high strain rate of 10^3 s^{-1} .

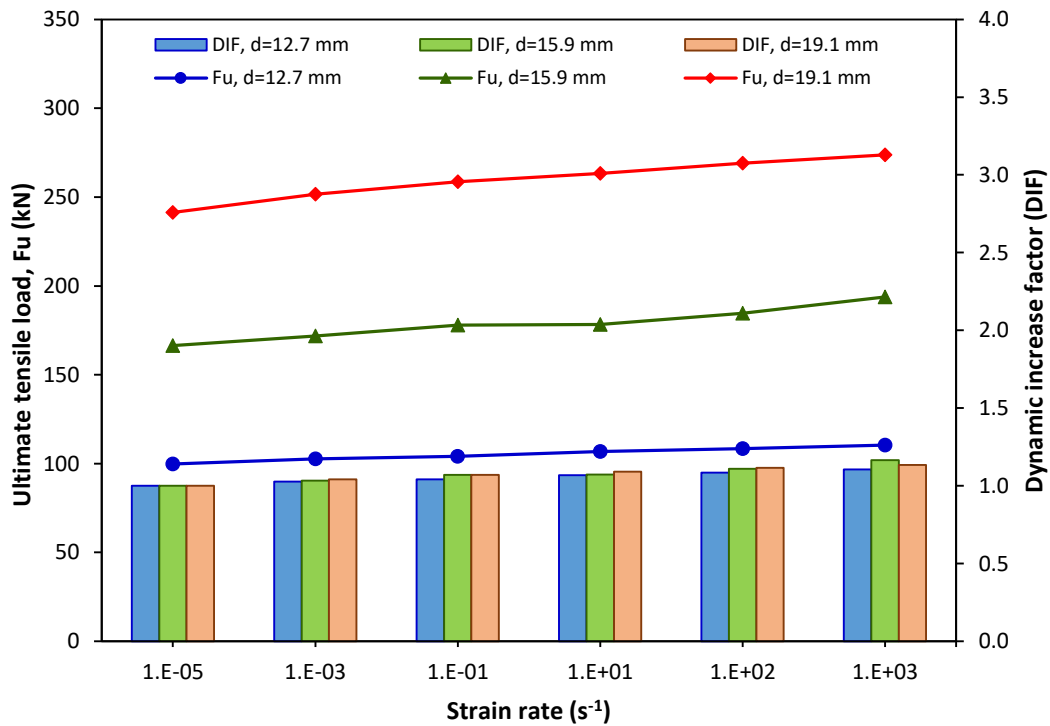


Figure 4-27: Ultimate tensile load and DIF versus strain rate for the cast-in-place anchor of 152.4 mm embedment depth

It can be seen that maximum tensile loads of 110.42 kN, 193.82 kN and 273.79 kN were obtained at high strain rate of 10^3 s^{-1} and embedment depth of 152.4 mm for the 12.7-mm, 15.9-mm and 19.1-mm diameter cast-in-place anchors respectively.

The increase in the ultimate load with the increase in strain rate is attributed to the fact that the strain rate has an effect on the mechanical properties of the concrete and steel materials. For the concrete material, the tensile and compressive strengths increase with the increase in the strain rate (Hentz et al., 2004). Hence, the concrete resistance increase results in increase of the ultimate load capacity of the anchorage system. Also, increasing the strain rate increases the modulus of elasticity of the concrete (Shkolnik, 2008) and its energy absorption capacity (Bischoff & Perry, 1991). Moreover, the yield and ultimate strength of the steel increase with increase in the strain rate (Fu et al., 1991). This is due to the increase in the deformations and dislocations of steel at high strain rate. The strain rate has an effect on the microstructure of the steel, increasing the strain rate resulted in increasing the deformation level (Lee et al., 2007). In general, the DIF increased with the increase in the strain rate where the concrete and steel strengths increased with the increase in strain rate. The increase in the tensile strength of concrete with the increase in the strain rate is higher than that for the steel (Malvar & Ross, 1998; Malvar & Crawford, 1998). Hence, maximum DIF of 1.23 was obtained for anchor diameter of 12.7 mm with embedment depth of 76.2 mm at strain rate of 10 s^{-1} where concrete cone breakout failure was observed. Maximum DIF of 2.11 and 2.62 were obtained for the anchor diameters of 15.9-mm and 19.1-mm respectively with anchor embedment depth of 76.2 mm at high strain rate of 10^2 s^{-1} .

The DIF of cast-in-place anchors at different strain rates can be represented as a function of the strain rate ratio in accordance with Equation (4.4).

$$DIF = \frac{F_{ud}}{F_{us}} = A \left(\frac{\dot{\epsilon}_d}{\dot{\epsilon}_s} \right)^B \quad (4.4)$$

$$F_{ud} = F_{us} \cdot A \left(\frac{\dot{\varepsilon}_d}{\dot{\varepsilon}_s} \right)^B \quad (4.5)$$

Where

F_{us} , F_{ud} are the ultimate static and dynamic tensile loads of the anchorage to concrete systems respectively. A and B are constants to be determined from experimental or numerical parametric studies, and $\dot{\varepsilon}_s$ and $\dot{\varepsilon}_d$ are the static and dynamic strain rates respectively.

Table 4-9 shows the maximum DIF for the cast-in-place anchors under tensile load where concrete cone breakout failure and steel anchor failure modes were observed.

Table 4-9: Maximum dynamic increase factor for the cast-in-place anchors under tensile load

Model No.	d (mm)	h _{ef} (mm)	$\dot{\varepsilon}$ (s ⁻¹)	DIF	$\dot{\varepsilon}$ (s ⁻¹)	DIF
				CC		S
1	12.7	76.2	10	1.23	10 ³	1.12
2	12.7	101.6	-	-	10 ³	1.13
3	12.7	127.0	-	-	10 ³	1.12
4	12.7	152.4	-	-	10 ³	1.11
5	15.9	76.2	10	1.43	10 ³	1.17
6	15.9	101.6	10	1.24	10 ³	1.17
7	15.9	127.0	-	-	10 ³	1.17
8	15.9	152.4	-	-	10 ³	1.17
9	19.1	76.2	10	1.74	10 ³	1.13
10	19.1	101.6	10	1.34	10 ³	1.13
11	19.1	127.0	10	1.21	10 ³	1.13
12	19.1	152.4	-	-	10 ³	1.13

4.1.10 Regression Analysis for cast-in-place anchors under tensile load

To develop an accurate predictive model based on the finite element results for determining the DIF of the cast-in-place anchorage to concrete systems, regression analysis was performed. The DIF is plotted as a function of the strain rate ratio ($\dot{\epsilon}_d/\dot{\epsilon}_s$) based on the numerical results obtained to account for the effect of the strain rate on the ultimate tensile load. Where the strain rate ratio ($\dot{\epsilon}_d/\dot{\epsilon}_s$) is the ratio of dynamic strain rate ($\dot{\epsilon}_d$) to the static strain rate ($\dot{\epsilon}_s$). Average value of the DIF for the cast-in-place anchorage systems with anchor diameters of 12.7-mm, 15.9-mm and 19.1-mm was calculated to adjust the DIF for the effect of anchor diameter. Figure 4-28 shows the relation between the DIF and the strain rate ratio ($\dot{\epsilon}_d/\dot{\epsilon}_s$) for the cast-in-place anchors exhibited concrete cone breakout failure mode. The increase in the strain rate increased the strengths of concrete and steel materials resulted in increasing the ultimate load and the DIF. Figure 4-29 shows the relation between the DIF and the strain rate ratio ($\dot{\epsilon}_d/\dot{\epsilon}_s$) for the cast-in-place anchors exhibited steel anchor failure mode.

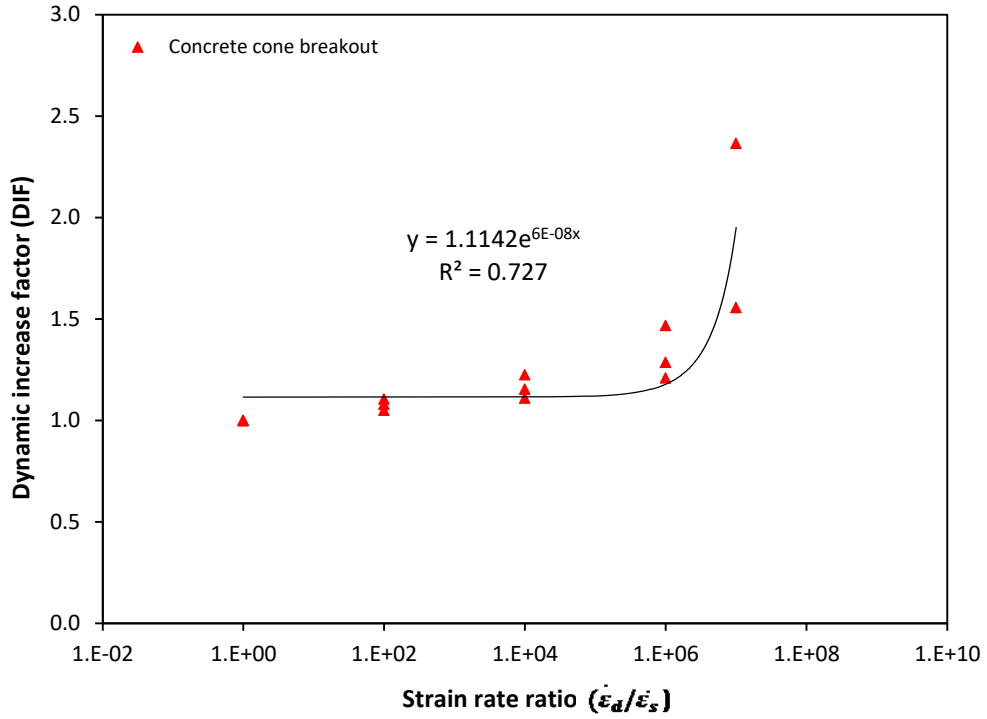


Figure 4-28: Effect of strain rate ratio on the DIF for cast-in-place anchor exhibiting concrete cone breakout failure

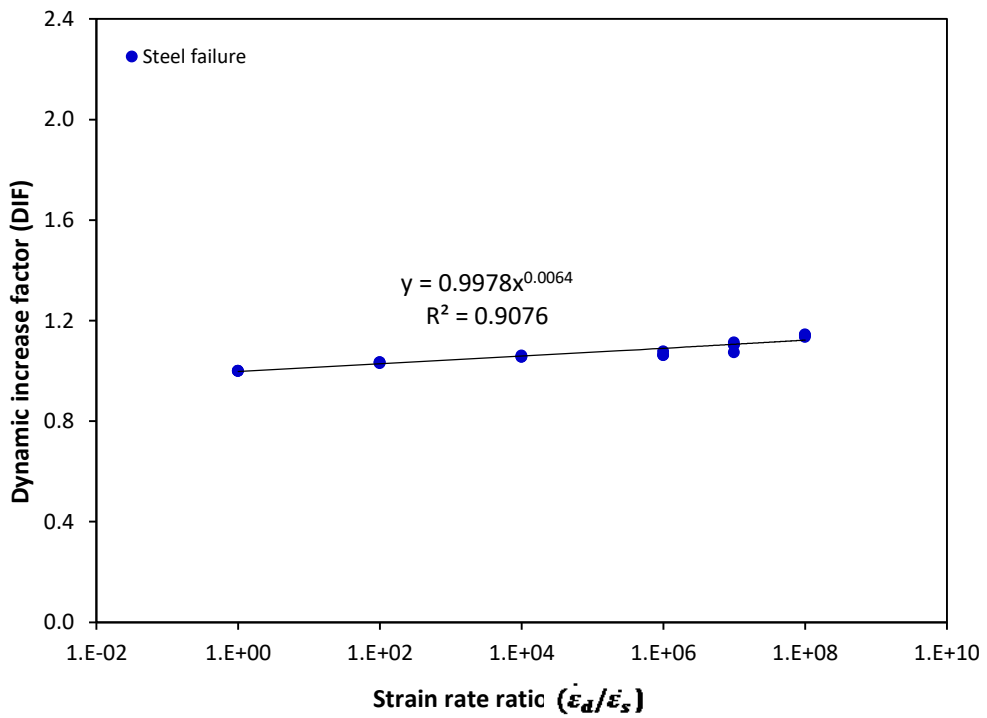


Figure 4-29: Effect of strain rate ratio on the DIF for cast-in-place anchor exhibiting steel failure

Various regression models; exponential, linear, logarithmic and power models were used to develop a formula that relates the DIF with the strain rate as shown in Tables 4-10 and 4-11 for concrete cone breakout and steel anchor failure respectively. The adequacy of the predicted model is verified according to the following tests: calculating coefficient of determination R^2 and residual analysis (Montgomery, 2013). A good probability distribution of the results is obtained when the coefficient of determination (R^2) is closer to one (Ceci et al., 2012).

Table 4-10: Statistical models and coefficient of determination to predict the DIF for cast-in-place anchors exhibited concrete cone breakout failure under tensile load

Statistical models	Formulae	Coefficient of determination (R^2)
Exponential	$DIF = 1.1142e^{6E-08\left(\frac{\dot{\epsilon}_d}{\dot{\epsilon}_s}\right)}$	0.727
Linear	$DIF = 9E - 08\left(\frac{\dot{\epsilon}_d}{\dot{\epsilon}_s}\right) + 1.1158$	0.726
Logarithmic	$DIF = 0.0435\ln\left(\frac{\dot{\epsilon}_d}{\dot{\epsilon}_s}\right) + 0.8996$	0.519
Power	$DIF = 0.9442\left(\frac{\dot{\epsilon}_d}{\dot{\epsilon}_s}\right)^{0.0313}$	0.640

Table 4-11: Statistical models and coefficient of determination to predict the DIF for cast-in-place anchors exhibited steel failure under tensile load

Statistical models	Formulae	Coefficient of determination (R^2)
Exponential	$DIF = 1.0505e^{9E-10\left(\frac{\dot{\epsilon}_d}{\dot{\epsilon}_s}\right)}$	0.600
Linear	$DIF = 9E - 10\left(\frac{\dot{\epsilon}_d}{\dot{\epsilon}_s}\right) + 1.051$	0.618
Logarithmic	$DIF = 0.0068\ln\left(\frac{\dot{\epsilon}_d}{\dot{\epsilon}_s}\right) + 0.9964$	0.899
Power	$DIF = 0.9978\left(\frac{\dot{\epsilon}_d}{\dot{\epsilon}_s}\right)^{0.0064}$	0.908

As shown in Tables 4-10 and 4-11, the highest coefficients of determination of 73% and 91% are obtained from the exponential model and power model for the concrete cone breakout and steel anchor failure modes respectively. The exponential model can represent 73% and 91% of the total variation between the DIF obtained from the finite element analysis and the predicted values for the concrete cone breakout and steel anchor failure modes respectively. The predicted formulae for the DIF can be presented in Equations (4.6) and (4.7) for the concrete cone breakout and steel anchor failure modes respectively as follows:

$$DIF = 1.1142e^{6E-08\left(\frac{\dot{\epsilon}_d}{\dot{\epsilon}_s}\right)} \quad (4.6)$$

$$DIF = 0.9978\left(\frac{\dot{\epsilon}_d}{\dot{\epsilon}_s}\right)^{0.0064} \quad (4.7)$$

Where $\dot{\epsilon}_s$ is the static strain rate= 10^{-5} s^{-1} , $\dot{\epsilon}_d$ is the dynamic strain rate ranging from 10^{-3} s^{-1} to 10^3 s^{-1} .

The proposed Equations (4.6) and (4.7) can be used to predict the ultimate dynamic load (F_{ud}) for the concrete cone breakout and steel anchor failure modes respectively as follows:

$$F_{ud} = F_{us} \times 1.1142e^{6E-08\left(\frac{\dot{\epsilon}_d}{\dot{\epsilon}_s}\right)} \quad (4.8)$$

$$F_{ud} = F_{us} \times 0.9978\left(\frac{\dot{\epsilon}_d}{\dot{\epsilon}_s}\right)^{0.0064} \quad (4.9)$$

Where the ultimate static load (F_{us}) can be determined from Equations 4.1 and 4.3 for the concrete cone breakout and from Equation (4.2) for steel anchor failure mode.

Residual analysis has been performed to measure the difference between the results obtained from finite element analysis of the cast-in-place anchors under tensile load and fitted results of DIF obtained from Equations (4.6) and (4.7). Where the residual is the difference between the observed values (FEA results) and the predicted values (obtained from the equations). The residual plots are presented in Figures 4-30 and 4-31.

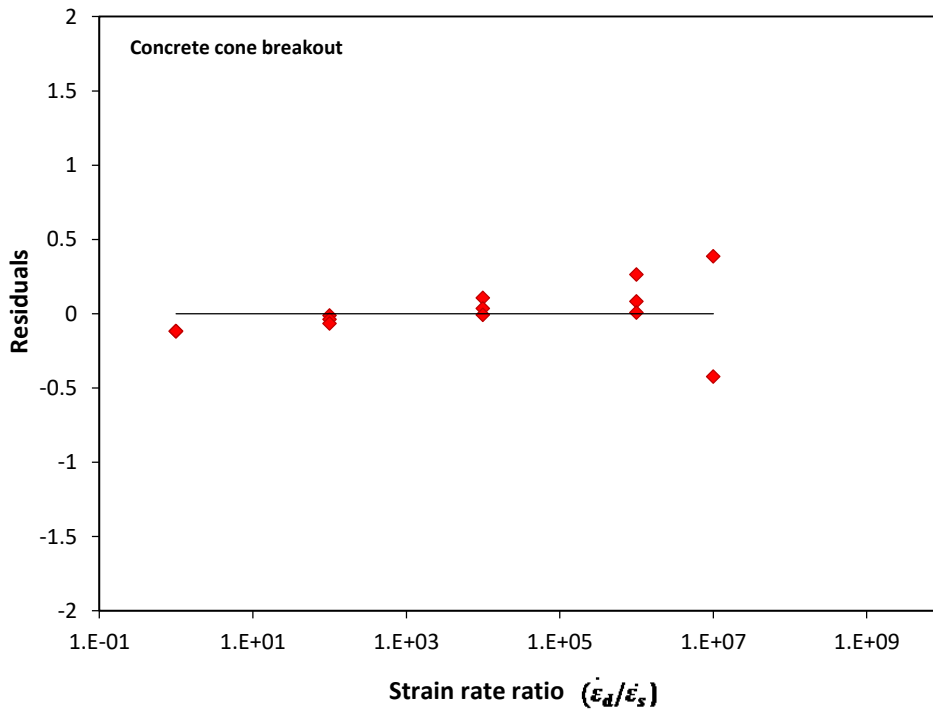


Figure 4-30: Residual versus strain rate ratio for the cast-in-place anchors exhibited concrete cone breakout failure

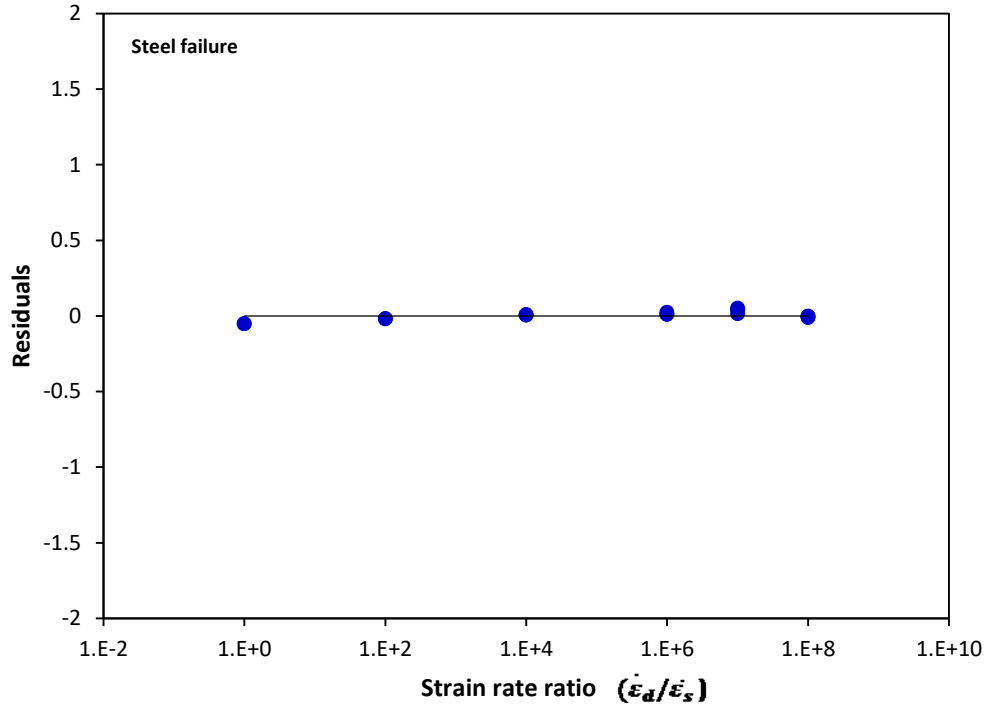


Figure 4-31: Residual versus strain rate ratio for the cast-in-place anchors exhibited steel failure

As shown in Figure 4-30, for the concrete cone breakout failure the variance in the residual increases with the increase in the strain rate ratio. For the steel anchor failure (Figure 4-31), the residual exhibited horizontal trend line at strain rate ratio up to 10^8 .

In addition, to evaluate the adequacy of the proposed equations, new cast-in-place anchor models with diameters of 9.5 mm, 12.7 mm, 15.9 mm and 19.1 mm and embedment depths of 89 mm, 114 mm and 140 mm were developed. The relation between the DIF results of the newly developed numerical models and the regression models (Equations (4.6) and (4.7)) are presented as shown in Figures 4-32 and 4-33 for the concrete cone breakout failure and steel failure modes respectively. As shown in the Figure 4-32, the DIF is observed distributed around the equality line with some divergence for the anchors

exhibited concrete cone breakout failure for the higher values of the DIF where the residual increased at higher strain rates. For the anchors exhibited steel failure as shown in Figure 4-33, the DIF is distributed around the equality line.

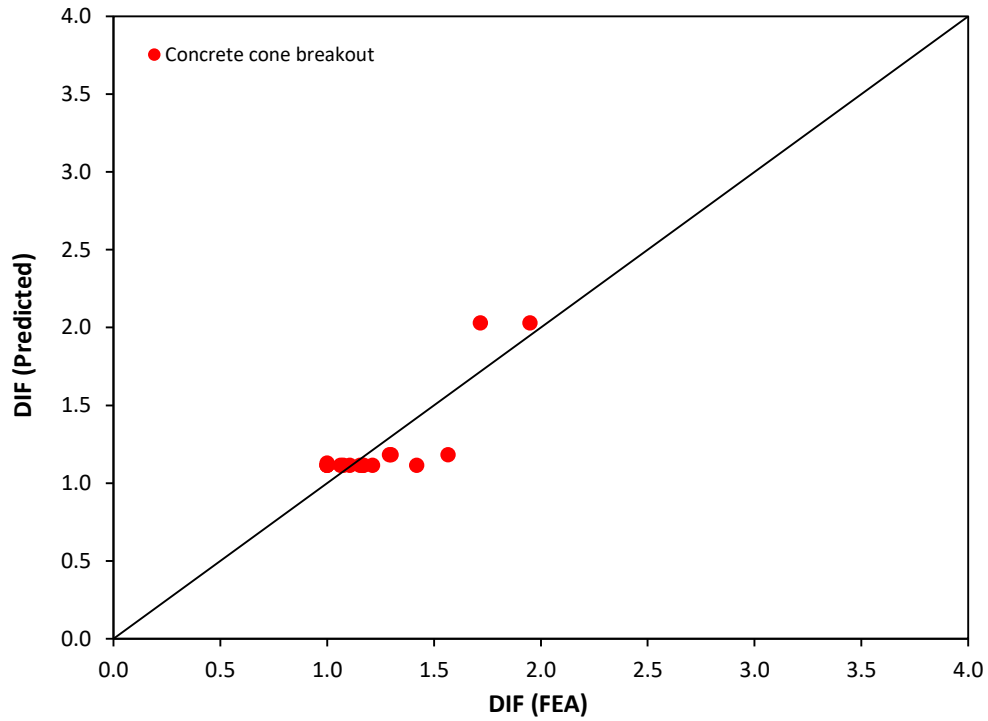


Figure 4-32: DIF obtained from the finite element analysis versus the predicted DIF for the cast-in-place anchor exhibited concrete cone breakout failure

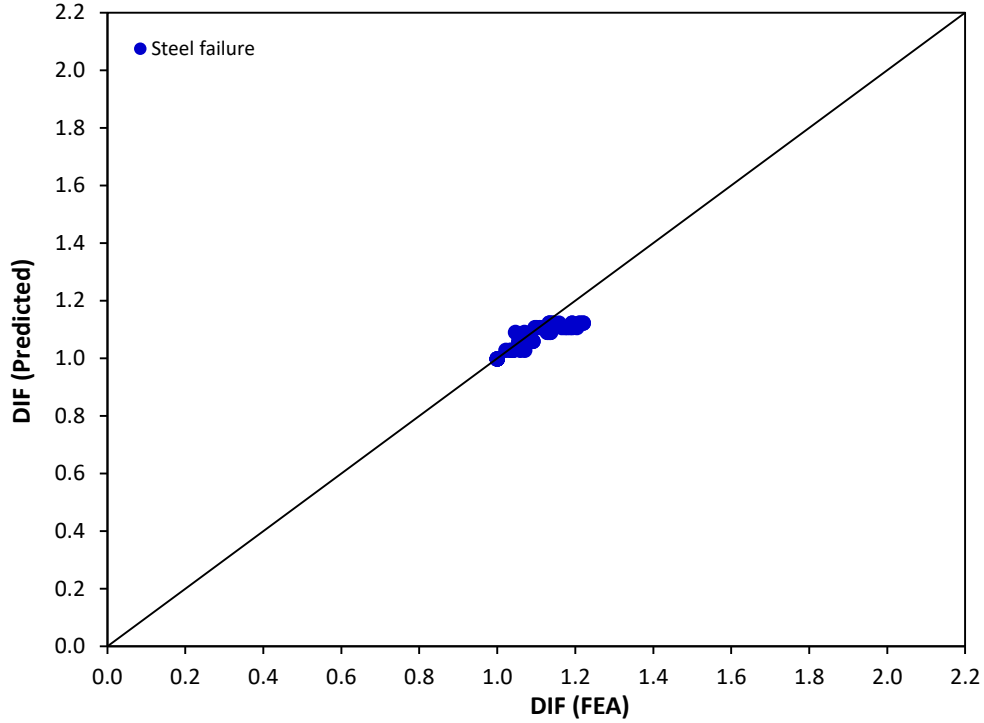


Figure 4-33: DIF obtained from the finite element analysis versus the predicted DIF for the cast-in-place anchor exhibited steel failure

In order to verify the results obtained from the finite element analysis, a comparison has been made between the ultimate dynamic load obtained from the finite element analysis for the cast-in-place anchors exhibited concrete cone breakout failure and the proposed Equation by Fujikake et al. (Equation (4.10)) (Fujikake et al., 2003). Fujikake et al. (2003) proposed an equation to determine the ultimate dynamic cone resistance for the shallow embedment depths (Fujikake et al., 2003) as follows:

$$F_{cd} = A_e \cdot F_{td} \cdot \frac{\alpha}{\sqrt{h_{ef}}} \quad (4.10)$$

$$A_e = \pi \cdot h_{ef} \cdot \tan\theta (d + h_{ef} \cdot \tan\theta) \quad (4.11)$$

Where, F_{td} is determined according to the proposed equation by Ross et al. (1989) (Ross et al., 1989) as follows:

$$\frac{F_{td}}{F_s} = \exp \left[0.00126 \left(\log_{10} \frac{\epsilon_d}{\epsilon_s} \right)^{3.373} \right] \quad (4.12)$$

$$F_s = 0.23(f'_c)^{2/3} \quad (4.13)$$

Where F_{cd} is the ultimate dynamic concrete cone breakout, A_e is the projected area of concrete cone failure, $\alpha = 3.48 \times 10^{-3}$, θ is the crack propagation angle ($\theta = 60^\circ$), where the concrete cone breakout angle is equal to 30° . F_s and F_{td} are the static and dynamic tensile strength of concrete respectively. Table 4-12 shows a comparison of the ultimate dynamic load obtained from the finite element analysis and the proposed equation by Fujikake et al. (Fujikake et al., 2003). As shown in the table, the FEA results for the anchors overpredict the ultimate load obtained by Fujikake et al. prediction equation.

Table 4-12: Comparison between ultimate dynamic load obtained from the FEA and proposed equations by Fujikake et al. (2003) for the cast-in-place anchor exhibited concrete cone breakout failure

d (mm)	h_{ef} (mm)	$\dot{\epsilon}_s$ (s⁻¹)	$\dot{\epsilon}_d$ (s⁻¹)	$\dot{\epsilon}_d/\dot{\epsilon}_s$	FEA		F_{ud} Regression (kN)	F_{ud} Fujikake (kN)	F_{ud} FEA/ F_{ud} Fujikake
					F_{us} (kN)	F_{ud} (kN)			
12.7	76.2	10 ⁻⁵	10 ⁻³	10 ²	64.48	68.63	71.84	53.80	1.28
12.7	76.2	10 ⁻⁵	10 ⁻¹	10 ⁴	64.48	72.16	71.89	60.79	1.19
15.9	76.2	10 ⁻⁵	10 ⁻³	10 ²	68.61	76.32	76.45	54.99	1.39
15.9	76.2	10 ⁻⁵	10 ⁻¹	10 ⁴	68.61	83.96	76.49	62.13	1.35
15.9	101.6	10 ⁻⁵	10 ⁻³	10 ²	104.17	110.25	116.07	82.38	1.34
15.9	101.6	10 ⁻⁵	10 ⁻¹	10 ⁴	104.17	116.33	116.14	93.09	1.25
19.1	76.2	10 ⁻⁵	10 ⁻³	10 ²	72.88	83.09	81.20	56.18	1.48
19.1	76.2	10 ⁻⁵	10 ⁻¹	10 ⁴	72.88	96.94	81.25	63.48	1.53
19.1	101.6	10 ⁻⁵	10 ⁻³	10 ²	116.65	128.44	129.97	83.76	1.53
19.1	101.6	10 ⁻⁵	10 ⁻¹	10 ⁴	116.65	138.88	130.05	94.64	1.47

*F_{us} FEA: ultimate static load obtained from FEA, F_{ud} FEA: ultimate dynamic load obtained from FEA

4.2 Cast-in-place anchors under shear load

4.2.1 Finite element modelling for cast-in-place anchors under shear load

Analysis on the behaviour of cast-in-place anchors embedded into concrete under shear load at different strain rates was performed using the explicit commercial finite element code LS-DYNA (LSTC, 2014). Figure 4-34 shows the geometric configuration and boundary conditions for the cast-in-place anchor model for investigating shear behaviour.

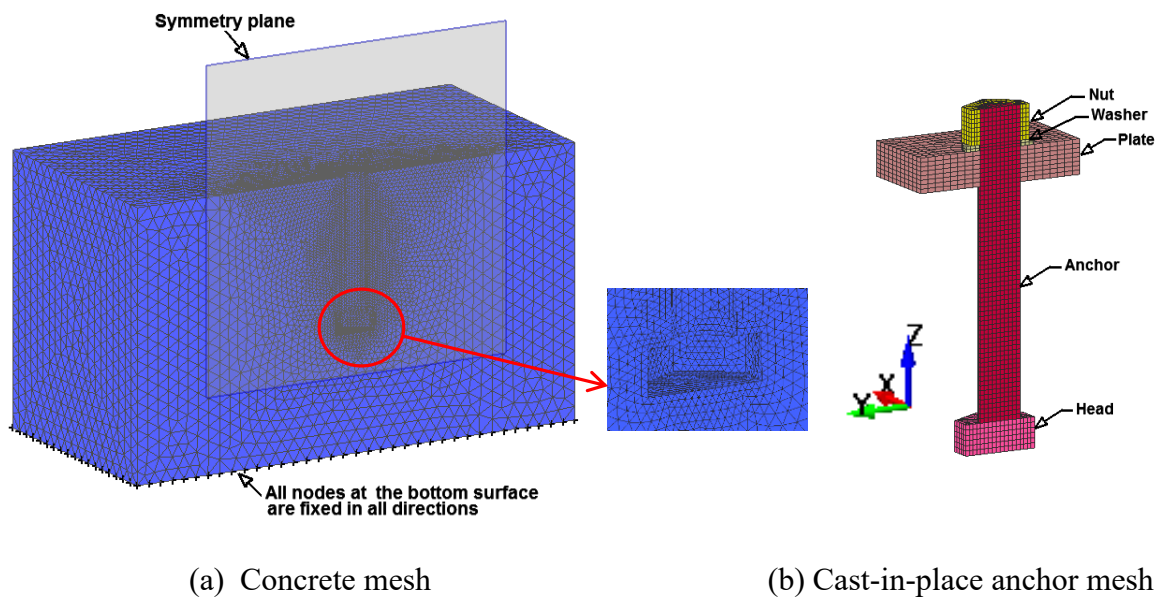


Figure 4-34: Geometric configuration of cast-in-place anchor model under shear load

4.2.2 Validation of cast-in-place anchor model under shear load

The finite element model was validated by modeling the specimens in an experimental investigation by Ueda et al. (1991) and comparing ultimate shear loads obtained from the analysis with experimental tests. Two finite element models, representative of the test specimens of Ueda et al. (1991) were developed. Two edge distances of 56 mm and 106 mm in the parallel direction (c_1) to direction of the applied load and a larger edge distance

perpendicular to the applied shear load direction (c_2) were investigated. Figure 4-35 shows the direction of the applied load and the edge distances c_1 and c_2 .

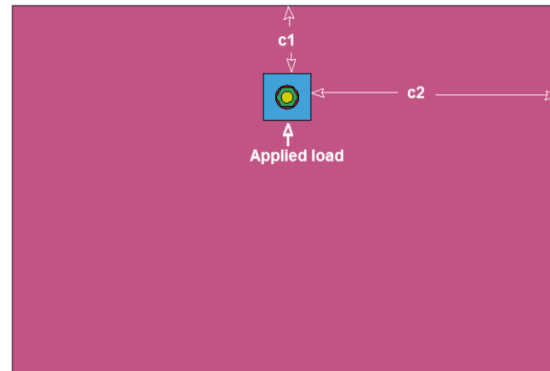


Figure 4-35: Applied shear load in the direction parallel to the edge distance c_1 and perpendicular to the edge distance c_2

The anchors had a diameter of 16-mm and embedment depth of 200 mm and were cast into concrete with compressive cylinder strength of 24 MPa. Mesh sensitivity analysis was performed to determine the suitable mesh size that can best represent the experimental results. The load-displacement relation was not presented in the experimental work conducted by Ueda et al., hence the ultimate shear loads were considered for comparison purpose. Table 4-13 presents a comparison of ultimate shear load from experimental tests by Ueda et al. (Ueda et al., 1991) and finite element analysis (FEA) results under static shear loading. Mesh sizes of $1 \times 2 \times 8$ mm, $1 \times 1 \times 8$ mm and $0.75 \times 1 \times 8$ mm were investigated. As shown in Table 4-13 the finite element analysis results with the mesh sizes of $1 \times 1 \times 8$ mm and $0.75 \times 1 \times 8$ mm give converged ultimate shear load results to the experimental results with a percentage difference of 4.5% and 2.9% respectively for the edge distance of 56 mm and a percentage difference of 4.1% and 3.2% for the edge distance of 106 mm. The finite element analysis results with mesh size of 0.75 mm for the steel anchor and a

biased mesh from 1 to 8 mm for the concrete show good agreement with the experimental results and was selected for the analysis.

Table 4-13: Effect of mesh size refinement on the convergence of ultimate shear load for cast-in-place anchor

Model No.	c ₁ (mm)	Mesh size (mm)			Ultimate shear load (kN)		Failure mode
		Anchor	Concrete		FEA	EXP.	
			Min.	Max.			
1	56	1	2	8	12.75	13.70	Concrete cone breakout
2		1	1	8	13.11		
3		0.75	1	8	14.10		
4	106	1	2	8	36.82	39.60	Concrete cone breakout
5		1	1	8	38.05		
6		0.75	1	8	40.88		

4.2.3 Comparison of finite element results with design method

When the anchors are installed far from the concrete free edge and subjected to shear loading, pryout failure and or steel anchor failure are the dominant failure modes. The pryout failure load of the anchor can be calculated according to ACI 318 (ACI Committee 318, 2011) as in Equation (4.14).

$$V_{cp} = k_{cp} N_{cb} \quad (4.14)$$

where

$$k_{cp} = \begin{cases} 1 & \text{for } h_{ef} < 63.5 \text{ mm} \\ 2 & \text{for } h_{ef} \geq 63.5 \text{ mm} \end{cases} \quad (4.15)$$

and

$$N_{cb} = \frac{A_N}{A_{No}} \psi_{ed,N} \cdot \psi_{c,N} \cdot \psi_{cp,N} \cdot N_b \quad (4.16)$$

$$N_b = K \sqrt{f'_{cc}} h_{ef}^{1.5} \quad (4.17)$$

N_{cb} is the concrete tensile breakout capacity for the anchor, A_N is the actual projected area, A_{No} is the projected area for the failure surface of concrete, $\psi_{ed,N}$ is a modification factor accounting for edge effects, $\psi_{c,N}$ is a modification factor accounting for cracking, $\psi_{cp,N}$ is a modification factor accounting for post-installed anchors embedded in concrete without reinforcement, N_b is the basic concrete breakout strength of a single anchor, k_{cp} is a modification factor for embedment depth effects. $K=15.5$ for the cast-in-place anchors and 13.5 for post installed anchors (Fuchs et al., 1995).

The steel anchor failure for cast-in-place headed bolt can be calculated according to ACI 318 as in Equation (4.18) (ACI Committee 318, 2011).

$$V_u = 0.6 A_s \cdot F_{ut} \quad (4.18)$$

where

A_s is the effective cross section area of the anchor, F_{ut} is ultimate tensile strength of the anchor.

Ultimate shear load obtained from the finite element analysis was compared with results obtained from ACI 318 method. The anchors were embedded in 30 MPa compressive

strength concrete. The ultimate shear load was observed to increase with the increase of the anchor diameter from 12.7 mm to 19.1 mm.

Table 4-14 presents a comparison of ultimate shear load obtained from the finite element analysis (FEA) and ACI 318 (ACI Committee 318, 2011) for the anchor diameters and embedment depths investigated. The failure mode observed from the finite element analysis is also presented in the Table. Minimum value of the ultimate shear load obtained from Equations (4.14) and (4.18) is considered for comparison with the finite element results and included in Table 4-14. It can be seen from Table 4-14 that the ACI method underpredicts the failure load for the anchor diameter of 12.7-mm. This can be attributed to the high bending, tensile and shear stresses that are generated in anchor diameter of 12.7-mm due to the applied shear load where the interaction of these stresses causes steel anchor failure. In general, the results show that the ultimate shear load obtained from the finite element analysis is in a good agreement with the ACI 318 method.

Table 4-14: Comparison between FEA and ACI 318 method

Model No.	d (mm)	h _{ef} (mm)	Failure Load (kN)		FEA/ACI	*Failure mode (FEA)
			FEA Static ($\dot{\epsilon} = 10^{-5} \text{ s}^{-1}$)	ACI 318		
1	12.7	76.2	86.64	78.59	1.10	S
2	12.7	101.6	88.81	78.59	1.13	S
3	12.7	152.4	90.16	78.59	1.15	S
4	15.9	76.2	104.37	123.18	0.85	PR
5	15.9	101.6	118.79	123.18	0.96	S
6	15.9	152.4	120.67	123.18	0.98	S

7	19.1	76.2	124.18	125.43	0.99	PR
8	19.1	101.6	152.14	177.75	0.86	PR
9	19.1	152.4	174.09	177.75	0.98	S

* Failure mode: PR=pryout, S=steel anchor failure

4.2.4 Crack pattern for cast-in-place anchors under shear load

Contours of effective plastic strain for cast-in-place anchors with different anchor diameters and embedment depths at failure are shown in Figure 4-36 at strain rate of 10^{-5} s^{-1} . Fringe levels in Figure 4-36 (level of plastic straining) represent the localized damage. As shown in the figure, concrete pryout failure is observed at low strain rate of 10^{-5} s^{-1} for anchor diameters of 15.9 mm and 19.1 mm with embedment depth of 76.2 mm, while steel anchor failure was observed for anchor diameter of 12.7 mm. Steel anchor failure was also observed for all the anchor diameters at embedment depths of 101.6 mm and 152.4 mm except for anchor diameter of 19.1 mm with embedment depth of 101.6 mm which exhibited concrete pryout failure. This is attributed to the increase in the anchor diameter which increased the strength of the anchor leading to initiation of cracking in the concrete at the bottom of the anchor that propagate diagonally towards the concrete surface and resulted in pryout failure. The pryout failure is characterized by concrete half cone breakout behind the anchor associated with concrete cracking/crushing in front of the anchor. The level of damage increased with the increase in the anchor diameter from 12.7-mm to 19.1 mm where more cracking was observed in the concrete.

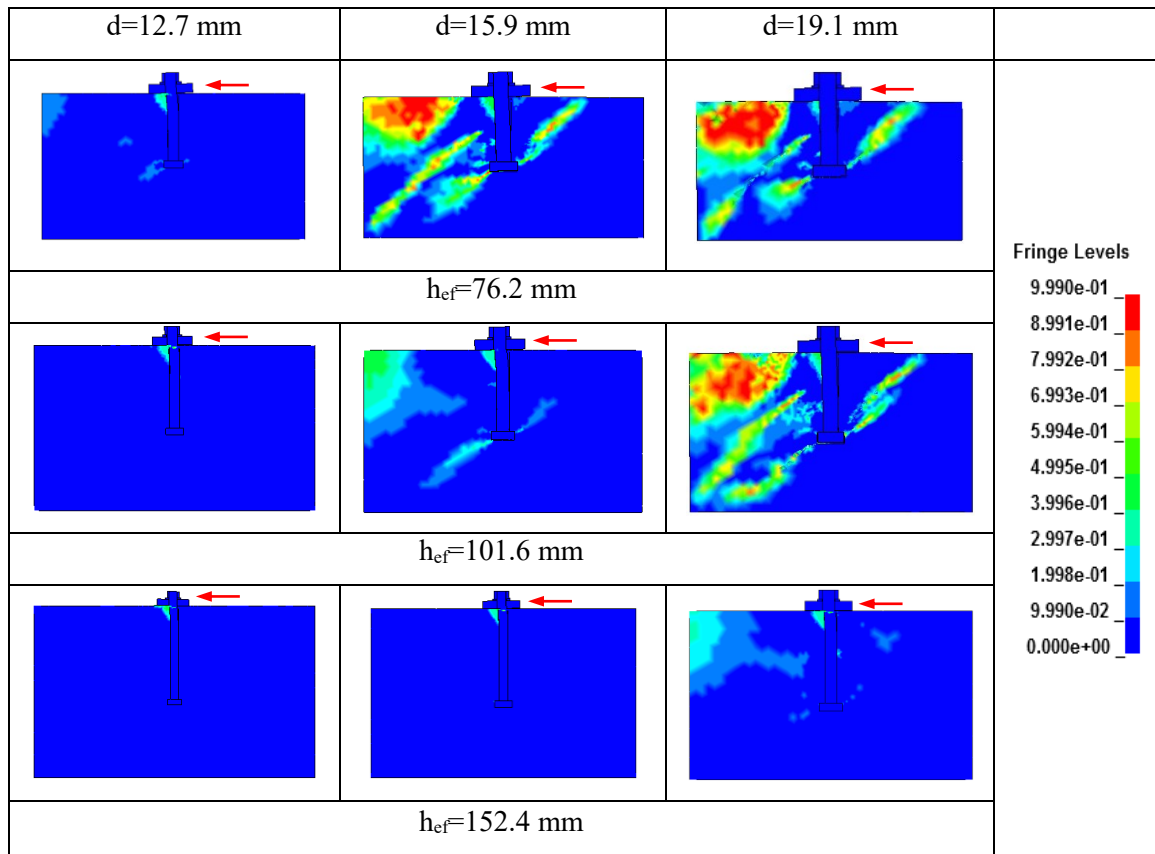


Figure 4-36: Plastic strain contours for cast-in-place anchor under shear load at strain rate of 10^{-5} s^{-1}

According to Zhao (Zhao, 1994) the applied shear load is transferred to the concrete through four mechanisms. The first is the friction force between the concrete and the anchor plate and oriented in opposite direction to the applied load (R_1). The second is the reaction force of the concrete towards the anchor bolt (R_2). The third is the reaction force at the front tip of the plate (R_3). The fourth is the tensile force of the anchor bolt (R_4) (Zhao, 1994). In addition, there is a reaction force on the anchor head that pushes on the concrete resulting in concrete pryout failure (R_5). Figure 4-37 presents the reaction forces on the concrete due to the applied shear load on the anchor.

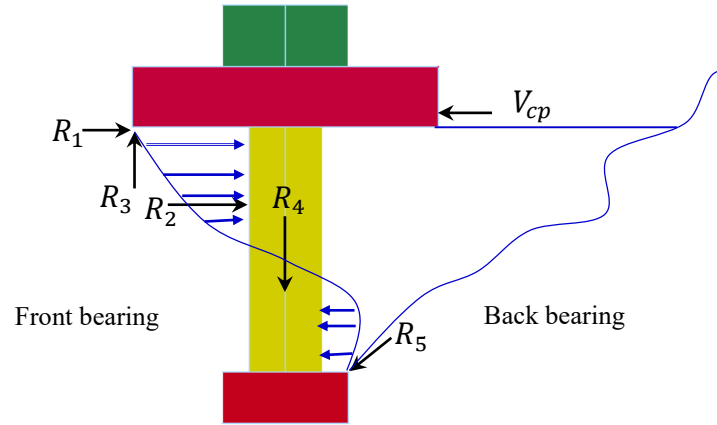


Figure 4-37: Pryout failure mechanism of the cast-in-place anchor

The shear load applied on the anchor plate develops stresses in the concrete in front of the anchor, produces a rotation moment of the anchor plate. As a result two forces are developed; compression force on the concrete under the tip of the anchor plate and tensile force in the anchor (Zhao, 1994). The stresses on the concrete in front of the anchor increase with the increase in the applied shear load, create concrete fracture under the anchor plate and increase the rotation of the anchor plate. As a result, half concrete cone breakout is formed at the back side of the anchor leads to pryout failure.

4.2.5 Effect of strain rate on the level of damage and failure mode

To demonstrate the effect of strain rate on the failure mechanism and level of damage, plastic strain contours for cast-in-place anchors subjected to different shear strain rates were investigated. Figures 4-38, 4-39 and 4-40 present the failure mode for the 12.7-mm, 15.9-mm and 19.1-mm diameter cast-in-place anchors respectively. As shown in Figure 4-38, steel anchor failure is the dominant failure mode for the 12.7-mm diameter cast-in-place anchor at strain rates ranging from 10^{-3} s^{-1} to 10^3 s^{-1} . Also, steel anchor failure is the

dominant failure mode for the anchor diameter of 15.9-mm (Figure 4-39) at the strain rates of 10^{-3} s^{-1} to 10^3 s^{-1} except for embedment depth of 76.2 mm at strain rate of 10^{-3} s^{-1} where pryout failure was observed. For the anchor diameter of 19.1 mm (Figure 4-40), pryout failure mode was observed at embedment depths of 76.2 mm and 101.6 mm at strain rate of 10^{-3} s^{-1} . At early stage of loading, the cracks initiated on the top surface of the concrete around the anchor in the direction of the applied load and propagated along the anchor embedment depth. Cracking in the concrete was subsequently transferred to a wider area in the concrete, leading to pryout failure. Steel anchor failure was observed at embedment depth of 152.4 mm. At strain rate of 10^{-1} s^{-1} , pryout failure mode was observed with embedment depth of 76.2 mm while steel anchor failure was observed at embedment depths of 101.6 mm and 152.4 mm. At strain rates of 10 s^{-1} , 10^2 s^{-1} and 10^3 s^{-1} steel anchor failure was observed for all the embedment depths investigated.

$\dot{\epsilon}$ (s^{-1})	Failure mode			Fringe Levels
	$h_{ef}=76.2 \text{ mm}$	$h_{ef}=101.6 \text{ mm}$	$h_{ef}=152.4 \text{ mm}$	
10^{-3}				9.990e-01 8.991e-01 7.992e-01 6.993e-01 5.994e-01 4.995e-01 3.996e-01 2.997e-01 1.998e-01 9.990e-02 0.000e+00
10^{-1}				
10				

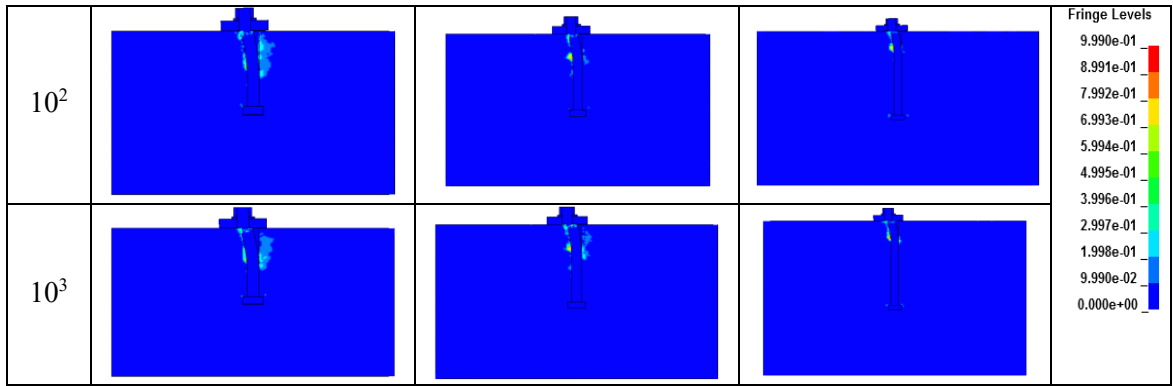


Figure 4-38: Failure mode for 12.7 mm diameter cast-in-place anchor at different strain rates

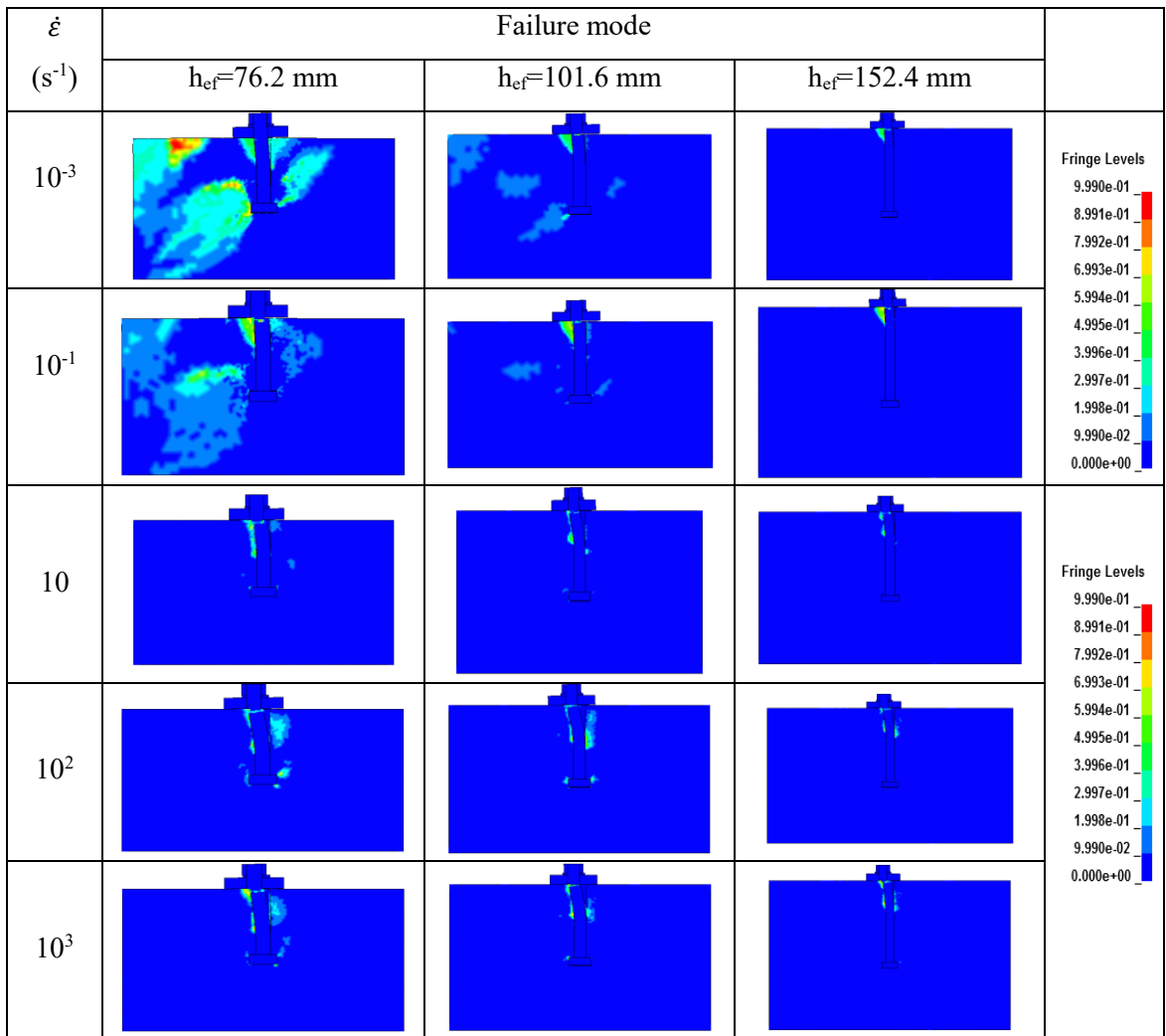


Figure 4-39: Failure mode for 15.9 mm diameter cast-in-place anchor at different strain rates

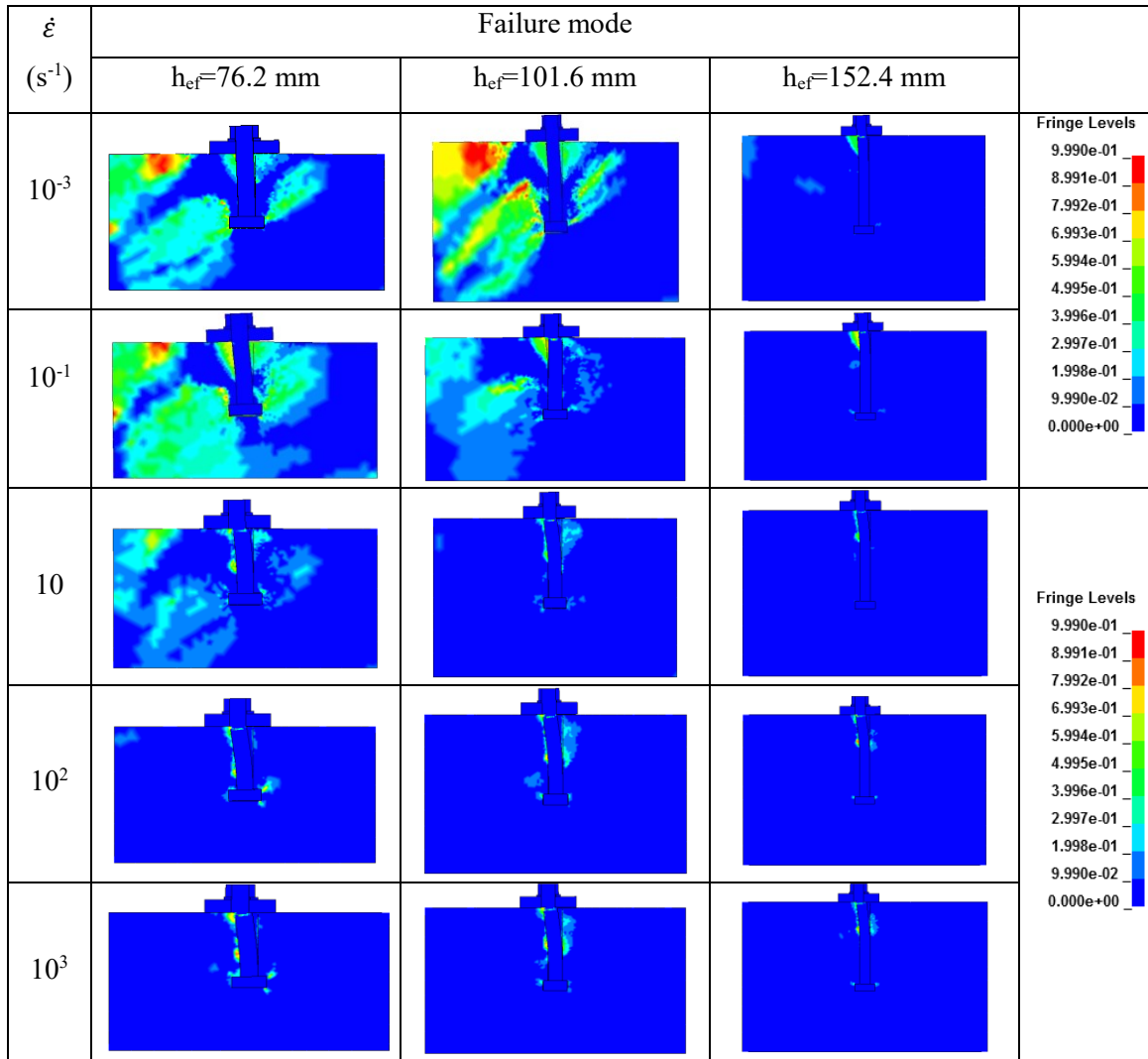


Figure 4-40: Failure mode for 19.1 mm diameter cast-in-place anchor at different strain rates

It can be seen from Figures 4-36, 4-38, 4-39 and 4-40 that as the anchor diameter increased from 12.7 mm to 19.1 mm cracking and level of damage in the concrete increased at all the strain rates investigated. Also, it can be seen that the increase in the strain rate has an effect on the failure mode of cast-in-place anchorage systems. Concrete pryout failure was observed at strain rates of 10^{-5} s^{-1} and 10^{-3} s^{-1} for 15.9 mm and 19.1 mm diameters with 76.2 mm embedment depth. Also, pryout failure was observed for 19.1-mm diameter with

embedment depth of 101.6 mm at strain rates of 10^{-5} s^{-1} and 10^{-3} s^{-1} . Concrete spalling followed by steel anchor failure was observed at higher strain rates of 10^{-1} s^{-1} to 10^3 s^{-1} .

In general, the failure mode for the cast-in-place anchors subjected to shear load depends on several factors such as edge distance, concrete compressive strength, embedment depth to diameter ratio (h_{ef}/d) and strain rate. In this section, concrete compressive strength of 30 MPa was investigated and the anchor was placed far from the free edge of the concrete. Thus, the ratio (h_{ef}/d) and strain rate are the factors that affect the failure mode and considered for the analysis. At static strain rate of 10^{-5} s^{-1} , the occurrence of pryout failure mode depends mainly on the ratio of (h_{ef}/d). The failure mode is governed by pryout failure for the large anchor diameters with shallow embedment depths. On the other hand, the failure mode is governed by steel anchor failure when the embedment depth is large enough compared to anchor diameter. Thus pryout failure mode was observed for the 15.9-mm and 19.1-mm diameter cast-in-place anchors for the shallow embedment depth of 76.2 mm. Also, the strain rate affects the failure mode where transition from pryout failure to steel anchor failure is observed with the increase in the strain rate.

The steel failure process of 19.1-mm diameter cast-in-place anchor with 101.6 mm embedment depth at strain rate of 10 s^{-1} is shown in Figure 4-41. Contours of Von Mises stresses (MPa) are presented in the figure. As shown, the stresses are concentrated around the top part of the anchor where the shear load is introduced followed by anchor bending and fracturing. When the shear load is applied on the anchor plate, friction forces between the anchor plate and the concrete surface are generated. When the applied shear load exceeds the friction force, the anchor plate will slip and transfer the shear load to the bolt

(Cook et al., 2013), which in turns transfers the load to the concrete through bearing. The concrete resists the shear forces transferred from the anchor causing concrete spall and fracture. In addition to the shear stress on the anchor, bending and tensile stresses are also generated. According to Cook et al., the interaction of these three stresses can lead to anchor fracture (Cook et al., 2013).

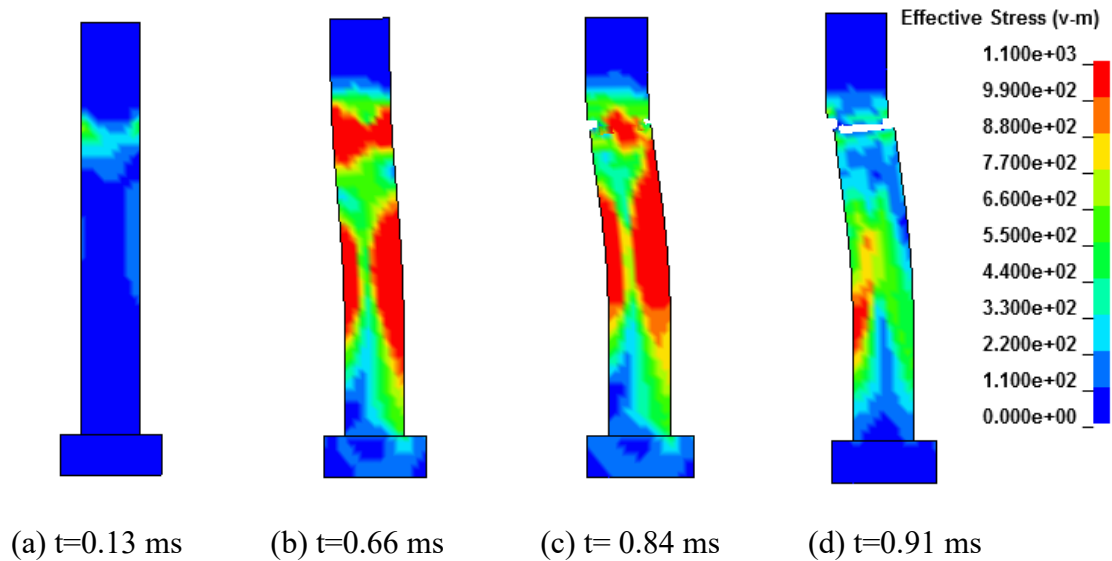


Figure 4-41: Steel failure process of 19.1 mm diameter cast-in-place anchor with 101.6 mm embedment depth; (a) stress concentration around the anchor, (b) anchor bending, (c) initiation of anchor fracture and (d) complete anchor fracture

The failure modes for the cast-in-place anchors at different strain rates is shown in Table 4-15. As shown in Table 4-15, at strain rates of 10^{-5} s^{-1} to 10^3 s^{-1} , steel anchor failure was observed for 12.7-mm diameter cast-in-place anchor. Pryout failure mode was observed for anchor diameters of 15.9-mm and 19.1-mm with embedment depth of 76.2 mm. Also, pryout failure mode is observed for anchor diameter of 19.1 mm with embedment depth of 101.6 mm at strain rates of 10^{-5} s^{-1} and 10^{-3} s^{-1} . Steel anchor failure is observed at the strain

rates of 10^{-1} s^{-1} up to 10^3 s^{-1} for all anchor diameters and embedment depths except for anchor diameter of 19.1 mm with embedment depth of 76.2 mm at strain rate of 10^{-1} s^{-1} where prout failure mode is observed.

Table 4-15: Failure mode for cast-in-place anchors under shear load at different strain rates

Model No.	d (mm)	h _{ef} (mm)	*Failure mode					
			Strain rate (s ⁻¹)					
			$\dot{\epsilon}=10^{-5}$	$\dot{\epsilon}=10^{-3}$	$\dot{\epsilon}=10^{-1}$	$\dot{\epsilon}=10$	$\dot{\epsilon}=10^2$	$\dot{\epsilon}=10^3$
1	12.7	76.2	S	S	S	S	S	S
2	12.7	101.6	S	S	S	S	S	S
3	12.7	152.4	S	S	S	S	S	S
4	15.9	76.2	PR	PR	S	S	S	S
5	15.9	101.6	S	S	S	S	S	S
6	15.9	152.4	S	S	S	S	S	S
7	19.1	76.2	PR	PR	PR	S	S	S
8	19.1	101.6	PR	PR	S	S	S	S
9	19.1	152.4	S	S	S	S	S	S

*Failure mode: PR= prout failure, S=steel anchor failure

4.2.6 Effect of design parameters on failure mode and ultimate shear load

Figures 4-42, 4-43 and 4-44 show the effect of strain rate on the failure mode and ultimate shear load for the 12.7-mm, 15.9-mm and 19.1-mm diameter cast-in-place anchors respectively. The figures indicate that the strain rate has an effect on the failure mode for the anchor diameters of 15.9 mm and 19.1 mm where transition from prout failure to steel anchor failure is observed. Furthermore, the anchor diameter and embedment depth have an effect on the failure mode. It can be seen from the figures that the ultimate shear load increased with the increase in the strain rate for the cast-in-place anchors.

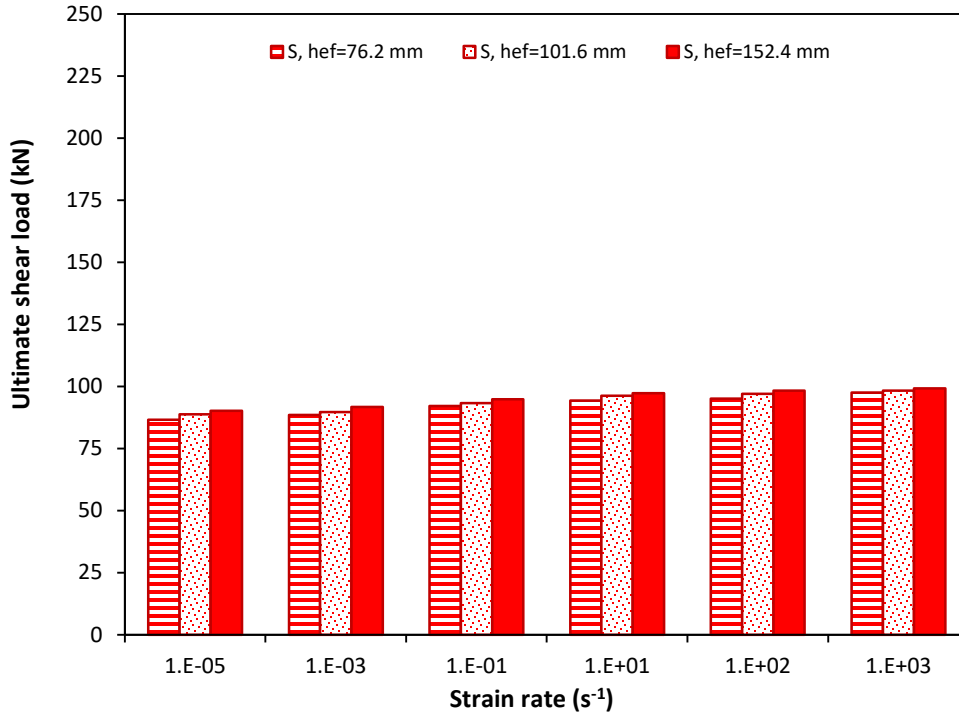


Figure 4-42: Effect of strain rate on the failure mode and ultimate shear load for the cast-in-place anchor diameter of 12.7 mm

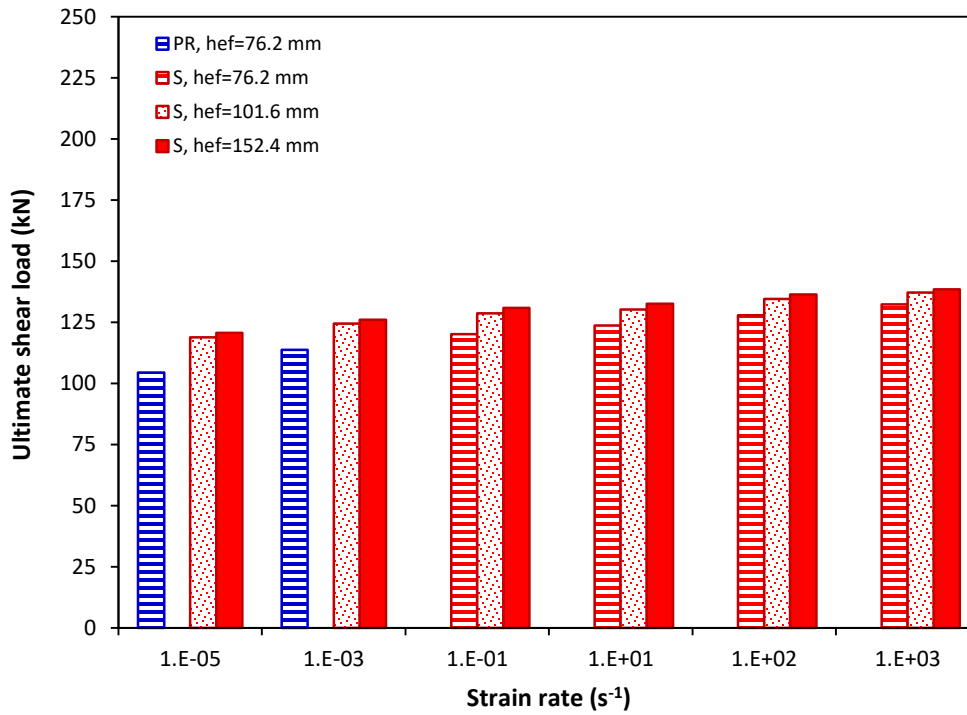


Figure 4-43: Effect of strain rate on the failure mode and ultimate shear load for the cast-in-place anchor diameter of 15.9 mm

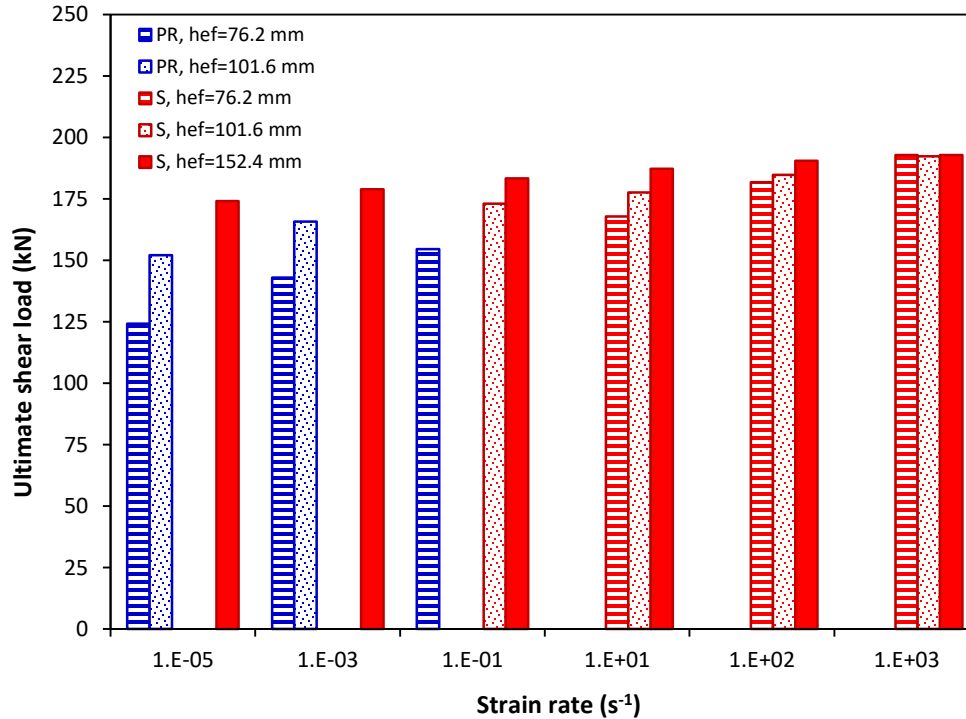


Figure 4-44: Effect of strain rate on the failure mode and ultimate shear load for the cast-in-place anchor diameter of 19.1 mm

4.2.7 Effect of strain rate on the shear behaviour of cast-in-place anchors

Shear behaviour of cast-in-place anchors embedded into concrete was investigated using LS-DYNA finite element software. Strain rates ranging from low to high strain rates (10^{-5} s^{-1} , 10^{-3} s^{-1} , 10^{-1} s^{-1} , 10 s^{-1} , 10^2 s^{-1} and 10^3 s^{-1}) were selected for the analysis. Effect of strain rate on the shear capacity for different cast-in-place anchor diameters and embedment depths was investigated. Load-displacement response for the 12.7-mm diameter cast-in-place anchor at strain rates of 10^{-5} s^{-1} , 10^{-3} s^{-1} , 10^{-1} s^{-1} , 10 s^{-1} , 10^2 s^{-1} and 10^3 s^{-1} is shown in Figures 4-45, 4-46, 4-47, 4-48, 4-49 and 4-50 respectively. Embedment depths of 76.2 mm, 101.6 mm and 152.4 mm were used for the analysis. The displacement in the y-direction (shown in Figure 4-34) was measured at the top of the anchor using History-Nodal-y-displacement in the LS-DYNA post processor.

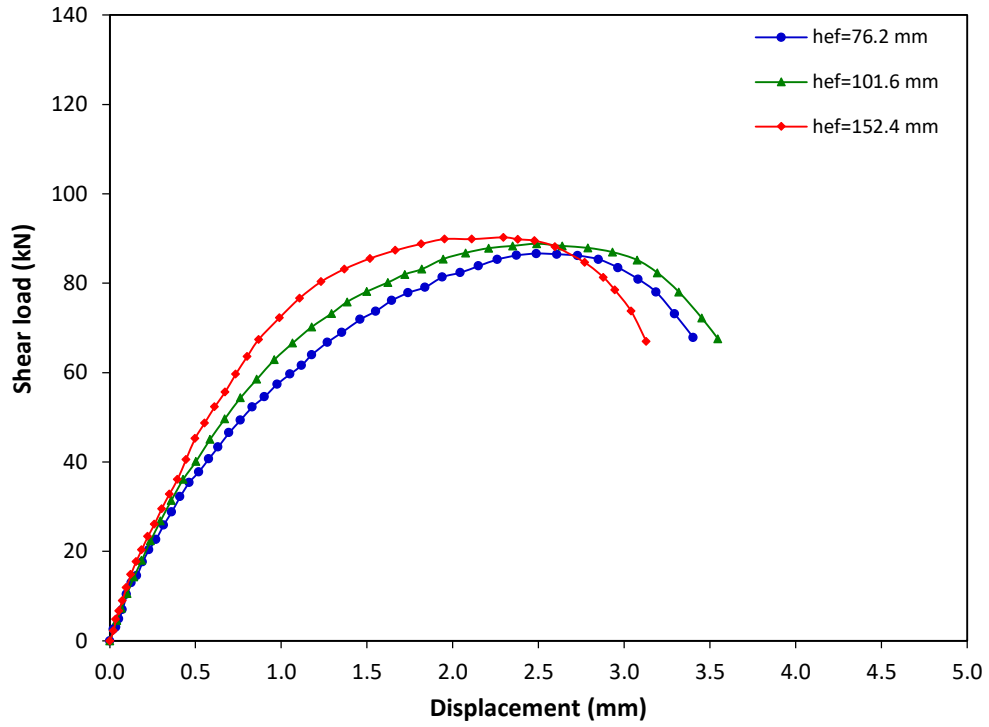


Figure 4-45: Shear load-displacement graph for 12.7 mm diameter cast-in-place anchor at strain rate of 10^{-5} s^{-1}

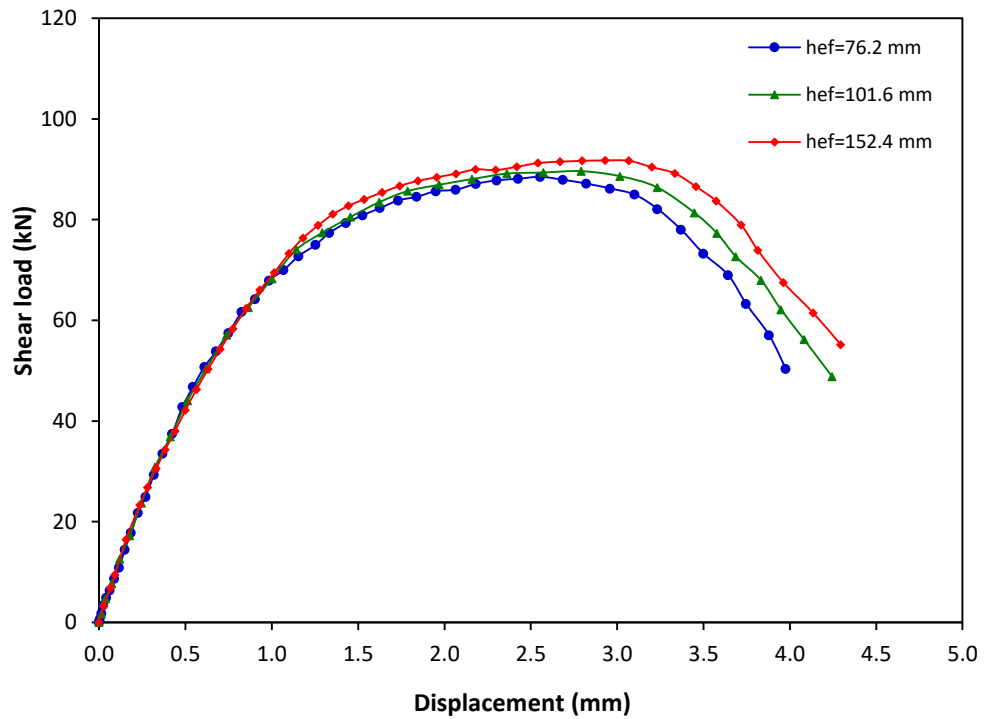


Figure 4-46: Shear load-displacement graph for 12.7 mm diameter cast-in-place anchor at strain rate of 10^{-3} s^{-1}

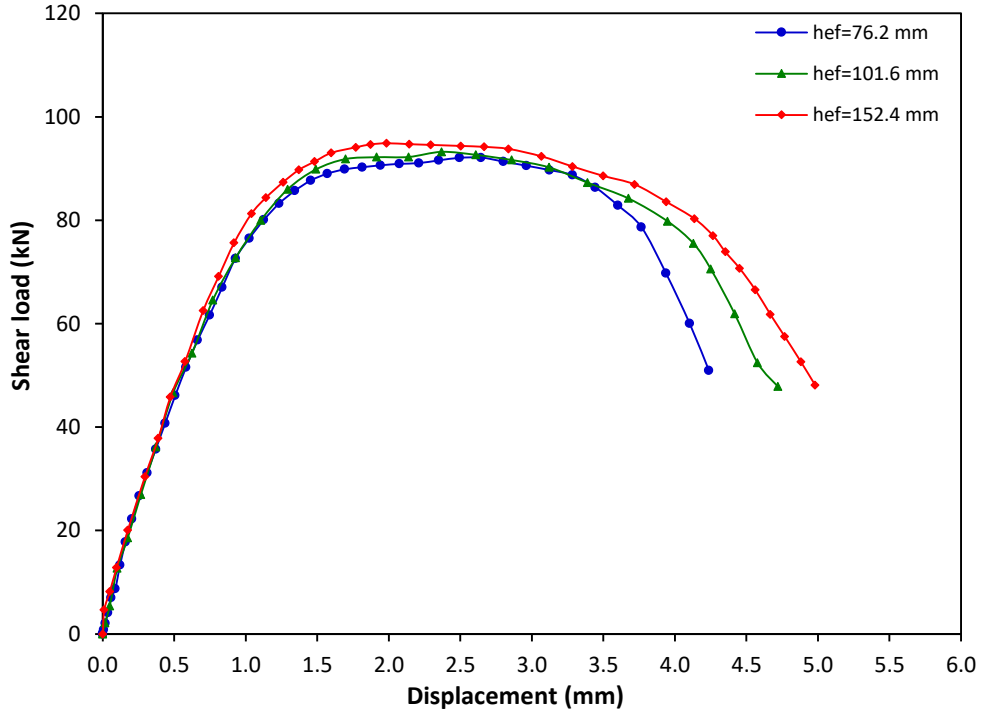


Figure 4-47: Shear load-displacement graph for 12.7 mm diameter cast-in-place anchor at strain rate of 10^{-1} s^{-1}

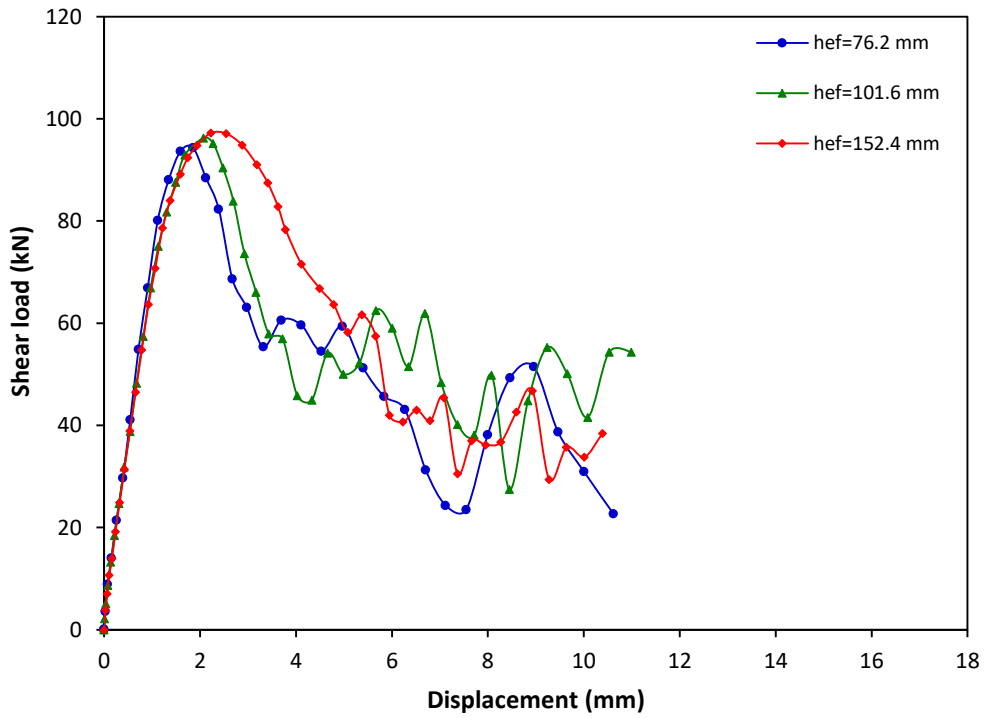


Figure 4-48: Shear load-displacement graph for 12.7 mm diameter cast-in-place anchor at strain rate of 10 s^{-1}

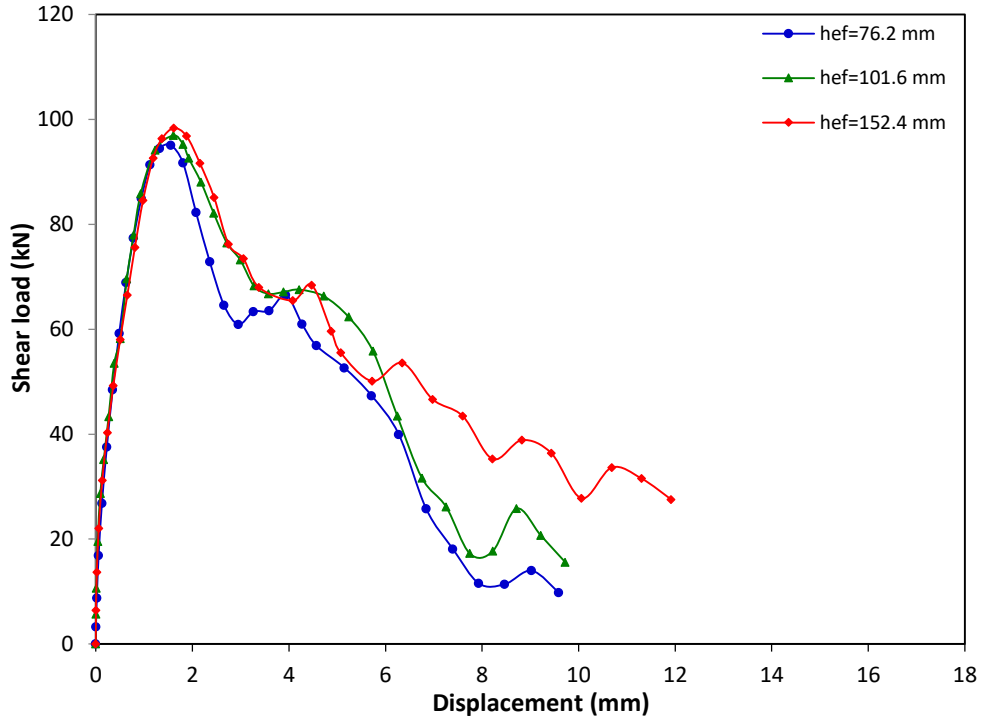


Figure 4-49: Shear load-displacement graph for 12.7 mm diameter cast-in-place anchor at strain rate of 10^2 s^{-1}

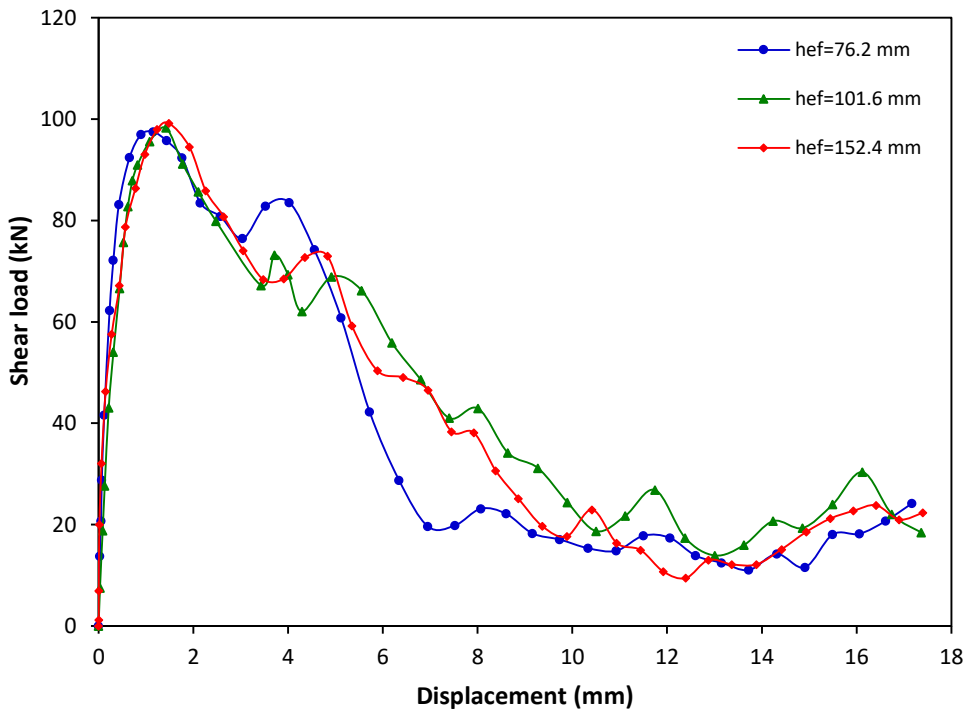


Figure 4-50: Shear load-displacement graph for 12.7 mm diameter cast-in-place anchor at strain rate of 10^3 s^{-1}

As shown from Figures 4-45 to 4-50, the increase in the strain rate increased the shear capacity for the 12.7-mm diameter cast-in-place anchor. At strain rates of 10^{-5} s^{-1} to 10^3 s^{-1} , the shear load increased with the displacement until the ultimate load was reached, and then decreased until complete failure. This is attributed to the progressive crack propagation in the concrete and anchor failure.

Shear load-displacement response for 15.9-mm and 19.1-mm diameter cast-in-place anchors with embedment depths of 76.2 mm, 101.6 mm and 152.4 mm at strain rates of 10^{-5} s^{-1} , 10^{-3} s^{-1} , 10^{-1} s^{-1} , 10 s^{-1} , 10^2 s^{-1} and 10^3 s^{-1} is presented in Appendix D. Tables 4-16, 4-17 and 4-18 present the ultimate shear load (V_u) and corresponding displacement (δ) for the 12.7-mm, 15.9-mm and 19.1-mm diameter cast-in-place anchors respectively.

Table 4-16: Ultimate shear load and displacement results for the 12.7 mm diameter cast-in-place anchor

Model No.	d (mm)	h_{ef} (mm)	$\dot{\epsilon}$ (s^{-1})	V_u (kN)	δ (mm)	Failure mode
1	12.7	76.2	10^{-5}	86.64	2.49	S
2		101.6		88.81	2.49	S
3		152.4		90.16	2.29	S
4	12.7	76.2	10^{-3}	88.49	2.56	S
5		101.6		89.63	2.79	S
6		152.4		91.78	2.93	S
7	12.7	76.2	10^{-1}	92.14	2.65	S
8		101.6		93.25	2.37	S
9		152.4		94.89	1.99	S
10	12.7	76.2	10	94.36	1.85	S
11		101.6		96.23	2.07	S
12		152.4		97.26	2.23	S

13	12.7	76.2	10^2	95.08	1.55	S
14		101.6		96.99	1.61	S
15		152.4		98.35	1.61	S
16	12.7	76.2	10^3	97.48	1.15	S
17		101.6		98.26	1.42	S
18		152.4		99.15	1.48	S

Table 4-17: Ultimate shear load and displacement results for the 15.9 mm diameter cast-in-place anchor

Model No.	d (mm)	h_{ef} (mm)	$\dot{\epsilon}$ (s^{-1})	V_u (kN)	δ (mm)	Failure mode
1	15.9	76.2	10^{-5}	104.37	2.05	PR
2		101.6		118.79	2.42	S
3		152.4		120.67	2.53	S
4	15.9	76.2	10^{-3}	113.74	3.67	PR
5		101.6		124.43	3.49	S
6		152.4		126.01	3.13	S
7	15.9	76.2	10^{-1}	120.13	3.58	S
8		101.6		128.58	3.52	S
9		152.4		130.87	3.27	S
10	15.9	76.2	10	123.65	1.98	S
11		101.6		130.21	2.12	S
12		152.4		132.51	2.74	S
13	15.9	76.2	10^2	127.89	1.61	S
14		101.6		134.47	1.67	S
15		152.4		136.36	1.78	S
16	15.9	76.2	10^3	132.30	1.87	S
17		101.6		137.16	1.85	S
18		152.4		138.42	1.78	S

Table 4-18: Ultimate shear load and displacement results for the 19.1 mm diameter cast-in-place anchor

Model No.	d (mm)	h_{ef} (mm)	$\dot{\epsilon}$ (s^{-1})	V_u (kN)	δ (mm)	Failure mode
1	19.1	76.2	10^{-5}	124.18	1.73	PR
2		101.6		152.14	2.12	PR
3		152.4		174.09	3.08	S
4	19.1	76.2	10^{-3}	143.04	2.47	PR
5		101.6		165.76	2.96	PR
6		152.4		178.96	3.29	S
7	19.1	76.2	10^{-1}	154.56	3.16	PR
8		101.6		173.03	3.34	S
9		152.4		183.29	3.47	S
10	19.1	76.2	10	167.89	1.92	S
11		101.6		177.59	2.41	S
12		152.4		187.20	2.53	S
13	19.1	76.2	10^2	181.72	2.04	S
14		101.6		184.83	2.09	S
15		152.4		190.48	1.98	S
16	19.1	76.2	10^3	192.91	1.79	S
17		101.6		192.28	2.09	S
18		152.4		192.81	2.01	S

4.2.8 Effect of strain rate on the ultimate shear load and DIF of cast-in-place anchors

The relation between the ultimate shear load, DIF and the strain rate for the cast-in-place anchor of 76.2 mm, 101.6 mm and 152.4 mm embedment depths and different anchor diameters is shown in Figures 4-51, 4-52 and 4-53. It can be seen that the ultimate shear load increased with the increase in the anchor diameter from 12.7 mm to 19.1 mm for all the embedment depths and strain rates investigated. Anchor diameter of 12.7 mm exhibited an increase in the ultimate shear load of 12.5%, 10.6% and 10.0% as the strain rate

increased from 10^{-5} s^{-1} to 10^3 s^{-1} for the 76.2 mm, 101.6 mm and 152.4 mm embedment depths respectively. Anchor diameter of 15.9 mm exhibited an increase in the ultimate shear load with the increase in the strain rate at embedment depth of 76.2 mm where the failure mode transitioned from pryout failure to steel anchor failure. An increase of 15.5% and 14.7% in the ultimate shear load is obtained with the increase in strain rate from 10^{-5} s^{-1} to 10^3 s^{-1} for anchor embedment depths of 101.6 mm and 152.4 mm respectively. For anchor diameter of 19.1 mm, the ultimate shear load increased from 124.2 kN to 192.9 kN and from 152.1 kN to 192.3 kN as the strain rate increased from 10^{-5} s^{-1} to 10^3 s^{-1} for anchor embedment depths of 76.2 mm and 101.6 mm respectively. An increase in the ultimate shear load of 10.75% was obtained with the increase in the strain rate from 10^{-5} s^{-1} to 10^3 s^{-1} at 152.4 mm embedment depth. Maximum ultimate shear loads of 99.2 kN, 138.4 kN and 192.8 kN were obtained for anchor diameters of 12.7 mm, 15.9 mm and 19.1 mm respectively with embedment depth of 152.4 mm at high strain rate of 10^3 s^{-1} . At low strain rate of 10^{-5} s^{-1} , ultimate shear loads of 90.2 kN, 120.7 kN and 174.1 kN were obtained for the anchor diameters of 12.7-mm, 15.9-mm and 19.1-mm respectively with embedment depth of 152.4 mm. It can be seen from Figures 4-51, 4-52 and 4-53, the relation between the ultimate shear load and the strain rate is almost linear for all the anchors investigated.

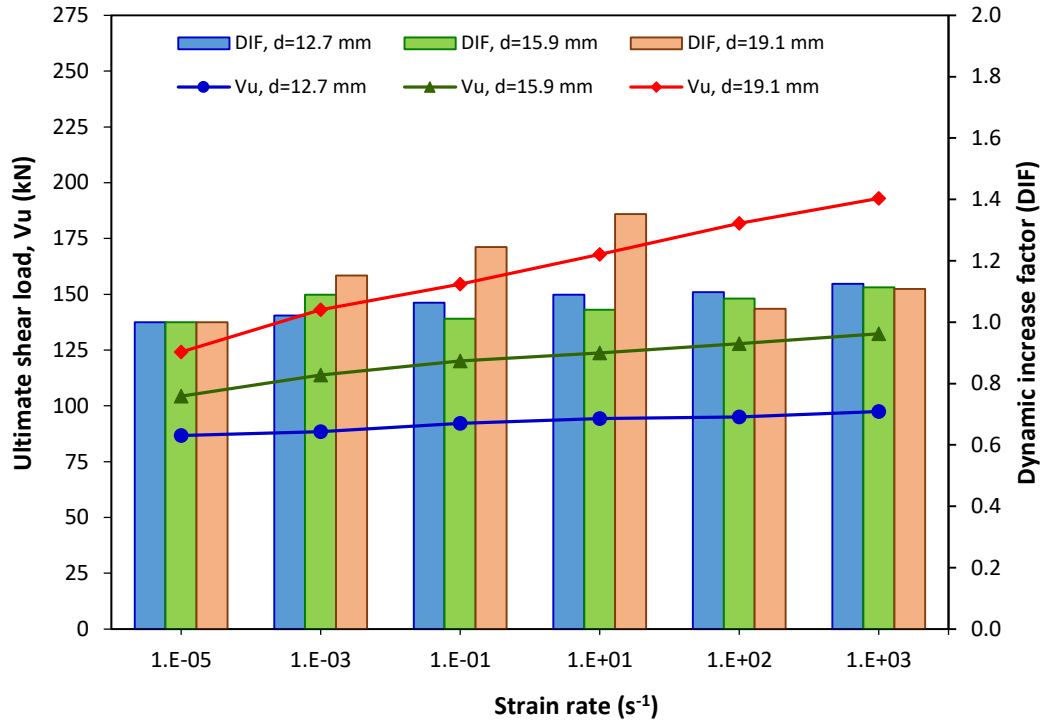


Figure 4-51: Ultimate shear load and DIF versus strain rate for cast-in-place anchor with 76.2 mm embedment depth

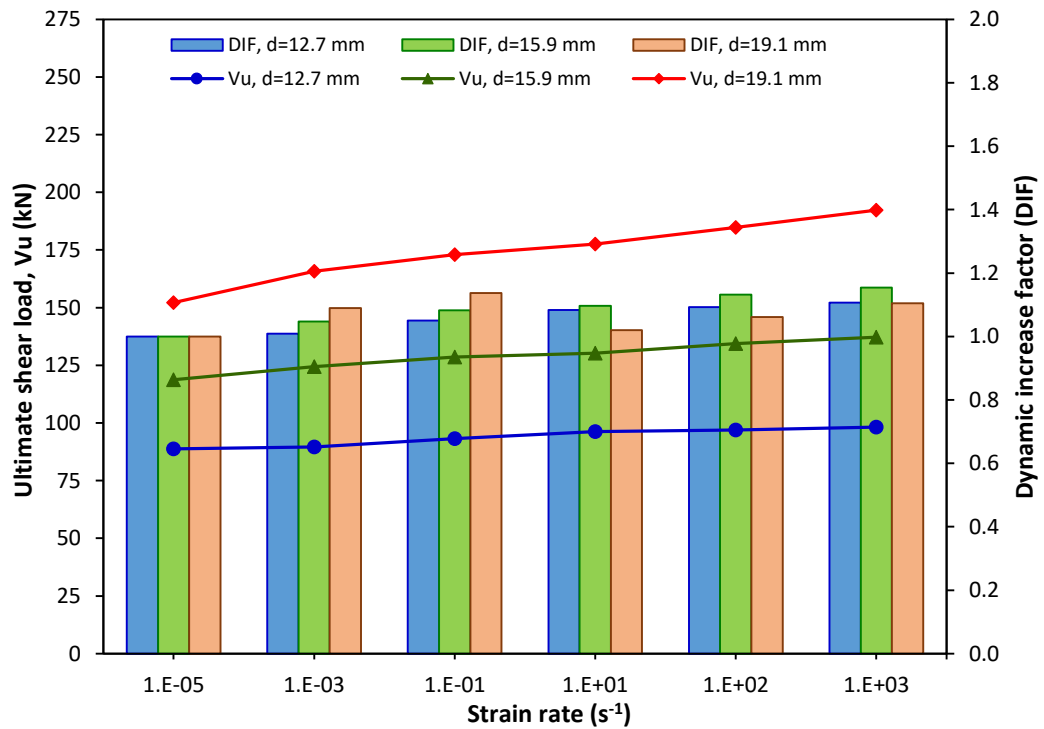


Figure 4-52: Ultimate shear load and DIF versus strain rate for cast-in-place anchor with 101.6 mm embedment depth

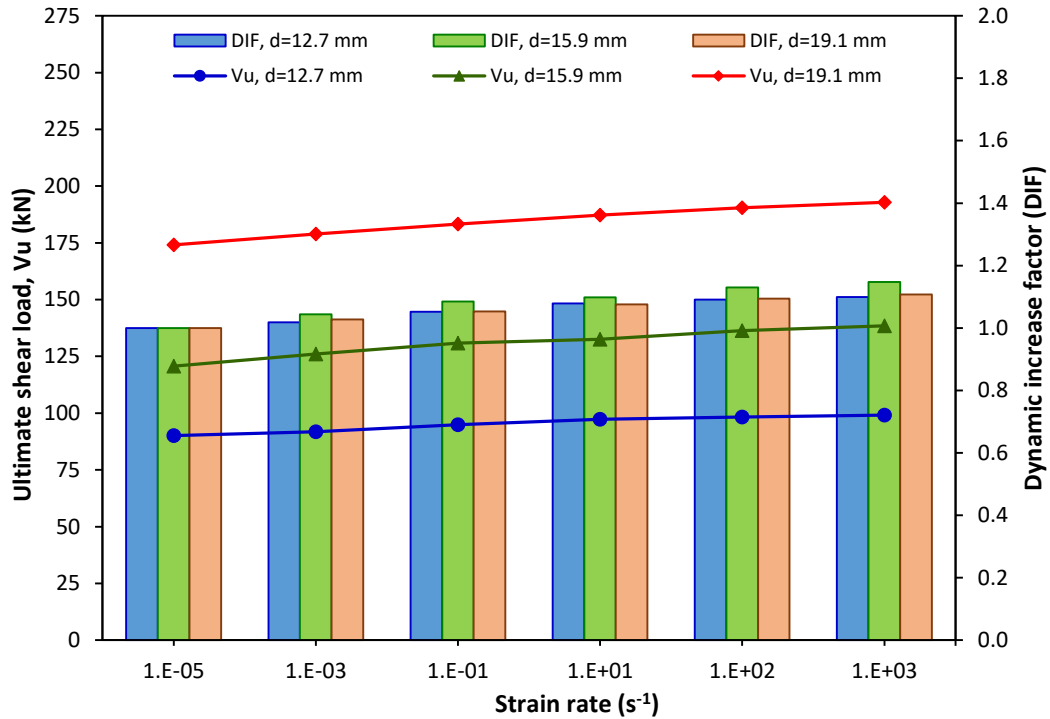


Figure 4-53: Ultimate shear load and DIF versus strain rate for cast-in-place anchor with 152.4 mm embedment depth

As shown in Figure 4-51, for the 12.7-mm diameter anchor the DIF increased slightly with the increase in the strain rate where steel anchor failure was observed at all the strain rates investigated. For anchor diameter of 15.9 mm with embedment depth of 76.2 mm the DIF increased from 1 to 1.09 at strain rate of 10^{-3} s^{-1} where pryout failure was observed. Further increase in the strain rate resulted in steel failure with DIF of 1.11 at high strain rate of 10^3 s^{-1} . The increase in the DIF is obvious for the anchor diameter of 19.1 mm with embedment depth of 76.2 mm where the failure mode transitioned from pryout failure at low strain rate of 10^{-5} s^{-1} to steel fracture at strain rate of 10 s^{-1} . At high strain rates of 10^2 s^{-1} and 10^3 s^{-1} , DIF of 1.04 and 1.11 were obtained for the 19.1 mm anchor diameter where steel failure was observed. From Figure 4-52, DIF of 1.14 was obtained for the 19.1 mm anchor diameter at strain rate of 10^{-1} s^{-1} where transition in the failure mode from pryout to steel

anchor failure is observed at higher strain rates. DIF of 1.1 was obtained at high strain rate of 10^3 s^{-1} . Very close DIF values were obtained for the 12.7-mm and 15.9-mm diameter anchors that all fail by steel fracture at all strain rates investigated. From Figure 4-53, for embedment depth of 152.4 mm, the DIF values are very close for all anchor diameters where steel failure is the dominant failure mode at all the strain rates. Maximum DIF of 1.35 is obtained for the 19.1-mm diameter cast-in-place anchor with 76.2 mm embedment depth at strain rate of 10 s^{-1} . The DIF of cast-in-place anchors at different strain rates is represented as a function for the strain rate ratio as follows:

$$DIF = \frac{V_{ud}}{V_{us}} = A \left(\frac{\dot{\epsilon}_d}{\dot{\epsilon}_s} \right)^B \quad (4.19)$$

$$V_{ud} = V_{us} \cdot A \left(\frac{\dot{\epsilon}_d}{\dot{\epsilon}_s} \right)^B \quad (4.20)$$

Where V_{us} , V_{ud} are the ultimate static and dynamic shear loads respectively. A and B are constants to be determined by experimental testing or numerical parametric analysis.

Table 4-19 shows the maximum dynamic increase factor for the cast-in-place anchors under shear load where pryout failure and steel failure modes were observed.

Table 4-19: Maximum DIF for the cast-in-place anchors under shear load

Model No.	d (mm)	h _{ef} (mm)	ε̇ (s ⁻¹)	DIF	ε̇ (s ⁻¹)	DIF
				PR		S
1	12.7	76.2	-	-	10 ³	1.13
2	12.7	101.6	-	-	10 ³	1.11
3	12.7	152.4	-	-	10 ³	1.10
4	15.9	76.2	10 ⁻³	1.09	10 ³	1.11
5	15.9	101.6	-	-	10 ³	1.15
6	15.9	152.4	-	-	10 ³	1.15

7	19.1	76.2	10^{-1}	1.24	10^3	1.11
8	19.1	101.6	10^{-3}	1.09	10^3	1.10
9	19.1	152.4	-	-	10^3	1.11

4.2.9 Regression analysis for cast-in-place anchors under shear load

Regression analysis has been performed to predict the relation that accurately represents the finite element results of the cast-in-place anchor subjected to shear load. As shown in Figures 4-38, 4-39 and 4-40, steel anchor failure is the dominant failure mode for most of the cast-in-place anchors subjected to shear load and subjected to strain rate in the range of 10^{-3} s^{-1} to 10^3 s^{-1} , hence regression analysis is performed for the anchors exhibiting steel failure mode. Average values of the DIF for the 12.7-mm, 15.9-mm and 19.1-mm cast-in-place diameter anchors were considered to adjust the DIF for the effect of anchor diameter. The relation between the DIF and the strain rate ratio ($\dot{\epsilon}_d/\dot{\epsilon}_s$) is shown in Figure 4-54 for the cast-in-place anchors exhibited steel anchor failure mode.

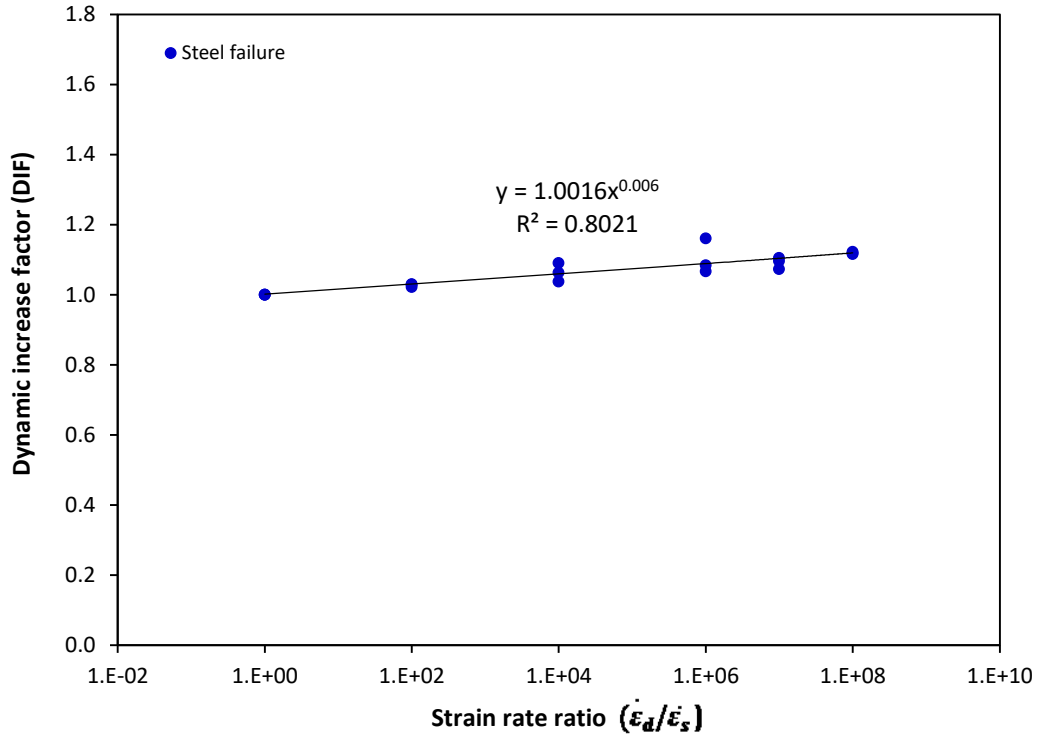


Figure 4-54: Effect of strain rate ratio on the DIF for cast-in-place anchors exhibit steel failure under shear load

Table 4-20 shows the statistical models used to predict a formula that relates the DIF with the strain rate for the cast-in-place anchors exhibited steel anchor failure.

Table 4-20: Statistical models and coefficient of determination to predict the DIF for cast-in-place anchor exhibited steel failure under shear load

Statistical models	Formulae	Coefficient of determination (R ²)
Exponential	$DIF = 1.0539e^{6E-10\left(\frac{\dot{\epsilon}_d}{\dot{\epsilon}_s}\right)}$	0.277
Linear	$DIF = 7E - 10\left(\frac{\dot{\epsilon}_d}{\dot{\epsilon}_s}\right) + 1.0548$	0.278
Logarithmic	$DIF = 0.0064\ln\left(\frac{\dot{\epsilon}_d}{\dot{\epsilon}_s}\right) + 1.0009$	0.790
Power	$DIF = 1.0016\left(\frac{\dot{\epsilon}_d}{\dot{\epsilon}_s}\right)^{0.006}$	0.802

As shown in Table 4-20 the highest coefficients of determination of 80% is obtained from the power model for the steel anchor failure mode. The predicted formulae for the DIF for cast-in-place anchors subjected to shear load and exhibited steel failure can be presented as in Equation (4.21).

$$DIF = 1.0016 \left(\frac{\dot{\epsilon}_d}{\dot{\epsilon}_s} \right)^{0.006} \quad (4.21)$$

The proposed Equation (4.21) can be used to predict the ultimate dynamic shear load (V_{ud}) for steel anchor failure mode as follows:

$$V_{ud} = V_{us} \times 1.0016 \left(\frac{\dot{\epsilon}_d}{\dot{\epsilon}_s} \right)^{0.006} \quad (4.22)$$

Where the ultimate static load (V_{us}) can be determined from Equation (4.18) for the cast-in-place anchors exhibited steel failure under shear load.

Residual analysis has been performed for the cast-in-place anchors subjected to shear load to determine the difference between the DIF results obtained from the finite element and the DIF results obtained from the proposed Equation (4.21). Figure 4-55 presents the residual plots for the cast-in-place anchors. As shown in Figure 4-55, the residual results exhibit horizontal trend line with strain rate ratio.

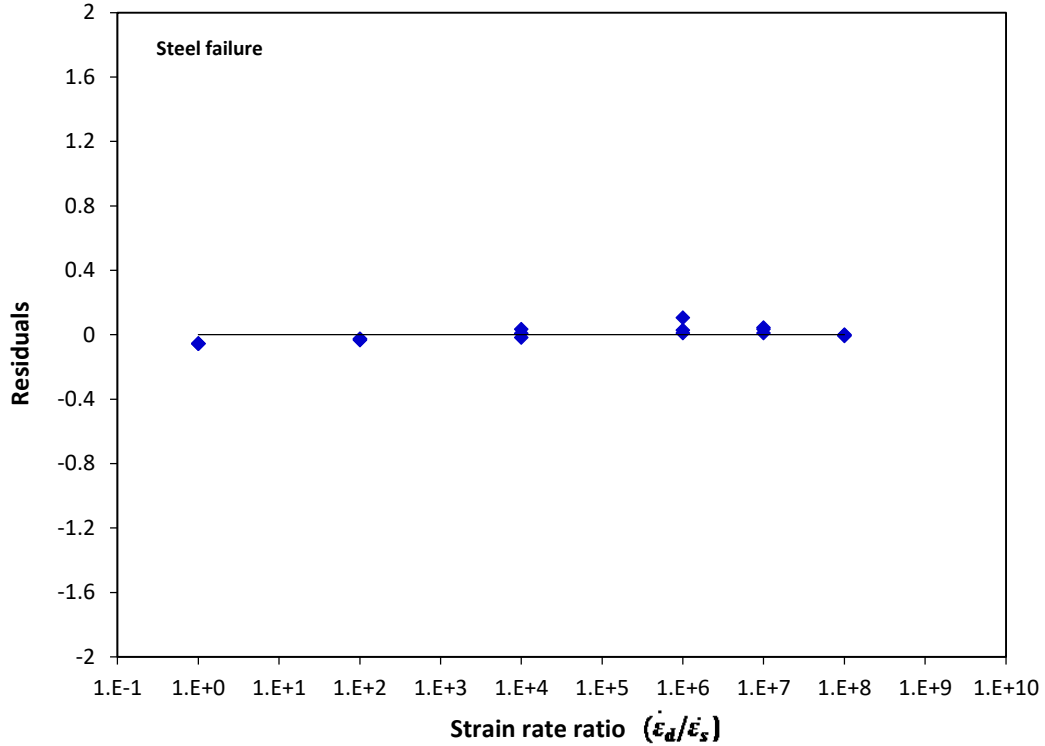


Figure 4-55: Residual versus strain rate ratio for the cast-in-place anchor subjected to shear load and exhibited steel failure

In addition, new cast-in-place anchor models were developed with diameters of 9.5 mm, 12.7 mm, 15.9 mm and 19.1 mm and embedment depths of 89 mm, 114 mm and 140 mm to verify the proposed equation. A comparison has been made between the proposed equation and the results of the new cast-in-place anchor models. Figure 4-56 presents the relation between the DIF obtained from newly developed numerical models and the regression models (Equation (4.21)) for cast-in-place anchors exhibited steel failure. As shown in the figure, the DIF is distributed normally around the equality line, however some divergence was observed for the high DIF values.

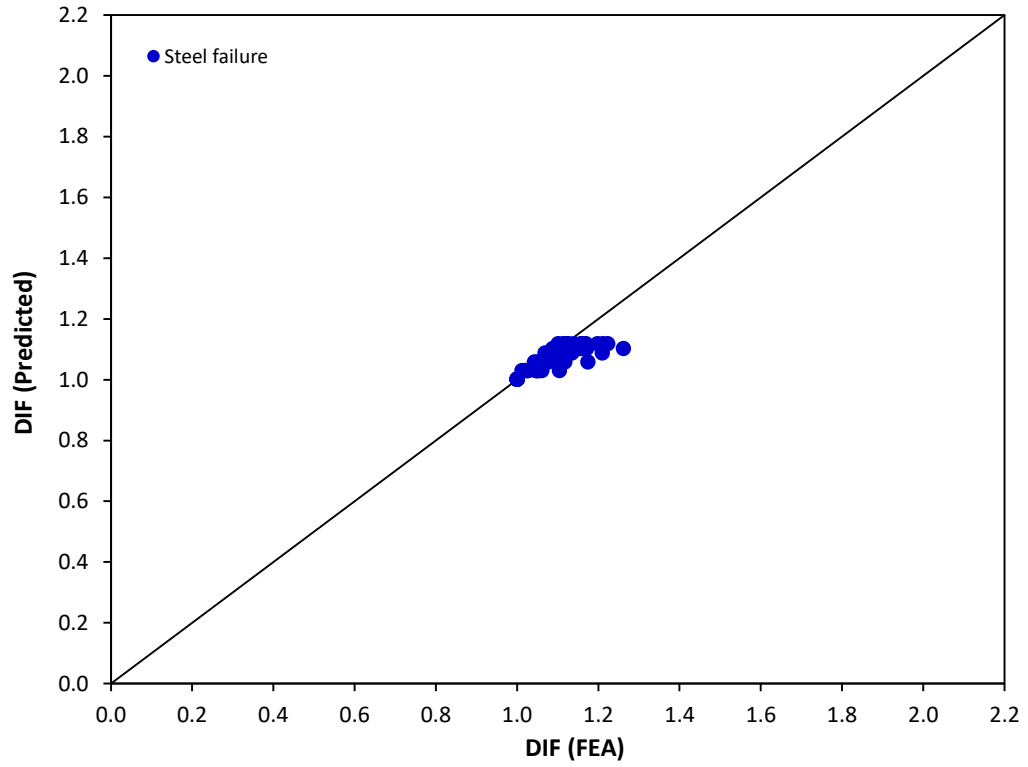


Figure 4-56: DIF obtained from the finite element analysis versus the predicted DIF for the cast-in-place anchor exhibited steel failure under shear load

4.2.10 Case study: effect of concrete compressive strength on the shear behaviour of cast-in-place anchors

4.2.10.1 Level of damage and failure mode

Cast-in-place anchor diameters of 12.7 mm and 19.1 mm with embedment depths of 76.2 mm and 152.4 mm subjected to shear load were investigated at static (10^{-5} s^{-1}) and high strain rate (10^3 s^{-1}). Three concrete compressive strengths of 20 MPa, 30 MPa and 40 MPa were selected for the analysis. Figures 4-57 and 4-58 show the failure mode for the 12.7-mm and 19.1-mm diameter cast-in-place anchors respectively embedded in concrete compressive strengths of 20 MPa, 30 MPa and 40 MPa at low and high strain rates of 10^{-5} s^{-1} and 10^3 s^{-1} . As shown in Figure 4-57, at the low strain rate of 10^{-5} s^{-1} , pryout failure mode is observed for the concrete compressive strength of 20 MPa and embedment depth of 76.2 mm. Steel anchor failure was observed for the concrete compressive strengths of 30 MPa and 40 MPa. Also, steel anchor failure was observed for the embedment depth of 152.4 mm at all concrete compressive strengths. At strain rate of 10^3 s^{-1} steel anchor failure was observed for all the concrete compressive strengths and embedment depths investigated. It can be seen from Figure 4-58, for the 19.1-mm diameter cast-in-place anchor at low strain rate of 10^{-5} s^{-1} , pryout failure was observed for all the concrete compressive strengths at embedment depth of 76.2 mm. At the embedment depth of 152.4 mm pryout failure is observed for the compressive strength of 20 MPa whereas steel anchor failure was observed for the compressive strengths of 30 MPa and 40 MPa. At high strain rate of 10^3 s^{-1} , steel anchor failure was observed for all the concrete compressive strengths and embedment depths investigated.

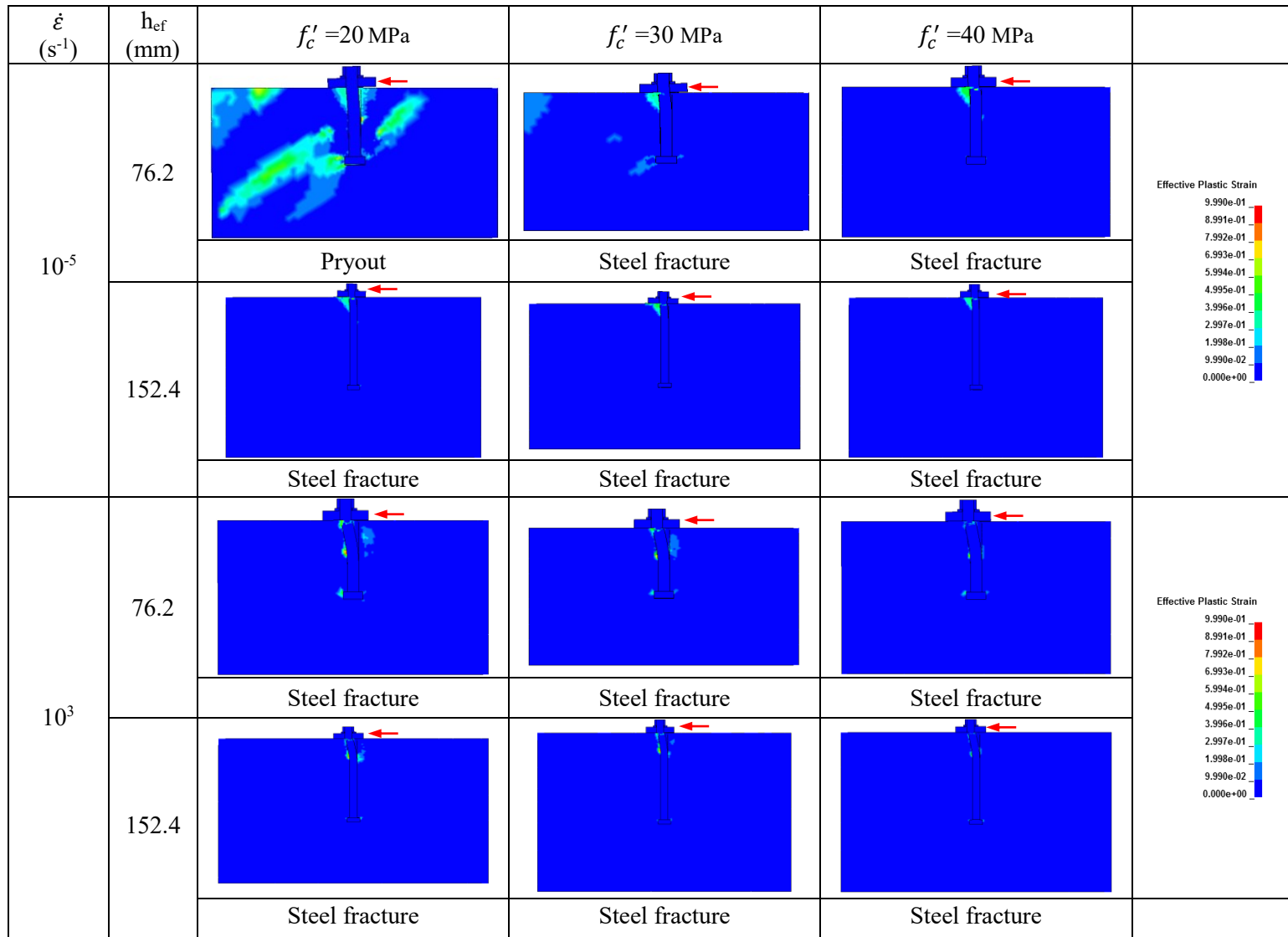


Figure 4-57: Effect of strain rate and concrete compressive strength on the failure mode for the 12.7 mm diameter cast-in-place anchors

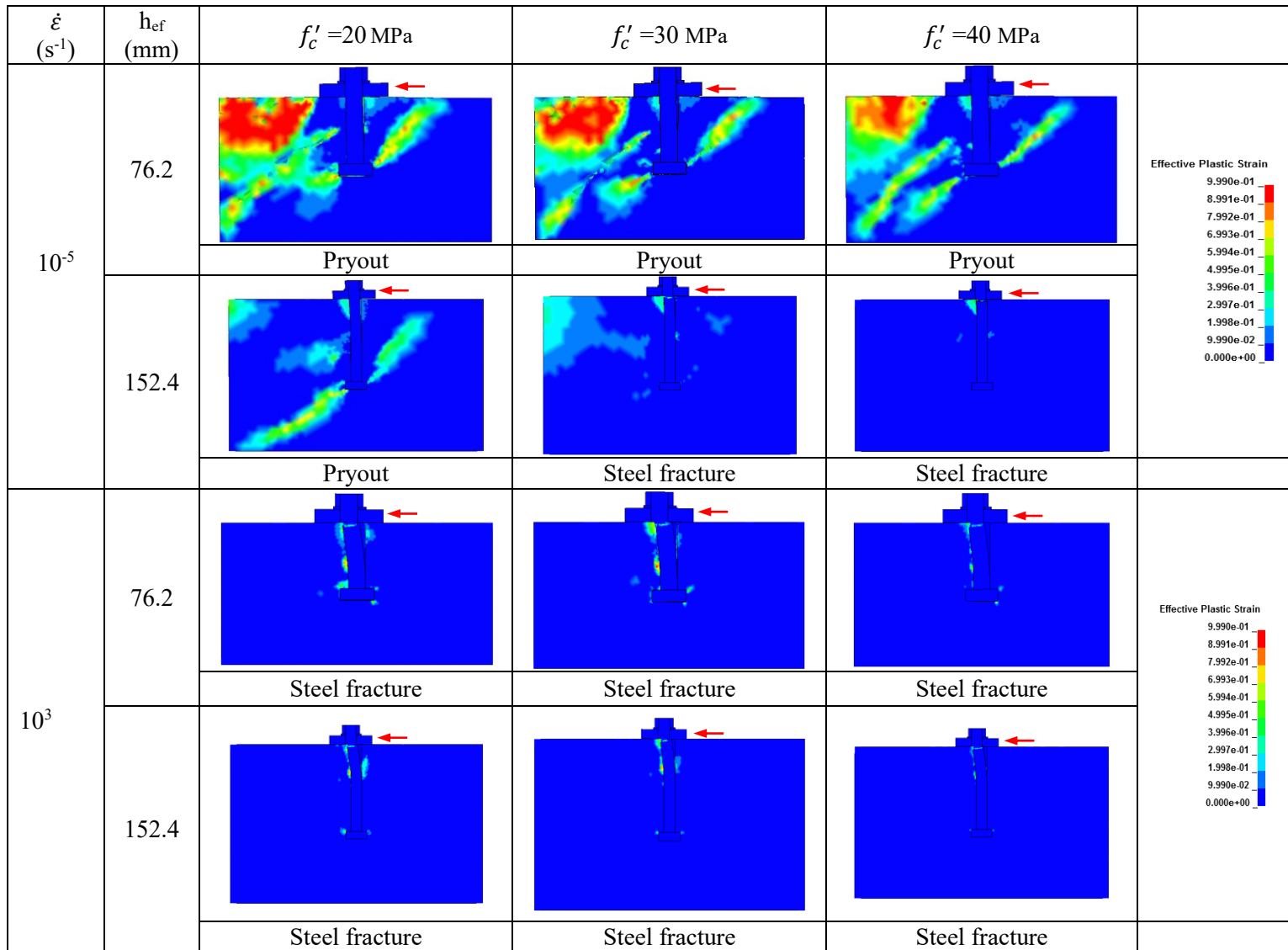


Figure 4-58: Effect of strain rate and concrete compressive strength on the failure mode for the 19.1 mm diameter cast-in-place anchors

From Figures 4-57 and 4-58, it can be seen that for cast-in-place anchorage systems failing in concrete pryout at the static strain rate transitioned to steel fracture failure at the high strain rates. This is attributed to the higher DIF of concrete at high strain rates compared with steel (Malvar and Crawford, 1998; Malvar and Ross, 1998).

It can be stated that at low strain rate of 10^{-5} s^{-1} , the failure mode is influenced by the concrete compressive strength where pryout failure is observed in most of the anchors at shallow embedment depth of 76.2 mm. However, at high strain rate, the failure mode of the anchorage system transitioned to steel failure for all the concrete compressive strengths investigated. More severe concrete cracking was observed for the cast-in-place anchors embedded in 20 MPa concrete compressive strength than that embedded in 30 MPa and 40 MPa concrete compressive strengths at low strain rate of 10^{-5} s^{-1} . At high strain rate, it can be seen that the damage extends to a small area in the concrete where anchor bending followed by fracturing was observed.

4.2.10.2 Effect of strain rate and concrete compressive strength on shear behaviour

Shear behaviour of cast-in-place anchors was investigated using LS-DYNA finite element software. Three concrete compressive strengths of 20 MPa, 30 MPa and 40 MPa were selected for the analysis to investigate the effect of concrete strength on the shear response of cast-in-place anchors. Anchor diameters of 12.7 mm and 19.1 mm with embedment depths of 76.2 mm and 152.4 mm were investigated at low and high strain rates of 10^{-5} s^{-1} and 10^3 s^{-1} respectively. Figures 4-59 and 4-60 show the effect of concrete compressive strength on the load-displacement response of the 12.7-mm diameter cast-in-place anchor at strain rate of 10^{-5} s^{-1} with embedment depths of 76.2 mm and 152.4 mm respectively.

Effect of concrete compressive strength on the load displacement response of cast-in-place anchor of 19.1 mm diameter with 76.2 mm and 152.4 mm embedment depths at low strain rate of 10^{-5} s^{-1} is shown in Figures 4-61 and 4-62 respectively. As shown in the figures, the ultimate shear load of the cast-in-place anchors increased with the displacement until the maximum load then it decreased until failure. Concrete compressive strength of 40 MPa resulted in higher ultimate shear load compared to the concrete compressive strength of 20 MPa. Similar observation was reported by Çalışkan et al. (Çalışkan et al., 2013) on the adhesive anchors embedded in low strength concrete of 5 MPa and 10 MPa and subjected to cyclic shear load (Çalışkan et al., 2013). The increment in the ultimate shear load is found to be higher at the shallow embedment depth of 76.2 mm, where pryout failure is observed, compared to deeper embedment depth of 152.4 mm where the failure mode was by steel fracture. The increase in the embedment depth showed an increased shear capacity when the pryout failure mode is the dominant.

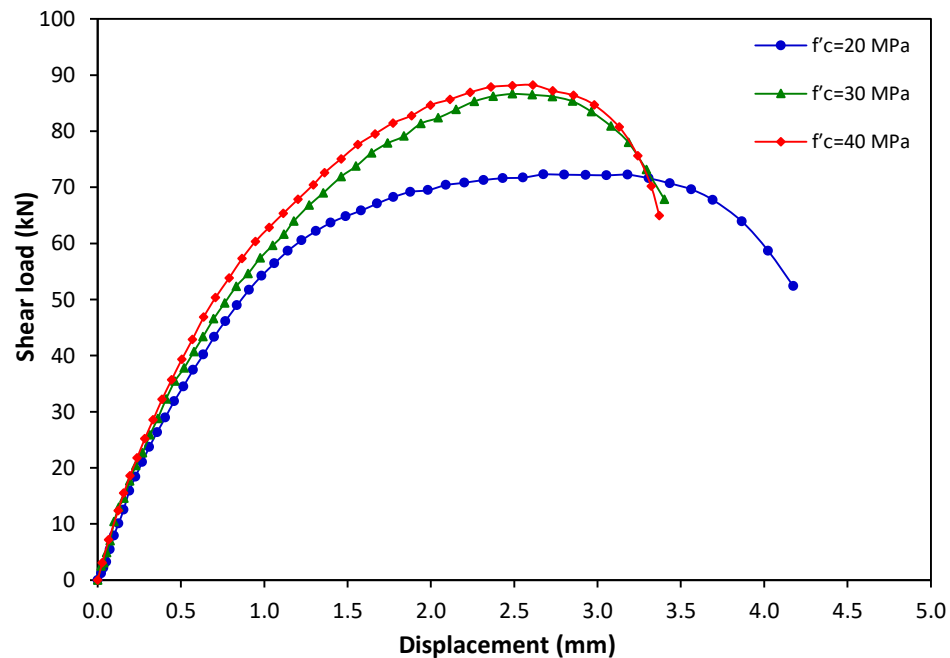


Figure 4-59: Shear load-displacement response of 12.7 mm cast-in-place anchor diameter with 76.2 mm embedment depth at strain rate of 10^{-5} s^{-1}

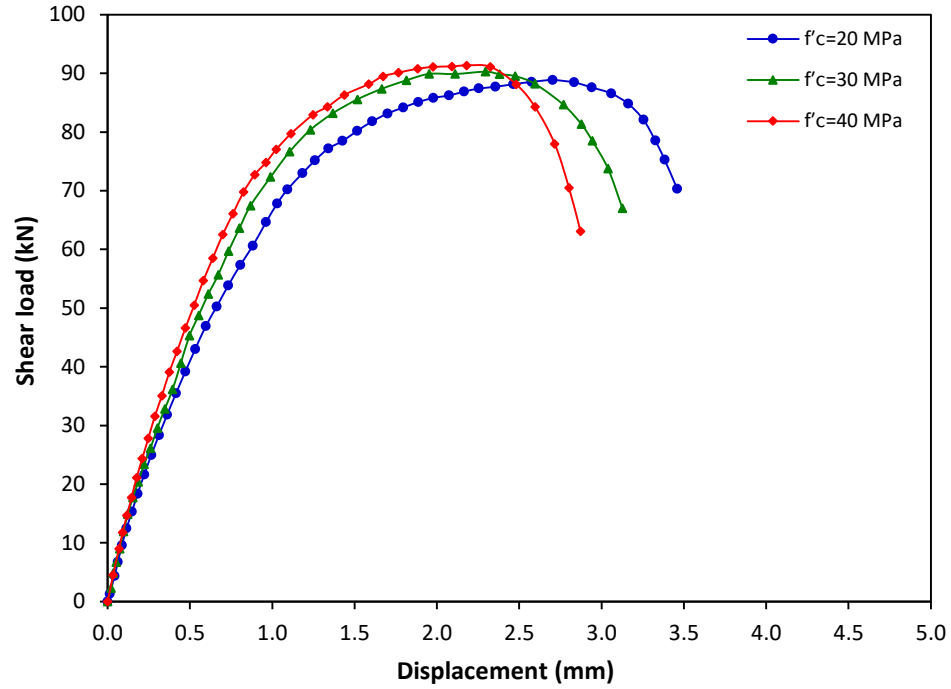


Figure 4-60: Shear load-displacement response of 12.7 mm cast-in-place anchor diameter with 152.4 mm embedment depth at strain rate of 10^{-5} s^{-1}

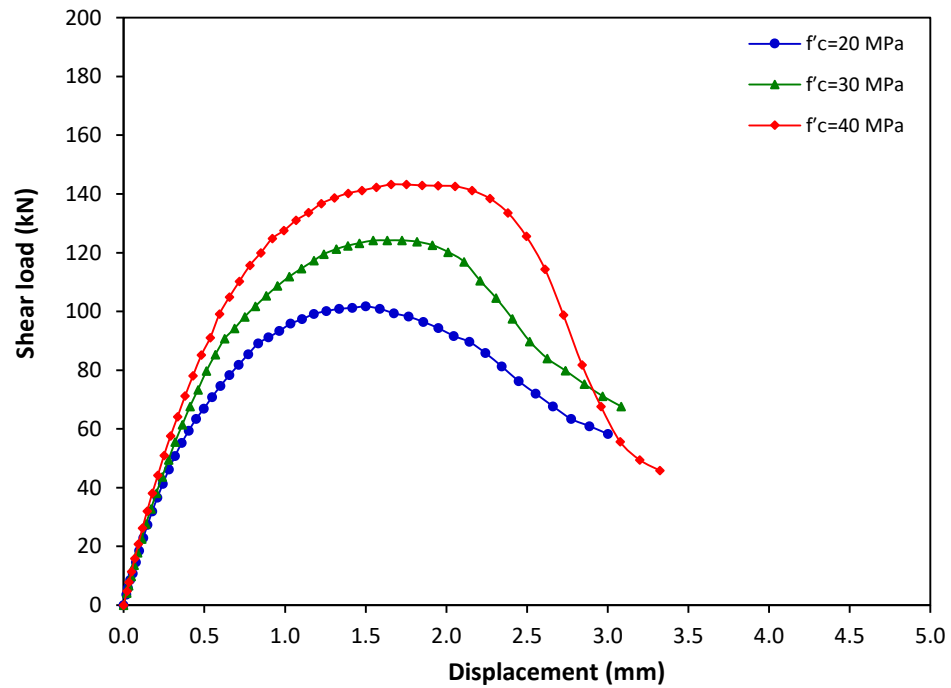


Figure 4-61: Shear load-displacement response of 19.1 mm cast-in-place anchor diameter with 76.2 mm embedment depth at strain rate of 10^{-5} s^{-1}

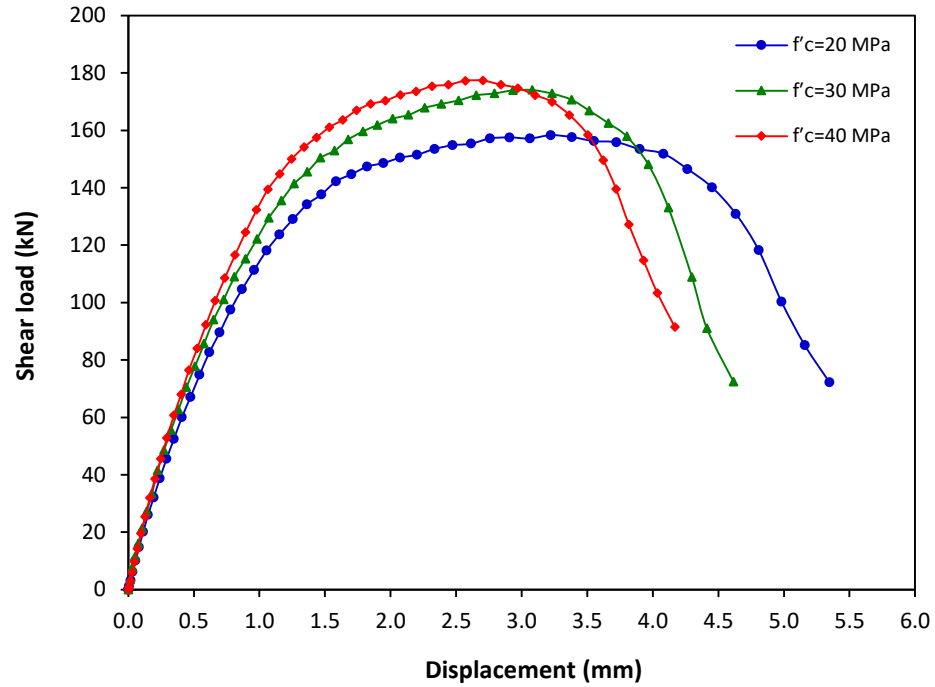


Figure 4-62: Shear load-displacement response of 19.1 mm cast-in-place anchor diameter with 152.4 mm embedment depth at strain rate of 10^{-5} s^{-1}

At high strain rate of 10^3 s^{-1} , the shear load increased with the displacement until the ultimate shear load, and then decreased with increased displacement until failure (Figures 4-63, 4-64, 4-65 and 4-66). The increase in the strain rate from 10^{-5} s^{-1} to 10^3 s^{-1} resulted in increased shear capacity of the cast-in-place anchorage systems.

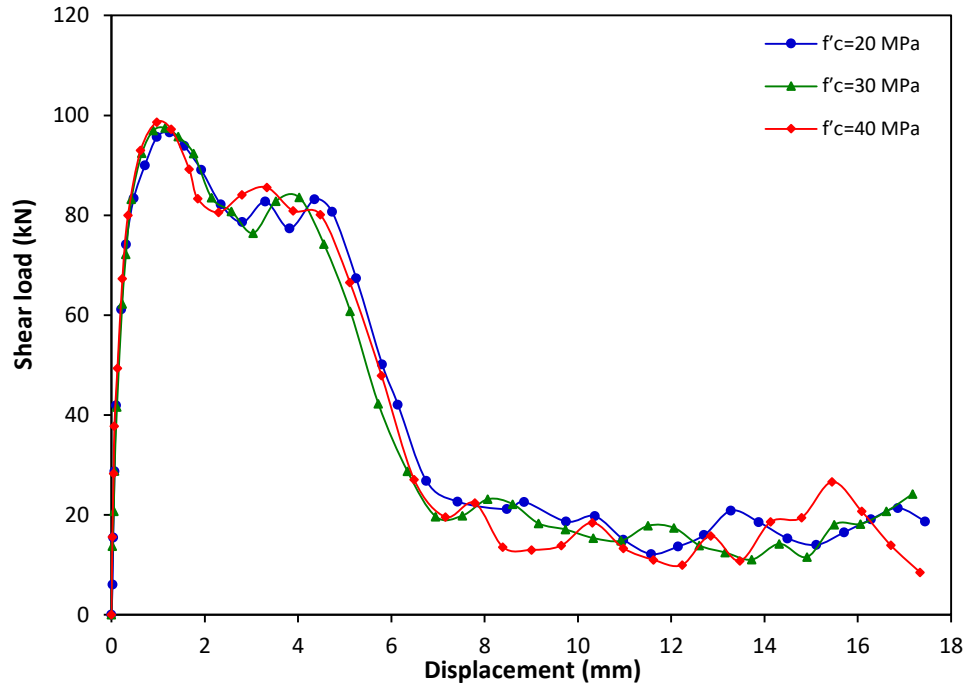


Figure 4-63: Shear load-displacement response of 12.7 mm cast-in-place anchor diameter with 76.2 mm embedment depth at strain rate of 10^3 s^{-1}

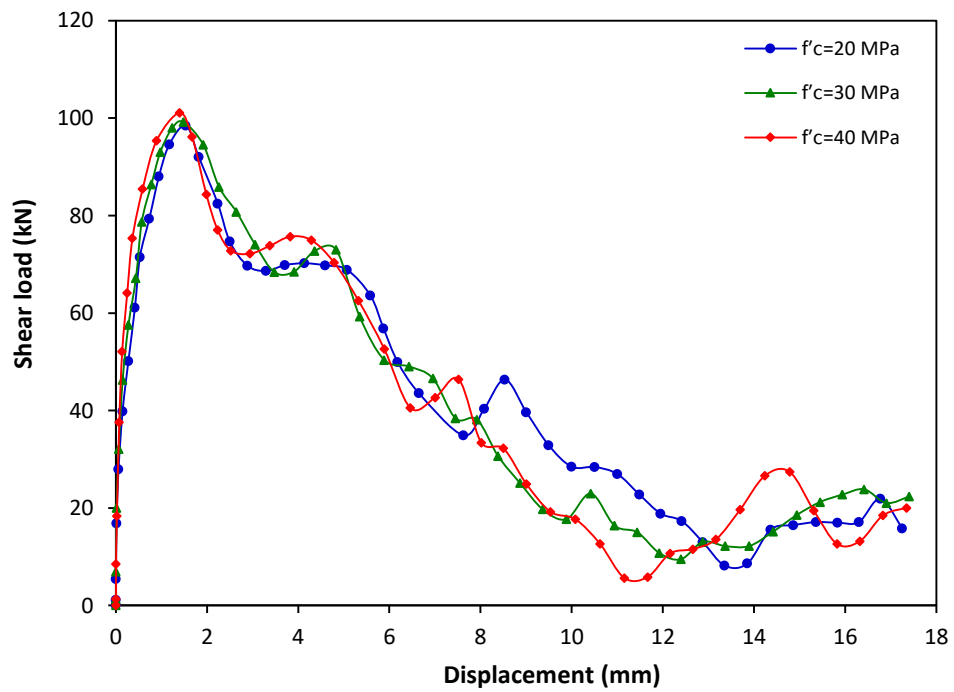


Figure 4-64: Shear load-displacement response of 12.7 mm cast-in-place anchor diameter with 152.4 mm embedment depth at strain rate of 10^3 s^{-1}

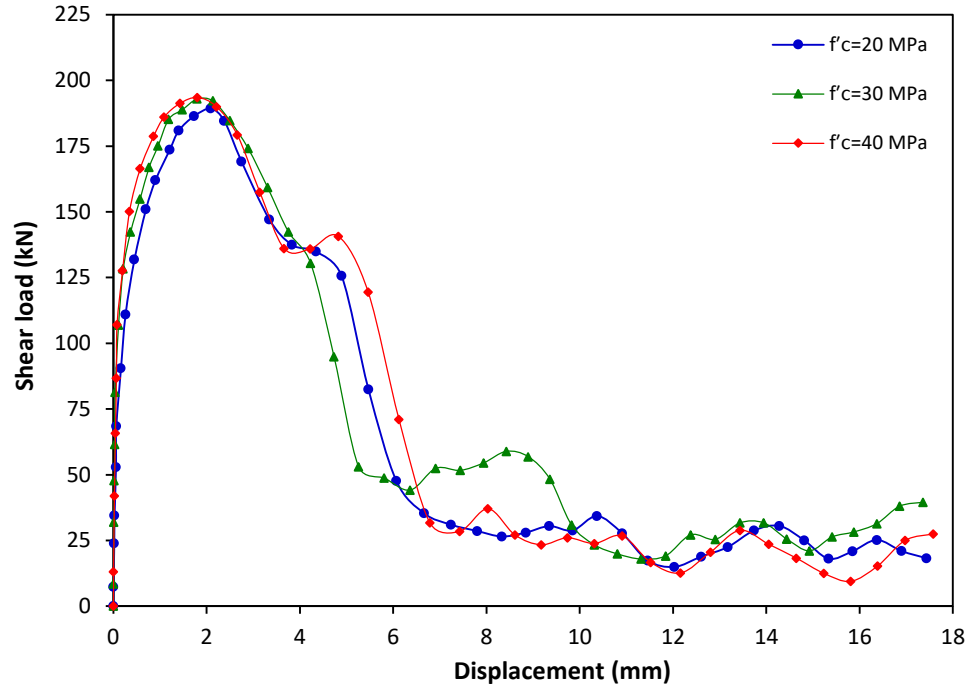


Figure 4-65: Shear load-displacement response of 19.1 mm diameter cast-in-place anchor with 76.2 mm embedment depth at strain rate of 10^3 s^{-1}

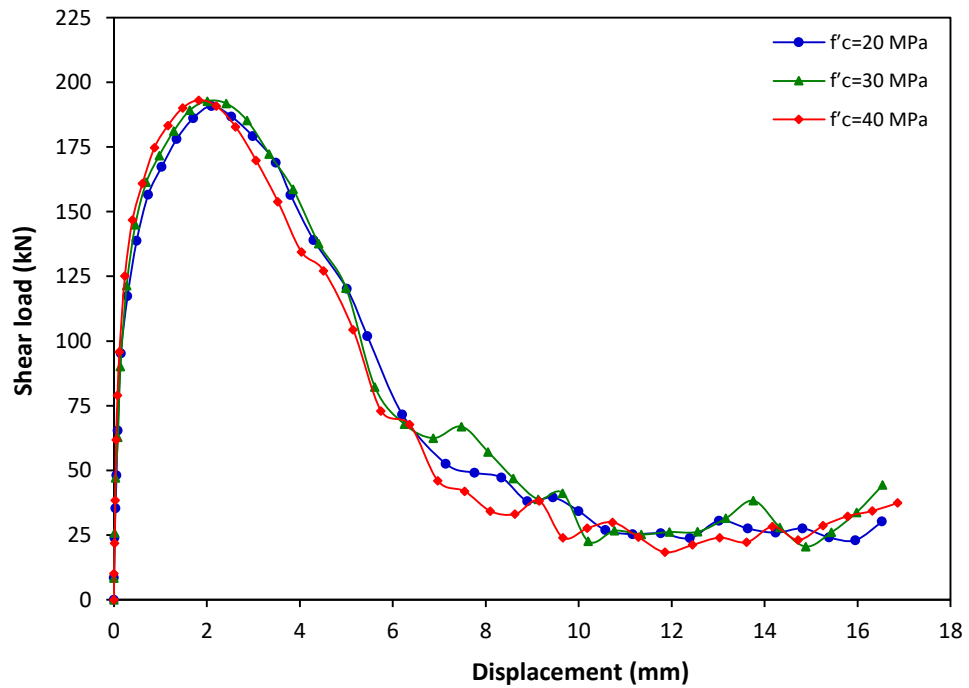


Figure 4-66: Shear load-displacement response of 19.1 mm cast-in-place anchor diameter with 152.4 mm embedment depth at strain rate of 10^3 s^{-1}

In general, it can be seen from Figures 4-59 to 4-66 that the increase in the anchor diameter from 12.7 mm to 19.1 mm increased the ultimate shear load for the cast-in-place anchors. Effect of concrete compressive strength is significant at low strain rate of 10^{-5} s^{-1} where pryout failure is observed while a slight (almost negligible) increase in the shear capacity is observed with the increase in the concrete compressive strength at the high strain rate of 10^3 s^{-1} . The increase in the shear load is attributed to increase concrete resistance to the applied shear load with the increase in the concrete compressive strength. Maximum increment in the ultimate shear load of 40.8% was obtained for the 19.1-mm diameter cast-in-place anchor at strain rate of 10^{-5} s^{-1} when the concrete compressive strength increased from 20 MPa to 40 MPa where pryout failure mode is observed. Maximum increment in the ultimate shear load of 2.7% is obtained at high strain rate of 10^3 s^{-1} when the concrete compressive strength increased from 20 MPa to 40 MPa where steel anchor failure is the dominant failure mode. At high strain rate the strength of concrete and steel materials increased. When steel failure occurs, the increment in the shear failure load is attributed to the increase in the steel strength at high strain rate rather than the increase in the concrete strength. Hence, the concrete compressive strength has a slight influence on the shear load at high strain rate.

4.3 Summary

This chapter introduces finite element analyses for the cast-in-place anchorage to concrete system models that were developed and presented in chapter three. Tensile and shear behaviour of the cast-in-place anchors at strain rates ranging from 10^{-5} s^{-1} to 10^3 s^{-1} were investigated. Different design parameters (anchor diameter and embedment depth) were

considered in the analyses. The chapter starts with validation of the cast-in-place anchor model with the experimental test data from the literature. Level of damage and failure mode for different strain rates was investigated. For the cast-in-place anchors subjected to tensile load; two types of failure modes were observed: concrete cone breakout failure and steel anchor failure. For the cast-in-place anchors subjected to shear load, two types of failure modes were observed; pryout and steel anchor failure. At high strain rate of 10^3 s^{-1} steel anchor failure was the dominant failure mode for all the cast-in-place anchors investigated. Concrete cone depth, concrete cone breakout diameter and concrete cone propagation angle were determined.

Tensile and shear load-displacement relations for the cast-in-place anchors at different strain rates were drawn and analyzed. The relation between the ultimate tensile load, strain rate and failure mode for different design parameters was introduced and discussed. Also, the relation between the ultimate shear load, strain rate and failure mode for different design parameters was introduced and discussed. Comparison has been made between the results obtained from the finite element analysis and the prediction analytical methods (ACI and CCD). Dynamic increase factor was determined for the cast-in-place anchors subjected to tensile and shear loads at all the strain rates investigated. Equations were developed to predict the relation between the strain rate and the DIF for the cast-in-place anchors under tensile and shear loads. Effect of strain rate on the concrete compressive strengths of 20 MPa, 30 MPa and 40 MPa for the cast-in-place anchors subjected to shear load was investigated. Plastic strain contours that represent the level of damage were drawn and discussed. Shear load-displacement relation for the cast-in-place anchors was drawn for the concrete compressive strengths investigated.

Chapter 5 : Strain rate effect on adhesive anchors

5.1 Finite element modelling for adhesive anchors under tensile load

Finite element models were developed using LS-DYNA software (LSTC, 2014) to investigate the tensile behaviour of adhesive anchors embedded into concrete at strain rates ranging from 10^{-5} s^{-1} to 10^3 s^{-1} . A single adhesive anchor was placed in the center of each concrete block to ensure that the edge distance was sufficient for concrete cone formation without edge effects. A biased mesh refinement towards the adhesive and anchor along the embedment depth was developed to improve the accuracy of the analysis and to minimize discretization error. A schematic view of the adhesive anchorage to concrete system is shown in Figure 5-1. Figure 5-2 shows the geometric configuration and boundary condition of the adhesive anchor model under tensile load.

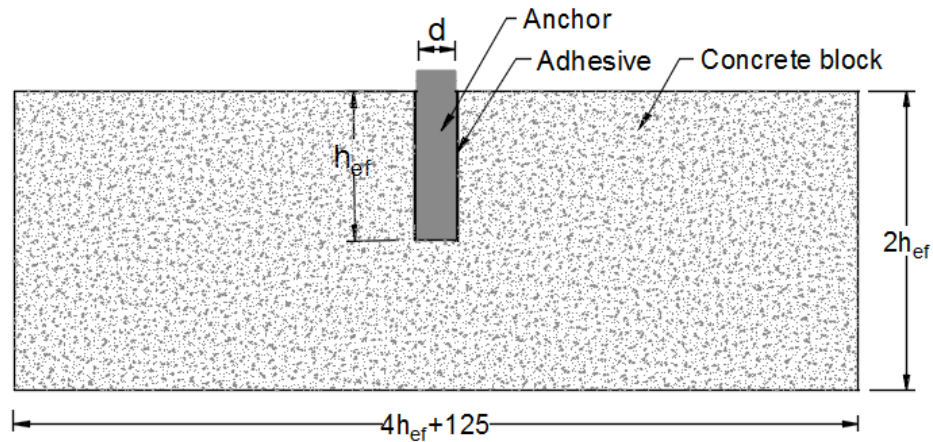


Figure 5-1: A schematic view of the adhesive anchorage to concrete system

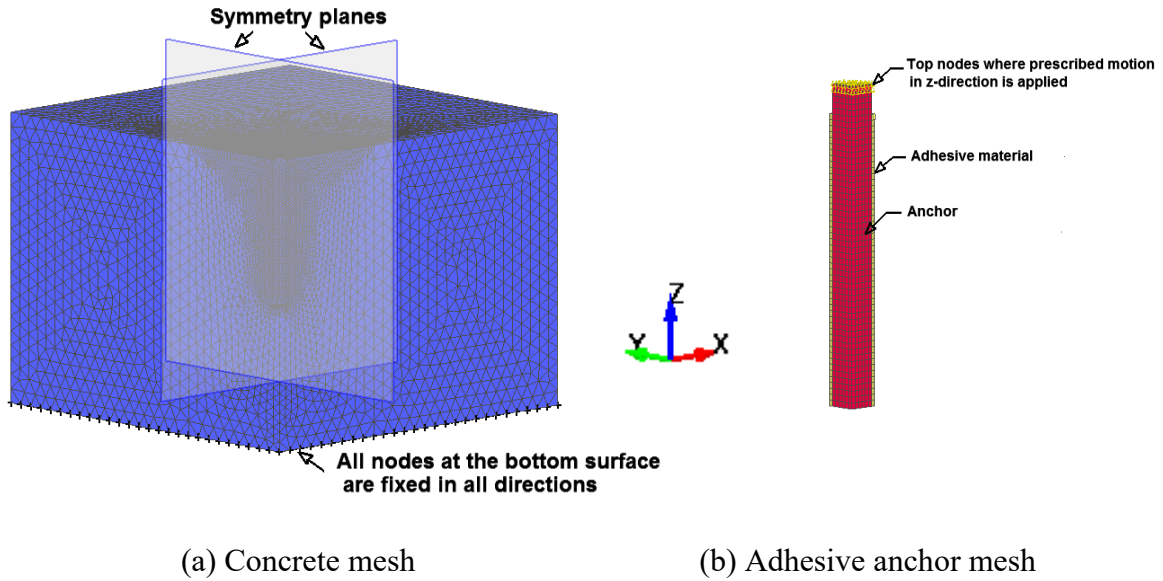


Figure 5-2: Geometric configuration with boundary condition for the adhesive anchor model

5.1.1 Validation of adhesive anchor model under tensile load

To ensure the material models chosen for the concrete, adhesive and steel elements are adequate for the research program, two finite element models of adhesive anchorage to concrete system representing drop-mass experimental program conducted by Braimah et al. (Braimah et al., 2004) were developed in LS-DYNA to validate the numerical model. The experimental test setup consisted of a 6.4-mm diameter steel anchor with embedment depth of 114 mm and 9.5-mm diameter anchor with embedment depth of 89 mm embedded into a 34.5 MPa compressive strength concrete. The 6.4-mm and 9.5-mm diameter adhesive anchors were modeled with yield strengths of 874 MPa and 1030 MPa respectively. The epoxy adhesive material was 1.5 mm thick with 30 MPa tensile strength, 23 MPa shear strength and 4900 MPa modulus of elasticity (Braimah et al., 2004). A mesh sensitivity analysis was carried out to achieve an optimum mesh size that resulted in high accuracy in comparison with experimental results and minimized computational effort. The

drop mass impact effect on the anchor was not modeled in the analysis. The experimental displacement profile from a drop-mass test was applied to the steel anchor in the numerical model by using BOUNDARY_PRESCRIBED_MOTION_SET in order to apply the tensile load. Mesh sizes of $0.75 \times 0.75 \times 3$ mm, $0.75 \times 0.75 \times 1$ mm, $0.75 \times 0.5 \times 1$ mm and $0.5 \times 0.5 \times 1$ mm were investigated. For the anchor diameter of 6.4 mm, mesh sizes of $0.75 \times 0.5 \times 1$ mm and $0.5 \times 0.5 \times 1$ mm give a percentage difference of 3.7% and 3.3% in the ultimate tensile load respectively compared to the experimental results. Less computational time is obtained using mesh size of $0.75 \times 0.5 \times 1$ mm than that obtained using mesh size of $0.5 \times 0.5 \times 1$ mm and hence was selected for the analysis. Table 5-1 shows the results of the mesh sensitivity analysis for the adhesive anchor models.

Table 5-1: Effect of mesh size refinement on the convergence of ultimate tensile load for adhesive anchor

Model No.	d (mm)	Mesh size (mm)				Ultimate tensile load (kN)		Displacement (mm)		Failure mode
		Anchor	Adhesive	Concrete		FEA	EXP.	FEA	EXP.	
				Min.	Max.					
1	6.4	0.75	0.75	3	8	29.50	34.37	0.83	0.99	Steel failure
2		0.75	0.75	1	8	32.11		0.86		Steel failure
3		0.75	0.50	1	8	33.14		0.89		Steel failure
4		0.50	0.50	1	8	33.28		0.89		Steel failure
5	9.5	0.75	0.75	3	8	69.55	74.53	0.93	0.80	Concrete cone
6		0.75	0.75	1	8	72.14		0.91		Concrete cone
7		0.75	0.50	1	8	76.71		0.88		Concrete cone
8		0.50	0.50	1	8	76.71		0.85		Concrete cone

For the anchor diameter of 9.5 mm, mesh sizes of 0.75 mm for the steel anchor, 0.5 mm for the adhesive and biased 1 to 8 mm for the concrete yielded converged results to the experimental results obtained by Braimah et al. (Braimah et al., 2004) (Table 5-1). Further decreasing the mesh size of the steel anchor to 0.5 mm did not result in better results however the computational time increased significantly. Hence mesh size of $0.75 \times 0.5 \times 1$ was selected for the analysis Figure 5-3 presents a comparison of load-displacement response of the experimental tests and the finite element analysis results for the 6.4-mm diameter adhesive anchor. The figure shows that as the mesh sizes decrease the load-displacement response approaches the experimental. The tensile load-displacement response was almost linear up to the peak load followed by a sharp drop in the load. Load fluctuation about the residual tensile load was observed. The load fluctuation can be attributed to the pullout of the anchor to a small displacement associated with concrete cracking in a small area around the anchor followed by steel anchor failure. The results obtained from the finite element analysis were in good agreement with the experimental results with the same failure mode (steel anchor failure) as shown in Figure 5-4.

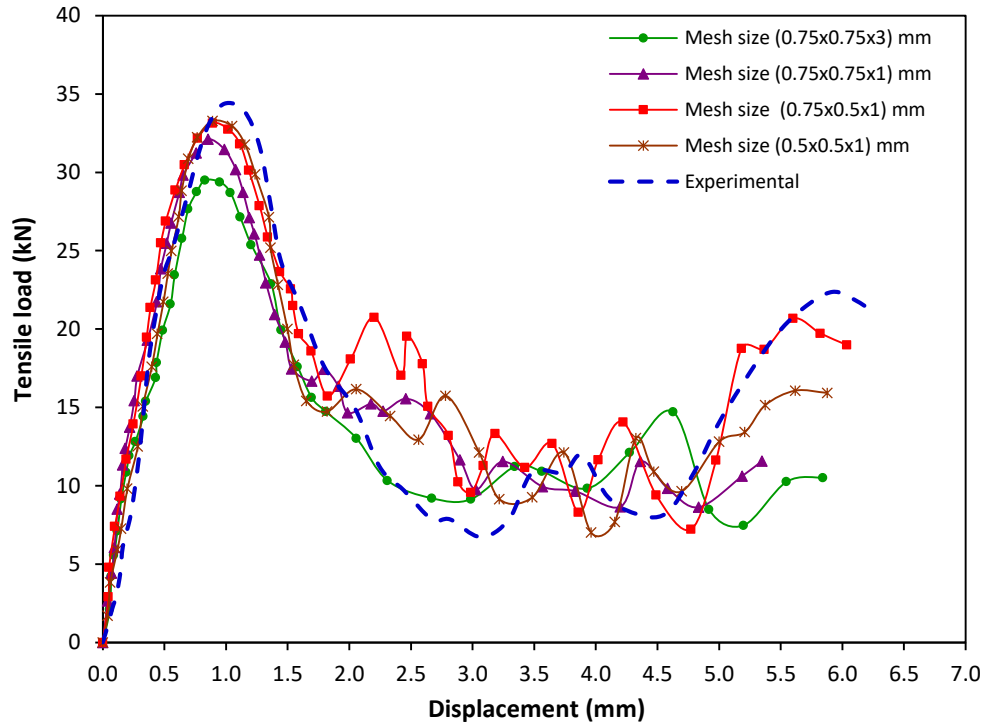


Figure 5-3: Comparison of tensile load-displacement response between FEA and experimental results obtained by Braimah et al. (Braimah et al., 2004) for anchor diameter of 6.4 mm

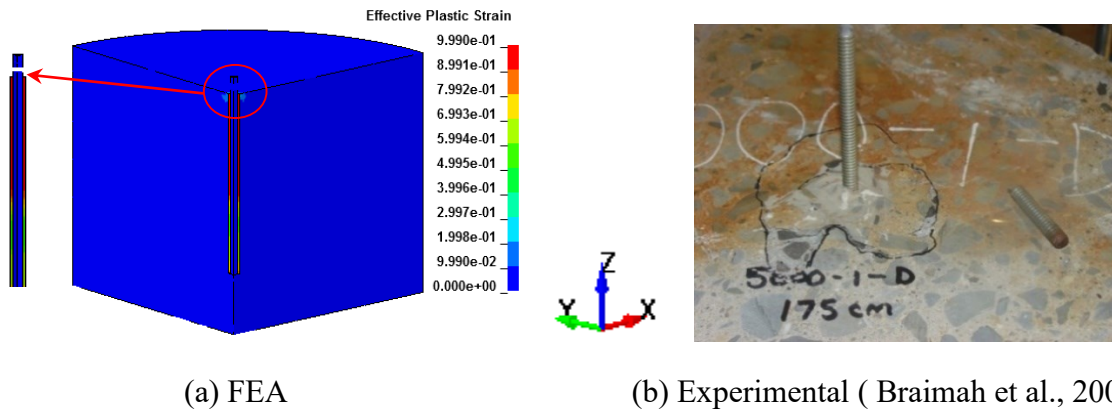


Figure 5-4: Failure mode obtained from the finite element analysis and the experimental results obtained by Braimah et al. (Braimah et al., 2004)

Figure 5-5 presents a comparison of load-displacement response of the experimental tests and the finite element analysis results for the 9.5-mm diameter adhesive anchor. A good agreement is obtained between the finite element analyses using mesh size of Model No. 7

and the experimental results. Shallow concrete cone breakout failure was observed similar to that obtained from the experimental results.

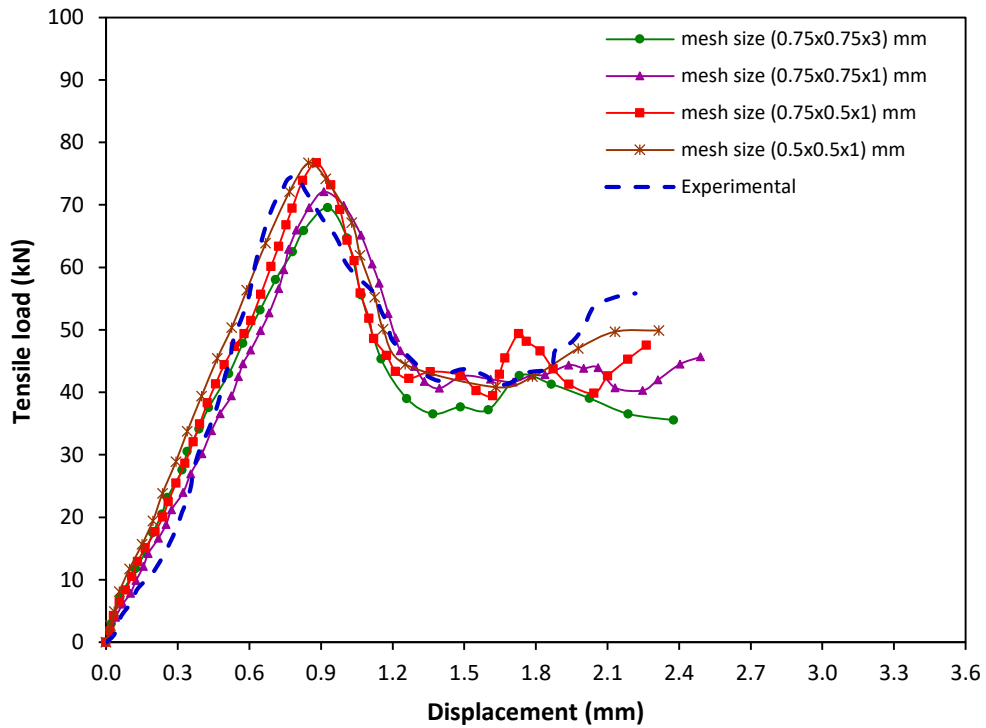


Figure 5-5: Comparison of tensile load-displacement response between FEA and experimental results obtained by Braimah et al. (Braimah et al., 2004) for anchor diameter of 9.5 mm

After the adhesive anchor system was validated against the experimental results, the appropriate mesh size for the concrete, adhesive and steel anchor together with material models were used in a parametric analysis to investigate the effect of various design parameters (anchor diameter and embedment depth) on the capacity of the adhesive anchorage system when subjected to strain rates ranging from the static strain rate of 10^{-5} s^{-1} to higher strain rate of 10^3 s^{-1} . The results of the investigation are presented and discussed in the following sections.

5.1.2 Comparison of finite element results with ACI and CCD design methods

Ultimate tensile loads of the adhesive anchors obtained from the finite element analysis (FEA) at the static strain rate of 10^{-5} s^{-1} were compared with the ACI design method (ACI 349-85) and CCD method as shown in Table 5-2. According to the ACI method (Fuchs et al., 1995), the ultimate tensile load of post-installed anchors failing by the concrete cone breakout failure mode can be determined by Equation (4.1). For the steel anchor failure, the ultimate tensile load can be determined using Equation (4.2). Hole diameters of 14.7 mm, 18 mm, and 22 mm were used for the 12.7-mm, 15.9-mm and 19.1-mm diameter adhesive anchors respectively. According to CCD design method (Committee Euro-International du Beton (CEB), 1994; Fuchs et al., 1995), the ultimate tensile load of anchors can be determined using Equation (4.3). Minimum value of the ultimate tensile load obtained from Equations (4.1) and (4.2) is considered for comparison of ACI method with the FEA results. Also, minimum value of ultimate tensile load obtained from Equations (4.2) and (4.3) is considered for comparison of CCD method with the FEA results and included in Table 5-2.

Table 5-2: Comparison of ultimate tensile loads obtained from FEA with ACI and CCD methods

d (mm)	h _{ef} (mm)	Ultimate tensile load (kN)			FEA/ACI	FEA/CCD	*Failure mode (FEA)
		ACI	CCD	FEA			
12.7	76.2	40.45	54.62	57.12	1.41	1.05	CC
	101.6	69.00	84.10	80.45	1.17	0.96	CC
	127.0	105.09	117.53	95.72	0.91	0.81	S
	152.4	130.98	130.98	96.79	0.74	0.74	S
15.9	76.2	41.92	54.62	65.69	1.57	1.20	CC

	101.6	70.96	84.10	87.31	1.23	1.04	CC
	127.0	107.53	117.53	126.18	1.17	1.07	CCB
	152.4	151.64	154.49	159.72	1.05	1.03	S
19.1	76.2	43.70	54.62	69.62	1.59	1.27	CC
	101.6	73.33	84.10	105.49	1.44	1.25	CC
	127.0	110.50	117.53	157.28	1.42	1.34	CC
	152.4	155.20	154.49	179.40	1.16	1.16	CC

*Failure mode: CC=concrete cone breakout, CCB=combined cone bond, S=steel failure

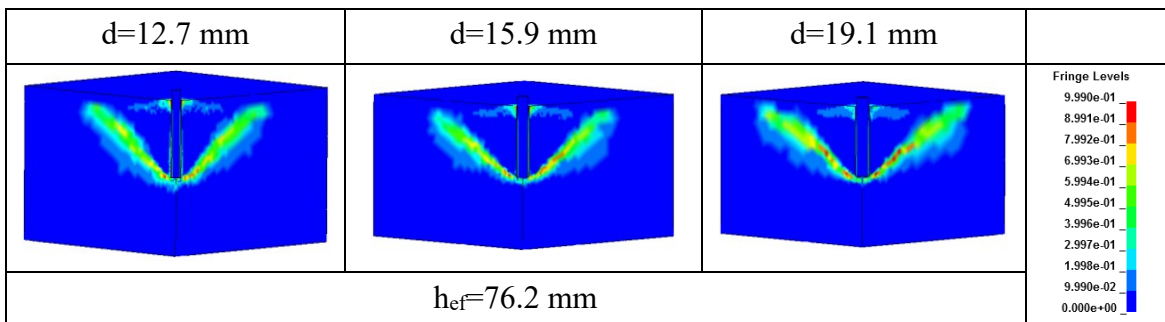
It can be observed from Table 5-2 that the ACI and CCD methods underpredict the ultimate tensile load in comparison with the FEA results for most of the adhesive anchors as the design methods incorporate more conservatism than the FEA. However, the CCD method gives a better agreement with the finite element results. Fuchs et al. (1995) found that the CCD method agree well with the experimental results in comparison to ACI method (Fuchs et al., 1995). This is attributed to the ACI method disregard the size effect (Fuchs et al., 1995). Same material properties were used for the finite element analysis and the design codes. However, in the finite element analysis assumptions such as materials model, boundary conditions and contact formulation, were considered to develop the numerical model for the adhesive anchorage to concrete system. These assumptions may have an influence on the variation between the FEA results and the design methods results.

5.1.3 Effect of strain rate on the level of damage and failure mode of adhesive anchors

Contours of effective plastic strain for adhesive anchor diameters of 12.7-mm, 15.9-mm and 19.1-mm with embedment depths of 76.2 mm, 101.6 mm, 127 mm and 152.4 mm at the static strain rate of 10^{-5} s^{-1} are shown in Figure 5-6. The crack patterns are presented

with the plastic strain contour fringe plots in the figure. As shown in the figure, concrete cone breakout failure was observed at low strain rate of 10^{-5} s^{-1} for most of the adhesive anchors investigated. Cracking started to appear on the top surface of the concrete around the anchor and subsequently the cracks generated at the bottom of the anchor propagated diagonally forming concrete cone and leading to failure of the anchorage system. Also, it can be seen that the level of concrete damage increased with the increase in the anchor diameter from 12.7 mm to 19.1 mm for the same embedment depth. The increase in the anchor diameter increases the pullout load. As the anchor diameter increase the contact area between the anchor and the adhesive and between the adhesive and the concrete increases leading to increase the friction resistance (Wang et al., 2015; Wang et al., 2017).

Combined cone bond failure was observed for the 15.9-mm diameter anchor at embedment depth of 127 mm; wherein a shallow cone was observed at the top of the concrete accompanied by adhesive bond failure at the remaining part of the embedment depth below the shallow concrete cone. Steel anchor failure was observed for the 12.7-mm diameter adhesive anchor at embedment depths of 127 mm and 152.4 mm. Also, steel anchor failure was observed for the 15.9-mm diameter anchor at embedment depth of 152.4 mm.



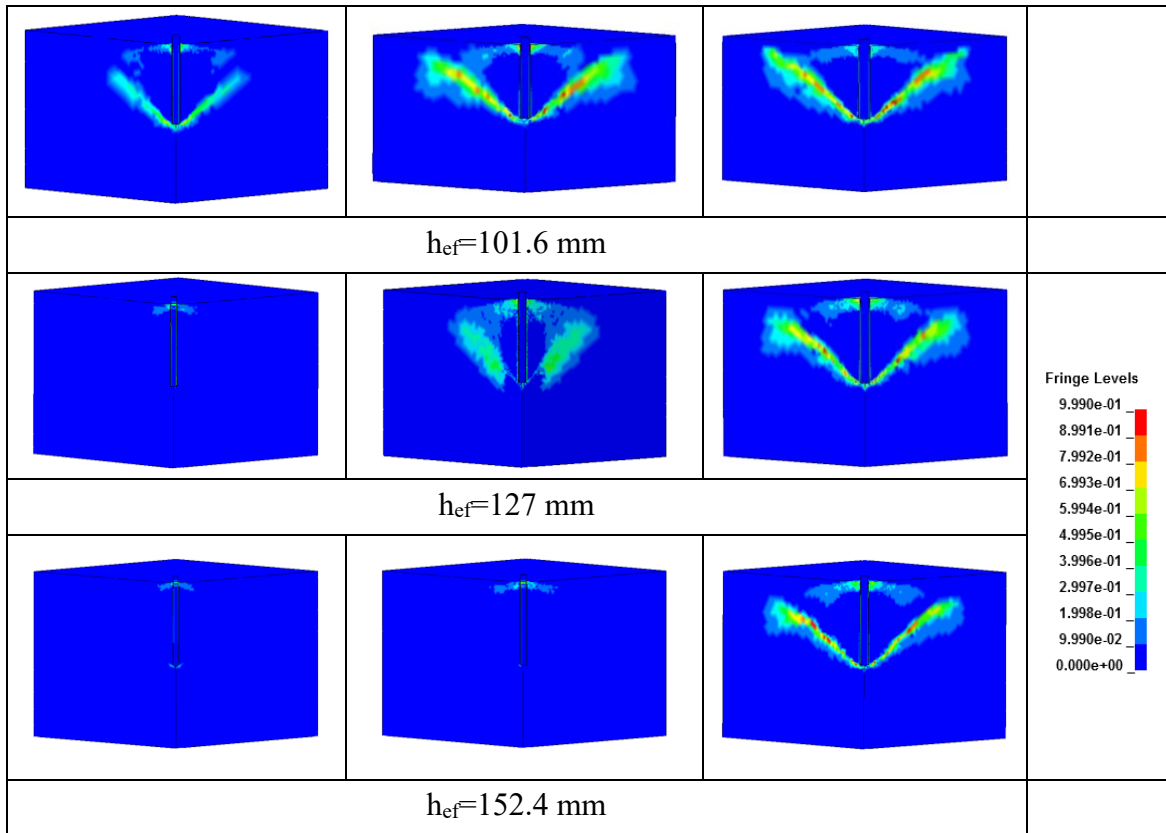


Figure 5-6: Plastic strain contours for adhesive anchor with different anchor diameters and embedment depths at strain rate of 10^{-5} s^{-1}

Table 5-3 shows the concrete cone breakout diameter (d_{cone}), cone breakout angle (θ_a) and corresponding failure mode of the adhesive anchor under tensile load. The increase in the embedment depth resulted in increase in the concrete cone diameter. The concrete cone breakout diameter for the 12.7-mm diameter adhesive anchor increases from 225 mm at embedment depth of 76.2 mm to 268 mm at embedment depth of 101.6 mm. Similarly, the concrete cone breakout diameter for the 15.9-mm anchor increased from 236 mm at embedment depth of 76.2 mm to 291 mm at embedment depth of 101.6 mm. Further increase in the anchor embedment depth resulted in steel anchor failure of the 12.7-mm diameter adhesive anchor and combined concrete cone bond failure for 15.9-mm diameter adhesive anchor, as shown in Figure 5-6. The increase in the concrete cone breakout

diameter was from 244 mm to 421 mm for the 19.1-mm diameter adhesive anchor for the increase in the embedment depth from 76.2 mm to 152.4 mm.

Concrete cone breakout angle was determined by measuring the angle of inclination of the failure surface. Figure 5-7 shows a sketch of the concrete cone breakout angle. As shown in Table 5-3, the concrete cone breakout angle (θ_a) varies between 32° and 35° for all anchors investigated. The average concrete cone angle was 33.5° mm. Crack propagation angle of 56.5° was obtained where the crack propagation angle is equal to $(90-\theta_a)$. According to ACI and CCD design methods, the concrete cone angle is 45° and 35° respectively. The concrete cone angle obtained from the finite element analysis is approximately comparable to the concrete cone breakout angle of the CCD method. The concrete cone angle has an influence on the ultimate tensile load where the decrease in the concrete cone angle increases the concrete cone area and hence increased ultimate tensile load.

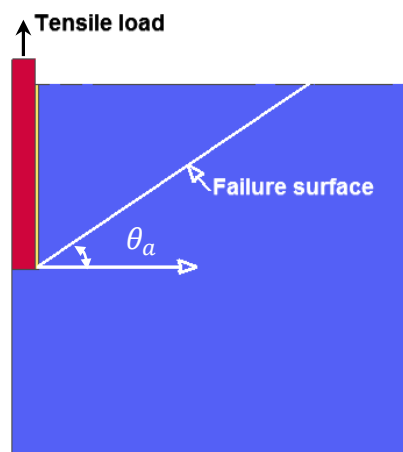


Figure 5-7: Cone breakout angle on the adhesive anchorage to concrete system.

Table 5-3: Concrete cone diameter and cone breakout angle for the adhesive anchor

h_{ef} (mm)	d (mm)	d_{cone} (mm)	θ_a (deg)	Failure mode
76.2	12.7	225	33	CC
	15.9	236	33	CC
	19.1	244	35	CC
101.6	12.7	268	34	CC
	15.9	291	34	CC
	19.1	295	33	CC
127.0	12.7	-	-	S
	15.9	-	-	CCB
	19.1	370	34	CC
152.4	12.7	-	-	S
	15.9	-	-	S
	19.1	421	32	CC

Figures 5-8, 5-9 and 5-10 show the failure mode of 12.7-mm, 15.9-mm and 19.1-mm diameter adhesive anchors at strain rates ranging from 10^{-3} s^{-1} to 10^3 s^{-1} . As shown in Figure 5-8 for the 12.7-mm diameter adhesive anchor, combined cone bond failure was observed for the 76.2 mm and 101.6 mm embedment depths at strain rates of 10^{-3} s^{-1} to 10^2 s^{-1} . Steel anchor failure was observed for the 127 mm and 152.4 mm embedment depths at all the strain rates investigated. As shown in Figure 5-9 for the 15.9-mm diameter adhesive anchor, combined cone bond failure was observed at embedment depths of 76.2 mm, 101.6 mm and 127 mm at strain rates of 10^{-3} s^{-1} to 10^2 s^{-1} ; whereas steel anchor failure was observed at embedment depth of 152.4 mm at strain rates ranging from 10^{-3} s^{-1} to 10^3 s^{-1} . Also, steel anchor failure was observed at strain rate of 10^3 s^{-1} for the embedment depths of 76.2 mm and 101.6 mm. As shown in Figure 5-10 for the 19.1-mm diameter adhesive

anchor at embedment depth of 76.2 mm, concrete cone breakout failure is observed at strain rate of 10^{-3} s^{-1} . The increase in the strain rate to 10^2 s^{-1} resulted in combined cone-bond failure. For the anchor embedment depths of 101.6 mm, 127 mm and 152.4 mm, combined cone-bond failure mode was observed at strain rates of 10^{-3} s^{-1} to 10^2 s^{-1} . At high strain rate of 10^3 s^{-1} steel anchor failure was observed for all the anchor diameters and embedment depths investigated.

It is clear from Figures 5-8, 5-9 and 5-10 that the strain rate has an influence on the failure mode. The failure mode is observed to transition from concrete cone or combined cone-bond failure mode to steel anchor failure mode with increase in strain rate. This behaviour can be attributed to the increase in concrete and steel capacity with increase in strain rate. The increase in the tensile capacity of the concrete is higher than the increase in the steel capacity (Malvar & Crawford, 1998; Malvar & Ross, 1998). Hence, the concrete resistance to the tensile load at high strain rate increase resulted in steel anchor failure.

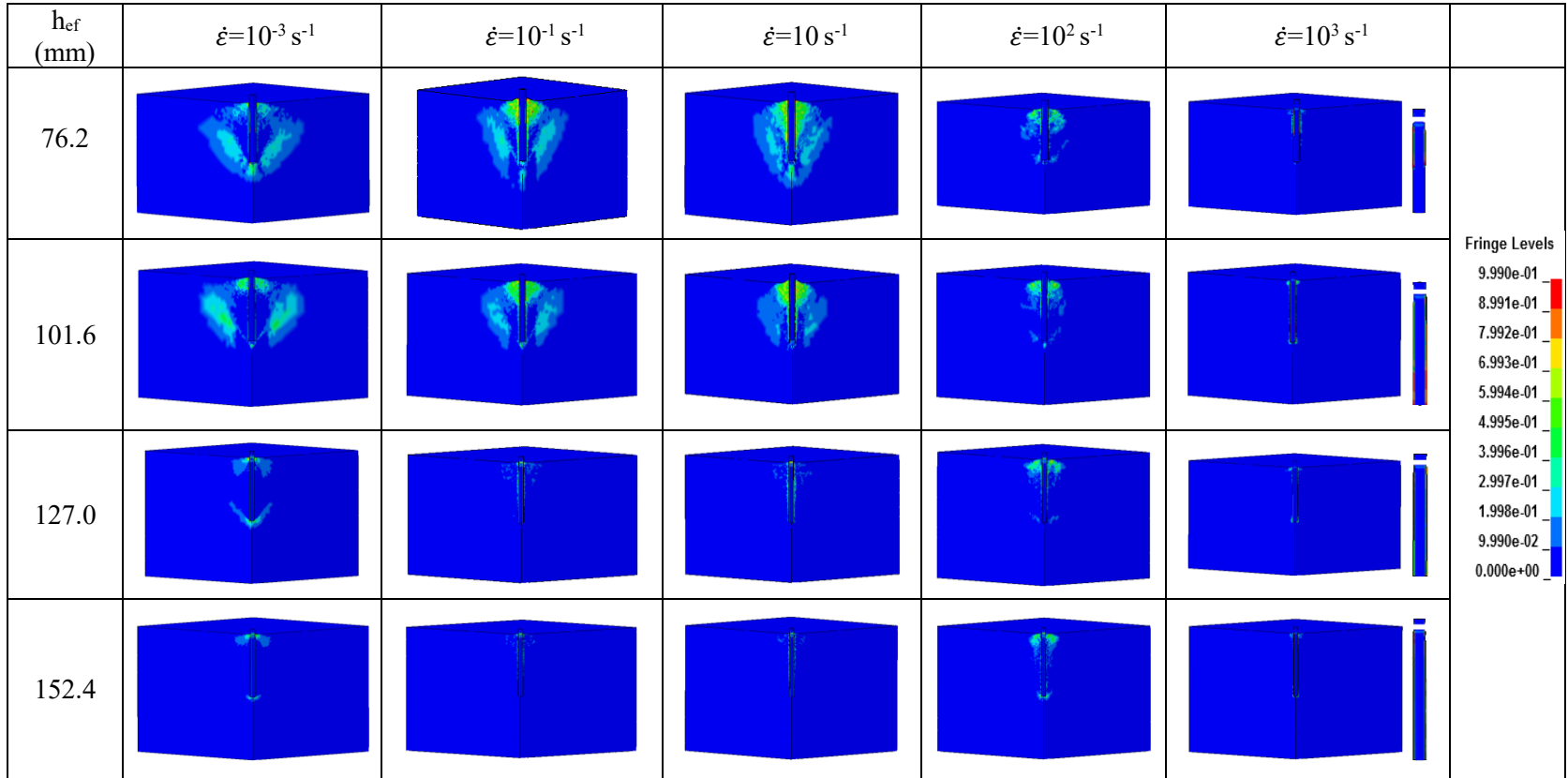


Figure 5-8: Failure mode of 12.7-mm diameter adhesive anchor at different strain rates

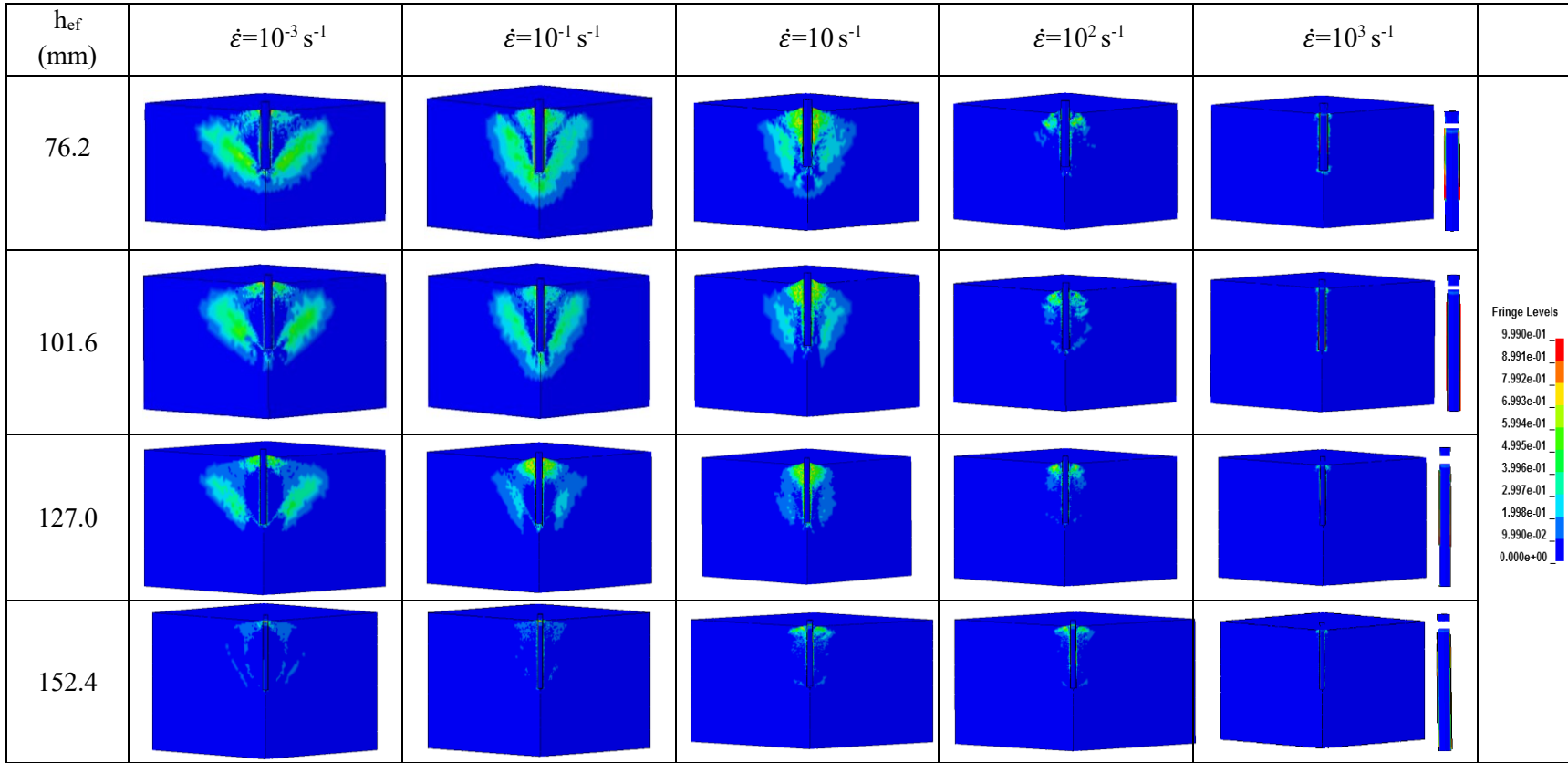


Figure 5-9: Failure mode of 15.9-mm diameter adhesive anchor at different strain rates

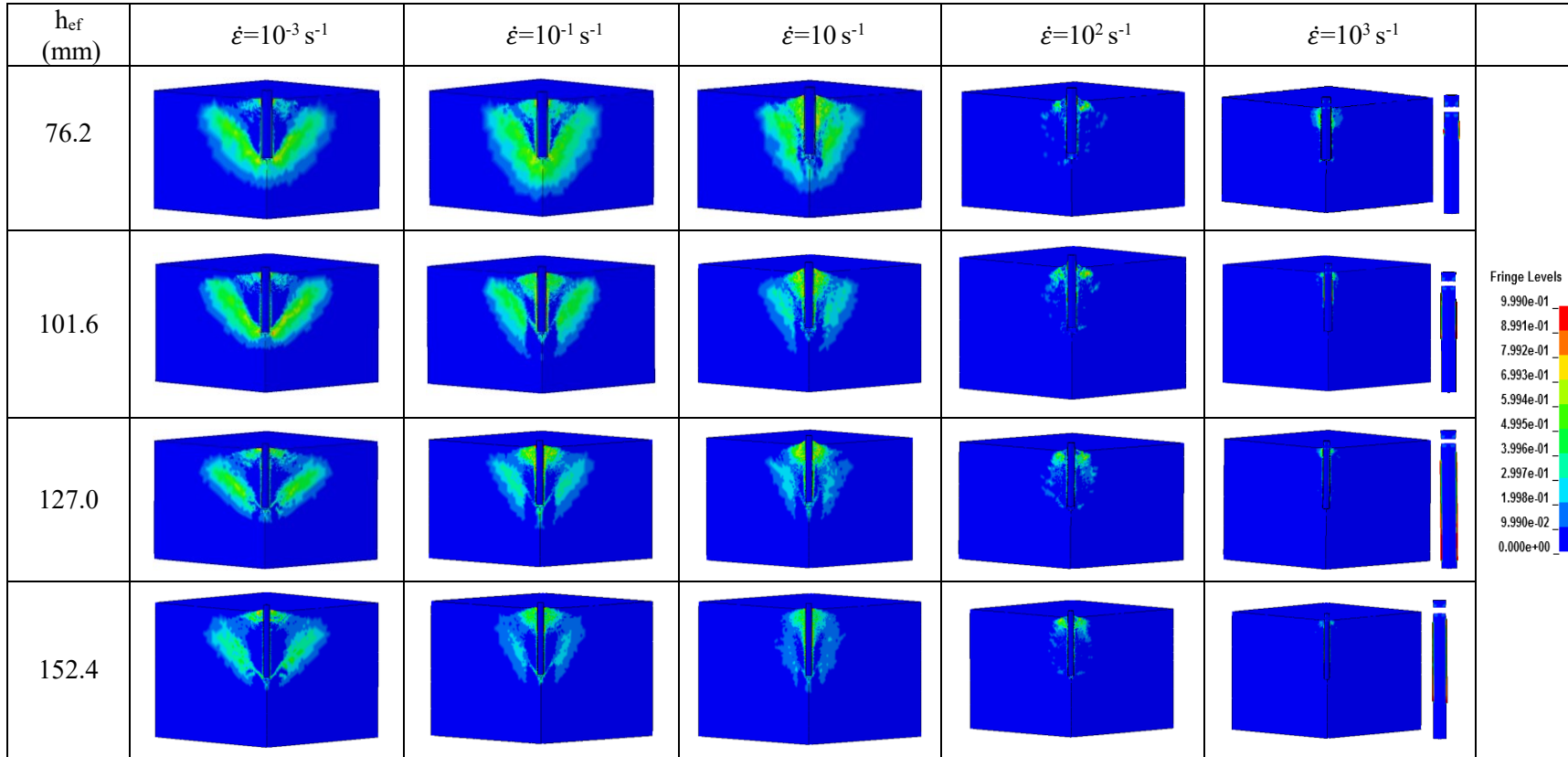


Figure 5-10: Failure mode of 19.1-mm diameter adhesive anchor at different strain rates

5.1.4 Effect of design parameters on failure mode and ultimate tensile load

Figures 5-11, 5-12 and 5-13 show the effect of strain rate on the failure mode and ultimate tensile load for the adhesive anchor. As shown in Figure 5-11 the tensile load increased from 57.1 kN to 107.2 kN and 80.5 kN to 107.9 kN for the anchor embedment depths of 76.2 mm and 101.6 mm respectively, where the failure mode transitioned from concrete cone breakout at strain rate of 10^{-5} s^{-1} to combined cone bond failure at strain rates up to 10^2 s^{-1} and steel anchor failure at strain rate of 10^3 s^{-1} . The ultimate tensile load increased 13.3% and 12.5% for the embedment depths of 127 mm and 152.4 mm respectively as the strain rate increased from 10^{-5} s^{-1} to 10^3 s^{-1} mm where steel anchor failure is the dominant failure mode at all the strain rates.

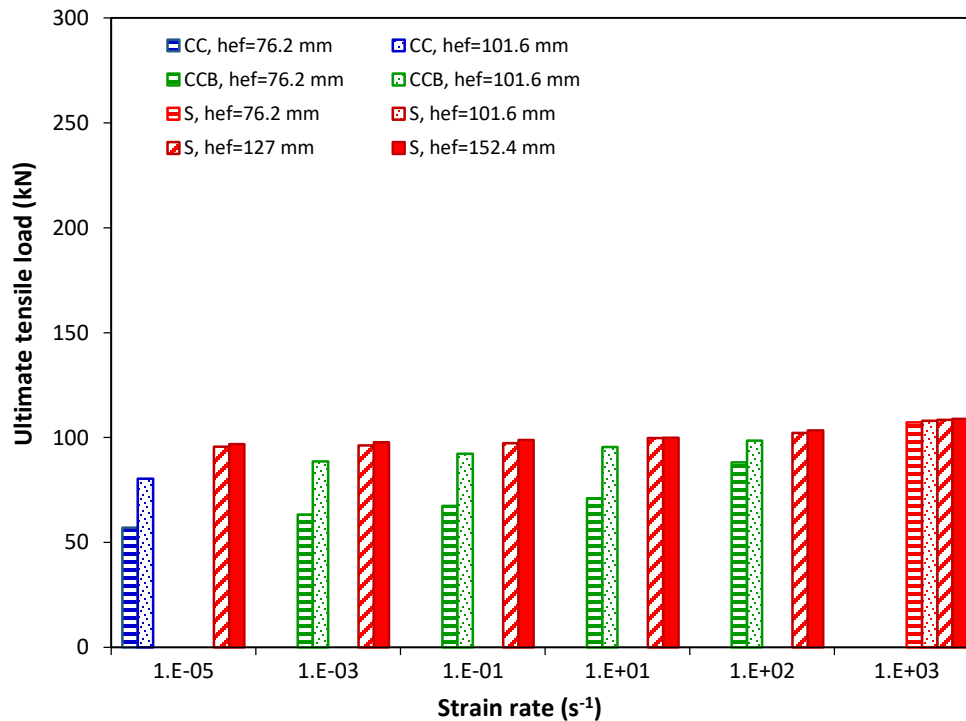


Figure 5-11: Strain rate effect on the failure mode and ultimate tensile load for adhesive anchor diameter of 12.7 mm

As shown in Figure 5-12, the ultimate tensile load increased with the increase in the strain rate. For the embedment depths of 76.2 mm and 101.6 mm, the failure mode transitioned from concrete cone breakout at strain rate of 10^{-5} s^{-1} to combined cone bond failure at strain rates up to 10^2 s^{-1} and steel anchor failure at strain rate of 10^3 s^{-1} . For anchor embedment depth of 127 mm, the failure mode transitioned from combined cone bond failure at strain rates up to 10^2 s^{-1} to steel anchor failure at strain rate of 10^3 s^{-1} . For anchor embedment depth of 152.4 mm, the ultimate tensile load increased 11.8% where steel anchor failure was observed at all strain rates investigated.

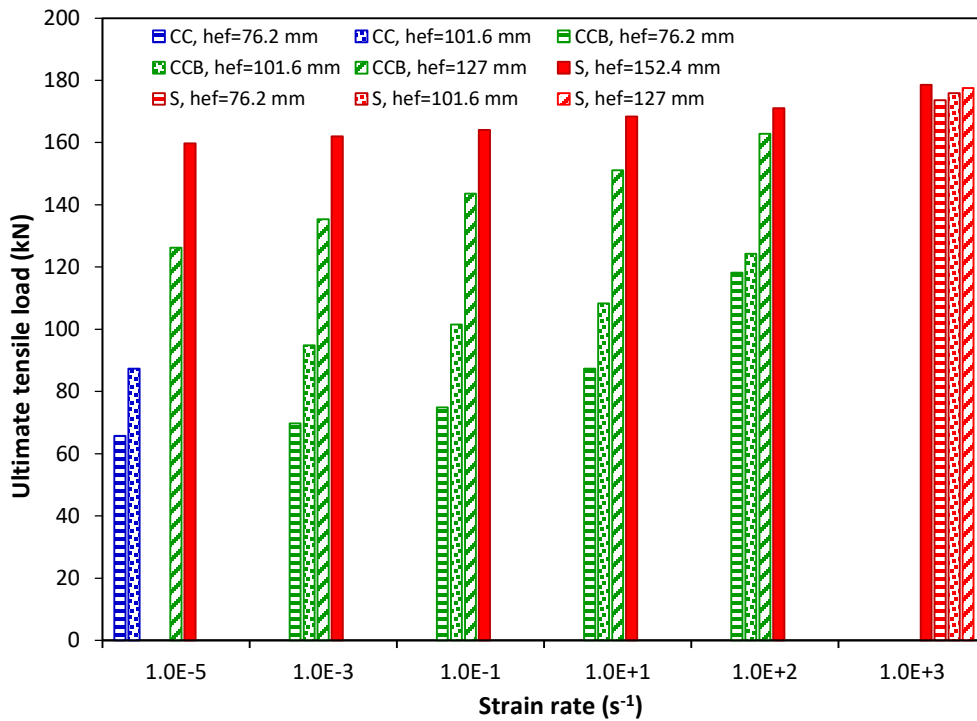


Figure 5-12: Strain rate effect on the failure mode and ultimate tensile load for adhesive anchor diameter of 15.9 mm

As shown in Figure 5-13, the ultimate tensile load increased with the increase in the strain rates for all the embedment depths investigated. For the 76.2 mm, 101.6 mm, 127 mm and

152.4 mm embedment depths, the failure mode transitioned from concrete cone breakout at strain rate of 10^{-5} s^{-1} to combined cone bond at strain rates up to 10^2 s^{-1} and then to steel anchor failure at strain rate of 10^3 s^{-1} . For the adhesive anchor of 76.2 mm embedment depth concrete cone breakout failure was observed at strain rate of 10^{-3} s^{-1} .

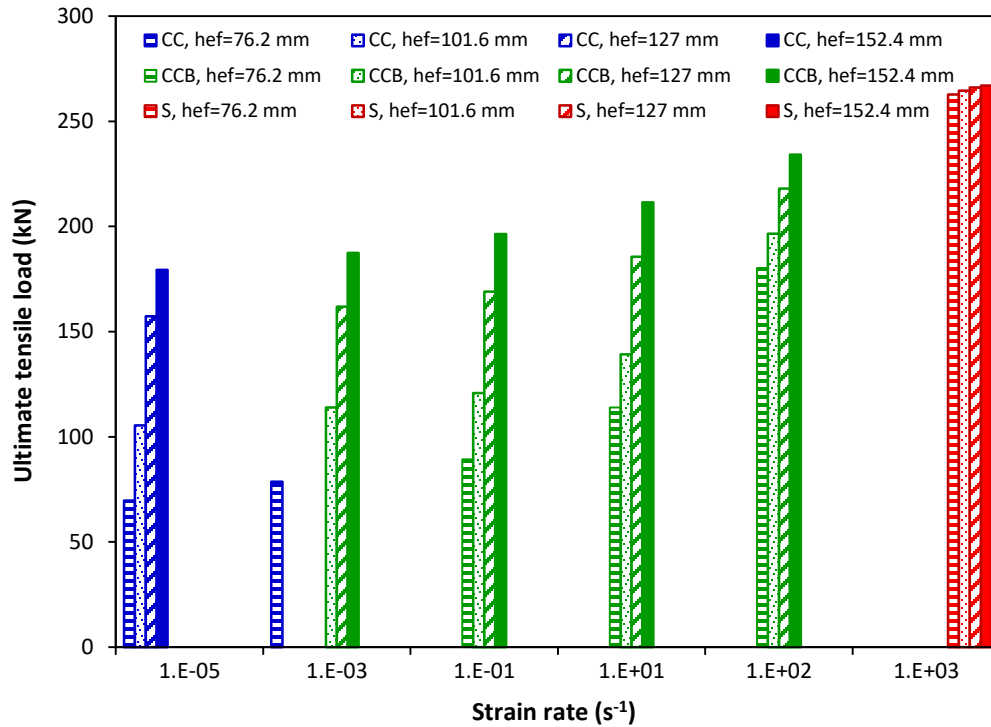


Figure 5-13: Strain rate effect on the failure mode and ultimate tensile load for adhesive anchor diameter of 19.1 mm

It can be seen from Figures 5-11, 5-12 and 5-13, that the failure mode of the adhesive anchor is affected by the strain rate. Also, it can be seen from the figures that, the failure mode is influenced by the embedment depth and anchor diameter. The increase in the embedment depth from 76.2 mm to 152.4 mm resulted in steel anchor failure for the anchor diameter of 12.7 mm at low strain rate of 10^{-5} s^{-1} . The increase in anchor diameter from 12.7 mm to 19.1 mm changed the failure mode from steel anchor failure to concrete cone breakout for the embedment depths of 127 mm and 152.4 mm at strain rate of 10^{-5} s^{-1} and

from steel failure to combined cone bond failure at strain rates of 10^{-3} s^{-1} , 10^{-1} s^{-1} , 10 s^{-1} and 10^2 s^{-1} for the same embedment depths. Also, it can be seen from the figures that the ultimate tensile load increased with the increase in the strain rate and embedment depth. The failure modes for the adhesive anchors under tensile load at different strain rates are summarized as in Table 5-4.

Table 5-4: Failure mode for adhesive anchors under tensile load at different strain rates

Model No.	d (mm)	h _{ef} (mm)	Failure mode*					
			Strain rate (s ⁻¹)					
			$\dot{\epsilon}=10^{-5}$	$\dot{\epsilon}=10^{-3}$	$\dot{\epsilon}=10^{-1}$	$\dot{\epsilon}=10$	$\dot{\epsilon}=10^2$	$\dot{\epsilon}=10^3$
1	12.7	76.2	CC	CCB	CCB	CCB	CCB	S
2	12.7	101.6	CC	CCB	CCB	CCB	CCB	S
3	12.7	127.0	S	S	S	S	S	S
4	12.7	152.4	S	S	S	S	S	S
5	15.9	76.2	CC	CCB	CCB	CCB	CCB	S
6	15.9	101.6	CC	CCB	CCB	CCB	CCB	S
7	15.9	127.0	CCB	CCB	CCB	CCB	CCB	S
8	15.9	152.4	S	S	S	S	S	S
9	19.1	76.2	CC	CC	CCB	CCB	CCB	S
10	19.1	101.6	CC	CCB	CCB	CCB	CCB	S
11	19.1	127.0	CC	CCB	CCB	CCB	CCB	S
12	19.1	152.4	CC	CCB	CCB	CCB	CCB	S

*Failure mode: CC= concrete cone breakout, CCB= combined cone bond, S=steel anchor failure

5.1.5 Effect of anchor embedment depth on concrete cone depth

Effect of anchor embedment depth on ultimate tensile load and concrete cone depth for the 12.7-mm, 15.9-mm and 19.1-mm diameter adhesive anchors is shown in Figures 5-14, 5-15 and 5-16 respectively. It can be seen from Figure 5-14 the ultimate tensile load of the 12.7-mm diameter adhesive anchor increased as the anchor embedment depth increased

from 76.2 mm to 127 mm under tensile loading at the static strain rate. The increase in the anchor embedment depth from 76.2 mm to 101.6 mm increased the concrete cone depth and hence the failure surface area. Further increase in the embedment depth to 152.4 mm shows no influence on the ultimate tensile load as the ultimate load was limited by the steel anchor failure.

For the 15.9-mm diameter adhesive anchor (Figure 5-15), the increase in the embedment depth from 76.2 mm to 152.4 mm increased the ultimate tensile load from 65.7 kN to 159.7 kN. The concrete cone depth increased with the increase in the anchor embedment depth from 76.2 mm to 101.6 mm. Combined cone bond failure was observed at embedment depth of 127 mm with cone depth of 40 mm and steel anchor failure is observed at embedment depth of 152.4 mm. For the anchor diameter of 19.1 mm (Figure 5-16), it can be seen that the ultimate tensile load and concrete cone depth increased with the increase in the anchor embedment depth from 76.2 mm to 152.4 mm.

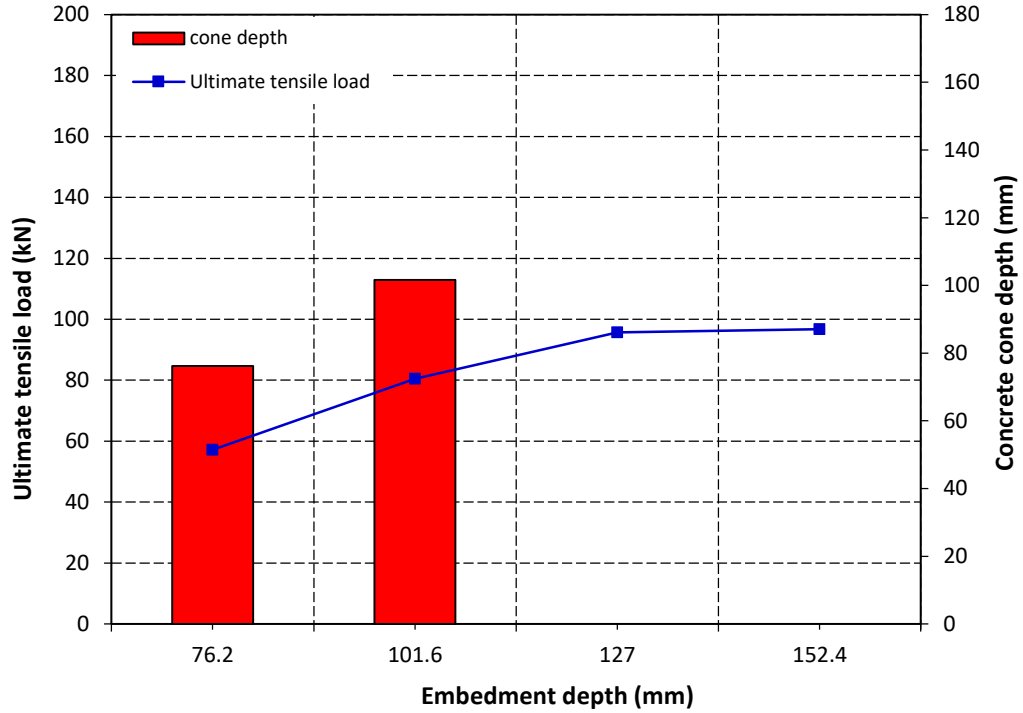


Figure 5-14: Effect of anchor embedment depth on the concrete cone depth and ultimate tensile load for 12.7 mm diameter adhesive anchor

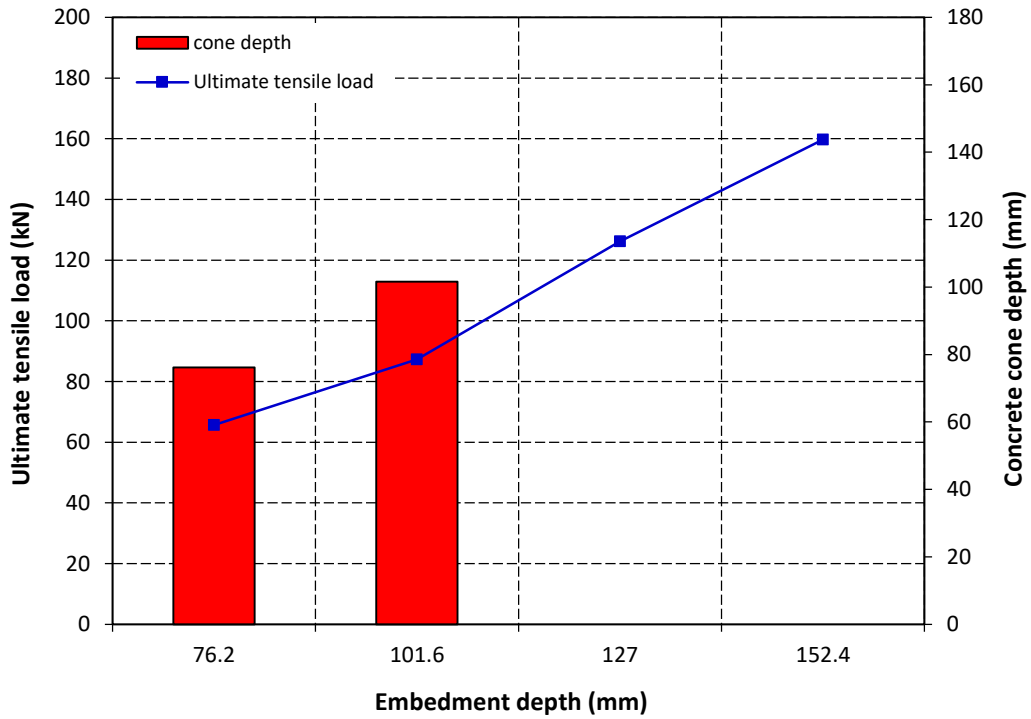


Figure 5-15: Effect of anchor embedment depth on the concrete cone depth and ultimate tensile load for 15.9 mm diameter adhesive anchor

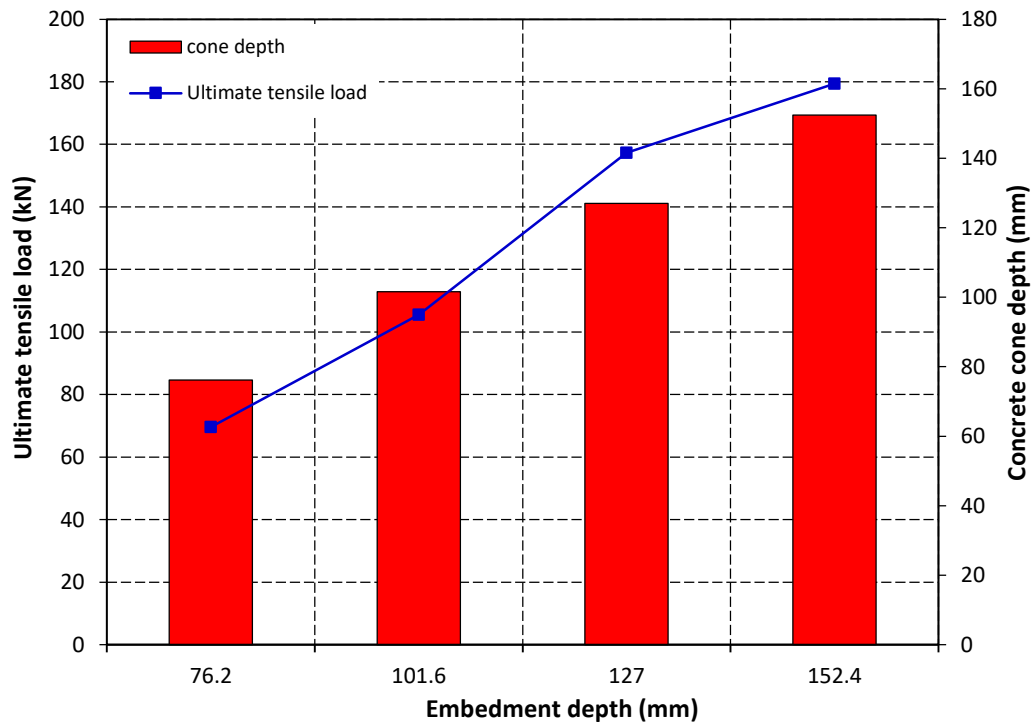
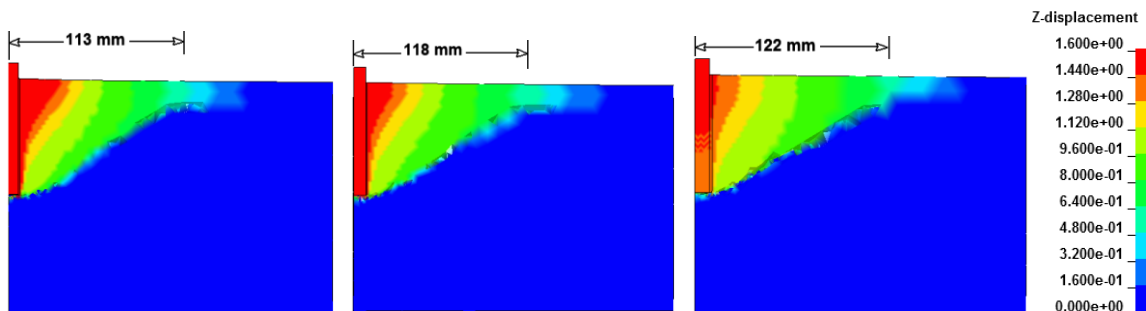


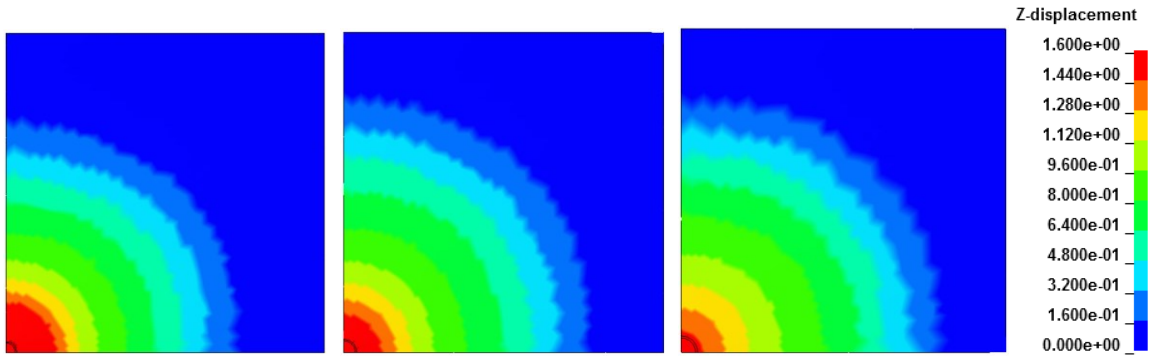
Figure 5-16: Effect of anchor embedment depth on the concrete cone depth and ultimate tensile load for 19.1 mm diameter adhesive anchor

5.1.6 Concrete cone breakout diameter for adhesive anchors

Figure 5-17 shows the displacement contours for adhesive anchors with embedment depth of 76.2 mm under tensile load at the static strain rate of 10^{-5} s^{-1} . As shown in the figure, the increase in the anchor diameter from 12.7 mm to 19.1 mm increased the concrete cone breakout radius from 113 mm to 122 mm.



Front view



Top view
 (a) (b) (c)

Figure 5-17: Displacement contours for adhesive anchors at strain rate of 10^{-5} with diameters of: (a) 12.7 mm, (b) 15.9 mm and (c) 19.1 mm

5.1.7 Effect of strain rate on the tensile behaviour of adhesive anchors

In order to investigate the tensile behaviour of the adhesive anchors, numerical models of adhesive anchorage to concrete systems were developed. Tensile capacity at different strain rates ($\dot{\epsilon}$) was investigated for different anchor diameters and embedment depths. Figures 5-18, 5-19, 5-20, 5-21, 5-22 and 5-23 present the load-displacement response for the 12.7-mm diameter adhesive anchor at strain rates of 10^{-5} s^{-1} , 10^{-3} s^{-1} , 10^{-1} s^{-1} , 10 s^{-1} , 10^2 s^{-1} and 10^3 s^{-1} respectively. The anchor embedment depths used in the investigation were 76.2 mm, 101.6 mm, 127 mm and 152.4 mm.

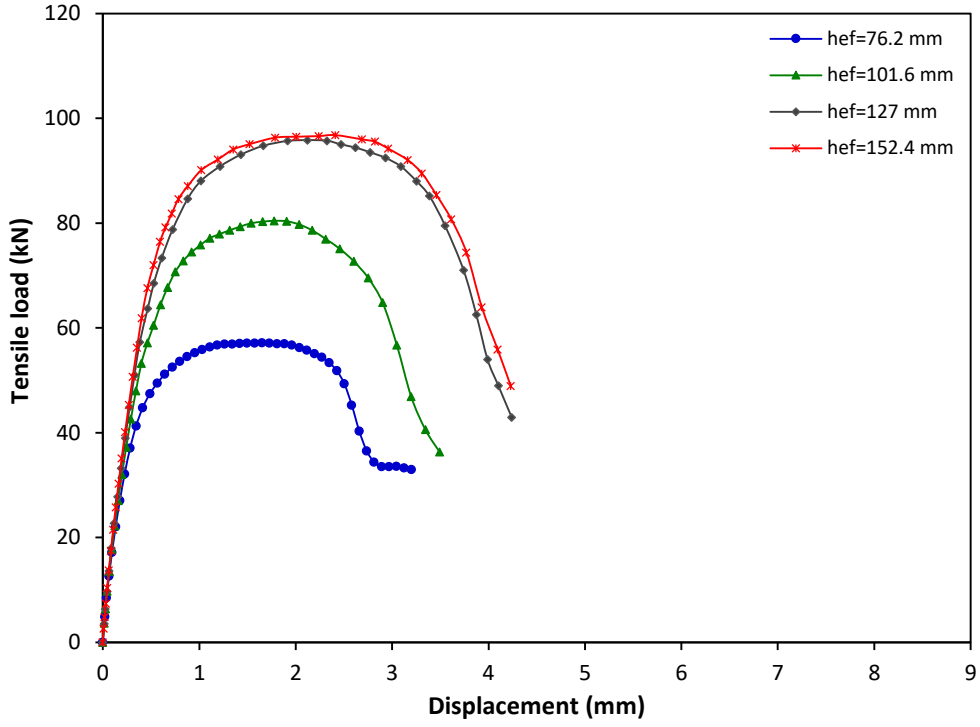


Figure 5-18: Tensile load-displacement graph for 12.7 mm diameter adhesive anchor at strain rate of 10^{-5} s^{-1}

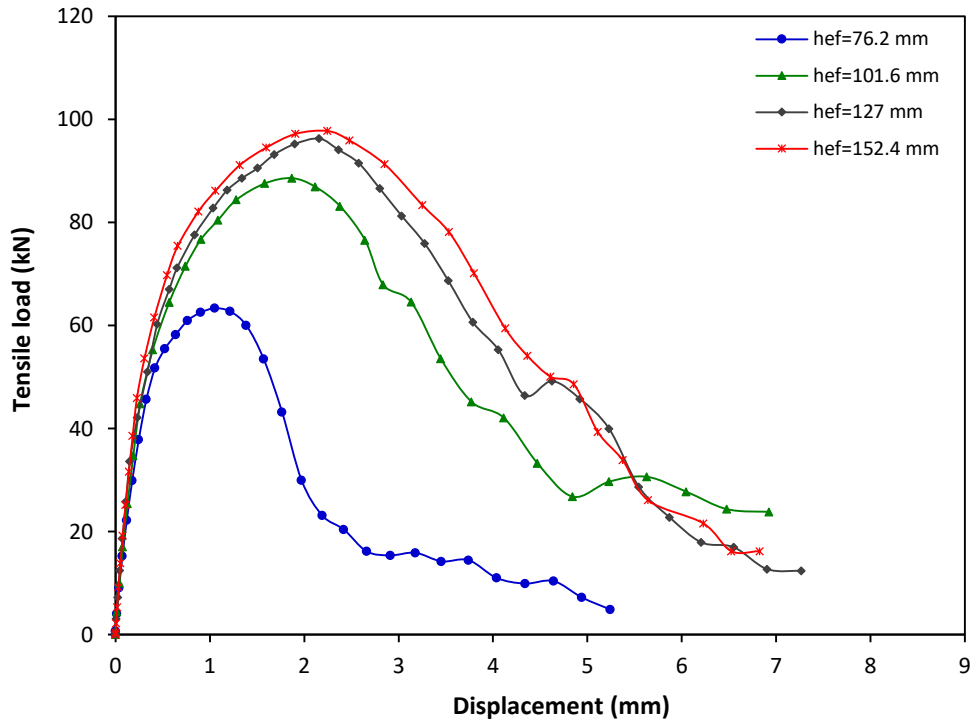


Figure 5-19: Tensile load-displacement graph for 12.7 mm diameter adhesive anchor at strain rate of 10^{-3} s^{-1}

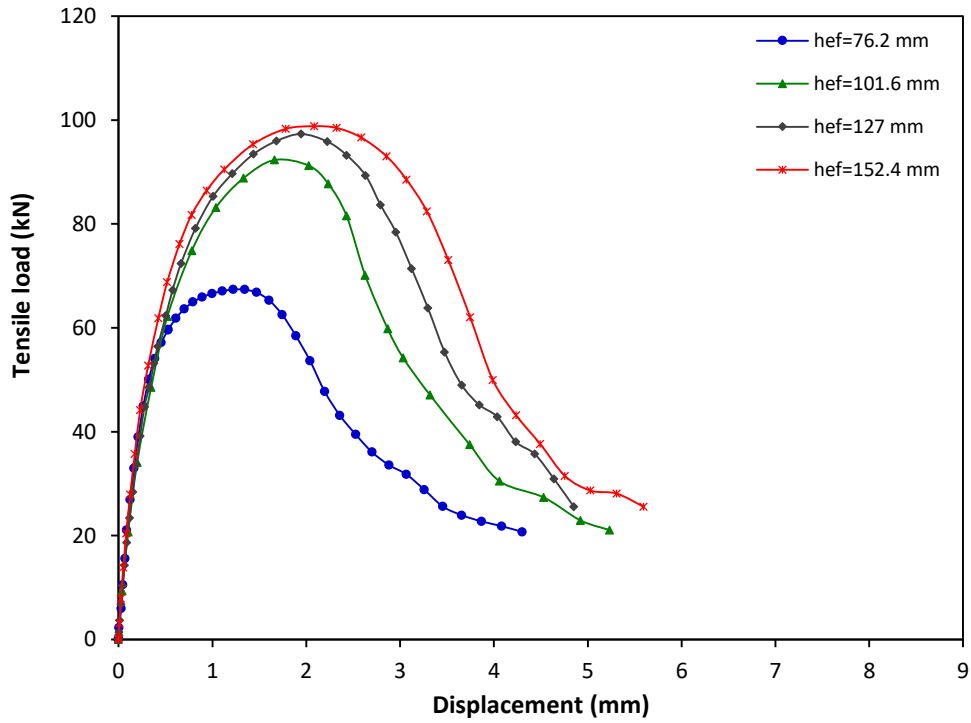


Figure 5-20: Tensile load-displacement graph for 12.7 mm diameter adhesive anchor at strain rate of 10^{-1} s^{-1}

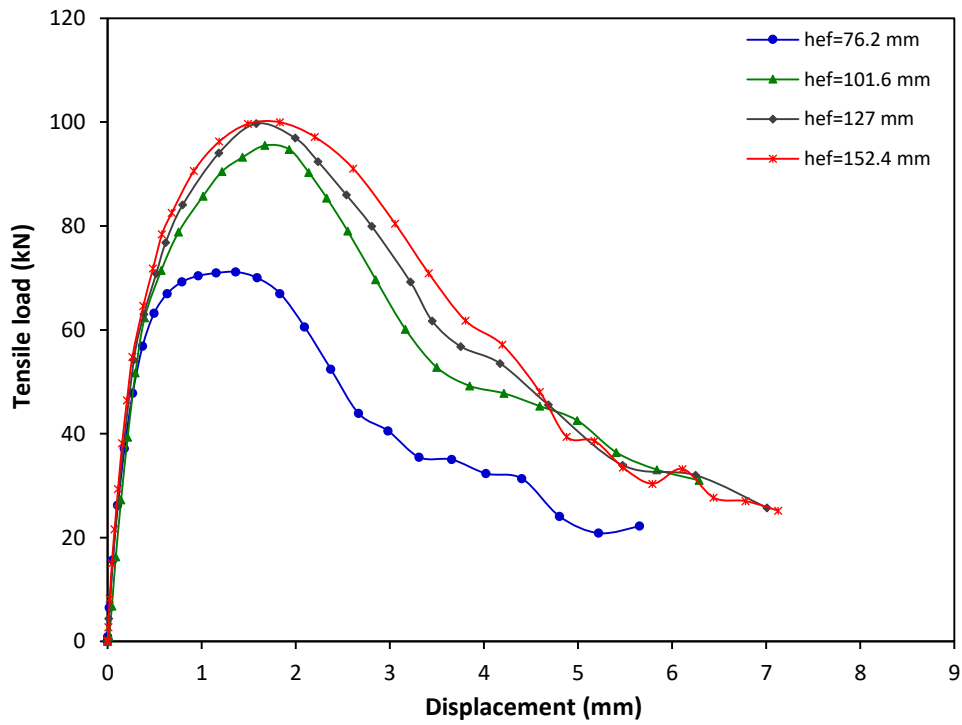


Figure 5-21: Tensile load-displacement graph for 12.7 mm diameter adhesive anchor at strain rate of 10 s^{-1}

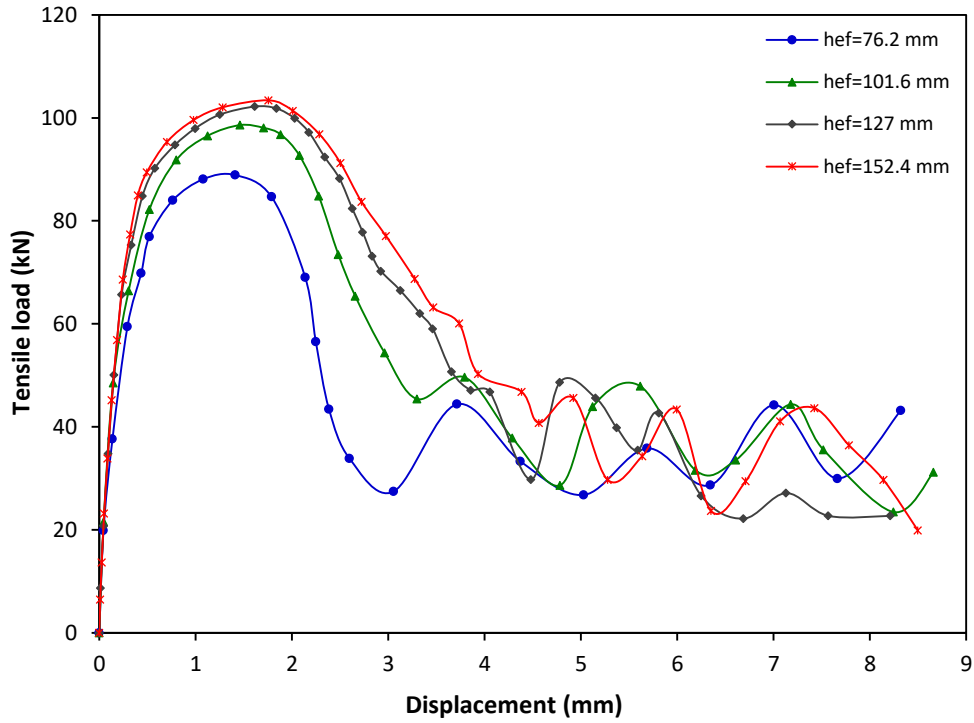


Figure 5-22: Tensile load-displacement graph for 12.7 mm diameter adhesive anchor at strain rate of 10^2 s^{-1}

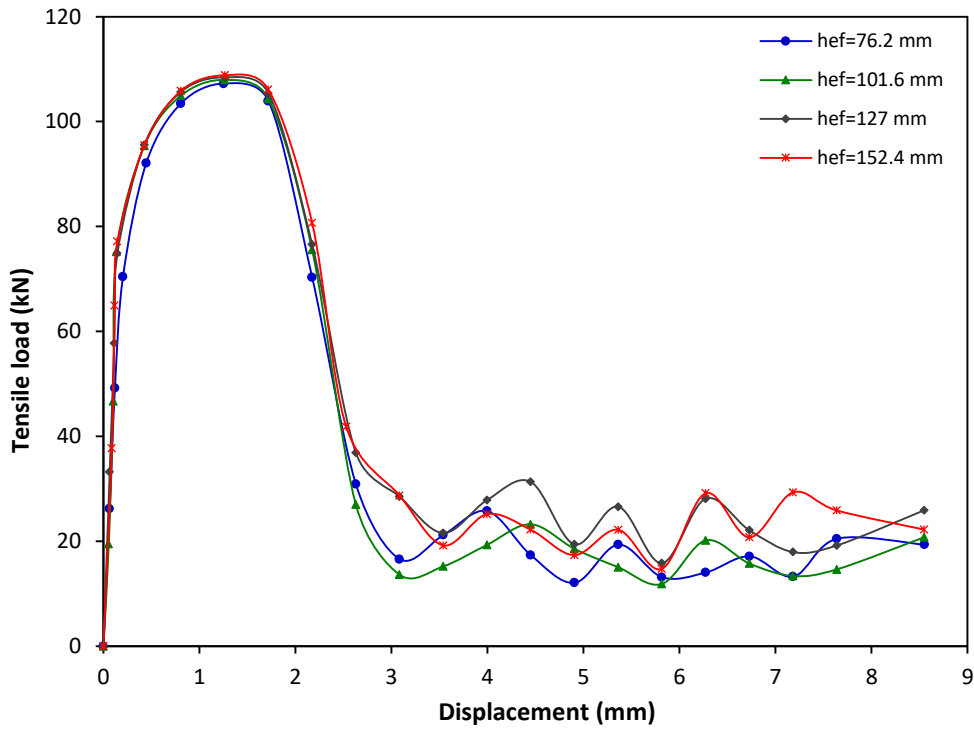


Figure 5-23: Tensile load-displacement graph for 12.7 mm diameter adhesive anchor at strain rate of 10^3 s^{-1}

Figures 5-18 to 5-23 show that the tensile load increased with the displacement until the ultimate load. This is attributed to the concrete resistance to the applied load where the tensile load transfers from the anchor to the concrete through the adhesive material. The post-peak response shows a reduction in the load with further increase in displacement until failure. The ultimate tensile load increased with the increase in the strain rate from 10^{-5} s^{-1} to 10^3 s^{-1} as shown in the figures and Table 5-5. Similar observation on the effect of loading rate for the adhesive anchors was obtained by Braimah et al., where the dynamic capacity increased at high loading rate of impulse (Braimah et al., 2009).

At intermediate strain rate of 10 s^{-1} , the tensile load increased as the embedment depth increased from 76.2 mm to 127 mm where the failure mode changed from combined cone-bond failure at embedment depth of 76.2 mm to steel anchor failure at embedment depth of 127 mm. Further increase in the embedment depth to 152.4 mm shows no increase of the tensile load as steel failure is observed. At embedment depths of 76.2 mm and 101.6 mm, the post peak behaviour at strain rate of 10 s^{-1} shows a decrease in the tensile load due to bond failure at the lower part of the anchor accompanied by crack initiation and propagation to the top surface of the concrete. The crack initiation and propagation lead to fracturing of the concrete and results in combined cone-bond failure as shown in Figure 5-8.

As the strain rate increased from 10 s^{-1} to 10^3 s^{-1} , the tensile load increased with the displacement until the maximum load. The post peak behaviour shows a decrease in the tensile load due to steel anchor failure. The failure mode transitioned from combined cone-bond failure to steel anchor failure for the embedment depths of 76.2 mm and 101.6 mm.

At embedment depths of 127 mm and 152.4 mm steel anchor failure was the dominant failure mode (Figure 5-8). At the large embedment depths, the ultimate failure load of the anchorage systems is the same as failure is dependent on steel anchor resistance.

The increase in the ultimate load with increase in strain rate is attributed to the fact that strain rate affects the mechanical properties of the concrete and steel materials. Concrete has been reported to have increased tensile and compressive strengths with increase in the strain rate (Hentz et al., 2004). Hence, the concrete resistance increases results in increase of the ultimate load capacity of the anchorage system when failure is by either cone or combined cone-bond failure.

Tensile load-displacement relations of the 15.9-mm and 19.1-mm diameter adhesive anchors with embedment depths of 76.2 mm, 101.6 mm, 127 mm and 152.4 mm at strain rates of 10^{-5} s^{-1} , 10^{-3} s^{-1} , 10^{-1} s^{-1} , 10 s^{-1} , 10^2 s^{-1} and 10^3 s^{-1} are presented in Appendix E.

Tables 5-5, 5-6 and 5-7 present the results of ultimate tensile load and corresponding displacement (δ) for the 12.7-mm, 15.9-mm and 19.1-mm diameter adhesive anchors respectively.

Table 5-5: Ultimate tensile load and displacement results for the 12.7 mm diameter adhesive anchor

Model No.	d (mm)	h_{ef} (mm)	$\dot{\epsilon}$ (s^{-1})	F_u (kN)	δ (mm)	Failure mode
1	12.7	76.2	10^{-5}	57.12	1.65	CC
2		101.6		80.45	1.78	CC
3		127		95.72	2.12	S
4		152.4		96.79	2.41	S

5	12.7	76.2	10^{-3}	63.33	1.05	CCB
6		101.6		88.59	1.87	CCB
7		127		96.27	2.16	S
8		152.4		97.74	2.23	S
9	12.7	76.2	10^{-1}	67.39	1.22	CCB
10		101.6		92.31	1.66	CCB
11		127		97.29	1.95	S
12		152.4		98.82	2.09	S
13	12.7	76.2	10	71.14	1.37	CCB
14		101.6		95.49	1.44	CCB
15		127		99.73	1.58	S
16		152.4		99.95	1.83	S
17	12.7	76.2	10^2	88.11	1.08	CCB
18		101.6		98.60	1.46	CCB
19		127		102.19	1.62	S
20		152.4		103.38	1.76	S
21	12.7	76.2	10^3	107.24	1.25	S
22		101.6		107.93	1.26	S
23		127		108.43	1.27	S
24		152.4		108.85	1.27	S

Table 5-6: Ultimate tensile load and displacement results for the 15.9 mm diameter adhesive anchor

Model No.	d (mm)	h_{ef} (mm)	ϵ (s^{-1})	F_u (kN)	δ (mm)	Failure mode
1	15.9	76.2	10^{-5}	65.69	1.11	CC
2		101.6		87.31	1.47	CC
3		127		126.18	1.82	CCB
4		152.4		159.72	2.09	S
5	15.9	76.2	10^{-3}	69.70	1.42	CCB
6		101.6		94.88	1.61	CCB
7		127		135.36	1.77	CCB

8		152.4		162.02	2.24	S
9	15.9	76.2	10^{-1}	74.94	1.25	CCB
10		101.6		101.48	1.53	CCB
11		127		143.56	1.61	CCB
12		152.4		164.08	2.36	S
13		76.2		87.36	1.04	CCB
14	15.9	101.6	10	108.31	1.03	CCB
15		127		151.14	1.22	CCB
16		152.4		168.41	1.54	S
17		76.2		118.21	1.06	CCB
18	15.9	101.6	10^2	124.28	1.02	CCB
19		127		162.82	1.60	CCB
20		152.4		171.08	1.76	S
21		76.2		173.63	1.26	S
22	15.9	101.6	10^3	175.89	1.26	S
23		127		177.57	1.42	S
24		152.4		178.59	1.37	S

Table 5-7: Ultimate tensile load and displacement results for the 19.1 mm diameter adhesive anchor

Model No.	d (mm)	h_{ef} (mm)	$\dot{\epsilon}$ (s^{-1})	F_u (kN)	δ (mm)	Failure mode
1	19.1	76.2	10^{-5}	69.62	0.80	CC
2		101.6		105.49	1.06	CC
3		127		157.28	1.36	CC
4		152.4		179.40	2.04	CC
5	19.1	76.2	10^{-3}	78.68	1.19	CC
6		101.6		113.94	1.59	CCB
7		127		161.79	1.77	CCB
8		152.4		187.48	1.99	CCB
9	19.1	76.2	10^{-1}	89.32	1.29	CCB
10		101.6		120.78	1.32	CCB

11		127		169.02	1.51	CCB
12		152.4		196.47	1.47	CCB
13	19.1	76.2	10	114.01	1.07	CCB
14		101.6		139.14	1.02	CCB
15		127		185.58	1.23	CCB
16		152.4		211.45	1.34	CCB
17		76.2		180.25	0.67	CCB
18	19.1	101.6	10 ²	196.53	0.84	CCB
19		127		217.96	1.47	CCB
20		152.4		234.18	1.40	CCB
21		76.2		262.69	1.26	S
22	19.1	101.6	10 ³	264.59	1.29	S
23		127		266.13	1.26	S
24		152.4		266.96	1.39	S

In general, it can be seen from Tables 5-5, 5-6 and 5-7 that the ultimate tensile load increased with the increase in the anchor diameter from 12.7 mm to 19.1 mm for the embedment depths and strain rates investigated. The increase in anchor diameter increases the contact area between the adhesive anchor and concrete and hence the bond capacity of the anchorage system. It can be seen from the tables that at the low strain rate of 10^{-5} s^{-1} for shallow embedment depths of 76.2 mm and 101.6 mm concrete cone breakout failure was observed for the 12.7-mm, 15.9-mm and 19.1-mm diameter adhesive anchors. Also, concrete cone breakout failure was observed for the 19.1-mm diameter adhesive anchor at embedment depths of 127 mm and 152.4 mm, where the tensile load was higher than the concrete strength. Steel anchor failure was observed for anchor embedment depth of 127 mm with anchor diameter of 12.7 mm. Also, steel anchor failure was observed at embedment depth of 152.4 mm for anchor diameters of 12.7 mm and 15.9 mm. For long embedment depths and smaller anchor diameters of 12.7 mm and 15.9 mm, the steel anchor

is not capable to withstand the applied load resulting in steel fracture. The tensile load is influenced by the strain rate. From Tables 5-5, 5-6 and 5-7 it can be seen that the adhesive anchors exhibited concrete cone breakout failure transitioned to steel failure at high strain rate. This can be attributed to the increased strength of concrete and steel due to increased strain rate and hence, the concrete resistance to the tensile load increased resulted in steel anchor failure.

In general, it can be seen that the displacement (δ) at the ultimate load decreased with the increase in anchor diameter from 12.7 mm to 19.1 mm, at the same embedment depths. At high strain rate the effect of anchor diameter on the ultimate displacement is insignificant. The tensile load was also observed to increase with increase in the embedment depth from 76.2 mm to 152.4 mm for the anchors exhibited concrete cone breakout failure mode. The increase in the anchor embedment depth increased the displacement at the ultimate tensile load. The embedment depth was observed to have a greater effect on the ultimate tensile load at the same strain rate when concrete cone breakout failure is the dominant failure mode. However, the increase in the embedment depth has no influence on the ultimate tensile load when steel anchor failure is the dominant failure mode.

5.1.8 Effect of strain rate on the ultimate tensile load and DIF of adhesive anchors

In order to predict the increase in strength of anchorage system due to increase in the steel and concrete strength with the increase in the strain rate, DIF for the anchorage to concrete system was investigated. The lowest strain rate of 10^{-5} s^{-1} is representative of static loading rate and was used as the baseline for comparison with adhesive anchor capacity at the higher strain rates for the adhesive anchors exhibiting concrete cone breakout failure and

combined cone bond failure. For the anchors exhibiting steel failure mode the dynamic increase factor is taken as the ratio of ultimate dynamic load to the ultimate static steel failure load. Effect of strain rate on the ultimate tensile load and DIF is shown in Figures 5-24, 5-25, 5-26 and 5-27 for the 12.7-mm, 15.9-mm and 19.1-mm diameter adhesive anchors with embedment depths of 76.2 mm, 101.6 mm, 127 mm and 152.4 mm respectively. It can be seen from the figures that the ultimate tensile load increased with increase in strain rate from 10^{-5} s^{-1} to 10^3 s^{-1} for all the adhesive anchors investigated. The increase in anchor embedment depth resulted in increase in ultimate tensile load at all strain rates investigated. Maximum tensile loads of 108.85 kN, 178.59 kN and 266.96 kN were obtained at high strain rate of 10^3 s^{-1} and embedment depth of 152.4 mm for the 12.7-mm, 15.9-mm and 19.1-mm diameter adhesive anchors, respectively. On the other hand, at low strain rate of 10^{-5} s^{-1} and for the same embedment depth of 152.4 mm, the ultimate tensile loads were 96.79 kN, 159.72 kN and 179.40 kN for the 12.7-mm, 15.9-mm and 19.1-mm diameter adhesive anchors, respectively.

As shown from Figures 5-24 and 5-25, the relationship between the ultimate tensile load and the strain rate appears to be bilinear with a change in slope at strain rate of 10 s^{-1} for all anchor diameters at embedment depths of 76.2 mm and 101.6 mm where concrete cone breakout failure was observed at low strain rate of 10^{-5} s^{-1} . Then the failure mode transitioned to combined concrete cone bond failure at strain rates up to 10^2 s^{-1} , and to steel anchor failure at high strain rate of 10^3 s^{-1} where higher load is required to fracture the anchor. This is similar to the reported relationship between tensile concrete strength and strain rate (Malvar & Crawford, 1998; Hentz et al., 2004). Also, Malvar & Crawford

reported that the relationship between compressive concrete strength and strain rate is bilinear (Malvar & Crawford, 1998).

It can be seen from Figures 5-24 and 5-25, the 19.1-mm diameter adhesive anchor exhibited higher DIF than that obtained for anchor diameters of 12.7 mm and 15.9 mm for the strain rates ranging from 10^{-5} s^{-1} to 10^2 s^{-1} . At high strain rate of 10^3 s^{-1} , average DIF of 1.1 was obtained for the anchor diameters of 12.7 mm, 15.9 mm and 19.1 mm where steel failure was observed. Also, it can be seen that the DIF is higher for the shallow embedment depth of 76.2 mm compared to the deep embedment depth of 152.4 mm. Maximum DIF of 1.54, 1.80 and 2.59 were obtained for the 12.7-mm, 15.9-mm and 19.1-mm diameter adhesive anchors with embedment depth of 76.2 mm at the high strain rate of 10^2 s^{-1} where combined cone bond failure is observed for all the adhesive anchors.

It can be seen from Figure 5-26 bilinear relationship between the ultimate tensile load and strain rate was obtained for the 15.9-mm and 19.1-mm anchor diameters at embedment depth of 127 mm; whereas almost linear relation was obtained for the 12.7-mm diameter adhesive anchor where steel anchor failure was observed at all the strain rates investigated. As shown in Figure 5-26, the DIF increased slightly from 1.01 at strain rate of 10^{-3} s^{-1} to 1.13 at strain rate of 10^3 s^{-1} for anchor diameter of 12.7 mm. The DIF increased from 1.07 to 1.29 and from 1.03 to 1.39 for the anchor diameters of 15.9 mm and 19.1 mm respectively when the strain rate increased from 10^{-3} s^{-1} to 10^2 s^{-1} . At high strain rate of 10^3 s^{-1} , average DIF of 1.11 was obtained for the 15.9 mm and 19.1 mm diameter adhesive anchors. Combined cone bond failure was observed for anchor diameters of 15.9 mm and

19.1 mm at strain rate of 10^{-3} s^{-1} and transitioned to steel anchor failure at high strain rate of 10^3 s^{-1} .

At embedment depth of 152.4 mm (Figure 5-27), bilinear relationship was obtained for the 19.1-mm diameter adhesive anchor where concrete cone breakout failure mode at low strain rate of 10^{-5} s^{-1} transitioned to combined cone bond failure at higher strain rates up to 10^2 s^{-1} followed by steel anchor failure at strain rate of 10^3 s^{-1} . While linear relation was obtained for the 12.7-mm and 15.9-mm diameter adhesive anchors where steel anchor failure was the dominant failure mode at all the strain rates investigated. The DIF increased slightly for anchor diameters of 12.7 mm and 15.9 mm. For the 19.1-mm diameter adhesive anchor, the DIF increased from 1.05 at strain rate of 10^{-3} s^{-1} to 1.31 at strain rate of 10^2 s^{-1} where combined cone bond failure was observed. At high strain rate of 10^3 s^{-1} DIF of 1.11 was obtained for the 19.1 mm diameter anchor where steel failure was observed.

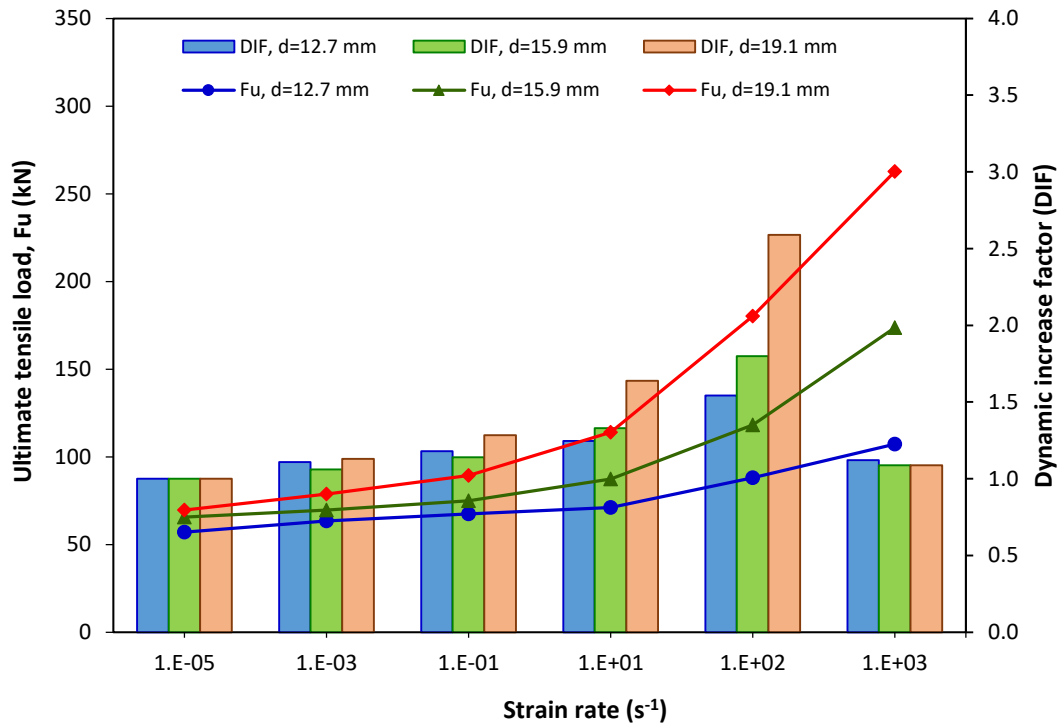


Figure 5-24: Ultimate tensile load and DIF versus strain rate for the adhesive anchor at 76.2 mm embedment depth

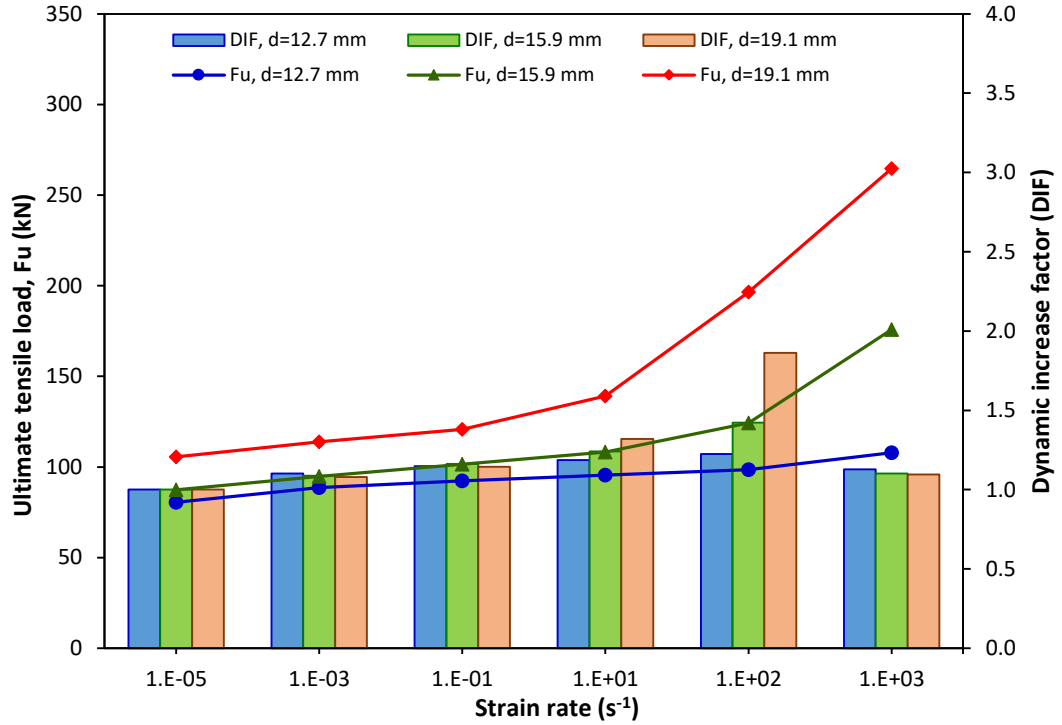


Figure 5-25: Ultimate tensile load and DIF versus strain rate for the adhesive anchor at 101.6 mm embedment depth

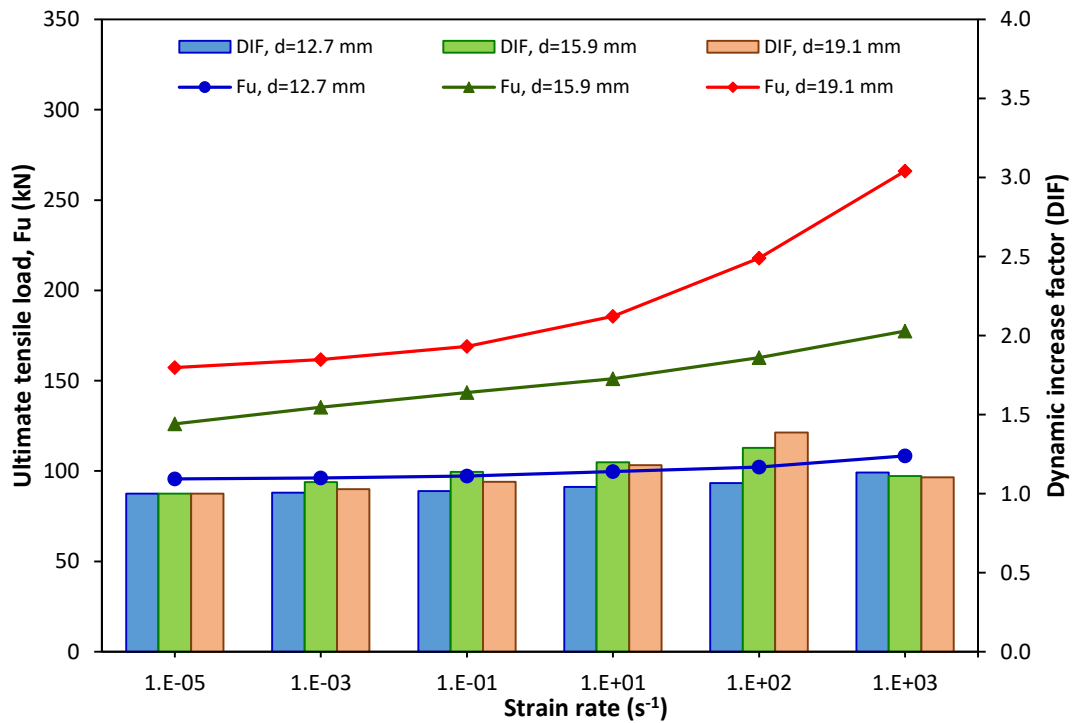


Figure 5-26: Ultimate tensile load and DIF versus strain rate for the adhesive anchor at 127 mm embedment depth

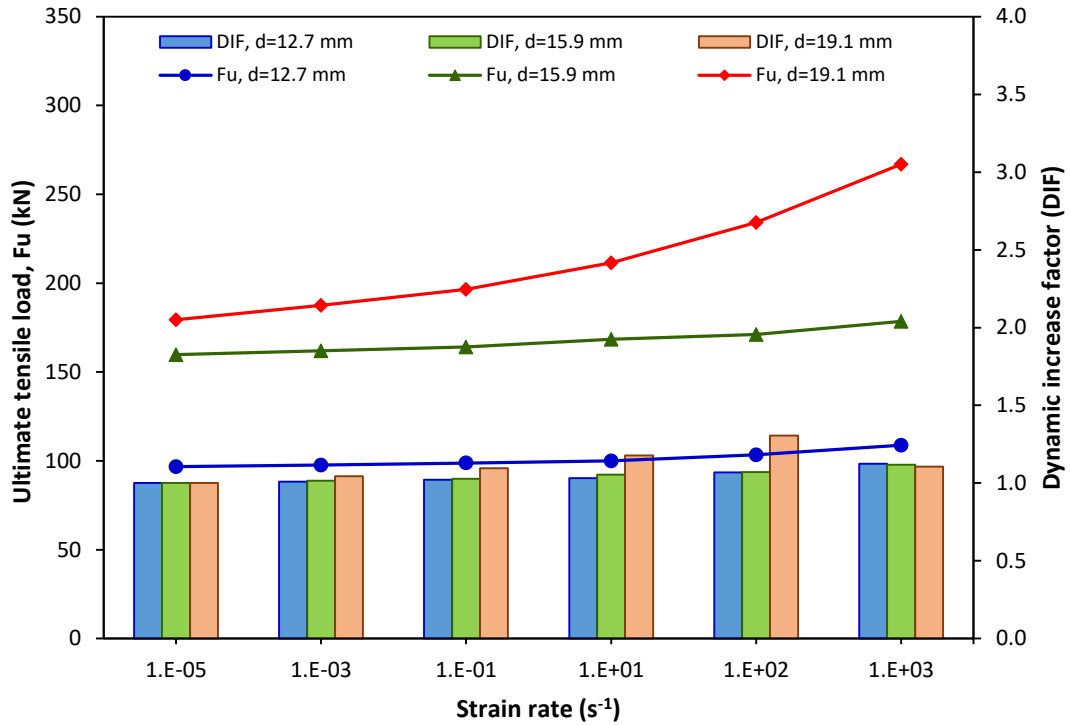


Figure 5-27: Ultimate tensile load and DIF versus strain rate for the adhesive anchor at 152.4 mm embedment depth

The increase in the strain rate increased the ultimate load and the DIF for the concrete and steel. The DIF for concrete tensile strength is much higher than that for steel (Malvar & Crawford, 1998; Malvar & Ross, 1998). Hence as the strain rate increases, the increase in the anchor capacity for concrete cone and combined concrete cone-bond failure exceeds the increase attributed to steel anchor failure where the concrete cone failure is observed at strain rates of 10^{-5} s^{-1} for most of the adhesive anchors (Figure 5-6). Combined cone-bond failure is observed at strain rates ranging from 10^{-3} s^{-1} to 10^2 s^{-1} for most of the adhesive anchors while steel failure is the dominant failure mode for all the adhesive anchors at high strain rate of 10^3 s^{-1} as shown in Figures 5-8, 5-9 and 5-10.

Table 5-8 shows the maximum DIF for the adhesive anchors under tensile load where concrete cone breakout, combined cone bond and steel failure modes were observed. The DIF at static strain rate of 10^{-5} s^{-1} ($\dot{\epsilon}_s$) is equal to one where concrete cone breakout failure was observed as shown in Table 5-8. For the anchor diameter of 12.7 mm with embedment depths of 127 mm and 152.4 mm and for the anchor diameter of 15.9 mm with embedment depth of 152.4 mm, steel anchor failure was observed at all the strain rates investigated. For the anchor diameter of 15.9 mm with embedment depth of 127 mm, combined cone bond failure was observed at strain rates of 10^{-5} s^{-1} and 10^2 s^{-1} , maximum DIF of 1.29 for the combined cone bond failure was obtained at strain rate of 10^2 s^{-1} . For anchor diameter of 19.1 mm with embedment depth of 76.2 mm concrete cone breakout failure was observed at strain rates of 10^{-5} s^{-1} and 10^{-3} s^{-1} , maximum DIF of 1.13 for the concrete cone breakout was obtained at strain rate of 10^{-3} s^{-1} .

Table 5-8: Maximum dynamic increase factor for the adhesive anchors under tensile load

Model No.	d (mm)	h_{ef} (mm)	$\dot{\epsilon}$ (s^{-1})	DIF	$\dot{\epsilon}$ (s^{-1})	DIF	$\dot{\epsilon}$ (s^{-1})	DIF
				CC		CCB		S
1	12.7	76.2	10^{-5}	1.00	10^2	1.54	10^3	1.12
2	12.7	101.6	10^{-5}	1.00	10^2	1.23	10^3	1.13
3	12.7	127.0	-	-	-	-	10^3	1.13
4	12.7	152.4	-	-	-	-	10^3	1.12
5	15.9	76.2	10^{-5}	1.00	10^2	1.80	10^3	1.09
6	15.9	101.6	10^{-5}	1.00	10^2	1.42	10^3	1.10
7	15.9	127.0	-	-	10^2	1.29	10^3	1.11
8	15.9	152.4	-	-	-	-	10^3	1.12
9	19.1	76.2	10^{-3}	1.13	10^2	2.59	10^3	1.09
10	19.1	101.6	10^{-5}	1.00	10^2	1.86	10^3	1.10
11	19.1	127.0	10^{-5}	1.00	10^2	1.39	10^3	1.10
12	19.1	152.4	10^{-5}	1.00	10^2	1.31	10^3	1.11

5.1.9 Regression Analysis for adhesive anchors under tensile load

Regression analysis was carried out to develop an accurate predictive formula for determining the DIF of the adhesive anchorage to concrete systems based on the finite element results. As shown from Figures 5-8, 5-9 and 5-10, most of the adhesive anchors investigated at strain rates ranging from 10^{-3} s^{-1} to 10^3 s^{-1} exhibited combined cone bond and steel anchor failure under tensile load. Hence regression analysis was performed for these failure modes. Average value of the DIF for the adhesive anchorage systems with anchor diameters of 12.7 mm, 15.9 mm and 19.1 mm was calculated to adjust the DIF for the effect of anchor diameter. Figures 5-28 and 5-29 present the relation between the DIF and the strain rate ratio ($\dot{\epsilon}_d/\dot{\epsilon}_s$) for the combined cone bond and steel anchor failure modes respectively.

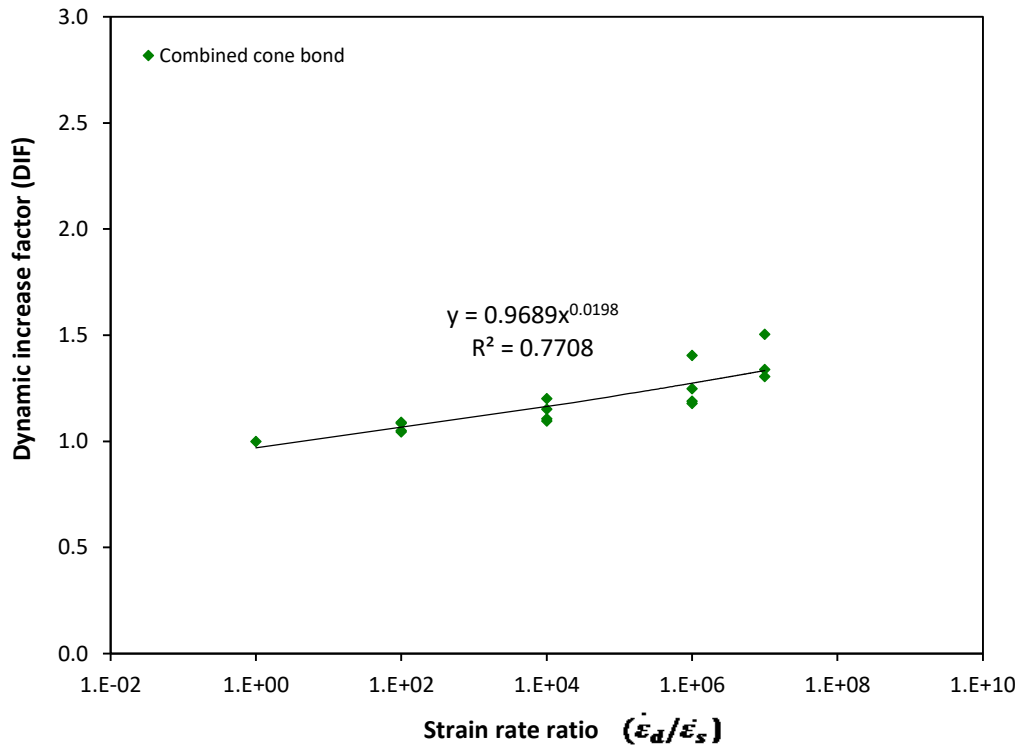


Figure 5-28: Effect of strain rate ratio on DIF for adhesive anchor exhibited combined cone bond failure under tensile load

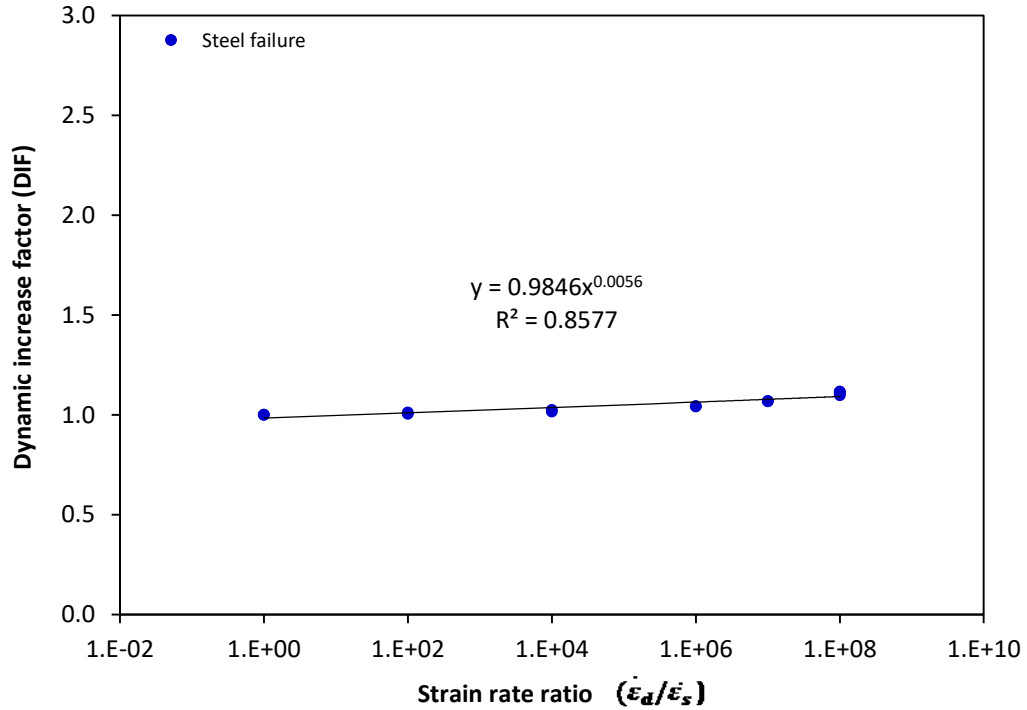


Figure 5-29: Effect of strain rate ratio on DIF for adhesive anchor exhibited steel failure under tensile load

Various statistical models are used to predict the relation between the DIF of the adhesive anchors and strain rate ratio as shown in Tables 5-9 and 5-10.

Table 5-9: Statistical models and coefficient of determination to predict the DIF for adhesive anchors exhibited combined cone bond failure under tensile load

Statistical models	Formulae	Coefficient of determination (R^2)
Exponential	$DIF = 1.1272e^{2E-8\left(\frac{\dot{\epsilon}_d}{\dot{\epsilon}_s}\right)}$	0.532
Linear	$DIF = 3E - 8\left(\frac{\dot{\epsilon}_d}{\dot{\epsilon}_s}\right) + 1.1306$	0.544
Logarithmic	$DIF = 0.0237\ln\left(\frac{\dot{\epsilon}_d}{\dot{\epsilon}_s}\right) + 0.9516$	0.733
Power	$DIF = 0.9689\left(\frac{\dot{\epsilon}_d}{\dot{\epsilon}_s}\right)^{0.0198}$	0.771

Table 5-10: Statistical models and coefficient of determination to predict the DIF for adhesive anchors exhibited steel failure under tensile load

Statistical models	Formulae	Coefficient of determination (R ²)
Exponential	$DIF = 1.0253e^{8E-10\left(\frac{\dot{\epsilon}_d}{\dot{\epsilon}_s}\right)}$	0.790
Linear	$DIF = 9E - 10\left(\frac{\dot{\epsilon}_d}{\dot{\epsilon}_s}\right) + 1.0255$	0.800
Logarithmic	$DIF = 0.0059\ln\left(\frac{\dot{\epsilon}_d}{\dot{\epsilon}_s}\right) + 0.9832$	0.849
Power	$DIF = 0.9846\left(\frac{\dot{\epsilon}_d}{\dot{\epsilon}_s}\right)^{0.0056}$	0.858

From Tables 5-9 and 5-10, it can be seen that power model exhibits the highest coefficient of determination of 77% and 86%. The predicted formula for the DIF for the adhesive anchors can be presented as in Equations (5.1) and (5.2) for the combined cone bond failure and steel failure respectively.

$$DIF = 0.9689\left(\frac{\dot{\epsilon}_d}{\dot{\epsilon}_s}\right)^{0.0198} \quad (5.1)$$

$$DIF = 0.9846\left(\frac{\dot{\epsilon}_d}{\dot{\epsilon}_s}\right)^{0.0056} \quad (5.2)$$

The ultimate dynamic load (F_{ud}) for the combined cone bond and steel anchor failure modes can be determined as in Equations (5.3) and (5.4) respectively as follows:

$$F_{ud} = F_{us} \times 0.9689\left(\frac{\dot{\epsilon}_d}{\dot{\epsilon}_s}\right)^{0.0198} \quad (5.3)$$

$$F_{ud} = F_{us} \times 0.9846\left(\frac{\dot{\epsilon}_d}{\dot{\epsilon}_s}\right)^{0.0056} \quad (5.4)$$

Where the ultimate static load (F_{us}) can be determined from Equation (B.11) for the combined cone bond and from Equation (4.2) for steel anchor failure mode.

The adequacy of the predicted model is verified by calculating coefficient of determination R^2 and residual analysis (Montgomery, 2013). Residual analysis has been performed to measure the difference between the results obtained from finite element analysis and fitted results of DIF obtained from Equations (5.1) and (5.2). Figures 5-30 and 5-31 present the residual plots. As shown in Figure 5-30, for the combined cone-bond failure, the variance in the residual increases with the increase in the strain rate ratio. For the steel anchor failure (Figure 5-31), the residual exhibits horizontal trend line at strain rate ratio up to 10^8 .

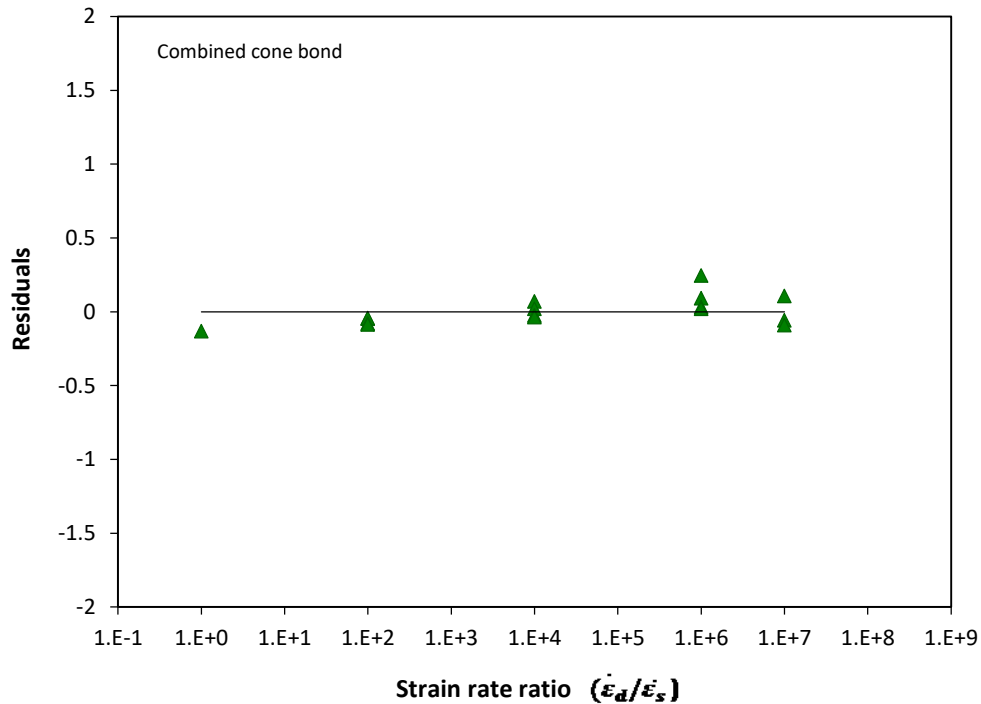


Figure 5-30: Residual versus strain rate ratio for the adhesive anchor exhibited combined cone bond failure

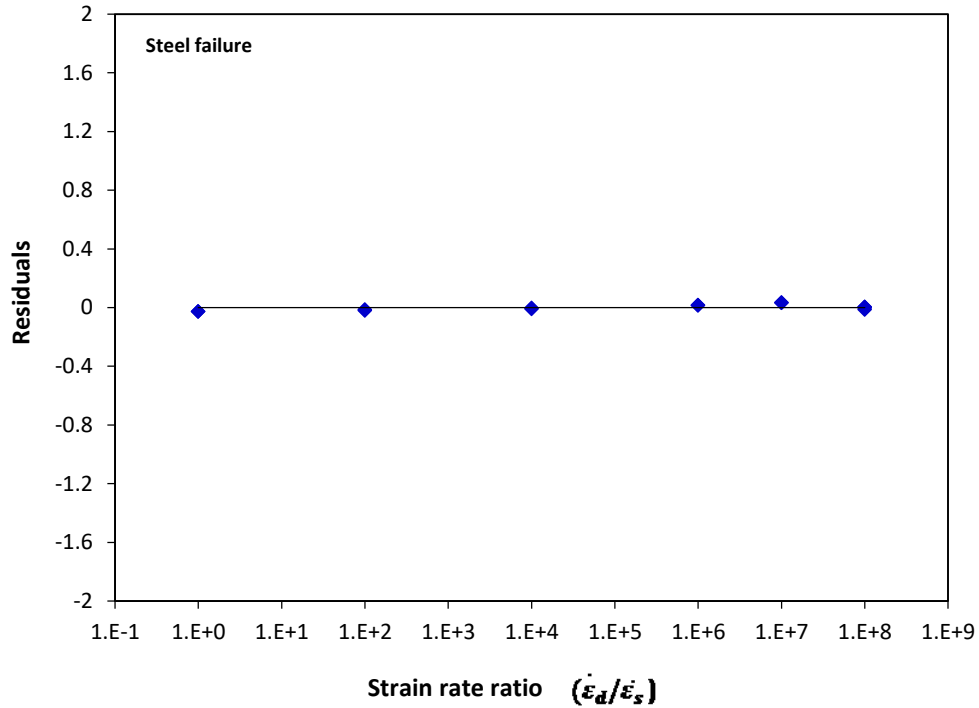


Figure 5-31: Residual versus strain rate ratio for the adhesive anchor exhibited steel failure

In addition, to evaluate the adequacy of the proposed equations, new adhesive anchor models with diameters of 9.5 mm, 12.7 mm, 15.9 mm and 19.1 mm and embedment depths of 89 mm, 114 mm and 140 mm were developed. The relation between the DIF obtained from the finite element analysis of the new developed models and the regression models (Equations (5.1) and (5.2)) are presented as shown in Figures 5-32 and 5-33 for the combined cone-bond failure and steel failure modes respectively. As shown in the figures, the DIF is distributed around the equality line. However, some divergence was observed for the higher values of the DIF for the combined cone bond failure mode where the residual increased at higher strain rates.

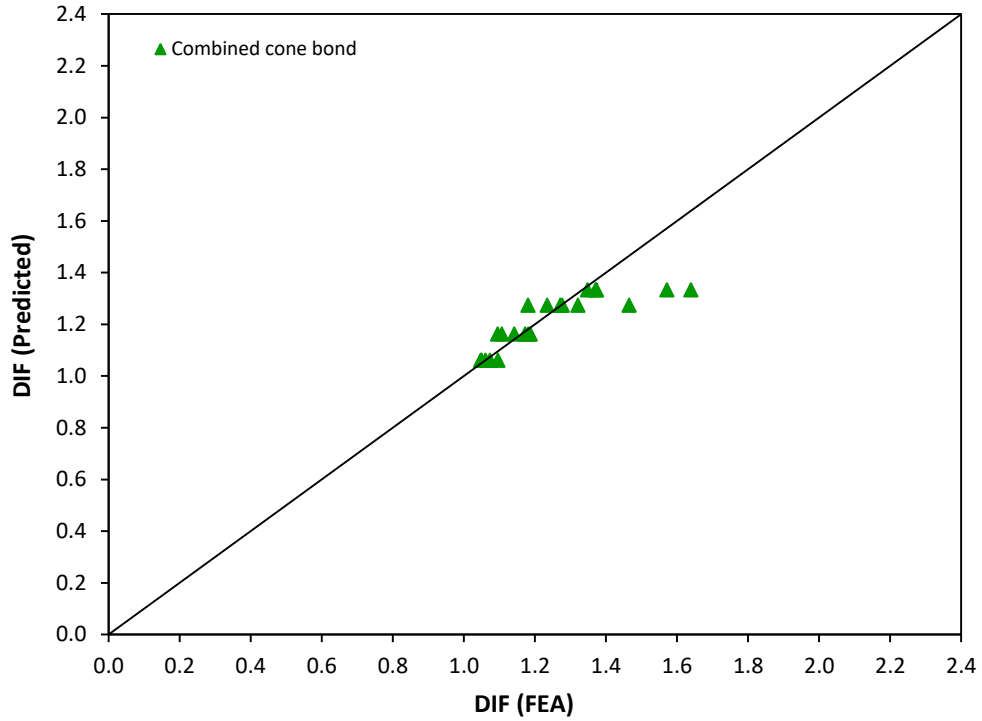


Figure 5-32: DIF obtained from the finite element analysis versus the predicted DIF for the adhesive anchors exhibited combined cone bond failure

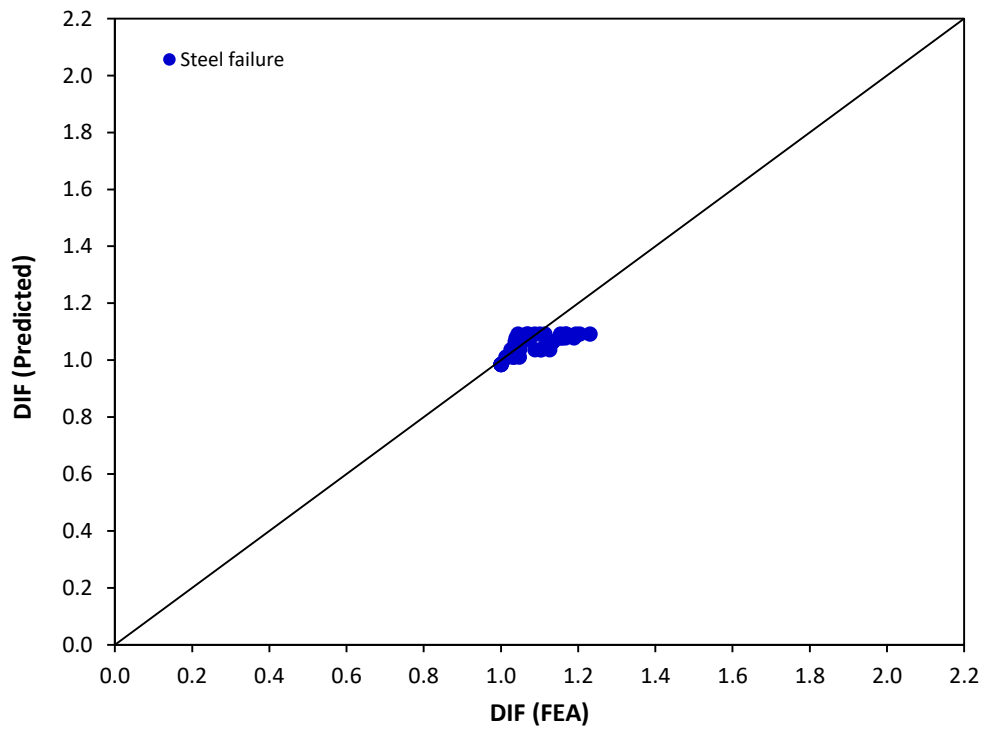


Figure 5-33: DIF obtained from the finite element analysis versus the predicted DIF for the adhesive anchors exhibited steel failure

As mentioned in Chapter 4, Fujikake et al. (2003) proposed equation to determine the ultimate dynamic load of the anchorage system exhibited concrete cone breakout failure (Equation 4.10). Also, Fujikake et al. (2003) proposed equations to determine the ultimate dynamic load for the combined cone bond failure mode (Fujikake et al., 2003) as follows:

$$F_{ccb} = F_{cd} + F_b \quad (5.5)$$

$$F_b = \pi \cdot d_h \cdot h_b \cdot \tau_{bs} \cdot \left(\frac{\dot{\epsilon}_d}{\dot{\epsilon}_s}\right)^{0.013} \quad (5.6)$$

Where F_{ccb} is the ultimate tensile load for the combined cone bond failure, F_{cd} is the ultimate dynamic concrete cone breakout calculated by Equation (4.10), F_b is the ultimate tensile load for the bond failure mode, h_b is the bond failure depth ($h_b = h_{ef} - h_c$), h_c is the failure cone depth in the combined cone bond failure mode ($h_c=35$ mm), $\alpha=3.48 \times 10^{-3}$, θ is the crack propagation angle ($\theta = 60^\circ$), where the concrete cone breakout angle is equal to 30° , τ_{bs} is the static bond strength ($\tau_{bs}=19$ MPa).

In order to verify the results obtained from the finite element analysis, a comparison has been made between the ultimate load obtained from the finite element analysis and the proposed equations by Fujikake et al. (Equations 4.10 and 5.5) for the concrete cone breakout failure and the combined cone-bond failure modes respectively (Fujikake et al., 2003). The embedment depth (h_{ef}) substituted in Equation (5.5) is equal to the cone failure depth (h_c) for the combined cone-bond failure mode. Tables 5-11 and 5-12 show a comparison of the ultimate load obtained from the finite element analysis for the concrete cone breakout failure and combined cone-bond failure modes and the proposed equations

by Fujikake et al. (Fujikake et al., 2003). It can be seen from Tables 5-11 and 5-12 that the ultimate loads obtained from the finite element analysis agree well with the proposed equations by Fujikake et al. (2003).

Table 5-11: Comparison between ultimate load obtained from the FEA and the proposed equations by Fujikake et al. (2003) for concrete cone breakout failure mode

d (mm)	h_{ef} (mm)	F_{us} FEA (kN)	F_{cd} Fujikake (kN)	F_{us} FEA/ F_{cd} Fujikake
12.7	76.2	57.12	53.10	1.08
12.7	101.6	80.45	79.96	1.01
15.9	76.2	65.69	54.27	1.21
15.9	101.6	87.31	81.31	1.07
19.1	76.2	69.62	55.45	1.26
19.1	101.6	105.49	82.67	1.28

Table 5-12: Comparison between ultimate dynamic load obtained from the FEA and the proposed equations by Fujikake et al. (2003) for combined cone bond failure mode

d (mm)	h _{ef} (mm)	$\dot{\epsilon}_s$ (s ⁻¹)	$\dot{\epsilon}_d$ (s ⁻¹)	$\dot{\epsilon}_d/\dot{\epsilon}_s$	FEA		Regression F _u (kN)	Fujikake Equation (5.5)			F _{ud} FEA/ F _{ccb} Fujikake
					F _{us} (kN)	F _{ud} (kN)		F _{cd} (kN)	F _b (kN)	F _{ccb} (kN)	
12.7	76.2	10 ⁻⁵	10 ⁻³	10 ²	57.12	63.33	60.63	18.48	38.38	56.86	1.11
12.7	76.2	10 ⁻⁵	10 ⁻¹	10 ⁴	57.12	67.39	66.42	20.88	40.75	61.63	1.09
12.7	76.2	10 ⁻⁵	10	10 ⁶	57.12	71.14	72.76	31.01	43.26	74.28	0.96
12.7	76.2	10 ⁻⁵	10 ²	10 ⁷	57.12	88.11	76.15	44.55	44.58	89.12	0.99
12.7	101.6	10 ⁻⁵	10 ⁻³	10 ²	80.45	88.59	85.39	18.48	62.04	80.52	1.10
12.7	101.6	10 ⁻⁵	10 ⁻¹	10 ⁴	80.45	92.31	93.54	20.88	65.87	86.75	1.06
12.7	101.6	10 ⁻⁵	10	10 ⁶	80.45	95.49	102.47	31.01	69.93	100.95	0.95
12.7	101.6	10 ⁻⁵	10 ²	10 ⁷	80.45	98.60	107.25	44.55	72.06	116.61	0.85
15.9	76.2	10 ⁻⁵	10 ⁻³	10 ²	65.69	69.70	69.72	19.28	47.00	66.28	1.05
15.9	76.2	10 ⁻⁵	10 ⁻¹	10 ⁴	65.69	74.94	76.38	21.79	49.90	71.69	1.05
15.9	76.2	10 ⁻⁵	10	10 ⁶	65.69	87.36	83.67	32.37	52.97	85.34	1.02
15.9	76.2	10 ⁻⁵	10 ²	10 ⁷	65.69	118.21	87.57	46.49	54.58	101.07	1.17
15.9	101.6	10 ⁻⁵	10 ⁻³	10 ²	87.31	94.88	92.67	19.28	75.97	95.25	1.00
15.9	101.6	10 ⁻⁵	10 ⁻¹	10 ⁴	87.31	101.48	101.52	21.79	80.66	102.45	0.99
15.9	101.6	10 ⁻⁵	10	10 ⁶	87.31	108.31	111.21	32.37	85.63	118.00	0.92
15.9	101.6	10 ⁻⁵	10 ²	10 ⁷	87.31	124.28	116.40	46.49	88.23	134.73	0.92
19.1	76.2	10 ⁻⁵	10 ⁻¹	10 ⁴	69.62	89.32	80.95	22.70	60.98	83.68	1.07
19.1	76.2	10 ⁻⁵	10	10 ⁶	69.62	114.01	88.68	33.72	64.75	98.47	1.16

19.1	101.6	10^{-5}	10^{-3}	10^2	105.49	113.94	111.97	20.09	92.85	112.94	1.01
19.1	101.6	10^{-5}	10^{-1}	10^4	105.49	120.78	122.66	22.70	98.58	121.28	1.00
19.1	101.6	10^{-5}	10	10^6	105.49	139.14	134.37	33.72	104.66	138.38	1.01
19.1	101.6	10^{-5}	10^2	10^7	105.49	196.53	140.63	48.44	107.84	156.28	1.26
19.1	127.0	10^{-5}	10^{-3}	10^2	157.28	161.79	166.94	20.09	128.26	148.35	1.09
19.1	127.0	10^{-5}	10^{-1}	10^4	157.28	169.02	182.87	22.70	136.18	158.88	1.06
19.1	127.0	10^{-5}	10	10^6	157.28	185.58	200.33	33.72	144.58	178.30	1.04
19.1	127.0	10^{-5}	10^2	10^7	157.28	217.96	209.68	48.44	148.97	197.41	1.10
19.1	152.4	10^{-5}	10^{-3}	10^2	179.40	187.48	190.42	20.09	163.67	183.76	1.02
19.1	152.4	10^{-5}	10^{-1}	10^4	179.40	196.47	208.59	22.70	173.77	196.47	1.00
19.1	152.4	10^{-5}	10	10^6	179.40	211.45	228.51	33.72	184.49	218.22	0.97
19.1	152.4	10^{-5}	10^2	10^7	179.40	234.18	239.17	48.44	190.10	238.54	0.98

*F_{us}: ultimate static load obtained from FEA, F_{ud}: ultimate dynamic load obtained from FEA

5.2 Adhesive anchors under shear load

5.2.1 Finite element modelling for adhesive anchors under shear load

Shear behaviour of adhesive anchors was investigated using LS-DYNA finite element program. Adhesive anchor diameters of 12.7 mm, 15.9 mm and 19.1 mm with embedment depths of 76.2 mm, 101.6 mm, and 152.4 mm, respectively, were investigated. Figure 5-34 shows the geometric configuration and boundary conditions for the adhesive anchor model.

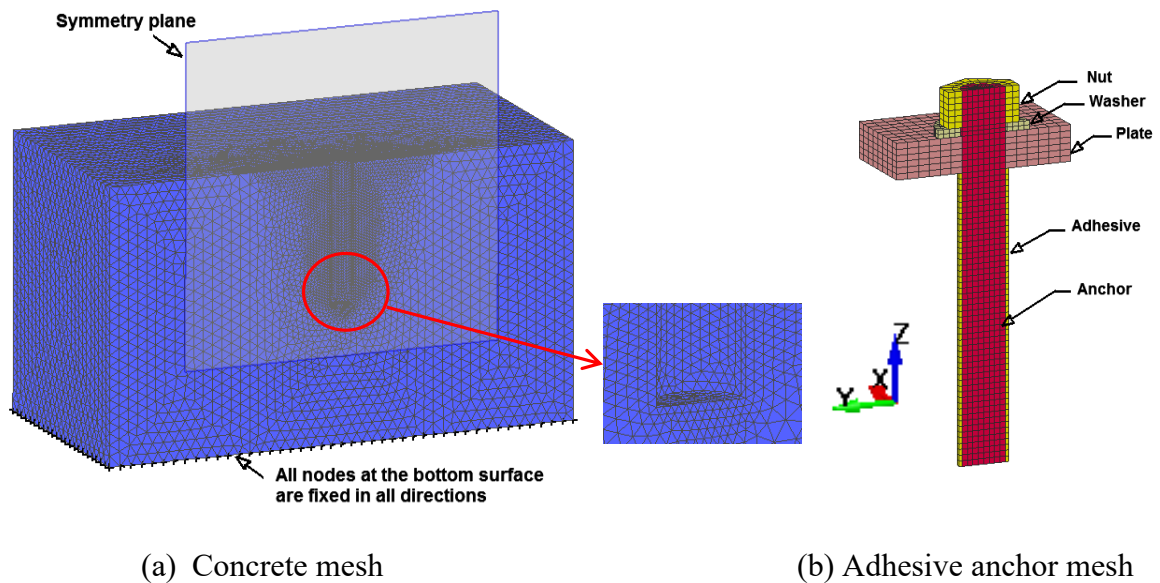


Figure 5-34: Geometric configuration and boundary conditions of adhesive anchor model

5.2.2 Validation of adhesive anchor model under shear load

The adhesive anchor model was validated by comparing the finite element results with the experimental results obtained by Cattaneo and Muciaccia (Cattaneo & Muciaccia, 2015).

A finite element model, representing the test conducted by Cattaneo and Muciaccia, was

developed using LS-DYNA. The adhesive anchor was placed at a distance of 40 mm from the concrete free edge. Epoxy adhesive of 1 mm thickness was used. The steel anchor used had yield strength of 400 MPa, diameter of 12-mm and embedment depth of 110 mm. The compressive strength of the concrete block used in the experimental test and numerical model was 90 MPa.

A mesh sensitivity analysis was carried out to obtain optimum mesh size that gives converged results to the experimental test results. BOUNDARY_PRESCRIBED_MOTION_SET in y direction was applied on the anchor plate to represent the shear load. Table 5-13 shows the results of the mesh sensitivity analysis for the adhesive anchor under shear load.

Table 5-13: Effect of mesh size refinement on the convergence of ultimate shear load for adhesive anchor

Model No.	Mesh size (mm)				Ultimate shear load (kN)		Displacement (mm)		Failure mode
	Anchor	Adhesive	Concrete		FEA	EXP.	FEA	EXP.	
			Min.	Max.					
1	1	1	2	8	17.26	18.65	1.27	0.85	Concrete cracking
2	1	1	1	8	17.96		1.27		Concrete cracking
3	0.75	0.50	1	8	19.31		1.24		Concrete cracking

Mesh sizes of 1×1×2 mm, 1×1×1 mm and 0.75×0.5×1 mm give percentage difference of 8.1%, 3.8% and 3.5% in the ultimate shear load respectively compared to the experimental work. Mesh size of model No. 3 yielded converged shear load–displacement behaviour to the experimental behaviour reported by Cattaneo and Muciaccia and selected for the analysis. A comparison of shear load–displacement response of the experimental tests and the finite element analysis is presented in Figure 5-35 and shows that the shear load

increased with the displacement up to the ultimate load followed by a reduction in the shear load until failure. A good agreement was obtained between the finite element analysis and the experimental results. Concrete cracking failure mode was observed from the finite element results similar to that observed by Cattaneo and Muciaccia as shown in Figure 5-36.

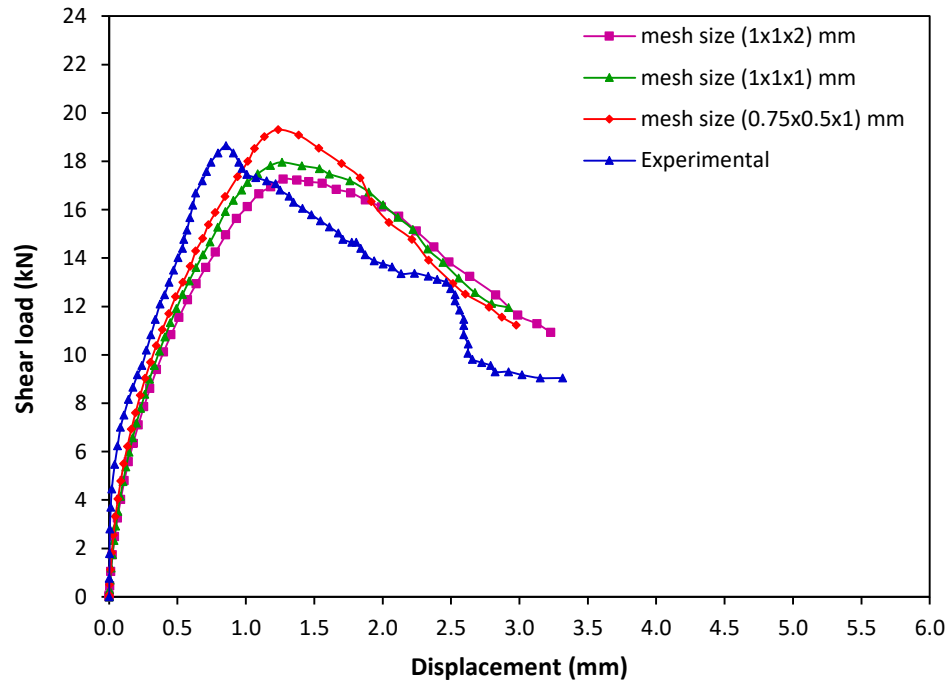


Figure 5-35: Comparison of shear load-displacement relation between FEA and experimental results obtained by Cattaneo et al. (Cattaneo & Muciaccia, 2015)

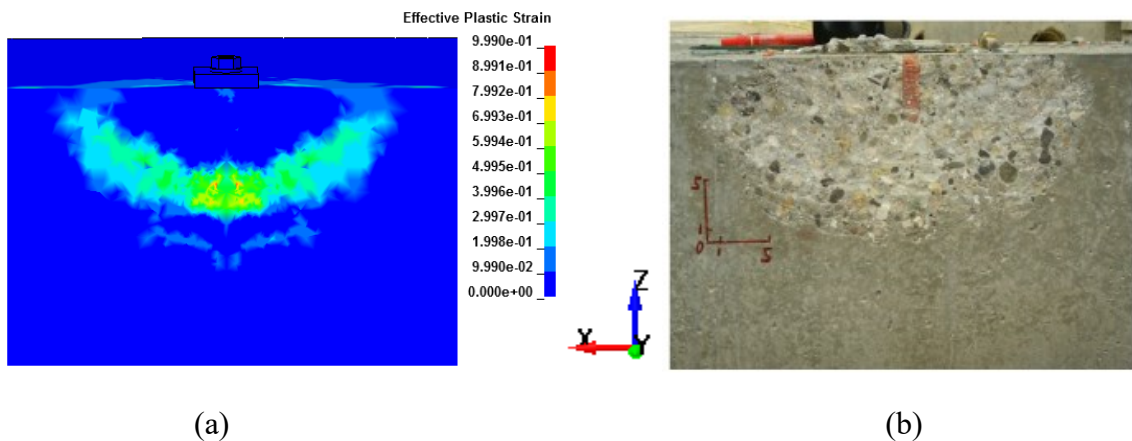


Figure 5-36: Failure mode obtained from:(a) finite element analysis and (b) experimental results obtained by Cattaneo et al. (Cattaneo & Muciaccia, 2015)

5.2.3 Comparison of finite element results with design methods

For the adhesive anchors placed far away from the concrete free edge, pryout failure mode or anchor failure is often the dominant failure modes. The shear failure load of anchors exhibiting pryout failure can be calculated according to ACI 318 (ACI Committee 318, 2011) Equation (4.14). The shear failure load of anchors that exhibit steel anchor failure can be calculated according to ACI 318 as in Equation (4.18) (ACI Committee 318, 2011). A comparison of the ultimate shear load obtained from the finite element analysis at strain rate of 10^{-5} s^{-1} and ACI 318 method (Equations 4.14 and 4.18) is presented in Table 5-14. It can be seen that the ultimate shear capacity increased with increase in the anchor diameter from 12.7 mm to 19.1 mm, at the same embedment depth. Similar observation on the effect of anchor diameter on the shear capacity was reported by Jebara et al. (Jebara et al., 2016). A good agreement is obtained between the ultimate shear load obtained from the finite element analysis and the ACI 318 method.

Table 5-14: Comparison between FEA and ACI 318 method

Model No.	d (mm)	h_{ef} (mm)	Failure load (kN)		FEA/ACI 318	*Failure mode (FEA)
			FEA static ($\dot{\epsilon} = 10^{-5} \text{ s}^{-1}$)	ACI 318		
1	12.7	76.2	79.93	78.59	1.02	S
2	12.7	101.6	81.64	78.59	1.04	S
3	12.7	152.4	81.85	78.59	1.04	S
4	15.9	76.2	94.31	109.24	0.86	PR
5	15.9	101.6	103.73	123.18	0.84	S
6	15.9	152.4	106.5	123.18	0.86	S
7	19.1	76.2	116.26	109.24	1.06	PR
8	19.1	101.6	146.45	168.19	0.87	PR
9	19.1	152.4	164.33	177.76	0.92	S

*Failure mode: S = Steel anchor failure, PR = Pryout failure

5.2.4 Crack pattern for adhesive anchors under shear load

Contours of effective plastic strain for adhesive anchors with 12.7 mm, 15.9 mm and 19.1 mm diameters and embedment depths of 76.2 mm, 101.6 mm and 152.4 mm at strain rate of 10^{-5} s^{-1} are shown in Figure 5-37. Two failure modes were observed for the adhesive anchors at low strain rate of 10^{-5} s^{-1} : pryout failure and steel anchor failure.

As shown in the figure, pryout failure was observed for the 15.9-mm and 19.1-mm diameter anchors with embedment depth of 76.2 mm whereas steel anchor failure was observed for the 12.7-mm anchor diameter. For the embedment depth of 101.6 mm pryout failure was observed for the anchor diameter of 19.1 mm. Steel anchor failure was observed for the 12.7-mm and 15.9-mm anchor diameters wherein the embedment depth to anchor diameter ratio was sufficient to prevent pryout failure. Also, steel anchor failure was observed for all the diameters at embedment depth of 152.4 mm. In general, the failure mode of the adhesive anchor system depends on the anchor stiffness (diameter) and embedment depth. For the same anchor diameter, increase in the embedment depth can change the failure mode from concrete pryout failure to steel anchor fracture. Conversely at the same embedment depth, increase in anchor diameter can lead to concrete pryout failure. When the shear load is applied on the anchor plate, the anchor resists the shear load and transfers the load to the adhesive and then to the concrete resulting in compressive stresses in the concrete in front of the anchor. These stresses increase with the increase in the applied shear load, create concrete cracking under the anchor plate, result in displacement of the anchor plate in vertical direction, rotation of the anchor plate and generating a compression force on the concrete at the front end tip of the plate. A rotational moment will be generated due to the tensile force in the steel anchor and the compression force on the concrete that

results in breaking half concrete cone at the back side on the anchor resulting in pryout failure. On the other hand, when the concrete resistance to the applied shear load is higher than the anchor strength, the anchor bends due to the applied shear load resulted in steel anchor failure. Cook et al. attributed the steel anchor failure of the anchorage to concrete system under shear load to the interaction of the shear, tensile and bending stresses (Cook et al., 2013).

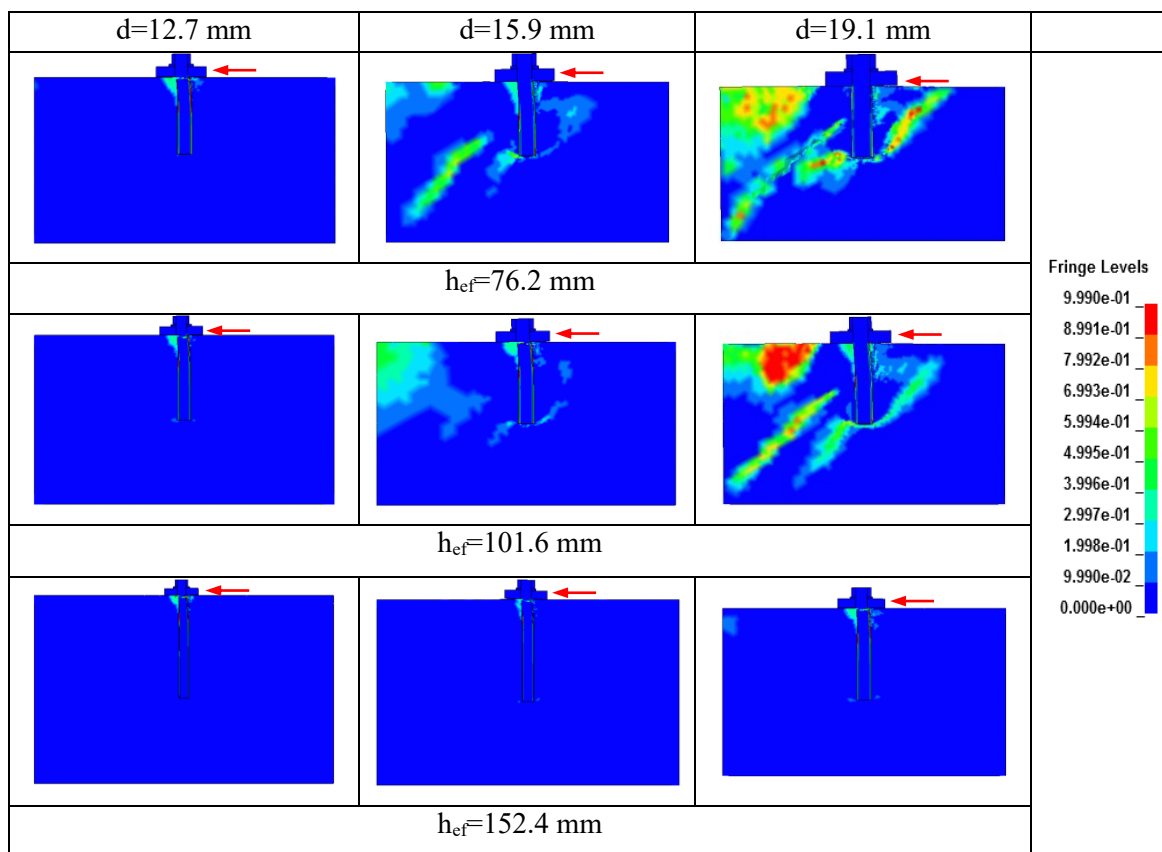
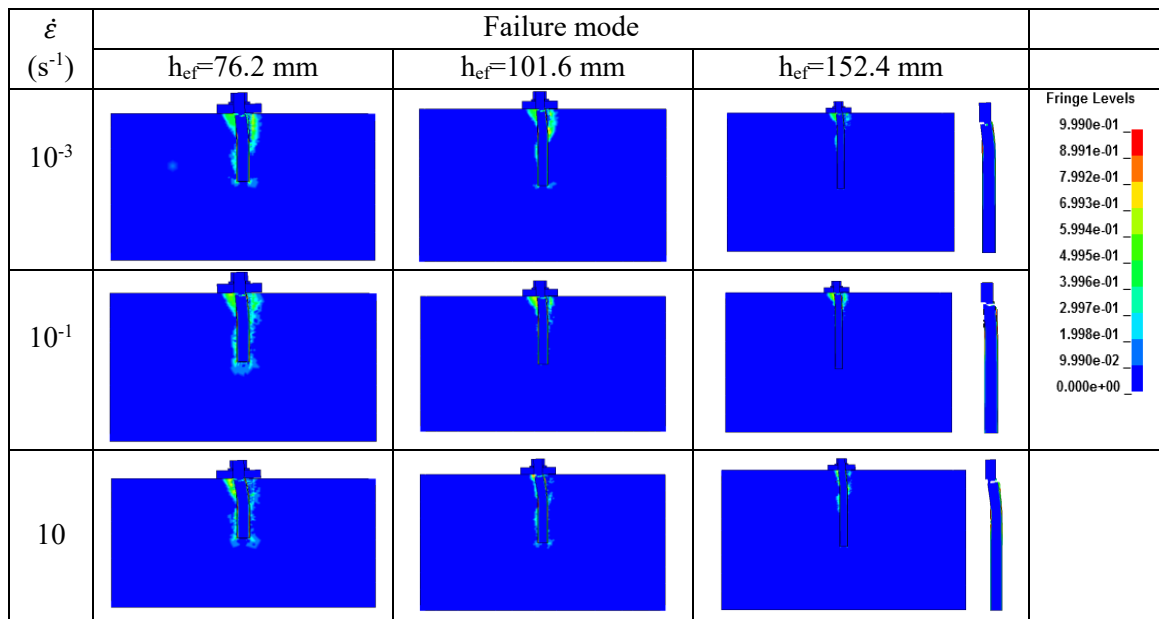


Figure 5-37: Plastic strain contours for adhesive anchor under shear load at strain rate of 10^{-5} s^{-1}

5.2.5 Effect of strain rate on the level of damage and failure mode

Figures 5-38, 5-39 and 5-40 present failure mechanism for 12.7-mm, 15.9-mm and 19.1-mm diameter adhesive anchors subjected to different shear strain rates of loading. The cracks initiated at the interface between concrete and adhesive on the top surface of the concrete in the direction of the applied load (ahead of the anchor) and propagated along the anchor embedment depth leading to failure. As shown in Figures 5-38 and 5-39, at strain rates ranging from 10^{-3} s^{-1} to 10^3 s^{-1} , concrete spalling followed by steel anchor failure was observed for the 12.7-mm and 15.9-mm diameter anchors. For anchor diameter of 19.1 mm (Figure 5-40) concrete spalling was observed at strain rates of 10^{-3} s^{-1} , 10^{-1} s^{-1} and 10 s^{-1} at embedment depth of 76.2 mm, while steel anchor failure was observed at strain rates of 10^2 s^{-1} and 10^3 s^{-1} . Also, steel anchor failure was observed for embedment depths of 101.6 mm and 152.4 mm at strain rates ranging from 10^{-3} s^{-1} to 10^3 s^{-1} . When concrete spalling occurs, the stresses are concentrated in the concrete in front of the anchor resulting in concrete cracking without breakout of a concrete cone behind the anchor.



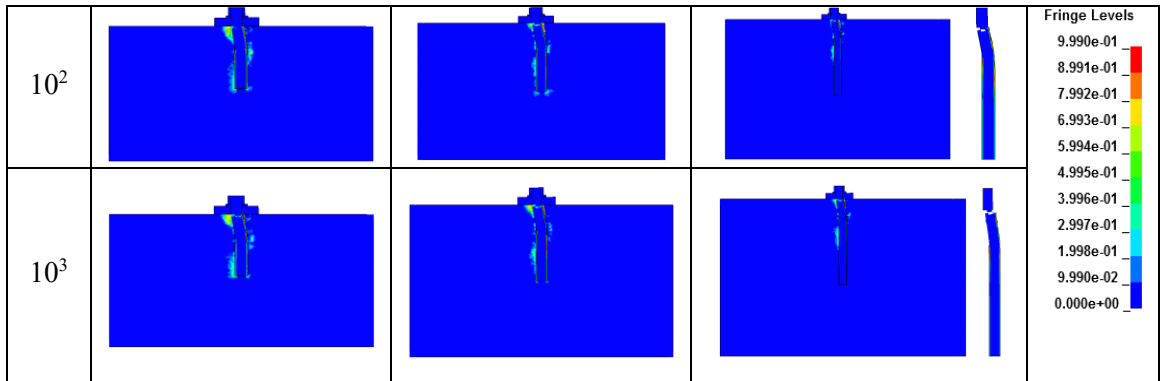


Figure 5-38: Failure mode for 12.7 mm diameter adhesive anchor at different strain rates

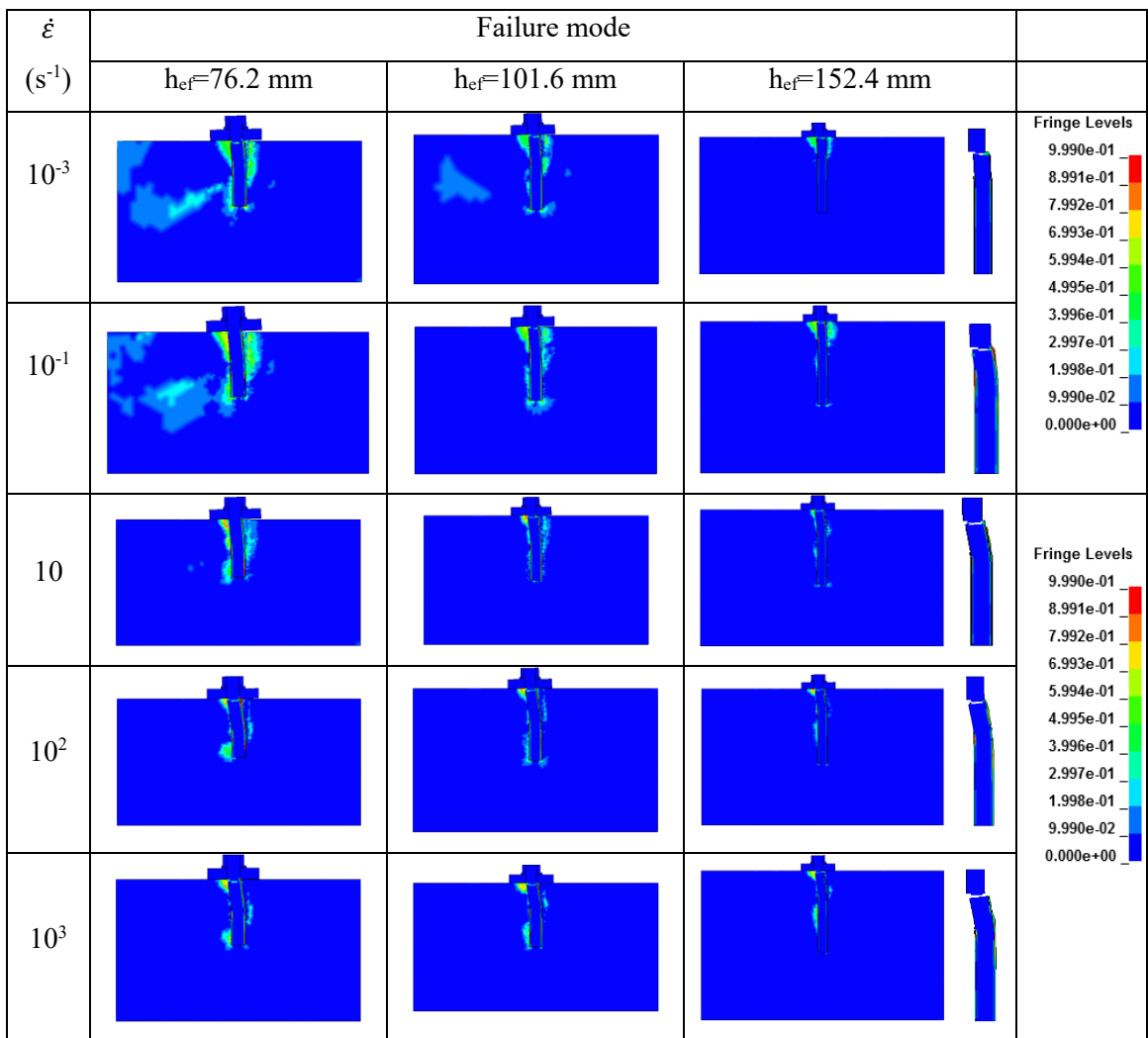


Figure 5-39: Failure mode for 15.9 mm diameter adhesive anchor at different strain rates

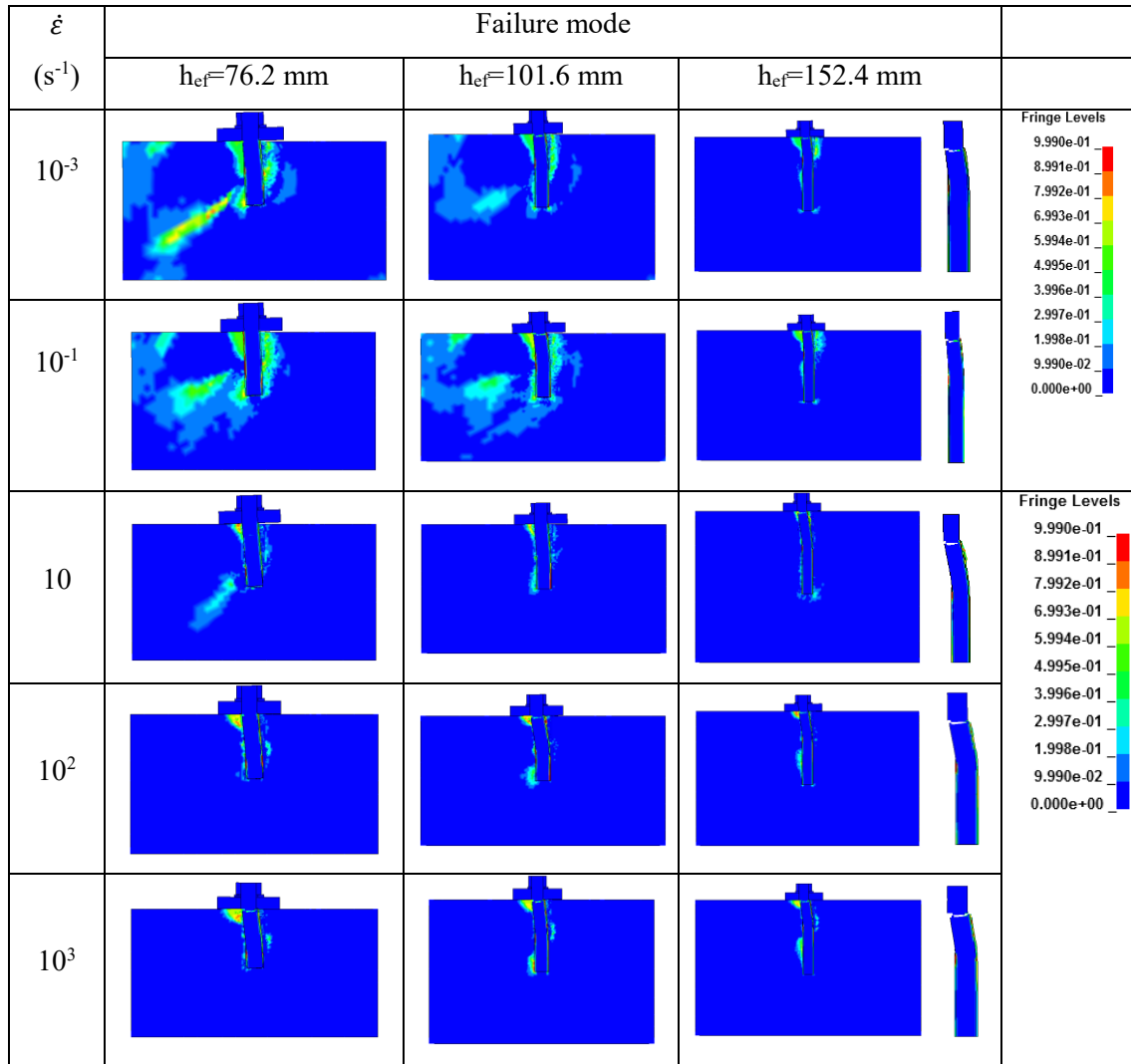


Figure 5-40: Failure mode for 19.1 mm diameter adhesive anchor at different strain rates

It can be seen from Figure 5-38, 5-39 and 5-40 that the strain rate has an influence on the failure mode. The figures show that, anchor diameter of 19.1 mm exhibited higher level of concrete damage compared to the smaller anchor diameter of 12.7-mm for all the strain rates investigated.

Typical Von-Mises stress contours (MPa) in the steel anchor are presented in Figure 5-41 to show the mechanism of steel anchor failure of 19.1-mm diameter adhesive anchor with 152.4 mm embedment depth at strain rate of 10 s⁻¹. As shown in the figure, the Von-Mises

stresses are concentrated around the top part of the anchor where the shear load is applied then propagated along the embedment depth of the anchor, followed by anchor bending, bond failure and steel anchor failure.

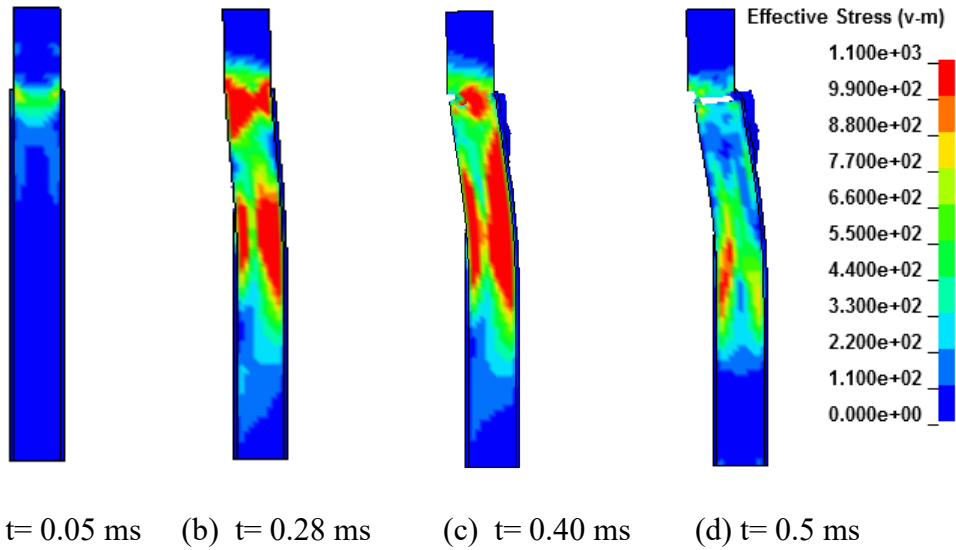


Figure 5-41: Failure mechanism of 19.1 mm diameter adhesive anchor with 152.4 mm embedment depth; (a) stress concentration around the anchor, (b) anchor bending with bond failure, (c) initiation of anchor fracture, (d) complete anchor failure

Table 5-15 presents the failure modes for the adhesive anchors at different strain rates.

Table 5-15: Failure mode for adhesive anchors under shear load at different strain rates

Model No.	d (mm)	h_{ef} (mm)	*Failure mode					
			Strain rate (s^{-1})					
			$\dot{\epsilon}=10^{-5}$	$\dot{\epsilon}=10^{-3}$	$\dot{\epsilon}=10^{-1}$	$\dot{\epsilon}=10$	$\dot{\epsilon}=10^2$	$\dot{\epsilon}=10^3$
1	12.7	76.2	S	S	S	S	S	S
2	12.7	101.6	S	S	S	S	S	S
3	12.7	152.4	S	S	S	S	S	S
4	15.9	76.2	PR	S	S	S	S	S
5	15.9	101.6	S	S	S	S	S	S
6	15.9	152.4	S	S	S	S	S	S
7	19.1	76.2	PR	CS	CS	CS	S	S
8	19.1	101.6	PR	S	S	S	S	S
9	19.1	152.4	S	S	S	S	S	S

*Failure mode: PR= pryout failure, CS= concrete spalling, S=steel anchor failure

5.2.6 Effect of design parameters on failure mode and ultimate shear load

Figures 5-42, 5-43 and 5-44 show the effect of strain rate on the failure mode and ultimate shear load for the adhesive anchors. As shown in Figure 5-42 and Figure 5-43, slight increase in the ultimate shear load with the increase in the strain rate is observed for the anchor diameters of 12.7 mm and 15.9 mm. Also, it can be seen that increasing the embedment depth from 76.2 mm to 152.4 mm at the same strain rate has insignificant influence on the ultimate shear load. Where, steel anchor failure was observed for the 12.7-mm and 15.9-mm diameter adhesive anchors at all the strain rates investigated except for the 15.9-mm diameter adhesive anchor with 76.2 mm embedment depth which exhibited pryout failure. This is attributed to the concrete resistance to the applied load is higher than the capacity of the small anchor diameters of 12.7-mm and 15.9-mm leads to steel fracture. However, the increase in the shear load with increasing the embedment depth is remarkable for the 19.1-mm diameter adhesive anchor (Figure 5-44).

As shown in Figure 5-44 for the 19.1-mm diameter adhesive anchor with embedment depth of 76.2 mm, the failure mode transitioned from pryout failure (PR) at strain rate of 10^{-5} s^{-1} to concrete spalling (CS) at strain rates of 10^{-3} s^{-1} , 10^{-1} s^{-1} , and 10 s^{-1} and then to steel failure (S) at strain rates of 10^2 s^{-1} and 10^3 s^{-1} . Concrete spalling failure mode occurs when the anchor placed far from the concrete free edge where the concrete resists the shear forces transferred from the anchor causing concrete spall. However, when the anchor placed near the concrete free edge, concrete breakout can occur. It can be seen from Figure 5-44, at strain rates of 10^{-3} s^{-1} , 10^{-1} s^{-1} and 10 s^{-1} transitions in the failure mode from concrete spalling to steel anchor failure is observed when the embedment depth increased from 76.2 mm to 152.4 mm. At the 101.6 mm and 152.4 mm embedment depths, steel anchor failure

was observed at all the strain rates investigated, while at low strain rate of 10^{-5} s^{-1} with embedment depth of 101.6 mm, pryout failure was observed.

It can be seen from Figure 5-44 the ultimate shear load for the 76.2 mm embedment depth increased from 116.26 kN at strain rate of 10^{-5} s^{-1} to 154.81 kN at strain rate of 10 s^{-1} . These values are 180.18 kN and 184.17 kN at strain rates of 10^2 s^{-1} and 10^3 s^{-1} respectively. The increase in the ultimate shear load is due to the increase in the concrete and steel strength with the increase in the strain rate from 10^{-5} s^{-1} to 10 s^{-1} , where concrete spalling failure mode is observed. However, at high strain rates of 10^2 s^{-1} and 10^3 s^{-1} , the increase in the ultimate shear load is due to the increase of steel strength at high strain rate where steel anchor failure is observed. For the embedment depth of 101.6 mm, the increase in the ultimate load was from 146.45 kN at strain rate of 10^{-5} s^{-1} to 170.49 kN at strain rate of 10^3 s^{-1} . Further increase in the strain rate exhibited slight increase in the ultimate shear load. Similar behaviour was observed for the anchor embedment depth of 152.4 mm where steel anchor failure is the dominant failure mode at all the strain rates investigated.

As shown in Figure 5-44, the strain rate affects the failure mode for the anchor diameter of 19.1-mm where transition from pryout failure to concrete spalling and then to steel anchor failure is observed. Also, it can be seen from Figures 5-43 and 5-44 that the failure mode is influenced by the anchor diameter and embedment depth. Pryout failure (PR) is observed at low strain rate of 10^{-5} s^{-1} for anchor diameters of 15.9-mm and 19.1 mm at embedment depth of 76.2 mm. Also, pryout failure was observed for anchor diameter of 19.1-mm at embedment depth of 101.6 mm. Concrete spalling (CS) was observed at strain rate of 10^2

3 s^{-1} to 10 s^{-1} for anchor diameter of 19.1-mm at embedment depth of 76.2 mm. Steel anchor failure (S) was observed for most of the adhesive anchors investigated. Also, it can be seen from the figures that the ultimate shear load increased with the increase in the strain rate and diameter for the adhesive anchors investigated. Anchor diameter of 19.1-mm gave the highest ultimate shear load at all the embedment depths investigated. This is attributed to the increase in the anchor stiffness and anchor resistance to the applied shear load and thus higher load is required for fracturing the anchor.

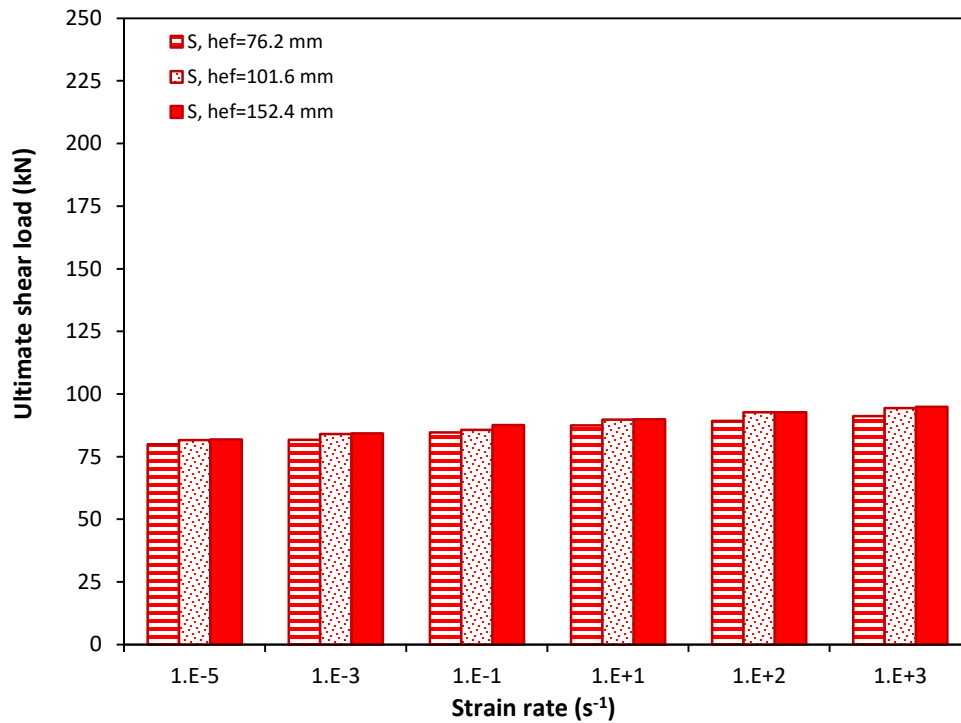


Figure 5-42: Effect of strain rate on the failure mode and ultimate shear load for the adhesive anchor diameter of 12.7 mm

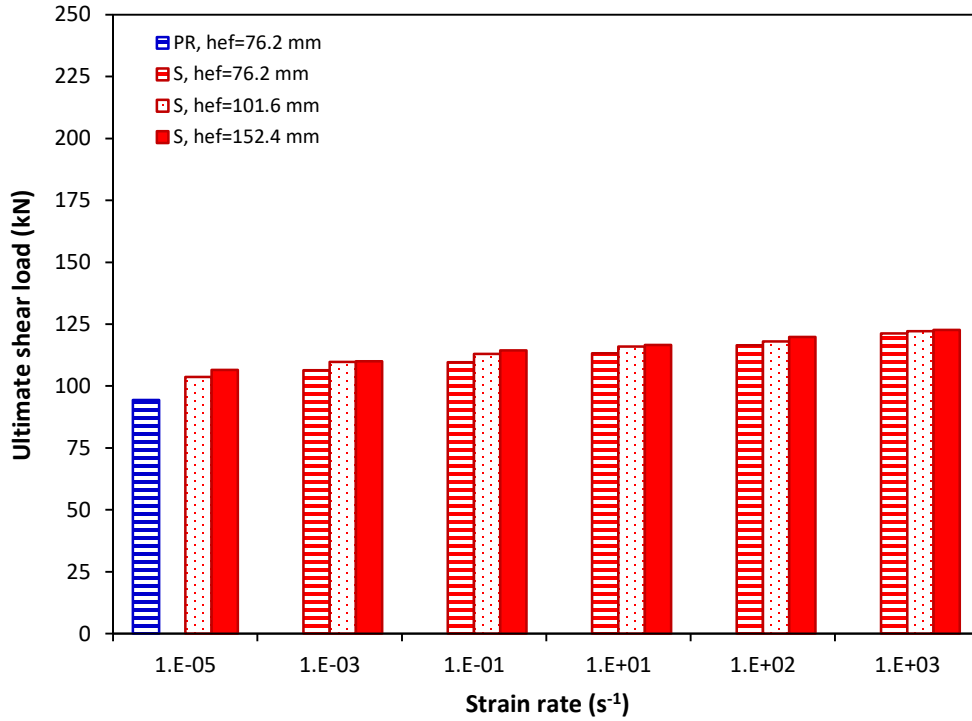


Figure 5-43: Effect of strain rate on the failure mode and ultimate shear load for the adhesive anchor diameter of 15.9 mm

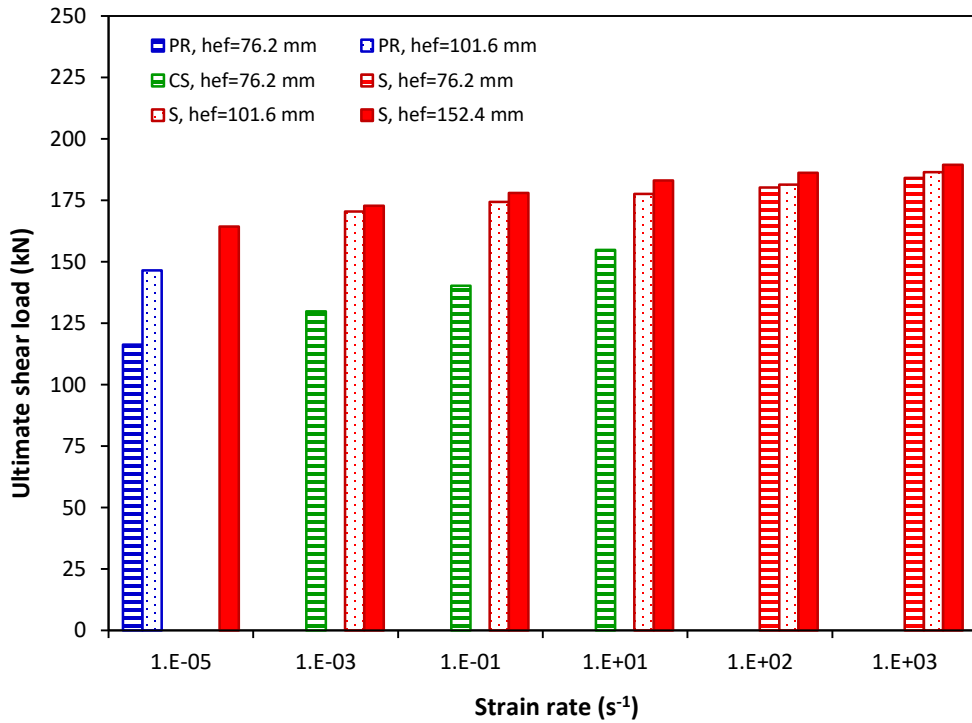


Figure 5-44: Effect of strain rate on the failure mode and ultimate shear load for the adhesive anchor diameter of 19.1 mm

5.2.7 Effect of strain rate on the shear behaviour of adhesive anchors

The shear behaviour of the adhesive anchors embedded into concrete at strain rates in the range of 10^{-5} s^{-1} to 10^3 s^{-1} was investigated. Load-displacement behaviour of the 12.7-mm diameter adhesive anchor at strain rates of 10^{-5} s^{-1} , 10^{-3} s^{-1} , 10^{-1} s^{-1} , 10 s^{-1} , 10^2 s^{-1} and 10^3 s^{-1} are shown in Figures 5-45, 5-46, 5-47, 5-48, 5-49 and 5-50 respectively at embedment depths of 76.2 mm, 101.6 mm and 152.4 mm.

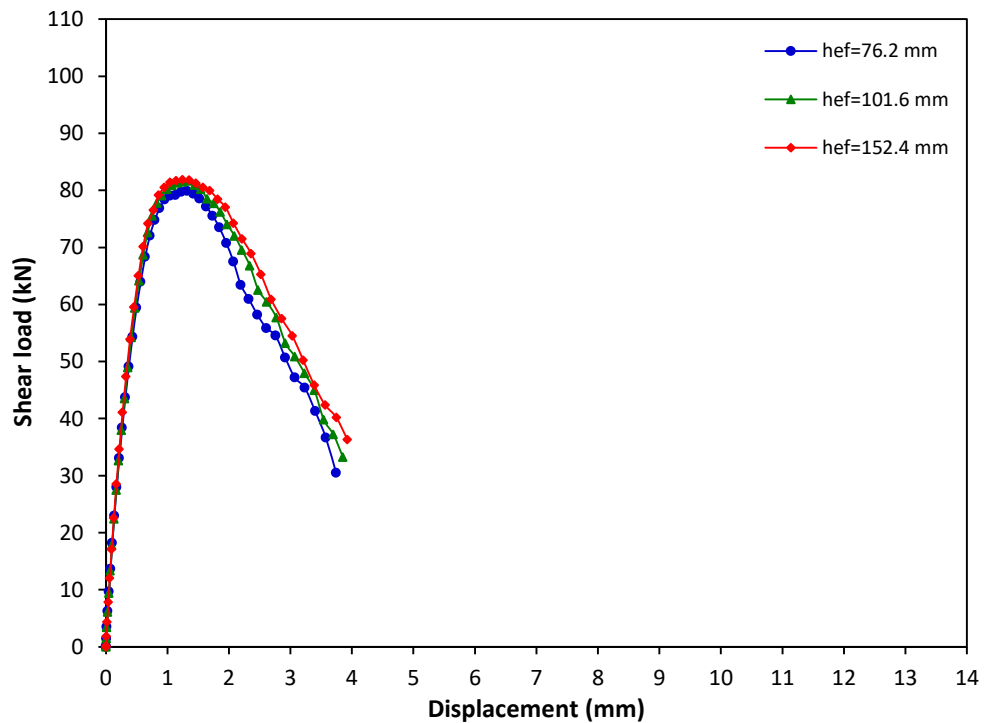


Figure 5-45: Shear load-displacement graph for 12.7-mm diameter adhesive anchor at strain rate of 10^{-5} s^{-1}

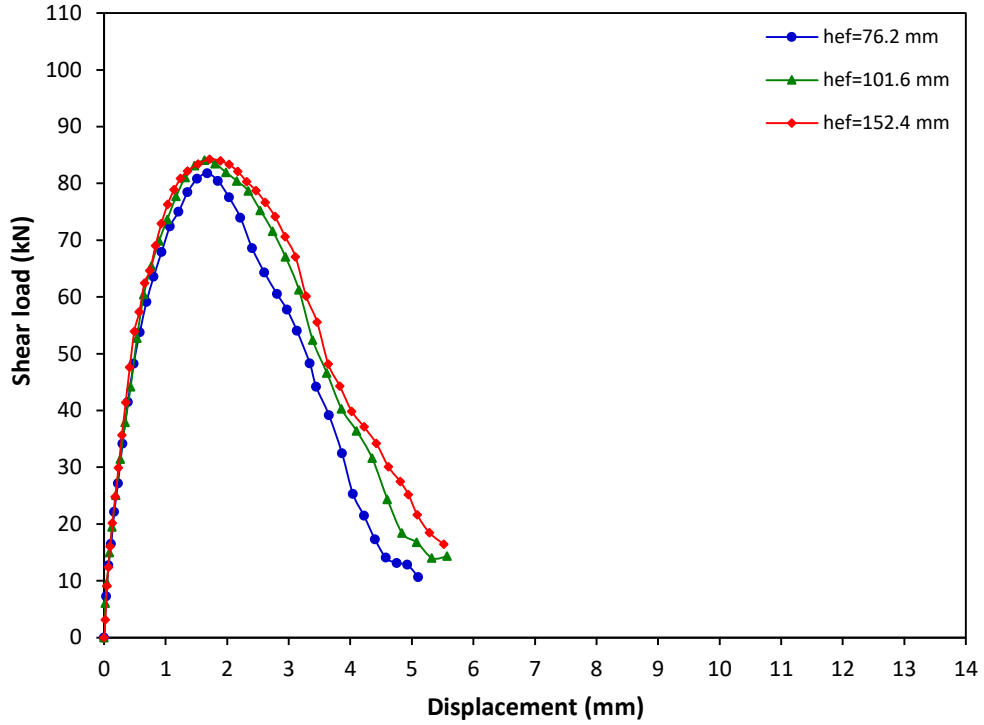


Figure 5-46: Shear load-displacement graph for 12.7-mm diameter adhesive anchor at strain rate of 10^{-3} s^{-1}

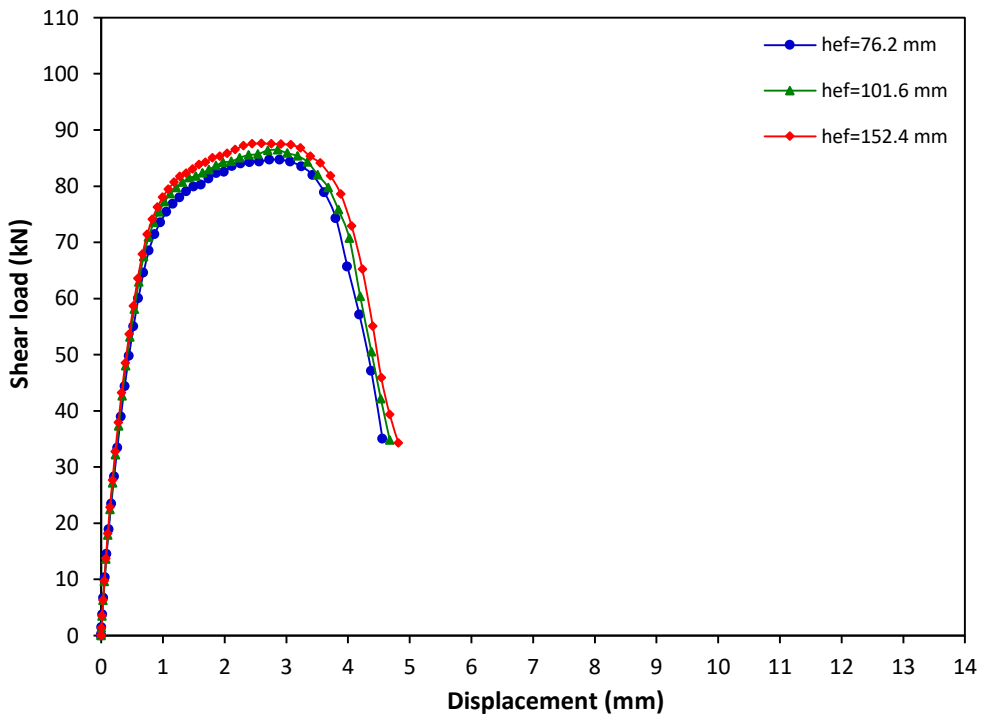


Figure 5-47: Shear load-displacement graph for 12.7-mm diameter adhesive anchor at strain rate of 10^{-1} s^{-1}

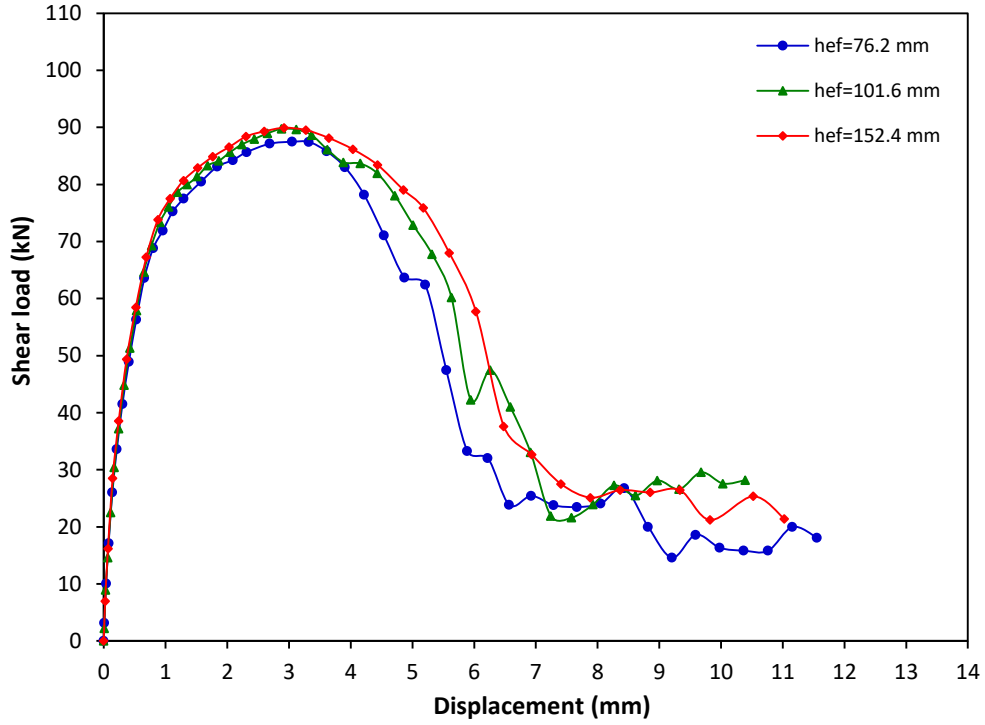


Figure 5-48: Shear load-displacement graph for 12.7-mm diameter adhesive anchor at strain rate of 10 s^{-1}

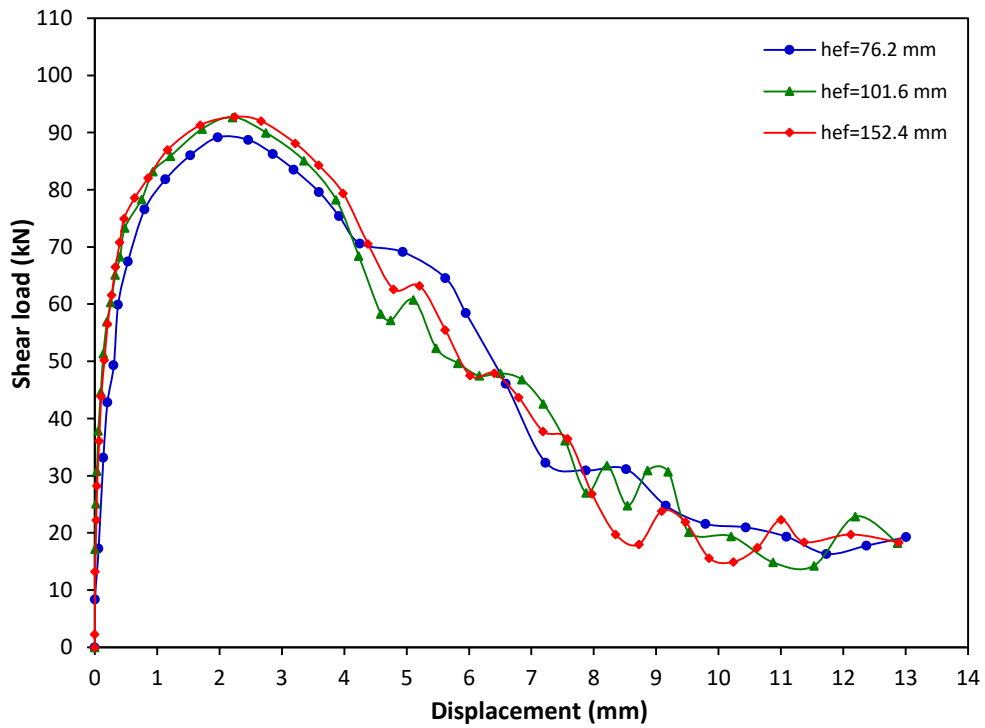


Figure 5-49: Shear load-displacement graph for 12.7-mm diameter adhesive anchor at strain rate of 10^2 s^{-1}

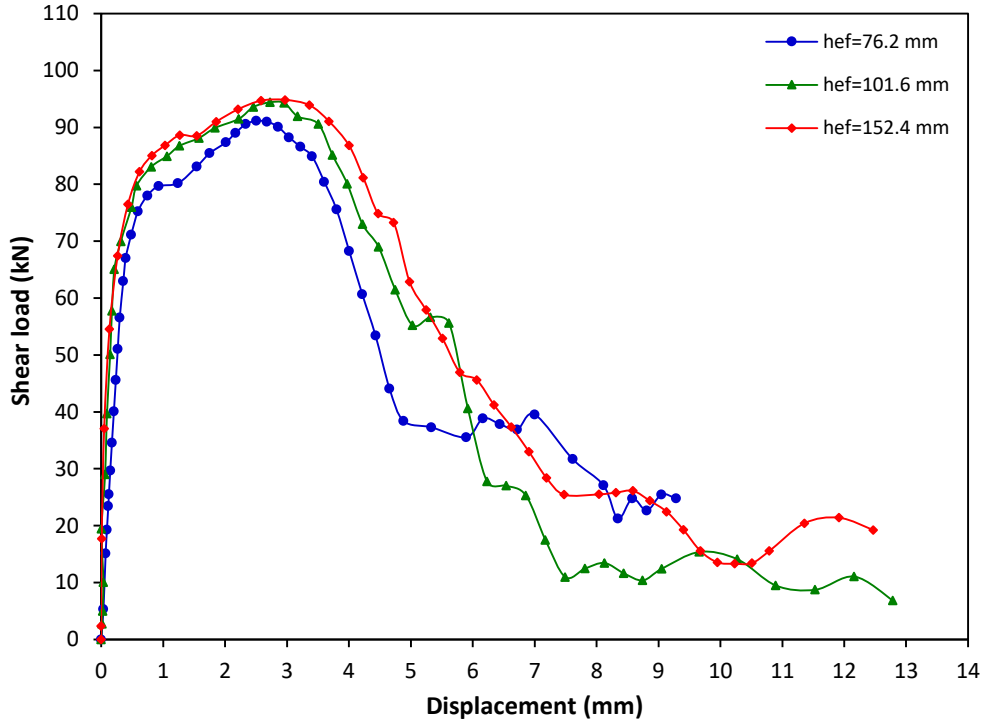


Figure 5-50: Shear load-displacement graph for 12.7-mm diameter adhesive anchor at strain rate of 10^3 s^{-1}

As shown from the Figures 5-45 to 5-50, the shear load increased with the displacement until the ultimate value. This is attributed to the concrete resistance to the applied load where the shear load is transferred from the anchor plate to the anchor and then to the concrete through the adhesive material. The post-peak response shows a reduction in the load with further increase in displacement until failure. It can be seen from Table 5-16 that the shear capacity of the adhesive anchor increased as the strain rate increased from 10^{-5} s^{-1} to 10^3 s^{-1} . At strain rates of 10^{-5} s^{-1} , 10^{-3} s^{-1} and 10^{-1} s^{-1} (Figures 5-45, 5-46 and 5-47) the shear load increased with the displacement until reaching the ultimate value, and then decreased until complete failure. At strain rates of 10 s^{-1} , 10^2 s^{-1} and 10^3 s^{-1} (Figures 5-48, 5-49 and 5-50), the shear load increased with the displacement up to the ultimate shear load followed by a decrease in the shear load and fluctuation about the residual shear load. It

can be seen from the figures that the ultimate shear loads of the anchors at strain rates ranging from 10^{-5} s^{-1} to 10^3 s^{-1} were almost the same irrespective of the embedment depth as the predominant failure mode was steel anchor fracture.

The shear load-displacement behaviour of 15.9-mm and 19.1-mm diameter adhesive anchors with embedment depths of 76.2 mm, 101.6 mm and 152.4 mm at strain rates in the range between 10^{-5} s^{-1} to 10^3 s^{-1} is showed similar response to the 12.7-mm diameter adhesive anchor. The results for these adhesive anchors are presented in Appendix F.

Tables 5-16, 5-17 and 5-18 present the ultimate shear load-displacement results for the 12.7-mm, 15.9-mm and 19.1-mm diameter adhesive anchors respectively. Where δ is the displacement at the ultimate shear load. It can be seen from Tables 5-16, 5-17 and 5-18 that as the strain rate increased the ultimate shear capacity of the adhesive anchorage systems increased. The increased shear capacity is enhanced with increased anchor diameter from 12.7-mm to 19.1-mm and for all the embedment depths investigated. It can be seen from Tables 5-16 and 5-17, steel failure is the dominant failure mode for adhesive anchor diameters of 12.7-mm and 15.9-mm for all embedment depths and strain rates investigated, except for the 15.9-mm diameter anchor with embedment depth of 76.2 mm at low strain rate of 10^{-5} s^{-1} that exhibited pryout failure, where the embedment depth to diameter ratio is sufficient to obtain pryout failure. For adhesive anchor diameter of 19.1-mm (Table 5-18), pryout failure was observed for the embedment depths of 76.2 mm and 101.6 mm while steel failure was observed at embedment depth of 152.4 mm at low strain rate of 10^{-5} s^{-1} . Concrete spalling was observed for the shallow embedment depth of 76.2 mm at strain

rates of 10^{-3} s^{-1} , 10^{-1} s^{-1} and 10 s^{-1} while steel anchor failure was observed for the embedment depths of 101.6 mm and 152.4 mm. Also, steel failure was observed at strain rates of 10^2 s^{-1} and 10^3 s^{-1} and for all embedment depths investigated. It can be stated that the strain rate has an effect on the shear load and failure mode.

Table 5-16: Ultimate shear load and displacement results for the 12.7-mm diameter adhesive anchor

Model No.	d (mm)	h_{ef} (mm)	$\dot{\epsilon}$ (s^{-1})	V_u (kN)	δ (mm)	Failure mode
1	12.7	76.2	10^{-5}	79.93	1.32	S
2		101.6		81.64	1.35	S
3		152.4		81.85	1.25	S
4	12.7	76.2	10^{-3}	81.75	1.68	S
5		101.6		84.07	1.63	S
6		152.4		84.26	1.72	S
7	12.7	76.2	10^{-1}	84.69	2.89	S
8		101.6		85.72	2.54	S
9		152.4		87.63	2.56	S
10	12.7	76.2	10^1	87.47	3.00	S
11		101.6		89.74	2.89	S
12		152.4		89.91	2.92	S
13	12.7	76.2	10^2	89.19	1.98	S
14		101.6		92.68	2.21	S
15		152.4		92.75	2.25	S
16	12.7	76.2	10^3	91.14	2.50	S
17		101.6		94.39	2.73	S
18		152.4		94.82	2.97	S

Table 5-17: Ultimate shear load and displacement results for the 15.9-mm diameter adhesive anchor

Model No.	d (mm)	h_{ef} (mm)	$\dot{\epsilon}$ (s^{-1})	V_u (kN)	δ (mm)	Failure mode
1	15.9	76.2	10^{-5}	94.31	1.57	PR
2		101.6		103.73	1.41	S
3		152.4		106.50	1.39	S
4	15.9	76.2	10^{-3}	106.38	3.07	S
5		101.6		109.69	2.81	S
6		152.4		109.98	2.57	S
7	15.9	76.2	10^{-1}	109.55	2.52	S
8		101.6		113.02	2.73	S
9		152.4		114.41	2.45	S
10	15.9	76.2	10	113.19	2.65	S

11		101.6		115.97	3.51	S
12		152.4		116.58	3.29	S
13	15.9	76.2	10^2	116.43	2.62	S
14		101.6		117.99	3.16	S
15		152.4		119.87	3.09	S
16	15.9	76.2	10^3	121.21	2.59	S
17		101.6		122.16	3.17	S
18		152.4		122.62	3.22	S

Table 5-18: Ultimate shear load and displacement results for the 19.1-mm diameter adhesive anchor

Model No.	d (mm)	h_{ef} (mm)	$\dot{\epsilon}$ (s^{-1})	V_u (kN)	δ (mm)	Failure mode
1	19.1	76.2	10^{-5}	116.26	1.12	PR
2		101.6		146.45	1.26	PR
3		152.4		164.33	1.47	S
4	19.1	76.2	10^{-3}	129.89	2.08	CS
5		101.6		170.49	1.93	S
6		152.4		172.78	1.91	S
7	19.1	76.2	10^{-1}	140.24	2.74	CS
8		101.6		174.37	3.56	S
9		152.4		178.02	3.43	S
10	19.1	76.2	10	154.81	1.36	CS
11		101.6		177.65	1.11	S
12		152.4		183.08	1.28	S
13	19.1	76.2	10^2	180.18	1.19	S
14		101.6		181.34	1.24	S
15		152.4		186.14	1.23	S
16	19.1	76.2	10^3	184.17	1.66	S
17		101.6		186.51	1.58	S
18		152.4		189.42	1.77	S

5.2.8 Effect of strain rate on the ultimate shear load and DIF of adhesive anchors

Figures 5-51, 5-52 and 5-53 present the effect of strain rate on the ultimate shear load and DIF for the 12.7-mm, 15.9-mm and 19.1-mm diameter adhesive anchors with different embedment depths. As shown in the figures, the ultimate shear load increased with the increase in the strain rate from $10^{-5} s^{-1}$ to $10^3 s^{-1}$ for the adhesive anchors investigated. Similar observation on the cast-in-place and post-installed (undercut and expansion)

anchors subjected to dynamic shear load was reported by Gross et al. (2001) (Gross et al., 2001). Gross et al. found that the ultimate shear loads for the investigated anchors under dynamic load is higher than that under static load.

The relationship between the ultimate shear load and strain rate is approximately linear for the 12.7-mm and 15.9-mm diameter adhesive anchors at all embedment depths. The linear relationship between the ultimate shear load and strain rate for the 12.7-mm and 15.9-mm diameter adhesive anchors is attributed to the slight increase in ultimate shear load with the increase in the strain rate from 10^{-5} s^{-1} to 10^3 s^{-1} where steel anchor failure is the dominant failure mode at all the strain rates. The steel strength increased with the increase in the strain rate resulting in increased ultimate shear load. However, for the 19.1 mm diameter adhesive anchor with embedment depth of 76.2 mm an almost bilinear relation is obtained with change in slope at strain rate of 10 s^{-1} . The change in slope is attributed to the transition from pryout failure mode to steel anchor failure. At embedment depth of 101.6 mm, linear relation was observed for the 19.1-mm diameter anchor for the strain rates ranging from 10^{-3} s^{-1} to 10^3 s^{-1} . At strain rate of 10^{-5} pryout failure was observed, transition from pryout failure mode to steel anchor failure was observed at strain rate of 10^{-3} s^{-1} . For pryout failure mode both steel and concrete materials contribute in increasing the shear load where their strength increased with increasing the strain rate. Increasing anchor embedment depth from 76.2 mm to 152.4 mm increased the ultimate shear load for the anchors exhibiting pryout or concrete spalling failure. Maximum ultimate shear loads of 94.82 kN, 122.62 kN and 189.42 kN were obtained for the 12.7-mm, 15.9-mm and 19.1-mm diameter adhesive anchors respectively with embedment depth of 152.4 mm at high strain rate of 10^3 s^{-1} . At

low strain rate of 10^{-5} s^{-1} the shear loads were 81.85 kN, 106.50 kN and 164.33 kN for the 12.7-mm, 15.9-mm and 19.1-mm diameter adhesive anchors, respectively.

Comparing with the ultimate shear load at embedment depth of 76.2 mm (Figure 5-51), the increase in the ultimate shear load for the 12.7-mm, 15.9-mm and 19.1-mm diameter adhesive anchors over the static (strain rate of 10^{-5} s^{-1}) was 14%, 28.5% and 58%, respectively at high strain rate of 10^3 s^{-1} . While the increase in the ultimate shear load was 16%, 18% and 27% for the 12.7-mm, 15.9-mm and 19.1-mm diameter adhesive anchors, respectively for the embedment depth of 101.6 mm at high strain rate of 10^3 s^{-1} (Figure 5-52). The increase in the ultimate shear load was 16%, 15% and 15% for the 12.7-mm, 15.9-mm and 19.1-mm diameter adhesive anchors, respectively for the embedment depth of 152.4 mm at high strain rate of 10^3 s^{-1} where steel anchor failure is observed at all the strain rates investigated (Figure 5-53). At high strain rates of 10^2 s^{-1} and 10^3 s^{-1} , the concrete strength increased and thus the concrete resistance to the applied shear load increased. The increase in the concrete strength at high strain rate is attributed to the internal cracking that is propagated severely in the concrete. The concrete is a brittle material when subjected to failure load there is no time for unloading and this resulted in confining stresses in the concrete and thus increase the dynamic strength (Bischoff & Perry, 1991). Also, the strain rate has an influence on the mechanical properties of the steel, both the tensile and yield strength of the steel increased with the increase in the strain rate (Fu et al., 1991; Hopperstad et al., 2003; Yu et al., 2009). Furthermore, the strain rate has an influence on the flow stress-strain response and the microstructure of the steel (Lee et al., 2007). The increase in the strain rate increased the level of deformation of the steel where severe strain

concentration is observed along narrow area called adiabatic shear band (Odeshi et al., 2005). The adiabatic shear band creates plastic instability that leads to fracture (Lee et al., 2007).

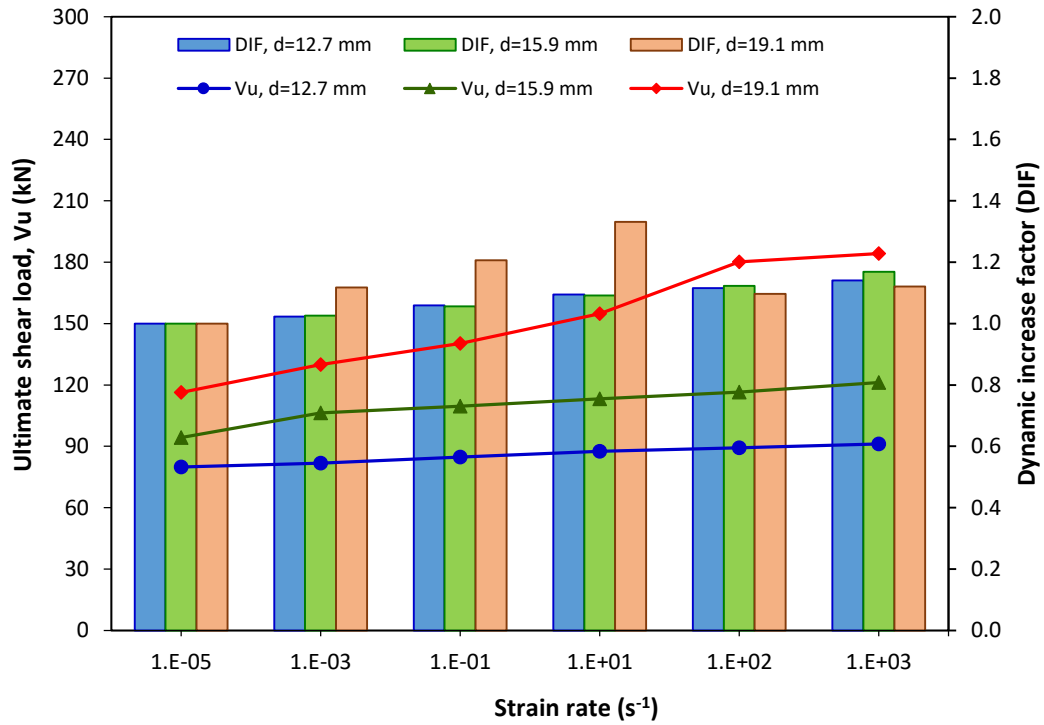


Figure 5-51: Ultimate shear load and DIF versus strain rate for adhesive anchors at 76.2 mm embedment depth

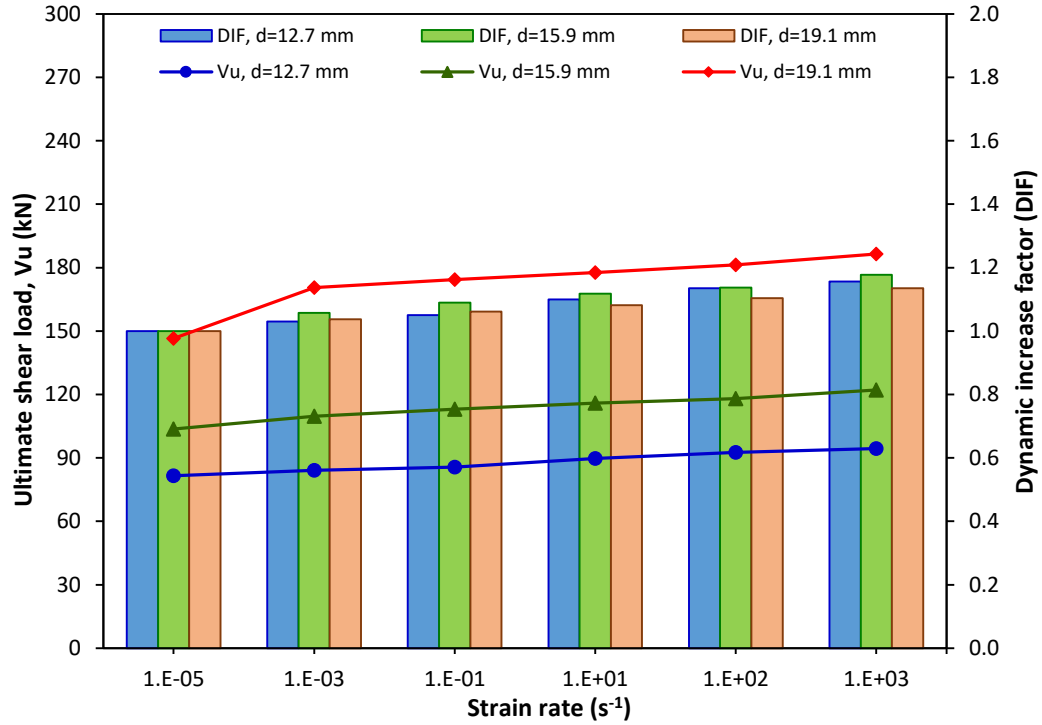


Figure 5-52: Ultimate shear load and DIF versus strain rate for adhesive anchors at 101.6 mm embedment depth

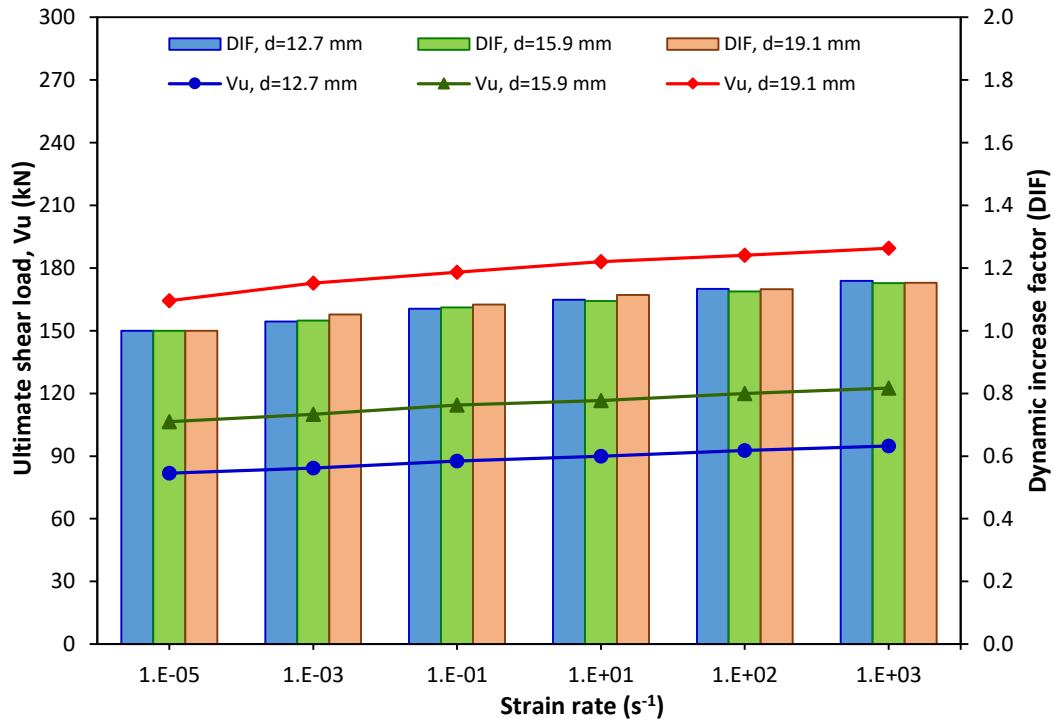


Figure 5-53: Ultimate shear load and DIF versus strain rate for adhesive anchors at 152.4 mm embedment depth

The findings in the Figures 5-51, 5-52 and 5-53 demonstrate that the DIF increased with the increase in the strain rate from 10^{-5} s^{-1} to 10^3 s^{-1} . For the 19.1 mm diameter adhesive anchor with 76.2 mm embedment depth (Figure 5-51), the DIF increased with the increase in the strain rate up to 10 s^{-1} where transition in the failure mode from pryout failure to concrete spalling was observed. Steel failure was observed at high strain rates of 10^2 s^{-1} and 10^3 s^{-1} with a slight increase in the DIF to 1.12. The increase in DIF is due to the increase in the strength of steel and concrete materials with the increase in strain rate. The increase in the concrete strength at high strain rate is higher than the increase in the steel strength. Maximum DIF of 1.33 was obtained for the 19.1 mm diameter adhesive anchor with embedment depth of 76.2 mm at strain rate of 10 s^{-1} . It can be noticed from Figure 5-53, that the influence of anchor diameter on the DIF at embedment depth of 152.4 mm is insignificant for the strain rates investigated where steel anchor failure is the dominant failure mode. Average DIF of 1.15 was obtained for adhesive anchors with embedment depth of 152.4 mm at high strain rate of 10^3 s^{-1} . This is comparable to the DIF of 1.2 reported by Braimah et al. for adhesive anchors subjected to impulse dynamic load and penetrated in normal substrate angle (Braimah et al., 2009). Cowell (1969) obtained DIF values of 1.25, 1.33 and 1.53 for A36 steel at strain rates of 0.03 s^{-1} , 0.1 s^{-1} and 1 s^{-1} respectively (Cowell, 1969). Wakabayashi et al. investigated the effect of strain rate on the yield strength of round and deformed steel. The authors obtained 1.07% and 1.08% increase in the yield strength at strain rate of $5 \times 10^{-3} \text{ s}^{-1}$ for the deformed and round steel bars respectively, the increase was 1.18% and 1.16% at strain rate of 10^{-1} s^{-1} (Wakabayashi et al., 1980).

Table 5-19 shows the maximum DIF for the adhesive anchors under shear load where pryout and steel anchor failure modes were observed. The value of DIF equal to one represents the DIF at the static strain rate of 10^{-5} s^{-1} , where pryout failure mode is observed. Steel anchor failure was observed for most of the adhesive anchors at low strain rate of 10^{-5} s^{-1} and higher strain rates up to 10^3 s^{-1} . Maximum DIF for the adhesive anchors exhibited steel failure was obtained at high strain rate of 10^3 s^{-1} and presented in Table 5-19.

Table 5-19: Maximum dynamic increase factor for the adhesive anchors under shear load

Model No.	d (mm)	h_{ef} (mm)	$\dot{\epsilon}$ (s^{-1})	DIF	$\dot{\epsilon}$ (s^{-1})	DIF
				PR		S
1	12.7	76.2	-	-	10^3	1.14
2	12.7	101.6	-	-	10^3	1.16
3	12.7	152.4	-	-	10^3	1.16
4	15.9	76.2	10^{-5}	1.00	10^3	1.17
5	15.9	101.6	-	-	10^3	1.18
6	15.9	152.4	-	-	10^3	1.15
7	19.1	76.2	10^{-5}	1.00	10^3	1.12
8	19.1	101.6	10^{-5}	1.00	10^3	1.13
9	19.1	152.4	-	-	10^3	1.15

5.2.9 Regression analysis for adhesive anchor under shear load

Regression analysis was carried out to predict the relation between the DIF and the strain rate ratio for the adhesive anchors subjected to shear load. Steel anchor failure was observed as the dominant failure mode for the adhesive anchors subjected to shear load investigated in this research (Figures 5-38, 5-39 and 5-40). Hence regression analysis was conducted to this failure mode. Average value of the DIF for anchor diameters of 12.7 mm, 15.9 mm and 19.1 mm was calculated to adjust the DIF for the effect of anchor diameter. Figure 5-54 presents the relation between the DIF and the strain rate ratio ($\dot{\epsilon}_d/\dot{\epsilon}_s$) for the

adhesive anchors exhibiting steel failure mode. The minimum recommended embedment depth for the adhesive anchor diameter of 19.1 mm is 89 mm (Hilti, 2014), hence anchor diameter of 19.1 mm with embedment depth of 76.2 mm was excluded from the regression analysis.

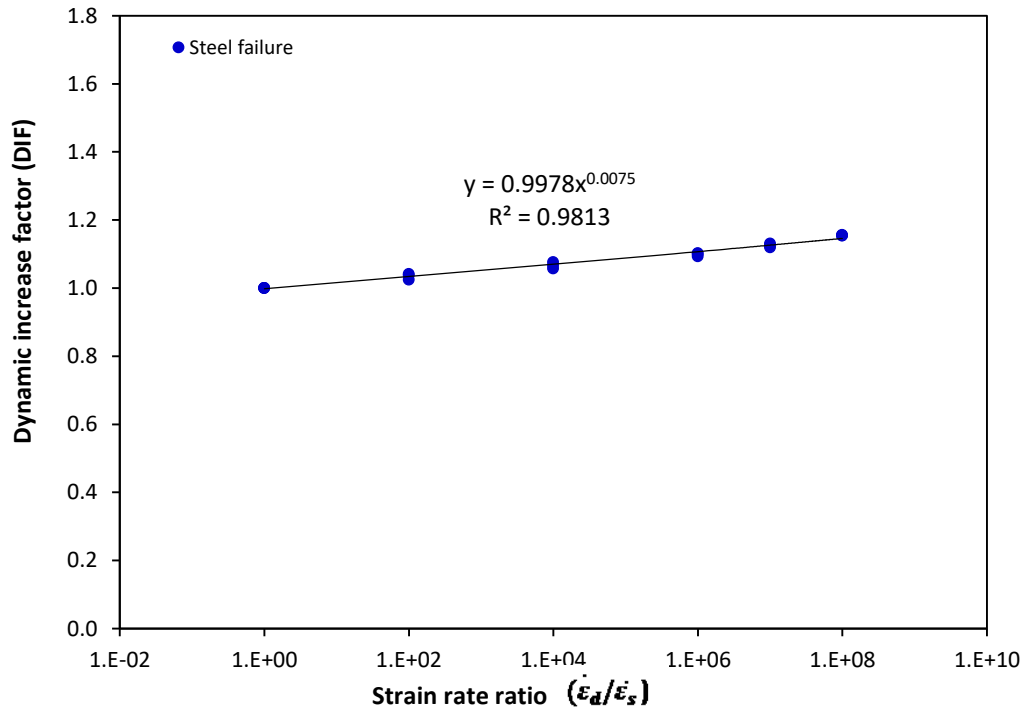


Figure 5-54: Effect of strain rate ratio on the DIF for adhesive anchor exhibiting steel failure under shear load

Various statistical models are used to predict the relation between the DIF and strain rate ratio as shown in Table 5-20.

Table 5-20: Statistical models and coefficient of determination to predict the DIF for adhesive anchor exhibited steel failure under shear load

Statistical models	Formulae	Coefficient of determination (R ²)
Exponential	$DIF = 1.0607e^{9E-10\left(\frac{\dot{\epsilon}_d}{\dot{\epsilon}_s}\right)}$	0.454
Linear	$DIF = 1E - 9\left(\frac{\dot{\epsilon}_d}{\dot{\epsilon}_s}\right) + 1.0616$	0.471
Logarithmic	$DIF = 0.0081\ln\left(\frac{\dot{\epsilon}_d}{\dot{\epsilon}_s}\right) + 0.9963$	0.978
Power	$DIF = 0.9978\left(\frac{\dot{\epsilon}_d}{\dot{\epsilon}_s}\right)^{0.0075}$	0.981

From Table 5-20, it can be seen that power model exhibits the highest coefficient of determination (R²) of 98% for the adhesive anchors exhibiting steel failure mode. The predicted formulae for the DIF of the adhesive anchor under shear load can be presented using the power model as in Equation (5.7).

$$DIF = 0.9978\left(\frac{\dot{\epsilon}_d}{\dot{\epsilon}_s}\right)^{0.0075} \quad (5.7)$$

The proposed Equation (5.7) can be used to predict the ultimate dynamic shear load (V_{ud}) as follows:

$$V_{ud} = V_{us} \times 0.9978\left(\frac{\dot{\epsilon}_d}{\dot{\epsilon}_s}\right)^{0.0075} \quad (5.8)$$

Where the ultimate static load (V_{us}) can be determined from Equation (4.18) for steel anchor failure mode.

Residual analysis has been performed for the adhesive anchors to measure the difference between the results obtained from finite element analysis and results of DIF obtained from

Equation (5.7). Figure 5-55 presents the residual plots for the adhesive anchors. As shown in Figure 5-55, the residual exhibits horizontal trend line with strain rate ratio.

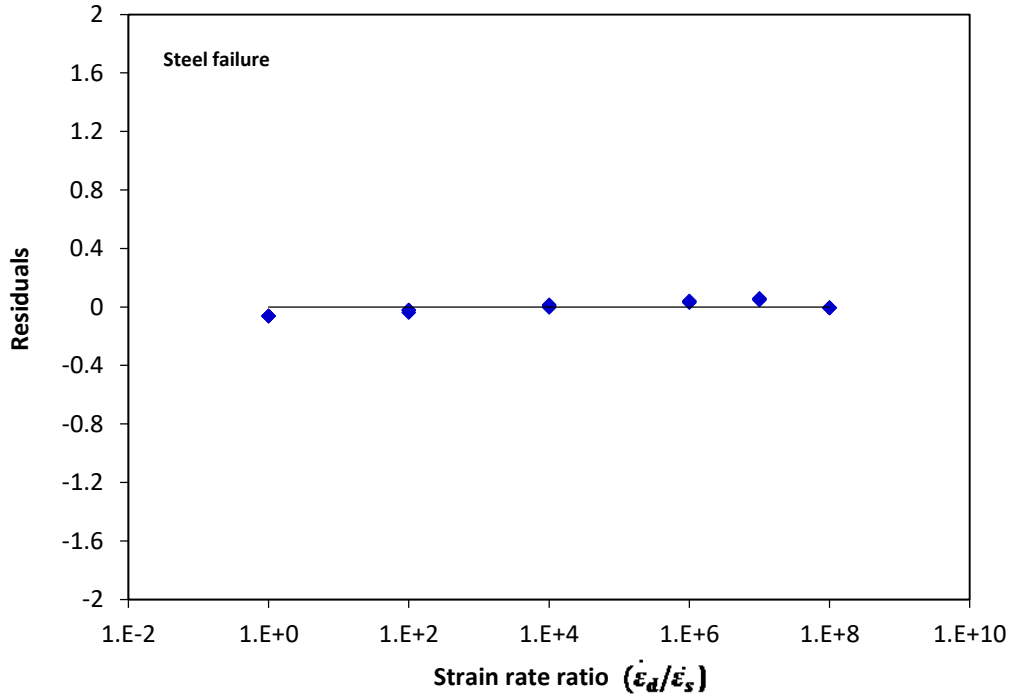


Figure 5-55: Residual versus strain rate ratio for the adhesive anchor subjected to shear load and exhibited steel failure

New adhesive anchor models with diameters of 9.5 mm, 12.7 mm, 15.9 mm and 19.1 mm and embedment depths of 89 mm, 114 mm and 140 mm were developed. The adequacy of the proposed equation was validated by comparing the results with the new adhesive anchor models with different design parameters. Figure 5-56 presents the relation between the DIF obtained from the finite element analysis of the newly developed models and the regression models (Equation (5.7)) for adhesive anchors exhibited steel failure. As shown in the figure, the DIF is observed distributed around the equality line.

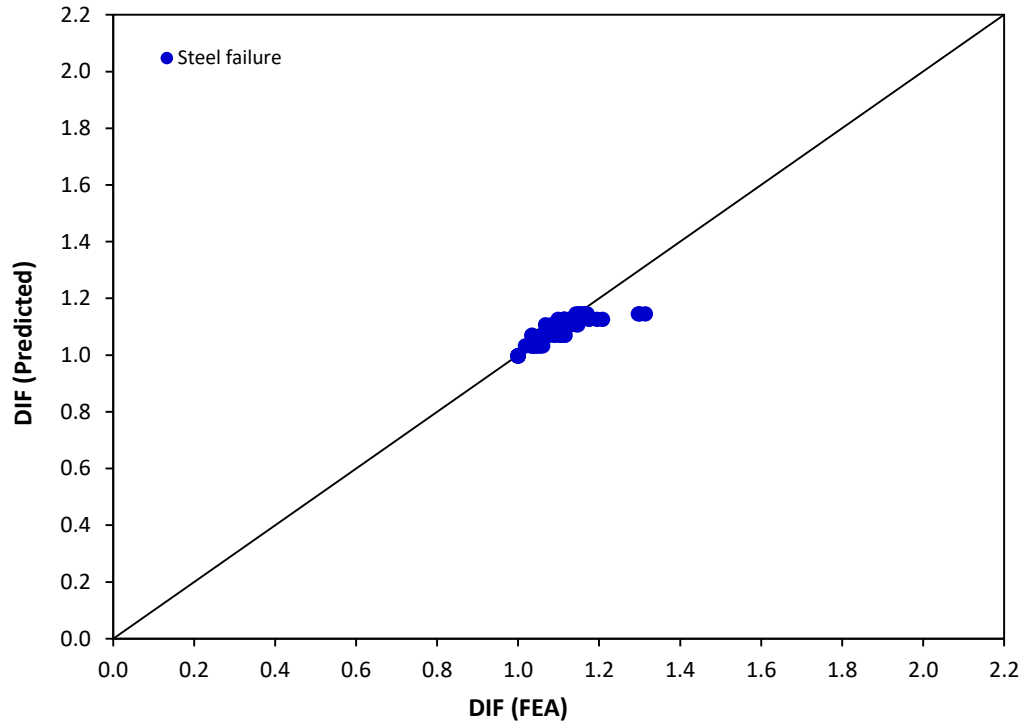


Figure 5-56: DIF obtained from the finite element analysis versus the predicted DIF for the adhesive anchor exhibited steel failure under shear load

5.3 Summary

In this chapter finite element analyses were performed to investigate the tensile and shear behaviour of the adhesive anchorage to concrete system models. The chapter began with validation of the adhesive anchor models with the experimental results from the literature. Mesh sensitivity analyses were performed to obtain the optimum mesh size that can represent the experimental results accurately. The results of the finite element analysis have been compared with the ACI and CCD design methods. Also, the results of the finite element analysis were compared with the results obtained from the literature. Level of damage and failure mode for the adhesive anchors subjected to tensile and shear loads at strain rates ranging from 10^{-5} s^{-1} to 10^3 s^{-1} were drawn and discussed. For the adhesive

anchors subjected to tensile load, three types of failure modes were observed: concrete cone breakout, combined cone-bond failure and steel anchor failure. For the adhesive anchors subjected to shear loads three types of failure modes were observed: pryout, concrete spalling and steel anchor failure. Concrete cone depth and concrete cone breakout diameter for adhesive anchor under tensile load were determined. Load-displacement relations for adhesive anchor under tensile and shear loads were drawn and analyzed. The relation between ultimate load, failure mode and strain rate for the adhesive anchors subjected to tensile and shear loads were drawn and discussed. Dynamic increase factor (DIF) was determined for the adhesive anchors at all the strain rates investigated. Equations were developed to determine the relation between the DIF and strain rate for the adhesive anchors investigated.

Chapter 6 : Strain rate effect on the undercut anchors

6.1 Finite element modelling for undercut anchors under tensile load

Finite element analyses were performed to investigate the tensile behaviour of the undercut anchors using LS-DYNA. Undercut anchor diameters of 12 mm, 16 mm and 20 mm with recommended effective embedment depths of 125 mm, 190 mm and 250 mm, respectively (Hilti, 2011) were investigated. In addition, embedment depth of 100 mm was investigated. Figure 6-1 shows a schematic view of the undercut anchorage to concrete system. Figure 6-2 shows the geometric configuration and boundary conditions for the undercut anchor model under tensile load.

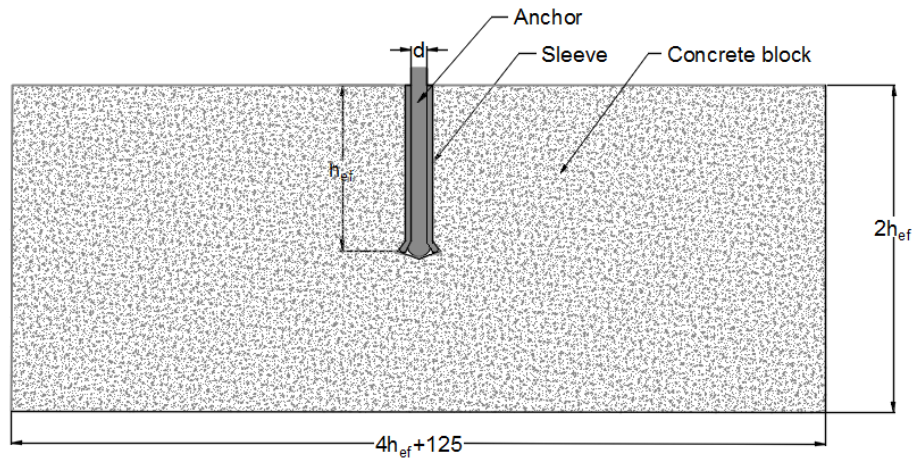


Figure 6-1: A schematic view for the undercut anchor model

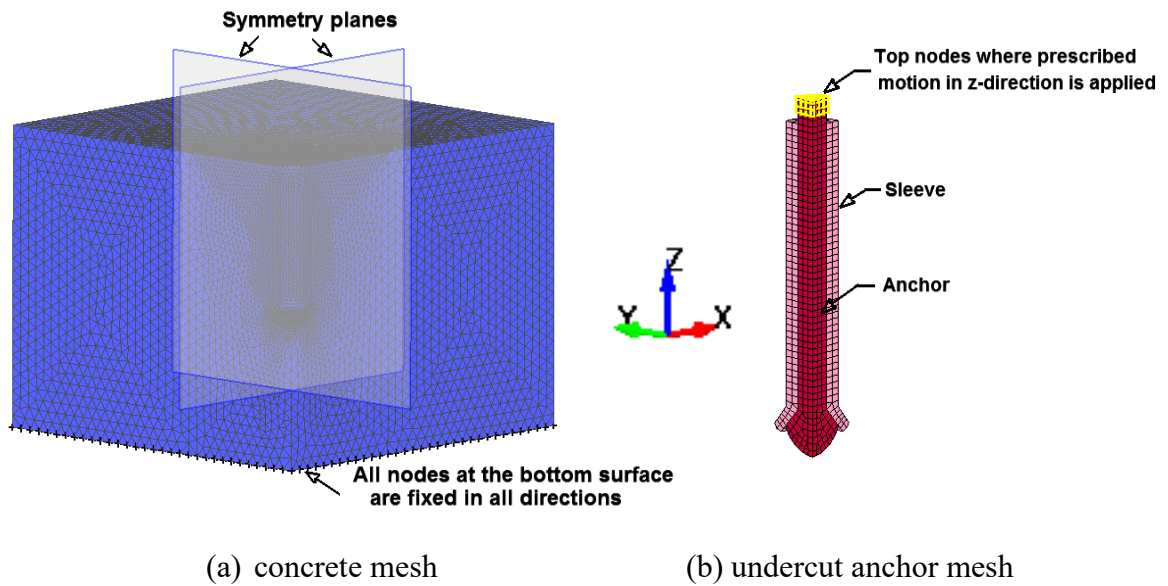


Figure 6-2: Geometric configuration and boundary conditions for the undercut anchor model

6.1.1 Validation of undercut anchor model under tensile load

To assess the ability of LS-DYNA model to predict the tensile behaviour of the undercut anchor, a finite element model representing the experimental test conducted by Mahadik et al. (Mahadik et al., 2016) was developed to validate the undercut anchor model. Concrete block size of (700×300×400) mm and cube compressive strength of 42.6 MPa ($f'_c = 33.5$ MPa) was used. Hilti undercut anchor, through-set type, of 12-mm diameter, 125 mm embedment depth and 640 MPa yield strength was used for the analysis. Mesh sensitivity analyses were carried out to determine the optimum mesh size for both the steel undercut anchor and concrete block to maximize accuracy of the results while minimizing required computer resources. Table 6-1 shows various element mesh sizes for the steel anchor and concrete, the ultimate load, and failure mode for each mesh size.

Table 6-1: Effect of mesh size refinement on the convergence of ultimate tensile load for undercut anchor

Model No.	Mesh size (mm)			Ultimate tensile load (kN)		Displacement (mm)		Failure mode
	Anchor	Concrete		FEA	EXP.	FEA	EXP.	
		Min.	Max.					
1	2	4	12	66.5	72.8	5.13	4.67	Steel failure
2	2	2	12	71.4		4.74		Steel failure
3	1	1	12	74.2		4.71		Steel failure

A percentage difference between the finite element analysis and the experimental results of 9.47%, 1.96% and 1.92% for the ultimate tensile load were obtained for the models No. 1, 2 and 3 respectively. Mesh size of model No. 2 gave converged results to the experimental results conducted by Mahadik et al. with better computation time and was selected for the analysis. Figure 6-3 shows a comparison of tensile load-displacement response between the experimental results obtained by Mahadik et al. (Mahadik et al., 2016) and the finite element results. Ultimate tensile loads of 71.4 kN and 72.8 kN were obtained from the finite element analysis and the experimental test conducted by Mahadik et al. (Mahadik et al., 2016), respectively. The experimental results exhibited 1.96% higher ultimate tensile load than the finite element analysis results. Both the finite element analysis and experimental test resulted in steel anchor failure mode as shown in Figure 6-4.

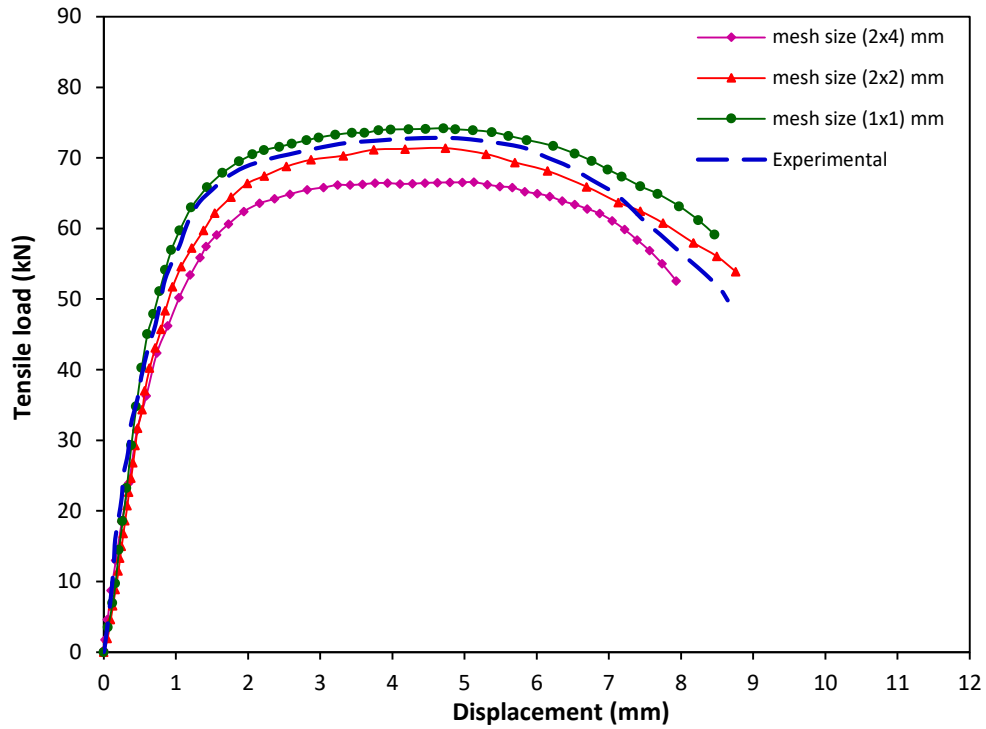
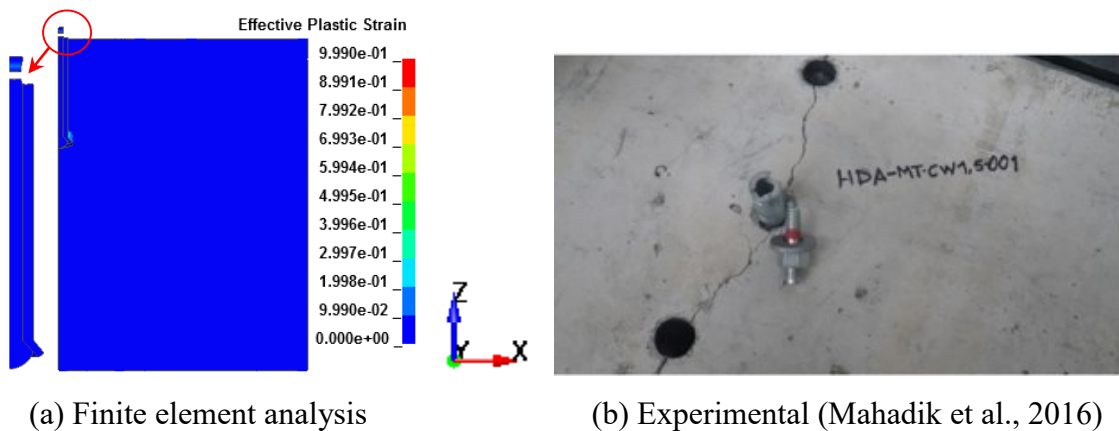


Figure 6-3: Tensile load-displacement response of the FEA and experimental results obtained by Mahadik et al. (Mahadik et al., 2016)



(a) Finite element analysis

(b) Experimental (Mahadik et al., 2016)

Figure 6-4: Failure mode of the undercut anchors under tensile load observed from the finite element analysis and the experimental results by (Mahadik et al., 2016)

6.1.2 Comparison of FEA results with the ACI and CCD design methods

Ultimate tensile loads obtained from the finite element analysis (FEA) at strain rate of 10^{-5} s^{-1} were compared with anchor capacity obtained by use of the American Concrete Institute ACI 349-85 (Equations 4.1 for concrete cone breakout failure and 4.2 for steel anchor failure) and Concrete Capacity Design (CCD) (Equation 4.3) methods, as presented in Table 6-2. Fuchs et al. (1995) proposed an equation to predict the concrete cone breakout failure for the cast-in-place and post-installed anchors (Equation 4.3) which was subsequently adopted by ACI 318 code (Eligehausen, et al., 2006; Fuchs et al., 1995). The equivalent anchor head diameter (d_h) (in Equation 4.1) of undercut anchors is $\geq 2.5d$ (Hilti, 2011). For safe anchorage to concrete design, minimum ultimate load obtained from (Equations 4.1 and 4.2) is considered for the comparison of the FEA results with the ACI method. Also, minimum ultimate value obtained from (Equations 4.2 and 4.3) is considered for the comparison of the FEA results with the CCD method and included in Table 6-2.

It can be seen from Table 6-2 that the ACI and CCD methods underpredict the ultimate load for the anchor with a diameter of 12 mm and embedment depth of 100 and anchor diameters of 16 mm and 20 mm with embedment depths of 100 mm and 125 mm. The ACI method underestimate the failure load for the shallow embedment depths (Fuchs et al., 1995). Also, the anchor diameter is not considered in the ACI (Equation 4.1) and CCD (Equation 4.3) methods. In general the finite element analysis results are in good agreement with the ACI and CCD methods.

Table 6-2: Comparison of ultimate tensile loads obtained from FEA with ACI and CCD methods

d (mm)	h _{ef} (mm)	Ultimate tensile load (kN)			δ (mm)	FEA/ACI	FEA/CCD	*Failure mode (FEA)
		FEA	ACI	CCD				
12	100	83.14	75.91	82.12	1.32	1.10	1.01	S
	125	83.22	90.48	90.48	1.34	0.92	0.92	S
	190	83.94	90.48	90.48	1.38	0.93	0.93	S
16	100	101.09	81.75	82.12	1.78	1.24	1.23	CC
	125	126.62	120.44	114.76	1.88	1.05	1.10	S
	190	127.16	160.85	160.85	1.87	0.79	0.79	S
20	100	118.41	87.59	82.12	1.27	1.35	1.44	CC
	125	168.66	127.74	114.76	1.81	1.32	1.47	CC
	190	211.46	251.33	215.06	2.03	0.84	0.98	S

*Failure mode: CC=concrete cone breakout, S=steel anchor fracture

6.1.3 Effect of strain rate on the level of damage and failure mode

Figure 6-5 shows the level of damage for the undercut anchor diameters of 12 mm, 16 mm and 20 mm with different embedment depths at low strain rate of 10^{-5} s^{-1} . As shown in the figure, two types of failure modes were observed at low strain rate of 10^{-5} s^{-1} : concrete cone breakout failure and steel failure. Concrete cone breakout failure was observed at embedment depth of 100 mm for anchor diameters of 16 mm and 20 mm whereas steel anchor failure was observed for the anchor diameter of 12 mm. At the beginning of the loading, cracks started to appear at the lower ends of the sleeve, then the cracks grow and propagate diagonally along the embedment depth and transferred to a wider area on the concrete forming concrete cone breakout failure. Steel anchor failure was observed at embedment depths of 125 mm, 190 mm and 250 mm for all the undercut anchor diameters except anchor diameter of 20 mm with embedment depth of 125 mm where concrete cone breakout failure was observed.

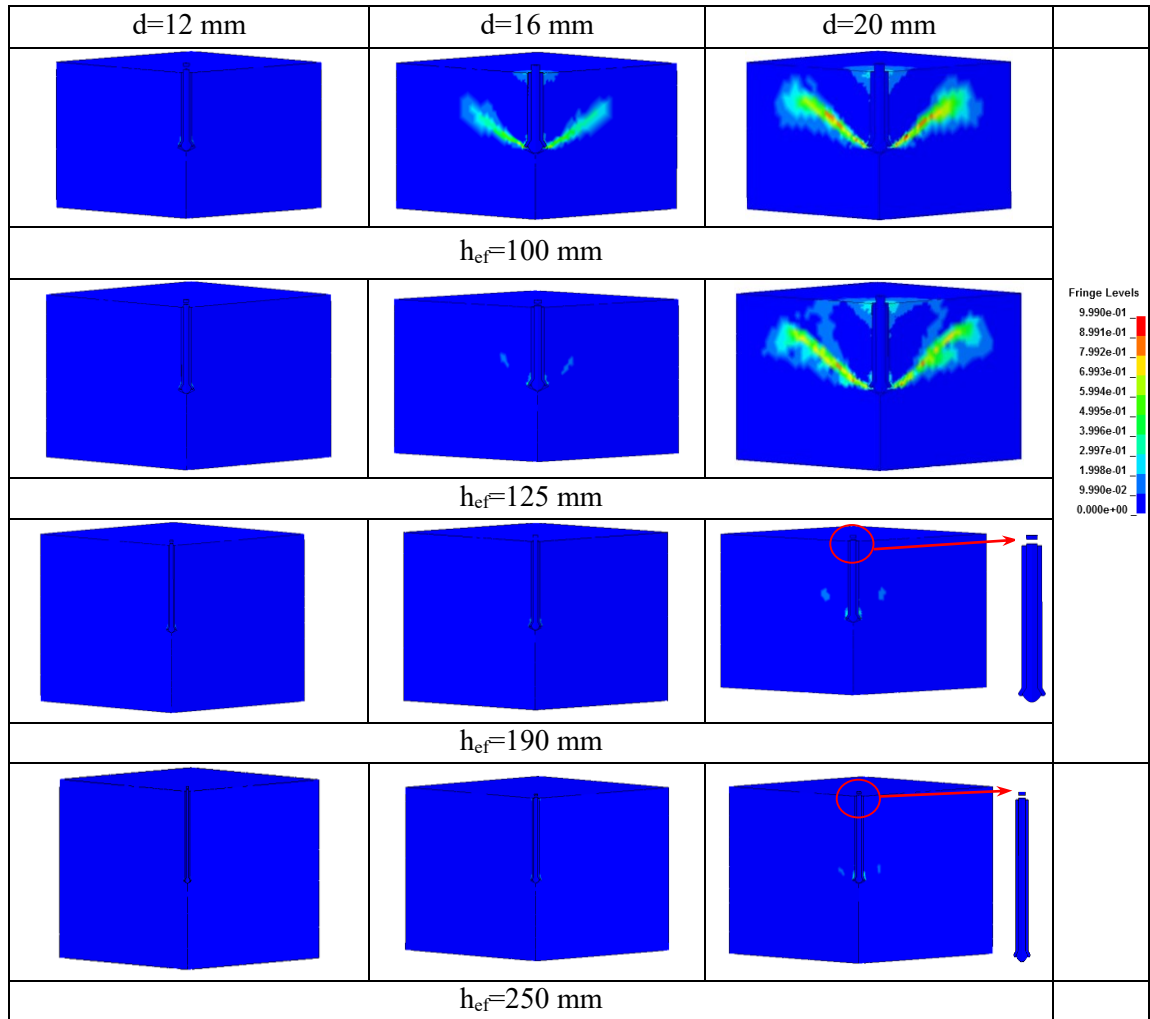


Figure 6-5: Plastic strain contours for the undercut anchors at strain rate of 10^{-5} s^{-1}

Figures 6-6, 6-7 and 6-8 present the failure mode of 12 mm, 16 mm and 20 mm diameter undercut anchors with 100 mm, 125 mm, 190 mm and 250 mm embedment depths at different strain rates. As shown in the Figures 6-6 and 6-7, steel anchor failure was the dominant failure mode for the 12-mm and 16-mm diameter undercut anchors at strain rates ranging from 10^{-3} s^{-1} to 10^3 s^{-1} .

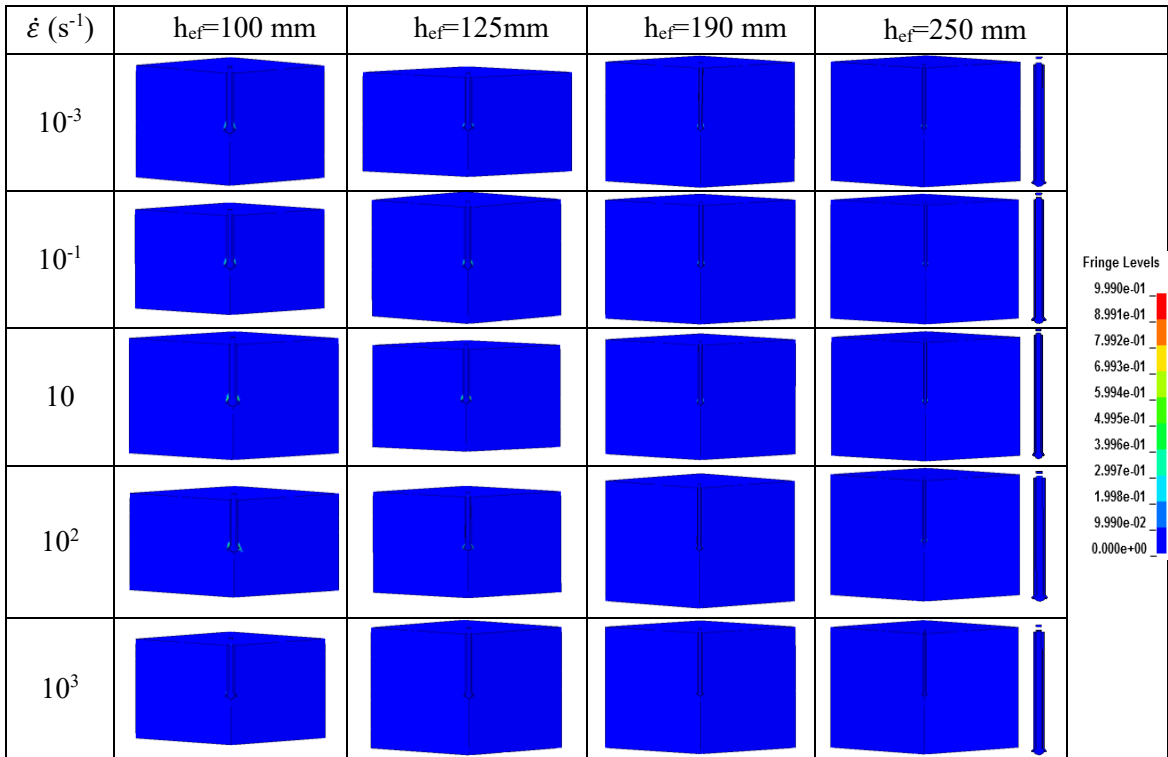


Figure 6-6: Failure mode of 12 mm diameter undercut anchor at different strain rates

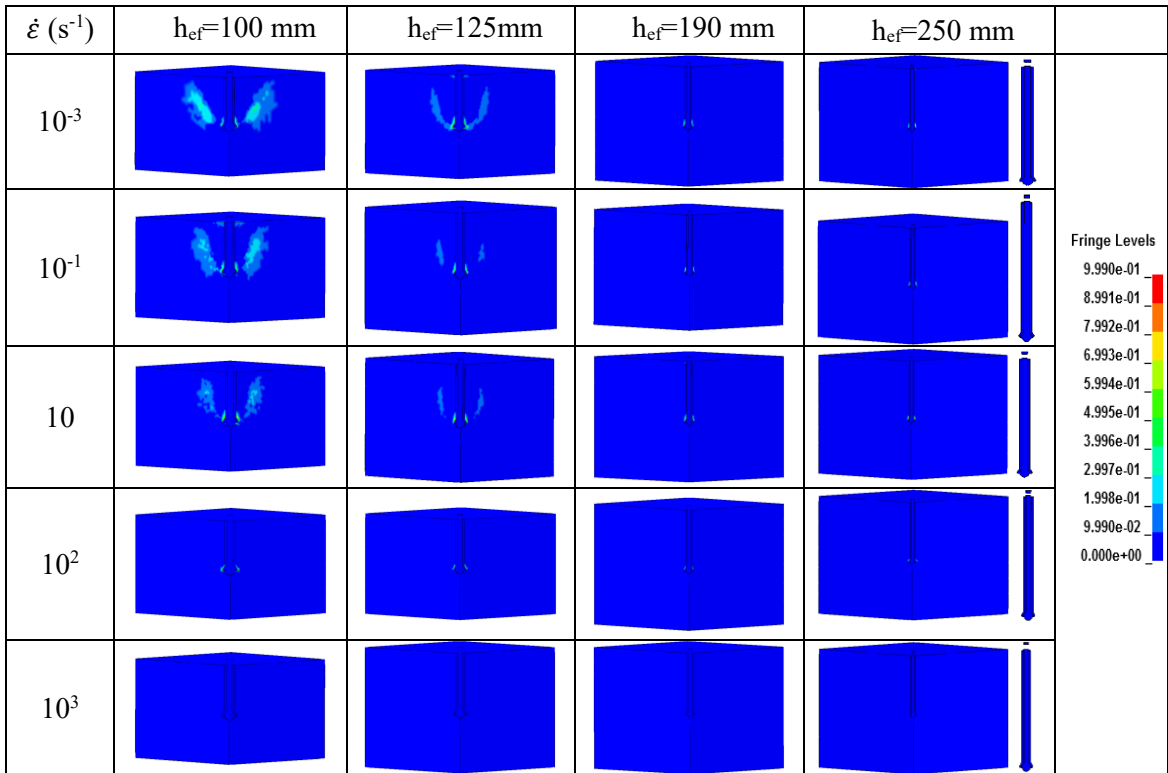


Figure 6-7: Failure mode of 16 mm diameter undercut anchor at different strain rates

As shown in Figure 6-8, concrete cone breakout failure was observed for the undercut anchor diameter of 20 mm with embedment depth of 100 mm at strain rates of 10^{-3} s^{-1} , 10^{-1} s^{-1} and 10 s^{-1} while steel anchor failure was observed at strain rates of 10^2 s^{-1} and 10^3 s^{-1} . At strain rates of 10^{-3} and 10^{-1} s^{-1} there was sufficient time to initiate and propagate the cracks in the concrete, formation of the conical shape resulting in concrete cone breakout failure. Whereas at high strain rates of 10^2 s^{-1} and 10^3 s^{-1} , the steel anchor failure is attributed to the fast pullout of the anchors and increase in the concrete tensile strength at high strain rate. At embedment depth of 125 mm, concrete cone breakout failure was observed at strain rates of 10^{-3} s^{-1} and 10^{-1} s^{-1} whereas steel anchor failure was observed at strain rates of 10 s^{-1} , 10^2 s^{-1} 10^3 s^{-1} . Also, steel anchor failure was observed at embedment depths of 190 mm and 250 mm for all the strain rates investigated.

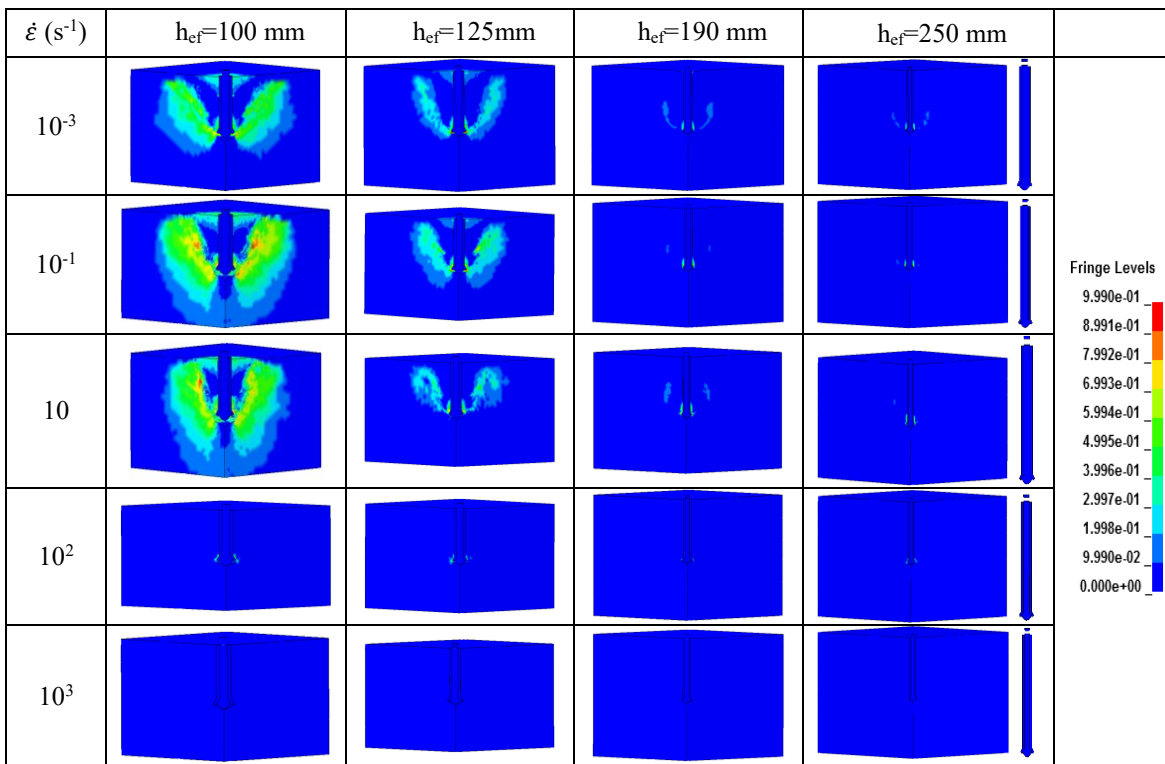


Figure 6-8: Failure mode of 20 mm diameter undercut anchor at different strain rates

6.1.4 Effect of design parameters on failure mode and ultimate tensile load

Effect of strain rate on the ultimate tensile load and failure mode for the undercut anchors is shown in Figures 6-9, 6-10 and 6-11 for the 12 mm, 16 mm and 20 mm diameter undercut anchors respectively. It can be seen from the figures that the tensile load increased with the increase in the strain rate from 10^{-5} s^{-1} to 10^3 s^{-1} where steel anchor failure is observed for most of the undercut anchors investigated. From Figures 6-9, 6-10 and 6-11, it can be seen that the strain rate has an influence on the failure mode of the undercut anchors.

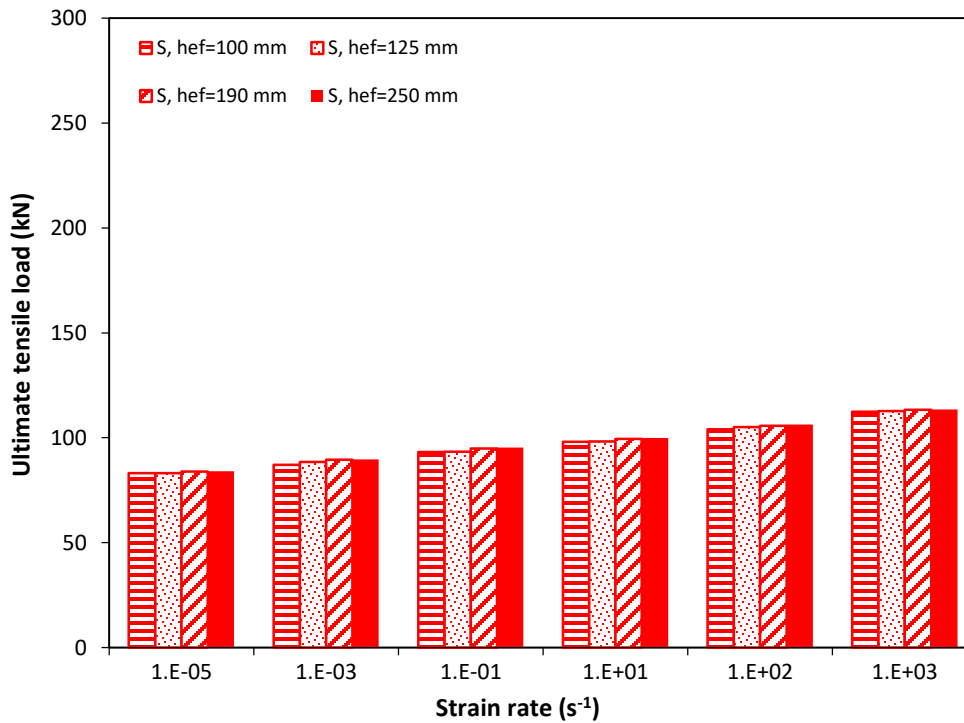


Figure 6-9: Strain rate effect on the failure mode and ultimate tensile load for undercut anchor diameter of 12 mm

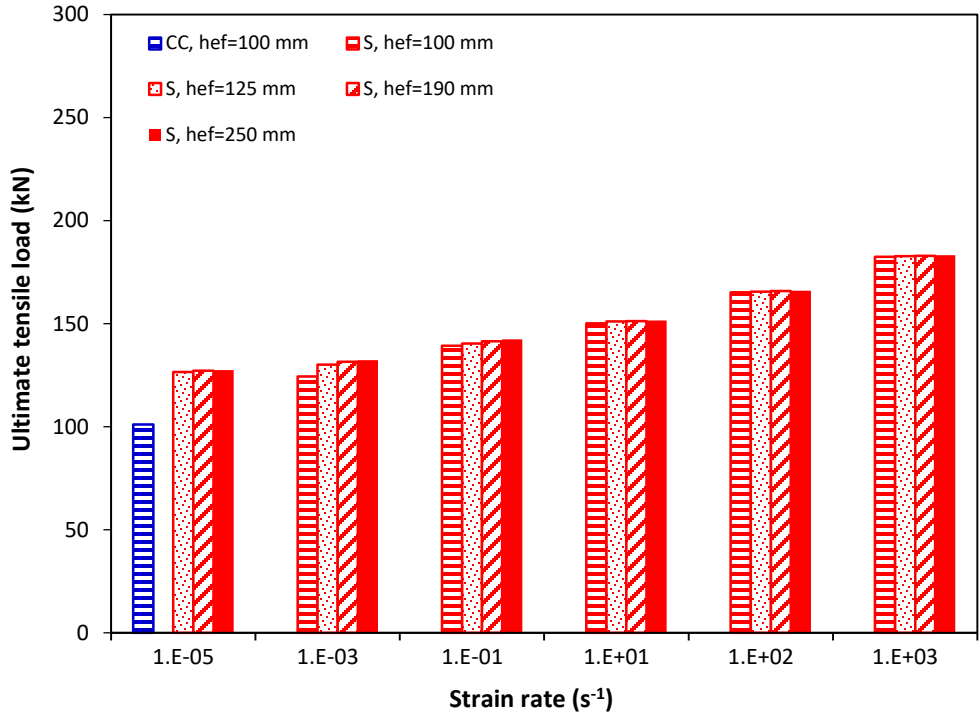


Figure 6-10: Strain rate effect on the failure mode and ultimate tensile load for undercut anchor diameter of 16 mm

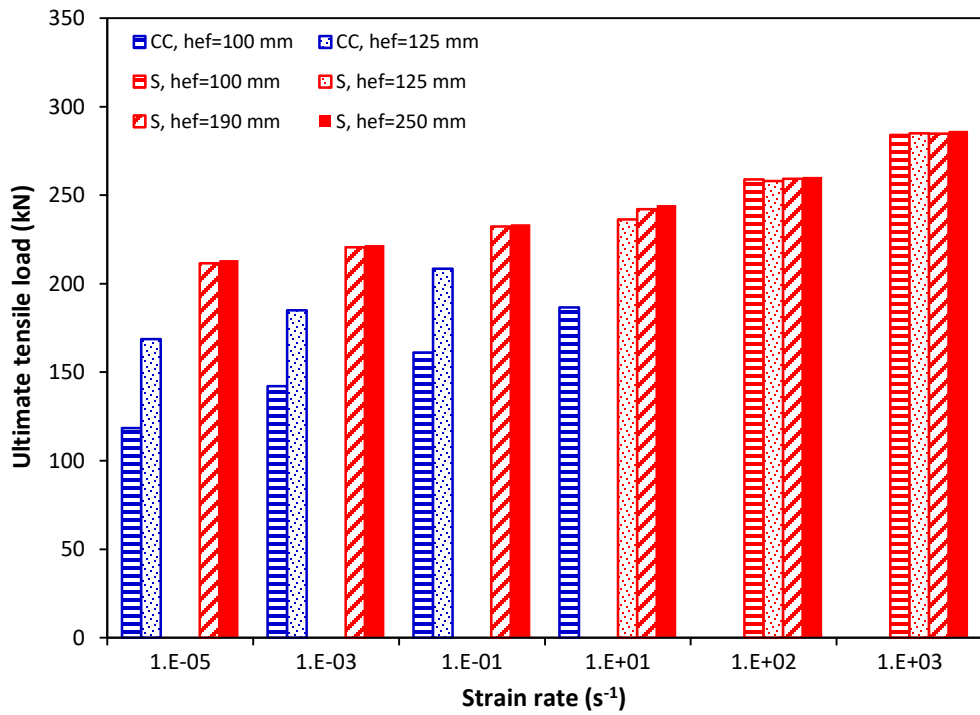


Figure 6-11: Strain rate effect on the failure mode and ultimate tensile load for undercut anchor diameter of 20 mm

Figures 6-9, 6-10 and 6-11, show that the embedment depth and anchor diameter also have an effect on the failure mode. Increasing the embedment depth from 100 mm to 190 mm resulted in steel anchor failure for the anchor diameter of 20 mm at low strain rate of 10^{-5} s^{-1} . Increasing the anchor diameter from 12 mm to 20 mm resulted in changing the failure mode from steel anchor failure to concrete cone breakout for the embedment depths of 100 mm and 125 mm at strain rates of 10^{-5} s^{-1} , 10^{-3} s^{-1} and 10^{-1} s^{-1} . Also, the failure mode changed from steel failure to concrete cone breakout for embedment depth of 100 mm at strain rate of 10 s^{-1} with the increase in the anchor diameter from 12 mm to 20 mm. Table 6-3 presents the failure mode for the undercut anchors under tensile load at different strain rates.

Table 6-3: Failure mode for undercut anchors under tensile load at different strain rates

Model No.	d (mm)	h _{ef} (mm)	*Failure mode					
			Strain rate (s ⁻¹)					
			$\dot{\epsilon}=10^{-5}$	$\dot{\epsilon}=10^{-3}$	$\dot{\epsilon}=10^{-1}$	$\dot{\epsilon}=10$	$\dot{\epsilon}=10^2$	$\dot{\epsilon}=10^3$
1	12	100	S	S	S	S	S	S
2	12	125	S	S	S	S	S	S
3	12	190	S	S	S	S	S	S
4	12	250	S	S	S	S	S	S
5	16	100	CC	S	S	S	S	S
6	16	125	S	S	S	S	S	S
7	16	190	S	S	S	S	S	S
8	16	250	S	S	S	S	S	S
9	20	100	CC	CC	CC	CC	S	S
10	20	125	CC	CC	CC	S	S	S
11	20	190	S	S	S	S	S	S
12	20	250	S	S	S	S	S	S

*Failure mode: CC= concrete cone breakout, S= steel anchor failure

6.1.5 Effect of anchor embedment depth on the ultimate tensile load

Figures 6-12, 6-13 and 6-14 show the ultimate tensile load and concrete cone depth for the 12-mm, 16-mm and 20-mm diameter undercut anchors for different embedment depths at low strain rate of 10^{-5} s^{-1} . It can be seen that nearly same ultimate tensile load is obtained for the 12-mm anchor diameter at all the embedment depths investigated where steel anchor failure is observed as shown in Figure 6-12. For the anchor diameter of 16 mm (Figure 6-13) the ultimate tensile load increased from 101.09 kN to 126.62 kN as the embedment depth increased from 100 mm to 125 mm. No increase in the ultimate tensile load was obtained for further increase in the embedment depth to 190 mm. Concrete cone breakout failure was observed at embedment depth of 100 mm with concrete cone breakout diameter of 291 mm. Steel anchor failure was observed at embedment depths of 125 mm and 190 mm.

For the anchor diameter of 20 mm as shown in Figure 6-14, the ultimate tensile load increased with the increase in the embedment depth from 100 mm to 190 mm. Concrete cone breakout failure mode was observed at embedment depths of 100 mm and 125 mm. The concrete cone breakout diameter increased from 340 mm to 378 mm as the embedment depth increased from 100 mm to 125 mm. Steel anchor failure was observed at embedment depth of 190 mm.

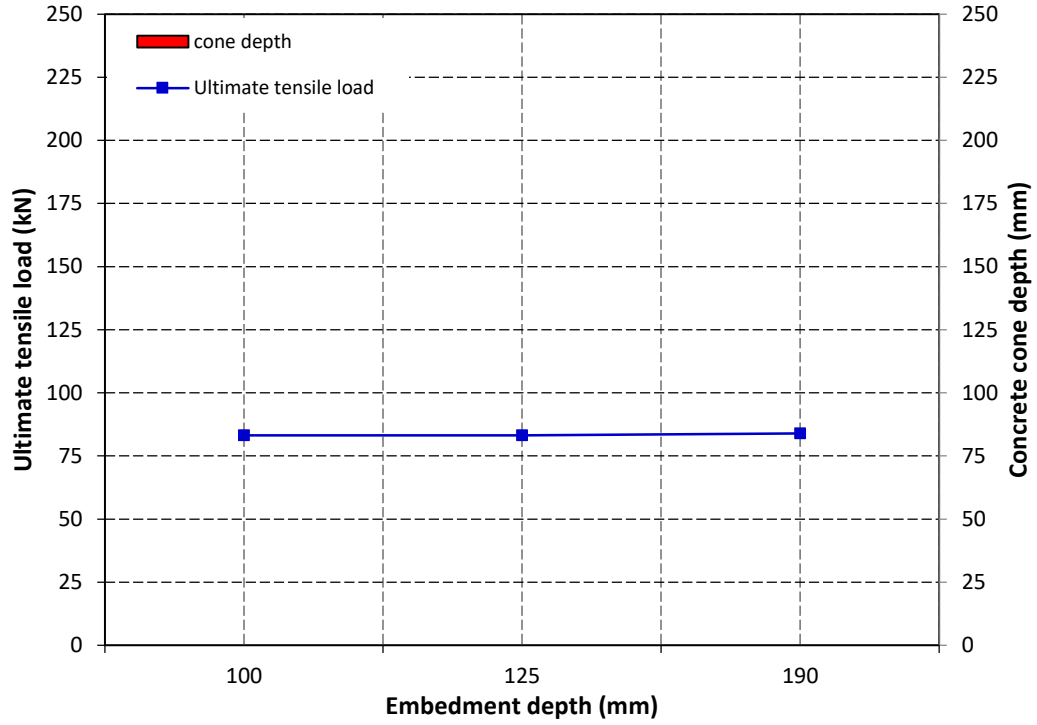


Figure 6-12: Effect of anchor embedment depth on the concrete cone depth and ultimate tensile load for 12 mm diameter undercut anchor

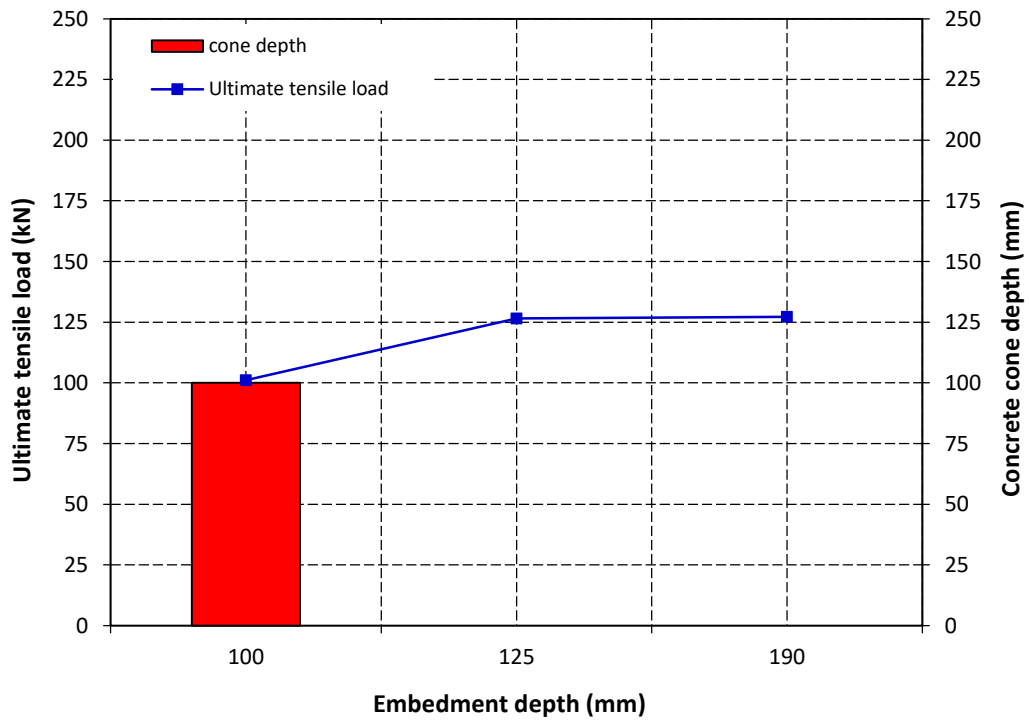


Figure 6-13: Effect of anchor embedment depth on the concrete cone depth and ultimate tensile load for 16 mm diameter undercut anchor

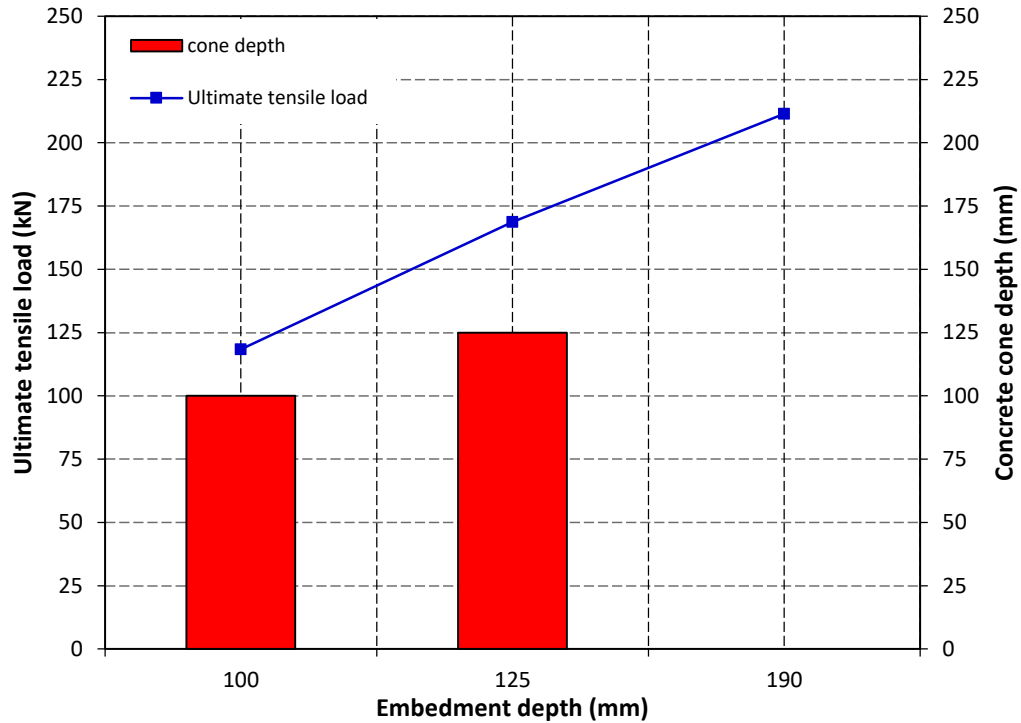


Figure 6-14: Effect of anchor embedment depth on the concrete cone depth and ultimate tensile load for 20 mm diameter undercut anchor

6.1.6 Effect of strain rate on concrete cone breakout diameter and cone propagation angle

Figure 6-15 shows the displacement contours of 20-mm diameter undercut anchor with embedment depth of 100 mm under tensile load at strain rates ranging from 10^{-5} s^{-1} to 10^3 s^{-1} . As shown in the figure, the increase in the strain rate from 10^{-5} s^{-1} to 10 s^{-1} decreased the concrete cone breakout diameter. At high strain rates of 10^2 s^{-1} and 10^3 s^{-1} , steel anchor failure is observed.

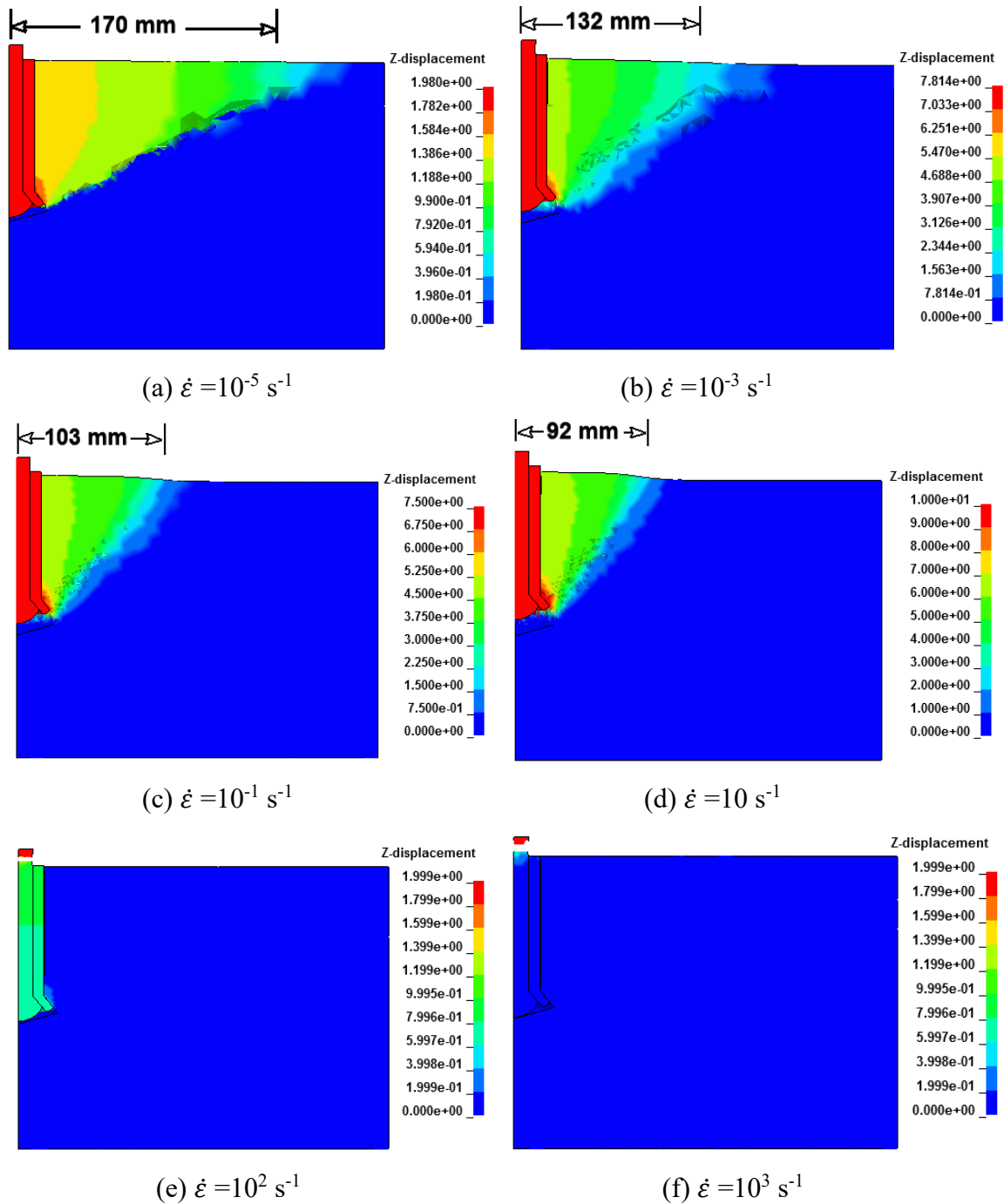


Figure 6-15: Displacement contours for 20 mm undercut anchor diameter at strain rates ranging from 10^{-5} s^{-1} to 10^3 s^{-1}

The crack propagation angle was monitored and recorded at the ultimate capacity and presented in Table 6-4. As shown in the table, the crack propagation angle decreases with

the increase in the strain rate for the undercut anchors exhibiting concrete cone breakout failure. The crack propagation angle was measured from the direction of the applied load to the failure surface.

Table 6-4: Crack propagation angle for the undercut anchors at different strain rates

Model No.	d (mm)	h _{ef} (mm)	Crack propagation angle (deg)					
			Strain rate (s ⁻¹)					
			$\dot{\epsilon}=10^{-5}$	$\dot{\epsilon}=10^{-3}$	$\dot{\epsilon}=10^{-1}$	$\dot{\epsilon}=10$	$\dot{\epsilon}=10^2$	$\dot{\epsilon}=10^3$
1	12	100	-	-	-	-	-	-
2	12	125	-	-	-	-	-	-
3	12	190	-	-	-	-	-	-
4	12	250	-	-	-	-	-	-
5	16	100	63	-	-	-	-	-
6	16	125	-	-	-	-	-	-
7	16	190	-	-	-	-	-	-
8	16	250	-	-	-	-	-	-
9	20	100	62	50	46	42	-	-
10	20	125	62	52	47	-	-	-
11	20	190	-	-	-	-	-	-
12	20	250	-	-	-	-	-	-

6.1.7 Effect of strain rate on the tensile behaviour of the undercut anchors

Tensile behaviour of 12-mm, 16-mm and 20-mm diameter undercut anchors with embedment depths of 100 mm, 125 mm, 190 mm and 250 mm were investigated. Figures 6-16, 6-17, 6-18, 6-19, 6-20 and 6-21 present the load-displacement relation for the 12-mm diameter undercut anchors subjected to tensile load. Strain rates from 10^{-5} s^{-1} to 10^3 s^{-1} were investigated.

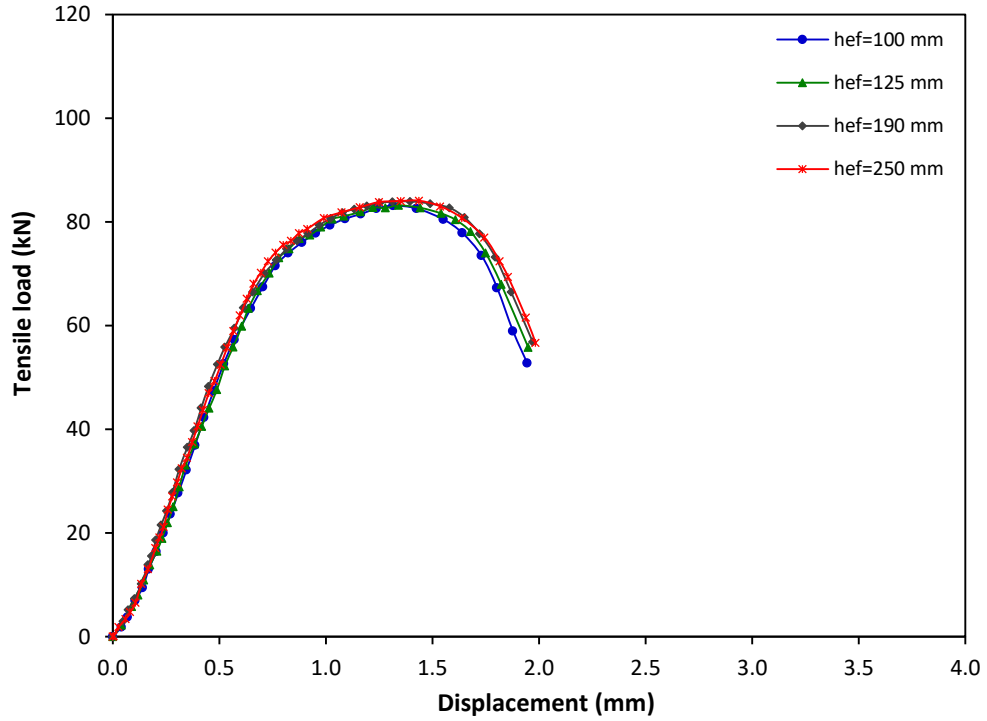


Figure 6-16: Tensile load-displacement graph for the 12-mm diameter undercut anchor at strain rate of 10^{-5} s^{-1}

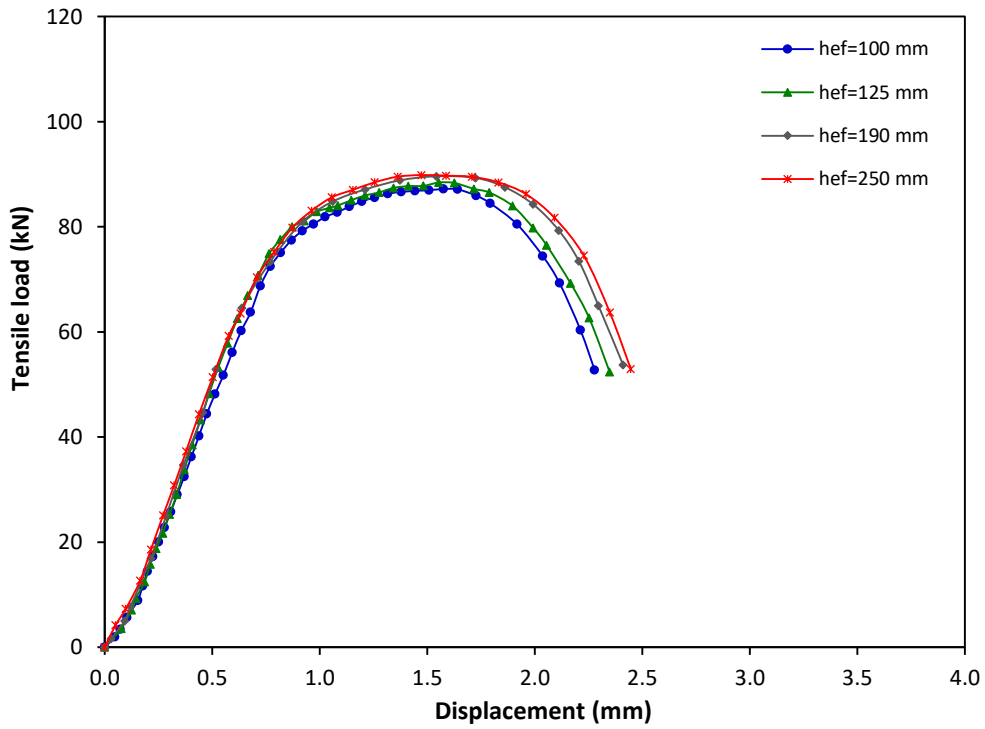


Figure 6-17: Tensile load-displacement graph for the 12-mm diameter undercut anchor at strain rate of 10^{-3} s^{-1}

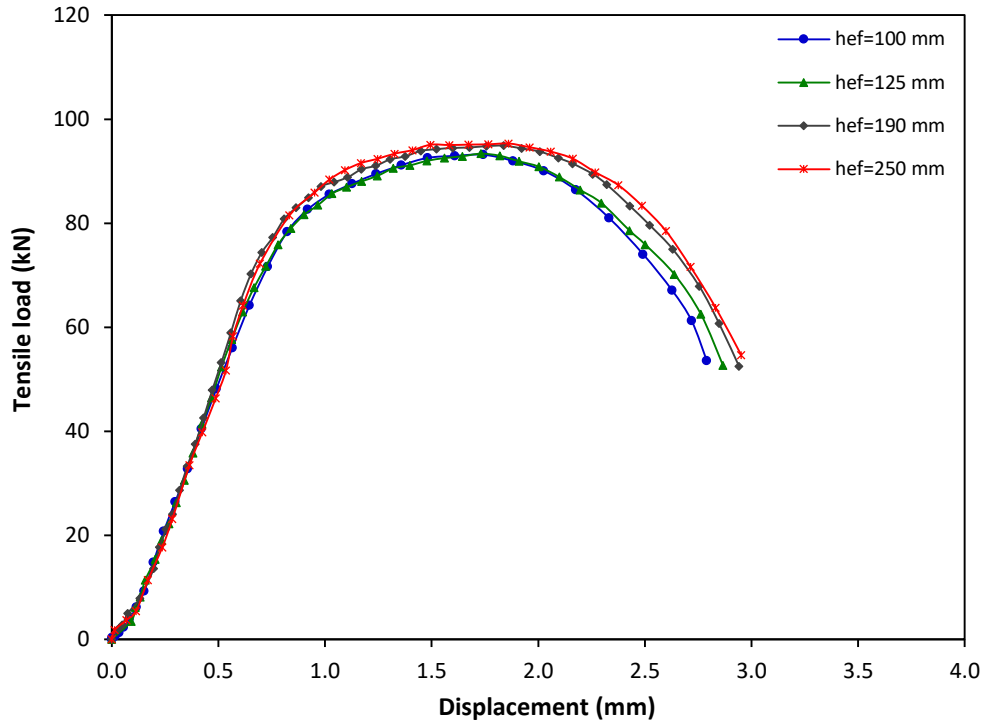


Figure 6-18: Tensile load-displacement graph for the 12-mm diameter undercut anchor at strain rate of 10^{-1} s^{-1}

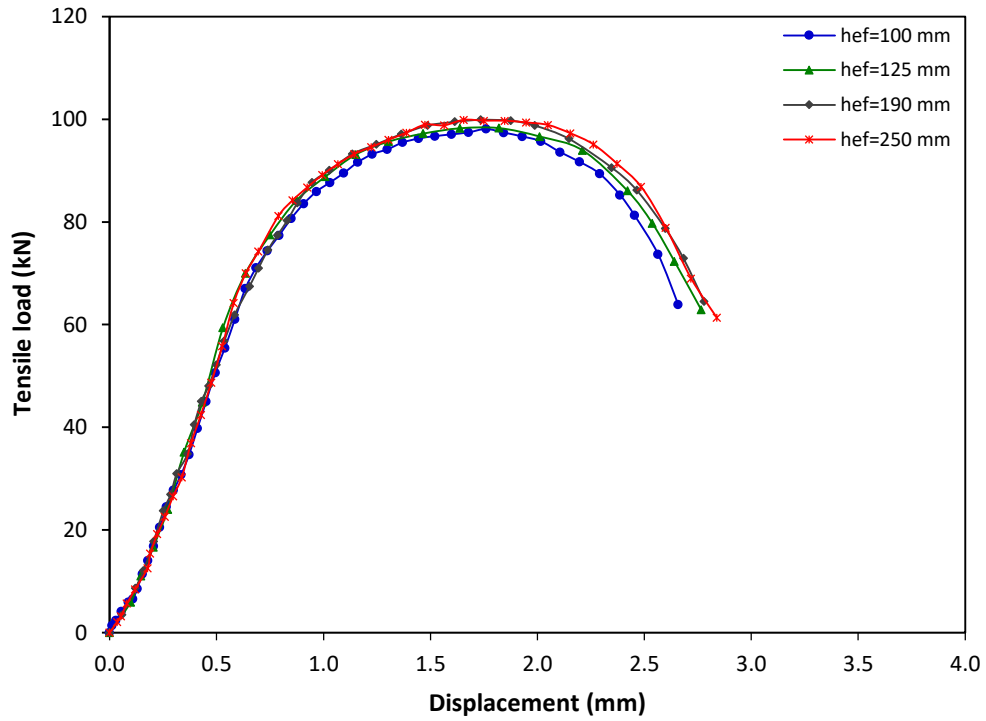


Figure 6-19: Tensile load-displacement graph for the 12-mm diameter undercut anchor at strain rate of 10 s^{-1}

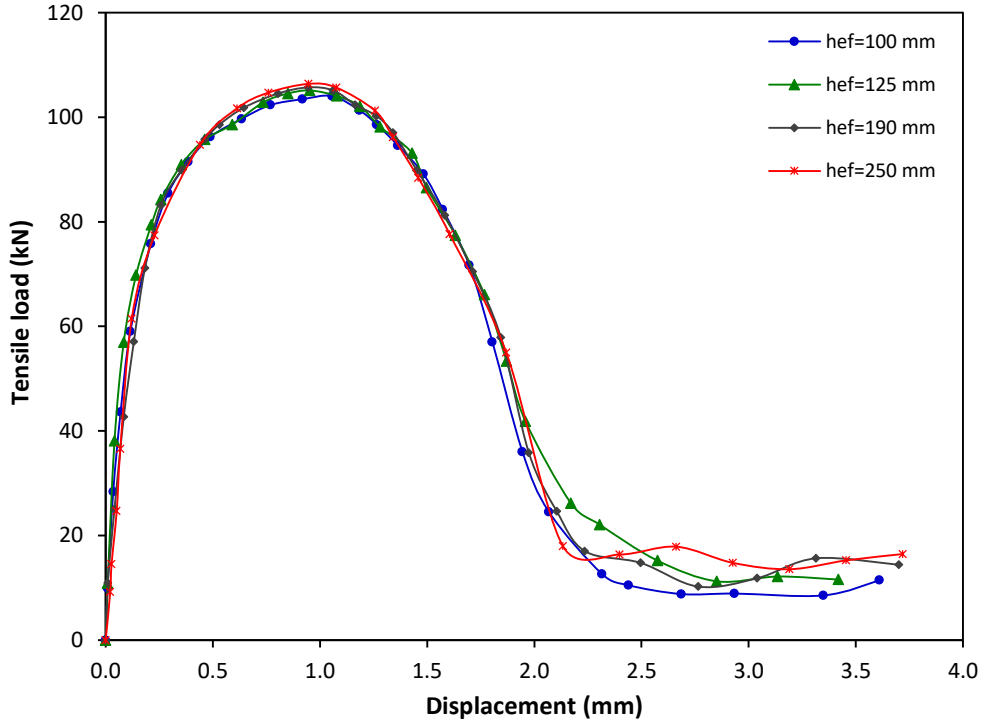


Figure 6-20: Tensile load-displacement graph for the 12-mm diameter undercut anchor at strain rate of 10^2 s^{-1}

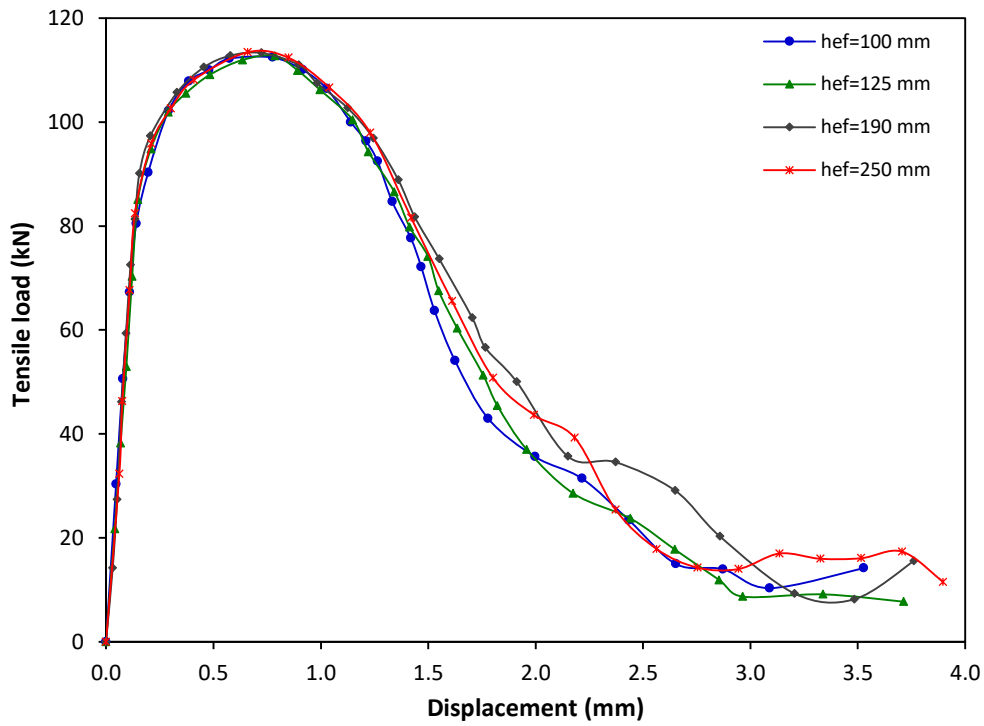


Figure 6-21: Tensile load-displacement graph for the 12-mm diameter undercut anchor at strain rate of 10^3 s^{-1}

As shown in the Figures 6-16 to 6-21, the load increased with displacement up to the ultimate capacity and then decreased until failure. Higher tensile loads were obtained at high strain rate of 10^3 s^{-1} compared to that obtained at low strain rate of 10^{-5} s^{-1} . Maximum tensile load for the 12-mm diameter undercut anchor of 113.46 kN was obtained at high strain rate of 10^3 s^{-1} . The increase in the embedment depth has no effect on the tensile capacity where steel anchor failure is observed.

The results of the load-displacement graphs for the 16-mm and 20-mm diameter undercut anchors with embedment depths of 100 mm, 125 mm, 190 mm and 250 mm at different strain rates are presented in Appendix G. Similar behaviour for the load-displacement relation of the 16-mm and 20-mm diameter undercut anchors were observed at the different strain rates.

Figures 6-22 and 6-23, show the load-displacement behaviour for undercut anchors with embedment depths of 100 mm and 190 mm respectively at the static strain rate of 10^{-5} s^{-1} .

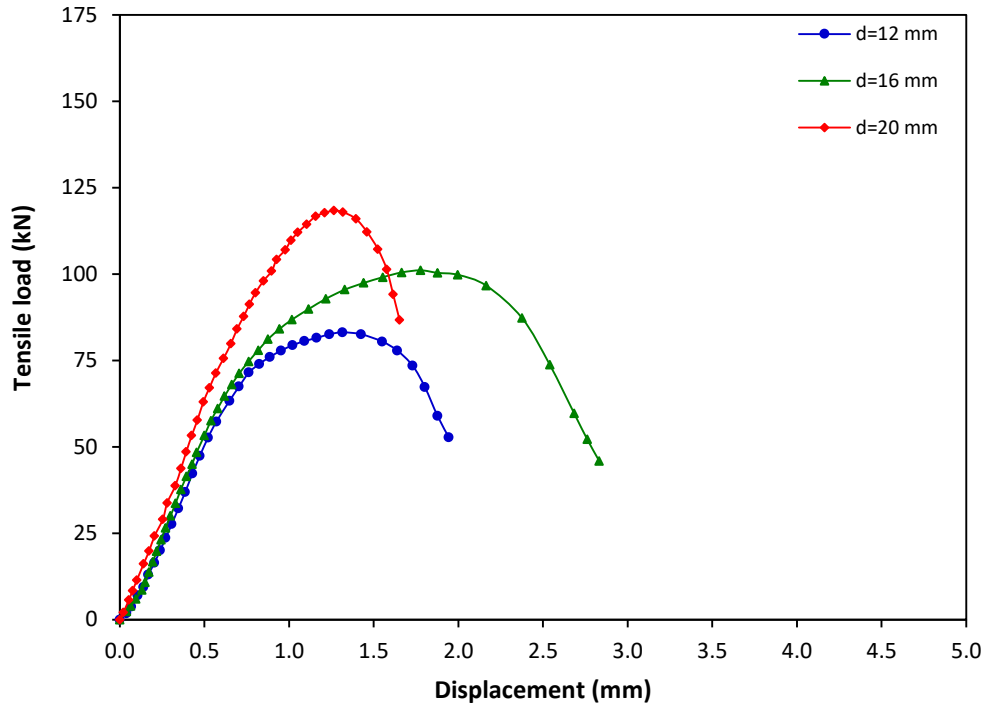


Figure 6-22: Tensile load-displacement response of 100 mm embedment depth undercut anchors at strain rate of 10^{-5} s^{-1}

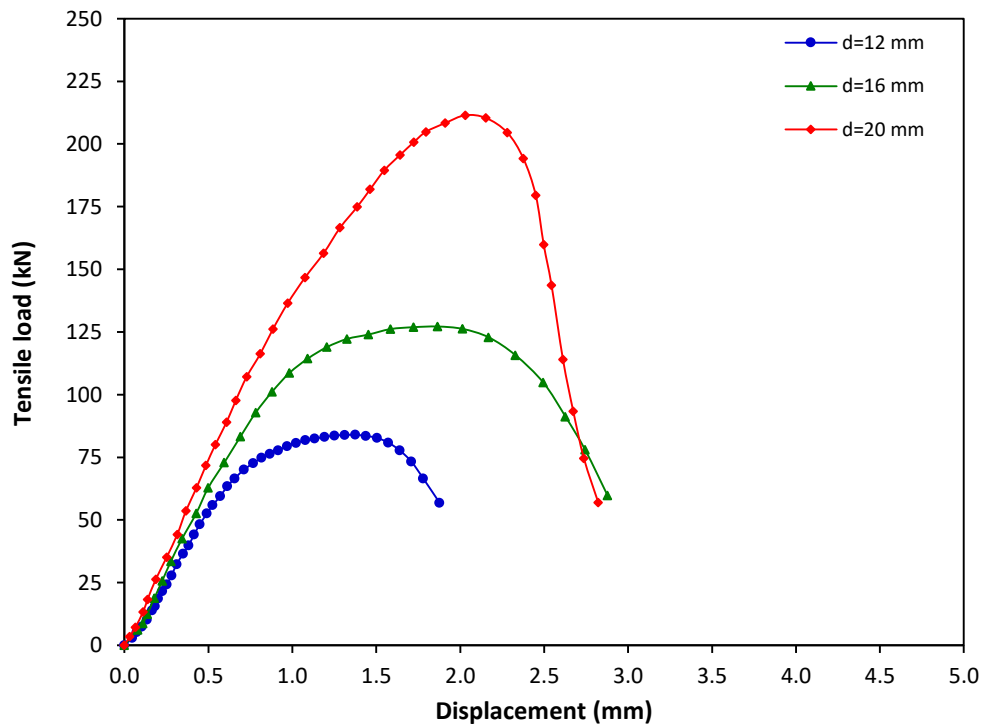


Figure 6-23: Tensile load-displacement response of 190 mm embedment depth undercut anchors at strain rate of 10^{-5} s^{-1}

As shown in Figure 6-22 the increase in the anchor diameter from 12 mm to 20 mm resulted in an increase in tensile capacity from 83.1 kN to 118.4 kN and from 83.9 kN to 211.5 kN for embedment depths of 100 mm and 190 mm respectively. At embedment depth of 100 mm, steel anchor failure was observed for anchor diameter of 12 mm. Concrete cone breakout failure was observed for the anchor diameters of 16 mm and 20 mm. At embedment depth of 190 mm steel anchor failure was observed for all the anchor diameters.

Tables 6-5, 6-6 and 6-7, show the ultimate tensile load and corresponding displacement (δ) for the 12-mm, 16-mm and 20-mm diameter undercut anchors respectively at strain rates ranging from 10^{-5} s^{-1} to 10^3 s^{-1} . As shown in the tables, the increase in the strain rate resulted in increased ultimate tensile load for the undercut anchors investigated. It can be seen that the increase in the anchor diameter increased the ultimate tensile load for the undercut anchors. This is attributed to the increase in the cross-sectional area of the anchor and this requires higher load to cause steel failure. On the other hand, the increase in the anchor diameter increased the concrete cone breakout diameter that require higher load to breakout the concrete cone and hence increasing the tensile capacity.

Table 6-5: Ultimate tensile load and displacement for the 12 mm diameter undercut anchor

Model No.	d (mm)	h_{ef} (mm)	$\dot{\epsilon}$ (s^{-1})	F_u (kN)	δ (mm)	Failure mode
1	12	100	10^{-5}	83.14	1.32	S
2		125		83.22	1.34	S
3		190		83.94	1.39	S
4		250		84.07	1.44	S
5	12	100	10^{-3}	87.19	1.58	S
6		125		88.43	1.55	S
7		190		89.61	1.54	S
8		250		89.72	1.59	S
9	12	100	10^{-1}	93.18	1.74	S
10		125		93.37	1.73	S

11		190		94.90	1.84	S
12		250		95.30	1.86	S
13	12	100	10	98.09	1.76	S
14		125		98.25	1.64	S
15		190		99.52	1.61	S
16		250		99.86	1.65	S
17	12	100	10 ²	104.06	1.06	S
18		125		105.13	0.95	S
19		190		105.70	0.95	S
20		250		106.40	0.95	S
21	12	100	10 ³	112.46	0.78	S
22		125		112.74	0.79	S
23		190		113.32	0.72	S
24		250		113.46	0.66	S

Table 6-6: Ultimate tensile load and displacement for the 16 mm diameter undercut anchor

Model No.	d (mm)	h _{ef} (mm)	$\dot{\epsilon}$ (s ⁻¹)	F _u (kN)	δ (mm)	Failure mode
1	16	100	10 ⁻⁵	101.09	1.78	CC
2		125		126.62	1.88	S
3		190		127.16	1.87	S
4		250		127.43	1.82	S
5	16	100	10 ⁻³	124.46	2.29	S
6		125		130.07	2.26	S
7		190		131.56	2.19	S
8		250		132.25	2.31	S
9	16	100	10 ⁻¹	139.35	1.96	S
10		125		140.31	1.93	S
11		190		141.42	2.05	S
12		250		142.33	1.95	S
13	16	100	10	150.14	1.79	S
14		125		151.05	1.66	S
15		190		151.19	1.59	S
16		250		151.63	1.73	S
17	16	100	10 ²	165.21	0.99	S
18		125		165.58	0.99	S
19		190		165.84	0.99	S
20		250		165.94	1.02	S
21	16	100	10 ³	182.46	0.87	S
22		125		182.76	0.88	S
23		190		182.88	0.79	S
24		250		183.16	0.79	S

Table 6-7: Ultimate tensile load and displacement for the 20 mm diameter undercut anchor

Model No.	d (mm)	h_{ef} (mm)	$\dot{\epsilon}$ (s ⁻¹)	F_u (kN)	δ (mm)	Failure mode
1	20	100	10 ⁻⁵	118.41	1.27	CC
2		125		168.66	1.81	CC
3		190		211.46	2.10	S
4		250		213.29	2.14	S
5	20	100	10 ⁻³	142.16	3.2	CC
6		125		185.01	2.75	CC
7		190		220.52	2.81	S
8		250		221.83	2.79	S
9	20	100	10 ⁻¹	161.18	3.19	CC
10		125		208.53	3.31	CC
11		190		232.39	2.74	S
12		250		233.64	2.84	S
13	20	100	10	186.60	3.49	CC
14		125		236.30	3.59	S
15		190		242.02	4.02	S
16		250		244.50	4.10	S
17	20	100	10 ²	258.89	0.99	S
18		125		258.05	0.95	S
19		190		259.19	1.09	S
20		250		260.39	1.07	S
21	20	100	10 ³	283.96	0.83	S
22		125		284.84	0.65	S
23		190		284.66	0.74	S
24		250		286.36	0.78	S

6.1.8 Effect of strain rate on the ultimate tensile load and DIF of undercut anchors

Figures 6-24, 6-25, 6-26 and 6-27 present the relation between the ultimate tensile load, DIF and the strain rate, for undercut anchor diameters of 12 mm, 16 mm and 20 mm, at embedment depths of 100 mm, 125 mm, 190 mm and 250 mm respectively. The ultimate tensile load increases with increasing anchor diameter from 12 mm to 20 mm for the same strain rate. The ultimate tensile load increased almost linearly with the strain rate for anchor diameters of 12 mm and 16 mm where steel anchor failure is the dominant failure mode at all the strain rates investigated (Figure 6-24, 6-25, 6-26 and 6-27). Hence the increase in

the tensile load is attributed to the increase in steel strength at high strain rate. For 20-mm diameter undercut anchor, as the strain rate increased from 10^{-5} s^{-1} to 10 s^{-1} , the ultimate tensile load was observed to increase according to a nearly bilinear relationship with a change in slope at a strain rate of about 10 s^{-1} where concrete cone breakout failure was observed (Figures 6-24, 6-25, 6-26 and 6-27). The ultimate tensile load increased with further increase in the strain rate to 10^2 s^{-1} where the failure mode transitioned to steel anchor failure. The increase in the ultimate load with the increase in the strain rate is attributed to the increase in the tensile strength of the concrete and steel materials with the increase in the strain rate. Maximum tensile loads of 113.5 kN, 183.2 kN and 286.4 kN were obtained for the 12-mm, 16-mm and 20-mm diameter undercut anchors respectively at high strain rate of 10^3 s^{-1} .

Strain rate of 10^{-5} s^{-1} represents the static strain rate and is taken as the base line to determine the DIF at different strain rates for the anchors exhibited concrete cone failure. For the anchors exhibited steel failure, the DIF is taken as the ratio of the ultimate dynamic load at strain rates higher than 10^{-5} s^{-1} to the ultimate static steel failure load for the anchors. As shown in Figures 6-24 and 6-25, the DIF for anchor diameters of 12 mm and 16 mm increases with the increase in the strain rate from 10^{-3} s^{-1} to 10^3 s^{-1} where steel failure was observed. The increase in the DIF is attributed to the increase in the steel strength with the increase in the strain rate. For anchor diameter of 20 mm with embedment depth of 100 mm (Figure 6-24), the DIF increased to 1.58 at strain rate of 10 s^{-1} where concrete cone failure was observed. At high strain rates of 10^2 s^{-1} and 10^3 s^{-1} steel failure was observed and the DIF was taken as the ratio of the dynamic ultimate load to the static steel failure

load with DIFs of 1.22 and 1.34 respectively. For anchor diameter of 20 mm with embedment depth of 125 mm (Figure 6-25), the DIF increased to 1.24 at strain rate of 10^{-1} s^{-1} where concrete cone failure was observed. At higher strain rates of 10 s^{-1} up to 10^3 s^{-1} steel failure was observed with maximum DIF of 1.35.

It can be seen from Figures 6-26 and 6-27, the DIF increased with the increase in the strain rate from 10^{-5} s^{-1} to 10^3 s^{-1} for all anchor diameters investigated. Maximum DIF of 1.35 and 1.44 are obtained for the anchor diameters of 12 mm, 16 mm respectively at highest strain rate of 10^3 s^{-1} where steel failure was the dominant failure mode at all the strain rates investigated. For the anchor diameter of 20 mm maximum DIF of 1.58 was obtained at strain rate of 10 s^{-1} with embedment depth of 100 mm where concrete cone breakout failure was observed. The failure mode transitioned from concrete cone breakout failure to steel failure at high strain rates of 10^2 s^{-1} and 10^3 s^{-1} .

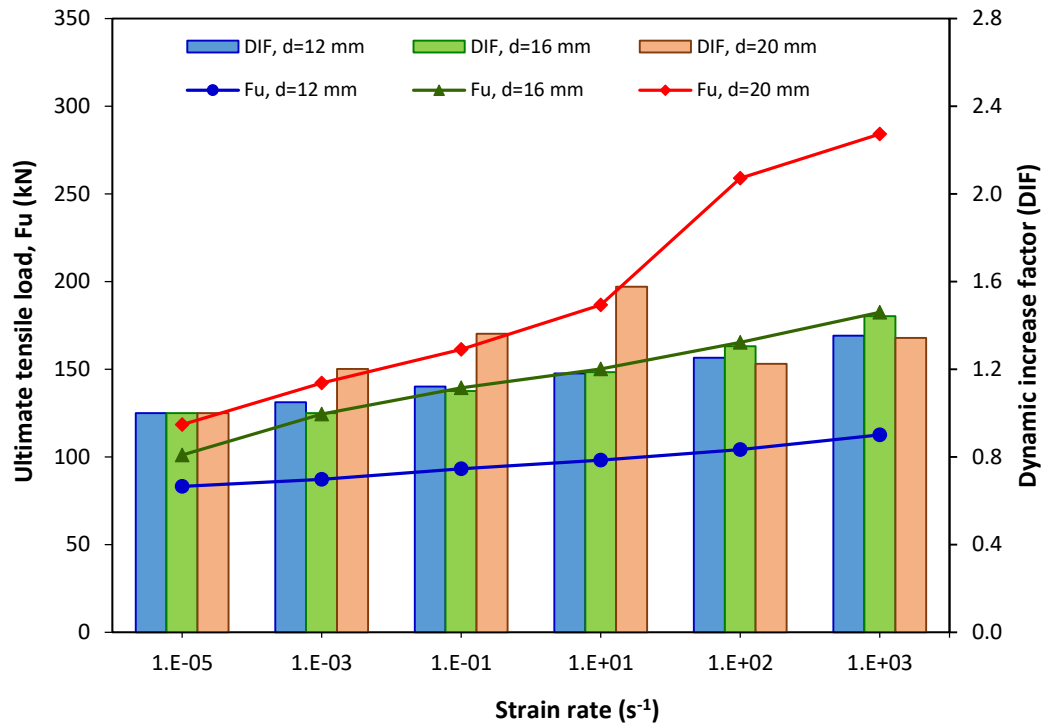


Figure 6-24: Ultimate tensile load and DIF versus strain rate for the undercut anchor at 100 mm embedment depth

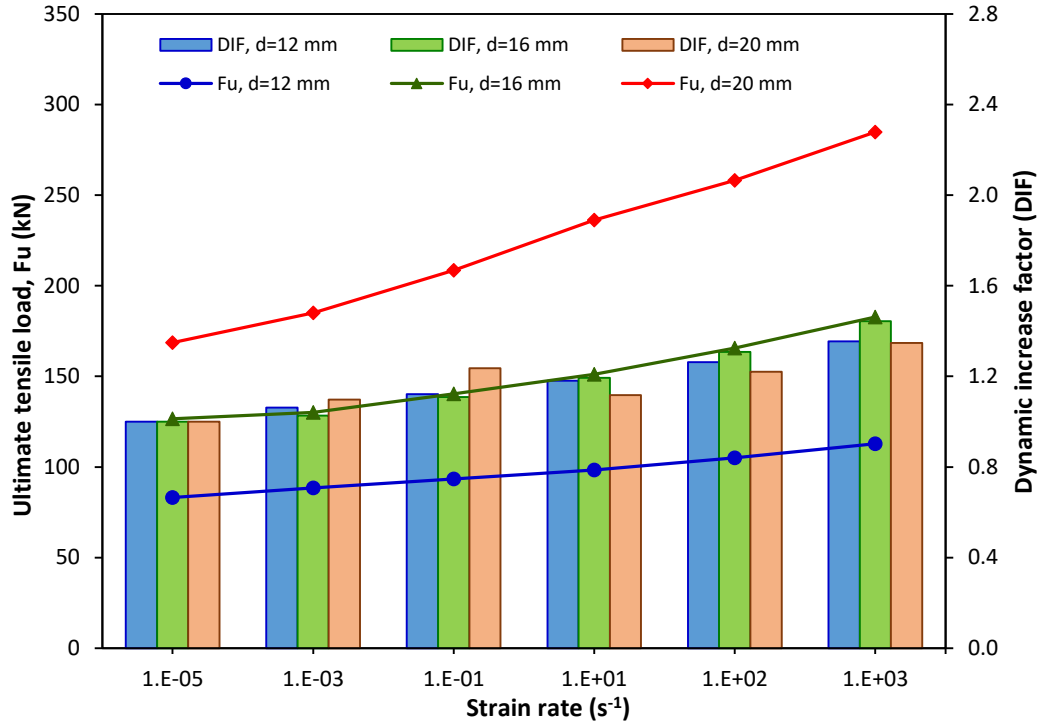


Figure 6-25: Ultimate tensile load and DIF versus strain rate for the undercut anchor at 125 mm embedment depth

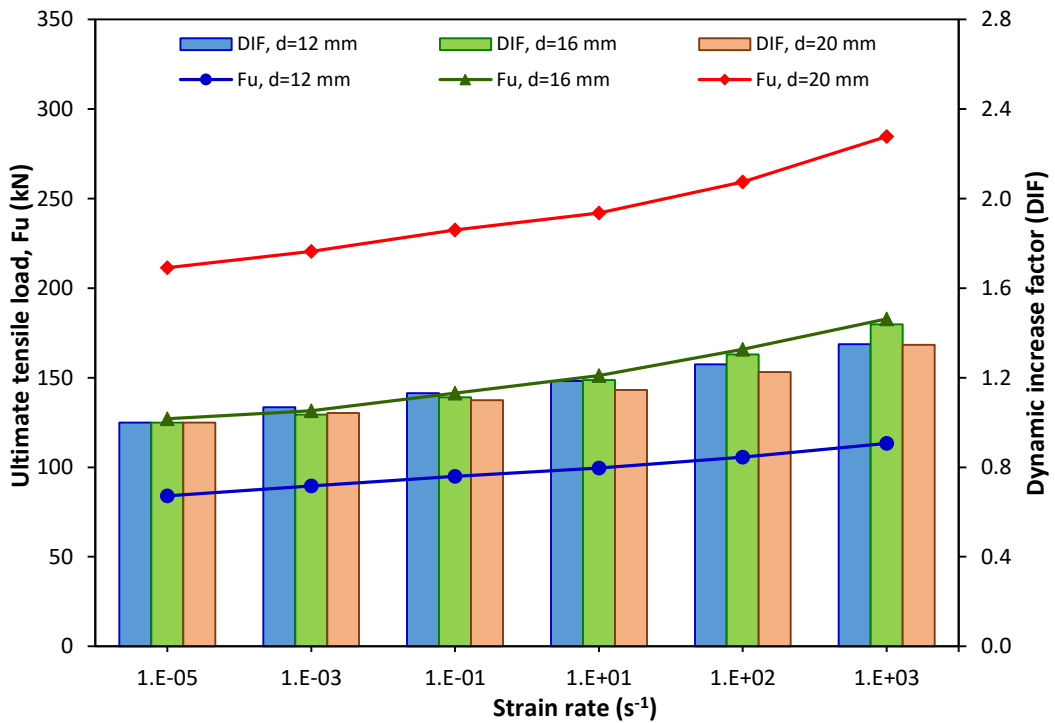


Figure 6-26: Ultimate tensile load and DIF versus strain rate for the undercut anchor at 190 mm embedment depth

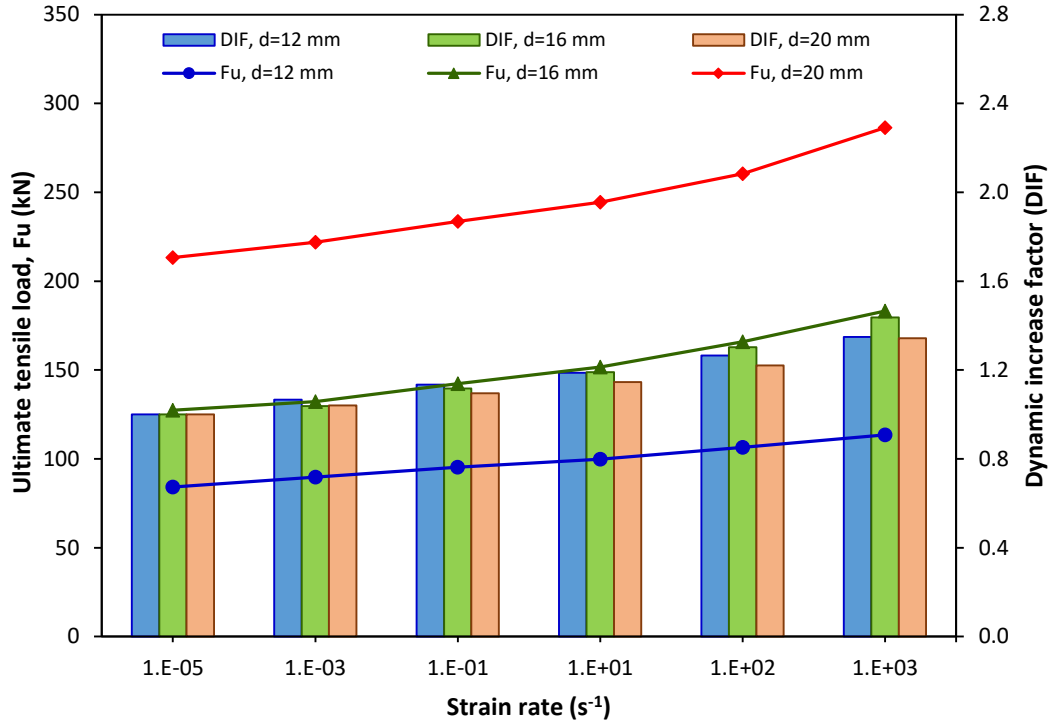


Figure 6-27: Ultimate tensile load and DIF versus strain rate for the undercut anchor at 250 mm embedment depth

Table 6-8 shows maximum DIF for the undercut anchors under tensile load where concrete cone breakout and steel anchor failure modes were observed. The value of DIF equal to one represents the DIF at the static strain rate of 10^{-5} s^{-1} where concrete cone breakout failure mode is observed for the 16 mm and 20 mm diameter undercut anchors with embedment depth of 100 mm. Also, concrete cone breakout failure was observed for the 20 mm diameter with 125 mm embedment depth. Steel anchor failure was the dominant failure mode for most of the undercut anchors at the static strain rate of 10^{-5} s^{-1} and higher strain rates up to 10^3 s^{-1} . Maximum value of the DIF for the undercut anchors exhibited steel failure was obtained at high strain rate of 10^3 s^{-1} and presented in Table 6-8.

Table 6-8: Maximum Dynamic increase factor for the undercut anchors under tensile load

Model No.	d (mm)	h _{ef} (mm)	ε̇ (s ⁻¹)	DIF	ε̇ (s ⁻¹)	DIF
				CC		S
1	12	100	-	-	10 ³	1.35
2	12	125	-	-	10 ³	1.35
3	12	190	-	-	10 ³	1.35
4	12	250	-	-	10 ³	1.35
5	16	100	10 ⁻⁵	1.00	10 ³	1.44
6	16	125	-	-	10 ³	1.44
7	16	190	-	-	10 ³	1.44
8	16	250	-	-	10 ³	1.44
9	20	100	10	1.58	10 ³	1.34
10	20	125	10 ⁻¹	1.24	10 ³	1.35
11	20	190	-	-	10 ³	1.35
12	20	250	-	-	10 ³	1.34

6.1.9 Regression analysis for the undercut anchors under tensile load

Regression analysis was performed for the undercut anchors under tensile load to develop an accurate predictive model based on the finite element results for determining the DIF of undercut anchors. Most of the undercut anchors exhibited steel anchor failure when subjected to strain rates in the range of 10^{-3} s^{-1} to 10^3 s^{-1} , hence regression analysis has been performed for the steel anchor failure mode. The relation between the DIF and the strain rate ratio ($\dot{\epsilon}_d/\dot{\epsilon}_s$) for the undercut anchor diameters of 12 mm, 16 mm and 20 mm exhibited steel failure is shown in Figure 6-28.

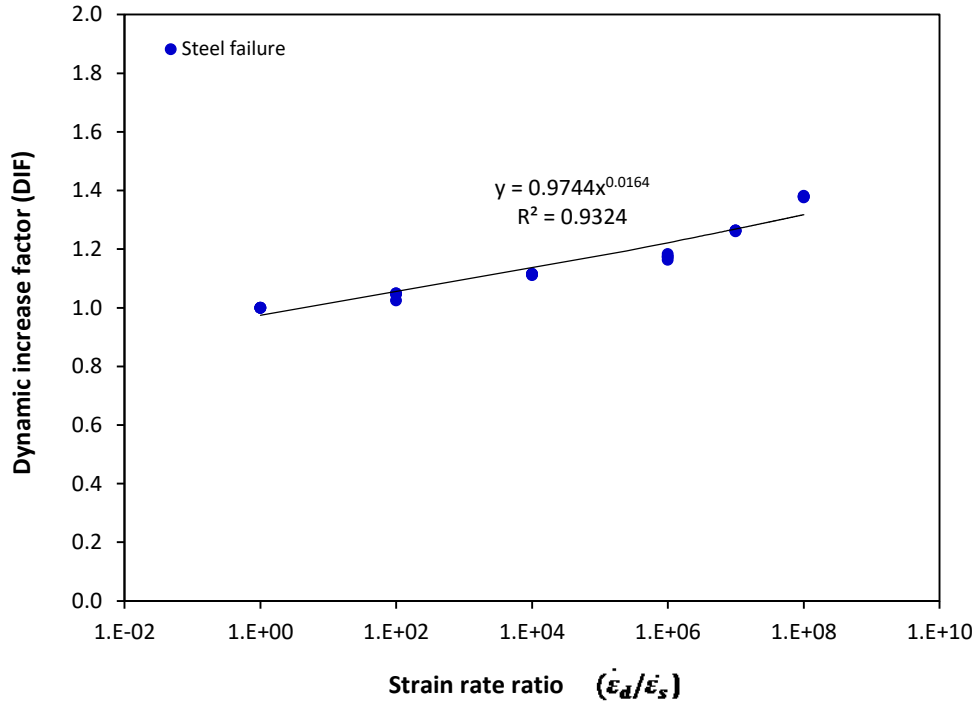


Figure 6-28: Effect of strain rate ratio on the DIF for the undercut anchors exhibited steel failure under tensile load

A formula relating DIF with the strain rate was developed using various regression models; namely, exponential, linear, logarithmic and power regression models. The predicted formulae obtained from various regression models is shown in Table 6-9.

Table 6-9: Statistical models and coefficient of determination to predict the DIF for the undercut anchors exhibited steel failure under tensile load

Statistical models	Formulae	Coefficient of determination (R^2)
Exponential	$DIF = 1.1061e^{2E-09(\frac{\dot{\epsilon}_d}{\dot{\epsilon}_s})}$	0.597
Linear	$DIF = 3E - 09(\frac{\dot{\epsilon}_d}{\dot{\epsilon}_s}) + 1.1094$	0.639
Logarithmic	$DIF = 0.019 \ln\left(\frac{\dot{\epsilon}_d}{\dot{\epsilon}_s}\right) + 0.9645$	0.908
Power	$DIF = 0.9744\left(\frac{\dot{\epsilon}_d}{\dot{\epsilon}_s}\right)^{0.0164}$	0.932

As shown in Table 6-9, the power regression model was observed to be best fit for the results with coefficients of determination (R^2) of 93% for the undercut anchors exhibited steel failure. The DIF is represented by Equation (6.1) for the undercut anchors subjected to tensile load and exhibited steel failure.

$$DIF = 0.9744 \left(\frac{\dot{\epsilon}_d}{\dot{\epsilon}_s} \right)^{0.0164} \quad (6.1)$$

The ultimate dynamic load (F_{ud}) for the undercut anchors exhibited steel anchor failure can be determined as in Equation (6.2) as follows:

$$F_{ud} = F_{us} \times 0.9744 \left(\frac{\dot{\epsilon}_d}{\dot{\epsilon}_s} \right)^{0.0164} \quad (6.2)$$

Where the ultimate static load (F_{us}) can be determined from Equation (4.2) for steel anchor failure mode.

Figure 6-29 presents the residual analysis for undercut anchor subjected to tensile load and exhibited steel anchor failure. Where the difference between the finite element analysis and the DIF results obtained from Equations (6.1) is presented. As shown in Figure 6-29, approximately horizontal trend line was observed for the residual with the increase in the strain rate ratio.

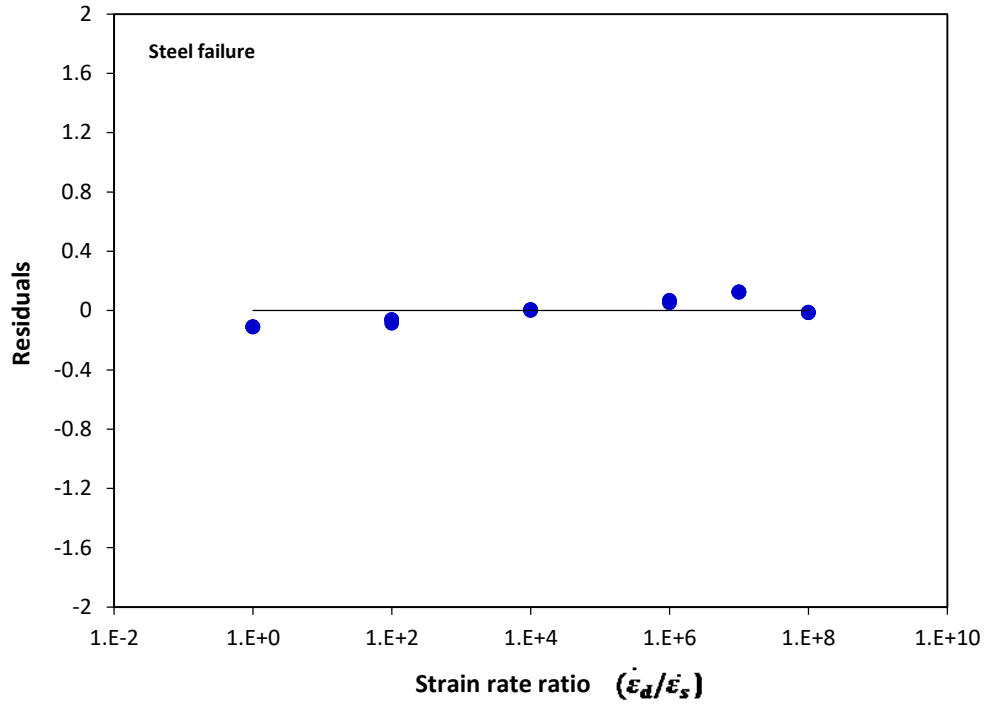


Figure 6-29: Residual versus strain rate ratio for the undercut anchors exhibited steel failure

In order to verify the accuracy of the proposed equation, new undercut anchors with diameters of 12 mm, 16 mm and 20 mm with embedment depths of 140 mm, 160 mm and 220 mm were developed. Figure 6-30 shows the relation between the DIF obtained from the newly developed numerical models and the predicted DIF obtained from Equation (6.1). As shown in the figure, the DIF values are uniformly distributed around the equality line. This means that power model presented in the Equation (6.1) can best represent the finite element results.

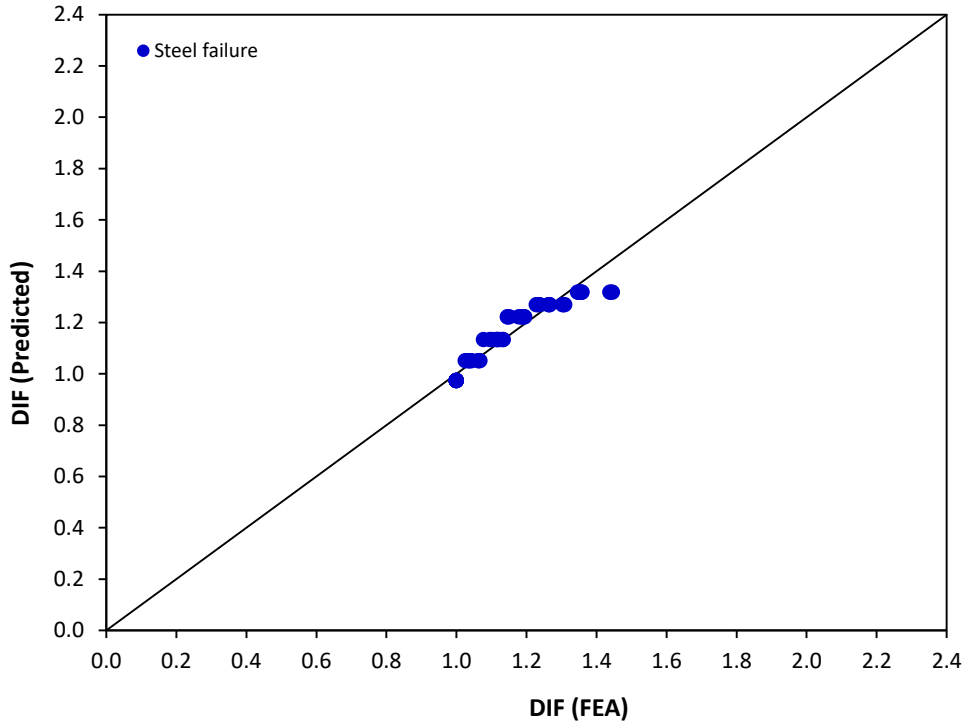


Figure 6-30: DIF obtained from the finite element analysis versus the predicted DIF for the undercut anchors exhibited steel failure

Also, in order to verify the results obtained from the finite element analysis, a comparison has been made between the ultimate dynamic load obtained from the finite element analysis for the undercut anchors exhibited concrete cone breakout and the proposed equation by Fujikake et al. (Fujikake et al., 2003) Equation (4.10) as shown in Table 6-10. As shown in the table the finite element results for the undercut anchors overpredict the dynamic load obtained from the proposed equation by Fujikake et al.

Table 6-10: Comparison between ultimate dynamic load for the undercut anchor obtained from the FEA and proposed equation by Fujikake et al. (2003)

d (mm)	h_{ef} (mm)	$\dot{\epsilon}_s$ (s⁻¹)	$\dot{\epsilon}_d$ (s⁻¹)	$\dot{\epsilon}_d/\dot{\epsilon}_s$	F_{us} FEA (kN)	F_{ud} FEA (kN)	F_{ud} Fujikake (kN)	F_{ud} FEA/ Fujikake
16	100	10 ⁻⁵	10 ⁻⁵	1	101.09	101.09	101.12	1.00
20	100	10 ⁻⁵	10 ⁻⁵	1	118.41	118.41	103.02	1.15
20	100	10 ⁻⁵	10 ⁻³	10 ²	118.41	142.16	104.38	1.36
20	100	10 ⁻⁵	10 ⁻¹	10 ⁴	118.41	161.18	117.94	1.37
20	100	10 ⁻⁵	10	10 ⁶	118.41	186.6	175.20	1.07
20	125	10 ⁻⁵	10 ⁻⁵	1	168.66	168.66	141.32	1.19
20	125	10 ⁻⁵	10 ⁻³	10 ²	168.66	185.01	143.17	1.29
20	125	10 ⁻⁵	10 ⁻¹	10 ⁴	168.66	208.53	161.78	1.29

6.2 Finite element modeling for undercut anchors under shear load

Finite element analyses were performed to investigate the shear behaviour of undercut anchors. Three anchor diameters of 12 mm, 16 mm and 20 mm with embedment depths of 100 mm, 125 mm, 190 mm and 250 mm were investigated. Figure 6-31 shows the geometric configuration and boundary conditions for the undercut anchor model under shear load.

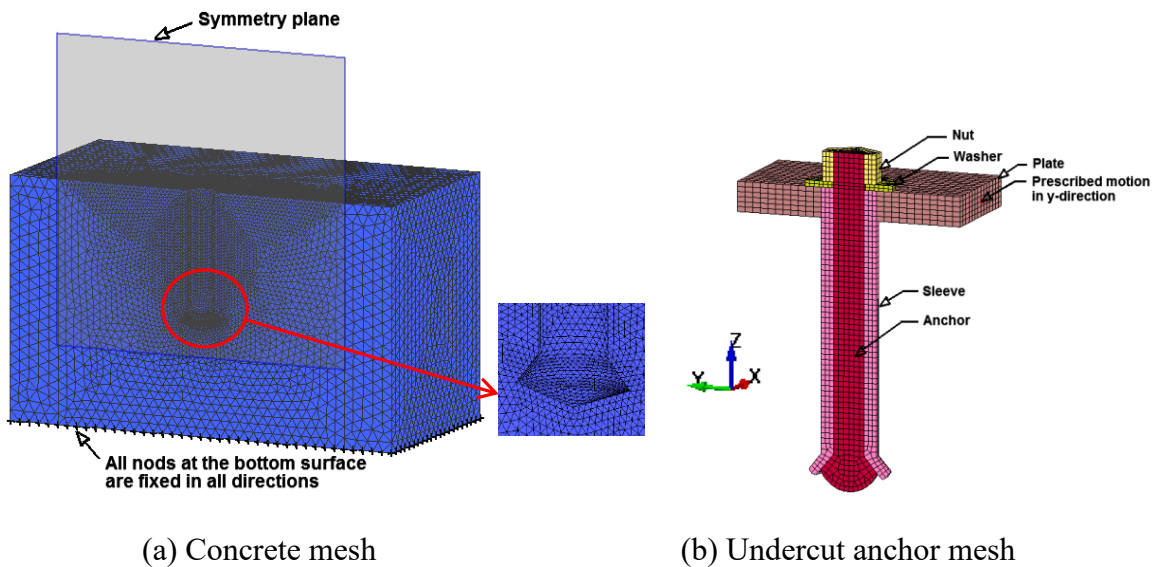


Figure 6-31: Geometric configuration and boundary conditions for the undercut anchor model

6.2.1 Validation of undercut anchor model under shear load

The numerical model of the undercut anchor under shear load was validated by comparing the finite element results with the experimental results obtained by Mahadik et al. (Mahadik et al., 2016). A finite element model, representing the test conducted by Mahadik et al., was developed using LS-DYNA software. Hilti undercut anchor through-set type was used. The undercut anchor used had yield strength of 640 MPa, tensile strength of 800 MPa,

diameter of 12 mm and embedment depth of 125 mm. The cube compressive strength of the concrete block used in the finite element analysis of 42.6 MPa ($f'_c = 33.5$ MPa) same as in the experimental test conducted by Mahadik et al. Mesh sensitivity analyses were carried out to obtain a mesh size that improve the accuracy and give converged results to the experimental results conducted by Mahadik et al. Table 6-11 shows the effect of mesh size refinement on the convergence of the ultimate shear load and failure mode.

Table 6-11: Effect of mesh size refinement on the convergence of ultimate shear load for undercut anchor

Model No.	Mesh size (mm)			Ultimate shear load (kN)		Displacement (mm)		Failure mode
	Anchor	Concrete		FEA	EXP.	FEA	EXP.	
		Min.	Max.					
1	2	4	12	126.21	131.9	19.10	18.71	Steel failure
2	2	2	12	128.65		18.89		Steel failure
3	1	1	12	134.73		18.82		Steel failure

The finite element analysis exhibited a percentage difference of 4.5%, 2.5% and 2.1% for the ultimate shear load for the models No. 1, 2 and 3 respectively in comparison with the experimental results. Mesh size of model No. 2 gave load-displacement results agree well with the experimental results reported by Mahadik et al. with better computation time and selected for the analysis. A comparison of shear load–displacement response of the finite element analysis and experimental results is shown in Figure 6-32. As shown in the figure same shear load-displacement behaviour was observed for the all mesh sizes investigated. Finite element analysis results exhibited steel anchor failure mode similar to that observed by Mahadik et al. as shown in Figure 6-33.

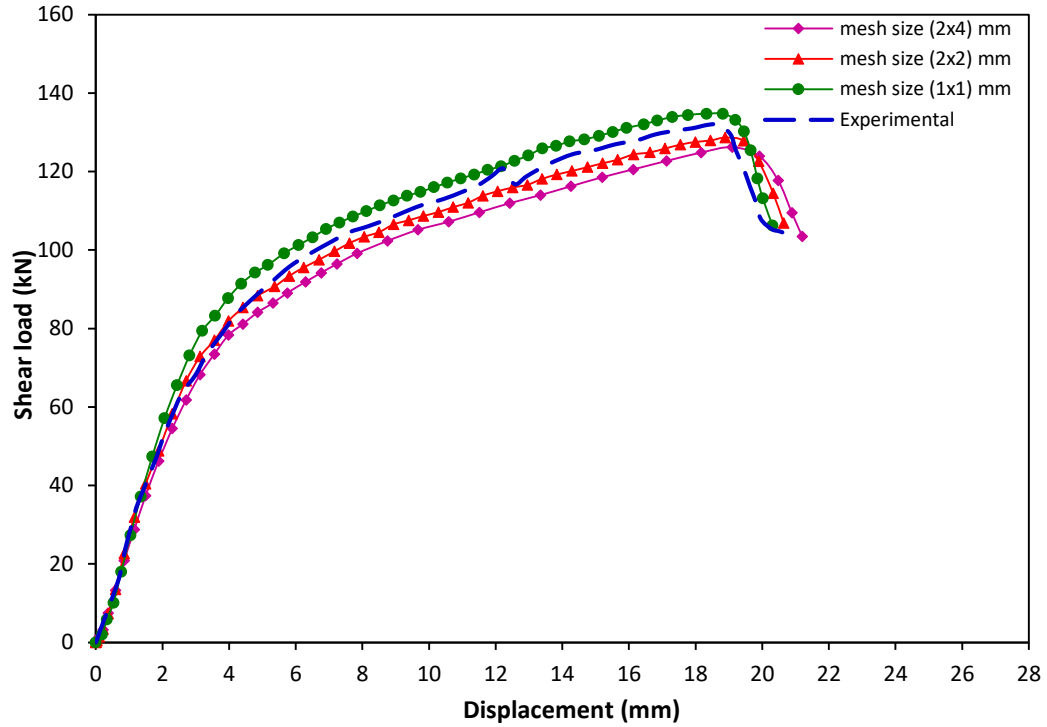


Figure 6-32: Comparison of shear load-displacement relation between FEA and experimental results obtained by Mahadik et al. (Mahadik et al., 2016)

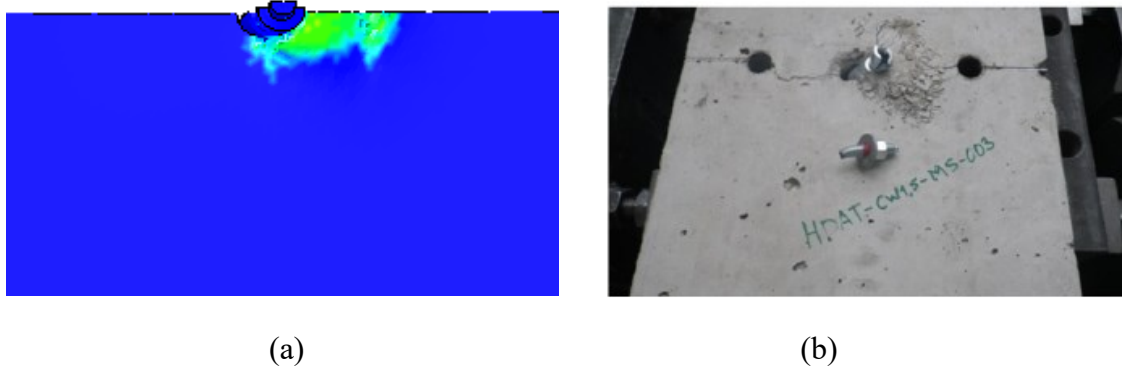


Figure 6-33: Failure mode obtained from:(a) finite element analysis and (b) experimental results obtained by Mahadik et al. (Mahadik et al., 2016)

6.2.2 Comparison of finite element results with design methods

For the anchors placed far away from the concrete free edge, pryout failure mode or anchor failure is often the dominant failure modes. The shear failure load of anchors exhibiting pryout failure can be calculated according to ACI 318 Equation (4.14) (ACI Committee

318, 2011). The shear failure load of anchors that exhibit steel fracture failure can be calculated according to ACI 318 method as in Equation (4.18) (ACI Committee 318, 2011). The ultimate shear load obtained from the finite element analysis was compared with ACI 318 method (Table 6-12). It can be seen that for the anchor diameter of 12-mm with embedment depths of 125 mm and 190 mm, a slight difference in the shear load where steel failure is observed. This can be attributed to the influence of embedment depth on the bending, tensile and shear stresses that are generated in the anchor due to the applied shear load. As shown in Table 6-12, the ACI 318 method overestimates the shear capacity for the undercut anchors investigated except for the anchor diameter of 20-mm where pryout failure mode was observed. The ACI method takes into account the effect of embedment depth, however the influence of anchor diameter is not considered in the case of pryout failure mode. In general, the FEA results show good agreement with the ACI 318 method.

Table 6-12: Comparison of ultimate shear load obtained from FEA and ACI 318 method

d (mm)	h _{ef} (mm)	Failure Load (kN)		FEA/ ACI 318	*Failure mode
		FEA static ($\dot{\epsilon} = 10^{-5} \text{ s}^{-1}$)	ACI 318		
12	100	132.27	164.23	0.81	PR
12	125	148.09	166.25	0.89	S
12	190	153.57	166.25	0.92	S
16	100	152.26	164.23	0.93	PR
16	125	199.42	229.52	0.87	PR
16	190	270.05	317.05	0.85	PR
16	250	304.6	317.05	0.96	S
20	100	175.37	164.23	1.07	PR
20	125	227.49	229.52	0.99	PR
20	190	344.63	430.13	0.80	PR
20	250	420.84	488.58	0.86	S

*Failure mode: PR= pryout failure; S= steel anchor fracture

6.2.3 Crack pattern for the undercut anchors under shear load

Figure 6-34 shows the crack patterns for the undercut anchors of different diameters and embedment depths at strain rate of 10^{-5} s^{-1} . As shown in the figure, pryout failure mode was observed for the undercut anchors with embedment depth of 100 mm. At embedment depths of 125 mm and 190 mm, steel anchor failure was observed for the 12-mm diameter anchor whereas pryout failure was observed for the 16-mm and 20-mm diameter anchors. At embedment depth of 250 mm, steel anchor failure was observed for all the anchor diameters investigated.

Level of damage and cracking in the concrete increased with the increase in the anchor diameter. It can be seen that, at the low strain rate of 10^{-5} s^{-1} the anchor diameter and embedment depth have an effect on the failure mode. The increase in the embedment depth from 100 mm to 125 mm resulted in concrete spalling followed by anchor fracture for the 12-mm diameter undercut anchor. The increase in the anchor diameter from 12 mm to 20 mm for the same embedment depth of 125 mm resulted in pryout failure of the anchor. It can be stated that, the increase in the undercut anchor diameter at low strain rate increases the probability of pryout failure as the anchor stiffness increases.

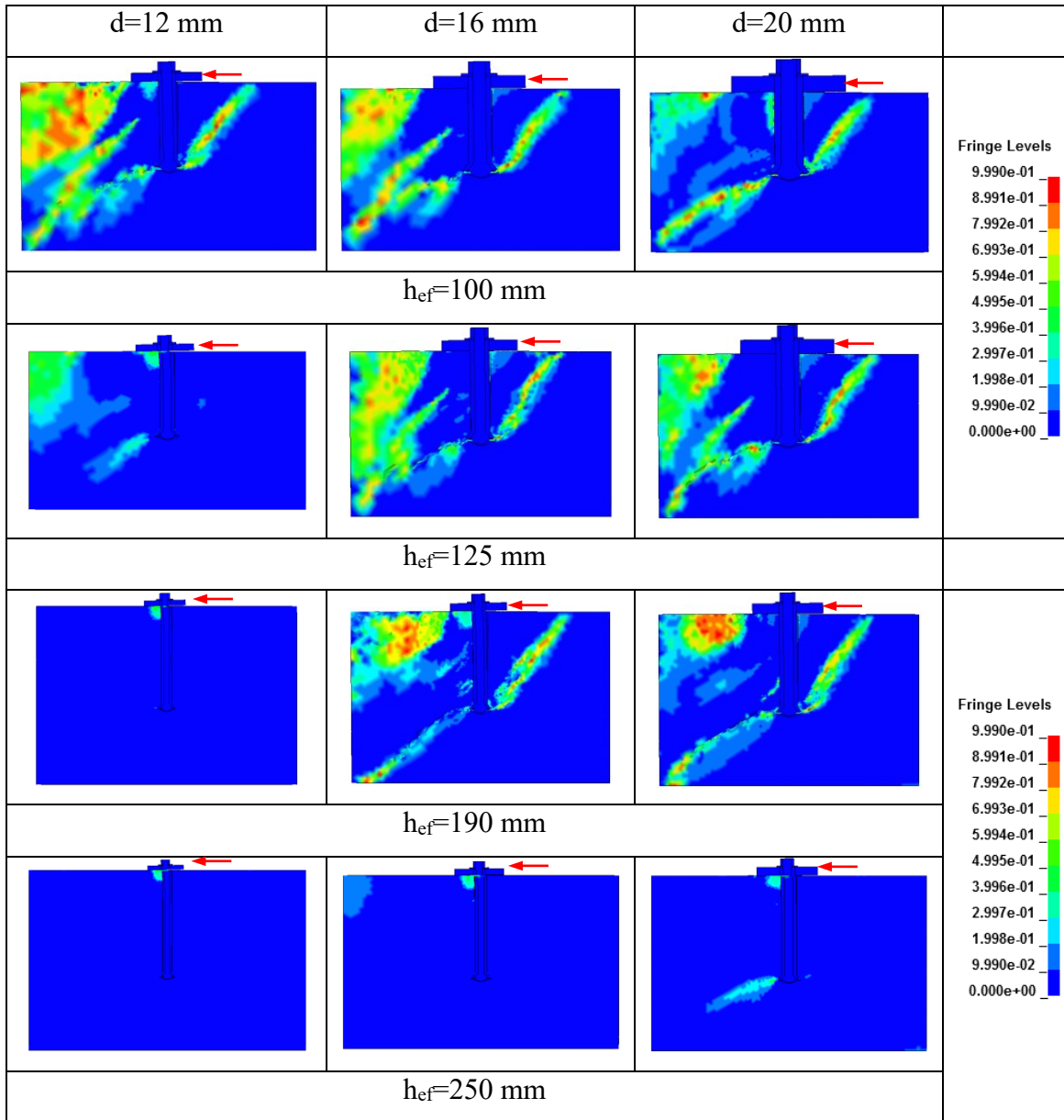


Figure 6-34: Plastic strain contours for undercut anchors under shear load at strain rate of 10^{-5} s^{-1}

6.2.4 Effect of strain rate on the level of damage and failure mode

When the shear load is applied on the anchor plate, the load is transferred from the anchor plate to the undercut anchor. For the through-set type undercut anchor used in the analysis, both the sleeve and the anchor body share in resisting the shear load and transfer it to the

concrete resulting in developing compressive stresses in the concrete in front of the anchor. These stresses increase with the increase in the applied shear load, create concrete cracking under the anchor plate and result in displacement of the anchor plate in vertical direction and rotation about the point of contact on the concrete surface. Three failure modes were observed; concrete pryout, concrete spalling and steel anchor failure modes. For the pryout failure mode, cracks initiate at the bottom of the sleeve and propagate diagonally towards the concrete surface resulting in breakout of a half concrete cone at the backside of the anchor, leading to pryout failure. For the concrete spalling, the stresses are concentrated in the concrete in front of the anchor resulting in concrete cracking without breakout of a half concrete cone behind the anchor. On the other hand, when the tensile, bending and shear stresses concentrated on the anchor, steel failure is observed. Failure mode for the 12-mm, 16-mm and 20-mm diameter undercut anchors at different strain rates is presented in Figures 6-35, 6-36 and 6-37 respectively.

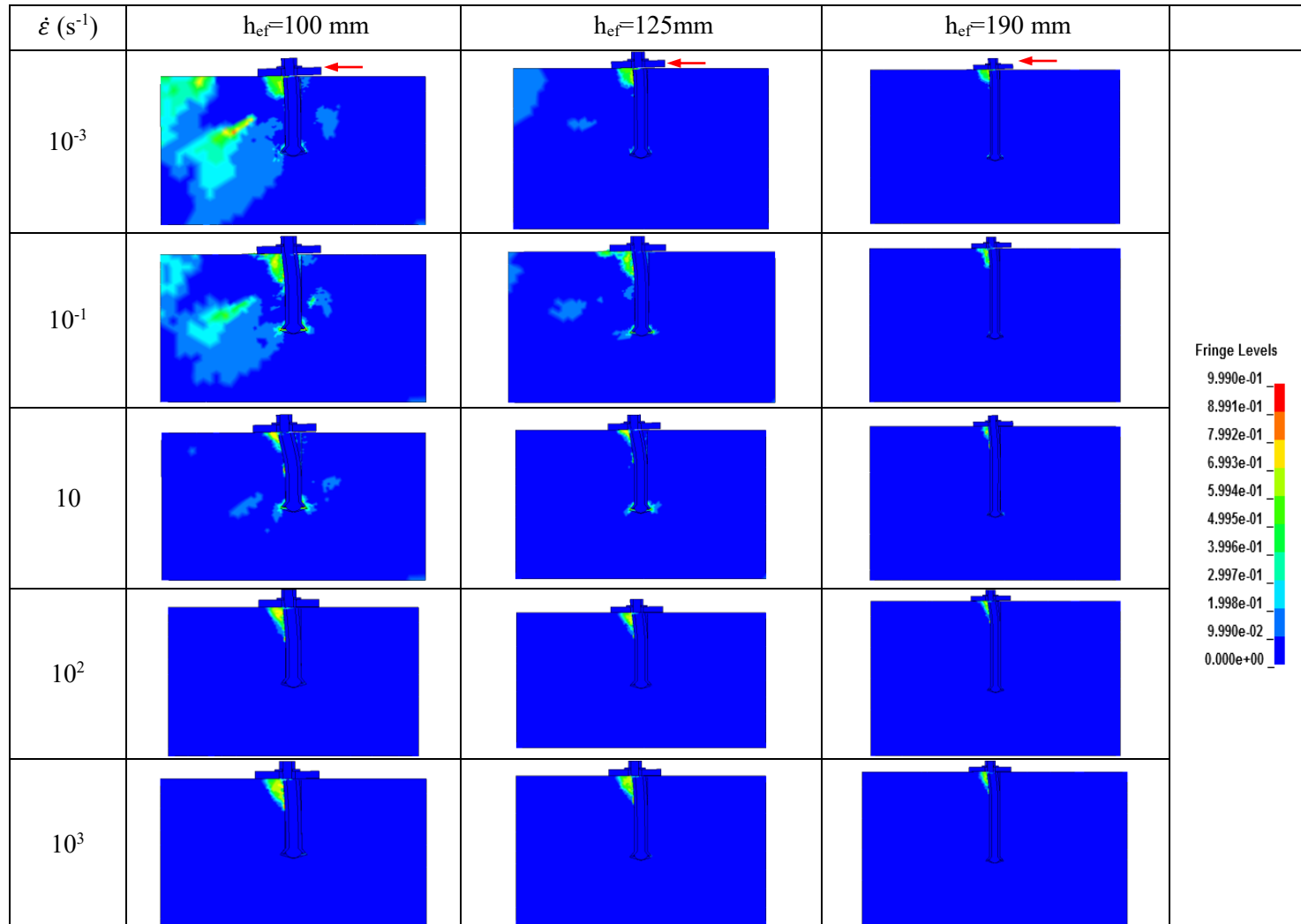


Figure 6-35: Failure mode of 12-mm diameter undercut anchor at different strain rates

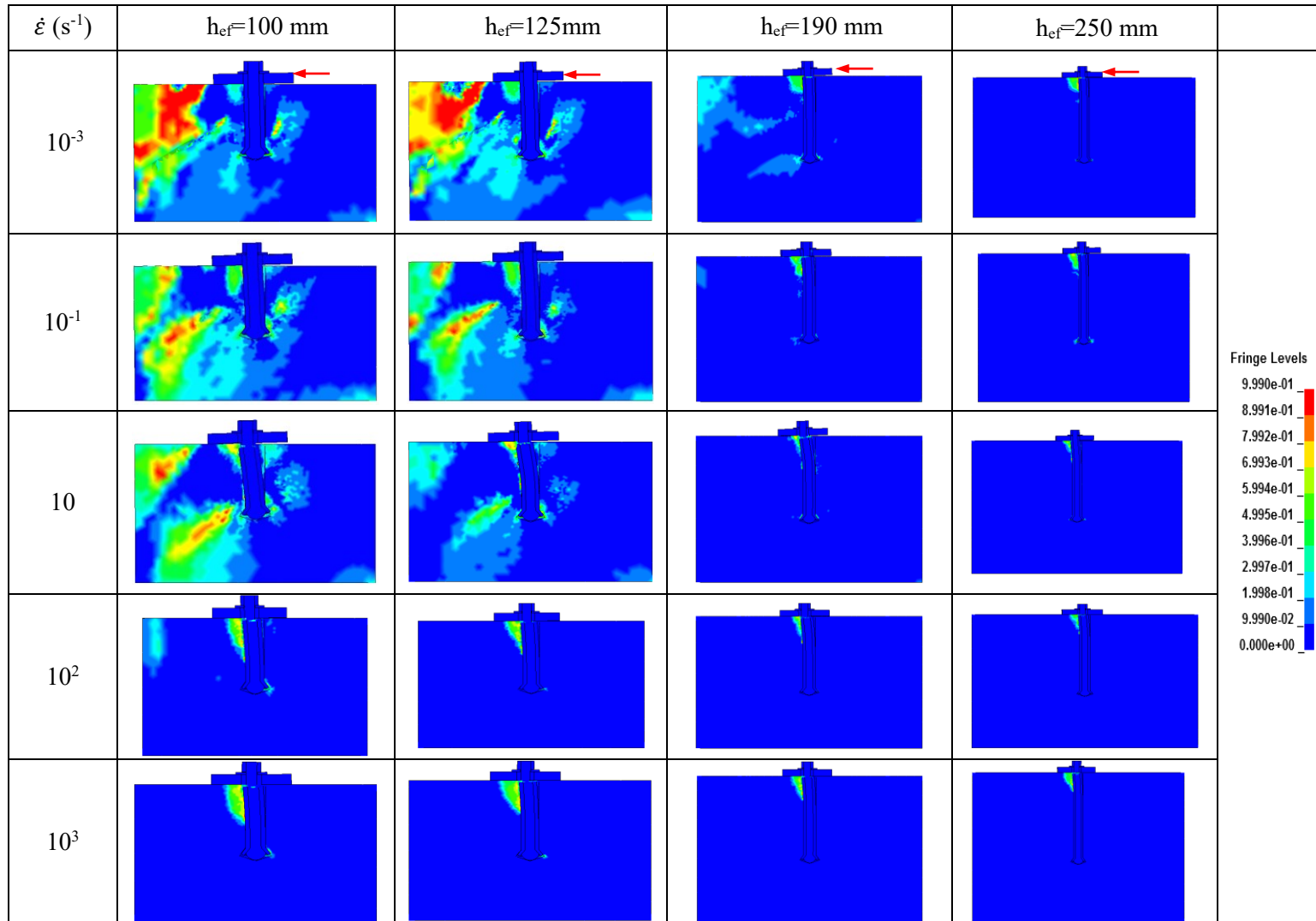


Figure 6-36: Failure mode of 16-mm diameter undercut anchor at different strain rates

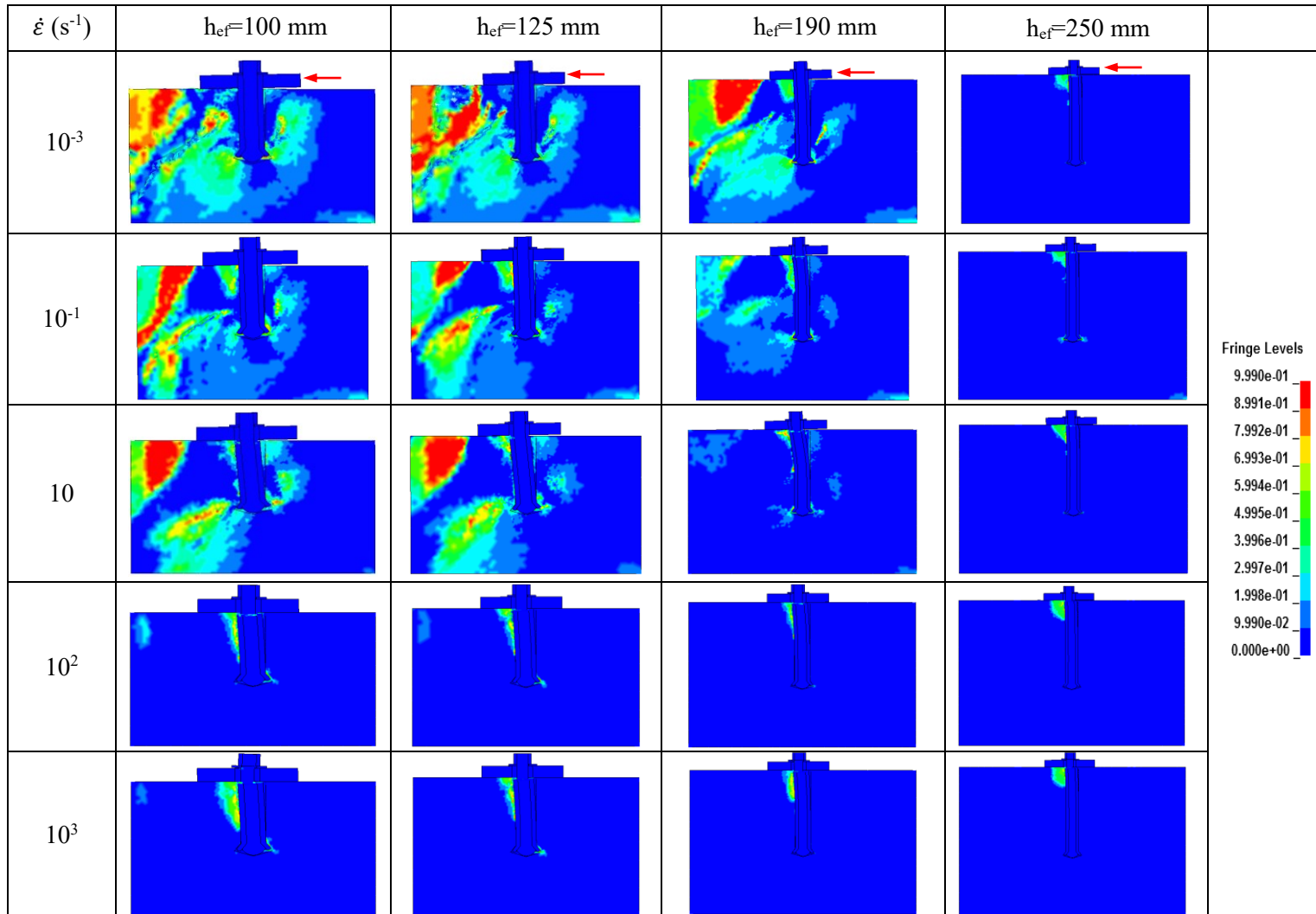


Figure 6-37: Failure mode of 20-mm diameter undercut anchor at different strain rates

From Figures 6-35, 6-36 and 6-37, it can be seen that the behaviour and failure mode of the undercut anchor is affected by the strain rate. As shown in Figure 6-35, steel anchor failure is observed for anchor diameter of 12 mm at strain rates of 10^{-3} s^{-1} to 10^3 s^{-1} . As shown in Figure 6-36 for the anchor diameter of 16 mm, at strain rates of 10^{-3} s^{-1} and 10^{-1} s^{-1} , concrete spalling is observed for embedment depths of 100 mm and 125 mm while steel anchor failure is observed for embedment depths of 190 mm and 250 mm. At strain rates of 10 s^{-1} , 10^2 s^{-1} and 10^3 s^{-1} concrete spalling followed by steel anchor failure is observed for all the embedment depths investigated. As shown in Figure 6-36 more concrete cracking and damage was observed for the embedment depths of 100 mm and 125 mm compared to the deeper embedment depths of 190 mm and 250 mm. For the shallow embedment depths of 100 mm and 125 mm the cracks initiated in front of the anchor and at the lower end of the anchor resulted in concrete cracking in a wider area. However, for the deeper embedment depths concrete spalling followed by steel anchor failure was observed.

It can be seen from Figure 6-37 for the 20-mm diameter undercut anchor, at strain rate of 10^{-3} s^{-1} , pryout failure is observed for embedment depths of 100 mm and 125 mm, concrete spalling is observed for embedment depth of 190 mm whereas steel anchor failure is observed for embedment depth of 250 mm. At strain rate of 10^{-1} s^{-1} concrete spalling is observed for embedment depths of 100 mm and 125 mm while steel anchor failure is observed for embedment depths of 190 mm and 250 mm. Also, steel anchor failure preceded by concrete spalling was observed for all embedment depths at strain rates of 10 s^{-1} , 10^2 s^{-1} and 10^3 s^{-1} . As shown in Figure 6-37 more concrete cracking is observed for the

shallow embedment depths. It can be seen from Figures 6-35, 6-36 and 6-37 that concrete cracks and damage increased with the increase in anchor diameter from 12 mm to 20 mm.

Figure 6-38 shows the failure progression of a 12-mm diameter undercut anchor embedded 190 mm in the concrete. Contours of Von Misses stresses (MPa) are shown in the figure. It can be seen that the stresses are concentrated around the sleeve and anchor at the top where the shear load is applied. Combination of the tensile, bending and shear stresses due to the applied load leads to initiation and propagation of cracks in the top part of the undercut anchor resulting in steel anchor failure.

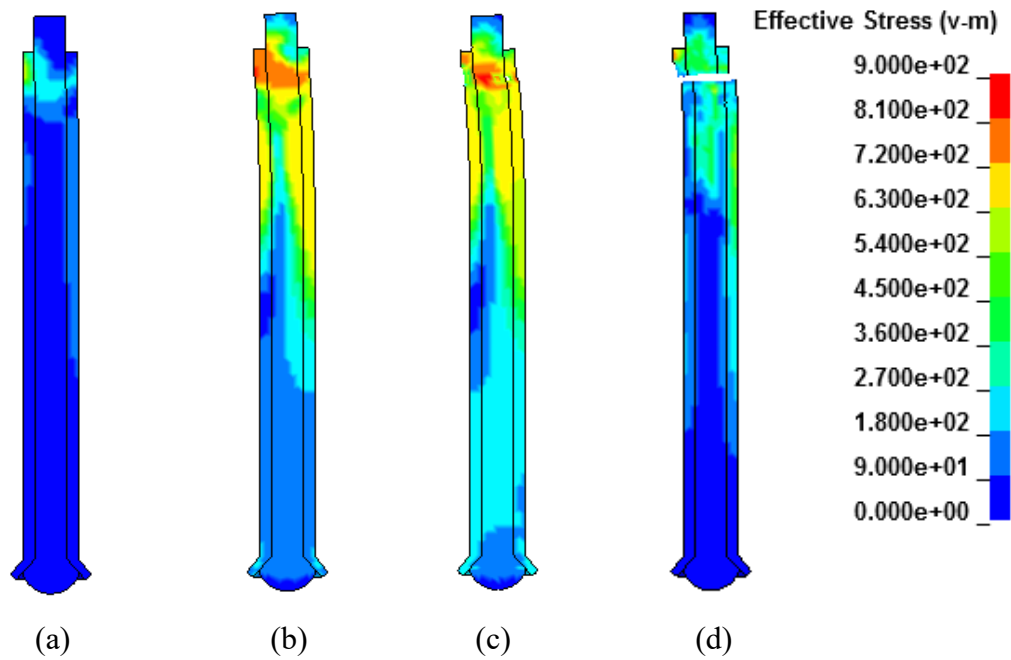


Figure 6-38: Failure process of 12-mm diameter undercut anchor with 190 mm embedment depth; (a) stress concentration around the undercut anchor, (b) anchor bending, (c) crack initiation and (d) anchor fracture

6.2.5 Effect of design parameters on failure mode and ultimate shear load

Figures 6-39, 6-40 and 6-41 show the effect of strain rate on the failure mode and ultimate shear load for the 12-mm, 16-mm and 20-mm diameter undercut anchors respectively. As shown in the figures, the strain rate affects the failure mode for the 16-mm and 20-mm diameter undercut anchors where transition from pryout failure to concrete spalling and then to steel anchor failure is observed. Also, the anchor diameter and embedment depth affect the failure mode. It can be seen from the figures that the ultimate shear load increased with the increase in the strain rate and anchor diameter for the undercut anchors.

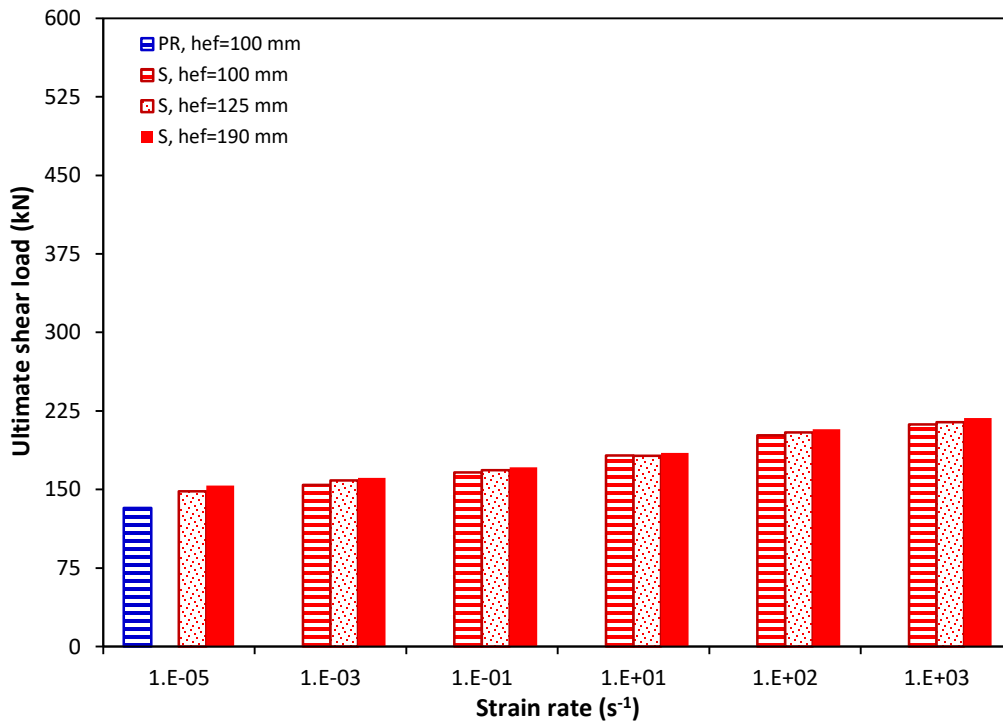


Figure 6-39: Effect of strain rate on the failure mode and ultimate shear load for the undercut anchor diameter of 12 mm

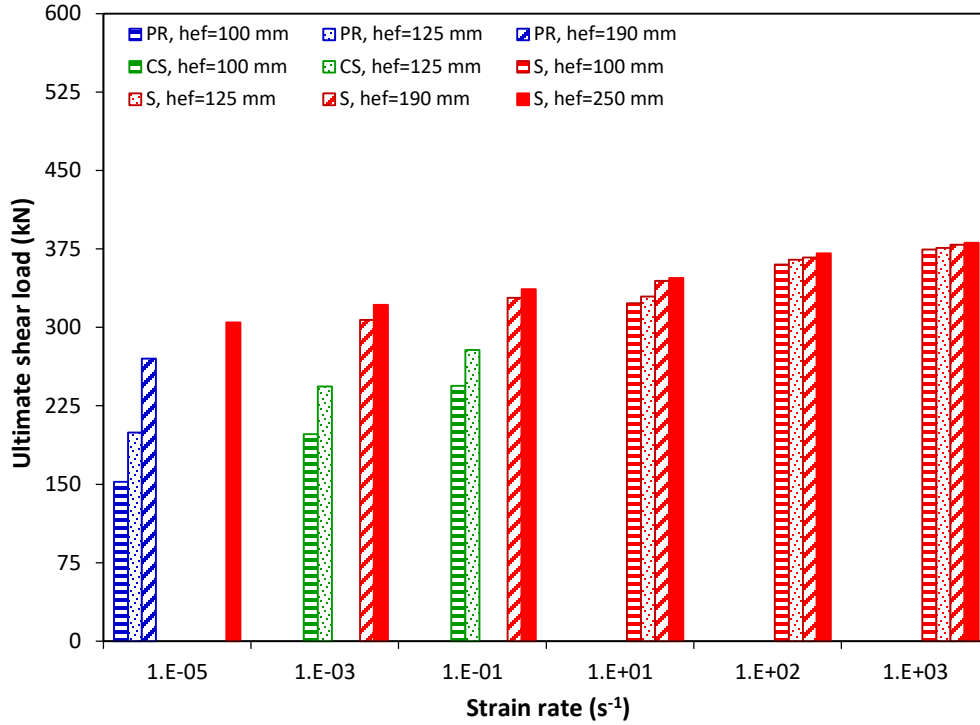


Figure 6-40: Effect of strain rate on the failure mode and ultimate shear load for the undercut anchor diameter of 16 mm

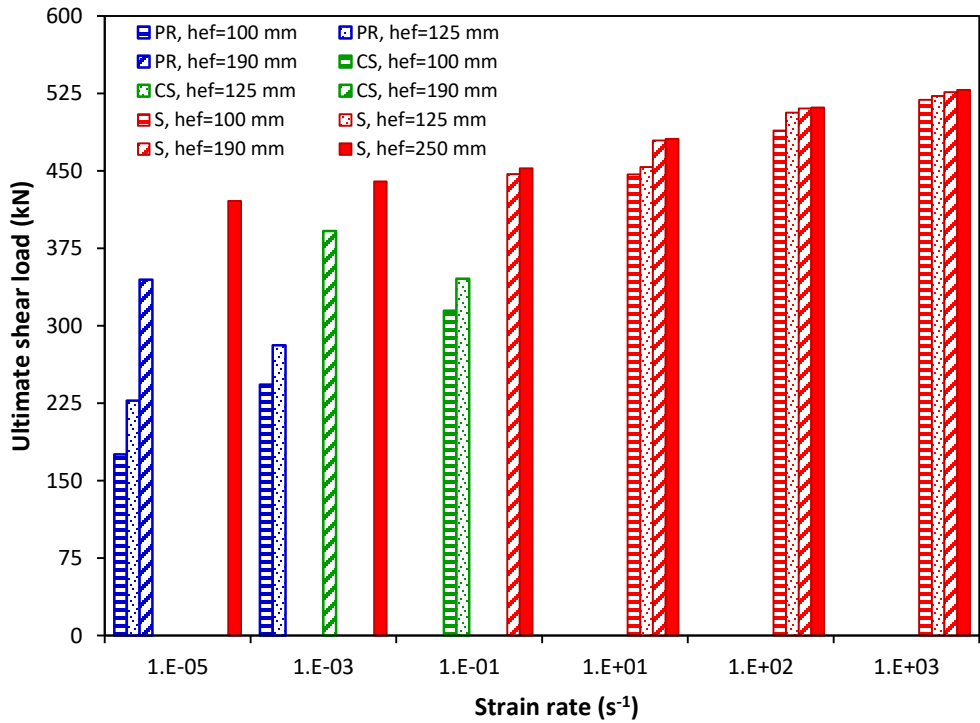


Figure 6-41: Effect of strain rate on the failure mode and ultimate shear load for the undercut anchor diameter of 20 mm

Table 6-13 presents the failure modes for the undercut anchors subjected to shear loads at different strain rates.

Table 6-13: Failure mode for the undercut anchors under shear load at different strain rates

Model No.	d (mm)	h _{ef} (mm)	*Failure mode						
			Strain rate (s ⁻¹)						
			$\dot{\epsilon}=10^{-5}$	$\dot{\epsilon}=10^{-3}$	$\dot{\epsilon}=10^{-1}$	$\dot{\epsilon}=10$	$\dot{\epsilon}=10^2$	$\dot{\epsilon}=10^3$	
1	12	100	PR	S	S	S	S	S	S
2	12	125	S	S	S	S	S	S	S
3	12	190	S	S	S	S	S	S	S
4	16	100	PR	CS	CS	S	S	S	S
5	16	125	PR	CS	CS	S	S	S	S
6	16	190	PR	S	S	S	S	S	S
7	16	250	S	S	S	S	S	S	S
8	20	100	PR	PR	CS	S	S	S	S
9	20	125	PR	PR	CS	S	S	S	S
10	20	190	PR	CS	S	S	S	S	S
11	20	250	S	S	S	S	S	S	S

*Failure mode: PR= pryout, CS=concrete spalling, S= steel anchor failure

6.2.6 Effect of strain rate on the shear behaviour of undercut anchors

Figures 6-42, 6-43, 6-44, 6-45, 6-46, and 6-47 present the shear load-displacement graphs for the 12-mm diameter undercut anchor at strain rates of 10^{-5} s^{-1} , 10^{-3} s^{-1} , 10^{-1} s^{-1} , 10 s^{-1} , 10^2 s^{-1} and 10^3 s^{-1} respectively.

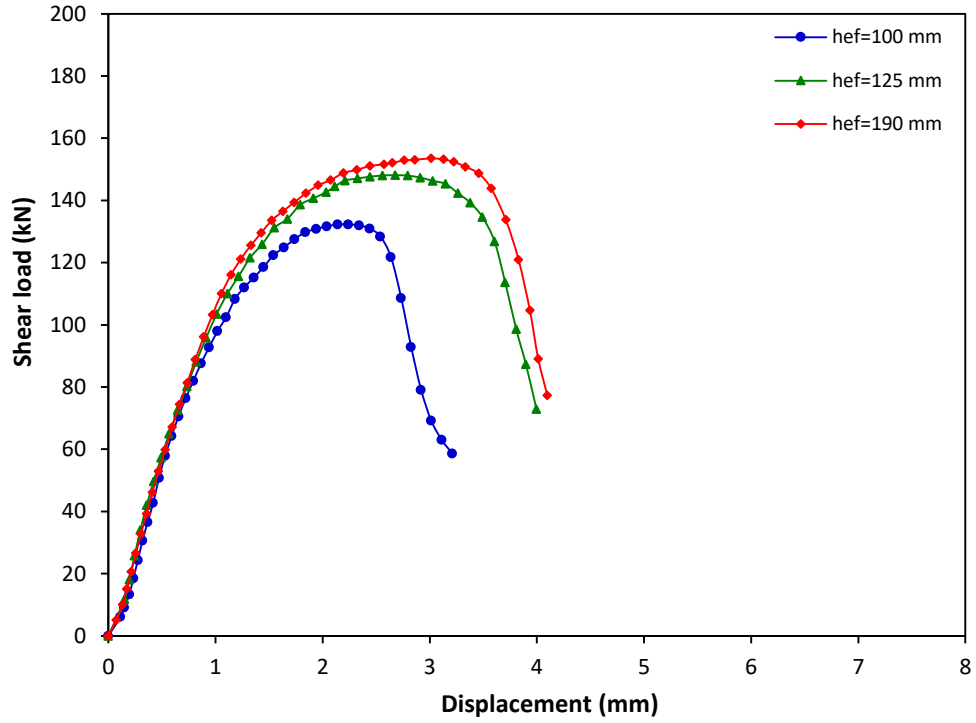


Figure 6-42: Shear load-displacement graph for 12-mm diameter undercut anchor at strain rate of 10^{-5} s^{-1}

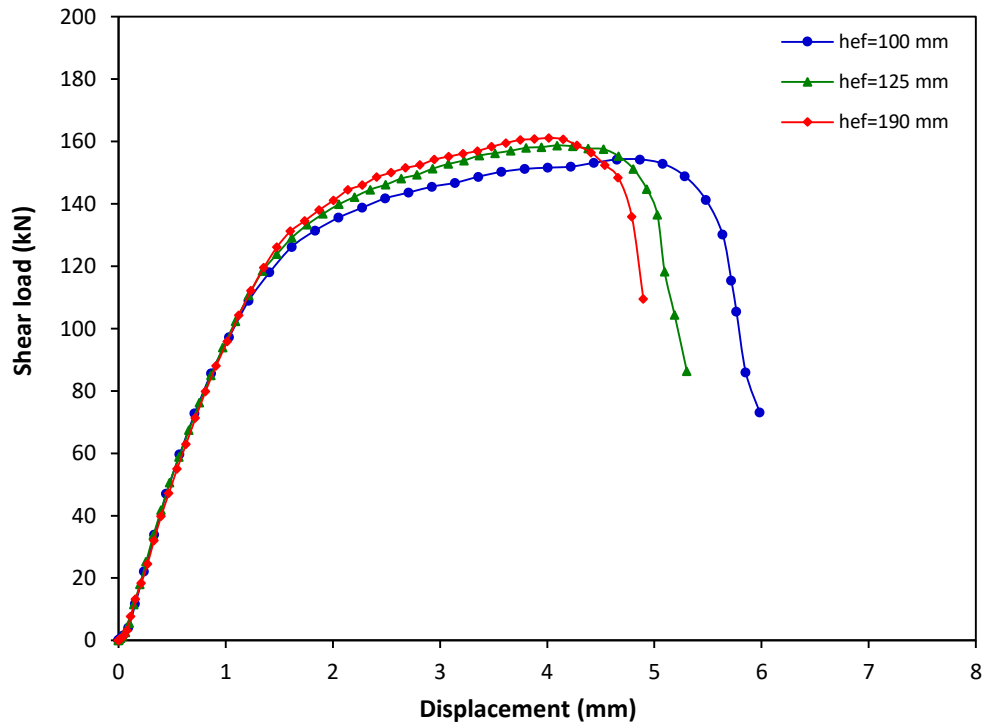


Figure 6-43: Shear load-displacement graph for 12-mm diameter undercut anchor at strain rate of 10^{-3} s^{-1}

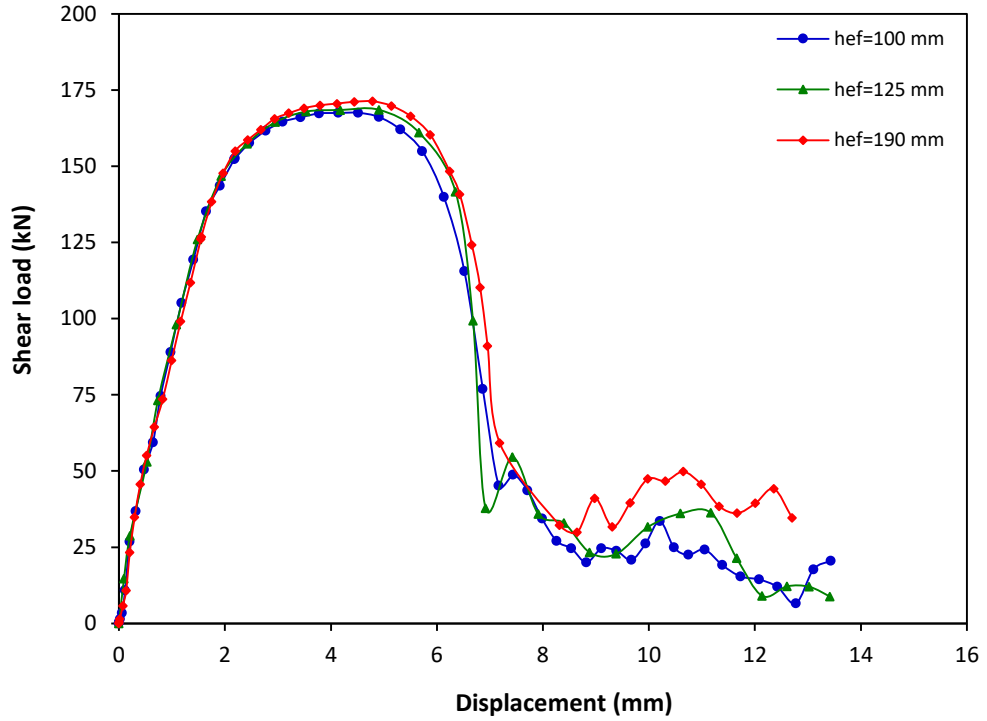


Figure 6-44: Shear load-displacement graph for 12-mm diameter undercut anchor at strain rate of 10^{-1} s^{-1}

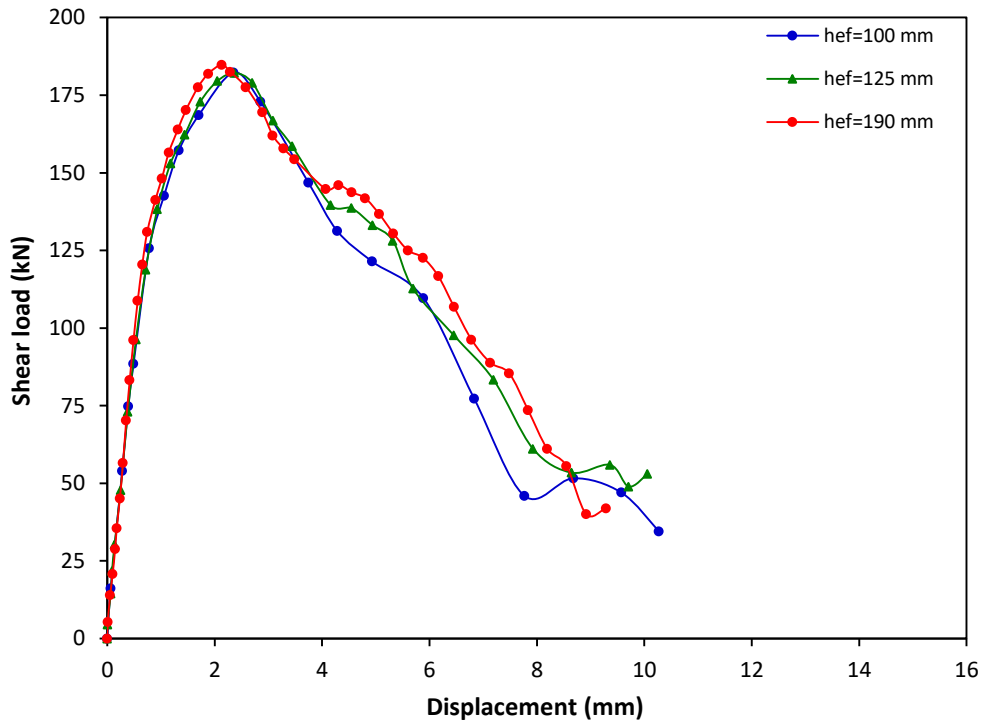


Figure 6-45: Shear load-displacement graph for 12-mm diameter undercut anchor at strain rate of 10 s^{-1}

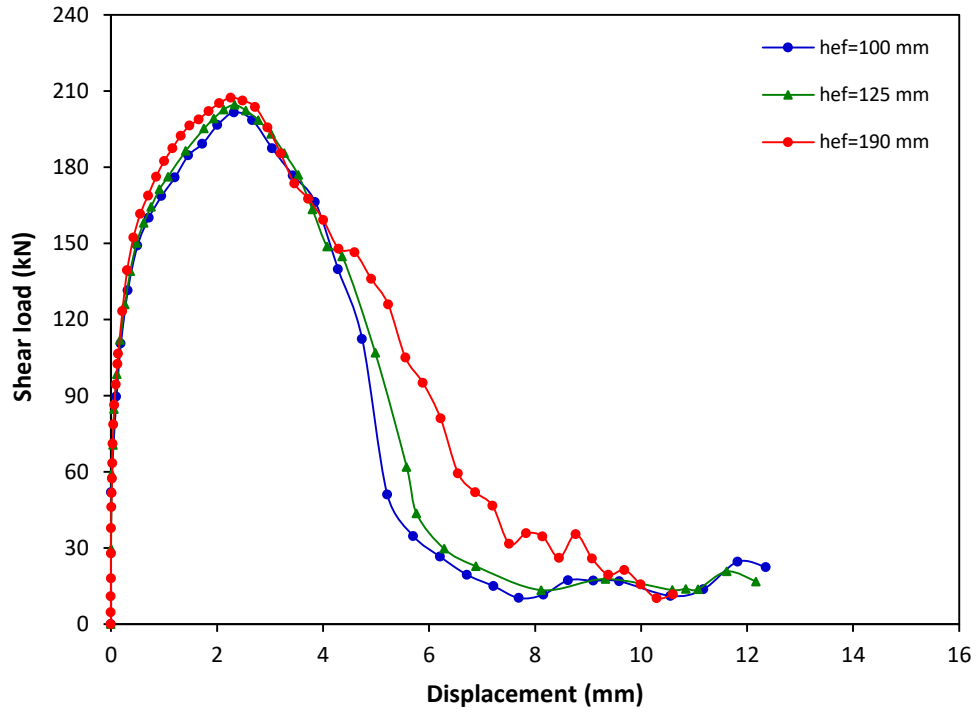


Figure 6-46: Shear load-displacement graph for 12-mm diameter undercut anchor at strain rate of 10^2 s^{-1}

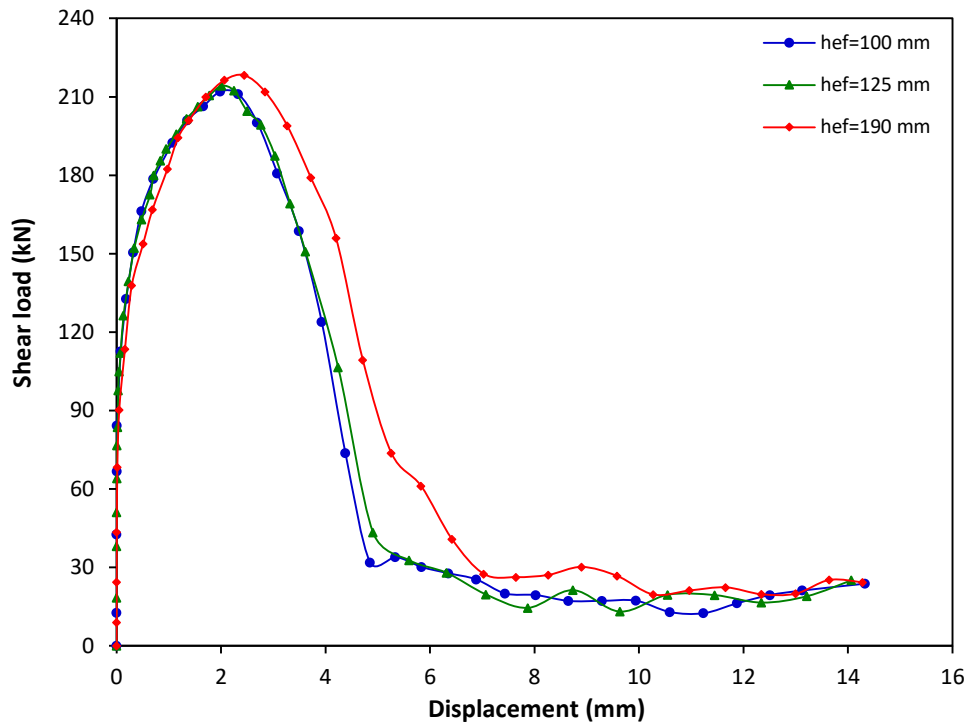


Figure 6-47: Shear load-displacement graph for 12-mm diameter undercut anchor at strain rate of 10^3 s^{-1}

As shown from Figures 6-42 to 6-47, Tables 6-14, 6-15 and 6-16 the shear load for the undercut anchors increased with the increase in the strain rate. At strain rates of 10^{-5} s^{-1} to 10^3 s^{-1} , the shear load increased with the displacement until maximum value then decreased with further increase in displacement until failure. At high strain rate, load fluctuations were observed in the post peak behaviour of the undercut anchors. This is attributed to the progressive propagation of the cracks in the concrete at high strain rate. Also, it can be seen that at low strain rate of 10^{-5} s^{-1} the increase in the embedment depth from 100 mm to 190 mm increased the ultimate shear capacity. However, at high strain rates the increase in the embedment depths increased the ultimate shear load slightly where steel anchor failure mode was observed.

Shear load-displacement graphs for 16-mm and 20-mm diameter undercut anchors with embedment depths of 100 mm, 125 mm, 190 mm and 250 mm at strain rates ranging from 10^{-5} s^{-1} to 10^3 s^{-1} are presented in Appendix H.

The ultimate shear load and displacement results for the 12-mm, 16-mm and 20-mm diameter undercut anchors are presented in Tables 6-14, 6-15 and 6-16 respectively. Where δ is the displacement of the undercut anchor at the ultimate shear load. As shown in the tables, the ultimate shear loads increased with the increase in the strain rate from 10^{-5} s^{-1} to 10^3 s^{-1} for all the undercut anchors investigated. Also, it can be seen that the ultimate shear load for the undercut anchors increased with the increase in the anchor diameter.

Table 6-14: Ultimate shear load and displacement results for the 12-mm diameter undercut anchor

Model No.	d (mm)	h _{ef} (mm)	$\dot{\epsilon}$ (s ⁻¹)	V _u (kN)	δ (mm)	Failure mode
1	12	100	10 ⁻⁵	132.27	2.14	PR
2		125		148.09	2.68	S
3		190		153.57	3.01	S
4	12	100	10 ⁻³	154.21	4.65	S
5		125		158.74	4.09	S
6		190		161.19	4.02	S
7	12	100	10 ⁻¹	166.17	4.91	S
8		125		168.49	4.91	S
9		190		171.25	4.79	S
10	12	100	10	182.34	2.35	S
11		125		182.16	2.36	S
12		190		184.79	2.13	S
13	12	100	10 ²	201.66	2.32	S
14		125		204.59	2.33	S
15		190		207.46	2.26	S
16	12	100	10 ³	211.98	1.98	S
17		125		214.21	2.01	S
18		190		218.27	2.44	S

Table 6-15: Ultimate shear load and displacement results for the 16-mm diameter undercut anchor

Model No.	d (mm)	h _{ef} (mm)	$\dot{\epsilon}$ (s ⁻¹)	V _u (kN)	δ (mm)	Failure mode
1	16	100	10 ⁻⁵	152.26	1.13	PR
2		125		199.42	1.65	PR
3		190		270.05	3.73	PR
4		250		304.60	3.76	S
5	16	100	10 ⁻³	197.88	2.14	CS
6		125		243.42	2.98	CS
7		190		307.24	4.44	S
8		250		321.59	3.67	S
9	16	100	10 ⁻¹	244.19	3.26	CS
10		125		278.38	3.94	CS
11		190		328.13	3.51	S
12		250		336.46	3.61	S
13	16	100	10	322.91	2.67	S
14		125		329.50	2.90	S
15		190		344.53	2.97	S
16		250		347.23	2.71	S
17	16	100	10 ²	360.02	2.55	S
18		125		364.76	2.92	S
19		190		366.70	2.34	S
20		250		370.66	2.28	S

21	16	100	10^3	374.52	1.95	S
22		125		376.11	1.84	S
23		190		379.07	1.89	S
24		250		380.84	2.10	S

Table 6-16: Ultimate shear load and displacement results for the 20-mm diameter undercut anchor

Model No.	d (mm)	h_{ef} (mm)	$\dot{\epsilon}$ (s^{-1})	V_u (kN)	δ (mm)	Failure mode
1	20	100	10^{-5}	175.37	0.86	PR
2		125		227.49	1.15	PR
3		190		344.63	2.22	PR
4		250		420.84	2.93	S
5	20	100	10^{-3}	242.86	1.90	PR
6		125		280.99	2.22	PR
7		190		391.77	4.04	CS
8		250		439.63	3.79	S
9	20	100	10^{-1}	314.72	3.47	CS
10		125		345.56	4.52	CS
11		190		446.87	6.41	S
12		250		452.59	3.89	S
13	20	100	10	446.46	2.41	S
14		125		453.73	2.33	S
15		190		479.50	2.19	S
16		250		480.93	2.79	S
17	20	100	10^2	489.11	2.42	S
18		125		506.24	2.44	S
19		190		510.41	2.81	S
20		250		511.22	2.17	S
21	20	100	10^3	518.84	1.18	S
22		125		522.53	1.34	S
23		190		526.32	1.59	S
24		250		528.37	1.61	S

6.2.7 Effect of strain rate on the ultimate shear load and DIF of undercut anchors

Figures 6-48, 6-49, 6-50 and 6-51 present the relation between the ultimate shear load, DIF and the strain rate for the 12-mm, 16-mm and 20-mm diameter undercut anchors at embedment depths of 100 mm, 125 mm, 190 mm and 250 mm respectively. It can be seen that the increase in the strain rate from $10^{-5} s^{-1}$ to $10^3 s^{-1}$ increased the ultimate shear load

for the undercut anchors. In general, the ultimate shear load increased with the increase in the anchor diameter and embedment depth. As shown in Figure 6-48 the ultimate shear load increased for anchor diameters of 16 mm and 20 mm with the increase in the strain rate from 10^{-5} s^{-1} to 10 s^{-1} where the failure mode changed from pryout to concrete spalling and then to steel failure at strain rate of 10 s^{-1} . A slight increase in the ultimate shear load of 4% and 6% is obtained with the increase in the strain rate from 10^2 s^{-1} and 10^3 s^{-1} for the 16-mm and 20-mm diameter undercut anchors respectively. The increase in the ultimate load is attributed to the increase in steel strength with the increase in strain rate. For the anchor diameter of 12 mm the ultimate shear load increased with the increase in the strain rate from 10^{-5} s^{-1} to 10^3 s^{-1} where transition in the failure mode from pryout failure at strain rate of 10^{-5} s^{-1} to steel anchor failure is observed.

At embedment depth of 125 mm (Figure 6-49), a similar behaviour of the ultimate shear load with the strain rate was observed for the anchor diameters of 16 mm and 20 mm. The ultimate shear load for the anchor diameter of 12 mm and embedment depth of 125 mm increased with the increase in the strain rate from 10^{-5} s^{-1} to 10^3 s^{-1} , where steel failure is the dominant failure mode at all the strain rates investigated.

As shown in Figure 6-50, for embedment depth of 190 mm, the ultimate shear load increased with the increase in the strain rate from 10^{-5} s^{-1} to 10^3 s^{-1} for anchor diameters of 12 mm, 16 mm and 20 mm respectively. At embedment depth of 250 mm (Figure 6-51) the ultimate shear load increased 25% and 25.6% for the 16-mm and 20-mm diameters undercut anchor with the increase in the strain rate from 10^{-5} s^{-1} to 10^3 s^{-1} where the steel fracture is the dominant failure mode. The increase in the ultimate shear load is attributed

to the fact that steel material is sensitive to the increase in the strain rate that increases the anchor capacity by increasing the yield and tensile strengths of the steel material.

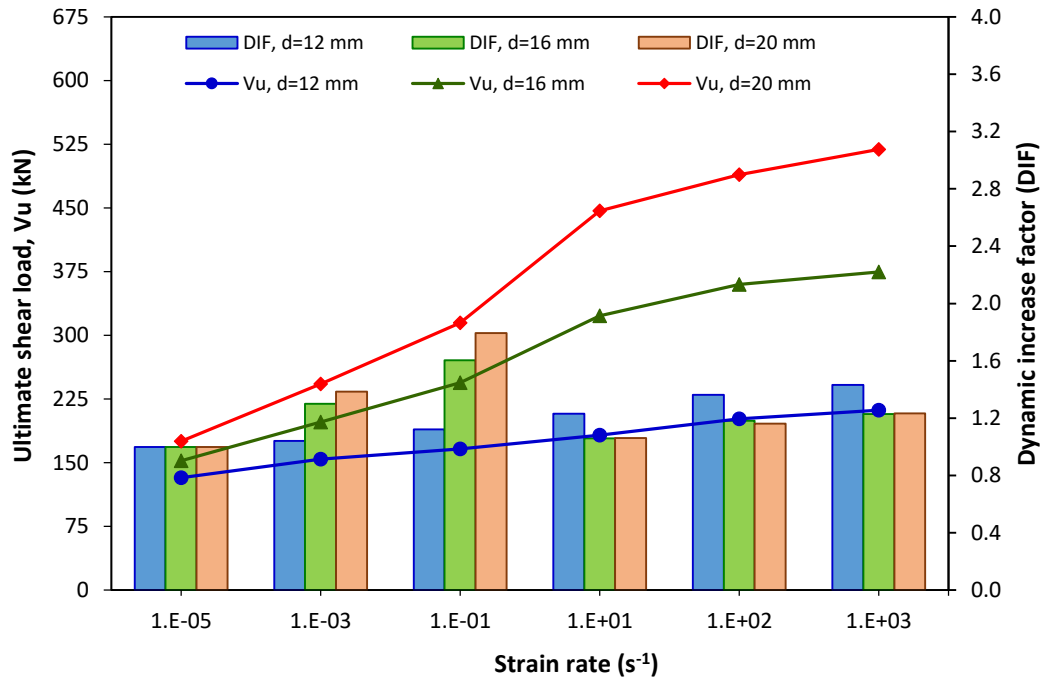


Figure 6-48: Ultimate shear load and DIF versus strain rate for undercut anchors at 100 mm embedment depth

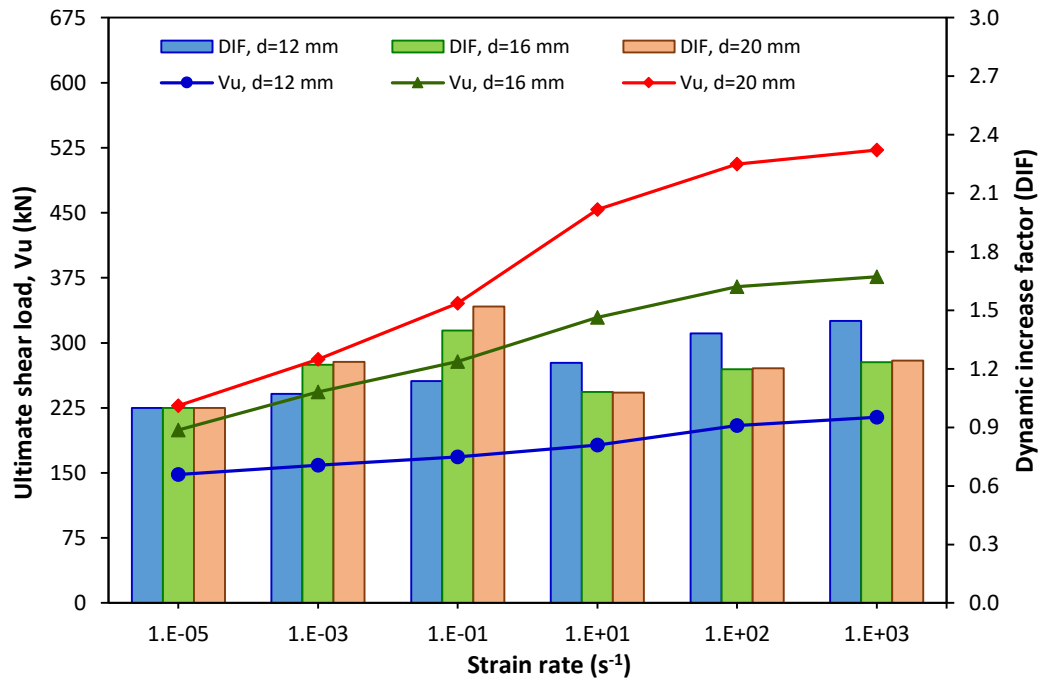


Figure 6-49: Ultimate shear load and DIF versus strain rate for undercut anchors at 125 mm embedment depth

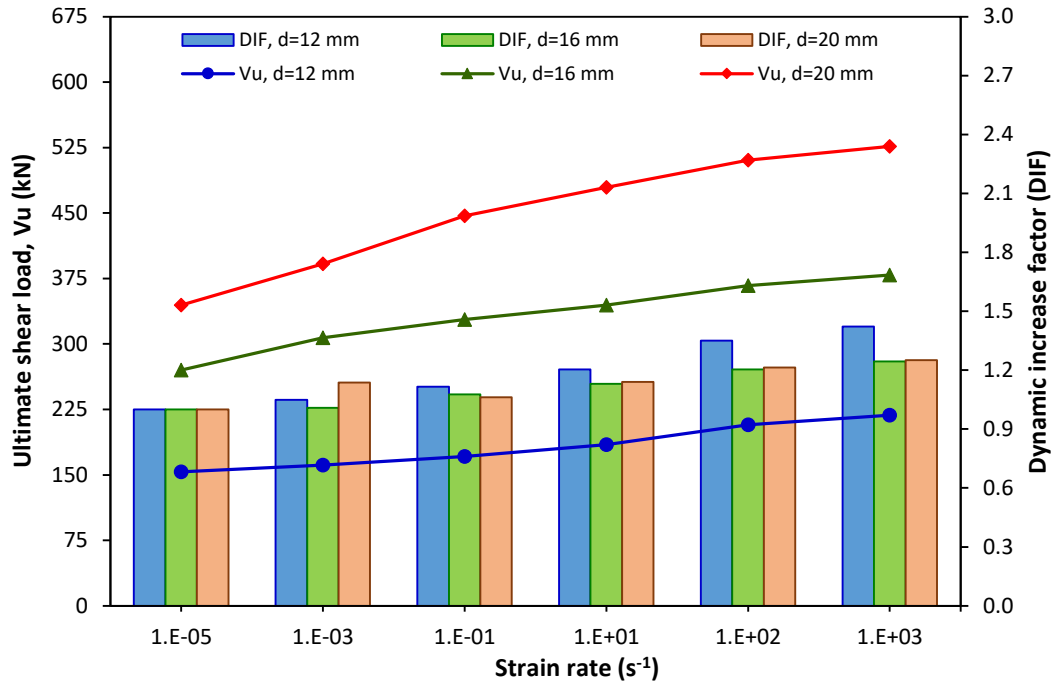


Figure 6-50: Ultimate shear load and DIF versus strain rate for undercut anchors at 190 mm embedment depth

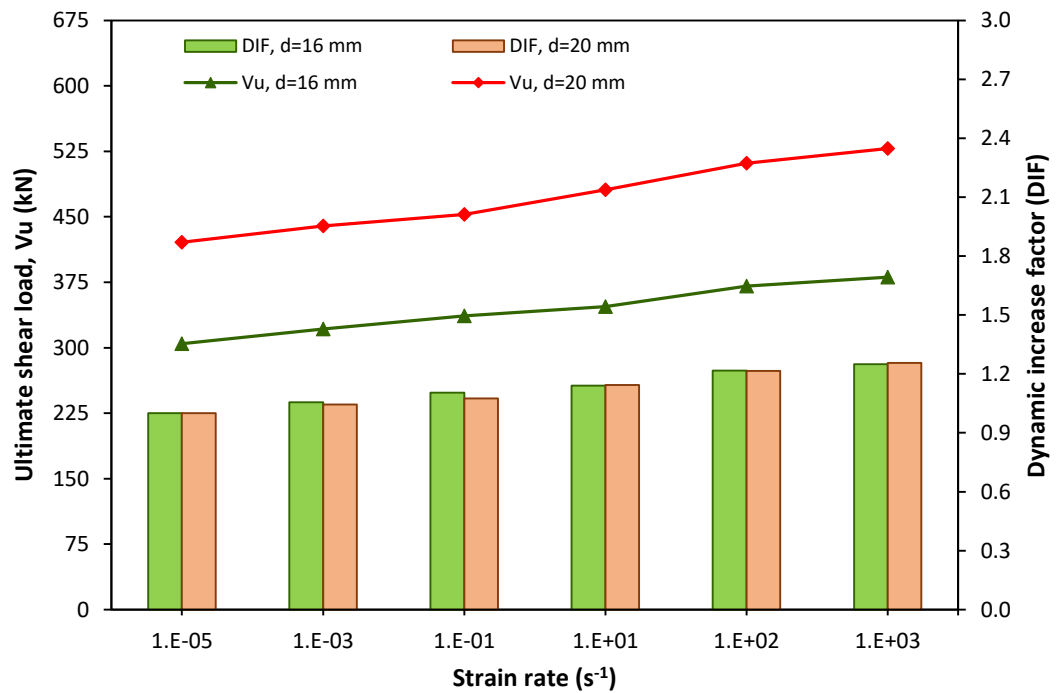


Figure 6-51: Ultimate shear load and DIF versus strain rate for undercut anchors at 250 mm embedment depth

It can be seen from Figures 6-48 and 6-49 that the DIF increased with the increase in the strain rate from 10^{-3} s^{-1} to 10^3 s^{-1} for anchor diameter of 12 mm where steel failure was observed. For anchor diameters of 16 mm and 20 mm, DIF increased with the increase in the strain rate up to 10^{-1} s^{-1} where transition in the failure mode from pryout to concrete spalling was observed. Steel failure was observed at strain rates higher than 10^{-1} s^{-1} . The increase in the strain rate from 10 s^{-1} to 10^3 s^{-1} increased the DIF from 1.06 to 1.23 for the anchor diameters of 16 mm and 20 mm respectively with embedment depth of 100 mm. The increase in the DIF was from 1.08 to 1.23 and from 1.08 to 1.24 for anchor diameters of 16 mm and 20 mm respectively with embedment depth of 125 mm.

As shown in Figure 6-50, the DIF increased with the increase in the strain rate from 10^{-5} s^{-1} to 10^3 s^{-1} for the 12 mm and 16 mm diameter anchors. For anchor diameter of 20 mm the DIF increased to 1.14 at strain rate of 10^{-3} s^{-1} where transition from pryout failure to concrete spalling was observed. The increase in the strain rate from 10^{-1} s^{-1} to 10^3 s^{-1} increased the DIF from 1.06 to 1.25 where steel failure was observed. As shown in Figure 6-51, average DIF of 1.25 was obtained for the undercut anchors with embedment depth of 250 mm at high strain rate of 10^3 s^{-1} .

It can be seen from Figures 6-48, 6-49, 6-50 and 6-51, maximum DIF of 1.6 and 1.79 were obtained at strain rate of 10^{-1} s^{-1} for the 16-mm and 20-mm diameter undercut anchors with 100 mm embedment depth where concrete spalling was observed. Maximum DIF of 1.45 was obtained for the 12 mm diameter anchor with embedment depth of 125 mm at high strain rate of 10^3 s^{-1} where steel failure was observed. It can be seen from the figures that the influence of anchor diameter on the DIF decreased with the increase in the embedment

depth from 100 mm to 250 mm. At the deeper embedment depth of 250 mm the influence of anchor diameter is insignificant where steel anchor failure is observed for all the strain rates.

Table 6-17 shows the maximum DIF for the undercut anchors under shear load where pryout, concrete spalling and steel anchor failure modes were observed.

Table 6-17: Maximum dynamic increase factor for the undercut anchors under shear load

Model No.	d (mm)	h _{ef} (mm)	$\dot{\epsilon}$ (s ⁻¹)	DIF	$\dot{\epsilon}$ (s ⁻¹)	DIF	$\dot{\epsilon}$ (s ⁻¹)	DIF
				PR		CS		S
1	12	100	10 ⁻⁵	1.00	-	-	10 ³	1.43
2	12	125	-	-	-	-	10 ³	1.45
3	12	190	-	-	-	-	10 ³	1.42
5	16	100	10 ⁻⁵	1.00	10 ⁻¹	1.60	10 ³	1.23
6	16	125	10 ⁻⁵	1.00	10 ⁻¹	1.40	10 ³	1.23
7	16	190	10 ⁻⁵	1.00	-	-	10 ³	1.24
8	16	250	-	-	-	-	10 ³	1.25
9	20	100	10 ⁻³	1.38	10 ⁻¹	1.79	10 ³	1.23
10	20	125	10 ⁻³	1.24	10 ⁻¹	1.52	10 ³	1.24
11	20	190	10 ⁻⁵	1.00	10 ⁻³	1.14	10 ³	1.25
12	20	250	-	-	-	-	10 ³	1.26

6.2.8 Regression analysis for undercut anchors under shear load

Regression analysis was performed for the undercut anchors subjected to shear loading to predict the relation between the DIF and the strain rate. Steel anchor failure is observed as the dominant failure mode for most of the undercut anchors investigated. Average DIF for the anchor diameters of 12 mm, 16 mm and 20 mm were considered in the regression analysis for the undercut anchors to adjust DIF for the effect of anchor diameter. The relation between the DIF and the strain rate ratio ($\dot{\epsilon}_d/\dot{\epsilon}_s$) is shown in Figure 6-52 for the undercut anchors exhibiting steel failure mode.

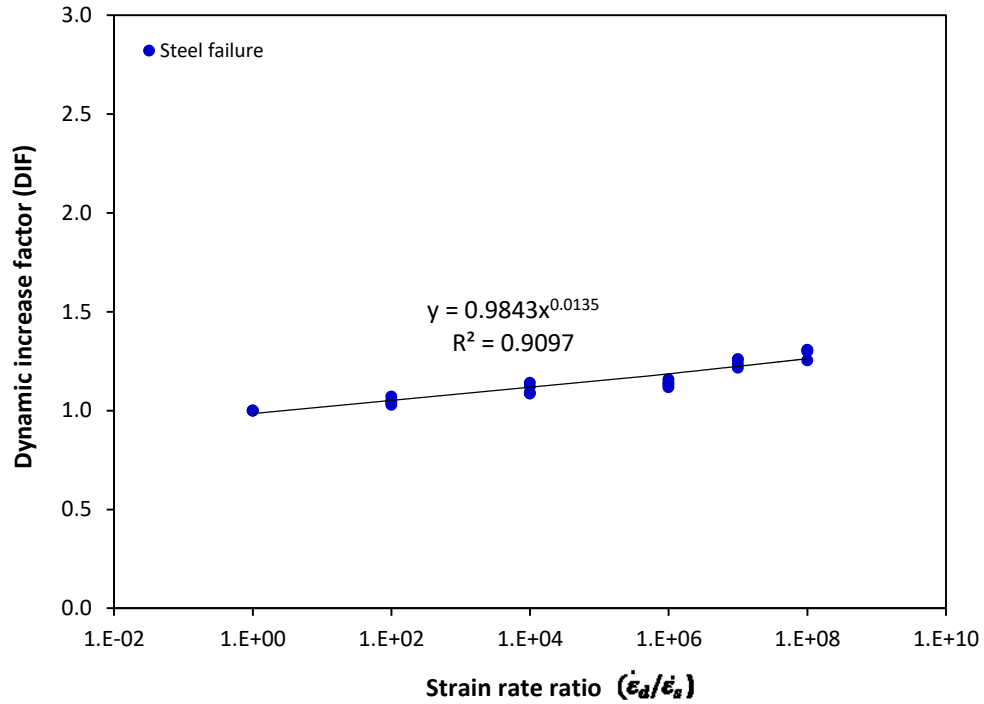


Figure 6-52: Effect of strain rate ratio on the DIF for undercut anchors exhibited steel failure under shear load

Various regression models were used to develop a formula that relates the DIF with the strain rate. Table 6-18 shows the statistical models used to predict the relation between the DIF with the strain rate for the undercut anchors subjected to shear load.

Table 6-18: Statistical models and coefficient of determination to predict the DIF for the undercut anchors exhibited steel failure under shear load

Statistical models	Formulae	Coefficient of determination (R^2)
Exponential	$DIF = 1.1028e^{2E-9\left(\frac{\dot{\epsilon}_d}{\dot{\epsilon}_s}\right)}$	0.499
Linear	$DIF = 2E - 9\left(\frac{\dot{\epsilon}_d}{\dot{\epsilon}_s}\right) + 1.1055$	0.525
Logarithmic	$DIF = 0.0154\ln\left(\frac{\dot{\epsilon}_d}{\dot{\epsilon}_s}\right) + 0.9774$	0.894
Power	$DIF = 0.9843\left(\frac{\dot{\epsilon}_d}{\dot{\epsilon}_s}\right)^{0.0135}$	0.910

As shown in the table, the power regression model gave the highest coefficient of determination of 0.91 and was used for prediction of DIF of undercut anchors exhibited steel failure as in Equation (6.3).

$$DIF = 0.9843 \left(\frac{\dot{\epsilon}_d}{\dot{\epsilon}_s} \right)^{0.0135} \quad (6.3)$$

The ultimate dynamic load (V_{ud}) for the undercut anchors subjected to shear load exhibited steel anchor failure can be determined as in Equations (6.4) as follows:

$$V_{ud} = V_{us} \times 0.9843 \left(\frac{\dot{\epsilon}_d}{\dot{\epsilon}_s} \right)^{0.0135} \quad (6.4)$$

Where the ultimate static load (V_{us}) can be determined from Equation (4.18) for steel anchor failure mode.

Residual analysis is performed for the undercut anchors subjected to shear load to determine the difference between the DIF obtained from the finite element analysis and the predictive equation (Equation 6.3). The relation between the residual and the strain rate ratio is shown in Figure 6-53. As shown in the figure, the residual exhibits a horizontal trend line with the strain rate ratio. However, a slight divergence of the residual is observed.

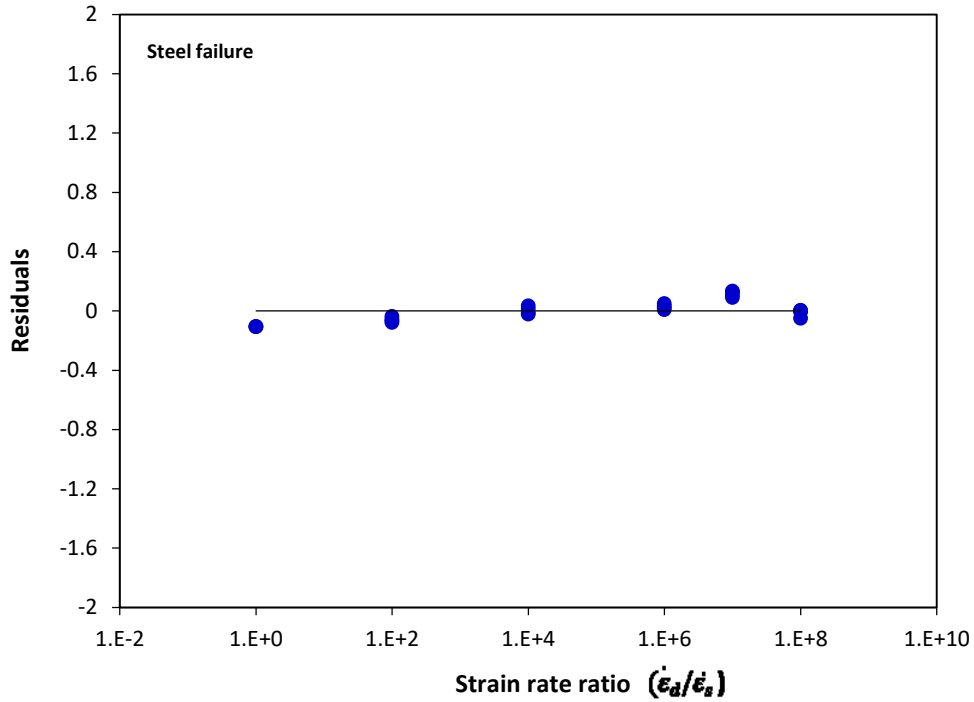


Figure 6-53: Residual versus strain rate ratio for the undercut anchors under shear load exhibited steel failure

New undercut anchorage to concrete models subjected to shear load were developed to verify the accuracy of the proposed equation (Equation 6.3). Undercut anchor diameters of 12 mm, 16 mm and 20 mm with embedment depths of 160 mm and 220 mm were investigated. The DIF results obtained from Equation (6.3) were compared with the DIF results of the newly developed numerical models. Figure 6-54 shows the relation between the DIF obtained from the finite element analysis and the DIF results obtained from the predictive equation. Normal distribution of the DIF values around the equality line is observed. This indicates that the finite element results well represented using the power model proposed in Equation (6.3).

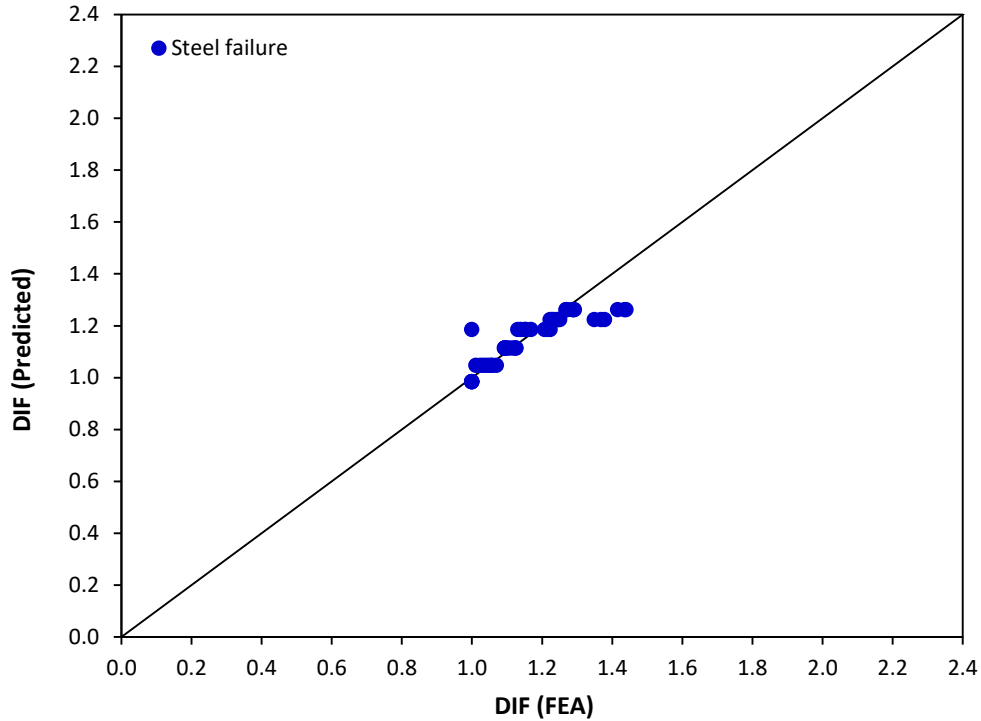


Figure 6-54: DIF obtained from the finite element analysis versus the predicted DIF for the undercut anchors exhibited steel failure under shear load

6.3 Summary

This chapter addressed the tensile and shear behaviour for the undercut anchorage to concrete systems subjected to strain rates of 10^{-5} s^{-1} , 10^{-3} s^{-1} , 10^{-1} s^{-1} , 10 s^{-1} , 10^2 s^{-1} and 10^3 s^{-1} . The chapter begins with validation of the undercut anchor model with the experimental results in the literature. To improve the accuracy of the analysis, mesh sensitivity analyses were performed to determine the adequate mesh size that can best represent the experimental results in the literature. The results obtained from the finite element analysis were compared with the ACI and CCD prediction analytical methods. Level of damage and failure mode for the undercut anchorage to concrete systems for different design parameters and at different strain rates were presented and discussed. For the undercut

anchors subjected to tensile load, two failure modes were observed: concrete cone breakout and steel anchor failure. On the other hand, for the undercut anchors subjected to shear load, three types of failure modes were observed: pryout, concrete spalling and steel anchor failure.

It is observed that the strain rate has influence on the failure mode of the undercut anchors, where the failure mode transitioned from concrete cone breakout failure or pryout failure to steel anchor failure with the increase in the strain rate from 10^{-5} s^{-1} to 10^3 s^{-1} . Concrete cone depth, concrete cone breakout diameter and cone propagation angle for the undercut anchors subjected to tensile load were determined. Ultimate load-displacement, failure mode and strain rate relations for the undercut anchorage to concrete systems subjected to tensile and shear loads were analyzed. Predicting the failure mode and the ultimate load for the undercut anchorage to concrete systems can improve the level of safety for the structures that contain undercut anchors.

DIFs for the undercut anchorage to concrete systems subjected to tensile and shear loads were determined at different strain rates. Equations were developed to determine the relation between the DIF and the strain rate for the undercut anchorage to concrete systems subjected to tensile and shear loads.

Chapter 7 :Conclusions and recommendations for future research

7.1 Introduction

In this research, numerical models for cast-in-place, adhesive and undercut anchorage to concrete systems were developed to investigate the tensile and shear behaviour of the anchorage systems subjected to strain rates in the range from 10^{-5} s^{-1} to 10^3 s^{-1} using LS-DYNA– a multi-physics based finite element analysis program. Various design parameters (anchor diameter and embedment depths) of the anchorage systems were investigated. A procedure was considered for developing the numerical model for the anchorage to concrete systems, to best represent the tensile and shear behaviour of the anchorage to concrete systems, started with selecting the design parameters for the anchors and concrete block, contact formulation and boundary conditions. The commonly used material constitutive models in LS-DYNA for concrete, steel and adhesive materials were evaluated to select the most suitable material models that can best represent the behaviour of the anchorage to concrete systems under different strain rates. The selected material models have the required features to represent the strain rate effect, damage and failure criteria of the material. The numerical model results were validated with the experimental results and with the design prediction methods. The contributions of this thesis is in providing a comprehensive and validated database on the behaviour of anchorage to concrete systems subjected to different strain rates, that can assist designers to predict the performance of anchorage systems under different strain rate loading conditions and accordingly put the suitable measures to mitigate or prevent the failure.

7.2 General conclusions

The main conclusions obtained from the finite element analyses on the cast-in-place, adhesive and undercut anchors can be summarized as follows:

- The developed cast-in-place, adhesive and undercut anchorage to concrete system models are capable to predict the tensile and shear behaviour, failure load and failure mode of the anchorage systems subjected to different strain rates.
- Increasing the strain rate from 10^{-5} s^{-1} to 10^3 s^{-1} increases the ultimate tensile and shear capacity of cast-in-place, adhesive and undercut anchors. Irrespective of the anchor diameter or embedment depth.
- The ultimate tensile load increased with the increase in the embedment depth at the same strain rate when concrete cone breakout failure is dominant.
- The ultimate shear load capacity of anchors depends on embedment depth when the pryout failure mode is the dominant failure mode. The longer the embedment depth the higher the ultimate shear load.
- The ultimate shear load capacity of the anchors depends on the anchor diameter; the larger the diameter the higher the ultimate shear load. This is also observed for the tensile capacity of the anchors.
- The DIF for the cast-in-place, adhesive and undercut anchors under tensile and shear loads increases with the increase in the strain rate from 10^{-5} s^{-1} to 10^3 s^{-1} .
- Crack propagation is influenced by the anchor diameter and embedment depth. The increase in the anchor diameter from 12.7 mm to 19.1 mm increased the concrete cracking and level of damage sustained by the concrete substrate.

- Crack propagation angle decreased with the increase in the strain rate from 10^{-5} s^{-1} to 10^3 s^{-1} for the cast-in-place, adhesive and undercut anchors subjected to tensile load.
- The failure mode of the cast-in-place, adhesive and undercut anchors subjected to tensile and shear loads is influenced by the strain rate.
- The concrete cone breakout diameter increased with the increase in the anchor diameter. However, the concrete breakout diameter decreased with the increase in the strain rate.
- Regression analysis was performed to develop an accurate predictive formula to relate the DIF and the strain rate of the cast-in-place, adhesive and undercut anchors at different strain rates and proposed for use in design of anchors under high strain rate loading.

7.3 Behaviour of cast-in-place anchorage system under different strain rates

- For cast-in-place anchors subjected to tensile load, maximum DIF of 1.74 was obtained for the anchors exhibited concrete cone breakout failure at strain rate of 10 s^{-1} . Maximum DIF of 1.17 was obtained for the cast-in-place anchors exhibited steel failure at high strain rate of 10^3 s^{-1} .
- For cast-in-place anchors subjected to shear load, maximum DIF of 1.24 was obtained for the anchors exhibited pryout failure at strain rate of 10^{-1} s^{-1} . Maximum DIF of 1.15 was obtained for the anchors exhibited steel failure at high strain rate of 10^3 s^{-1} .

- Average value of the crack propagation angle decreased from 58° at strain rate of 10^{-5} s^{-1} to 48° at strain rate of 10 s^{-1} for the cast-in-place anchors subjected to tensile load. Steel failure was observed at high strain rates of 10^2 s^{-1} and 10^3 s^{-1} .
- The failure mode transitioned from concrete cone breakout failure at low strain rate of 10^{-5} s^{-1} to steel anchor failure at higher strain rates for the cast-in-place anchors subjected to tensile load. While the failure mode transitioned from pryout failure to steel anchor failure with the increase in the strain rate from 10^{-5} s^{-1} to 10^3 s^{-1} for the cast-in-place anchors subjected to shear load.
- Concrete cone breakout diameter increased from 230 mm to 255 mm for the increase in anchor diameter from 12.7 mm to 19.1 mm at embedment depth of 76.2 mm. The increase in the concrete cone breakout diameter at embedment depth of 101.6 mm was from 292 mm to 314 mm when the anchor diameter increased from 15.9 mm to 19.1 mm. While steel anchor failure was observed for the 12.7 mm anchor diameter.
- The ultimate shear load increased with the increase in the concrete compressive strength when pryout failure is the dominant failure mode. Maximum increase in the ultimate shear load of 40.8% was obtained for the cast-in-place anchors when the concrete compressive strength increased from 20 MPa to 40 MPa at low strain rate of 10^{-5} s^{-1} . While at high strain rate of 10^3 s^{-1} increasing concrete compressive strength has no influence on the failure mode.

7.4 Behaviour of adhesive anchorage system under different strain rates

- For adhesive anchors subjected to tensile load, maximum DIF of 1.13 was obtained for the adhesive anchors exhibited concrete cone breakout failure at strain rate of 10^{-3} s^{-1} . Maximum DIF of 2.59 was obtained for the adhesive anchors exhibited combined cone bond failure at strain rate of 10^2 s^{-1} . Maximum DIF of 1.13 was obtained for the adhesive anchors exhibited steel failure at high strain rate of 10^3 s^{-1} .
- For adhesive anchors subjected to shear load, maximum DIF of 1.18 was obtained for the adhesive anchors exhibited steel failure at high strain rate of 10^3 s^{-1} .
- Concrete cone failure was observed at the static strain rate of 10^{-5} s^{-1} , while combined cone-bond failure was observed at strain rates of 10^{-3} s^{-1} , 10^{-1} s^{-1} and 10 s^{-1} for most of the adhesive anchors subjected to tensile load. Steel anchor failure was observed at high strain rate of 10^3 s^{-1} .
- Average crack propagation angle of 56.5° was observed at low strain rate of 10^{-5} s^{-1} for the adhesive anchors exhibited concrete cone breakout failure under tensile load. Increasing the strain rates higher than 10^{-5} s^{-1} exhibited combined cone bond failure and steel failure.
- Failure mode transition from pryout failure at low strain rate of 10^{-5} s^{-1} to steel anchor failure at high strain rate of 10^3 s^{-1} was observed for most of the adhesive anchors subjected to shear load. However, failure mode transition from pryout failure at low strain rate of 10^{-5} s^{-1} to concrete spalling and steel anchor failure at high strain rate of 10^3 s^{-1} was observed for 19.1 mm diameter adhesive anchor with embedment depth of 76.2 mm.

- The concrete cone breakout diameter increased from 225 mm to 236 mm with the increase in the anchor diameter from 12.7 mm to 15.9 mm at embedment depth of 76.2 mm. The increase was from 268 mm to 291 mm at embedment depth of 101.6 mm. At embedment depth of 127 mm, steel anchor failure was observed for the 12.7 mm diameter and combined concrete cone bond failure for 15.9 mm diameter adhesive anchor. Steel anchor failure was observed at embedment depth of 152.4 mm. The concrete cone breakout diameter increased from 244 mm to 421 mm for the 19.1 mm diameter adhesive anchor as the embedment depth increased from 76.2 mm to 152.4 mm.

7.5 Behaviour of undercut anchorage system under different strain rates

- Maximum DIF of 1.58 was obtained for the undercut anchors subjected to tensile load at strain rate of 10 s^{-1} , where concrete cone breakout failure is observed. Maximum DIF of 1.44 was obtained at strain rate of 10^3 s^{-1} , where steel failure is observed.
- For the undercut anchors subjected to shear load. Maximum DIF of 1.38 was obtained for the undercut anchors exhibited pryout failure at strain rate of 10^{-3} s^{-1} . Maximum DIF of 1.79 was obtained for the undercut anchors exhibited concrete spalling at strain rate of 10^{-1} s^{-1} . Maximum DIF of 1.45 was obtained for the undercut anchors exhibited steel failure at high strain rate of 10^3 s^{-1} .
- Steel anchor failure is the dominant failure mode for the 12-mm and 16-mm diameter undercut anchors subjected to tensile load at all the embedment depths and strain rates investigated. While concrete cone breakout failure is observed for

the 20-mm diameter undercut anchor with 100 mm and 125 mm embedment depths at strain rates up to 10^{-1} s^{-1} . Also, concrete cone breakout failure was observed for embedment depth of 100 mm at strain rate of 10 s^{-1} . Steel anchor failure is observed at high strain rates of 10^2 s^{-1} and 10^3 s^{-1} . Also, steel anchor failure was observed at embedment depths of 190 mm and 250 mm at all the strain rates investigated.

- Average crack propagation angle decreased from 62° at strain rate of 10^{-5} s^{-1} to 42° at strain rate of 10 s^{-1} for the undercut anchors exhibited concrete cone breakout failure.
- Failure mode transition from pryout failure at strain rate of 10^{-5} s^{-1} to concrete spalling and then to steel anchor failure at high strain rate of 10^3 s^{-1} was observed for the undercut anchors subjected to shear load.
- The concrete cone breakout diameter increased from 291 mm to 340 mm with the increase in the anchor diameter from 16 mm to 20 mm at embedment depth of 100 mm. While steel anchor failure was observed for anchor diameter of 12 mm. Further increase in the anchor embedment depths for the 12 mm, 16 mm diameter undercut anchors resulted in steel failure. Concrete cone breakout diameter of 378 mm was observed for the 20 mm diameter undercut anchor at 125 mm embedment depth.

7.6 Research limitations

In this research plain concrete was used. Effect of reinforcement confinement was not considered for the analysis. Effect of edge distance was not considered where single anchor

is placed at the center of the concrete block far from the concrete free edge. Effect of group anchors on the behaviour of anchorage to concrete system was not considered for the analysis. This research is limited to investigate the tensile and shear behaviour of anchorage to concrete system. Effect of combined tensile and shear loads on the behaviour of the anchorage to concrete system was not investigated.

7.7 Future research

The research performed in this thesis focused on the effect of strain rate on the tensile and shear capacity for the cast-in-place, adhesive and undercut anchors. The recommended future work can be summarized as follows:

- Effect of strain rate on the combination of the tensile and shear load of the anchorage systems.
- Influence of concrete confinement on the tensile and shear capacity of the anchorage system at different strain rates.
- Effect of hole shape (tapered shape) for the adhesive anchor on the tensile and shear capacity.
- Strain rate effect on the tensile and shear capacity for group of anchorage systems.
- Influence of temperature on the tensile and shear behaviour of anchorage to concrete systems at high strain rates.
- Strain rate effect on anchors near the concrete edge.

7.8 Contributions

7.8.1 Journal papers

- Lenda T. Ahmed and Abass Braimah (2019). Tensile behaviour of adhesive anchors under different strain rates. *Engineering Structures*, (192), 113-125.
- Lenda T. Ahmed and Abass Braimah (2017). Behaviour of undercut anchors subjected to high strain rate loading. *Procedia Engineering*, (210), 326-333.
- Lenda T. Ahmed and Abass Braimah (2019). Shear behaviour of adhesive anchors under different strain rates. (*Submitted to Engineering Structures*).

7.8.2 Conference papers

- Lenda T. Ahmed and Abass Braimah (2018). Shear behaviour of cast-in-place anchors at low and high strain rates. *CSCE 2018 Annual Conference*, New Brunswick, Canada.
- Lenda T. Ahmed and Abass Braimah (2016). Strain Rate Effect on the behaviour of cast-in-place anchors under tensile load. *2nd International Conference on Advances in Civil Architecture and Environmental Engineering (ICCAEE)*, KL, Malaysia.
- Lenda T. Ahmed and Abass Braimah (2016). Strain rate effect on the behaviour of cast-in-place concrete anchors under shear loading. *2nd International Conference on Advances in Civil Architecture and Environmental Engineering (ICCAEE)*, KL, Malaysia. (Best paper presentation award).

References

- A Mitek' Company. (1997). *DUC UNDERCUT ANCHORS*.
- Abebe, M. S., & Qiu, H. S. (2016). Numerical modeling of geotextile reinforcement of soft subgrade ballasted railway under high speed train. *Electronic Journal of Geotechnical Engineering*, 21(12), 4327–4343.
- ACI Committee (349). (1990). *Code requirements for nuclear safety related structures (ACI) 349-85, Appendix B- steel embedment"*. American concrete institute, Detroit.
- ACI Committee 318. (2005). *Building Code Requirements for Structural Concrete (ACI 318-05) and Commentrary (ACI 318R-05)*.
- ACI Committee 318. (2011). *Building Code Requirements for Structural Concrete (ACI 318-11) and Commentary*.
- ACI Committee 355. (2000). *Commentary on Evaluating the Performance of Post-Installed Mechanical Anchors in Concrete (ACI 355.2R-00)*.
- Ansell, A. (2006). Dynamic testing of steel for a new type of energy absorbing rock bolt. *Journal of Constructional Steel Research*, 62(5), 501–512.
- Ashour, A. F., & Alqedra, M. A. (2005). Concrete breakout strength of single anchors in tension using neural networks. *Advances in Engineering Software*, 36, 87–97.
- Bala, S. (2008). Tolerance used for Tying Slave Nodes in TIED contacts.
- Barnat, J., Bajer, M., & Vyhnanekova, M. (2012). Bond strength of chemical anchor in high-strength concrete. *Procedia Engineering*, 40, 38–43.
- Bathe, K.-J., Walczak, J., Guillermin, O., Bouzinov, P. A., & Chen, H.-Y. (1999). Advances in crush analysis. *Computers & Structures*, 72, 31–47.
- Benmokrane, B., Tighiouart, B., & Chaallal, O. (1996). Bond strength and load distribution

- of composite GFRP reinforcing bars in concrete. *ACI Materials Journal*, 93(3), 246–252.
- Bergan, P. G., Horrigmoe, G., Krakeland, B., & Soreide, T. H. (1978). Solution techniques for non-linear finite element problems. *International Journal for Numerical Methods in Engineering*, 12, 1677–1696.
- Bermejo, M., Goicolea, J. M., Gabald'on, F., & Santos, A. (2011). Impact And Explosive Loads On Concrete Buildings Using Shell And Beam Type Elements. *3rd ECCOMAS Thematic Conference on Computational Methods in Structural Dynamics and Earthquake Engineering*, 1–14.
- Bi, K., & Hao, H. (2013). Numerical simulation of pounding damage to bridge structures under spatially varying ground motions. *Engineering Structures*, 46, 62–76.
- Bickel, T. S., & Shaikh, A. F. (2002). Shear Strength of Adhesive Anchors. *PCI Journal*, 47(5), 92–101.
- Bischoff, P. H., & Perry, S. H. (1991). Compressive behaviour of concrete at high strain rates. *Materials and Structures*, 24(6), 425–450.
- Boh, J. W., Louca, L. A., & Choo, Y. S. (2004). Strain rate effects on the response of stainless steel corrugated firewalls subjected to hydrocarbon explosions. *Journal of Constructional Steel Research*, 60(1), 1–29.
- Børvik, T., Hopperstad, O. S., & Berstad, T. (2003). On the influence of stress triaxiality and strain rate on the behaviour of a structural steel. Part II. Numerical study. *European Journal of Mechanics, A/Solids*, 22, 15–32.
- Braimah, A., Contestabile, E., & Guilbeault, R. (2009). Behaviour of adhesive steel anchors under impulse-type loading. *Canadian Journal of Civil Engineering*, 36(11),

1835–1847.

Braimah, A., Guilbeault, R., & Contestabile, E. (2004). *High strain rate behaviour of chemically bonded steel anchors. Canadian explosives research laboratory (CERL), Report No. 20, Natural Resources Canada (Vol. 20).*

Braimah, A., Guilbeault, R., & Contestabile, E. (2014). Strain rate behaviour of adhesive anchors in masonry. *Engineering Structures, 67*, 96–108.

Bridge Design Aids. (2012). *Anchorage to Concrete.*

British Standards Institution Draft for development. (1992). *Concrete performance, production, placing, and compliance criteria.*

BS EN 206. (2013). BSI Standards Publication Concrete — Specification , performance , production and conformity. *British Standard*, (May), 1–93.

Cadoni, E., Labibes, K., Albertini, C., Berra, M., & Giangrasso, M. (2001). Strain-rate effect on the tensile behaviour of concrete at different relative humidity levels. *Materials and Structures, 34*, 21–26.

Cai, M., Champaigne, D., & Kaiser, P. K. (2010). Development of a fully debonded cone-bolt for rockburst support. In *5 th International Seminar on Deep and High Stress Mining* (pp. 329–342).

Çalışkan, Ö., Yılmaz, S., Kaplan, H., & Kıracı, N. (2013). Shear strength of epoxy anchors embedded into low strength concrete. *Construction and Building Materials, 38*, 723–730.

Cattaneo, S., & Muciaccia, G. (2015). Adhesive anchors in high performance concrete. *Materials and Structures, 1–12.*

Ceci, A. M., Casas, J. R., & Ghosn, M. (2012). Statistical analysis of existing models for

- flexural strengthening of concrete bridge beams using FRP sheets. *Construction and Building Materials*, 27(1), 490–520.
- Cement Association of Canada. (2010). *Concrete design handbook, third edition*.
- Chan, Y., Chen, Y., & Liu, Y. (2003). Development of bond strength of reinforcement steel in self-consolidating concrete. *ACI Structural Journal*, 100(4), 490–498.
- Chapman, R. A., & Shah, S. P. (1987). Early-Age bond strength in reinforced concrete. *ACI Materials Journal*, 501–510.
- Chen, S., Zang, M., Wang, D., Yoshimura, S., & Yamada, T. (2017). Numerical analysis of impact failure of automotive laminated glass: A review. *Composites Part B*, 122, 47–60.
- Chen, W., & Hao, H. (2012). Numerical study of a new multi-arch double-layered blast-resistance door panel. *International Journal of Impact Engineering*, 43, 16–28.
- Choi, S., Joh, C., & Chun, S.-C. (2015). Behavior and strengths of single cast-in anchors in Ultra-High-Performance Fiber-Reinforced Concrete (UHPFRC) subjected to a monotonic tension or shear. *KSCCE Journal of Civil Engineering*, 19(4), 964–973.
- Chou, C., Chen, P., Le, J., & Tamini, N. (2004). A benchmark study of CAE sensor modeling using LS-DYNA. *Eighth International LS-DYNA User Conference*, (2), 3–22.
- Committee Euro-International du Beton (CEB). (1994). *Fastenings to concrete and masonry structures. State of the Art Report*. Thomas Telford Ltd.
- Cook, R. A. (1993). Behavior of chemically bonded anchors. *Journal of Structural Engineering*, 119(9), 2744–2762.
- Cook, R. A., Collins, D. M., Klingner, R. E., & Polyzois, D. (1992). Load-Deflection

- Behavior of Cast-in-Place and Retrofit Concrete Anchors. *ACI Structural Journal*, 89(6), 639–649.
- Cook, R. A., Doerr, G. T., & Klingner, R. E. (1993). Bond stress model for design of adhesive anchors. *ACI Structural Journal*, 90(5), 514–524.
- Cook, R. a., Eligehausen, R., & Appl, J. J. (2007). Overview: Behavior of Adhesive Bonded Anchors. *Beton- Und Stahlbetonbau*, 102, 16–21.
- Cook, R. A., Fagundo, F. E., Biller, M. H., & Richardson, D. E. (1991). Tensile behavior and design of single adhesive anchors. *Structures and Materials Res*, (91–3).
- Cook, R. A., & Konz, R. C. (2001). Factors Influencing Bond Strength of Adhesive Anchors. *ACI Structural Journal*, 98(1), 76–86.
- Cook, R. A., Kunz, J., Fuchs, W., & Konz, R. C. (1998). Behavior and design of single adhesive anchors under tensile load in uncracked concrete. *ACI Struct.*, 95(1), 9–26.
- Cook, R. A., Prevatt, D. O., McBride, K. E., & Potter, W. (2013). *Steel shear strength of anchors with stand-off base plates*.
- Cowell, W. L. (1969). *Dynamic tests on selected structural steels*.
- da Silva Lucas F. M., Öchsner, A., & Adams, R. D. (2011). *Handbook of Adhesion Technology*.
- Das, A., Ghosh, M., Tarafder, S., Sivaprasad, S., & Chakrabarti, D. (2017). Micromechanisms of deformation in dual phase steels at high strain rates. *Materials Science and Engineering A*, 680, 249–258.
- Davidson, J. S., Fisher, J. W., Hammons, M. I., Porter, J. R., & Dinan, R. J. (2005). Failure Mechanisms of Polymer-Reinforced Concrete Masonry Walls Subjected to Blast. *Journal of Structural Engineering*, 131(August), 1194–1205.

- de Larrard, F., Schaller, I., & Fuchs, J. (1993). Effect of bar diameter on the bond strength of passive reinforcement in high-performance concrete. *ACI Materials Journal*, 90(4), 333–339.
- Delhomme, F., Roure, T., Arrieta, B., & Limam, A. (2015a). Static and cyclic pullout behavior of cast-in-place headed and bonded anchors with large embedment depths in cracked concrete. *Nuclear Engineering and Design*, 287, 139–150.
- Delhomme, F., Roure, T., Arrieta, B., & Limam, A. (2015b). Tensile behaviour of cast-in-place headed anchors with different embedment depths. *European Journal of Environmental and Civil Engineering*, 19(6), 703–716.
- Dogan, F., Hadavinia, H., Donchev, T., & Bhonge, P. S. (2012). Delamination of impacted composite structures by cohesive zone interface elements and tiebreak contact. *Central European Journal of Engineering*, 2(4), 612–626.
- El-Hage, H., Mallick, P. K., & Zamani, N. (2005). A numerical study on the quasi-static axial crush characteristics of square aluminum tubes with chamfering and other triggering mechanisms. *International Journal of Crashworthiness*, 10(2), 183–195.
- Eligehausen, R. (1987). Anchorage to Concrete by Metallic Expansion Anchors. *Anchorage to Concrete, SP-103*, 181–201.
- Eligehausen, R., Bouska, P., Cervenka, V., & Pukl, R. (1992). Size effect of the concrete cone failure load of anchor bolts. In *First international conference on fracture mechanics of concrete structures (FraMCoS1)* (pp. 517–525).
- Eligehausen, R., Cook, R. A., & Appl, J. (2006). Behavior and Design of Adhesive Bonded Anchors. *ACI Structural Journal*, 103(6), 822–831.
- Eligehausen, R., Fuchs, W., & Sippel, T. M. (1998). Anchorage to concrete. *Progress in*

- Structural Engineering and Materials*, 1(4), 392–403.
- Eligehausen, R., Hofacker, I., & Lettow, S. (2001). Fastening technique-current status and future trends. In *International symposium on connections between steel and concrete* (pp. 11–27).
- Eligehausen, R., Mallee, R., & Rehm. (1984). Fastenings with bonded anchors. *Betonwerk+ Fertigteil -Technik*, 10, 686–692.
- Eligehausen, R., Mallée, R., & Silva, J. F. (2006). *Anchorage in concrete construction*. Ernst & Sohn, 1st edition.
- Epackachi, S., Esmaili, O., Mirghaderi, S. R., & Behbahani, A. A. T. (2015). Behavior of adhesive bonded anchors under tension and shear loads. *Journal of Constructional Steel Research*, 114, 269–280.
- Fabbrocino, G., Verderame, G. M., & Manfredi, G. (2005). Experimental behaviour of anchored smooth rebars in old type reinforced concrete buildings. *Engineering Structures*, 27(10), 1575–1585.
- Fang, Q., & Zhang, J. (2013). Three-dimensional modelling of steel fiber reinforced concrete material under intense dynamic loading. *Construction and Building Materials*, 44, 118–132.
- Fu, B. H. C., Erki, M. A., & Seckin, M. (1991). Review of effects of loading rate on reinforced concrete. *Journal of Structural Engineering*, 117(12), 3660–3679.
- Fu, X., & Chung, D. D. L. (1999). Interface between steel rebar and concrete, studied by electromechanical pull out testing. *Composite Interfaces*, 6(2), 81–92.
- Fuchs, W. (2001). Evolution of fastening design methods in Europe. In *International Symposium on connections between steel and concrete* (pp. 45–60).

- Fuchs, W., Eligehausen, R., & Breen, J. E. (1995). Concrete capacity design (CCD) approach for fastening to concrete. *ACI Structural Journal*, 92(1), 73–94.
- Fujikake, K., Nakayama, J., Sato, H., Mindess, S., & Ishibashi, T. (2003). Chemically Bonded Anchors Subjected to Rapid Pullout Loading. *ACI Materials Journal*, 100(3), 246–252.
- Gebbeken, N., Greulich, S., & Pietzsch, A. (2001). Performance of Concrete Based Building Materials Against Blast and Impact. In *Proceedings of the fib-Symposium on Concrete and Environment, Berlin* (pp. 1–11).
- Gebbeken, N., & Ruppert, M. (2000). A new material model for concrete in high-dynamic hydrocode simulations. *Archive of Applied Mechanics*, 70, 463–478.
- Georgin, J. F., & Reynouard, J. M. (2003). Modeling of structures subjected to impact: concrete behaviour under high strain rate. *Cement and Concrete Composites*, 25(1), 131–143.
- Gesoğlu, M., Güneyisi, E. M., Güneyisi, E., Yılmaz, M. E., & Mermerdaş, K. (2014). Modeling and analysis of the shear capacity of adhesive anchors post-installed into uncracked concrete. *Composites : Part B*, 60, 716–724.
- Gesoglu, M., Ozturan, T., Ozel, M., & Guneyisi, E. (2005). Tensile Behavior of Post-Installed Anchors in Plain and Steel Fiber-Reinforced Normal- and High-Strength Concretes. *Structural Journal*, 102(2), 224–231.
- Goncalves, M. C., & Margarido, F. (2015). *Materials for Construction and Civil Engineering*.
- González, F., Fernández, J., Agranati, G., & Villanueva, P. (2018). Influence of construction conditions on strength of post installed bonded anchors. *Construction*

- and Building Materials*, 165, 272–283.
- Graf, T., Haufe, A., & Andrade, F. (2014). *Adhesives modeling with LS-DYNA : Recent developments and future work*.
- Gross, H. J., Klingner, R. E., & Graves III, H. L. (2001). Dynamic Behavior of Single and Double Near-Edge Anchors Loaded in Shear. *ACI Structural Journal*, 98(5), 665–676.
- Hallquist, J. O. (2006). *LS-DYNA theory manual*. Livermore Software Technology Corporation.
- Han, H., Taheri, F., Pegg, N., & Lu, Y. (2007). A numerical study on the axial crushing response of hybrid pultruded and $\pm 45^\circ$ braided tubes. *Composite Structures*, 80(2), 253–264.
- Hariyadi, Munemoto, S., & Sonoda, Y. (2017). Experimental Analysis of Anchor Bolt in Concrete under the Pull-Out Loading. *Procedia Engineering*, 171, 926–933.
- Hashimoto, J., & Takiguchi, K. (2004). Experimental study on pullout strength of anchor bolt with an embedment depth of 30 mm in concrete under high temperature. *Nuclear Engineering and Design*, 229, 151–163.
- Hawkins, N. (1987). Strength in shear and tension of cast-in-place anchor bolts. *American Concrete Institute (ACI)*, 103(12), 233–255.
- Hentz, S., Donzé, F. V., & Daudeville, L. (2004). Discrete element modelling of concrete submitted to dynamic loading at high strain rates. *Computers & Structures*, 82, 2509–2524.
- Hilti. (2011). Anchor Fastening Technical Guide 2011.
- Hilti. (2014). Adhesive anchoring systems.

- Hopperstad, O. S., Børvik, T., Langseth, M., Labibes, K., & Albertini, C. (2003). On the influence of stress triaxiality and strain rate on the behaviour of a structural steel. Part I. Experiments. *European Journal of Mechanics, A/Solids*, 22, 1–13.
- Jaime, M. C. (2011). *Numerical modeling of rock cutting and its associated fragmentation process using the finite element method. PHD Thesis, Civil Engineering Department, University of Pittsburgh.*
- Jang, J. B., & Suh, Y. P. (2006). The experimental investigation of a crack's influence on the concrete breakout strength of a cast-in-place anchor. *Nuclear Engineering and Design*, 236(9), 948–953.
- Jebara, K., Ozbolt, J., & Hofmann, J. (2016). Pryout failure capacity of single headed stud anchors. *Materials and Structures*, 49, 1775–1792.
- Jensen, M. R., Hallquist, J., Grimes, R., Day, J., Lu, H., & Tabiei, A. (2007). Introduction to LS-DYNA, 1–145.
- Johnsonwindowfilms.com. (2018). <http://www.johnsonwindowfilms.com/protective-films/anchoring-systems/>.
- Kashani, M. H., Alavijeh, H. S., Akbarshahi, H., & Shakeri, M. (2013). Bitubular square tubes with different arrangements under quasi-static axial compression loading. *Materials and Design*, 51, 1095–1103.
- Keller, T., & Vallée, T. (2005). Adhesively bonded lap joints from pultruded GFRP profiles. Part I: Stress-strain analysis and failure modes. *Composites Part B: Engineering*, 36(4), 331–340.
- Kim, J.-S., Jung, W.-Y., Kwon, M.-H., & Ju, B.-S. (2013). Performance evaluation of the post-installed anchor for sign structure in South Korea. *Construction and Building*

- Materials*, 44, 496–506.
- Kinsho, T., Satake, M., & Miyazaki, T. (2000). Epoxy curing agent and one component (type) epoxy resin composition.
- Kulkarni, S. M., & Shah, S. P. (1998). Response of Reinforced Concrete Beams at High Strain Rates. *ACI Structural Journal*, 95(6), 705–715.
- Kwasniewski, L. (2010). Nonlinear dynamic simulations of progressive collapse for a multistory building. *Engineering Structures*, 32(5), 1223–1235.
- Kyei, C., & Braimah, A. (2013). Seismic Reinforcement Detailing Effects on Blast Resistance of Reinforced Concrete Columns. In *3rd Specialty Conference on Diasaster Prevention and Mitigation* (pp. 1–9).
- Lee, N. H., Park, K. R., & Suh, Y. P. (2011). Shear behavior of headed anchors with large diameters and deep embedments in concrete. *Nuclear Engineering and Design*, 241(3), 608–616.
- Lee, W.-S., & Lam, H.-F. (1996). The deformation behaviour and microstructure evolution of high-strength alloy steel at high rate of strain. *Journal of Materials Processing Technology*, 57(3–4), 233–240.
- Lee, W.-S., Lin, C.-F., & Liu, T.-J. (2007). Impact and fracture response of sintered 316L stainless steel subjected to high strain rate loading. *Materials Characterization*, 58(4), 363–370.
- Li, Y., Eligehausen, R., Ozbolt, J., & Lehr, B. (2002). Numerical Analysis of Quadruple Fastenings with Bonded Anchors. *ACI Structural Journal*, 99(2), 149–156.
- Liu, Y. (2008). ANSYS and LS-DYNA used for structural analysis. *International Journal of Computer Aided Engineering and Technology*, 1(1), 31–44.

- Livermore software technology Corporation, L. (2012). *LS-DYNA Keyword User' S Manual VOLUME II Material Models* (Vol. II).
- Livermore Software Technology Corporation, L. (2015). *LS-DYNA Theory Manual*.
- Lou, K.-A., & Perciballi, W. (2008). Finite Element Modeling of Preloaded Bolt Under Static Three-Point Bending Load. In *10th International LS-DYNA Users Conference* (pp. 1–10).
- LSTC, Livermore Software Technology Corporation. (2015). *LS-DYNA Keyword User'S Manual Volume II material models*.
- LSTC, Livermore Software Technology Corporation. (2014a). *LS-DYNA Keyword User's Manual Volume II Material Models. Livermore California* (Vol. II).
- LSTC, Livermore Software Technology Corporation. (2014b). Strain rate LS-DYNA support.
- Lu, J. Z., Zhong, J. S., Luo, K. Y., Zhang, L., Qi, H., Luo, M., XU, X. J., Zhou, J. Z. (2013). Strain rate correspondence of fracture surface features and tensile properties in AISI304 stainless steel under different LSP impact time. *Surface and Coatings Technology*, 221, 88–93.
- Mackay-Sim, R. (1990). *Limit State Design: Fastening to Concrete* (Vol. 355).
- Madico Safety Shield Premier Partener. (2012). <http://www.windowfilmuk.com/window-film-bomb-blast-protection/lifeline-anchoring-window-film.html>.
- Mahadik, V., Sharma, A., & Hofmann, J. (2016). Inelastic seismic behavior of post-installed anchors for nuclear safety related structures: Generation of experimental database. *Nuclear Engineering and Design*, 297, 231–250.
- Mahrenholtz, C., & Eligehausen, R. (2013). Dynamic performance of concrete undercut

- anchors for Nuclear Power Plants. *Nuclear Engineering & Design*, 265, 1091–1100.
- Mahrenholtz, P., & Eligehausen, R. (2015). Post-installed concrete anchors in nuclear power plants: Performance and qualification. *Nuclear Engineering and Design*, 287, 48–56.
- Maker, B., & Zhu, X. (2000). Input parameters for metal forming simulation using LS-DYNA. *Livermore Software Technology Corporation*, 2, 1–10.
- Mallonee, S., Shariat, S., Stennies, G., Waxweiler, R., Hogan, D., & Jordan, F. (1996). Physical Injuries and Fatalities Resulting From the Oklahoma City Bombing. *JAMA*, 276(5), 382–387.
- Malvar, L. J., & Crawford, J. E. (1998). Dynamic Increase Factors for Concrete. In *Twenty-Eight DDESB Seminar, Orlando, FL* (pp. 1–17).
- Malvar, L. J., & Ross, C. A. (1998). Review of Strain Rate Effects for Concrete in Tension. *ACI Materials Journal*, 95(6), 735–739.
- Marcon, M., Ninčević, K., Boumakis, I., Czernuschka, L.-M., & Wan-Wendner, R. (2018). Aggregate effect on the concrete cone capacity of an undercut anchor under quasi-static tensile load. *Materials*, 11(5), 1–17.
- Marzi, S., Hesebeck, O., Brede, M., & Kleiner, F. (2009). A Rate-Dependent Cohesive Zone Model for Adhesively Bonded Joints Loaded in Mode I. *Journal of Adhesion Science and Technology*, 23(6), 881–898.
- Marzi, S., Ramon-villalonga, L., Poklitar, M., & Kleiner, F. (2008). Usage of Cohesive Elements in Crash Analysis of Large, Bonded Vehicle Structures Experimental Tests and Simulation. In *LS DYNA FORUM, Bamberg*.
- May, M., Voß, H., & Hiermaier, S. (2014). Predictive modeling of damage and failure in

- adhesively bonded metallic joints using cohesive interface elements. *International Journal of Adhesion and Adhesives*, 49, 7–17.
- McMullin, P. W., Price, J. S., & Persellin, E. H. (2016). *Concrete design*, Routledge Taylor and Francis Group, New York.
- McVay, M., Cook, R. A., & Krishnamurthy, K. (1996). Pullout Simulation Of Postinstalled Chemically Bonded Anchors. *Structural Engineering*, 122(9), 1016–1024.
- Min, F., Yao, Z., & Jiang, T. (2014). Experimental and numerical study on tensile strength of concrete under different strain rates. *The Scientific World Journal*, 1–11.
- Montgomery, D. C. (2013). *Design and Analysis of Experiments (8th Edition)*. John Wiley & Sons, New York.
- Mousavi, R., Champiri, M. D., & Willam, K. J. (2016). Efficiency of damage-plasticity models in capturing compaction-expansion transition of concrete under different compression loading conditions. In *VII European Congress on Computational Methods in Applied Sciences and Engineering* (pp. 1–12).
- Moutoussamy, L., Herve, G., & Barbier, F. (2011). Qualification of * Constrained _ Lagrange_In_Solid command for steel / concrete interface modeling. In *8th European LS-DYNA Conference*.
- Muratli, H., Klingner, R. E., & Graves III, H. L. (2001). Behavior of shear anchors in concrete: statistical analysis and design recommendations. In *International Symposium on connections between steel and concrete* (pp. 220–230).
- Muratli, H., Klingner, R. E., & Graves III, H. L. (2004). Breakout Capacity of Anchors in Concrete - Part 2 : Shear. *ACI Structural Journal*, 101(6), 821–829.
- Murray, Y. (2007). *Users Manual for LS-DYNA Concrete Material Model 159*.

- Nammur Jr, G., & Naaman, A. (1989). Bond stress model for fiber reinforced concrete based on bond stress-slip relationship. *ACI Materials Journal*, 45–57.
- Nilforoush, R., Nilsson, M., & Elfgren, L. (2017). Experimental evaluation of tensile behaviour of single cast-in-place anchor bolts in plain and steel fibre-reinforced normal- and high-strength concrete. *Engineering Structures*, 147, 195–206.
- Nilforoush, R., Nilsson, M., & Elfgren, L. (2018). Experimental evaluation of influence of member thickness, anchor-head size, and orthogonal surface reinforcement on the tensile capacity of headed anchors in uncracked concrete. *Journal of Structural Engineering*, 144(4), 1–14.
- Norville, H. S., & Conrath, E. J. (2001). Considerations for blast-resistant glazing design. *Journal of Architectural Engineering*, 7(3), 80–86.
- Norville, H. S., & Conrath, E. J. (2006). Blast-Resistant Glazing Design. *Journal of Architectural Engineering*, 12(3), 129–136.
- Norville, H. S., Harvill, N., Conrath, E. J., Shariat, S., & Mallonee, S. (1999). Glass-related injuries in Oklahoma City Bombing. *Journal of Performance of Constructed Facilities*, 13(2), 50–56.
- Odeshi, A. G., Al-Ameeri, S., & Bassim, M. N. (2005). Effect of high strain rate on plastic deformation of a low alloy steel subjected to ballistic impact. *Journal of Materials Processing Technology*, 162–163(SPEC. ISS.), 385–391.
- Ozbolt, J., & Eligehausen, R. (1990). Numerical analysis of headed studs embedded in large plain concrete blocks. *Computer Aided Analysis and Design of Concrete Structures*, 1, 645–656.
- Ožbolt, J., Rah, K. K., & Meštrović, D. (2006). Influence of loading rate on concrete cone

- failure. *International Journal of Fracture*, 139, 239–252.
- Pallarés, L., & Hajjar, J. F. (2009). Headed steel stud anchors in composite structures, Part II: Tension and interaction. *Journal of Constructional Steel Research*, 66, 1–38.
- Park, S. W., Xia, Q., & Zhou, M. (2001). Dynamic behavior of concrete at high strain rates and pressures : II . numerical simulation. *International Journal of Impact Eng*, 25, 887–910.
- Paultre, P. (2010). *Dynamics of Structures*. ISTE Ltd, UK and John Wiley & Sons, Inc, USA. John Wiley & Sons, Inc, Hoboken, USA.
- Petersen, D., Lin, Z., & Zhao, J. (2013). *Behavior and Design of Cast-in-Place Anchors under Simulated Seismic Loading* (Vol. II).
- precast-prestressed concrete Institute. (1999). *PCI design handbook*.
- Primavera, E. J., Pinelli, J. P., & Kalajian, E. H. (1997). Tensile behavior of cast-in-place and undercut anchors in high-strength concrete. *ACI Structural Journal*, 94(5), 583–592.
- Qian, S., & Li, V. C. (2011). Headed Anchor/Engineered Cementitious Composites (ECC) Pullout Behavior. *Journal of Advanced Concrete Technology*, 9(3), 339–351.
- Rao, G. A., & Arora, J. (2013). Strength and Modes of Failure of Adhesive Anchors in Confined Concrete Under Direct Tensile Loading. In *VIII International Conference on Fracture Mechanics of Concrete and Concrete Structures FraMCOS-8* (pp. 1–11).
- Reinhardt, H., Rossi, P., & van Mier, J. (1990). Joint investigation of concrete at high rates of loading. *Materials and Structures*, 23, 213–216.
- Remani, C. (2013). *Methods for Solving Systems of Nonlinear Equations*.
- Rodriguez, M., Zhang, Y., Lotez, D., Graves III, H. L., & Klingner, R. E. (1997). Dynamic

- behaviour of anchors in cracked and uncracked concrete: a progress report 1. *Nuclear Engineering and Design*, 168, 23–34.
- Ross, C. A., Jerome, D. M., Tedesco, J. W., & Hughes, M. L. (1996). Moisture and Strain Rate Effects on Concrete Strength. *ACI Materials Journal*, 93(3), 293–298.
- Ross, C. A., Tedesco, J. W., & Kuennen, S. T. (1995). Effects of Strain Rate on Concrete Strength. *ACI Materials Journal*, 92(1), 37–45.
- Ross, C. A., Thompson, P. Y., & Tedesco, J. W. (1989). Split-Hopkinson Pressure-Bar Tests on Concrete and Mortar in Tension and Compression. *ACI Materials Journal*, 86(5), 475–481.
- Rossi, P., Mier, J. G. M. Van, Toutlemonde, F., Maou, fabrice le, & Boulay, C. (1994). Effect of loading rate on the strength of concrete subjected to uniaxial tension. *Materials and Structures*, 27, 260–264.
- Rust, W., & Schweizerhof, K. (2003). Finite element limit load analysis of thin-walled structures by ANSYS (implicit), LS-DYNA (explicit) and in combination. *Thin-Walled Structures*, 41(2–3), 227–244.
- Sagals, G., Orbovic, N., & Blahoianu, A. (2011). Sensitivity Studies of Reinforced Concrete Slabs Under Impact Loading. In *Transactions, SMiRT 21* (pp. 1–8).
- Sato, H., Fujikake, K., & Mindess, S. (2004). Study on dynamic pullout strength of anchors based on failure modes. *13th World Conference on Earthquake Engineering*, 1–7.
- Shariat, S., Mallonee, S., & Stidham, S. S. (1998). *Summary of Reportable Injuries in Oklahoma: Oklahoma City Bombing Injuries*.
- Shima, H., Chou, L. L., & Okamura, H. (1987). Micro and macro models for bond in reinforced concrete. *Journal of the Faculty of Engineering, The University of Tokyo*,

XXXIX(2), 133–194.

- Shkolnik, I. E. (2008). Influence of high strain rates on stress–strain relationship, strength and elastic modulus of concrete. *Cement and Concrete Composites*, 30(10), 1000–1012.
- Solomos, G., & Berra, M. (2006). Testing of anchorages in concrete under dynamic tensile loading. *Materials and Structures*, 39, 695–706.
- Spyridis, P., & Bergmeister, K. (2014). Effects of Assembly Tolerances on Bolted Anchorages in Concrete. *Journal of Structural Engineering*, 140(1), 1–12.
- Subramanian, N. (2000). Recent developments in the design of anchor bolts. *The Indian Concrete Journal*, 407–414.
- Sugiman, S., & Ahmad, H. (2017). Comparison of cohesive zone and continuum damage approach in predicting the static failure of adhesively bonded single lap joints. *Journal of Adhesion Science and Technology*, 31(5), 552–570.
- Tedesco, J. W., Hughes, M. L., & Ross, C. a. (1994). Numerical simulation of high strain rate concrete compression tests. *Computers & Structures*, 51(1), 65–77.
- Toikka, L., Braimah, A., Razaqpur, G., & Foo, S. (2015). Strain Rate Effect on Development Length of Steel Reinforcement. *Journal of Structural Engineering*, 141(11), 1–14.
- Trautwein, B. (2017). Anchor US Patent, US9677586 B2.
- Tserpes, K. I., & Koumpias, A. S. (2012). Comparison between a Cohesive Zone Model and a Continuum Damage Model in Predicting Mode-I Fracture Behavior of Adhesively Bonded Joints. *CMES*, 83(2), 169–181.
- Tu, Z., & Lu, Y. (2009). Evaluation of typical concrete material models used in hydrocodes

- for high dynamic response simulations. *International Journal of Impact Engineering*, 36(1), 132–146.
- Ueda, T., Kitipornchai, S., & Ling, K. (1990). Experimental Investigation of Anchor Bolts Under Shear. *Structural Engineering*, 116(4), 910–924.
- Ueda, T., Stitmannathum, B., & Matupayont, S. (1991). Experimental Investigation on Shear Strength of Bolt Anchorage Group. *ACI Structural Journal*, 88(3), 292–300.
- Upadhyaya, P., & Kumar, S. (2015). Pull-out capacity of adhesive anchors: An analytical solution. *International Journal of Adhesion and Adhesives*, 60, 54–62.
- Vuletic, R., & Pearson, J. (2008). Use of Adhesive Anchors to Resist Long-Term Loads. *Structural Engineering Magazine*, (January), 1–6.
- Wakabayashi, M., Nakamura, T., Yoshida, N., Iwai, S., & Watanabe, Y. (1980). Dynamic loading effects on the structural performance of concrete and steel materials and beams. *Proceedings of the Seventh World Conference on Earthquake Engineering*, 6(3), 271–278.
- Wang, D., Wu, D., He, S., Zhou, J., & Ouyang, C. (2015). Behavior of post-installed large-diameter anchors in concrete foundations. *Construction and Building Materials*, 95, 124–132.
- Wang, D., Wu, D., Ouyang, C., He, S., & Sun, X. (2017). Simulation analysis of large-diameter post-installed anchors in concrete. *Construction and Building Materials*, 143, 558–565.
- Wu, Y., Crawford, J. E., & Magallanes, J. M. (2012). Performance of LS-DYNA Concrete Constitutive Models. In *12 th International LS-DYNA Users Conference* (pp. 1–13).
- Xing, G., Zhou, C., Wu, T., & Liu, B. (2015). Experimental study on bond behavior

- between plain reinforcing bars and concrete. *Advances in Materials Science and Engineering*, 1–9.
- Xiong, R., Fu, R. Y., Su, Y., Li, Q., Wei, X.-C., & Li, L. (2009). Tensile Properties of TWIP Steel at High Strain Rate. *Journal of Iron and Steel Research International*, 16(1), 81–86.
- Xu, S., Ruan, D., Beynon, J. H., & Rong, Y. (2013). Dynamic tensile behaviour of TWIP steel under intermediate strain rate loading. *Materials Science and Engineering A*, 573, 132–140.
- Yilmaz, S., Özen, M. A., & Yardim, Y. (2013). Tensile behavior of post-installed chemical anchors embedded to low strength concrete. *Construction and Building Materials*, 47, 861–866.
- Yoon, Y.-S., Kim, H.-S., & Kim, S.-Y. (2001). Assessment of fracture behaviors for CIP anchors fastened to cracked and uncracked concretes. *KCI Concrete Journal*, 13(2), 33–41.
- Yu, H., Guo, Y., & Lai, X. (2009). Rate-dependent behavior and constitutive model of DP600 steel at strain rate from 10^{-4} to 10^3 s⁻¹. *Materials and Design*, 30, 2501–2505.
- Zamora, N. A., Cook, R. A., Konz, R. C., & Consolazio, G. R. (2003). Behavior and Design of Single, Headed and Unheaded, Grouted Anchors under Tensile Load. *ACI Structural Journal*, 100(2), 222–230.
- Zhao, C. F., Chen, J. Y., Wang, Y., & Lu, S. J. (2012). Damage mechanism and response of reinforced concrete containment structure under internal blast loading. *Theoretical and Applied Fracture Mechanics*, 61, 12–20.
- Zhao, G. (1994). *Load-Carrying Behavior of Headed Stud Anchors in Concrete Breakout*

Away From an Edge. University Stuttgart, Germany.

Zhao, J. (2014). Seismic behavior of single anchors in plastic hinge zones of RC columns.

In Tenth U.S. National Conference on Earthquake Engineering.

Zhao, T., Guo, W., Yin, Y., & Tan, Y. (2015). Bolt Pull-Out Tests of Anchorage Body under Different Loading Rates. *Shock and Vibration*, 1–8.

Zhou, X. Q., Kuznetsov, V. A., Hao, H., & Waschl, J. (2008). Numerical prediction of concrete slab response to blast loading. *International Journal of Impact Engineering*, 35, 1186–1200.

Appendix A: Design methods for cast-in-place anchors

A.1 Design methods for cast-in-place anchors under tensile load

A.1.1 American Concrete Institute (ACI)

According to ACI 349-85 design method, the ultimate tensile failure load for cast-in-place headed anchors can be determined by Equation (4.1) (Fuchs et al., 1995; Subramanian, 2000; Fuchs, 2001). Equation (4.1) is derived assuming sufficient thickness of the concrete member to ensure that there is no decrease in the failure load (Fuchs et al. 1995). For anchors with edge distance (c) less than h_{ef} , and/or the distance between anchors (spacing) (s) less than $2 \times h_{ef}$, the ultimate failure load can be determined by Equation (A.1) (Fuchs et al., 1995; Subramanian, 2000).

$$N_u = \frac{A_N}{A_{No}} \cdot N_{uo} \quad (\text{A.1})$$

$$A_{No} = \pi \cdot h_{ef}^2 \left(1 + \frac{d_h}{h_{ef}} \right) \quad (\text{A.2})$$

Where A_N is the actual projected area of stress cone of a single anchor, A_{No} is the projected area of stress cone of a single anchor unlimited by edge effect or spacing between the anchors. According to Fuchs et al. (1995), the strength of anchor with shallow embedment depth is underestimated by using ACI 349 and is unconservative for anchors with large embedment depth. In addition, the ACI 349-85 method calculates the failure surface area using complex calculations (Subramanian, 2000). The complexity appears in determining

the angle and the actual projected area (A_N) for the case of multiple anchors and thin concrete member (member thickness less than edge distance) (Fuchs et al., 1995).

ACI 318-11 Appendix D is proposed to design structural anchors that transfer structural loads to the concrete by tension, shear or combination of tension and shear. These anchors are used either to connect the structural elements or in safety related attachments that are assembled externally to the structure such as sprinkler system, pipes and barrier rails. The ACI 318-11 code is concerned with the levels of safety for the structural anchors. The combination of the load factor and the capacity reduction factors (ϕ factors) represent the levels of safety. These levels of safety are suitable for structural applications. The load factors are used to increase the load to consider the uncertainties in determining the dead and live loads. Capacity reduction factors are used to reduce the strength of the material to consider the uncertainties in material strengths and dimensions. The ACI 318-11 design provisions depend on the CCD method theory in predicting the concrete breakout capacity, where the failure surface forms a 35° cone. The CCD method coefficients were calibrated based on extensive experimental tests, the theory is based on 5% fractile failure, 90% confidence level, this means that for 95% of the performed tests the actual strength of the anchor is more than the nominal strength. Adhesive anchors were included in the design provisions of ACI 318-11 for the first time, as the previous versions of ACI code didn't include the adhesive anchors in the design (ACI Committee 318, 2011).

ACI 318 proposed equations to calculate the tensile load for each failure mode. Steel anchor failure (Figure 2-5a) is likely to happen in high strength concrete, the strength of

the steel anchor can be determined by Equation (4.2). Where the ultimate tensile strength is calculated as the minimum value of $1.9 f_y$ and 125000 psi, to assure there is no steel anchor yielding during the service loads (Cement Association of Canada, 2010).

According to ACI 318 the nominal concrete breakout capacity (Fig. 2-5b) for a single anchor can be determined as in Equation (4.16). For group of anchors, the concrete breakout capacity can be determined as follows:

$$N_{cbg} = \frac{A_N}{A_{No}} \psi_{ec,N} \cdot \psi_{ed,N} \cdot \psi_{c,N} \cdot \psi_{cp,N} \cdot N_b \quad (\text{A.3})$$

$$\psi_{ec,N} = \frac{1}{1 + 2e'_N / (3h_{ef})} \leq 1 \quad (\text{A.4})$$

$$\psi_{ed,N} = 1 \text{ if } c \geq 1.5h_{ef} \quad (\text{A.5})$$

$$\psi_{ed,N} = 0.7 + 0.3 \frac{c}{1.5h_{ef}} \text{ if } c < 1.5h_{ef} \quad (\text{A.6})$$

For cracked concrete at service load:

$$\psi_{c,N} = 1 \text{ for both cast in place and postinstalled anchors}$$

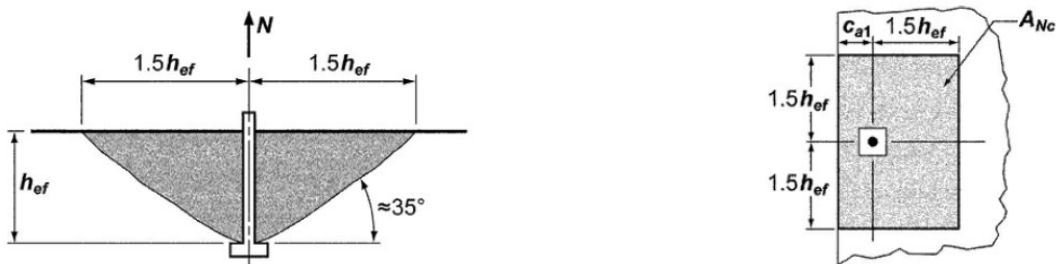
For the uncracked concrete at service load:

$$\psi_{c,N} = \begin{cases} 1.25 & \text{for cast in anchors} \\ 1.4 & \text{for postinstalled anchors} \end{cases}$$

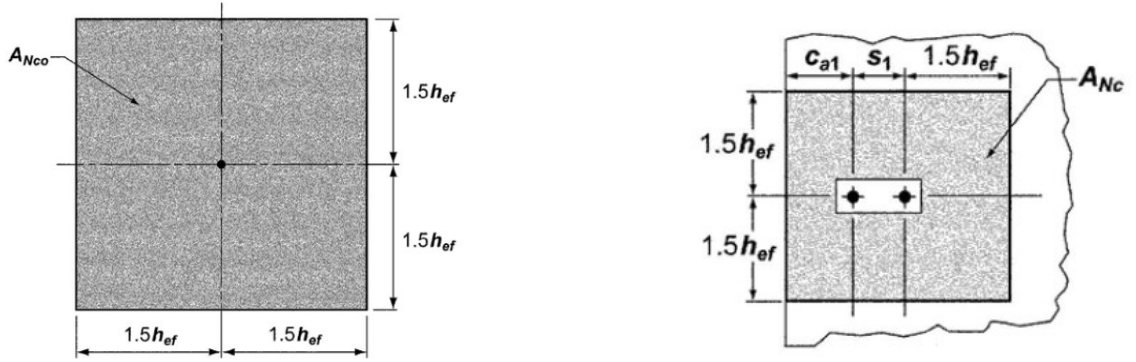
$$\psi_{cp,N} = \begin{cases} 1 & \text{if } c_{min} \geq c_c \\ \frac{c_{min}}{c_c} \geq \frac{1.5 h_{ef}}{c_c} & \text{if } c_{min} < c_c \end{cases}$$

Where A_N is the actual projected area, A_{No} is the projected area for the failure surface of concrete where $A_N \leq nA_{No}$, $\psi_{ec,N}$ is a modification factor account for eccentricity effect for group anchors, $\psi_{ed,N}$ is a modification factor account for edge effect, $\psi_{c,N}$ is a modification factor account for cracking, $\psi_{cp,N}$ is a modification factor account for post installed anchors embedded in uncracked concrete without reinforcement to control concrete splitting, c_c is the critical distance, N_b is the basic concrete breakout strength of a single anchor and can be determined using Equation (4.17), e'_N is the distance between the resultant tensile force of the group anchors and the centroid of the group anchors.

The geometrical calculations of the projected area A_{No} and the actual area A_N are shown in Figure A-1.



$$A_N = (c_{a1} + 1.5h_{ef}) \times (2 \times 1.5h_{ef}) \text{ For } c_{a1} < 1.5h_{ef}$$



$$A_{No} = (2 \times 1.5h_{ef}) \times (2 \times 1.5h_{ef}) = 9h_{ef}^2 \quad A_N = (c_{a1} + s_1 + 1.5h_{ef}) \times (2 \times 1.5h_{ef})$$

For $c_{a1} < 1.5h_{ef}$ and $s_1 < 3h_{ef}$

Figure A-1: Calculation of Projected area A_{No} and actual area A_N for single anchor and double anchors (Cement Association of Canada 2010; ACI Committee 318 2011)

Side-face blowout failure (Figure 2-5c) occurs for single cast-in-place anchors with deep embedment depths and located near the concrete free edge (Cement Association of Canada, 2010; ACI Committee 318, 2011). The side face blowout strength can be determined as follows:

$$N_{sb} = 160 c_1 \sqrt{A_{brg}} \sqrt{f'_c} \quad (A.7)$$

Where $c_1 < 0.4h_{ef}$

If $c_2 < 3c_1$ Equation (A.7) shall be multiplied by $(1 + \frac{c_2}{c_1})/4$ where the proportion of $(\frac{c_2}{c_1})$ should be in the range of $1 \leq \frac{c_2}{c_1} \leq 3$.

For group of anchors with deep embedment depths and $c_1 < 0.4h_{ef}$, $s < 6c_1$, the strength of the anchors can be calculated as follows:

$$N_{sbg} = (1 + \frac{s}{6c_1}) N_{sb} \quad (A.8)$$

Where A_{brg} is the bearing area, N_{sb} is the blowout strength for a single anchor, N_{sbg} is the blowout strength for a group of anchors.

According to ACI 318 the pullout load of single anchor in tension can be determined as in Equation (A.9).

$$N_{pn} = \psi_{c,p} \cdot N_p \quad (A.9)$$

$$\psi_{c,p} = \begin{cases} 1 & \text{for cracked concrete} \\ 1.4 & \text{for uncracked concrete} \end{cases}$$

$$N_p = 8A_{brg} \cdot f'_c \quad (A.10)$$

Where N_{pn} is the pullout force of a single anchor, N_p is the nominal pullout stress.

A.1.2 Concrete Capacity Design (CCD)

According to Concrete Capacity Design Method (CCD) the ultimate tensile load of the cast-in-place and post installed anchors in uncracked concrete can be determined as in Equation (4.3), where complete concrete cone is formed (Fuchs, 2001; Fuchs et al., 1995; Committee Euro-International du Beton (CEB), 1994; Subramanian, 2000; Ashour and Alqedra, 2005).

Large strain gradient in concrete for fastenings resulted in increasing the size effect and this behaviour is similar to linear elastic fracture mechanics (LEFM) mode. This means

that, the nominal failure stress decreases with $\frac{1}{\sqrt{h_{ef}}}$ and the failure load increases with $h_{ef}^{1.5}$ (Fuchs et al., 1995).

When the anchor is placed near to the edge of the concrete, complete concrete cone will not be produced and resulted in a decrease in the ultimate tensile load. Also, when the anchors located near to each other, the ultimate tensile load will decrease due to the overlap in the concrete cone breakout. The CCD method takes into consideration the effect of edge distance, spacing, and eccentricity effect in determining the tensile load, and it uses simple geometric relations in calculating these effects (Fuchs et al., 1995).

For the edge distance effect, assuming that the tensile load is applied concentrically on the anchors, the ultimate tensile strength can be determined as in Equation (A.11).

$$N_u = \frac{A_N}{A_{No}} \cdot \psi_2 \cdot N_{uo} \quad (\text{A.11})$$

Where A_N is the actual projected area of stress cone of a single anchor. A_{No} , is the projected area of single anchor, unlimited by edge effect or spacing between the anchors, adopting the approach of four-sided pyramids cone to predict the failure surface.

$$A_{No} = 9h_{ef}^2 \quad (\text{A.12})$$

ψ_2 is a modification factor considering the disorder of the radial symmetric stress distribution due to the edge effect for the anchors far from the edge. Existence of free edge causes distortion in the stress distribution of the concrete around the anchor, this distortion

is similar to that occurs in case of crack existence in the concrete around the anchor (Cement Association of Canada, 2010).

$$\psi_2 = 1 \text{ if } c_l \geq 1.5 h_{ef}, \psi_2 = 0.7 + 0.3 \frac{c_l}{1.5h_{ef}} \text{ if } c_l \leq 1.5 h_{ef} \quad (\text{A.13})$$

where c_l is the distance from center of anchor to edge of concrete in the direction of the applied load.

For the eccentricity effect and/or edge distance effect, the ultimate tensile strength can be determined as in Equation (A.14).

$$N_u = \frac{A_N}{A_{NO}} \cdot \psi_1 \cdot \psi_2 \cdot N_{uo} \quad (\text{A.14})$$

ψ_1 is factor considering the eccentricity of the resultant tensile force on the anchors.

$$\psi_1 = \frac{1}{1 + 2e'_N / (3h_{ef})} \leq 1 \quad (\text{A.15})$$

Where e'_N is the distance between the resultant tensile force of the set anchors and the centroid of these anchors. If the tensile load acts on one anchor of group anchors, the ultimate tensile load of the group of anchors is same as the ultimate tensile load of one anchor without spacing effects (Fuchs et al., 1995).

When the largest edge distance (c_{\max}) is less than or equal to $1.5 h_{ef}$, embedment depth of $h_{ef} = \frac{c_{\max}}{1.5}$ is used in Equations (A.17) and (A.18) (Fuchs et al., 1995).

A.2 Design methods for cast-in-place anchors under shear load

A.2.1 American concrete institute (ACI)

ACI 349-85 design method assumes fully developed semi concrete cone with height equal to edge distance to predict the concrete failure surface. The concrete capacity for a single anchor is determined by assuming the angle between failure surface and the concrete surface 45° . ACI 349 is applied for the anchors used in safety related structures and nuclear power plant. The ultimate shear failure load for single anchor can be determined by Equation (A.16) (Fuchs et al., 1995; Subramanian, 2000; Fuchs, 2001; Zamora et al., 2003).

$$V_{no} = 0.48 \sqrt{f'_{cc}} (c_1)^2 \quad (\text{A.16})$$

Where V_{no} is the ultimate shear load (N), f'_{cc} is the cube compressive strength of concrete (MPa), and c_1 is the edge distance parallel to the direction of the applied load (mm).

For small concrete depth (h less than c_1) or anchor spacing, s , (less than $2 \times c_1$) or the edge distance perpendicular to the load direction, c_2 , less than the edge distance parallel to the load, c_1 , the ultimate shear failure load (V_n) can be determined by the modified Equation (A.17) (Fuchs et al., 1995; Gross et al., 2001).

$$V_n = \frac{A_v}{A_{vo}} V_{no} \quad (\text{A.17})$$

$$A_{vo} = \frac{\pi}{2} c_1^2 \quad (\text{A.18})$$

Where A_v is the actual projected area considering edge effects and overlap with adjacent anchors and A_{vo} is the projected area for one anchor unlimited by edge effects, concrete depth or cone overlapping.

According to ACI 318-11 the shear strength for the anchors can be calculated depending on the steel strength of the anchor, edge distance, concrete strength, and anchor spacing that in turn affects the failure mode.

Steel anchor failure (Figure 2-6a) occurs for anchors with deep embedment depths and far from the concrete edge, where the bending stresses in the anchor are higher than the tensile strength of the steel anchor. This failure characterized by bending followed by yielding and fracture the steel anchor. Concrete spall may be observed at the surface of the concrete in front of the anchor because of the high local pressure generated in front of the anchor (Cement Association of Canada, 2010). Steel strength of cast-in-place anchor under shear loading can be calculated as in Equation (4.18).

Concrete cone breakout failure (Figure 2-6c) occurs when the anchors located close to the concrete free edge and subjected to shear load towards the edge, where the tensile strength of the steel anchor is sufficient to prevent anchorage failure. According to ACI 318-11,

assuming the failure surface makes 35° cone with the surface of the concrete, the nominal concrete breakout strength for a single anchor subjected to shear load perpendicular to an edge can be determined as in the following Equation:

$$V_{cb} = \frac{A_{vc}}{A_{vco}} \cdot \psi_{ed,v} \cdot \psi_{c,v} \cdot V_b \quad (\text{A.19})$$

The concrete breakout strength for a group of anchors subjected to shear load can be determined as follows:

$$V_{cbg} = \frac{A_{vc}}{A_{vco}} \psi_{ec,v} \cdot \psi_{ed,v} \cdot \psi_{c,v} \cdot V_b \quad (\text{A.20})$$

$$A_{vco} = 4.5 c_1^2 \quad (\text{A.21})$$

$$\psi_{ec,v} = \frac{1}{1+2e'_v/(3c_1)} \leq 1 \quad (\text{A.22})$$

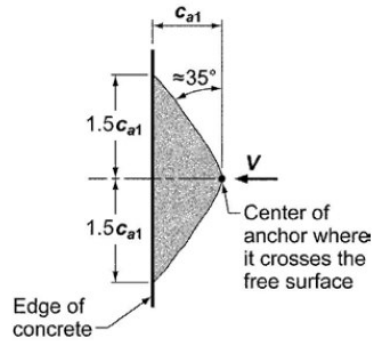
$$\psi_{ed,v} = 1 \text{ if } c_2 \geq 1.5c_1 \quad (\text{A.23})$$

$$\psi_{ed,v} = 0.7 + 0.3 \frac{c_2}{1.5c_1} \text{ if } c_2 < 1.5c_1 \quad (\text{A.24})$$

Where

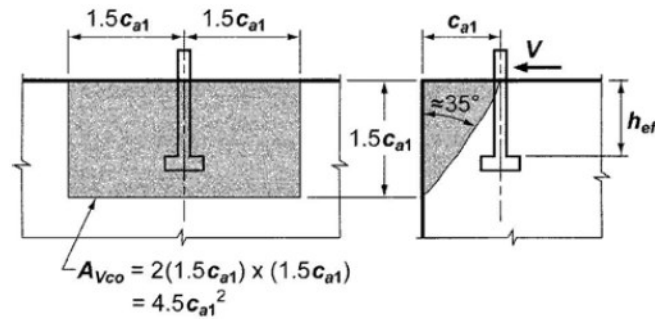
$\psi_{c,v} = 1.4$ in uncracked concrete

The geometrical calculations of the projected area A_{CO} are shown in Figure A-2.



The critical edge distance is equal to $1.5 c_{a1}$ for headed studs, headed bolts, expansion anchors, and undercut anchors

(a) Plan view



(b) Front view

(c) side view

Figure A-2: Calculation of projected area A_{VCO} for single anchor (Cement Association of Canada, 2010; ACI Committee 318, 2011)

Where A_{vc} is the actual projected area, A_{VCO} is the projected area for the failure surface of concrete, A_{vc} and A_{VCO} are calculated assuming the failure surface as a half pyramid projected on the face of the concrete near the edge, where $A_{vc} \leq nA_{VCO}$, $\psi_{ec,v}$ is a modification factor accounts for eccentricity effect for group anchors subjected to eccentrically shear load, $\psi_{ed,v}$ is a modification factor accounts for edge effect, $\psi_{c,v}$ is a modification factor accounts for cracking, V_b is the basic concrete breakout strength of a single anchor subjected to shear load in cracked concrete, V_{cb} is the nominal shear strength

acting perpendicular to the free edge of a single anchor, V_{cbg} is the shear strength acting perpendicular to the free edge of a group anchors.

When the shear load acts parallel to the concrete free edge the shear load value obtained from Equations (A.19) and (A.20) will be doubled, with $\psi_{ed,v} = 1$. For the anchors located far from the concrete free edge Equations (A.19 and A.20) will not be used where the concrete break out failure will not occur (ACI Committee 318, 2011).

Concrete pryout failure (Figure 2-6b) occurs when the anchors located far from the concrete free edge. The failure characterized by concrete cracking in the direction of the applied shear load accompanied by concrete spalling in the opposite direction. The concrete spalling initiated behind the anchor at its lower end and propagates forming a conical shape towards the surface of the concrete. This type of failure occurs for stiff anchors with shallow embedment depths (Cement Association of Canada, 2010). The shear load of the anchor that exhibits pryout failure can be calculated as in Equation (4.14) (ACI Committee 318, 2011). The ACI 318 calculates the pryout capacity depending on the tensile concrete breakout capacity multiplied by a factor to consider the shear effect (ACI Committee 318, 2011). The ACI 318 method takes into account the effect of embedment depth and didn't consider the influence of anchor diameter in the calculation of the shear load for the case of the pryout failure.

Jebara et al. (Jebara et al., 2016) proposed an equation to determine the pryout capacity of cast-in-place concrete anchors embedded in concrete based on a regression analysis made as follows:

$$V_{cp} = 6 \sqrt{d} \sqrt{f_{cc}} (h_{ef})^{1.5} \quad (\text{A.25})$$

A.2.2 Concrete Capacity Design (CCD)

The ultimate shear load of single anchor in uncracked concrete can be determined in accordance with the CCD method as in Equation (A.26) (Fuchs, 2001; Fuchs et al., 1995; Committee Euro-International du Beton (CEB), 1994; Subramanian, 2000; Ashour and Alqedra 2005). The shear load is calculated based on the test results of a single anchor diameter of $d \leq 25$ and effective length of $h_{ef} \leq 8 d_o$ embedded in thick uncracked concrete (Fuchs et al., 1995).

$$V_{no} = \left(\frac{h_{ef}}{d}\right)^{0.2} \sqrt{d f'_{cc}} (c_1)^{1.5} \quad (\text{A.26})$$

Where h_{ef} is the effective length or embedment depth of cast-in-place anchors (mm), and d is the diameter of the anchor (mm). As presented in Equation (A.26), the increment in the ultimate shear load is proportional to $c_1^{1.5}$ due to the size effect. Also, the failure load is affected by the anchor stiffness and diameter (Fuchs et al., 1995; Subramanian, 2000).

When the anchor or group of anchors is located near the edge of concrete specimen, the shear capacity for the concrete calculated in accordance with the CCD method is adjusted in accordance with Equation (A.27).

$$V_n = \frac{A_v}{A_{vo}} \cdot \psi_4 \cdot \psi_5 \cdot V_{no} \quad (\text{A.27})$$

$$\psi_4 = \frac{1}{1+2e'_v/(3c_1)} \quad (\text{A.28})$$

$$\psi_5 = \begin{cases} 1 & \text{for } c_2 \geq 1.5c_1 \\ 0.7 + 0.3 \frac{c_2}{1.5c_1} & \text{for } c_2 \leq 1.5c_1 \end{cases} \quad (\text{A.29})$$

Where A_v is the actual shear breakout area, A_{vo} is the projected area for one anchor unlimited by edge effects, concrete depth or cone overlapping, adopting the approach of half-pyramids to predict the failure surface, ψ_4 is the eccentricity effect of shear load on anchor groups, ψ_5 is a modification factor takes into consideration disorder of symmetric stress distribution resulting from edge effects, e'_v is the distance between resultant shear force of the anchor group and the centroid of the anchors.

The CCD method assumes the fracture shear area as a half pyramid, the effect of edge distance and spacing is calculated based on rectangular projected area. This assumption makes the CCD method relatively simple compared to the ACI 349 method that assumes circular projected area in the calculation. In addition, the CCD method is concerned in the disorder of the stresses in the concrete due to the edge effect or eccentricity effect, while ACI 349 neglect this effect (Fuchs et al., 1995; Subramanian, 2000).

Appendix B: Design methods for adhesive anchors

B.1 Design methods for adhesive anchors under tensile load

B.1.1 Concrete cone breakout failure

According to the Concrete Capacity Design Method (CCD), the pullout capacity for adhesive anchors under tensile load was introduced by Eligehausen et al.(1984) as in Equation (B.1)(Cook et al., 1998).

$$N_u = 0.92 h_{ef}^2 \sqrt{f'_c} \quad (B.1)$$

Where N_u is the pullout force (N).

Cook et al. 1998 introduced another equation for determining the pullout capacity of adhesive anchors under tensile load and based on the model developed by Fuchs et al. 1995 for cast-in-place anchors (Cook et al.,1998).

$$N_u = 16.5 h_{ef}^{1.5} \sqrt{f'_c} \quad (B.2)$$

Anchor pullout failure occurs for the adhesive anchor when the friction between the anchor and the concrete is less than the applied tensile load. According to the American Concrete Institute method, the pullout capacity for adhesive anchors under tensile load is given as in the following equation (Eligehausen, 1987; Fuchs et al., 1995; Gesoglu et al., 2005):

$$N_u = f_{ct} A_N \quad (\text{B.3})$$

$$f_{ct} = 0.33 \sqrt{f'_c} \quad (\text{B.4})$$

$$A_N = \pi h_{ef}^2 \left(1 + \frac{d_h}{h_{ef}} \right) \quad (\text{B.5})$$

Where

f_{ct} is the concrete capacity, A_N is the projected area of a single anchor, d_h is the diameter of the anchor head, where anchor diameter (d) is used instead of d_h for the adhesive anchors (Gesoglu et al., 2005).

Hence, the equation (B.3) can be expressed as follows (Eligehausen, 1987)

$$N_u = 1.043 \sqrt{f'_c} h_{ef}^2 \left(1 + \frac{d_h}{h_{ef}} \right) \quad (\text{B.6})$$

B.1.2 Anchor steel failure

The pullout failure load for the steel anchor can be determined using Equation (4.2).

B.1.3 Bond failure

For the uniform bond stress model, where the bond failure occurs at the steel/adhesive interface, the pullout force can be predicted as follows (McVay et al., 1996; Cook et al., 1998; Cook, 1993; Eligehausen et al., 2007):

$$N_u = \tau_o \pi d_o h_{ef} \quad (\text{B.7})$$

Where N_u is the pullout force (N), τ_o is the uniform bond stress in the adhesive layer (MPa), d_o is the diameter of the hole (mm), h_{ef} is the effective embedment depth (mm).

According to Cook et al. (1991) and McVay et al.(1996), the uniform bond stress of the adhesive is in the range between (9-13 MPa). Equation (B.7) is suitable for $4 \leq \frac{h_{ef}}{d} \leq 20$, $d \leq 50 \text{ mm}$ and bond area of $\pi d h_{ef} \leq 58000 \text{ mm}^2$ (Eligehausen et al., 2006).

On the other hand, for the uniform bond stress model, where the bond failure occurs at the adhesive/concrete interface, the pullout force can be predicted as follows (Cook et al., 1998).

$$N_u = \tau_o \pi d_o h_{ef} \sqrt{\frac{f'_c}{f'_{c,low}}} \quad (\text{B.8})$$

Where $f'_{c,low}$ is the low strength concrete.

For the elastic bond stress model, the bond strength can be predicted as in the following Equation (McVay et al., 1996; Cook et al., 1998; Cook et al., 1993; Cook, 1993):

$$N_u = \tau_{max} \pi d_o \left[\frac{\sqrt{d_o}}{\lambda'} \tanh \frac{\lambda' h_{ef}}{\sqrt{d_o}} \right] \quad (\text{B.9})$$

Where τ_{max} is the maximum bond stress in the adhesive layer, λ' is the elastic constant that depends on the shear stiffness of the adhesive-concrete system and axial stiffness of the anchor, λ' is independent of the hole diameter. The maximum bond stress of the adhesive

is in the range between (10-14.5 MPa) according to Cook et al. (Cook et al., 1991) and McVay et al. (McVay et al., 1996).

Similar results can be obtained from the uniform bond stress model and elastic bond stress model for embedment depths up to $40 \sqrt{d_o}$. Over prediction of the pullout force can be seen in the uniform bond stress model for the embedment depths higher than $40 \sqrt{d_o}$ (McVay et al., 1996; Cook et al., 1993).

B.1.4 Combined cone-bond failure

According to Cook (1993), the pullout failure load for the combined cone-bond model can be determined as in Equation (B.10).

$$N_u = N_{cone} + N_{bond} \quad (B.10)$$

So that, by combining concrete cone breakout failure with bond failure, combined cone-bond capacity equation can be written as follows for the uniform bond stress (McVay et al., 1996; Cook, 1993):

$$N_u = 0.92 h_{cone}^2 \sqrt{f_c} + \tau_o \pi d_o (h_{ef} - h_{cone}) \quad (B.11)$$

The concrete cone depth (h_{cone}) at the minimum failure load can be determined by taking the derivative of the combined cone-bond capacity equation with respect to the cone depth as follows:

$$\frac{dN_u}{dh_{cone}} = 0 \quad (B.12)$$

So that,

$$h_{cone} = \frac{\tau_o \pi d_o}{1.84 \sqrt{f'_c}} \quad (B.13)$$

For the elastic bond stress, the combined cone-bond failure load can be determined as in the following Equation (McVay et al., 1996; Cook, 1993):

$$N_u = 0.92 h_{cone}^2 \sqrt{f'_c} + \tau_{max} \pi d_o \left[\frac{d_o}{\lambda} \tan \frac{\lambda'(h_{ef} - h_{cone})}{\sqrt{d_o}} \right] \quad (B.14)$$

By taking the derivative for Equation (B.14) with respect to h_{cone} , resulted in the following Equation for the concrete cone depth:

$$h_{cone} = \frac{\tau_{max} \pi d_o}{1.84 \sqrt{f'_c}} \left(\operatorname{sech}^2 \frac{\lambda'(h_{ef} - h_{cone})}{\sqrt{d_o}} \right) \quad (B.15)$$

The uniform shear stress (τ_o) and maximum shear stress (τ_{max}) are identical for shallow embedment depths. While, the maximum shear stress (τ_{max}) becomes higher than the uniform shear stress (τ_o) for the large embedment depths (Cook, 1993).

For small concrete size, anchors located near to the edge of the concrete or small spacing distance between the anchors, concrete splitting would occur as shown in Figure 2-3d (Cement Association of Canada, 2010; Rao and Arora, 2013).

B.2 Design methods for adhesive anchors under shear load

The shear load of adhesive anchors can be determined according to Concrete Capacity Design method (CCD), American Concrete Institute (ACI) method and Precast/ Pre-stressed Concrete Institute (PCI) method.

The failure surface of the concrete become a semi-cone when the concrete thickness is less than edge distance parallel to the direction of the applied load (c_1), and or the spacing between two anchors (s) is less than $2c_1$, or (c_2) is less than c_1 (Alqedra and Ashour, 2005; Fuchs et al., 1995).

The shear load of the adhesive anchor can be calculated based on (ACI 349-78) as follows (Ueda et al., 1990):

$$V_u = 0.522 c_1^2 \sqrt{f'_c} \quad (\text{B.16})$$

The anchor shear strength in Equation (B.16) is derived based on the tensile strength of the concrete acts on the projected area of half cone shaped (Ueda et al., 1990).

ACI 318 can be used to predict the ultimate load for cast-in-place and post installed expansion and undercut anchors (ACI Committee 318, 2005). According to ACI 318-05, the ultimate shear load can be predicted as follows:

$$V_b = 0.6 \left(\frac{h_{ef}}{d_o} \right)^{0.2} \sqrt{d_o} \sqrt{f'_c} (c_1)^{1.5} \quad (\text{B.17})$$

ACI 318-11 deals with the structural anchors and can be used to predict the ultimate load for cast-in-place and post installed anchors including the adhesive anchors (ACI Committee 318, 2011). The failure surface of the concrete makes a 35° angle with the contact concrete edge. Impact and blast loads on anchors are not included in the ACI 318-11.

For single anchor, where the shear force perpendicular to the edge, the concrete breakout shear strength can be calculated as follows:

$$V_{cb} = \frac{A_{vc}}{A_{vco}} \psi_{ed,v} \cdot \psi_{c,v} \cdot \psi_{h,v} \cdot V_b \quad (\text{B.18})$$

$$\psi_{c,v} = \begin{cases} 1 & \text{for anchors in cracked concrete without reinforcement} \\ 1.2 & \text{for anchors in cracked concrete with reinforcement} \\ 1.4 & \text{for anchors in uncracked concrete} \end{cases}$$

$$\psi_{h,v} = \sqrt{\frac{1.5c_1}{h}} \quad (\text{B.19})$$

According to CCD method, the shear load of the adhesive anchor can be calculated as follows (Gesoglu et al., 2014; Bickel and Shaikh, 2002):

$$V_u = 1.1 \left(\frac{h_{ef}}{d_o} \right)^{0.2} \sqrt{d_o} \sqrt{f'_{cc}} c_1^{1.5} \quad (\text{B.20})$$

Equation (B.20) can be used for calculating the shear force of a single anchor embedded into thick uncracked concrete, where the shear load is applied towards the free edge (Bickel and Shaikh 2002).

Fuchs et al (1995) proposed equation (B.20) based on experimental shear tests for a single anchor with diameter $d_o \leq 25 \text{ mm}$ and $h_{ef} \leq 8d_o$. In order to include a wide range of anchor diameters and embedment depths Equation (B.20) is modified. The modification of the Equation (B.20) is based on experimental tests and numerical simulations. According to the modified CCD method the shear capacity of the adhesive anchor can be calculated as follows (Lee et al., 2011; Spyridis and Bergmeister, 2014):

$$V_u = 3 d_o^a h_{ef}^b \sqrt{f'_{cc}} c_1^{1.5} \quad (\text{B.21})$$

Where

$$a = 0.1 \left(\frac{h_{ef}}{c_1}\right)^{0.5}, \quad b = 0.1 \left(\frac{d_o}{c_1}\right)^{0.2} \quad (\text{B.22})$$

Where V_u is the shear capacity of the anchor near to edge and h_{ef} is the effective length.

PCI 1978 can predict the failure of the concrete based on a conical failure surface. Since 2004 the PCI method relied on the ACI 318 which is in turn based on the CCD method by adopting the approach of four-sided pyramids cone to predict the failure surface (Pallarés and Hajjar, 2009). PCI method is more suitable for predicting the shear capacity for adhesive anchors than cast-in-place anchors (Bickel and Shaikh, 2002). According to Precast/ Prestressed Concrete Institute (PCI) Design Handbook (precast-prestressed concrete Institute, 1999), the shear capacity of single anchor in uncracked concrete can be calculated as follows:

$$V_u = 5.2 c_1^{1.5} \sqrt{f'_c} \quad (\text{B.23})$$

Appendix C: Tensile load-displacement relation for cast-in place anchors

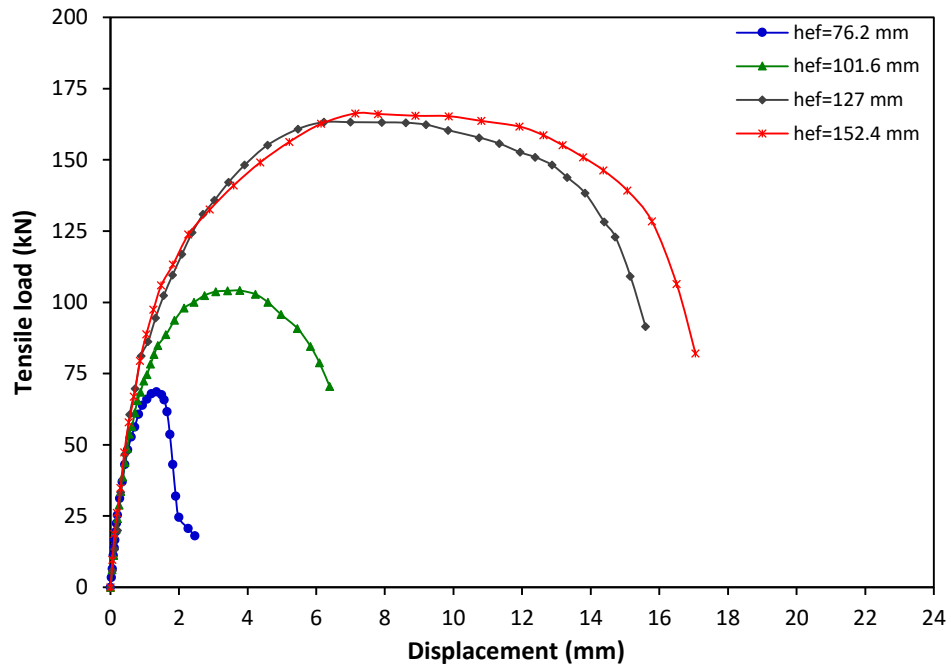


Figure C-1: Tensile load-displacement graph for 15.9 mm diameter cast-in-place anchor at strain rate of 10^{-5} s^{-1}

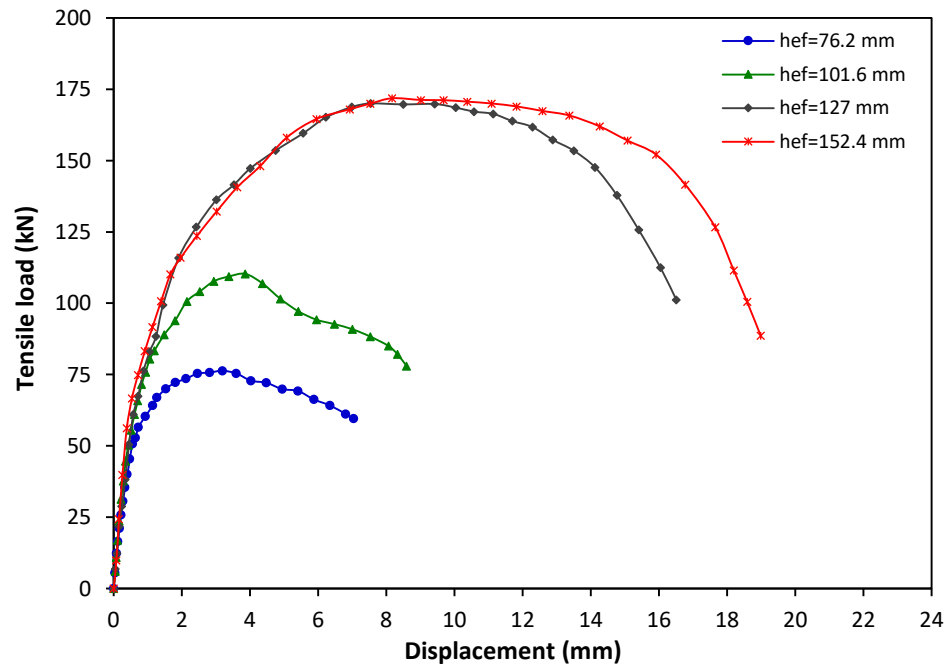


Figure C-2: Tensile load-displacement graph for 15.9 mm diameter cast-in-place anchor at strain rate of 10^{-3} s^{-1}

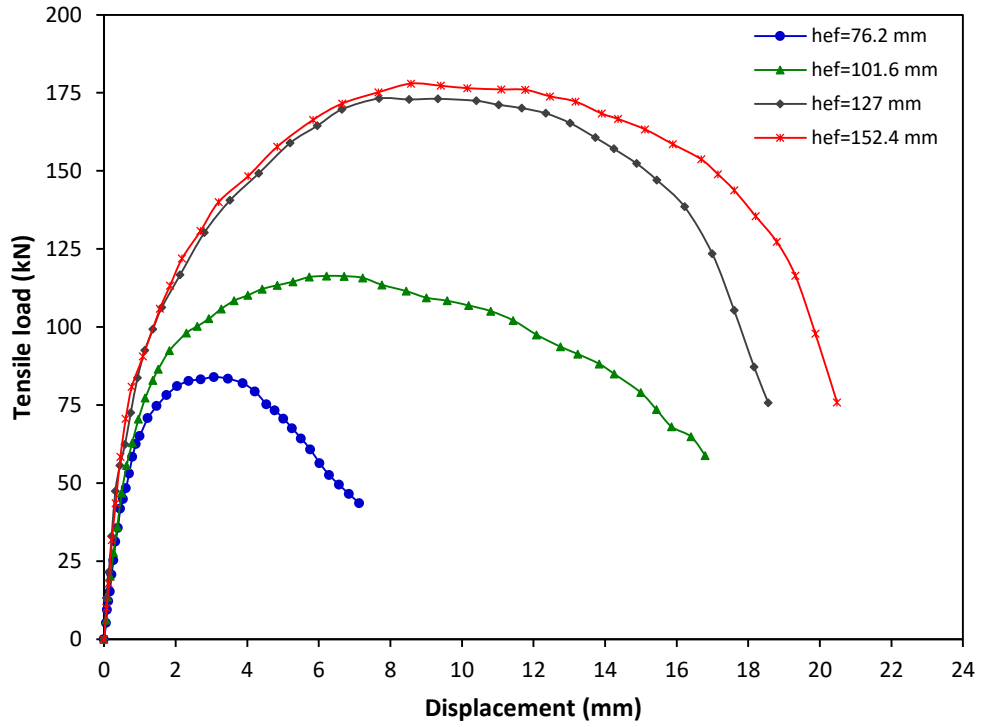


Figure C-3: Tensile load-displacement graph for 15.9 mm diameter cast-in-place anchor at strain rate of 10^{-1} s^{-1}

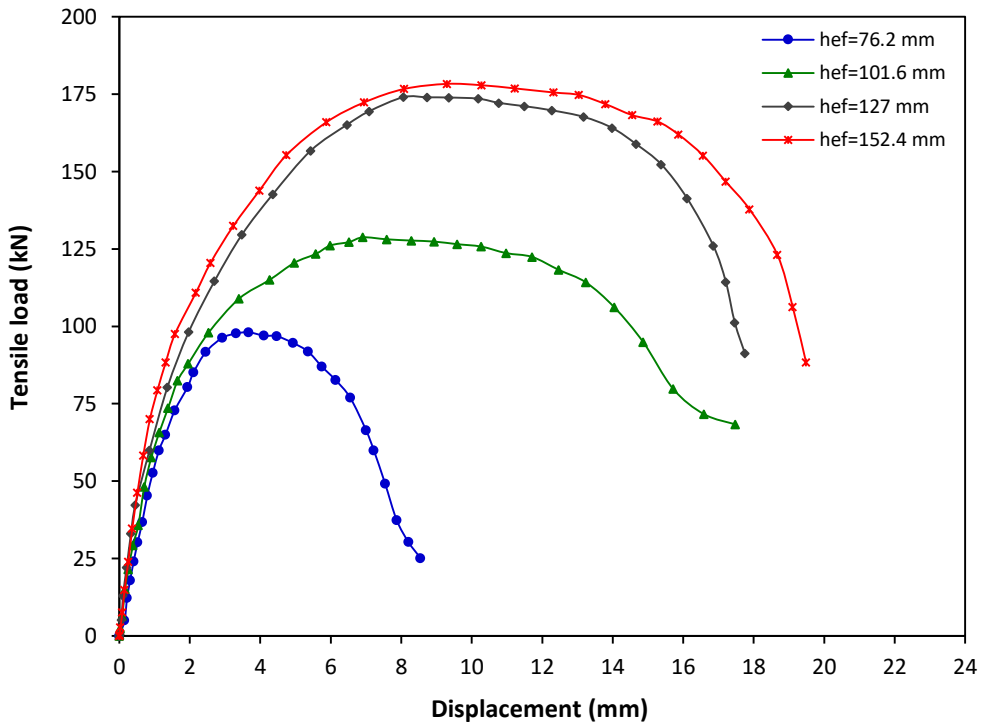


Figure C-4: Tensile load-displacement graph for 15.9 mm diameter cast-in-place anchor at strain rate of 10 s^{-1}

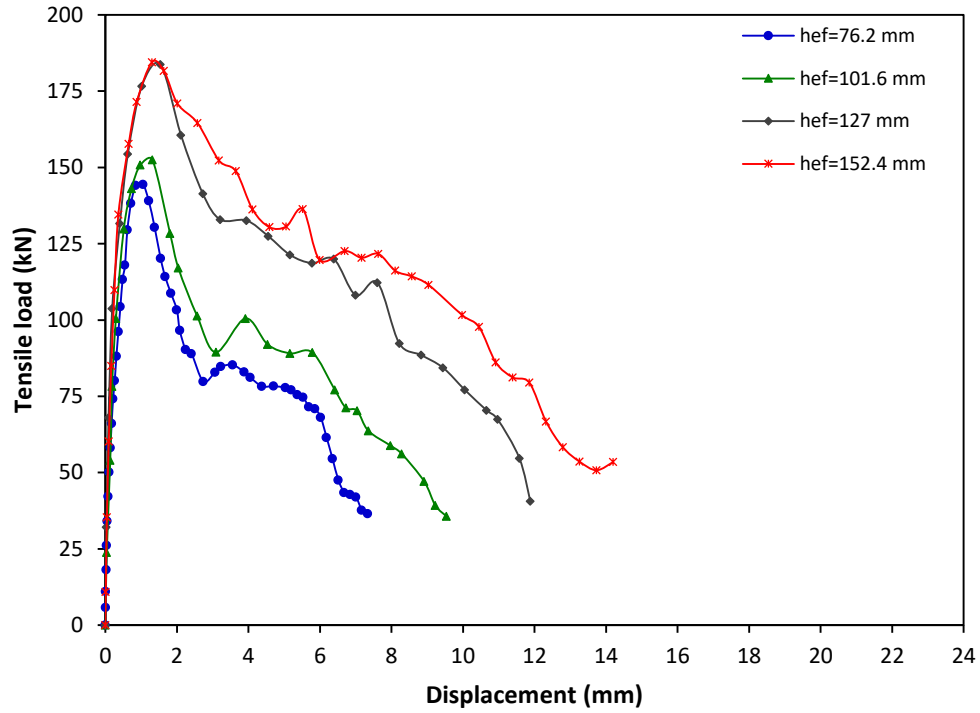


Figure C-5: Tensile load-displacement graph for 15.9 mm diameter cast-in-place anchor at strain rate of 10^2 s^{-1}

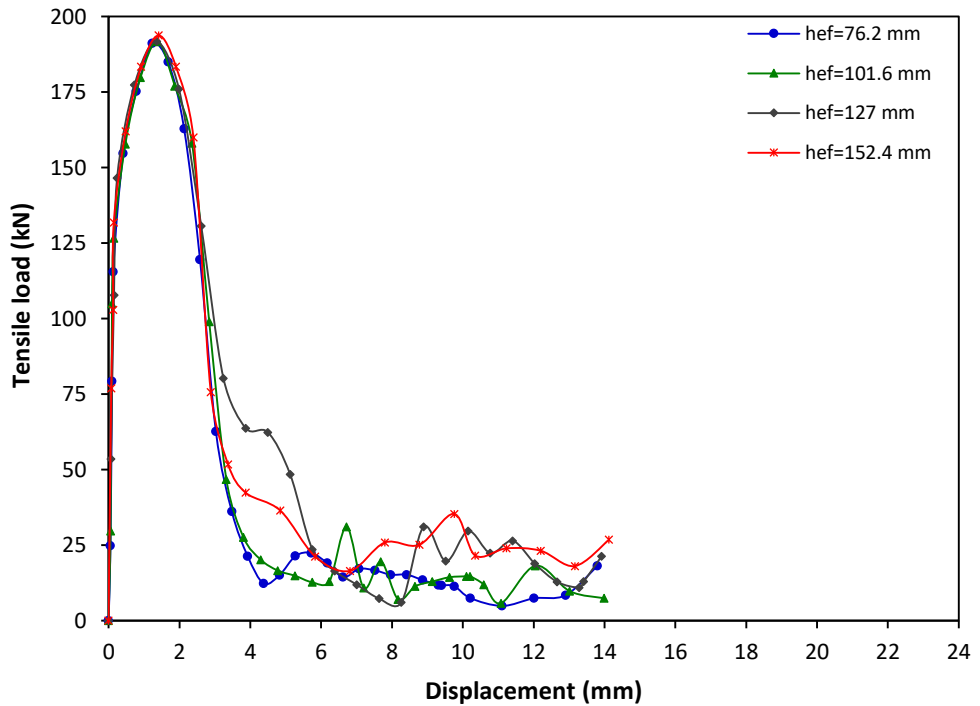


Figure C-6: Tensile load-displacement graph for 15.9 mm diameter cast-in-place anchor at strain rate of 10^3 s^{-1}

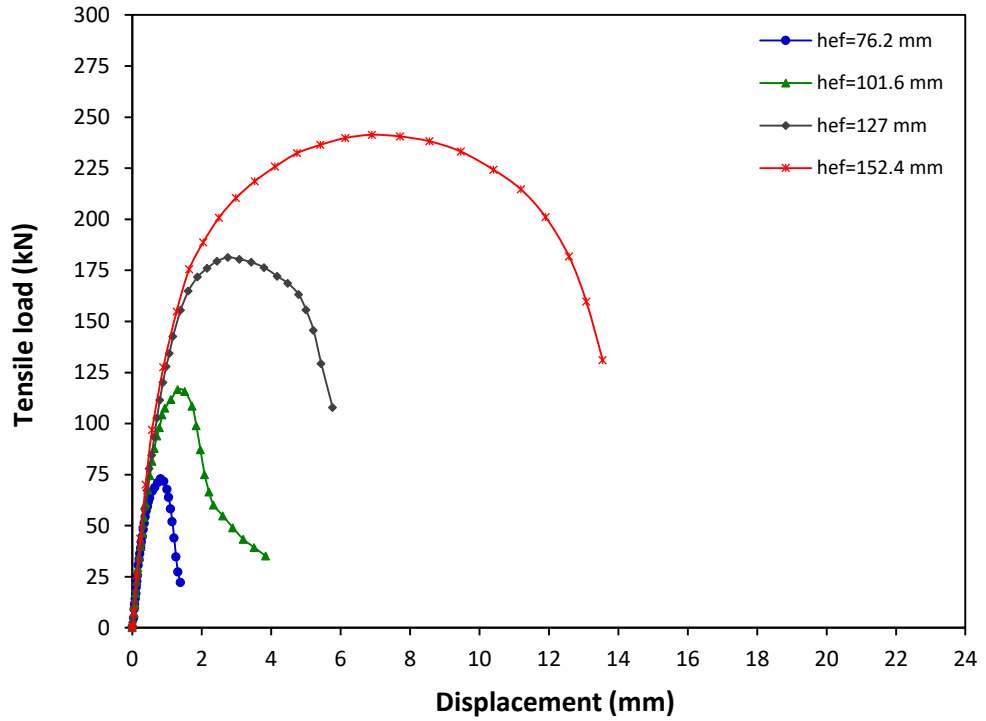


Figure C-7: Tensile load-displacement graph for 19.1 mm diameter cast-in-place anchor at strain rate of 10^{-5} s^{-1}

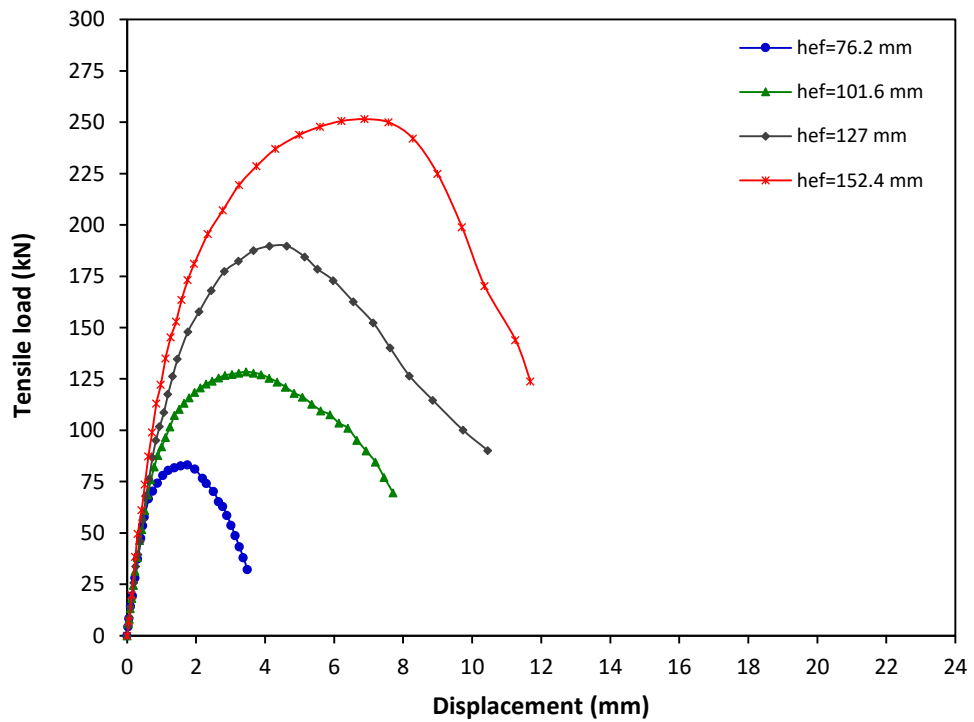


Figure C-8: Tensile load-displacement graph for 19.1 mm diameter cast-in-place anchor at strain rate of 10^{-3} s^{-1}

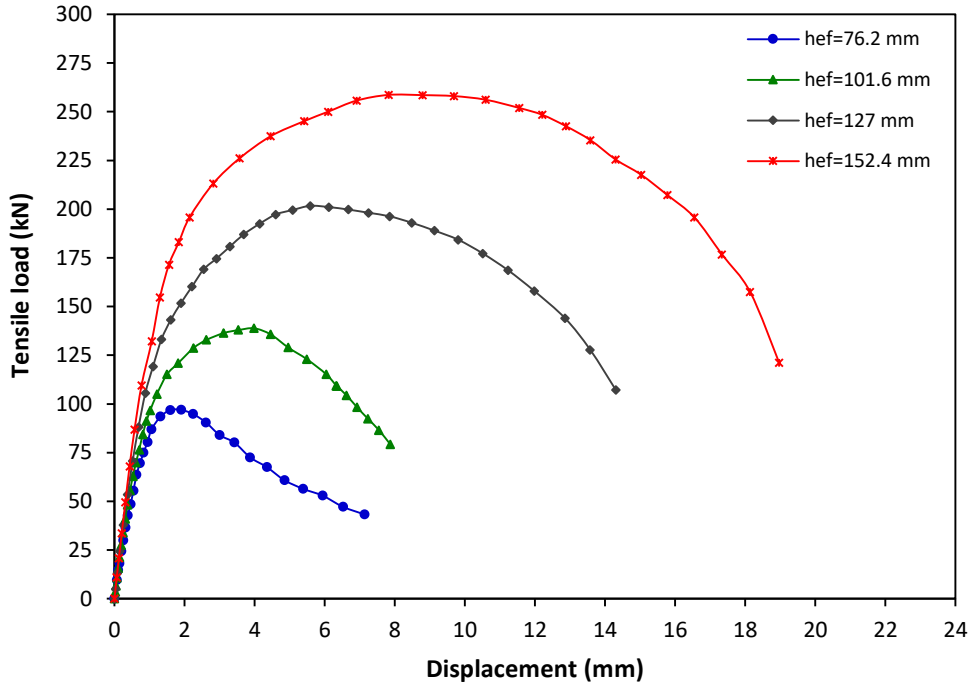


Figure C-9: Tensile load-displacement graph for 19.1 mm diameter cast-in-place anchor at strain rate of 10^{-1} s^{-1}

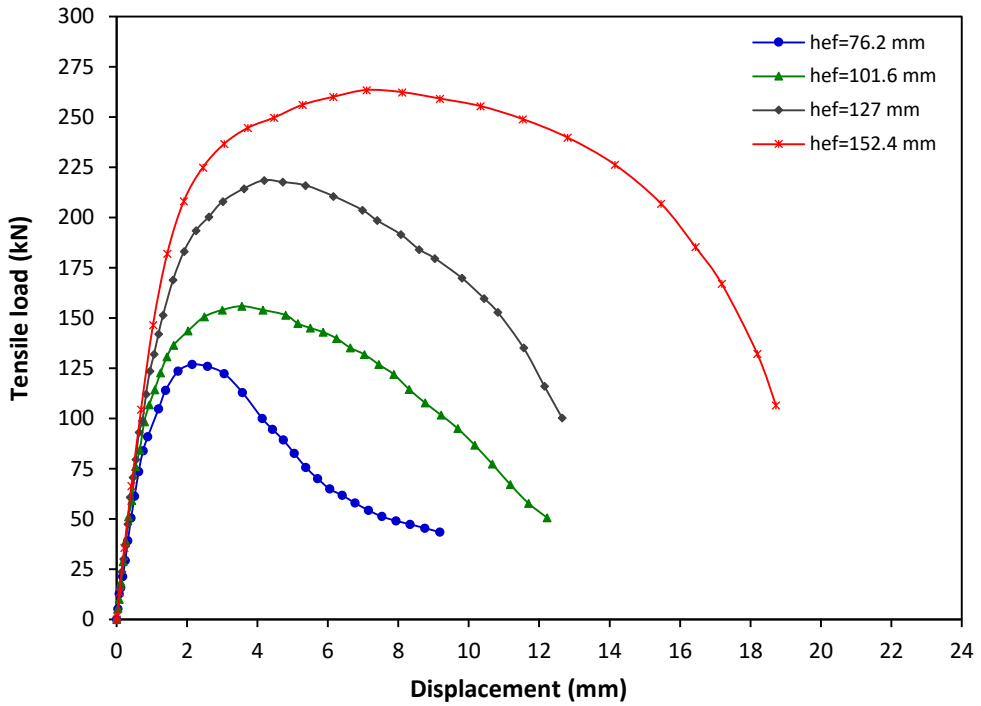


Figure C-10: Tensile load-displacement graph for 19.1 mm diameter cast-in-place anchor at strain rate of 10 s^{-1}

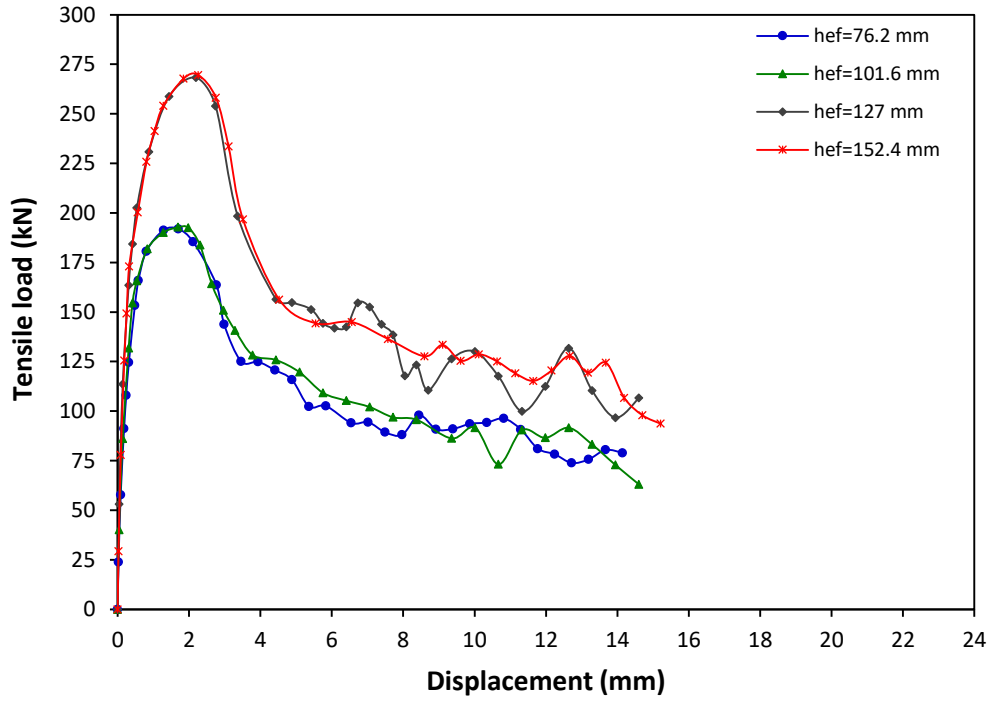


Figure C-11: Tensile load-displacement graph for 19.1 mm diameter cast-in-place anchor at strain rate of 10^2 s^{-1}

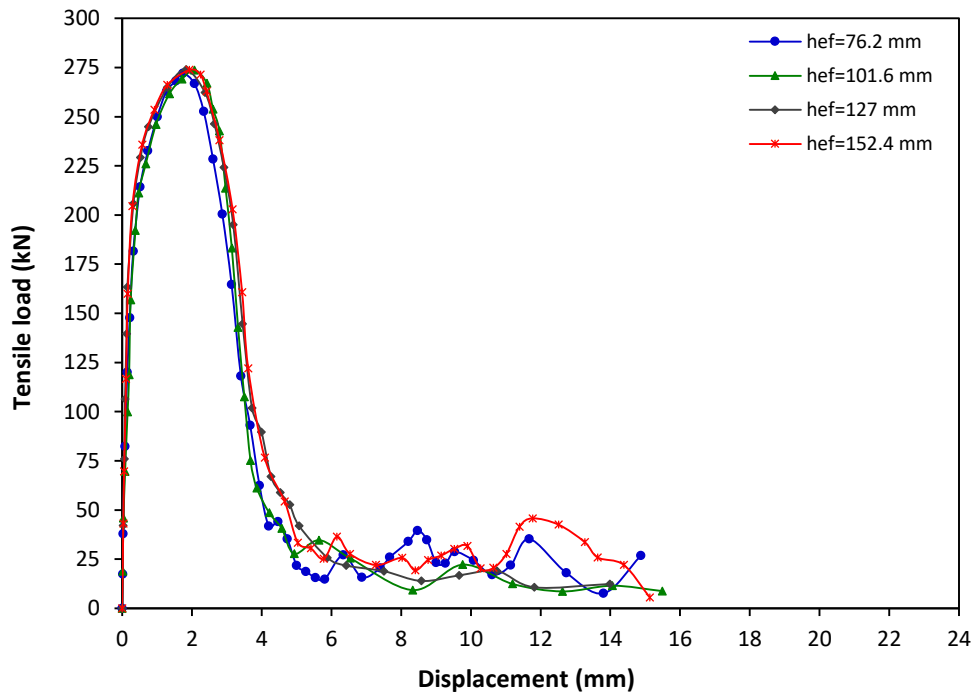


Figure C-12: Tensile load-displacement graph for 19.1 mm diameter cast-in-place anchor at strain rate of 10^3 s^{-1}

Appendix D: Shear load-displacement relation for cast-in-place anchors

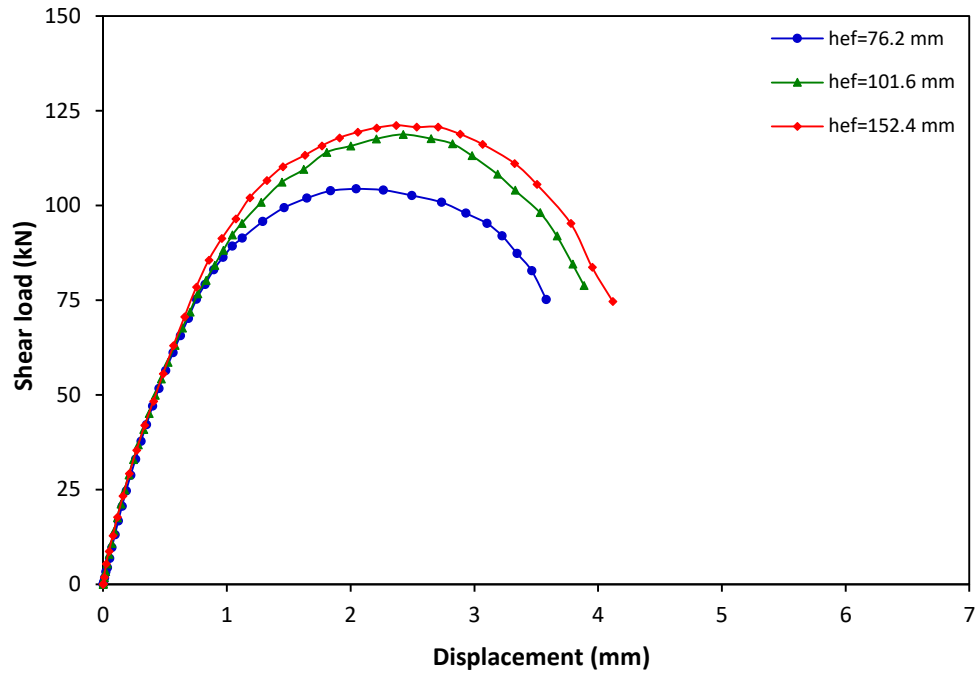


Figure D-1: Shear load-displacement graph for 15.9 mm diameter cast-in-place anchor at strain rate of 10^{-5} s^{-1}

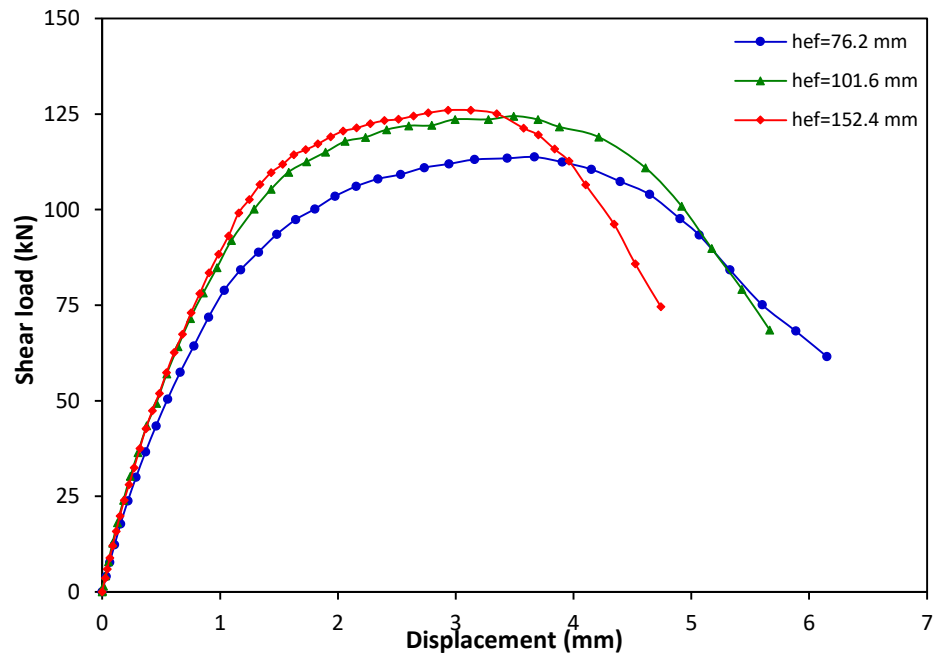


Figure D-2: Shear load-displacement graph for 15.9 mm diameter cast-in-place anchor at strain rate of 10^{-3} s^{-1}

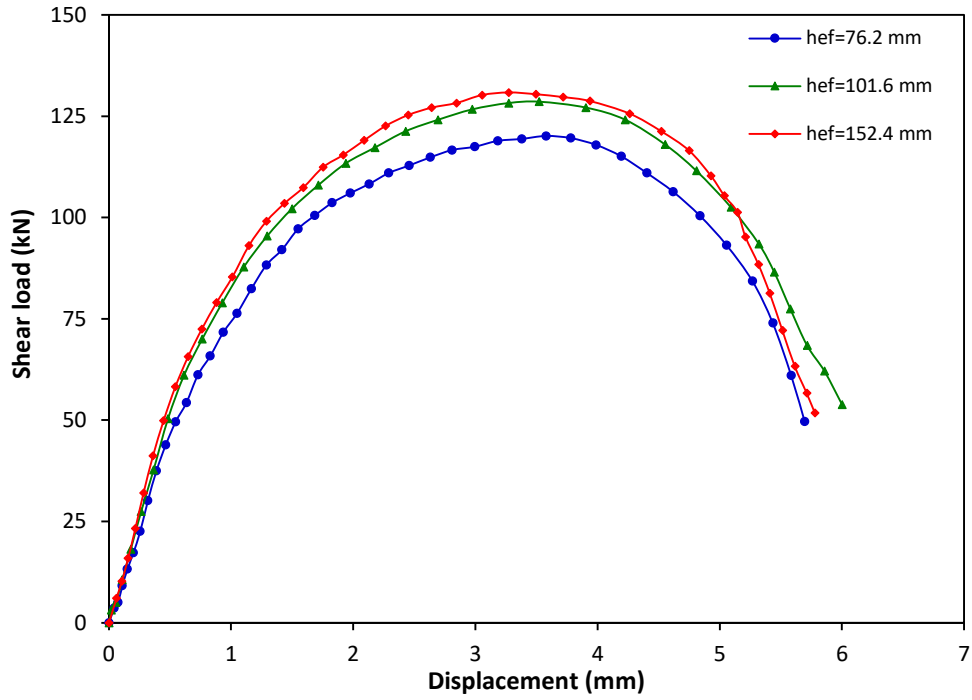


Figure D-3: Shear load-displacement graph for 15.9 mm diameter cast-in-place anchor at strain rate of 10^{-1} s^{-1}

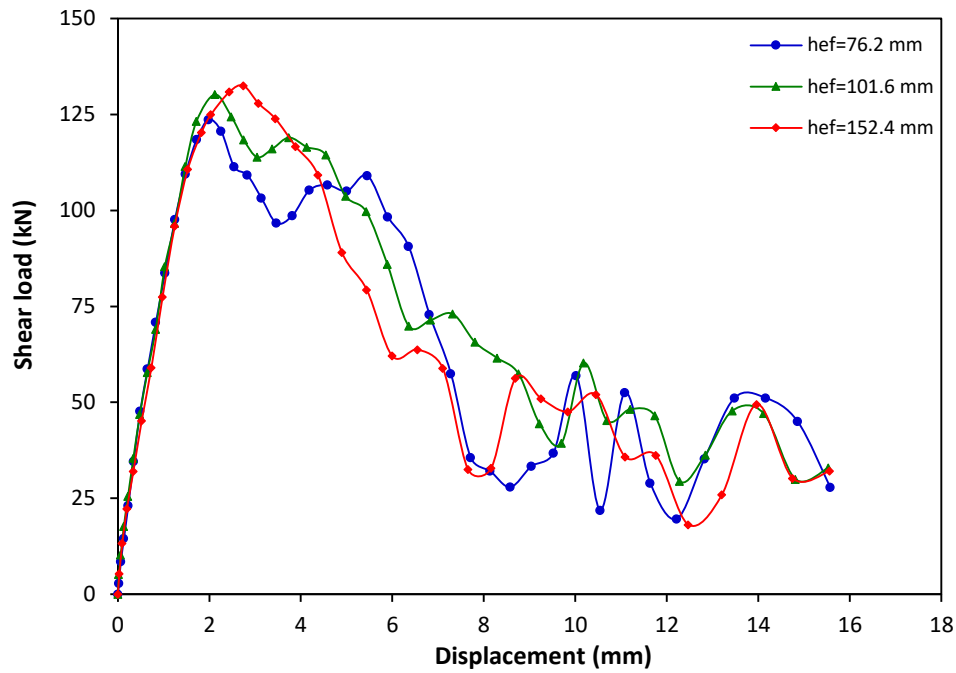


Figure D-4: Shear load-displacement graph for 15.9 mm diameter cast-in-place anchor at strain rate of 10 s^{-1}

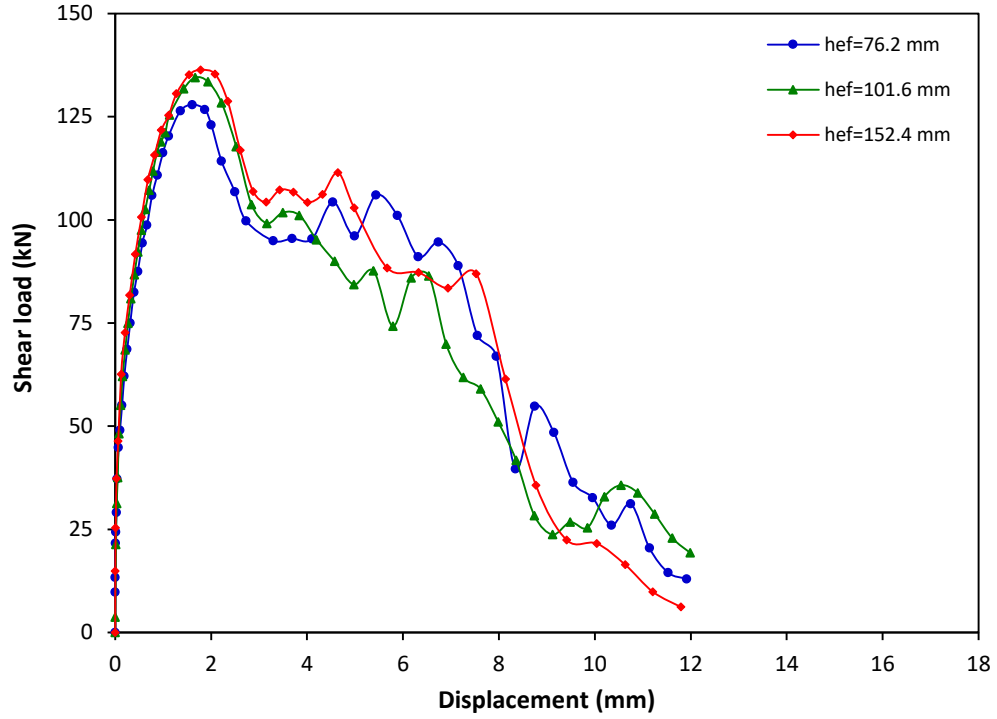


Figure D-5: Shear load-displacement graph for 15.9 mm diameter cast-in-place anchor at strain rate of 10^2 s^{-1}

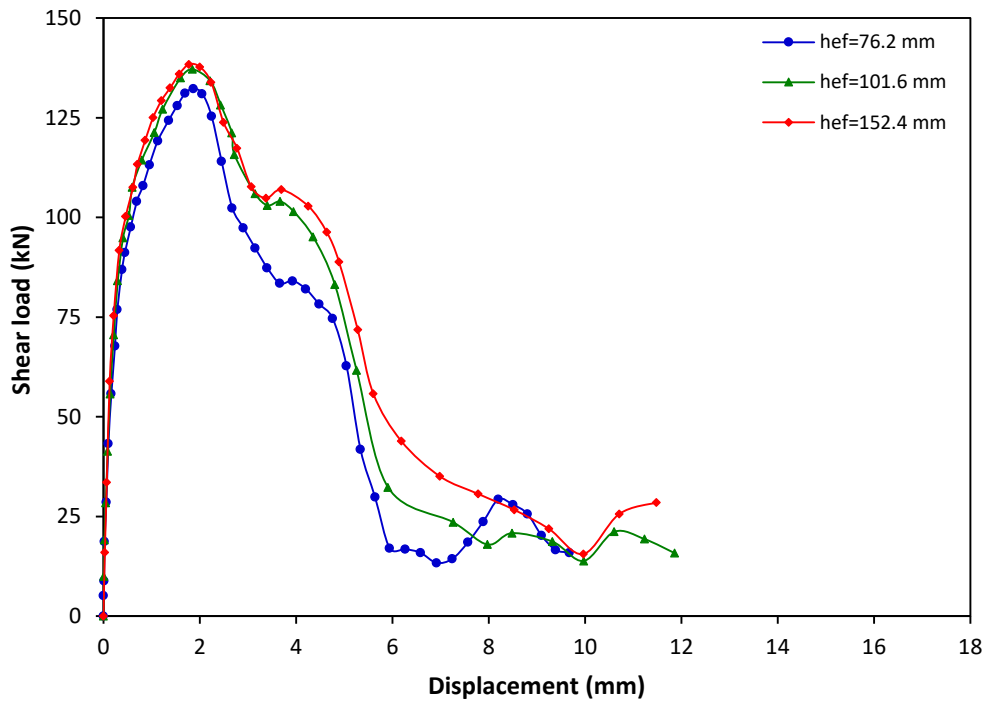


Figure D-6: Shear load-displacement graph for 15.9 mm diameter cast-in-place anchor at strain rate of 10^3 s^{-1}

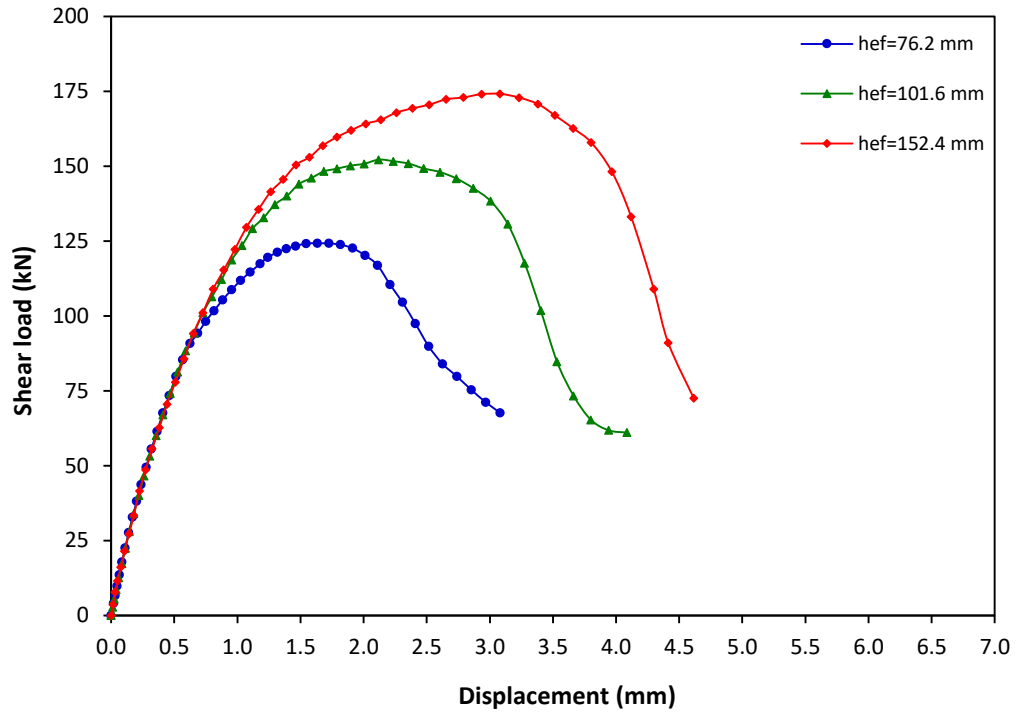


Figure D-7: Shear load-displacement graph for 19.1 mm diameter cast-in-place anchor at strain rate of 10^{-5} s^{-1}

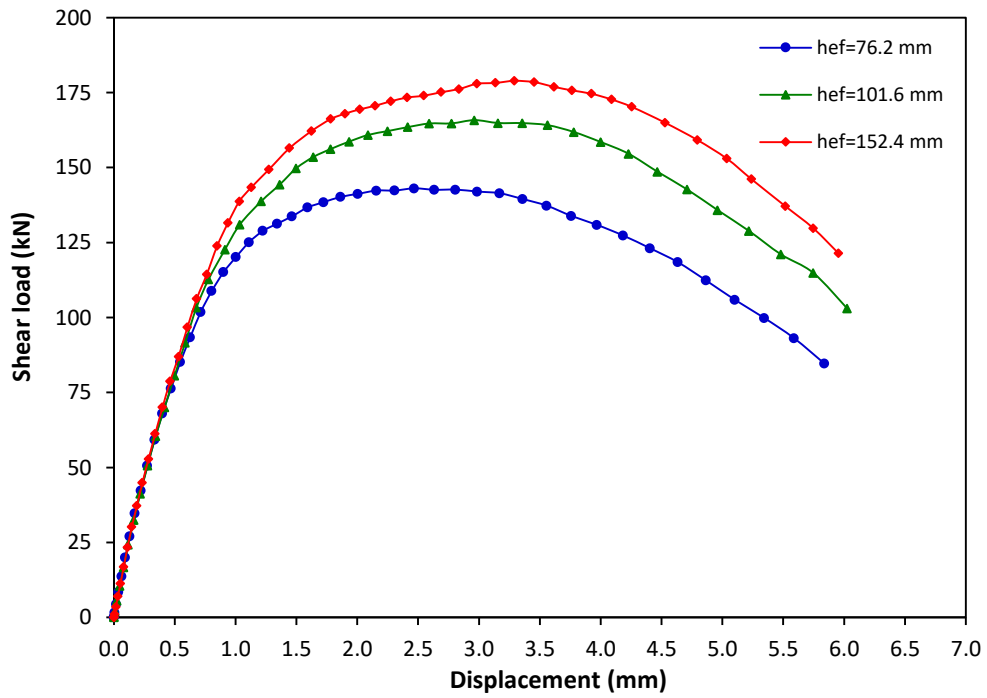


Figure D-8: Shear load-displacement graph for 19.1 mm diameter cast-in-place anchor at strain rate of 10^{-3} s^{-1}

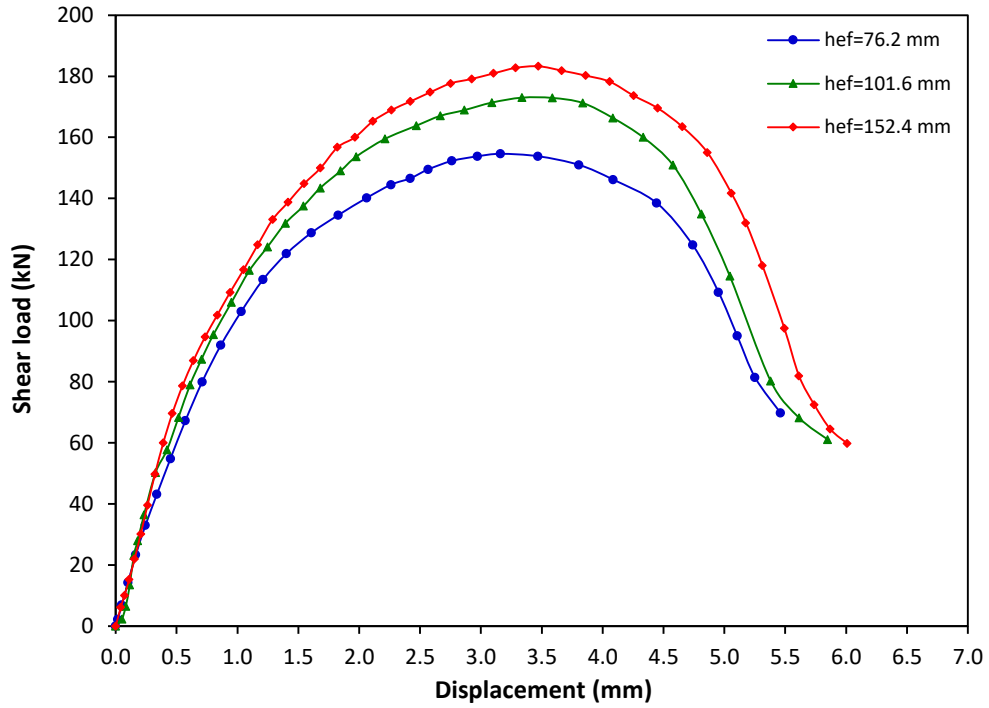


Figure D-9: Shear load-displacement graph for 19.1 mm diameter cast-in-place anchor mm at strain rate of 10^{-1} s^{-1}

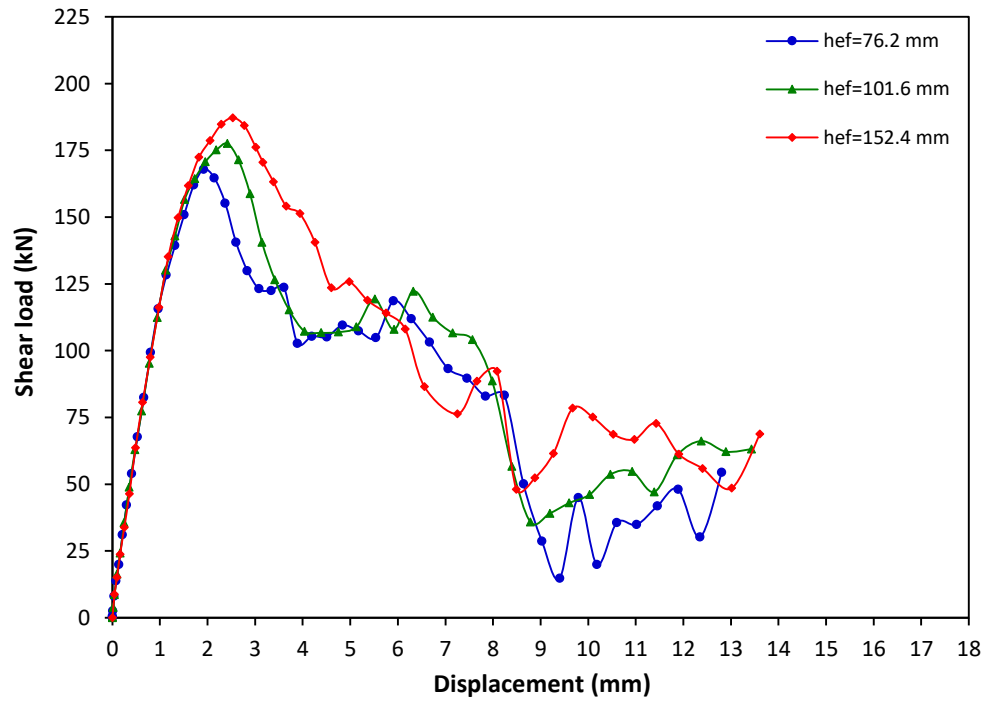


Figure D-10: Shear load-displacement graph for 19.1 mm diameter cast-in-place anchor at strain rate of 10 s^{-1}

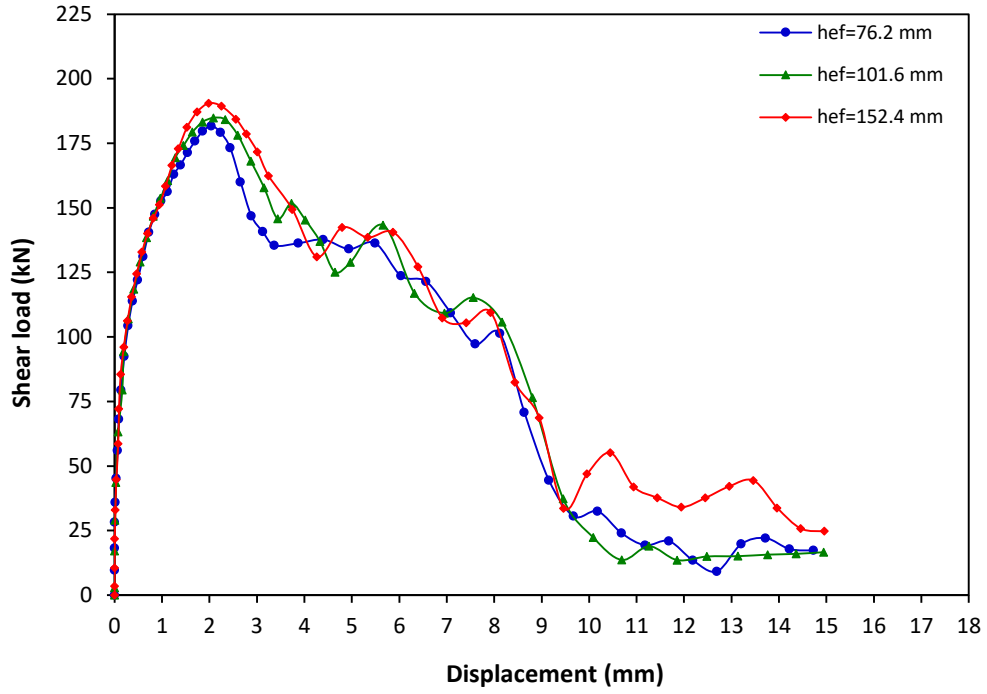


Figure D-11: Shear load-displacement graph for 19.1 mm diameter cast-in-place anchor at strain rate of 10^2 s^{-1}

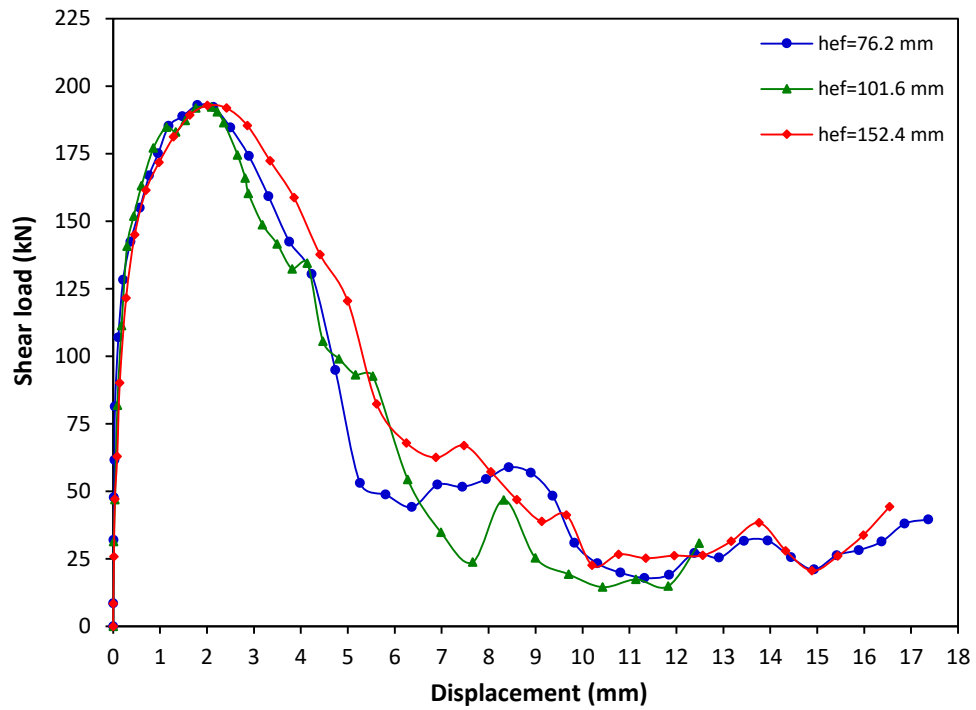


Figure D-12: Shear load-displacement graph for 19.1 mm diameter cast-in-place anchor at strain rate of 10^3 s^{-1}

Appendix E: Tensile load-displacement relation for adhesive anchors

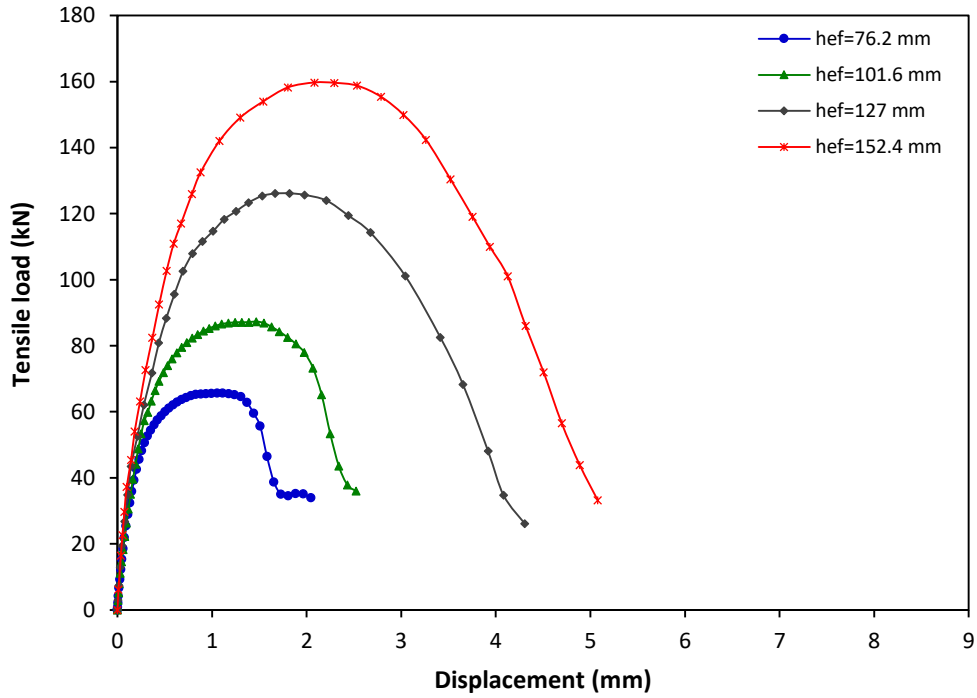


Figure E-1: Tensile load-displacement graph for 15.9 mm diameter adhesive anchor at strain rate of 10^{-5} s^{-1}

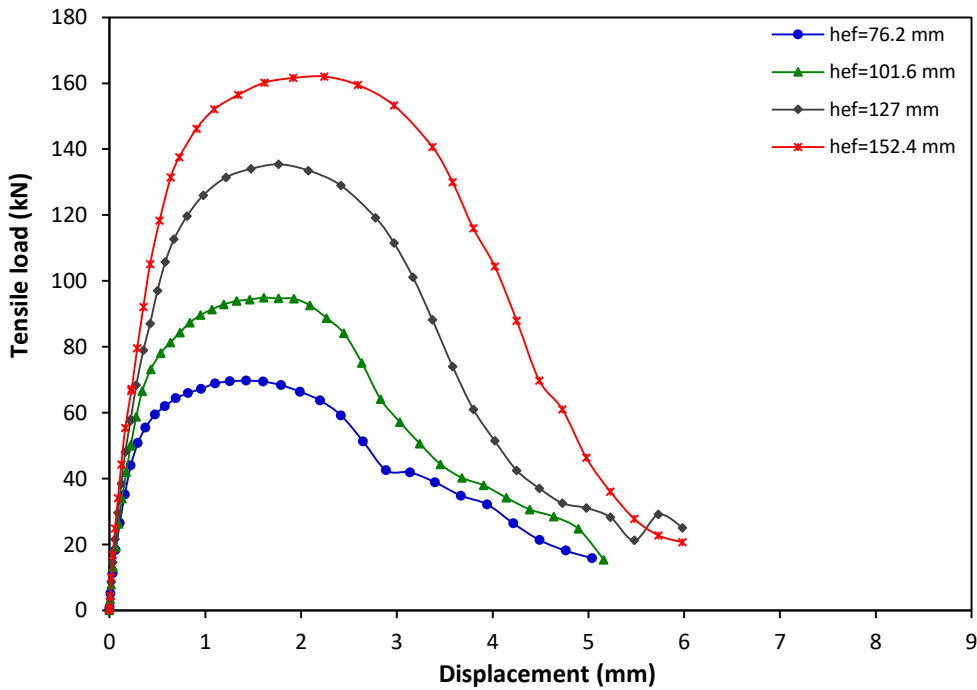


Figure E-2: Tensile load-displacement graph for 15.9 mm diameter adhesive anchor at strain rate of 10^{-3} s^{-1}

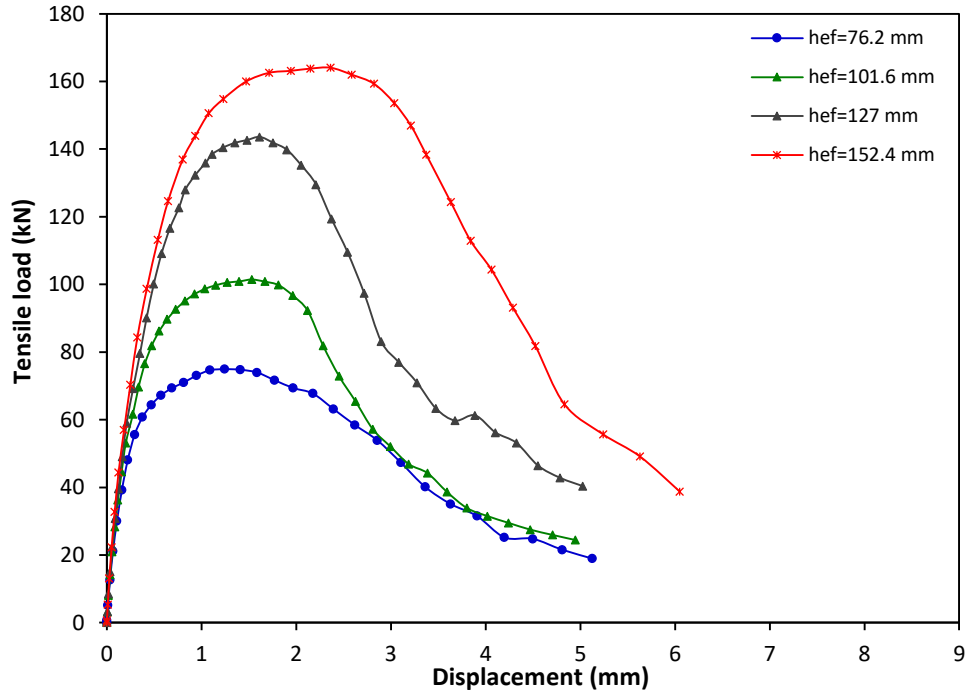


Figure E-3: Tensile load-displacement graph for 15.9 mm diameter adhesive anchor at strain rate of 10^{-1} s^{-1}

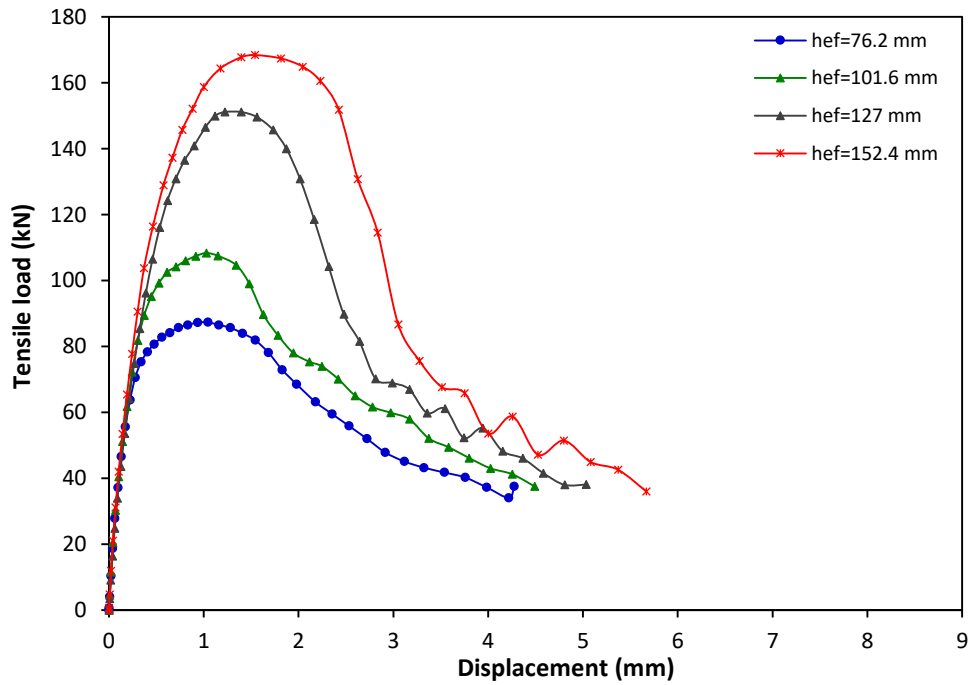


Figure E-4: Tensile load-displacement graph for 15.9 mm diameter adhesive anchor at strain rate of 10 s^{-1}

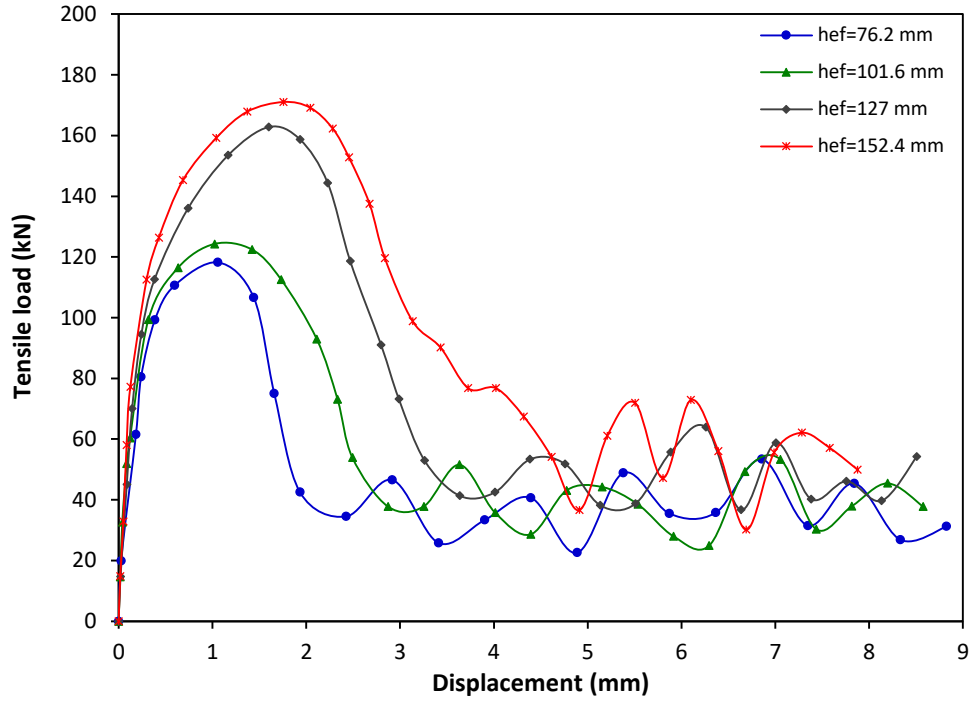


Figure E-5: Tensile load-displacement graph for 15.9 mm diameter adhesive anchor at strain rate of 10^2 s^{-1}

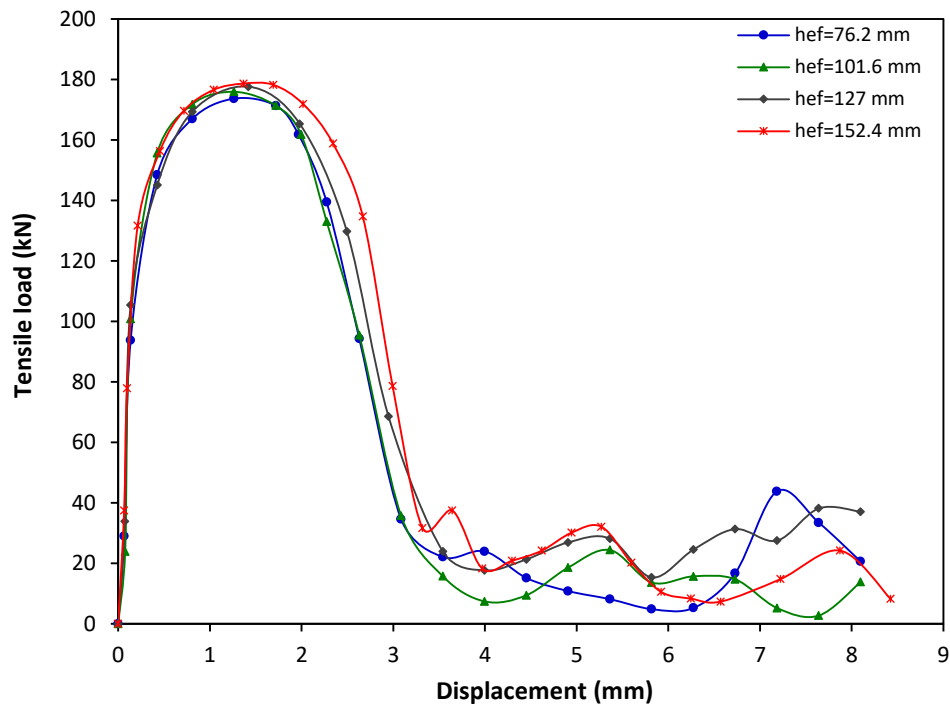


Figure E-6: Tensile load-displacement graph for 15.9 mm diameter adhesive anchor at strain rate of 10^3 s^{-1}

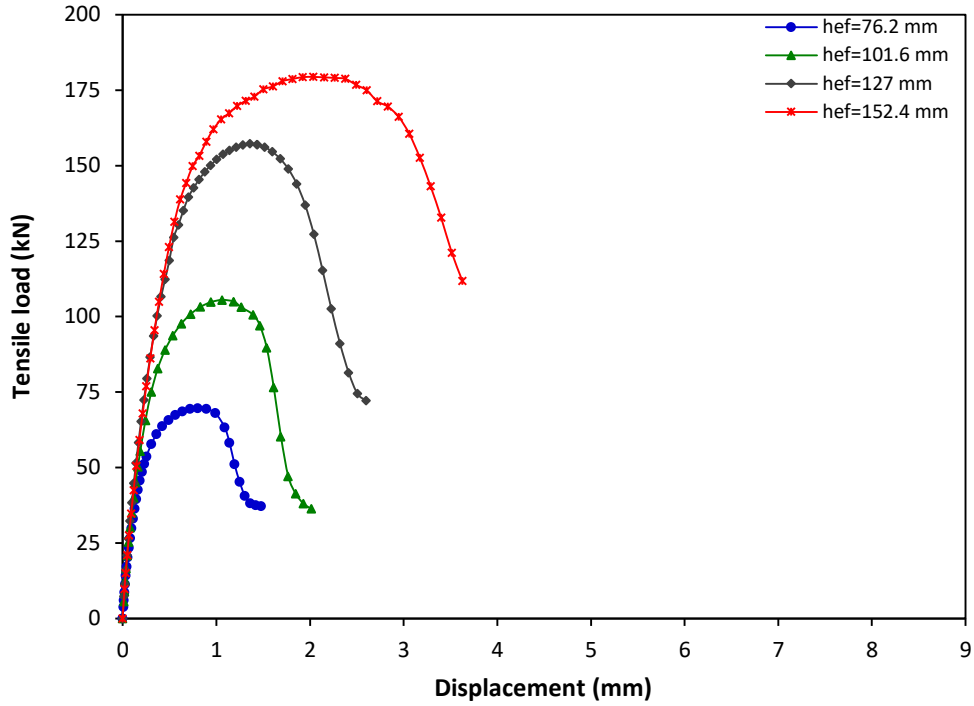


Figure E-7: Tensile load-displacement graph for 19.1 mm diameter adhesive anchor at strain rate of 10^{-5} s^{-1}

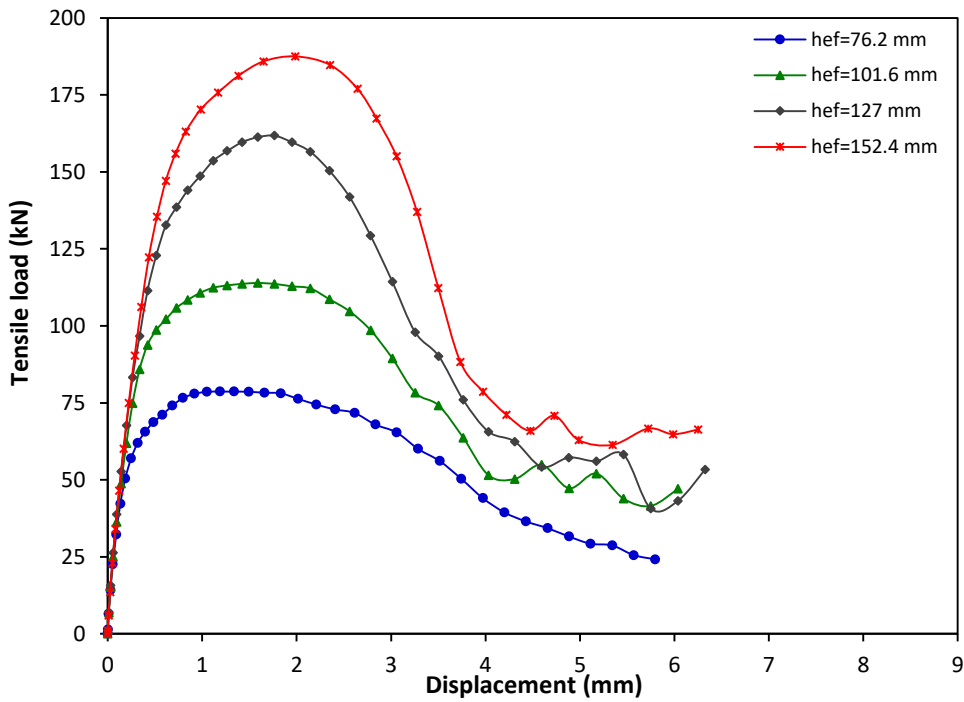


Figure E-8: Tensile load-displacement graph for 19.1 mm diameter adhesive anchor at strain rate of 10^{-3} s^{-1}

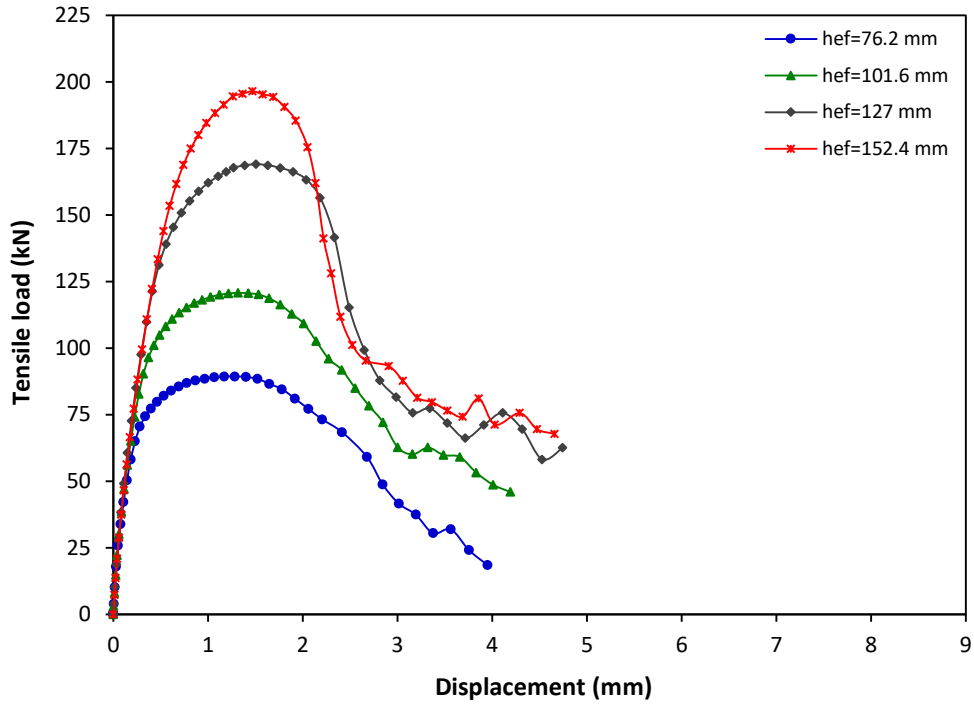


Figure E-9: Tensile load-displacement graph for 19.1 mm diameter adhesive anchor at strain rate of 10^{-1} s^{-1}

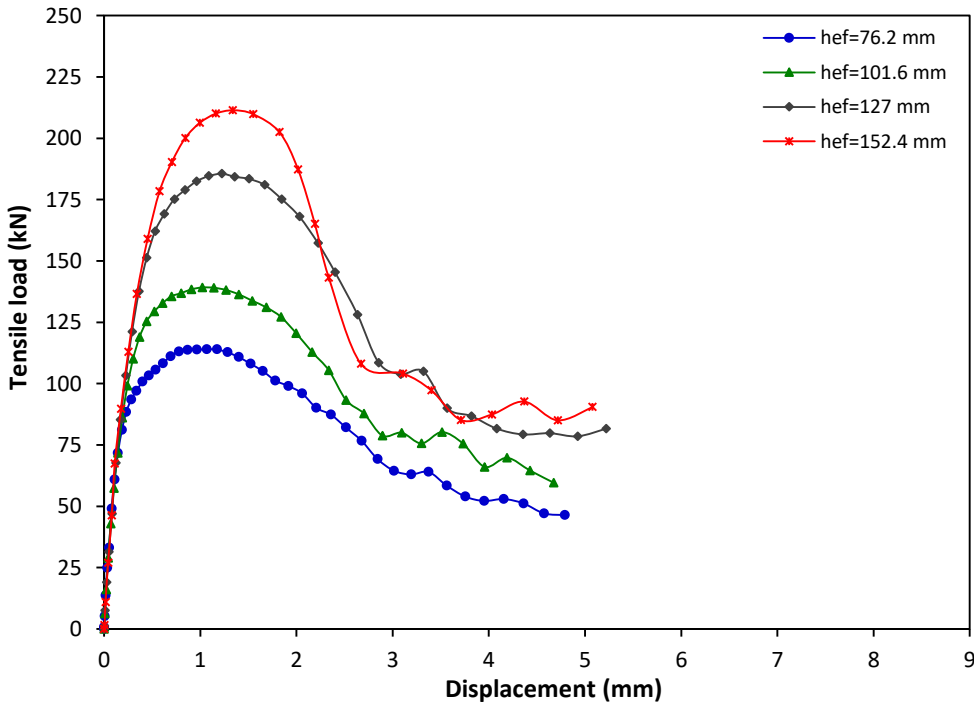


Figure E-10: Tensile load-displacement graph for 19.1 mm diameter adhesive anchor at strain rate of 10 s^{-1}

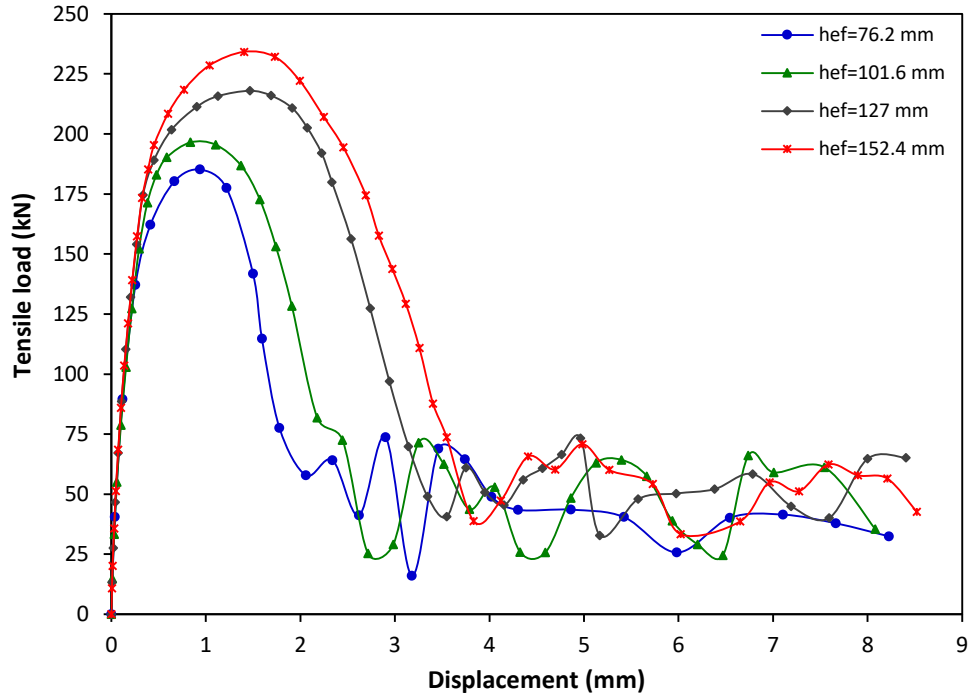


Figure E-11: Tensile load-displacement graph for 19.1 mm diameter adhesive anchor at strain rate of 10^2 s^{-1}

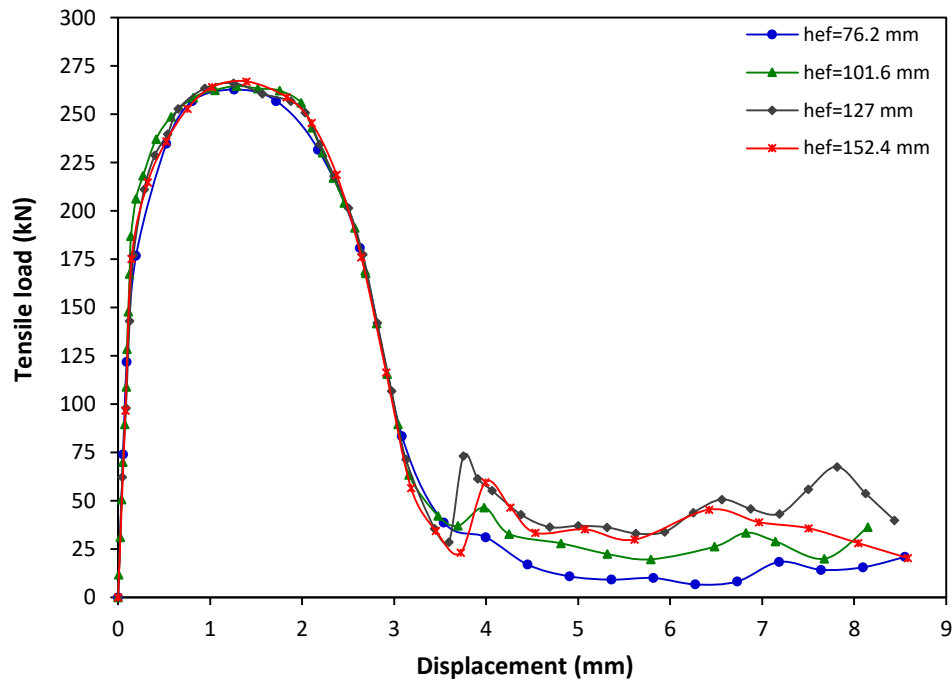


Figure E-12: Tensile load-displacement graph for 19.1 mm diameter adhesive anchor at strain rate of 10^3 s^{-1}

Appendix F: Shear load-displacement relation for adhesive anchors

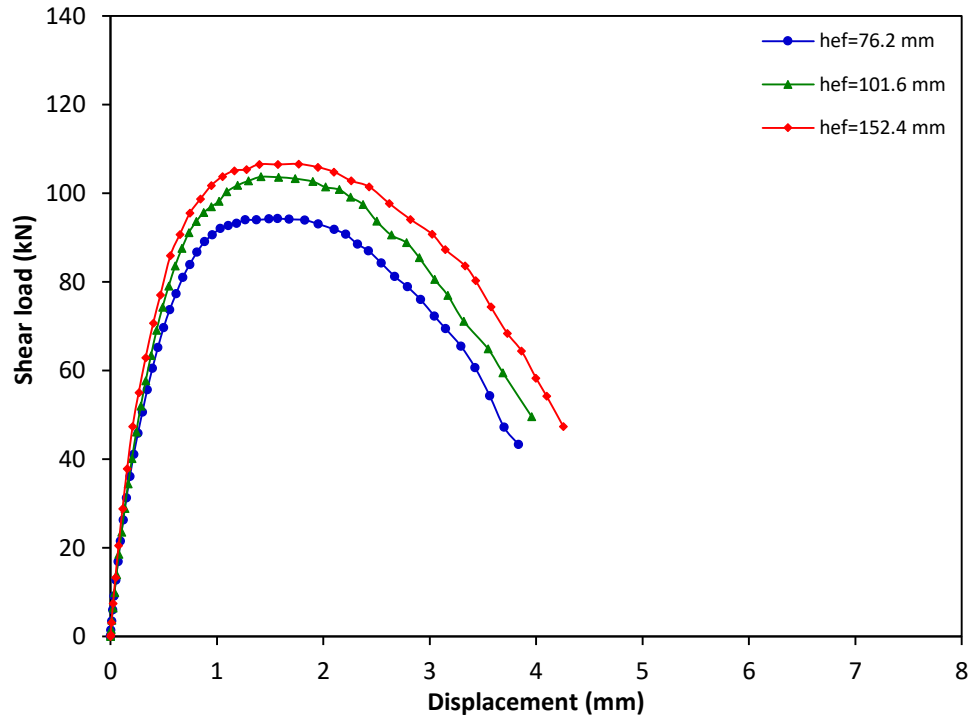


Figure F-1: Shear load-displacement graph for 15.9 mm diameter adhesive anchor at strain rate of 10^{-5} s^{-1}

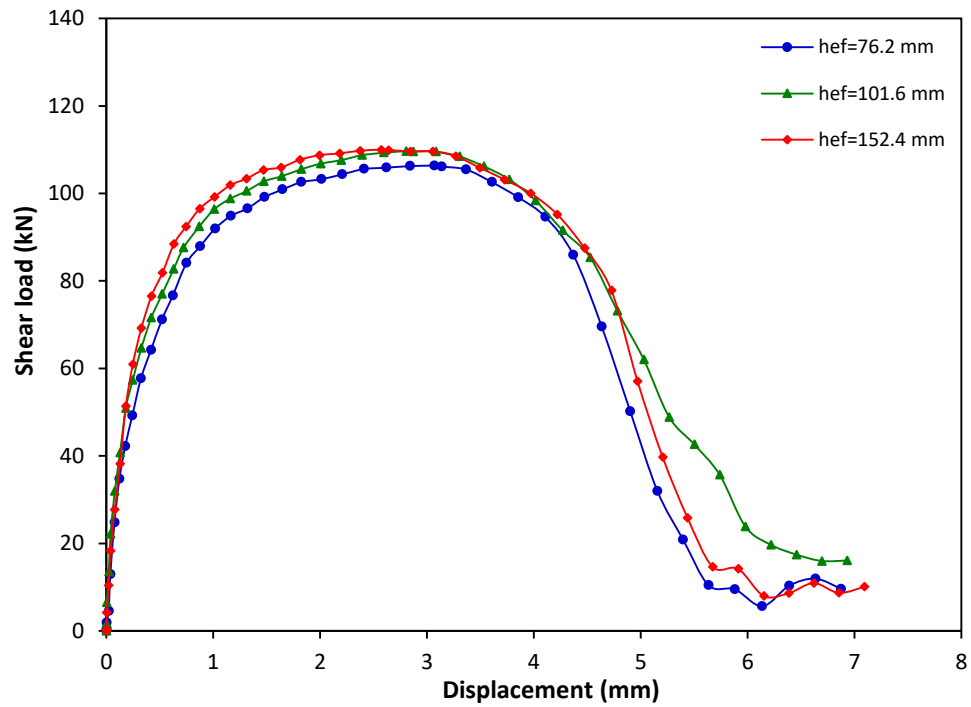


Figure F-2: Shear load-displacement graph for 15.9 mm diameter adhesive anchor at strain rate of 10^{-3} s^{-1}

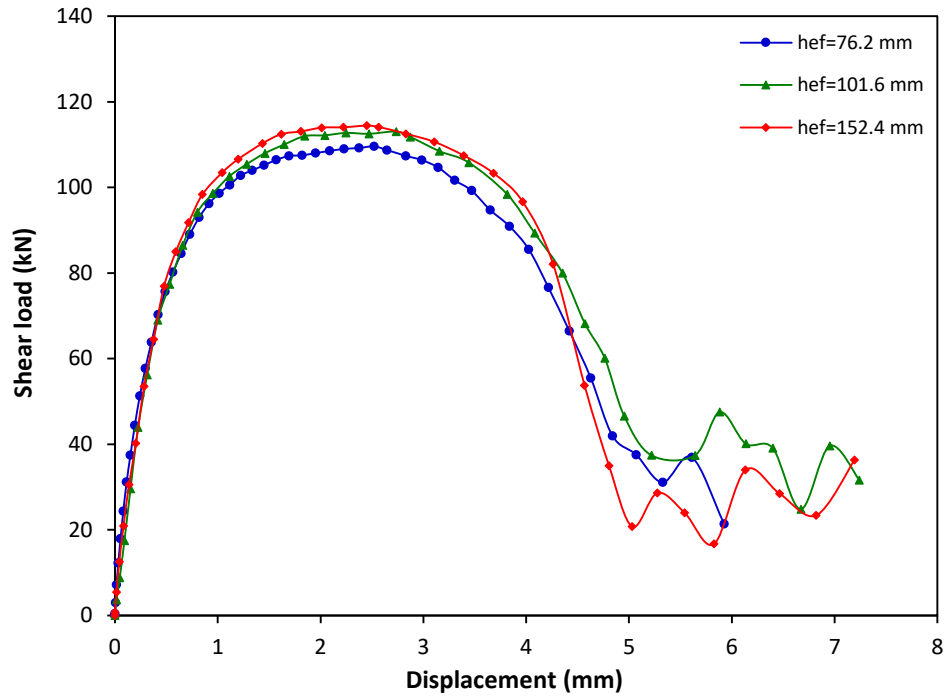


Figure F-3: Shear load-displacement graph for 15.9 mm diameter adhesive anchor at strain rate of 10^{-1} s^{-1}

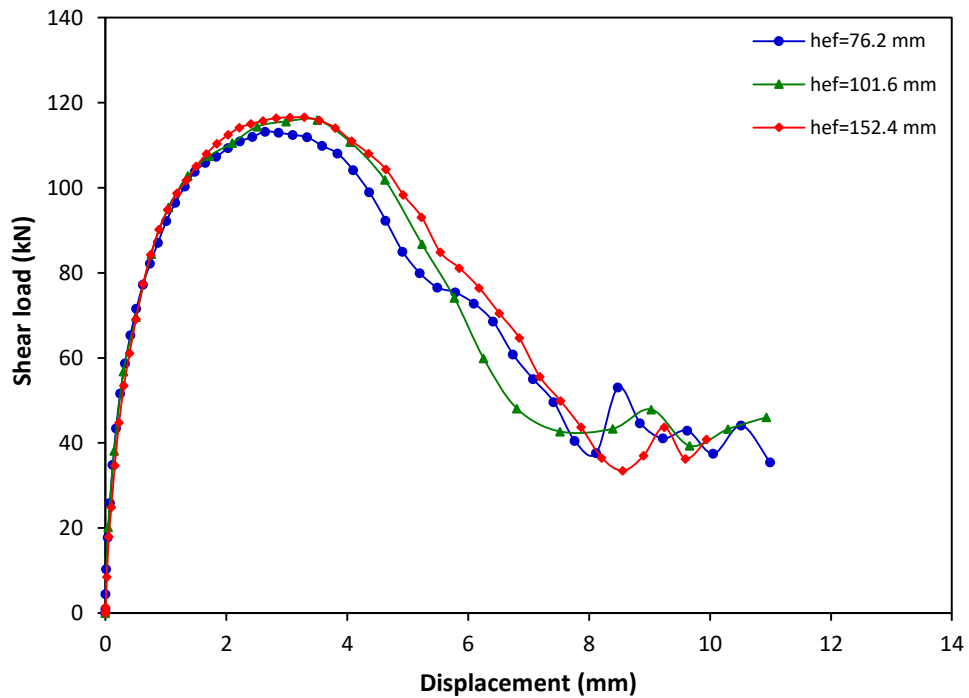


Figure F-4: Shear load-displacement graph for 15.9 mm diameter adhesive anchor at strain rate of 10 s^{-1}

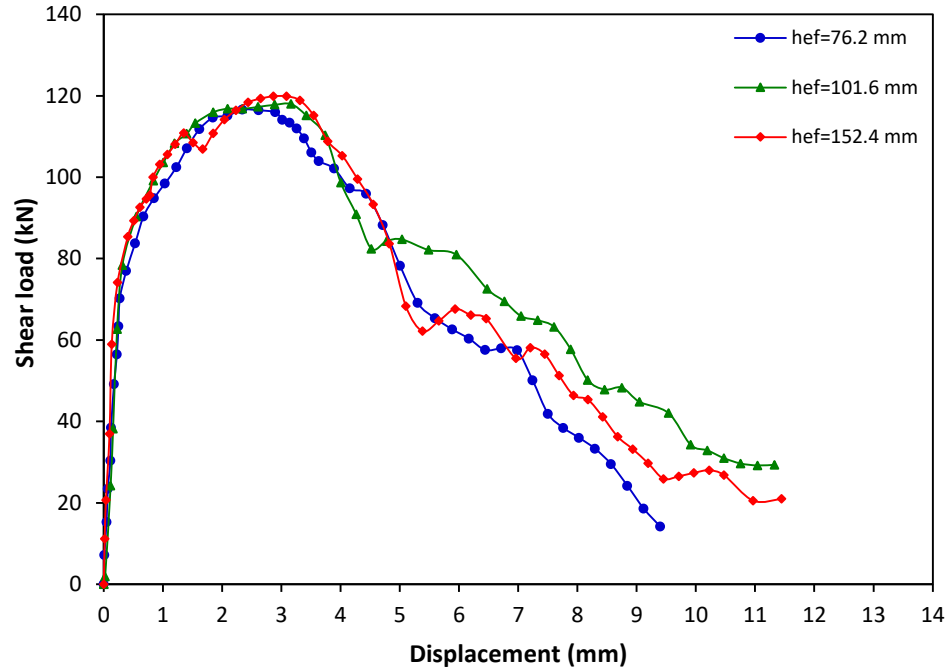


Figure F-5: Shear load-displacement graph for 15.9 mm diameter adhesive anchor at strain rate of 10^2 s^{-1}

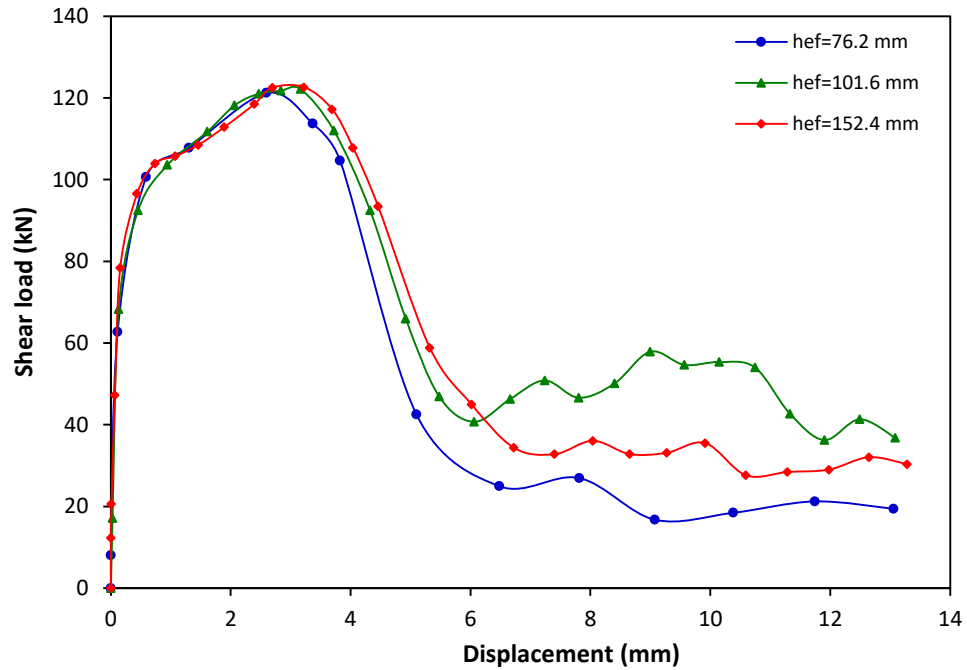


Figure F-6: Shear load-displacement graph for 15.9 mm diameter adhesive anchor at strain rate of 10^3 s^{-1}

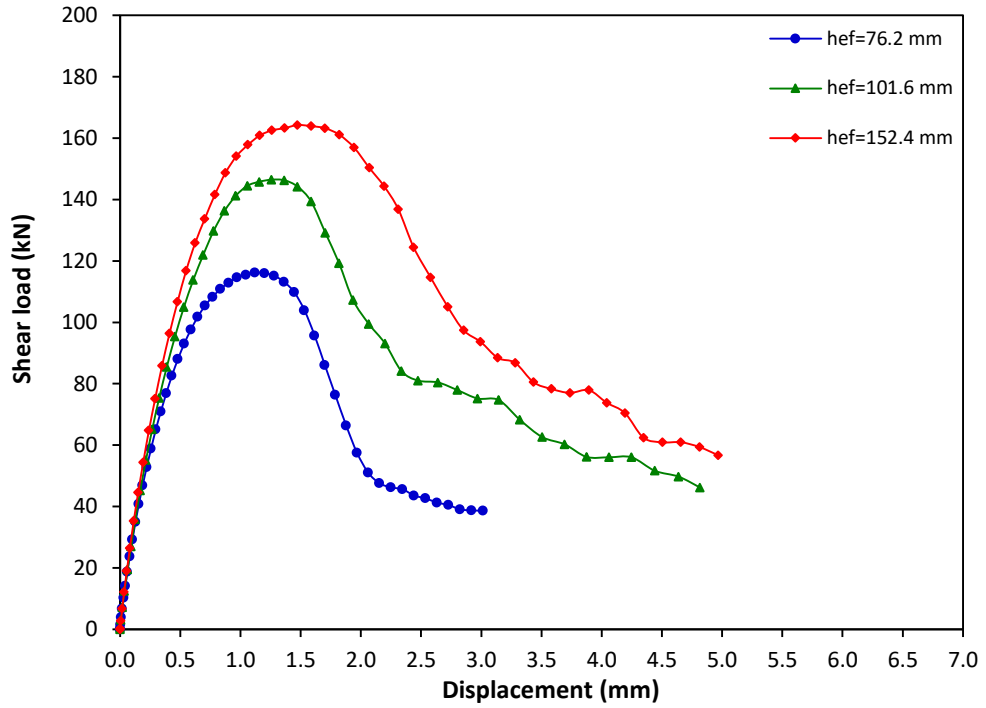


Figure F-7: Shear load-displacement graph for 19.1 mm diameter adhesive anchor at strain rate of 10^{-5} s^{-1}

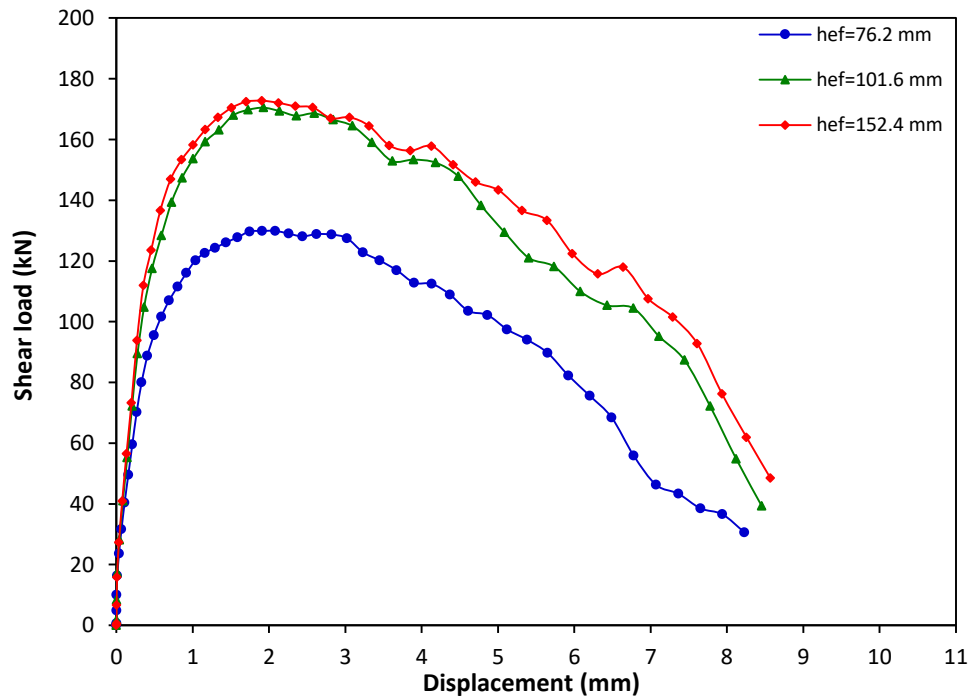


Figure F-8: Shear load-displacement graph for 19.1 mm diameter adhesive anchor at strain rate of 10^{-3} s^{-1}

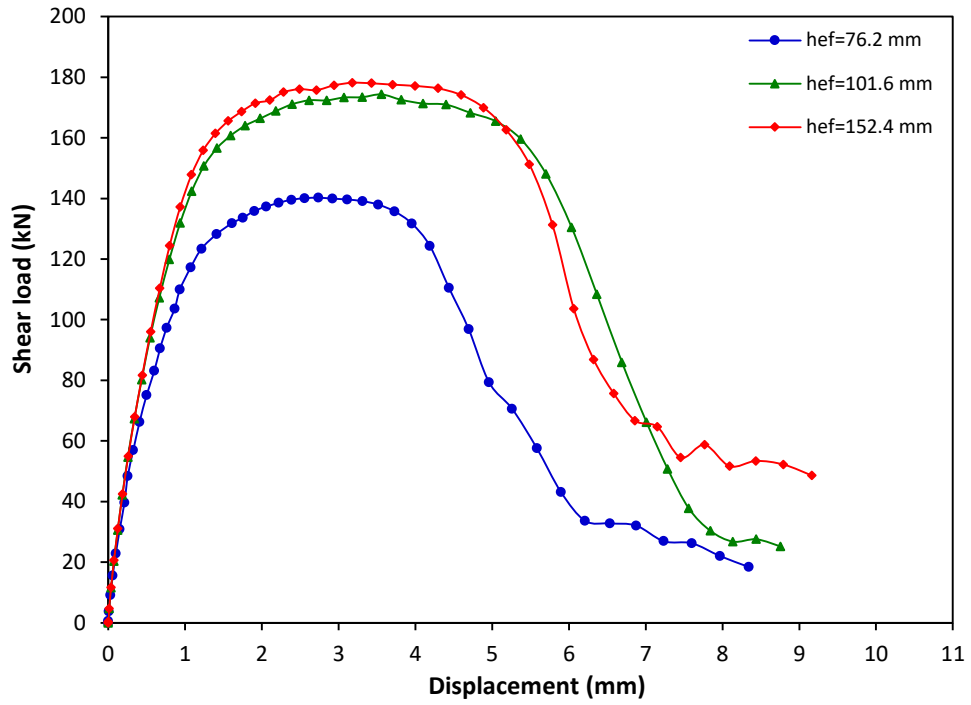


Figure F-9: Shear load-displacement graph for 19.1 mm diameter adhesive anchor at strain rate of 10^{-1} s^{-1}

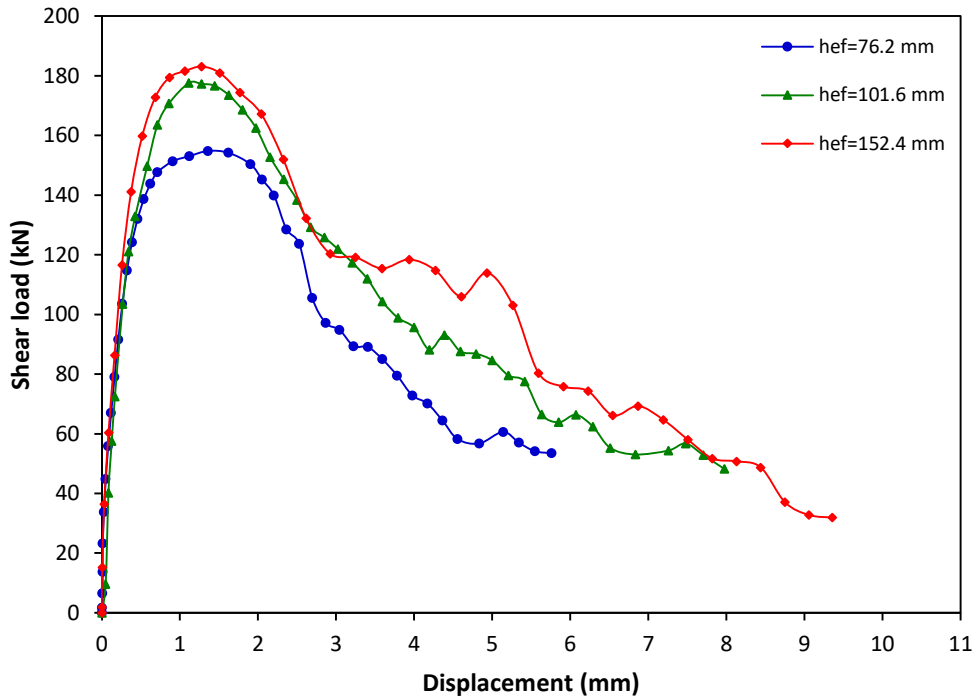


Figure F-10: Shear load-displacement graph for 19.1 mm diameter adhesive anchor at strain rate of 10 s^{-1}

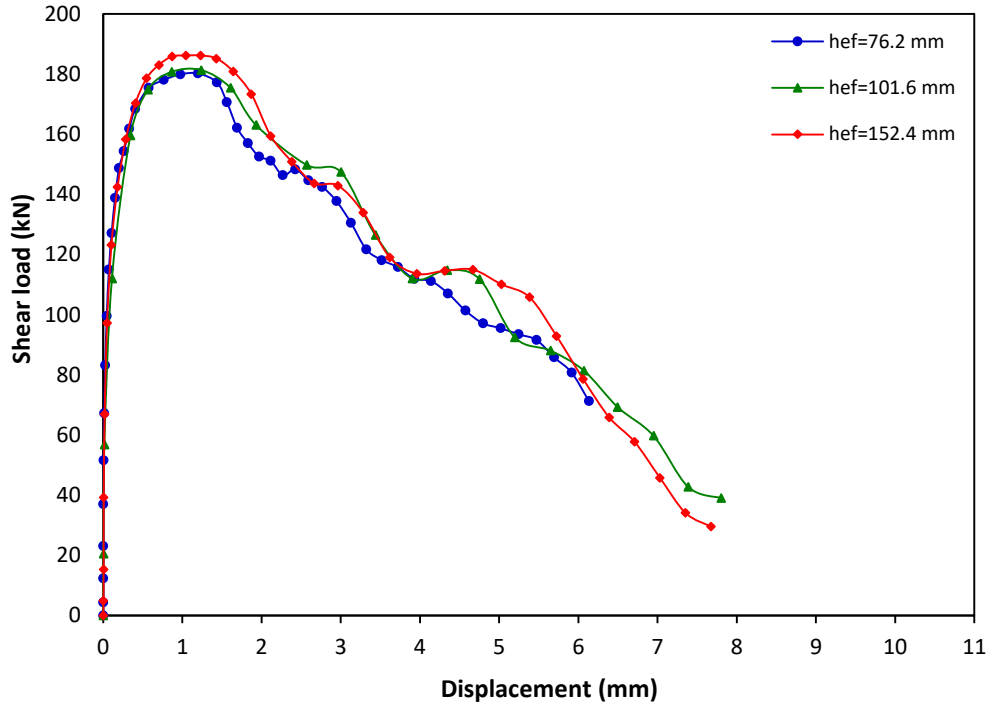


Figure F-11: Shear load-displacement graph for 19.1 mm diameter adhesive anchor at strain rate of 10^2 s^{-1}

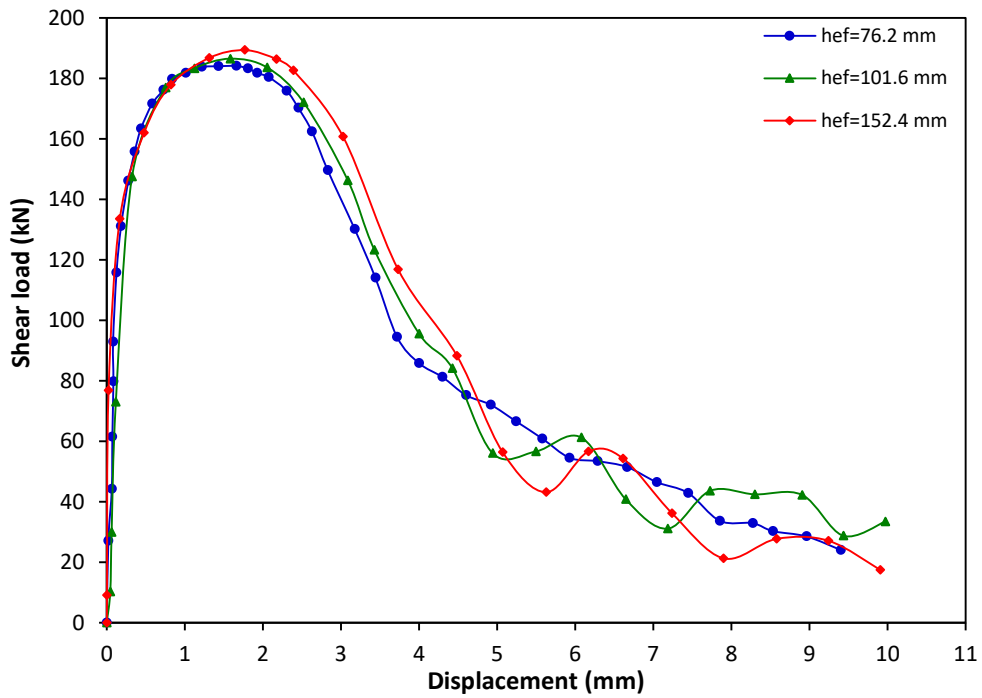


Figure F-12: Shear load-displacement graph for 19.1 mm diameter adhesive anchor at strain rate of 10^3 s^{-1}

Appendix G: Tensile load-displacement relation for undercut anchors

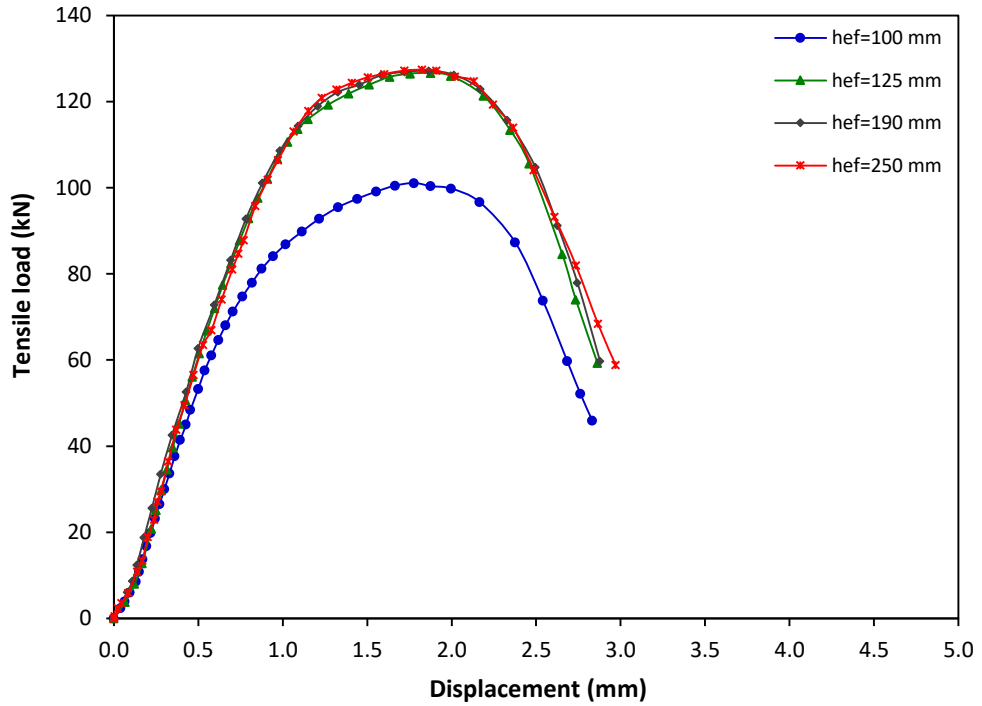


Figure G-1: Tensile load-displacement graph for the 16 mm diameter undercut anchor at strain rate of 10^{-5} s^{-1}

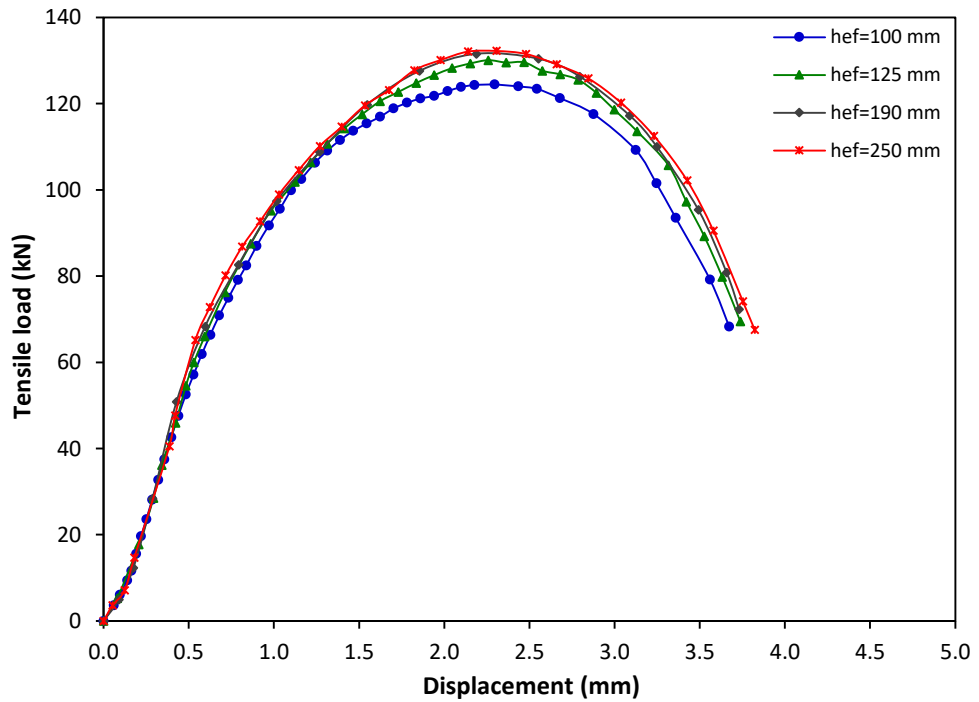


Figure G-2: Tensile load-displacement graph for the 16 mm diameter undercut anchor at strain rate of 10^{-3} s^{-1}

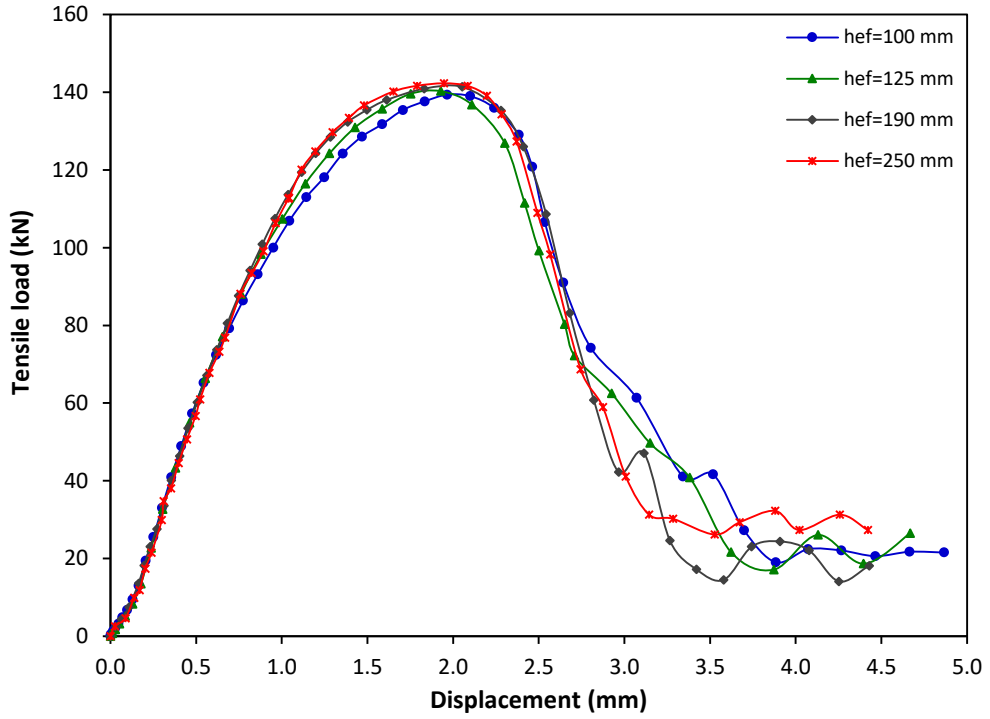


Figure G-3: Tensile load-displacement graph for the 16 mm diameter undercut anchor at strain rate of 10^{-1} s^{-1}

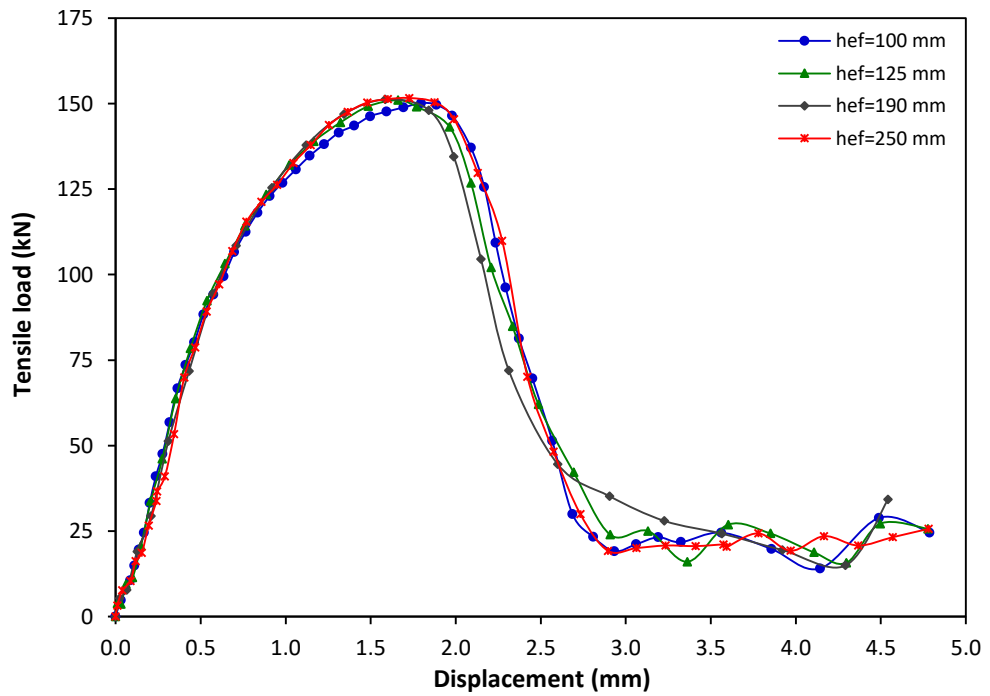


Figure G-4: Tensile load-displacement graph for the 16 mm diameter undercut anchor at strain rate of 10 s^{-1}

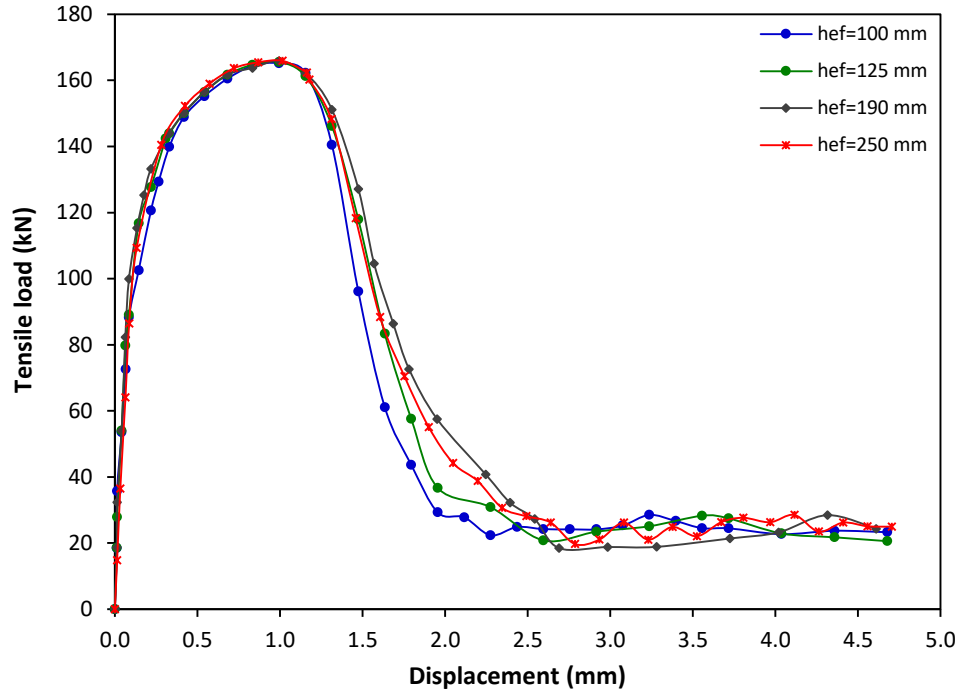


Figure G-5: Tensile load-displacement graph for the 16 mm diameter undercut anchor at strain rate of 10^2 s^{-1}

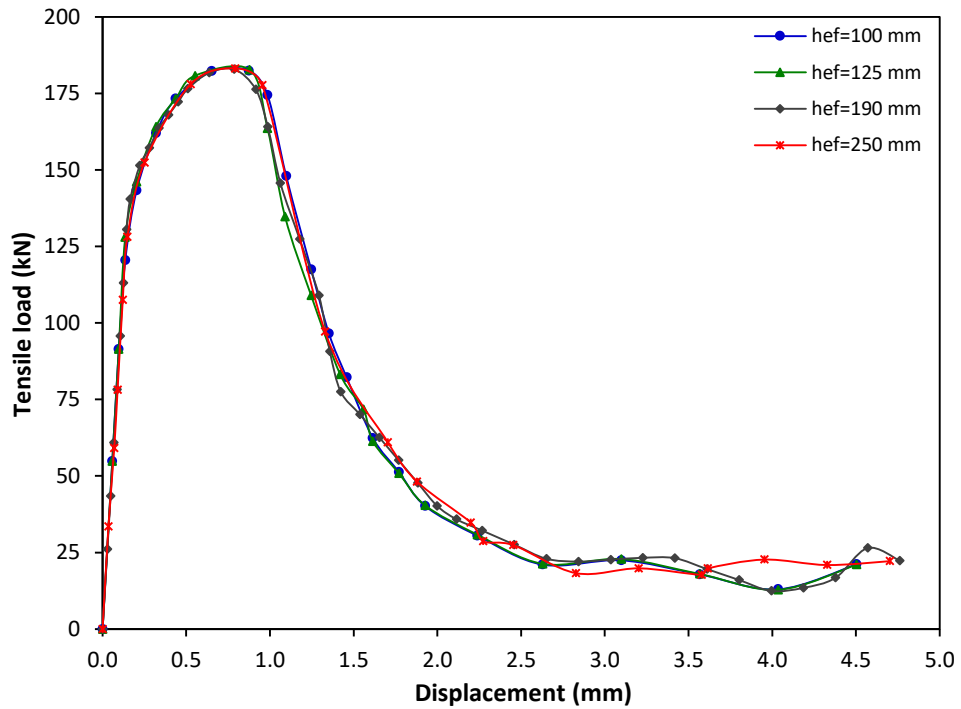


Figure G-6: Tensile load-displacement graph for the 16 mm diameter undercut anchor at strain rate of 10^3 s^{-1}

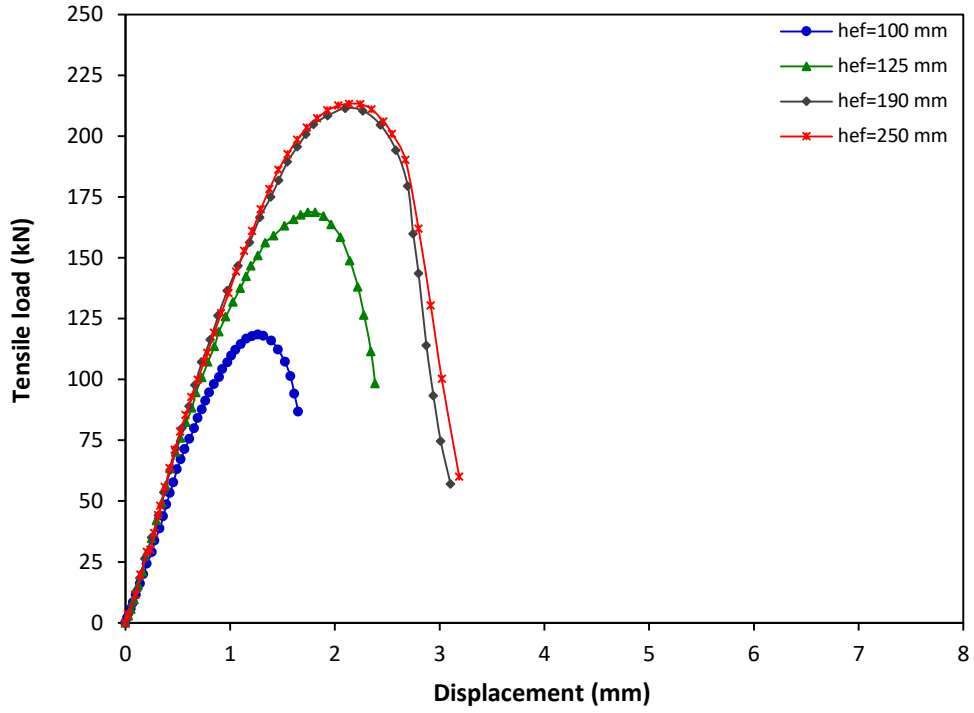


Figure G-7: Tensile load-displacement graph for the 20 mm diameter undercut anchor at strain rate of 10^{-5} s^{-1}

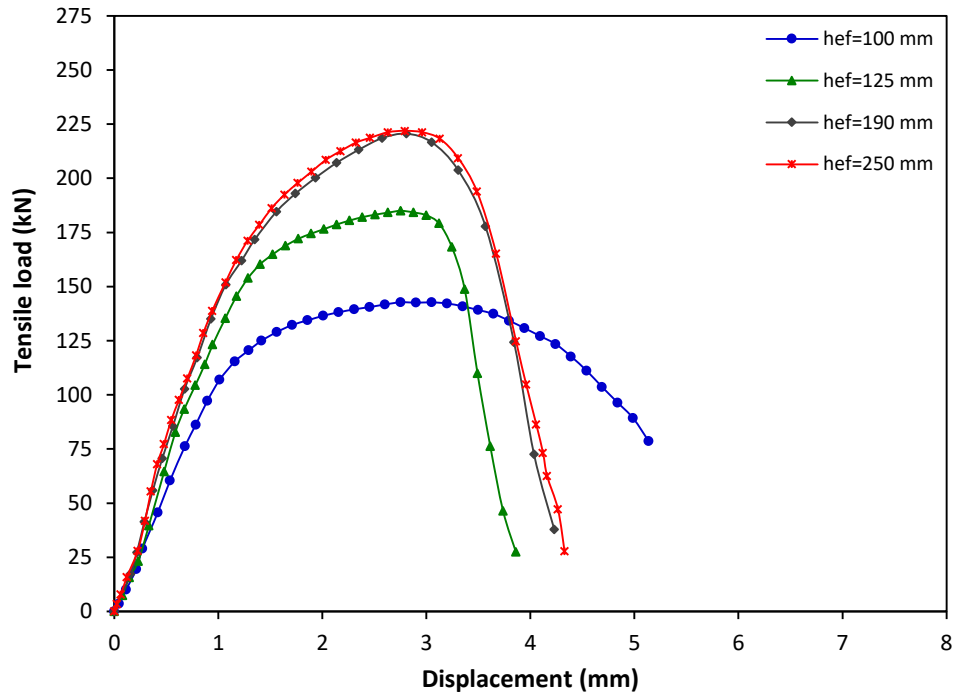


Figure G-8: Tensile load-displacement graph for the 20 mm diameter undercut anchor at strain rate of 10^{-3} s^{-1}

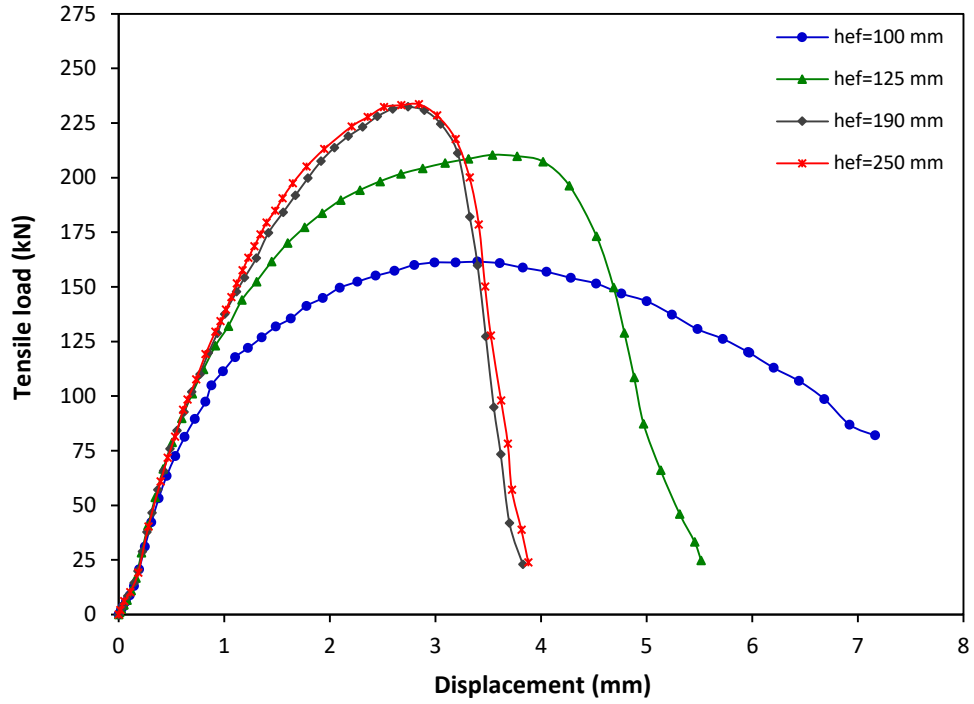


Figure G-9: Tensile load-displacement graph for the 20 mm diameter undercut anchor at strain rate of 10^{-1} s^{-1}

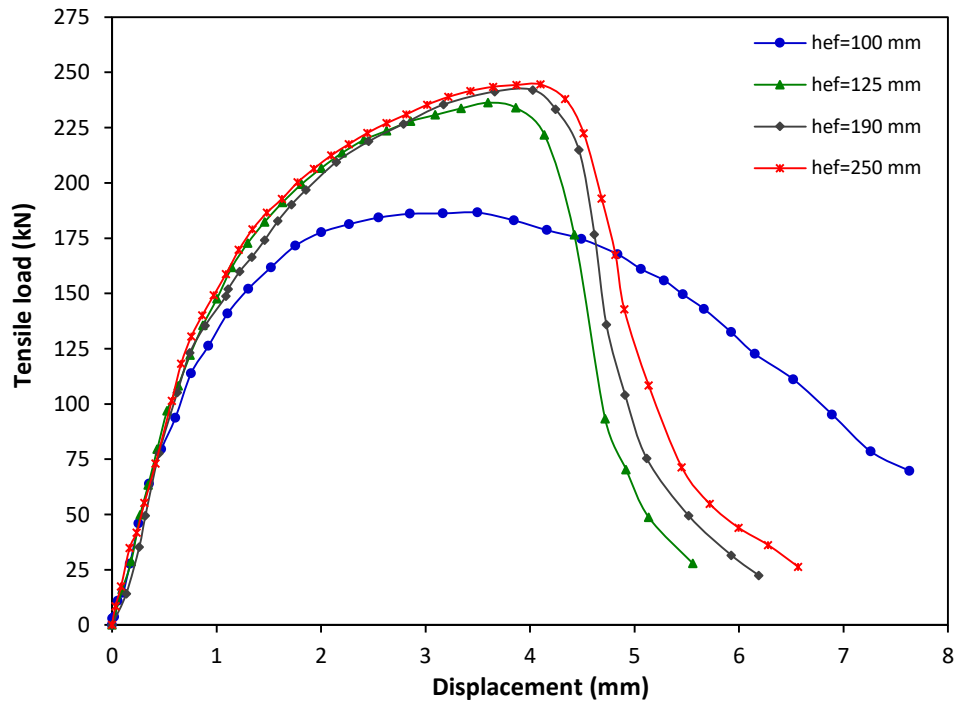


Figure G-10: Tensile load-displacement graph for the 20 mm diameter undercut anchor at strain rate of 10 s^{-1}

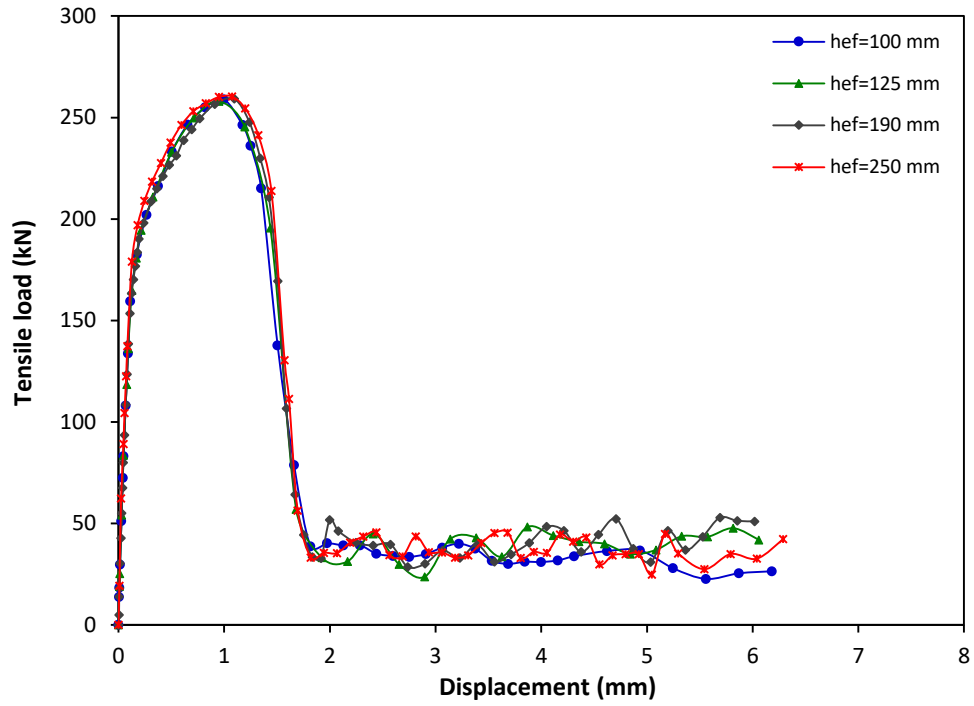


Figure G-11: Tensile load-displacement graph for the 20 mm diameter undercut anchor at strain rate of 10^2 s^{-1}

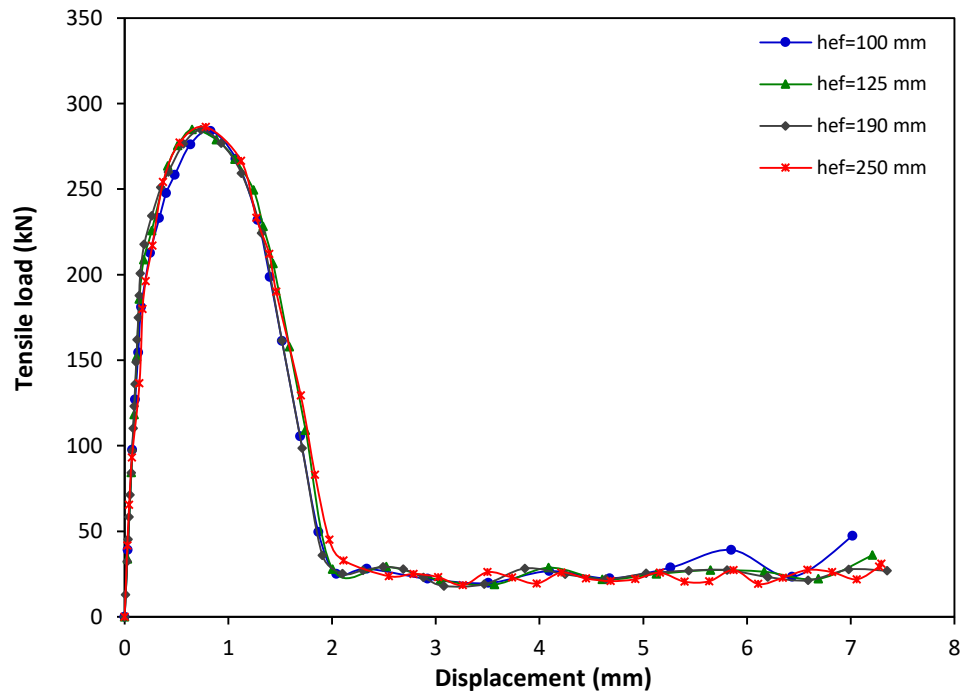


Figure G-12: Tensile load-displacement graph for the 20 mm diameter undercut anchor at strain rate of 10^3 s^{-1}

Appendix H: Shear load-displacement relation for undercut anchors

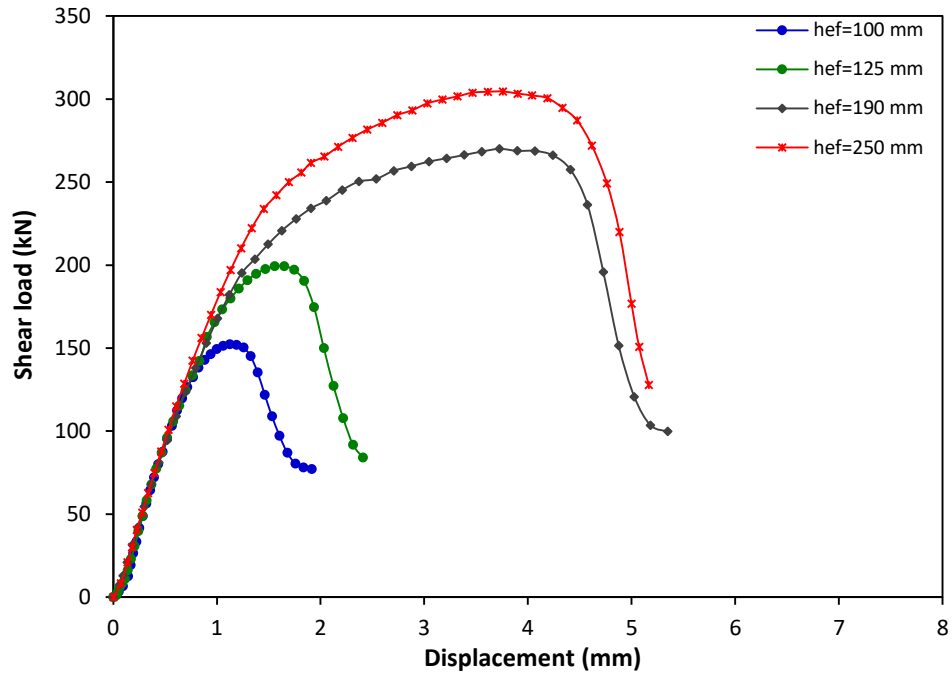


Figure H-1: Shear load-displacement graph for 16 mm diameter undercut anchor at strain rate of 10^{-5} s^{-1}

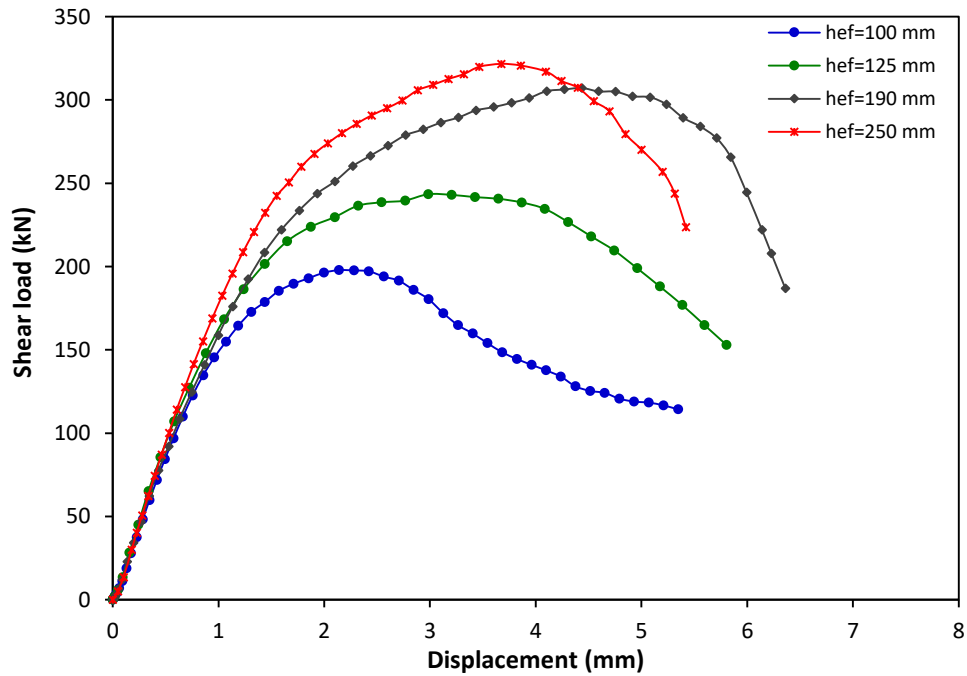


Figure H-2: Shear load-displacement graph for 16 mm diameter undercut anchor at strain rate of 10^{-3} s^{-1}

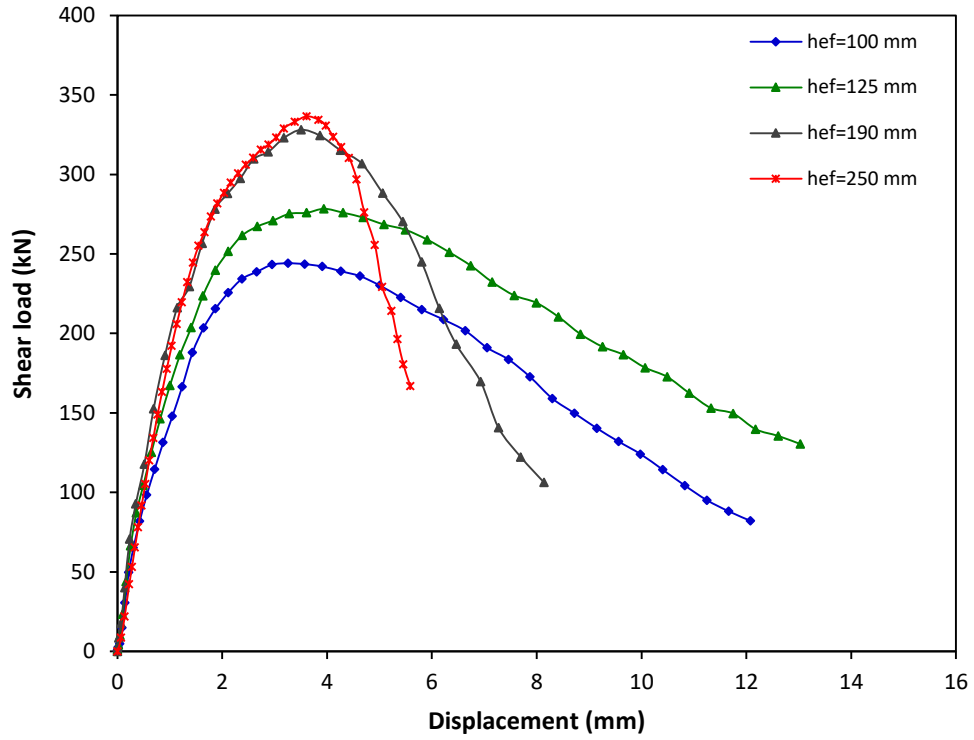


Figure H-3: Shear load-displacement graph for 16 mm diameter undercut anchor at strain rate of 10^{-1} s^{-1}

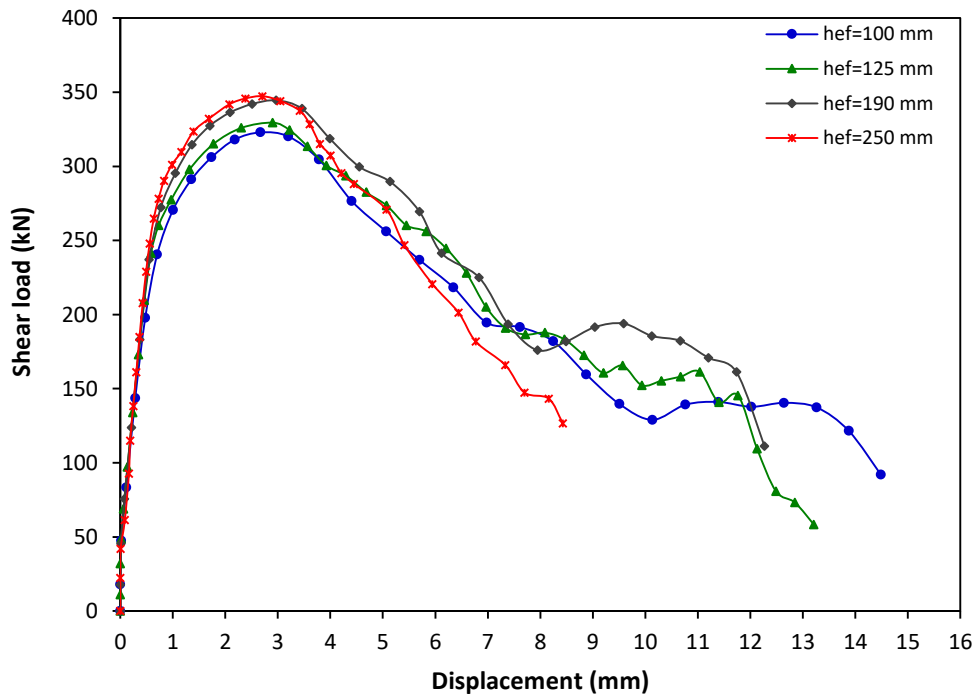


Figure H-4: Shear load-displacement graph for 16 mm diameter undercut anchor at strain rate of 10 s^{-1}

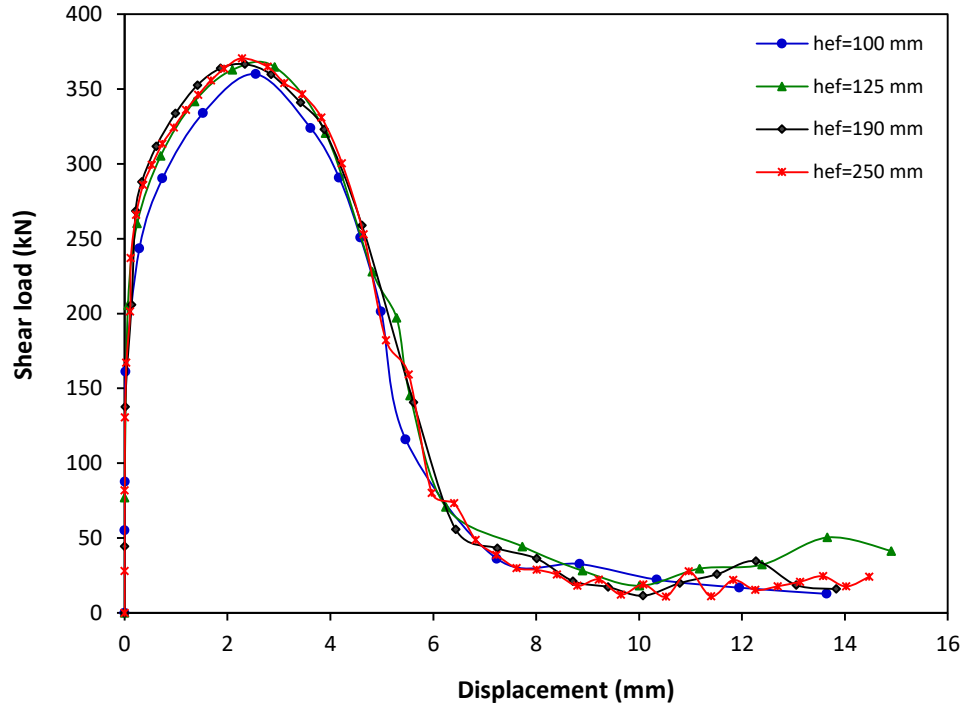


Figure H-5: Shear load-displacement graph for 16 mm diameter undercut anchor at strain rate of 10^2 s^{-1}

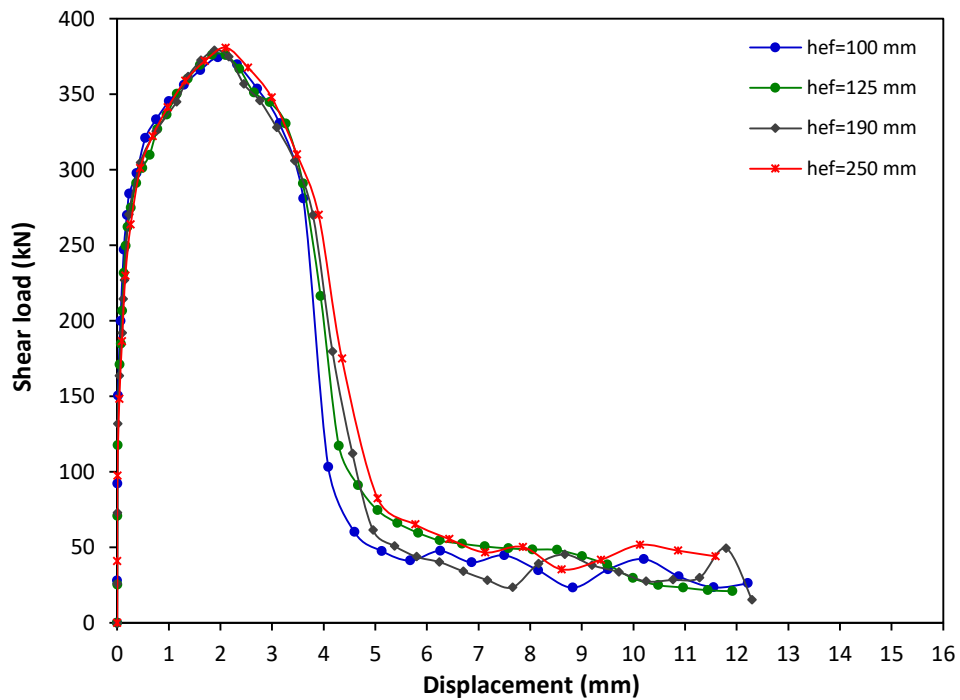


Figure H-6: Shear load-displacement graph for 16 mm diameter undercut anchor at strain rate of 10^3 s^{-1}

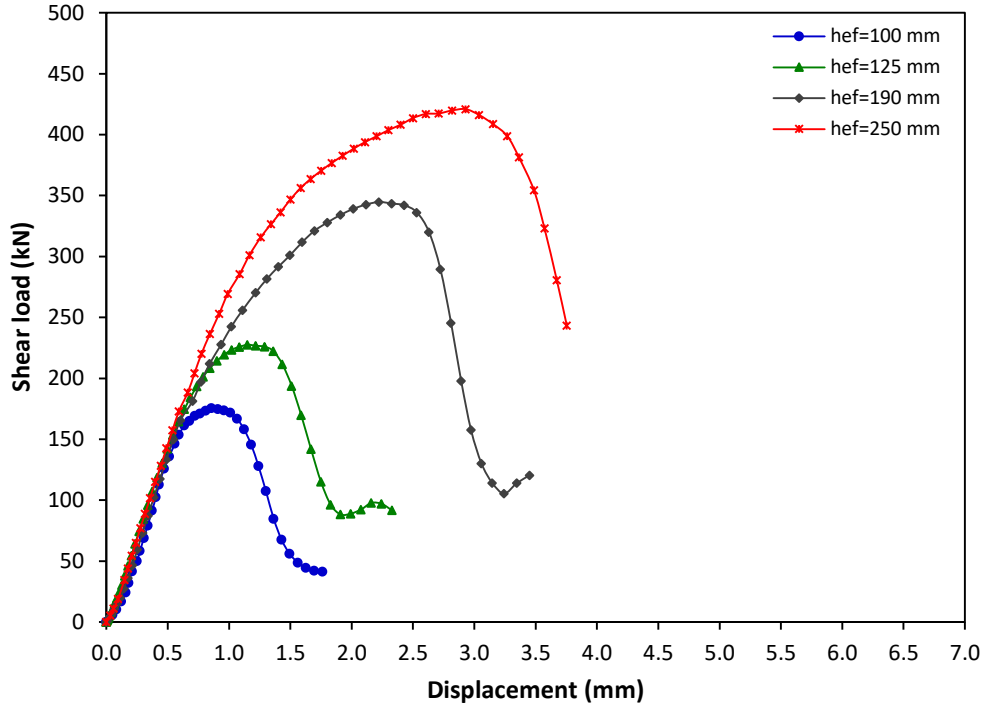


Figure H-7: Shear load-displacement graph for 20 mm diameter undercut anchor at strain rate of 10^{-5} s^{-1}

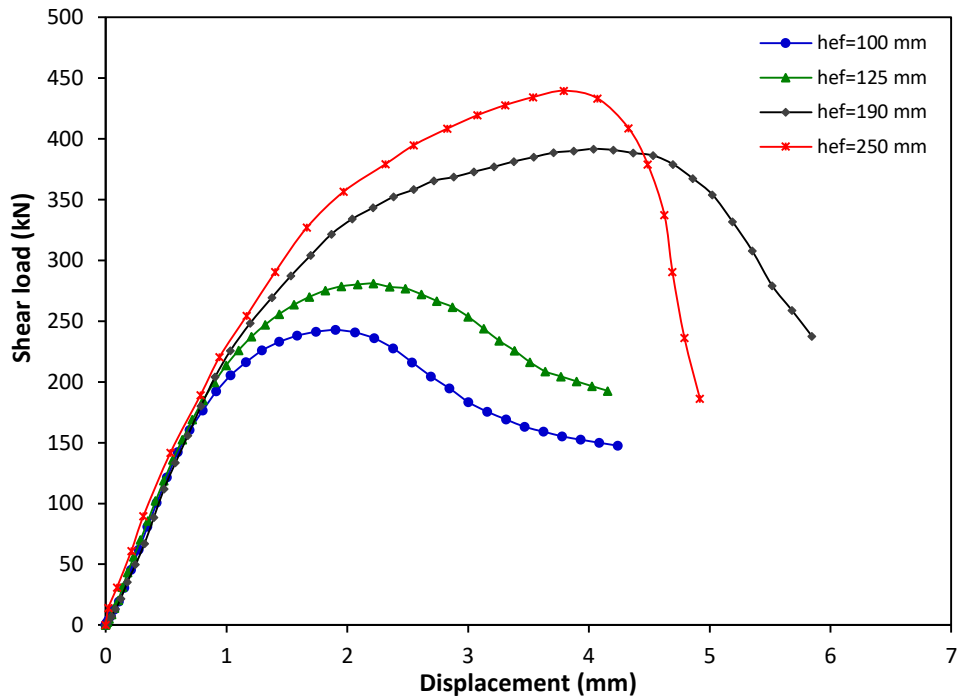


Figure H-8: Shear load-displacement graph for 20 mm diameter undercut anchor at strain rate of 10^{-3} s^{-1}

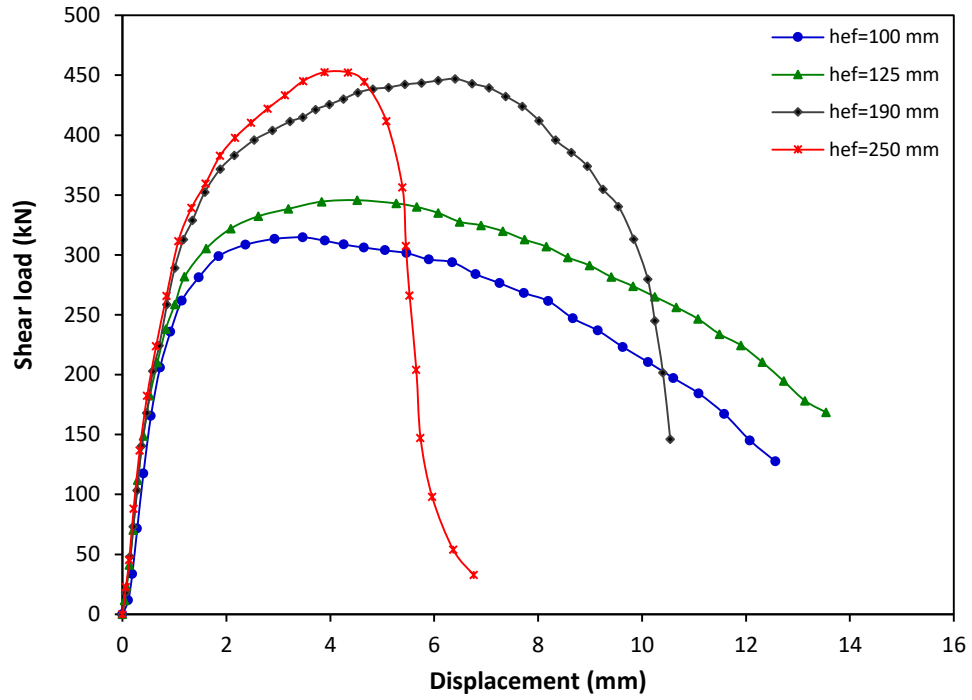


Figure H-9: Shear load-displacement graph for 20 mm diameter undercut anchor at strain rate of 10^{-1} s^{-1}

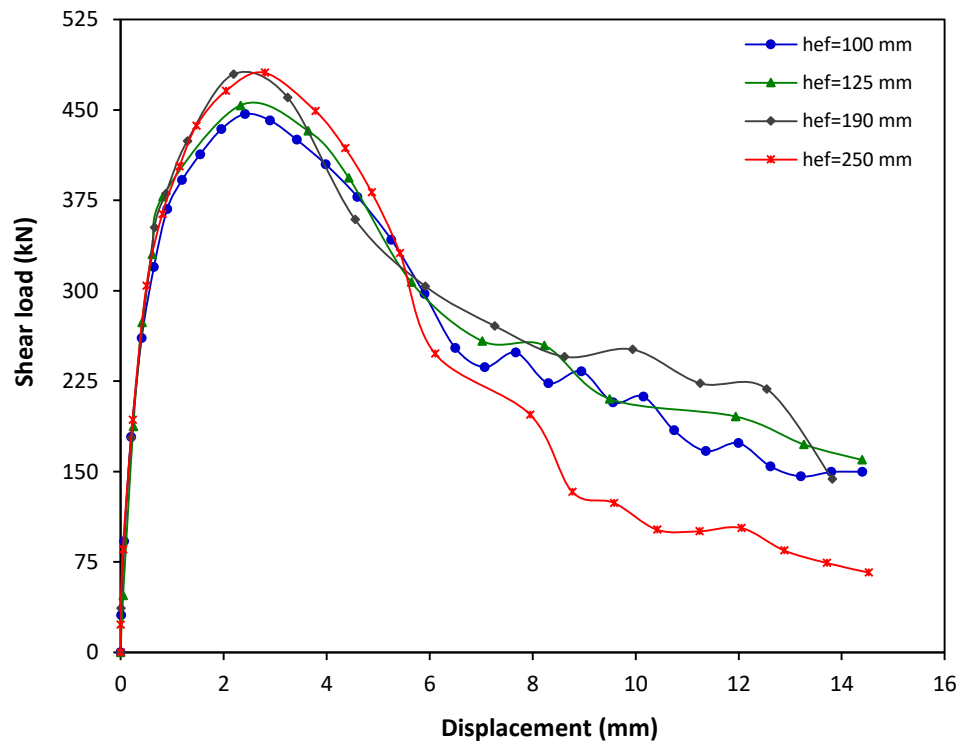


Figure H-10: Shear load-displacement graph for 20 mm diameter undercut anchor at strain rate of 10 s^{-1}

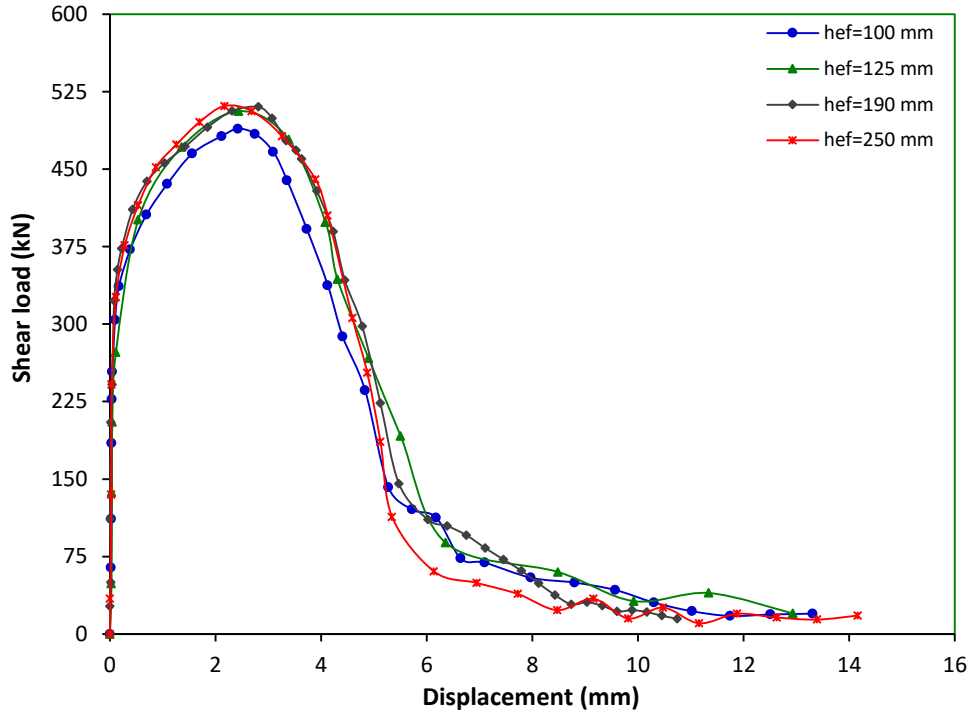


Figure H-11: Shear load-displacement graph for 20 mm diameter undercut anchor at strain rate of 10^2 s^{-1}

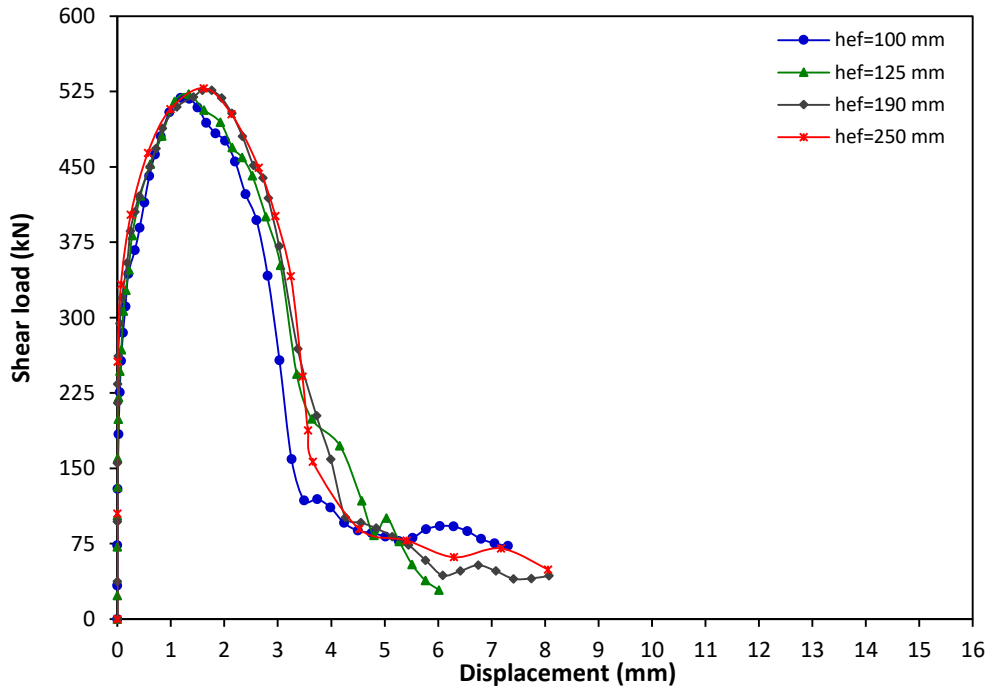


Figure H-12: Shear load-displacement graph for 20 mm diameter undercut anchor at strain rate of 10^3 s^{-1}

Appendix I: LS-DYNA keyword files for anchorage to concrete systems

Cast-in-place anchor under tensile load

```

$# LS-DYNA Keyword file
$# Created on Jan-15-2018 (19:25:44)
*KEYWORD MEMORY=900000000 NCFU=4
*TITLE
$#
title
LS-DYNA keyword deck by LS-PrePost
*DATABASE_SECFORC
$#      dt      binary      lcur      iopt
      0.05      0          0          1
*DATABASE_BINARY_D3PLOT
$#      dt      lcdt      beam      npltc      psetid
      0.5      0          0          0          0
$#      iopt
      0
*DATABASE_CROSS_SECTION_PLANE_ID
$#      csid
title
      8
$#      psid      xct      yct      zct      xch      ych
zch      radius
      0          0.0      3.82 -4.01051      0.0      3.82
13.241      0.0
$#      xhev      yhev      zhev      lenl      lenm      id
itype
      0.0      0.0      0.0      0.0      0.0      0
0
*BOUNDARY_PRESCRIBED_MOTION_SET
$#      nsid      dof      vad      lcid      sf      vid
death      birth
      4          3          0          1          1.0
01.00000E28      0.0
*BOUNDARY_SPC_SET
$#      nsid      cid      dofx      dofy      dofz      dofrx
dofry      dofrz
      5          0          1          1          1          1
1          1
*SET_NODE_LIST_TITLE
NODESET(SPC) 5
$#      sid      da1      da2      da3      da4      solver
      5          0.0      0.0      0.0      0.0MECH
$#      nid1      nid2      nid3      nid4      nid5      nid6
nid7
*BOUNDARY_SPC_SET
$#      nsid      cid      dofx      dofy      dofz      dofrx
dofry      dofrz
      6          0          0          1          0          1
0          1
*SET_NODE_LIST_TITLE

```

```

NODESET(SPC) 6
$#      sid      da1      da2      da3      da4      solver
        6        0.0      0.0      0.0      0.0MECH
$#      nid1      nid2      nid3      nid4      nid5      nid6
nid7
*BOUNDARY_SPC_SET
$#      nsid      cid      dofz      dofry      dofyz      dofz      dofry
dofry      dofz
        7        0        1        0        0        0
1        1
*SET_NODE_LIST_TITLE
NODESET(SPC) 7
$#      sid      da1      da2      da3      da4      solver
        7        0.0      0.0      0.0      0.0MECH
$#      nid1      nid2      nid3      nid4      nid5      nid6
nid7
*CONTACT_AUTOMATIC_SURFACE_TO_SURFACE_ID
$#      cid
title
        0anhea con
$#      ssid      msid      sstyp      mstyp      sboxid      mboxid
spr      mpr
        1        26        2        3        0        0
0        0
$#      fs      fd      dc      vc      vdc      penchk
bt      dt
        0.0      0.0      0.0      0.0      0.0      0
0.01.00000E20
$#      sfs      sfm      sst      mst      sfst      sfmt
fsf      vsf
        1.0      1.0      0.0      0.0      1.0      1.0
1.0      1.0
$#      soft      sofsc1      lcidab      maxpar      sbopt      depth
bsort      frcfrq
        1        0.1      0      1.025      2.0      2
0        1
$#      penmax      thkopt      shlthk      snlog      isym      i2d3d
sldthk      sldstf
        0.0      0      0      0      1      0
0.0      0.0
*SET_PART_LIST_TITLE
an head
$#      sid      da1      da2      da3      da4      solver
        1        0.0      0.0      0.0      0.0MECH
$#      pid1      pid2      pid3      pid4      pid5      pid6
pid7      pid8
        20      21      0      0      0      0
0        0
*PART
$#
title
an
$#      pid      secid      mid      eosid      hgid      grav
adpopt      tmid

```

```

20      1      1      0      0      0
0      0
*SECTION_SOLID
$#  secid  elform  aet
    1      1      0
*MAT_PIECEWISE_LINEAR_PLASTICITY_TITLE
anchor
$#  mid      ro      e      pr      sigy      etan
fail  tdel
    1      7.85  200000.0  0.3  896.0  1018.0
0.14  0.0
$#  c      p      lcsm  lcsr  vp      lcf
    40.0    5.0    0      0      0.0    0
$#  eps1    eps2    eps3    eps4    eps5    eps6
eps7  eps8
    0.0    0.0    0.0    0.0    0.0    0.0
0.0    0.0
$#  es1     es2     es3     es4     es5     es6
es7  es8
    0.0    0.0    0.0    0.0    0.0    0.0
0.0    0.0
*PART
$#
title
head
$#  pid      secid  mid  eosid  hgid  grav
adpopt  tmid
    21      1      1      0      0      0
0      0
*PART
$#
title
con
$#  pid      secid  mid  eosid  hgid  grav
adpopt  tmid
    26      2      2      0      0      0
0      0
*SECTION_SOLID_TITLE
con
$#  secid  elform  aet
    2      10    0
*MAT_CSCM_CONCRETE_TITLE
concrete
$#  mid      ro      nplot  incre  irate  erode
recov  itretrc
    2      2.4    1      0.0    1      1.05
0.0    0
$#  pred
    0.0
$#  fpc      dagg  units
    30.0    19.0  1
*DEFINE_CURVE
$#  lcid  sidr  sfa  sfo  offa  offo
dattyp  lcint

```

```

          1          0          1.0          1.0          0.0          0.0
0          0
$#          a1          o1
          0.0          0.0
          250.0          0.02
          300.0          0.02
*SET_NODE_LIST_TITLE
top
$#  sid      da1      da2      da3      da4      solver
      4      0.0      0.0      0.0      0.0MECH
$#  nid1     nid2     nid3     nid4     nid5     nid6
nid7
*CONTROL_ACCURACY
$#  osu      inn      pidosu     iacc
      0      1      0      0
*CONTROL_ENERGY
$#  hgen     rwen     slnten     rylen
      2      2      1      1
*CONTROL_TERMINATION
$#  endtim   endcyc   dtmin     endeng     endmas
      298.0   0      0.0      0.01.000000E8
*CONTROL_TIMESTEP
$#  dtinit   tssfacs  isdo      tslimt     dt2ms     lctm
erode     mslst
      0.0     0.9      0      0.0      0.0      0
0          0
$#  dt2msf   dt2mslc  imslc     unused     rmscl
      0.0     0      0      0.0      0.0
*ELEMENT_SOLID
$#  eid      pid      n1      n2      n3      n4      n5      n6
n7
*END

```

Cast-in-place anchor under shear load

```

$# LS-DYNA Keyword file
$# Created on Feb-09-2018 (10:15:11)
*KEYWORD MEMORY=900000000 NCPU=4
*TITLE
$#
title
LS-DYNA keyword deck by LS-PrePost
*CONTROL_ACCURACY
$#  osu      inn      pidosu     iacc
      0      1      0      0
*CONTROL_CONTACT
$#  slsfacs  rwpnal   islchk     shlthk     penopt     thkchg
orien     enmass
      0.1     0.0      2      0      1      0
1          1
$#  usrstr   usrfrc   nsbcs     interm     xpene     ssthk
ecdt     tiedprj

```

```

0          0          0          0          0          4.0          0
0          0
$#  sfric      dfri      edc      vfc      th      th_sf
pen_sf
0.0          0.0          0.0          0.0          0.0          0.0
0.0
$#  ignore     frceng   skipr      outseg   spotstp   spotdel
spothin
0          0          0          0          0          0
0.0
$#  isym      nserod   rwgaps    rwgdth   rwksf     icov
swradf      ithoff
0          0          1          0.0      1.0       0
0.0          0
$#  shledg    pstiff    ithcnt    tdcnof   ftall     unused
shltrw
0          0          0          0          0          0
0.0
*CONTROL_ENERGY
$#  hgen      rwen      slnten    rylen
2          2          1          1
*CONTROL_TERMINATION
$#  endtim     endcyc     dtmin     endeng    endmas    nosol
358.0      0          0.0      0.01.000000E8  0
*CONTROL_TIMESTEP
$#  dtinit     tssfacc    isdo      tslimt    dt2ms     lctm
erode      mslst
0.0          0.9          0          0.0      0.0       0
0          0
$#  dt2msf     dt2mslc    imslc     unused    unused    rmscl
0.0          0          0          0.0      0.0       0.0
*DATABASE_SECFORC
$#  dt         binary     lcur      ioopt
0.05        0          0          1
*DATABASE_BINARY_D3PLOT
$#  dt         lcdt      beam      npltc    psetid
0.5          0          0          0          0
$#  ioopt
0
*DATABASE_CROSS_SECTION_PLANE_ID
$#  csid
title
9
$#  psid      xct      yct      zct      xch      ych
zch      radius
0          0.0      0.0      -74.1947  0.0      37.0974 -
74.1947    0.0
$#  xhev      yhev     zhev     lenl     lenm     id
itype
0.0          0.0      0.0      0.0      0.0      0
0
*BOUNDARY_PRESCRIBED_MOTION_SET
$#  nsid      dof      vad      lcid     sf      vid
death      birth

```

```

3          2          0          1          1.0
01.00000E28      0.0
*BOUNDARY_SPC_SET
$#   nsid      cid      dofz      dofry      dofz      dofz      dofz      dofz      dofz
dofry      dofz
1          1          0          1          1          1          1          1
1          1
*SET_NODE_LIST_TITLE
NODESET(SPC) 1
$#   sid      da1      da2      da3      da4      solver
1          0.0      0.0      0.0      0.0MECH
$#   nid1      nid2      nid3      nid4      nid5      nid6
nid7
nid8
*BOUNDARY_SPC_SET
$#   nsid      cid      dofz      dofry      dofz      dofz      dofz      dofz
dofry      dofz
1          2          0          1          0          0          0          0
1          1
*SET_NODE_LIST_TITLE
NODESET(SPC) 2
$#   sid      da1      da2      da3      da4      solver
2          0.0      0.0      0.0      0.0MECH
$#   nid1      nid2      nid3      nid4      nid5      nid6
nid7      nid8
*CONTACT_AUTOMATIC_SURFACE_TO_SURFACE_ID
$#   cid
title
0anhea con
$#   ssid      msid      sstyp      mstyp      sboxid      mboxid
spr      mpr
1          108      2          3          0          0
0          0
$#   fs      fd      dc      vc      vdc      penchk
bt      dt
0.0      0.0      0.0      0.0      0.0      2
0.01.00000E20
$#   sfs      sfm      sst      mst      sfst      sfmt
fsf      vsf
1.0      1.0      0.0      0.0      1.0      1.0
1.0      1.0
$#   soft      sofsc1      lcidab      maxpar      sbopt      depth
bsort      frcfrq
1          1      0.1      0          1.025      2.0      2
15      2
$#   penmax      thkopt      shlthk      snlog      isym      i2d3d
sldthk      sldstf
0.0      0.0      0          0          0          1          0
0.0      0.0
*SET_PART_LIST_TITLE
anhe
$#   sid      da1      da2      da3      da4      solver
1          0.0      0.0      0.0      0.0MECH

```

```

$#      pid1      pid2      pid3      pid4      pid5      pid6
pid7    pid8
      21      100      0      0      0      0
0      0
*CONTACT_AUTOMATIC_SURFACE_TO_SURFACE_ID
$#      cid
title
      2plate con
$#      ssid      msid      sstyp      mstyp      sboxid      mboxid
spr      mpr
      106      108      3      3      0      0
0      0
$#      fs      fd      dc      vc      vdc      penchk
bt      dt
      0.0      0.0      0.0      0.0      0.0      2
0.01.00000E20
$#      sfs      sfm      sst      mst      sfst      sfmt
fsf      vsf
      1.0      1.0      0.0      0.0      1.0      1.0
1.0      1.0
$#      soft      sofsc1      lcidab      maxpar      sbopt      depth
bsort      frcfrq
      1      0.1      0      1.025      2.0      2
15      2
$#      penmax      thkopt      shlthk      snlog      isym      i2d3d
sldthk      sldstf
      0.0      0      0      0      1      0
0.0      0.0
*CONTACT_AUTOMATIC_SURFACE_TO_SURFACE_ID
$#      cid
title
      3plate an
$#      ssid      msid      sstyp      mstyp      sboxid      mboxid
spr      mpr
      106      100      3      3      0      0
0      0
$#      fs      fd      dc      vc      vdc      penchk
bt      dt
      0.0      0.0      0.0      0.0      0.0      2
0.01.00000E20
$#      sfs      sfm      sst      mst      sfst      sfmt
fsf      vsf
      1.0      1.0      0.0      0.0      1.0      1.0
1.0      1.0
$#      soft      sofsc1      lcidab      maxpar      sbopt      depth
bsort      frcfrq
      1      0.1      0      1.025      2.0      2
15      2
$#      penmax      thkopt      shlthk      snlog      isym      i2d3d
sldthk      sldstf
      0.0      0      0      0      1      0
0.0      0.0
*CONTACT_AUTOMATIC_SURFACE_TO_SURFACE_ID

```

```

$#      cid
title
      4plate washer
$#      ssid      msid      sstyp      mstyp      sboxid      mboxid
spr      mpr
      106      104      3      3      0      0
0      0
$#      fs      fd      dc      vc      vdc      penchk
bt      dt
      0.0      0.0      0.0      0.0      0.0      2
0.01.00000E20
$#      sfs      sfm      sst      mst      sfst      sfmt
fsf      vsf
      1.0      1.0      0.0      0.0      1.0      1.0
1.0      1.0
$#      soft      sofsc1      lcidab      maxpar      sbopt      depth
bsort      frcfrq
      1      0.1      0      1.025      2.0      2
15      2
$#      penmax      thkopt      shlthk      snlog      isym      i2d3d
sldthk      sldstf
      0.0      0      0      0      1      0
0.0      0.0
*CONTACT_AUTOMATIC_SURFACE_TO_SURFACE_ID
$#      cid
title
      5washer an
$#      ssid      msid      sstyp      mstyp      sboxid      mboxid
spr      mpr
      104      100      3      3      0      0
0      0
$#      fs      fd      dc      vc      vdc      penchk
bt      dt
      0.0      0.0      0.0      0.0      0.0      2
0.01.00000E20
$#      sfs      sfm      sst      mst      sfst      sfmt
fsf      vsf
      1.0      1.0      0.0      0.0      1.0      1.0
1.0      1.0
$#      soft      sofsc1      lcidab      maxpar      sbopt      depth
bsort      frcfrq
      1      0.1      0      1.025      2.0      2
15      2
$#      penmax      thkopt      shlthk      snlog      isym      i2d3d
sldthk      sldstf
      0.0      0      0      0      1      0
0.0      0.0
*CONTACT_AUTOMATIC_SURFACE_TO_SURFACE_ID
$#      cid
title
      6nut anc
$#      ssid      msid      sstyp      mstyp      sboxid      mboxid
spr      mpr

```

```

102      100      3      3      0      0
0        0
$#      fs      fd      dc      vc      vdc      penchk
bt      dt
0.0      0.0      0.0      0.0      0.0      0.0      2
0.01.00000E20
$#      sfs      sfm      sst      mst      sfst      sfmt
fsf      vsf
1.0      1.0      0.0      0.0      1.0      1.0
1.0      1.0
$#      soft      sofsc1      lcidab      maxpar      sbopt      depth
bsort      frcfrq
1        0.1      0      1.025      2.0      2
15      2
$#      penmax      thkopt      shlthk      snlog      isym      i2d3d
sldthk      sldstf
0.0      0      0      0      1      0
0.0      0.0
*CONTACT_AUTOMATIC_SURFACE_TO_SURFACE_ID
$#      cid
title
7washer nut
$#      ssid      msid      sstyp      mstyp      sboxid      mboxid
spr      mpr
104      102      3      3      0      0
0        0
$#      fs      fd      dc      vc      vdc      penchk
bt      dt
0.0      0.0      0.0      0.0      0.0      0.0      2
0.01.00000E20
$#      sfs      sfm      sst      mst      sfst      sfmt
fsf      vsf
1.0      1.0      0.0      0.0      1.0      1.0
1.0      1.0
$#      soft      sofsc1      lcidab      maxpar      sbopt      depth
bsort      frcfrq
1        0.1      0      1.025      2.0      2
15      2
$#      penmax      thkopt      shlthk      snlog      isym      i2d3d
sldthk      sldstf
0.0      0      0      0      1      0
0.0      0.0
*PART
$#
title
head
$#      pid      secid      mid      eosid      hgid      grav
adpopt      tmid
21      1      1      0      0      0
0        0
*SECTION_SOLID
$#      secid      elform      aet
1        1      0
*MAT_PIECEWISE_LINEAR_PLASTICITY_TITLE

```

```

anchor
$#      mid      ro      e      pr      sigy      etan
fail      tdel
      1      7.85  200000.0      0.3      896.0      1018.0
0.14      0.0
$#      c      p      lcsc      lcsr      vp
      40.0      5.0      0      0      0.0
$#      eps1      eps2      eps3      eps4      eps5      eps6
eps7      eps8
      0.0      0.0      0.0      0.0      0.0      0.0
0.0      0.0
$#      es1      es2      es3      es4      es5      es6
es7      es8
      0.0      0.0      0.0      0.0      0.0      0.0
0.0      0.0
*PART
$#
title
anc
$#      pid      secid      mid      eosid      hgid      grav
adpopt      tmid
      100      1      1      0      0      0
0      0
*PART
$#
title
nut
$#      pid      secid      mid      eosid      hgid      grav
adpopt      tmid
      102      1      1      0      0      0
0      0
*PART
$#
title
washer
$#      pid      secid      mid      eosid      hgid      grav
adpopt      tmid
      104      1      1      0      0      0
0      0
*PART
$#
title
plate
$#      pid      secid      mid      eosid      hgid      grav
adpopt      tmid
      106      1      1      0      0      0
0      0
*PART
$#
title
con
$#      pid      secid      mid      eosid      hgid      grav
adpopt      tmid

```

```

108      2      2      0      0      0
0      0
*SECTION_SOLID_TITLE
con
$#  secid  elform  aet
      2      10      0
*MAT_CSCM_CONCRETE_TITLE
concrete
$#  mid  ro  nplot  incre  irate  erode
recov  itretrc
      2      2.4      1      0.0      1      1.05
0.0      0
$#  pred
      0.0
$#  fpc  dagg  units
      30.0  19.0      1
*DEFINE_CURVE
$#  lcid  sidr  sfa  sfo  offa  offo
dattyp  lcint
      1      0      1.0      1.0      0.0      0.0
0      0
$#
      a1  o1
      0.0  0.0
      300.0  0.015
      360.0  0.015
*SET_NODE_LIST
$#  sid  da1  da2  da3  da4  solver
      3  0.0  0.0  0.0  0.0MECH
$#  nid1  nid2  nid3  nid4  nid5  nid6
nid7  nid8
      180413  0  0  0  0  0
0  0
*SET_NODE_LIST_TITLE
NODESET(CNRB)
$#  sid  da1  da2  da3  da4  solver
      4  0.0  0.0  0.0  0.0MECH
$#  nid1  nid2  nid3  nid4  nid5  nid6
nid7  nid8
*CONSTRAINED_NODAL_RIGID_BODY
$#  pid  cid  nsid  pnode  iprt  drflag
rrflag
      109  0  4  0  0  0
0
*ELEMENT_SOLID
$#  eid  pid  n1  n2  n3  n4  n5  n6
n7  n8
*END

```

Adhesive anchor under tensile load

```
$# LS-DYNA Keyword file
$# Created on Feb-10-2018 (16:49:30)
*KEYWORD MEMORY=900000000 NCPU=4
*TITLE
$#
title
LS-DYNA keyword deck by LS-PrePost
*CONTROL_ACCURACY
$#   osu       inn     pidosu     iacc
      0         1         0         0
*CONTROL_ENERGY
$#   hgen      rwen     slnten     rylen
      2         2         1         1
*CONTROL_TERMINATION
$#   endtim     endcyc     dtmin     endeng     endmas     nosol
      218.0     0         0.0     0.01.000000E8     0
*CONTROL_TIMESTEP
$#   dtinit     tssfac     isdo     tslimt     dt2ms     lctm
erode     mslst
      0.0         0.9         0         0.0         0.0         0
0         0
$#   dt2msf     dt2mslc     imslc     unused     unused     rmscl
      0.0         0         0         0         0         0.0
*DATABASE_SECFORC
$#   dt       binary     lcur     iopt
      0.05     0         0         1
*DATABASE_BINARY_D3PLOT
$#   dt       lcdt     beam     npltc     psetid
      0.5     0         0         0         0
$#   iopt
      0
*DATABASE_CROSS_SECTION_PLANE_ID
$#   csid
title
      4
$#   psid      xct      yct      zct      xch      ych
zch     radius
      0         0.0     7.63449  74.2458  0.0     7.63449
111.564     0.0
$#   xhev      yhev      zhev      lenl     lenm     id
itype
      0.0         0.0     0.0     0.0     0.0     0
0
*BOUNDARY_PRESCRIBED_MOTION_SET
$#   nsid      dof      vad      lcid      sf      vid
death     birth
      4         3         0         1         1.0
01.00000E28     0.0
*BOUNDARY_SPC_SET
$#   nsid      cid      dofz     dofry     dofz     dofry
dofry     dofz
```

```

5      0      1      1      1      1
1      1
*SET_NODE_LIST_TITLE
NODESET(SPC) 5
$#    sid      da1      da2      da3      da4      solver
      5      0.0      0.0      0.0      0.0MECH
$#    nid1     nid2     nid3     nid4     nid5     nid6
nid7     nid8
*BOUNDARY_SPC_SET
$#    nsid     cid      dofx     dofy     dofz     dofrx
dofry     dofz
      6      0      1      0      0      0
1      1
*SET_NODE_LIST_TITLE
NODESET(SPC) 6
$#    sid      da1      da2      da3      da4      solver
      6      0.0      0.0      0.0      0.0MECH
$#    nid1     nid2     nid3     nid4     nid5     nid6
nid7     nid8
*BOUNDARY_SPC_SET
$#    nsid     cid      dofx     dofy     dofz     dofrx
dofry     dofz
      7      0      0      1      0      1
0      1
*SET_NODE_LIST_TITLE
NODESET(SPC) 7
$#    sid      da1      da2      da3      da4      solver
      7      0.0      0.0      0.0      0.0MECH
$#    nid1     nid2     nid3     nid4     nid5     nid6
nid7     nid8
*CONTACT_AUTOMATIC_ONE_WAY_SURFACE_TO_SURFACE_TIEBREAK_ID
$#    cid
title
      0adan
$#    ssid     msid     sstyp     mstyp     sboxid     mboxid
spr      mpr
      11      10      3      3      0      0
0      0
$#    fs      fd      dc      vc      vdc      penchk
bt      dt
      0.8      0.7      0.0      0.0      0.0      0
0.01.00000E20
$#    sfs      sfm      sst      mst      sfst      sfmt
fsf      vsf
      1.0      1.0      0.0      0.0      1.0      1.0
1.0      1.0
$#    option   nfls     sfls     param     eraten     erates
ct2cn      cn
      9      0.0      0.0      0.0      0.0      0.0
0.0      0.0
$#    soft     sofsc1   lcidab   maxpar     sbopt     depth
bsort     frcfrq
      1      0.1      0      1.025     2.0      2
0      1

```

```

$# penmax thkopt shlthk snlog isym i2d3d
sldthk sldstf
0.0 0.0 0 0 0 1 0
0.0 0.0
*CONTACT_TIED_SURFACE_TO_SURFACE_ID
$# cid
title
0adco
$# ssid msid sstyp mstyp sboxid mboxid
spr mpr
11 16 3 3 0 0
0 0
$# fs fd dc vc vdc penchk
bt dt
0.8 0.7 0.0 0.0 0.0 0
0.01.00000E20
$# sfs sfm sst mst sfst sfmt
fsf vsf
1.0 1.0 0.0 0.0 1.0 1.0
1.0 1.0
$# soft sofsc1 lcidab maxpar sbopt depth
bsort frcfrq
1 0.1 0 1.025 2.0 2
0 1
$# penmax thkopt shlthk snlog isym i2d3d
sldthk sldstf
0.0 0.0 0 0 0 1 0
0.0 0.0
*CONTACT_ERODING_SINGLE_SURFACE
$# cid
title
$# ssid msid sstyp mstyp sboxid mboxid
spr mpr
1 0 0 0 0 0
0 0
$# fs fd dc vc vdc penchk
bt dt
0.0 0.0 0.0 0.0 0.0 0
0.01.00000E20
$# sfs sfm sst mst sfst sfmt
fsf vsf
1.0 1.0 0.0 0.0 1.0 1.0
1.0 1.0
$# isym erosop iadj
1 1 0
$# soft sofsc1 lcidab maxpar sbopt depth
bsort frcfrq
1 0.1 0 1.025 2.0 2
0 1
$# penmax thkopt shlthk snlog isym i2d3d
sldthk sldstf
0.0 0.0 0 0 0 1 0
0.0 0.0
*SET_SEGMENT_TITLE

```

```

ad
$#      sid      da1      da2      da3      da4      solver
      1      0.0      0.0      0.0      0.0MECH
$#      n1      n2      n3      n4      a1      a2
a3      a4
*PART
$#
title
an
$#      pid      secid      mid      eosid      hgid      grav
adpopt      tmid
      10      1      1      0      0      0
0      0
*SECTION_SOLID_TITLE
an
$#      secid      elform      aet
      1      1      0
*MAT_PIECEWISE_LINEAR_PLASTICITY_TITLE
anchor
$#      mid      ro      e      pr      sigy      etan
fail      tdel
      1      7.85 200000.0      0.3      896.0      1018.0
0.14      0.0
$#      c      p      lcss      lcsr      vp
      40.0      5.0      0      0      0.0
$#      eps1      eps2      eps3      eps4      eps5      eps6
eps7      eps8
      0.0      0.0      0.0      0.0      0.0      0.0
0.0      0.0
$#      es1      es2      es3      es4      es5      es6
es7      es8
      0.0      0.0      0.0      0.0      0.0      0.0
0.0      0.0
*PART
$#
title
ad
$#      pid      secid      mid      eosid      hgid      grav
adpopt      tmid
      11      1      3      0      0      0
0      0
*MAT_ARUP_ADHESIVE_TITLE
Adhes
$#      mid      ro      e      pr      tenmax      gcten
shrmax      gcshr
      3      1.2      3034.0      0.4      56.0      3.0
44.0      8.0
$#      pwrt      pwrs      shrp      sht_sl      edot0      edot2
thkdir      extra
      2.0      2.0      0.0      0.01.00000E-5      0.0
0.0      0.0
*PART
$#
title

```

```

New part from tetrahedron mesher
$#   pid      secid      mid      eosid      hgid      grav
adpopt      tmid
      16      2          2          0          0          0
0          0
*SECTION_SOLID_TITLE
co
$#   secid      elform      aet
      2          10          0
*MAT_CSCM_CONCRETE_TITLE
concrete
$#   mid      ro      nplot      incre      irate      erode
recov      itretc
      2          2.4          1          0.0          1          1.05
0.0          0
$#   pred
      0.0
$#   fpc      dagg      units
      30.0      19.0          1
*DEFINE_CURVE
$#   lcid      sidr      sfa      sfo      offa      offo
dattyp      lcint
      1          0          1.0          1.0          0.0          0.0
0          0
$#
      a1          o1
          0.0          0.0
          200.0          0.02
          220.0          0.02
*SET_NODE_LIST_TITLE
top
$#   sid      da1      da2      da3      da4      solver
      4          0.0          0.0          0.0          0.0MECH
$#   nid1      nid2      nid3      nid4      nid5      nid6
nid7      nid8
*SET_PART_LIST_TITLE
conc
$#   sid      da1      da2      da3      da4      solver
      1          0.0          0.0          0.0          0.0MECH
$#   pid1      pid2      pid3      pid4      pid5      pid6
pid7      pid8
      16          0          0          0          0          0
0          0
*SET_PART_LIST_TITLE
an
$#   sid      da1      da2      da3      da4      solver
      2          0.0          0.0          0.0          0.0MECH
$#   pid1      pid2      pid3      pid4      pid5      pid6
pid7      pid8
      10          0          0          0          0          0
0          0
*ELEMENT_SOLID
$#   eid      pid      n1      n2      n3      n4      n5      n6
n7      n8
*END

```

Adhesive anchor under shear load

```

$# LS-DYNA Keyword file
$# Created on Feb-02-2018 (02:34:40)
*KEYWORD MEMORY=900000000
*TITLE
$#
title
LS-DYNA keyword deck by LS-PrePost
*CONTROL_ACCURACY
$#      osu      inn      pidosu      iacc
          0          1          0          0
*CONTROL_CONTACT
$#  slsfac  rwpnal  islchk  shlthk  penopt  thkchg
orien  enmass
          0.1      0.0          2          0          1          0
1          1
$#  usrstr  usrfrc  nsbcs  interm  xpene  ssthk
ecdt  tiedprj
          0          0          0          0          4.0          0
0          0
$#  sfric  dfric  edc  vfc  th  th_sf
pen_sf
          0.0      0.0      0.0      0.0      0.0      0.0
0.0
$#  ignore  frceng  skiprwg  outseg  spotstp  spotdel
spothin
          0          0          0          0          0          0
0.0
$#  isym  nserod  rwgaps  rwgdth  rwksf  icov
swradf  ithoff
          0          0          1          0.0      1.0          0
0.0          0
$#  shldg  pstiff  ithcnt  tdcnof  ftall  unused
shltrw
          0          0          0          0          0
0.0
*CONTROL_ENERGY
$#  hgen  rwen  slnten  rylene
          2          2          1          1
*CONTROL_TERMINATION
$#  endtim  endcyc  dtmin  endeng  endmas  nosol
          378.0      0          0.0      0.01.000000E8      0
*CONTROL_TIMESTEP
$#  dtinit  tssfacc  isdo  tslimt  dt2ms  lctm
erode  mslst
          0.0      0.9          0          0.0      0.0          0
0          0
$#  dt2msf  dt2mslc  imsc1  unused  unused  rmsc1
          0.0          0          0          0          0          0.0
*DATABASE_SECFORC
$#  dt  binary  lcur  ioopt
          0.05      0          0          1
*DATABASE_BINARY_D3PLOT

```

```

$#      dt      lcdt      beam      npltc      psetid
      0.5      0      0      0      0
$#      iopt
      0
*DATABASE_CROSS_SECTION_PLANE_ID
$#      csid
title
      9
$#      psid      xct      yct      zct      xch      ych
zch      radius
      0      0.0      0.0      -74.1947      0.0      37.0974 -
74.1947      0.0
$#      xhev      yhev      zhev      lenl      lenm      id
itype
      0.0      0.0      0.0      0.0      0.0      0
0
*BOUNDARY_PRESCRIBED_MOTION_SET
$#      nsid      dof      vad      lcid      sf      vid
death      birth
      3      2      0      1      1.0
01.000000E28      0.0
*BOUNDARY_SPC_SET
$#      nsid      cid      dofx      dofy      dofz      dofrx
dofry      dofrz
      5      0      1      1      1      1
1      1
*SET_NODE_LIST_TITLE
NODESET(SPC) 5
$#      sid      da1      da2      da3      da4      solver
      5      0.0      0.0      0.0      0.0MECH
$#      nid1      nid2      nid3      nid4      nid5      nid6
nid7      nid8
*BOUNDARY_SPC_SET
$#      nsid      cid      dofx      dofy      dofz      dofrx
dofry      dofrz
      9      0      1      0      0      0
1      1
*SET_NODE_LIST_TITLE
NODESET(SPC) 9
$#      sid      da1      da2      da3      da4      solver
      9      0.0      0.0      0.0      0.0MECH
$#      nid1      nid2      nid3      nid4      nid5      nid6
nid7      nid8
*SET_SEGMENT_TITLE
conc
$#      sid      da1      da2      da3      da4      solver
      2      0.0      0.0      0.0      0.0MECH
$#      n1      n2      n3      n4      a1      a2
a3      a4
*CONTACT_AUTOMATIC_SURFACE_TO_SURFACE_ID
$#      cid
title
      2plate con

```

```

$#      ssid      msid      sstyp      mstyp      sboxid      mboxid
spr          mpr
      106        110          3          3          0          0
0          0
$#      fs        fd        dc        vc        vdc        penchk
bt          dt
      0.0        0.0        0.0        0.0        0.0          2
0.01.00000E20
$#      sfs        sfm        sst        mst        sfst        sfmt
fsf          vsf
      1.0        1.0        0.0        0.0        1.0        1.0
1.0        1.0
$#      soft      sofsc1    lcidab    maxpar    sbopt    depth
bsort      frcfrq
      1          0.1          0        1.025    2.0          2
15         2
$#      penmax    thkopt    shlthk    snlog    isym    i2d3d
sldthk      sldstf
      0.0          0          0          0          1          0
0.0        0.0
*CONTACT_AUTOMATIC_SURFACE_TO_SURFACE_ID
$#      cid
title
      3plate an
$#      ssid      msid      sstyp      mstyp      sboxid      mboxid
spr          mpr
      106        100          3          3          0          0
0          0
$#      fs        fd        dc        vc        vdc        penchk
bt          dt
      0.0        0.0        0.0        0.0        0.0          2
0.01.00000E20
$#      sfs        sfm        sst        mst        sfst        sfmt
fsf          vsf
      1.0        1.0        0.0        0.0        1.0        1.0
1.0        1.0
$#      soft      sofsc1    lcidab    maxpar    sbopt    depth
bsort      frcfrq
      1          0.1          0        1.025    2.0          2
15         2
$#      penmax    thkopt    shlthk    snlog    isym    i2d3d
sldthk      sldstf
      0.0          0          0          0          1          0
0.0        0.0
*CONTACT_AUTOMATIC_SURFACE_TO_SURFACE_ID
$#      cid
title
      4plate washer
$#      ssid      msid      sstyp      mstyp      sboxid      mboxid
spr          mpr
      106        104          3          3          0          0
0          0
$#      fs        fd        dc        vc        vdc        penchk
bt          dt

```

```

0.0      0.0      0.0      0.0      0.0      0.0      2
0.01.00000E20
$#      sfs      sfm      sst      mst      sfst      sfmt
fsf      vsf
1.0      1.0      1.0      0.0      0.0      1.0      1.0
1.0      1.0
$#      soft      sofsc1      lcidab      maxpar      sbopt      depth
bsort      frcfrq
1      1      0.1      0      1.025      2.0      2
15      2
$#      penmax      thkopt      shlthk      snlog      isym      i2d3d
sldthk      sldstf
0.0      0      0      0      0      1      0
0.0      0.0
*CONTACT_AUTOMATIC_SURFACE_TO_SURFACE_ID
$#      cid
title
5washer an
$#      ssid      msid      sstyp      mstyp      sboxid      mboxid
spr      mpr
104      100      3      3      0      0
0      0
$#      fs      fd      dc      vc      vdc      penchk
bt      dt
0.0      0.0      0.0      0.0      0.0      0.0      2
0.01.00000E20
$#      sfs      sfm      sst      mst      sfst      sfmt
fsf      vsf
1.0      1.0      1.0      0.0      0.0      1.0      1.0
1.0      1.0
$#      soft      sofsc1      lcidab      maxpar      sbopt      depth
bsort      frcfrq
1      1      0.1      0      1.025      2.0      2
15      2
$#      penmax      thkopt      shlthk      snlog      isym      i2d3d
sldthk      sldstf
0.0      0      0      0      0      1      0
0.0      0.0
*CONTACT_AUTOMATIC_SURFACE_TO_SURFACE_ID
$#      cid
title
6nut anc
$#      ssid      msid      sstyp      mstyp      sboxid      mboxid
spr      mpr
102      100      3      3      0      0
0      0
$#      fs      fd      dc      vc      vdc      penchk
bt      dt
0.0      0.0      0.0      0.0      0.0      0.0      2
0.01.00000E20
$#      sfs      sfm      sst      mst      sfst      sfmt
fsf      vsf
1.0      1.0      1.0      0.0      0.0      1.0      1.0
1.0      1.0

```

```

$#      soft      sofsc1      lcidab      maxpar      sbopt      depth
bsort      frcfrq
          1          0.1          0          1.025          2.0          2
15          2
$#      penmax      thkopt      shlthk      snlog      isym      i2d3d
sldthk      sldstf
          0.0          0          0          0          1          0
0.0          0.0
*CONTACT_AUTOMATIC_SURFACE_TO_SURFACE_ID
$#      cid
title
          7washer nut
$#      ssid      msid      sstyp      mstyp      sboxid      mboxid
spr      mpr
          104          102          3          3          0          0
0          0
$#      fs      fd      dc      vc      vdc      penchk
bt      dt
          0.0          0.0          0.0          0.0          0.0          2
0.01.00000E20
$#      sfs      sfm      sst      mst      sfst      sfmt
fsf      vsf
          1.0          1.0          0.0          0.0          1.0          1.0
1.0          1.0
$#      soft      sofsc1      lcidab      maxpar      sbopt      depth
bsort      frcfrq
          1          0.1          0          1.025          2.0          2
15          2
$#      penmax      thkopt      shlthk      snlog      isym      i2d3d
sldthk      sldstf
          0.0          0          0          0          1          0
0.0          0.0
*CONTACT_AUTOMATIC_ONE_WAY_SURFACE_TO_SURFACE_TIEBREAK_ID
$#      cid
title
          0ad an
$#      ssid      msid      sstyp      mstyp      sboxid      mboxid
spr      mpr
          1          100          2          3          0          0
0          0
$#      fs      fd      dc      vc      vdc      penchk
bt      dt
          0.8          0.7          0.0          0.0          0.0          0
0.01.00000E20
$#      sfs      sfm      sst      mst      sfst      sfmt
fsf      vsf
          1.0          1.0          0.0          0.0          1.0          1.0
1.0          1.0
$#      option      nfls      sfls      param      eraten      erates
ct2cn      cn
          9          0.0          0.0          0.0          0.0          0.0
0.0          0.0
$#      soft      sofsc1      lcidab      maxpar      sbopt      depth
bsort      frcfrq

```

```

15      1      0.1      0      1.025      2.0      2
15      1
$# penmax      thkopt      shlthk      snlog      isym      i2d3d
sldthk      sldstf
0.0      0.0      0      0      0      1      0
0.0      0.0
*SET_PART_LIST_TITLE
adh
$#      sid      da1      da2      da3      da4      solver
1      0.0      0.0      0.0      0.0MECH
$#      pid1      pid2      pid3      pid4      pid5      pid6
pid7      pid8
113      0      0      0      0      0
0      0
*CONTACT_TIED_SURFACE_TO_SURFACE_ID
$#      cid
title
0ad con
$#      ssid      msid      sstyp      mstyp      sboxid      mboxid
spr      mpr
3      2      0      0      0      0
0      0
$#      fs      fd      dc      vc      vdc      penchk
bt      dt
0.0      0.0      0.0      0.0      0.0      0
0.01.00000E20
$#      sfs      sfm      sst      mst      sfst      sfmt
fsf      vsf
1.0      1.0      0.0      0.0      1.0      1.0
1.0      1.0
$#      soft      sofsc1      lcidab      maxpar      sbopt      depth
bsort      frcfrq
1      0.1      0      1.025      2.0      2
15      1
$# penmax      thkopt      shlthk      snlog      isym      i2d3d
sldthk      sldstf
0.0      0.0      0      0      0      1      0
0.0      0.0
*SET_SEGMENT_TITLE
ad
$#      sid      da1      da2      da3      da4      solver
3      0.0      0.0      0.0      0.0MECH
$#      n1      n2      n3      n4      a1      a2
a3      a4
*CONTACT_ERODING_SINGLE_SURFACE_ID
$#      cid
title
0ad
$#      ssid      msid      sstyp      mstyp      sboxid      mboxid
spr      mpr
3      0      0      0      0      0
0      0
$#      fs      fd      dc      vc      vdc      penchk
bt      dt

```

```

0.0      0.0      0.0      0.0      0.0      0.0      0
0.01.00000E20
$#      sfs      sfm      sst      mst      sfst      sfmt
fsf      vsf
1.0      1.0      0.0      0.0      1.0      1.0
1.0      1.0
$#      isym      erosop      iadj
1      1      0
$#      soft      sofscl      lcidab      maxpar      sbopt      depth
bsort      frcfrq
1      0.1      0      1.025      2.0      2
0      1
$#      penmax      thkopt      shlthk      snlog      isym      i2d3d
sldthk      sldstf
0.0      0      0      0      1      0
0.0      0.0
*PART
$#
title
anc
$#      pid      secid      mid      eosid      hgid      grav
adpopt      tmid
100      1      1      0      0      0
0      0
*SECTION_SOLID
$#      secid      elform      aet
1      1      0
*MAT_PIECEWISE_LINEAR_PLASTICITY_TITLE
anchor
$#      mid      ro      e      pr      sigy      etan
fail      tdel
1      7.85      200000.0      0.3      896.0      1018.0
0.14      0.0
$#      c      p      lcss      lcsr      vp
40.0      5.0      0      0      0.0
$#      eps1      eps2      eps3      eps4      eps5      eps6
eps7      eps8
0.0      0.0      0.0      0.0      0.0      0.0
0.0      0.0
$#      es1      es2      es3      es4      es5      es6
es7      es8
0.0      0.0      0.0      0.0      0.0      0.0
0.0      0.0
*PART
$#
title
nut
$#      pid      secid      mid      eosid      hgid      grav
adpopt      tmid
102      1      1      0      0      0
0      0
*PART
$#
title

```

```

washer
$#      pid      secid      mid      eosid      hgid      grav
adpopt      tmid
      104      1      1      0      0      0
0      0
*PART
$#
title
plate
$#      pid      secid      mid      eosid      hgid      grav
adpopt      tmid
      106      1      1      0      0      0
0      0
*PART
$#
title
conc
$#      pid      secid      mid      eosid      hgid      grav
adpopt      tmid
      110      2      2      0      0      0
0      0
*SECTION_SOLID_TITLE
con
$#      secid      elform      aet
      2      10      0
*MAT_CSCM_CONCRETE_TITLE
concrete
$#      mid      ro      nplot      incre      irate      erode
recov      itretrc
      2      2.4      1      0.0      1      1.05
0.0      0
$#      pred
      0.0
$#      fpc      dagg      units
      30.0      19.0      1
*PART
$#
title
ad
$#      pid      secid      mid      eosid      hgid      grav
adpopt      tmid
      113      1      3      0      0      0
0      0
*MAT_ARUP_ADHESIVE_TITLE
adhesive
$#      mid      ro      e      pr      tenmax      gcten
shrmax      gcshr
      3      1.2      3034.0      0.4      56.0      3.0
44.0      8.0
$#      pwrt      pwrs      shrp      sht_sl      edot0      edot2
thkdir      extra
      2.0      2.0      0.0      0.01.00000E-5      0.0
0.0      0.0
*DEFINE_CURVE

```

```

$#      lcid      sidr      sfa      sfo      offa      offo
dattyp      lcint
          1          0          1.0          1.0          0.0          0.0
0          0
$#              a1              o1
              0.0              0.0
              280.0              0.014
              380.0              0.014
*SET_NODE_LIST
$#      sid      da1      da2      da3      da4      solver
          3      0.0      0.0      0.0      0.0MECH
$#      nid1      nid2      nid3      nid4      nid5      nid6
nid7      nid8
      180413          0          0          0          0          0
0          0
*SET_NODE_LIST_TITLE
NODESET(CNRB)
$#      sid      da1      da2      da3      da4      solver
          4      0.0      0.0      0.0      0.0MECH
$#      nid1      nid2      nid3      nid4      nid5      nid6
nid7      nid8
*CONSTRAINED_NODAL_RIGID_BODY
$#      pid      cid      nsid      pnode      iprt      drflag
rrflag
      109          0          4          0          0          0
0
*ELEMENT_SOLID
$#      eid      pid      n1      n2      n3      n4      n5      n6
n7      n8
*END

```

Undercut anchor under tensile load

```

$# LS-DYNA Keyword file
$# Created on Feb-16-2018 (11:30:16)
*KEYWORD MEMORY=900000000 NCPU=4
*TITLE
$#
title
LS-DYNA keyword deck by LS-PrePost
*CONTROL_ENERGY
$#      hgen      rwen      slnten      rylene
          2          2          1          1
*CONTROL_TERMINATION
$#      endtim      endcyc      dtmin      endeng      endmas      nosol
          549.0          0          0.0          0.01.000000E8          0
*CONTROL_TIMESTEP
$#      dtinit      tssfacc      isdo      tslimit      dt2ms      lctm
erode      mslst
          0.0          0.9          0          0.0          0.0          0
0          0

```

```

$# dt2msf dt2mslc imsc1 unused unused rmsc1
    0.0      0      0      unused      unused      0.0
*DATABASE_SECFORC
$# dt binary lcur iopt
    0.05     0      0      1
*DATABASE_BINARY_D3PLOT
$# dt lcdt beam npltc psetid
    0.5      0      0      0      0
$# iopt
    0
*DATABASE_CROSS_SECTION_PLANE_ID
$# csid
title
    12
$# psid xct yct zct xch ych
zch radius
    0      0.0  4.0  0.0  0.0  4.0
24.9375  0.0
$# xhev yhev zhev len1 lenm id
itype
    0.0    0.0  0.0  0.0  0.0  0
0
*BOUNDARY_PRESCRIBED_MOTION_SET
$# nsid dof vad lcid sf vid
death birth
    2      3      0      1      1.0
01.00000E28 0.0
*BOUNDARY_SPC_SET
$# nsid cid dofx dofy dofz dofrx
dofry dofrz
    5      0      1      1      1      1
1      1
*SET_NODE_LIST_TITLE
NODESET(SPC) 5
$# sid da1 da2 da3 da4 solver
    5      0.0  0.0  0.0  0.0MECH
$# nid1 nid2 nid3 nid4 nid5 nid6
nid7 nid8
*BOUNDARY_SPC_SET
$# nsid cid dofx dofy dofz dofrx
dofry dofrz
    6      0      1      0      0      0
1      1
*SET_NODE_LIST_TITLE
NODESET(SPC) 6
$# sid da1 da2 da3 da4 solver
    6      0.0  0.0  0.0  0.0MECH
$# nid1 nid2 nid3 nid4 nid5 nid6
nid7 nid8
*BOUNDARY_SPC_SET
$# nsid cid dofx dofy dofz dofrx
dofry dofrz
    7      0      0      1      0      1
0      1

```

```

*SET_NODE_LIST_TITLE
NODESET(SPC) 7
$#      sid      da1      da2      da3      da4      solver
        7        0.0      0.0      0.0      0.0MECH
$#      nid1      nid2      nid3      nid4      nid5      nid6
nid7      nid8
*CONTACT_AUTOMATIC_SURFACE_TO_SURFACE_ID
$#      cid
title
        0ansleco
$#      ssid      msid      sstyp      mstyp      sboxid      mboxid
spr      mpr
        1        43        2        3        0        0
0        0
$#      fs      fd      dc      vc      vdc      penchk
bt      dt
        0.0      0.0      0.0      0.0      0.0      0
0.01.00000E20
$#      sfs      sfm      sst      mst      sfst      sfmt
fsf      vsf
        1.0      1.0      0.0      0.0      1.0      1.0
1.0      1.0
$#      soft      sofsc1      lcidab      maxpar      sbopt      depth
bsort      frcfrq
        1        0.1      0      1.025      2.0      2
0        1
$#      penmax      thkopt      shlthk      snlog      isym      i2d3d
sldthk      sldstf
        0.0      0      0      0      1      0
0.0      0.0
*SET_PART_LIST_TITLE
ans1
$#      sid      da1      da2      da3      da4      solver
        1        0.0      0.0      0.0      0.0MECH
$#      pid1      pid2      pid3      pid4      pid5      pid6
pid7      pid8
        4        40      0      0      0      0
0        0
*CONTACT_AUTOMATIC_SURFACE_TO_SURFACE_ID
$#      cid
title
        3an sle
$#      ssid      msid      sstyp      mstyp      sboxid      mboxid
spr      mpr
        4        40      3      3      0      0
0        0
$#      fs      fd      dc      vc      vdc      penchk
bt      dt
        0.0      0.0      0.0      0.0      0.0      0
0.01.00000E20
$#      sfs      sfm      sst      mst      sfst      sfmt
fsf      vsf
        1.0      1.0      0.0      0.0      1.0      1.0
1.0      1.0

```

```

$#      soft      sofsc1      lcidab      maxpar      sbopt      depth
bsort      frcfrq
          1          0.1          0          1.025          2.0          2
0          1
$#      penmax      thkopt      shlthk      snlog      isym      i2d3d
sldthk      sldstf
          0.0          0          0          0          1          0
0.0          0.0
*PART
$#
title
sleeve
$#      pid      secid      mid      eosid      hgid      grav
adpopt      tmid
          4          1          1          0          0          0
0          0
*SECTION_SOLID_TITLE
an
$#      secid      elform      aet
          1          1          0
*MAT_PIECEWISE_LINEAR_PLASTICITY_TITLE
an
$#      mid      ro      e      pr      sigy      etan
fail      tdel
          1          7.85 200000.0      0.3      640.0      1170.0
0.14      0.0
$#      c      p      lcss      lcsr      vp
          40.0      5.0      0      0      0.0
$#      eps1      eps2      eps3      eps4      eps5      eps6
eps7      eps8
          0.0      0.0      0.0      0.0      0.0      0.0
0.0      0.0
$#      es1      es2      es3      es4      es5      es6
es7      es8
          0.0      0.0      0.0      0.0      0.0      0.0
0.0      0.0
*PART
$#
title
an
$#      pid      secid      mid      eosid      hgid      grav
adpopt      tmid
          40          1          1          0          0          0
0          0
*PART
$#
title
con
$#      pid      secid      mid      eosid      hgid      grav
adpopt      tmid
          43          2          2          0          0          0
0          0
*SECTION_SOLID_TITLE
co

```

```

$#   secid   elform   aet
      2      10      0
*MAT_CSCM_CONCRETE_TITLE
co
$#   mid      ro   nplot   incre   irate   erode
recov   itretrc
      2      2.4      1      0.0      1      1.05
0.0      0
$#   pred
      0.0
$#   fpc      dagg   units
      30.0     19.0      1
*DEFINE_CURVE
$#   lcid      sidr   sfa     sfo     offa     offo
dattyp   lcint
      1      0      1.0     1.0     0.0     0.0
0      0
$#
      a1      o1
      0.0      0.0
      500.0     0.01
      550.0     0.01
*SET_NODE_LIST_TITLE
top
$#   sid      da1     da2     da3     da4     solver
      2      0.0     0.0     0.0     0.0MECH
$#   nid1     nid2     nid3     nid4     nid5     nid6
nid7     nid8
*ELEMENT_SOLID
$#   eid     pid     n1     n2     n3     n4     n5     n6
n7     n8
*END

```

Undercut anchor under shear load

```

$# LS-DYNA Keyword file
$# Created on Feb-25-2018 (20:28:00)
*KEYWORD MEMORY=900000000
*TITLE
$#
title
LS-DYNA keyword deck by LS-PrePost
*CONTROL_ENERGY
$#   hgen     rwen     slnten     rylen
      2      2      1      1
*CONTROL_TERMINATION
$#   endtim     endcyc     dtmin     endeng     endmas     nosol
      398.0     0      0.0     0.01.000000E8     0
*CONTROL_TIMESTEP
$#   dtinit     tssfacc     isdo     tslimt     dt2ms     lctm
erode     mslst

```

```

0          0.0          0.9          0          0.0          0.0          0
0          0
$# dt2msf dt2mslc imsc1 unused unused rmscl
0.0          0          0          0.0
*DATABASE_SECFORC
$# dt binary lcur iopt
0.05          0          0          1
*DATABASE_BINARY_D3PLOT
$# dt lcdt beam npltc psetid
0.5          0          0          0          0
$# iopt
0
*DATABASE_CROSS_SECTION_PLANE_ID
$# csid
title
1
$# psid xct yct zct xch ych
zch radius
0          0.0-3.942E-16 -43.5094          0.0          21.7547 -
43.5094          0.0
$# xhev yhev zhev len1 lenm id
itype
0.0          0.0          0.0          0.0          0.0          0
0
*SET_PART_LIST_TITLE
ansle
$# sid da1 da2 da3 da4 solver
1          0.0          0.0          0.0          0.0MECH
$# pid1 pid2 pid3 pid4 pid5 pid6
pid7 pid8
128          129          0          0          0          0
0          0
*BOUNDARY_PRESCRIBED_MOTION_SET
$# nsid dof vad lcid sf vid
death birth
3          2          0          1          1.0
01.00000E28          0.0
*BOUNDARY_SPC_SET
$# nsid cid dofx dofy dofz dofrx
dofry dofrz
5          0          1          1          1          1
1          1
*SET_NODE_LIST_TITLE
NODESET(SPC) 5
$# sid da1 da2 da3 da4 solver
5          0.0          0.0          0.0          0.0MECH
$# nid1 nid2 nid3 nid4 nid5 nid6
nid7 nid8
*BOUNDARY_SPC_SET
$# nsid cid dofx dofy dofz dofrx
dofry dofrz
6          0          1          0          0          0
1          1
*SET_NODE_LIST

```

```

$#      sid      da1      da2      da3      da4      solver
      6      0.0      0.0      0.0      0.0MECH
$#      nid1      nid2      nid3      nid4      nid5      nid6
nid7      nid8
*CONTACT_AUTOMATIC_SURFACE_TO_SURFACE_ID
$#      cid
title
      0ansleco
$#      ssid      msid      sstyp      mstyp      sboxid      mboxid
spr      mpr
      1      142      2      3      0      0
0      0
$#      fs      fd      dc      vc      vdc      penchk
bt      dt
      0.0      0.0      0.0      0.0      0.0      0
0.01.00000E20
$#      sfs      sfm      sst      mst      sfst      sfmt
fsf      vsf
      1.0      1.0      0.0      0.0      1.0      1.0
1.0      1.0
$#      soft      sofsc1      lcidab      maxpar      sbopt      depth
bsort      frcfrq
      1      0.1      0      1.025      2.0      2
0      1
$#      penmax      thkopt      shlthk      snlog      isym      i2d3d
sldthk      sldstf
      0.0      0      0      0      1      0
0.0      0.0
*CONTACT_AUTOMATIC_SURFACE_TO_SURFACE_ID
$#      cid
title
      2plco
$#      ssid      msid      sstyp      mstyp      sboxid      mboxid
spr      mpr
      139      142      3      3      0      0
0      0
$#      fs      fd      dc      vc      vdc      penchk
bt      dt
      0.0      0.0      0.0      0.0      0.0      0
0.01.00000E20
$#      sfs      sfm      sst      mst      sfst      sfmt
fsf      vsf
      1.0      1.0      0.0      0.0      1.0      1.0
1.0      1.0
$#      soft      sofsc1      lcidab      maxpar      sbopt      depth
bsort      frcfrq
      1      0.1      0      1.025      2.0      2
0      1
$#      penmax      thkopt      shlthk      snlog      isym      i2d3d
sldthk      sldstf
      0.0      0      0      0      1      0
0.0      0.0
*CONTACT_AUTOMATIC_SURFACE_TO_SURFACE_ID

```

```

$#      cid
title
      4waspl
$#      ssid      msid      sstyp      mstyp      sboxid      mboxid
spr      mpr
      131      139      3      3      0      0
0      0
$#      fs      fd      dc      vc      vdc      penchk
bt      dt
      0.0      0.0      0.0      0.0      0.0      0
0.01.00000E20
$#      sfs      sfm      sst      mst      sfst      sfmt
fsf      vsf
      1.0      1.0      0.0      0.0      1.0      1.0
1.0      1.0
$#      soft      sofsc1      lcidab      maxpar      sbopt      depth
bsort      frcfrq
      1      0.1      0      1.025      2.0      2
0      1
$#      penmax      thkopt      shlthk      snlog      isym      i2d3d
sldthk      sldstf
      0.0      0      0      0      1      0
0.0      0.0
*CONTACT_AUTOMATIC_SURFACE_TO_SURFACE_ID
$#      cid
title
      5wasanslee
$#      ssid      msid      sstyp      mstyp      sboxid      mboxid
spr      mpr
      131      1      3      2      0      0
0      0
$#      fs      fd      dc      vc      vdc      penchk
bt      dt
      0.0      0.0      0.0      0.0      0.0      0
0.01.00000E20
$#      sfs      sfm      sst      mst      sfst      sfmt
fsf      vsf
      1.0      1.0      0.0      0.0      1.0      1.0
1.0      1.0
$#      soft      sofsc1      lcidab      maxpar      sbopt      depth
bsort      frcfrq
      1      0.1      0      1.025      2.0      2
0      1
$#      penmax      thkopt      shlthk      snlog      isym      i2d3d
sldthk      sldstf
      0.0      0      0      0      1      0
0.0      0.0
*CONTACT_AUTOMATIC_SURFACE_TO_SURFACE_ID
$#      cid
title
      6wasnut
$#      ssid      msid      sstyp      mstyp      sboxid      mboxid
spr      mpr

```

```

131      135      3      3      0      0
0      0
$#      fs      fd      dc      vc      vdc      penchk
bt      dt
0.0      0.0      0.0      0.0      0.0      0.0      0
0.01.00000E20
$#      sfs      sfm      sst      mst      sfst      sfmt
fsf      vsf
1.0      1.0      0.0      0.0      1.0      1.0
1.0      1.0
$#      soft      sofsc1      lcidab      maxpar      sbopt      depth
bsort      frcfrq
1      0.1      0      1.025      2.0      2
0      1
$#      penmax      thkopt      shlthk      snlog      isym      i2d3d
sldthk      sldstf
0.0      0      0      0      1      0
0.0      0.0
*CONTACT_AUTOMATIC_SURFACE_TO_SURFACE_ID
$#      cid
title
7ansleepla
$#      ssid      msid      sstyp      mstyp      sboxid      mboxid
spr      mpr
1      139      2      3      0      0
0      0
$#      fs      fd      dc      vc      vdc      penchk
bt      dt
0.0      0.0      0.0      0.0      0.0      0.0      0
0.01.00000E20
$#      sfs      sfm      sst      mst      sfst      sfmt
fsf      vsf
1.0      1.0      0.0      0.0      1.0      1.0
1.0      1.0
$#      soft      sofsc1      lcidab      maxpar      sbopt      depth
bsort      frcfrq
1      0.1      0      1.025      2.0      2
0      1
$#      penmax      thkopt      shlthk      snlog      isym      i2d3d
sldthk      sldstf
0.0      0      0      0      1      0
0.0      0.0
*CONTACT_AUTOMATIC_SURFACE_TO_SURFACE_ID
$#      cid
title
8Sleean
$#      ssid      msid      sstyp      mstyp      sboxid      mboxid
spr      mpr
129      128      3      3      0      0
0      0
$#      fs      fd      dc      vc      vdc      penchk
bt      dt
0.0      0.0      0.0      0.0      0.0      0.0      0
0.01.00000E20

```

```

$#      sfs      sfm      sst      mst      sfst      sfmt
fsf      vsf
      1.0      1.0      0.0      0.0      1.0      1.0
1.0      1.0
$#      soft      sofsc1      lcidab      maxpar      sbopt      depth
bsort      frcfrq
      1      0.1      0      1.025      2.0      2
0      1
$#      penmax      thkopt      shlthk      snlog      isym      i2d3d
sldthk      sldstf
      0.0      0      0      0      1      0
0.0      0.0
*PART
$#
title
an
$#      pid      secid      mid      eosid      hgid      grav
adpopt      tmid
      128      1      1      0      0      0
0      0
*SECTION_SOLID_TITLE
an
$#      secid      elform      aet
      1      1      0
*MAT_PIECEWISE_LINEAR_PLASTICITY_TITLE
an
$#      mid      ro      e      pr      sigy      etan
fail      tdel
      1      7.85 200000.0      0.3      640.0      1170.0
0.14      0.0
$#      c      p      lcss      lcsr      vp
      40.0      5.0      0      0      0.0
$#      eps1      eps2      eps3      eps4      eps5      eps6
eps7      eps8
      0.0      0.0      0.0      0.0      0.0      0.0
0.0      0.0
$#      es1      es2      es3      es4      es5      es6
es7      es8
      0.0      0.0      0.0      0.0      0.0      0.0
0.0      0.0
*PART
$#
title
sleeve
$#      pid      secid      mid      eosid      hgid      grav
adpopt      tmid
      129      1      1      0      0      0
0      0
*PART
$#
title
washer
$#      pid      secid      mid      eosid      hgid      grav
adpopt      tmid

```

```

0      131      1      1      0      0      0
0      0
*PART
$#
title
nut
$#      pid      secid      mid      eosid      hgid      grav
adpopt      tmid
0      135      1      1      0      0      0
0      0
*PART
$#
title
plate
$#      pid      secid      mid      eosid      hgid      grav
adpopt      tmid
0      139      1      1      0      0      0
0      0
*PART
$#
title
co
$#      pid      secid      mid      eosid      hgid      grav
adpopt      tmid
0      142      2      2      0      0      0
0      0
*SECTION_SOLID_TITLE
co
$#      secid      elform      aet
0      2      10      0
*MAT_CSCM_CONCRETE_TITLE
co
$#      mid      ro      nplot      incre      irate      erode
recov      itretrc
0.0      2      2.4      1      0.0      1      1.05
0.0      0
$#      pred
0.0
$#      fpc      dagg      units
30.0      19.0      1
*DEFINE_CURVE
$#      lcid      sidr      sfa      sfo      offa      offo
dattyp      lcint
0      1      0      1.0      1.0      0.0      0.0
0      0
$#      a1      o1
0.0      0.0
300.0      0.014
400.0      0.014
*SET_NODE_LIST
$#      sid      da1      da2      da3      da4      solver
3      0.0      0.0      0.0      0.0MECH
$#      nid1      nid2      nid3      nid4      nid5      nid6
nid7      nid8

```

```

    523359      0      0      0      0      0
0      0
*SET_NODE_LIST_TITLE
NODESET(CNRB)
$#   sid      da1      da2      da3      da4      solver
      4      0.0      0.0      0.0      0.0MECH
$#   nid1     nid2     nid3     nid4     nid5     nid6
nid7     nid8
*SET_PART_LIST_TITLE
con
$#   sid      da1      da2      da3      da4      solver
      2      0.0      0.0      0.0      0.0MECH
$#   pid1     pid2     pid3     pid4     pid5     pid6
pid7     pid8
      142      0      0      0      0      0
0      0
*CONSTRAINED_NODAL_RIGID_BODY
$#   pid      cid      nsid     pnode     iprt     drflag
rrflag
      140      0      4      0      0      0
0
*ELEMENT_SOLID
$#   eid      pid      n1      n2      n3      n4      n5      n6
n7      n8
*END

```